Physics and Applications of Scintillation Detectors

Francis Dey Brooks

Papers submitted in support of
candidacy for the DSc degree of
Rhodes University.

Cape Town,
October 1994.

Acknowledgements

I wish to express my appreciation and gratitude to many people, including some deceased, all of whom played important roles in providing the research opportunities which I have been privileged to experience. I thank particularly:

my parents, both of whom were scientists and teachers, for their inspiration, example, support and encouragement;

my wife, Kathleen, our daughter, Louise, and our sons, William, Peter and James, for their support and encouragement;

my mentors during the years spent at Rhodes University, especially John Birks, Jack Gledhill and Gordon Wright;

my colleagues during the years spent at A.E.R.E. Harwell and at the University of Cape Town, especially Dr Ernest Rae, and Professor Walter Schaffer; and

the collaborators and research students with whom I have worked, including all co-authors of the papers presented in this volume.

ABSTRACT

The papers submitted in this volume present contributions and reviews on the physics of the scintillation process together with contributions to the development of scintillation detection techniques and the use of these techniques in nuclear physics research and in the applications of nuclear methods to other fields.

Table of contents

1. Introduction

Photomultiplier scintillation detectors were still a novelty in 1950, when Professor J.B. Birks was appointed to the Chair of Physics at Rhodes University. John Birks was one of the leading pioneers then developing this new technique and he promptly formed a research group in the Rhodes Physics Department, specialising in the physics of the scintillation mechanism in organic scintillators. I became an MSc student in this group in 1953 and was assigned a research problem posed by the "Birks theory" of the organic scintillation process. The project involved studying the pulse height response of the organic crystal anthracene to low-energy x-rays. John Birks returned to England in 1954, but his brief stay at Rhodes was of great significance to myself and several others. My MSc thesis was completed under the guidance of his successor, Professor J.A. Gledhill, and of Dr. G.T. Wright, who was also well known for his work on scintillation mechanisms and had been attracted to Rhodes by Birks in 1953.

From Rhodes I moved to the Nuclear Physics Division of the Atomic Energy Research Establishment (AERE) Harwell, England, in 1955, to take up a Commonwealth Junior Research Fellowship. This appointment left me free to continue research into the physics of scintillation mechanisms but also encouraged me to become involved in the AERE research programme in neutron physics related to nuclear energy. The research interests developed during my years at Rhodes and AERE continued and were extended to other areas of nuclear physics when I moved back to South Africa in 1964, to take up my present position at the University of Cape Town. In pursuing this research I have been greatly assisted by the close association of UCT with the staff and facilities of the South African National Accelerator Centre and its predecessor, the Southern Universities Nuclear Institute, at Faure, near Cape Town.

The papers presented here are selected from research which was published during the years alluded to above, 1954-1994. They deal with topics in three broad fields: the physics of scintillation mechanisms; the techniques of scintillation detection; and research in pure and applied nuclear physics using scintillation techniques. The scintillator is the common factor in all of this work and it links the activities in these different research fields. The scintillation pulse shape discrimination technique, for example, emerged directly from work aimed at investigating the physics of the scintillation process. This technique, in turn, has enabled new approaches to problems in nuclear physics and has enhanced the application of nuclear technology to other fields of science, engineering and medicine.

To simplify presentation, the research papers introduced in sections 2-5 below, are grouped under the following headings:

(a) the physics and characteristics of scintillators;

(b) scintillators in radiation detection;

(c) nuclear physics using scintillation detectors; and

(d) scintillation methods in nuclear applications technology, for example in medicine and industry.

The authors, titles and references of the papers are listed in chronological order of publication in section 6. Papers other than those of which I am the sole author are marked either *s* or *j*, to indicate my part as either a *senior* co-author or a *junior* co-author respectively. The designation as senior co-author implies that I made a leading contribution to the initiation and execution of the research and to the preparation of the paper.

Reprints of the papers are collected in section 7. In sections 2-5 the papers are referred to by the numbers allocated to them in section 6. Some of the papers are referred to in more than one of the sections 2-5.

2. Physics and characteristics of scintillators

Eight papers [1-3,5,6,15,22,27], including two review articles [3,22], deal with characteristics of the organic scintillators and the physics of the scintillation mechanism in these systems.

2.1 Review papers

The review articles, published in 1956 [3] and 1979 [22], were prepared in response to invitations from Professor O.R. Frisch (Cambridge), editor of "Progress in Nuclear Physics", and Professor D. Allan Bromley (Yale), guest editor of a special issue of Nuclear Instruments and Methods entitled "Detectors in Nuclear Science", respectively.

2.2 Work carried out at Rhodes University

Papers [1] and [2] describe work carried out at Rhodes University under the supervision of Professor J.B. Birks. The pulse height response characteristics of anthracene crystals to 6-30 keV x-rays were investigated and compared with predictions based on the Birks theory (refs. Phys. Rev. 84 (1951) 364 and Proc. Phys. Soc. (London) A64 (1951) 874).

2.3 Scintillation pulse shapes

Paper [5] includes a discussion of the physics underlying the technique, later to become known as pulse shape discrimination (PSD), which identifies different types of detected particle, e.g. neutron or gamma quantum, by means of characteristics of the scintillation decay, or pulse shape. The dependence of pulse shape on the type of particle causing the scintillation was originally discovered at Rhodes by Dr. G.T. Wright (ref. Proc. Phys. Soc. (London) B49 (1956) 358). Papers [3-6,15,22] include work which followed up Wright's discovery, aiming to understand and to exploit the mechanisms responsible for the pulse shape differences exhibited by organic scintillators when

excited by different types of ionizing particle.

2.4 Anisotropy of crystal scintillator characteristics

Paper [15] describes studies aimed at mapping and understanding the direction-dependence of the response and pulse-shape characteristics of organic crystal scintillators to heavily ionizing particles, such as protons and alpha-particles.

2.5 Thin film plastic scintillators

Paper [27] presents an investigation and discussion of the response of thin-film plastic scintillators to fission fragments.

3. Scintillation detectors

3.1 Review articles

The review papers [3,22] cited in section 2.1 also covered new developments in the applications of scintillators in radiation detection. This topic was also reviewed in two other invited papers presented at international conferences: paper [7], presented at the Conference on Neutron Time-of-Flight Methods, Paris, 1961; and paper [38], presented at the Conference on Nuclear Techniques for Analytical and Industrial Applications, Mykonos, Greece, 1993.

3.2 The pulse shape discrimination technique

Papers [3-7] describe contributions to the development of the technique of pulse shape discrimination (see section 2.3). The first report of the successful application of scintillation pulse shape differences as a means for discriminating between different types of particle is that made on page 284 of paper [3]. Paper [4] was the first presentation on PSD at an international conference (held at Evanston, Illinois, in August 1957) and paper [5] presents a description of the first PSD system, together with a comparison of the PSD capabilities of a range of organic scintillators, crystal, liquid and plastic. Paper [7] describes developments which followed soon after, concerning the PSD performance of plastic scintillators.

3.3 Further developments in pulse shape discrimination

Papers [14-18,20,26,28,30,31,39,42] describe subsequent developments in which the PSD technique was used:

(i) to sense the directions of recoil protons (deuterons) in anthracene (deuterated anthracene) crystals, in order to determine left-right asymmetries in neutron polarization experiments [14-17,20,31];

(ii) to distinguish between protons and recoil deuterons released in neutron interactions in deuterated liquid scintillators [18];

(iii) in two new types of neutron spectrometer, based on deuterated scintillators [26,30,42];

(iv) in the study of deuteron photodisintegration [28]; and

(v) to identify deuterons resulting from neutron-proton radiative capture in liquid scintillators [39].

3.4 Other scintillation detectors

Papers [27,36,41] describe contributions to the development of thin-film plastic scintillators as detectors of fission fragments [27] and alpha particles [36,41]. Papers [10,13] describe contributions to detection techniques for low-energy neutron scattering measurements, using lithium-loaded glass scintillators and sodium iodide crystals.

4. Nuclear physics using scintillation detectors

"Nuclear physics", as used here, embodies any physics in which interactions with nuclei are significant. Thus neutron cross section measurements motivated by nuclear energy considerations are included, and phenomena such as muon-catalyzed nuclear fusion, as well as work work which would comply with a stricter (more conventional) definition of nuclear physics.

4.1 Neutron cross section measurements

Papers [5,8-13] describe neutron cross section measurements, including scattering, capture and fission, at low neutron energies (< 120 keV). Paper [11] is an invited paper which was presented at a national topical meeting of the American Nuclear Society, held in San Diego, USA, in February 1966.

4.2 Few-nucleon systems

Papers [14,17,18,20,25,28,31,39] describe studies of 2-nucleon and 3-nucleon systems at energies between 2 and 64 MeV. Papers [14,17,20,31] describe measurements of the analysing power in n-p and n-d elastic scattering, using the new technique (see section 3.3) based on the direction sensing capabilities of anthracene and deuterated anthracene scintillation crystals. Paper [18] describes a study of deuteron breakup induced by 8-22 MeV neutrons, using the PSD properties of deuterated liquid scintillators to distinguish between protons from the breakup reaction and recoil deuterons from neutron elastic scattering. Paper [25] describes a search for neutron-proton bremsstrahlung using a novel technique in which the proton target was an organic crystal scintillator. Paper [28] presents an investigation of deuteron photodisintegration carried out using

a deuterated anthracene scintillator as the target for the nuclear reaction. Paper [39] describes a study of the inverse process, neutron-proton radiative capture, for which a liquid scintillator served as the proton target.

4.3 Neutrons from fission and (d,n) reactions

Paper [19] describes an investigation of neutrons from the spontaneous fission of ^{252}Cf, which was facilitated by the use of PSD in neutron detection. Paper [26] describes studies of vector analyzing powers in some $(d,\vec{n})$ reactions, using the deuterated anthracene crystal as a neutron spectrometer.

4.4 Muon-catalyzed fusion

Papers [29,32-35,40,41] deal with experimental studies of the alpha-muon sticking coefficient in muon-catalyzed d-t fusion, and include simulations [35,40] of experiments designed to measure this quantity. Experiments that have succeeded in determining the initial sticking coefficient directly have shown [32-34] that neutron detectors having good PSD characteristics are essential to the success of these measurements. Papers [36,41] describe developments related to the detection of alpha particles in muon-catalyzed fusion experiments.

5. Scintillation methods in applied nuclear technology

Review paper [38], also cited in section 3.1, was in invited paper, presented at an international conference devoted to analytical and industrial applications of nuclear techniques. It deals specifically with neutron detection in this context, and largely by the scintillation method. Paper [42] is a follow-up on some of the work discussed in [38] and describes an investigation to test the feasibility of elemental analysis by neutron backscattering, using the deuterated anthracene neutron spectrometer [30].

Papers [21,23,37] deal with radiation detection by means of scintillators in medical applications. They describe a new method for estimating high-LET and low-LET radiation doses, simultaneously and independently, in tissue-equivalent media irradiated by neutrons [21,23] and measurements of neutron fluence and kerma spectra from a neutron radiotherapy system, using scintillation detection techniques [37].

Paper [24] describes a high-flux associated particle neutron source, used to calibrate neutron detectors, especially scintillators, used in both applied and basic nuclear physics measurements.

6. List of papers

1. J.B. Birks and F.D. Brooks
j *Scintillation response of anthracene to soft x-rays*
Phys. Rev. 94 (1954) 1800-1801

2. J.B. Birks and F.D. Brooks
j *Scintillation response of anthracene to 6-30 keV photoelectrons*
Proc. Phys. Soc. B69 (1956) 721-730

3. F.D. Brooks
Organic scintillators
Progress in Nuclear Physics 5 (1956) 252-313

4. F.D. Brooks
Scintillation counters with pulse shape selection to distinguish neutrons from gamma-rays
Liquid Scintillation Counting, ed. C.G. Bell and F.N. Hayes (Pergamon, New York, 1958) 268-269

5. F.D. Brooks
A scintillation counter with neutron and gamma-ray discriminators
Nucl. Instr. and Meth. 4 (1959) 151-163

6. F.D. Brooks, R.W. Pringle and B.L. Funt
s *Pulse shape discrimination in a plastic scintillator*
I.R.E. Trans. on Nucl. Sci. NS7 (1960) 35-38

7. F.D. Brooks
General survey on choice of the detector for a time-of-flight experiment
Neutron Time-of-Flight Methods, ed. A. Spaepen (EANDC, Brussels, 1961) 389-405

8. F.D. Brooks
A measurement of eta versus energy for ^{235}U
Neutron Time-of-Flight Methods, ed. A. Spaepen (EANDC, Brussels, 1961) 131-137

9. F.D. Brooks and J.R. Bird
s *Partial cross section measurements with the Harwell 28 MeV linear accelerator*
Neutron Physics, ed. M.L. Yeater (Academic Press, New York, 1962) 109-123

10. M. Asghar and F.D. Brooks
s *Neutron resonance scattering measurements with ^{6}Li-glass detectors*
Nucl. Instr. and Meth. 39 (1966) 68-76

11. F.D. Brooks
Measurements of alpha and eta in the intermediate energy range
Reactor Physics in the Resonance and Thermal Regions, ed. A.J. Goodjohn and G.C. Pomraning (M.I.T. Press, 1966) Vol. 2, 193-222

12. L.M. Spitz, E. Barnard and F.D. Brooks
s *Neutron capture cross sections of Cr, Mn, Ni, Nb, Ag, In, Sb and Au in the 8 to 120 keV region*
Nucl. Phys. A121 (1968) 655-672

13. C.A.R. Bain and F.D. Brooks
s *Inelastic scattering of neutrons to the 59 keV level of ^{127}I*
Nucl. Phys. A125 (1969) 312-320

14. F.D. Brooks and D.T.L. Jones
s *Polarization in n-p scattering at 21.6 MeV*
Proc. 3rd Int. Symposium on Polarization Phenomena in Nuclear Reactions, ed. H.H. Barschall and W. Haeberli (Univ. of Wisconsin Press, 1971) 430-432

15. F.D. Brooks and D.T.L. Jones
s *Directional anisotropy in organic scintillation crystals*
Nucl. Instr. and Meth. 121 (1974) 69-76

16. F.D. Brooks and D.T.L. Jones
s *A scintillation polarimeter for n-p scattering studies*
Nucl. Instr. and Meth. 121 (1974) 77-85

17. D.T.L. Jones and F.D. Brooks
s *Polarization in neutron-proton scattering at 16.4 and 21.6 MeV*
Nucl. Phys. A222 (1974) 79-92

18. G. Pauletta and F.D. Brooks
s *Cross sections for the n+d breakup reaction*
Nucl. Phys. A255 (1975) 267-274

19. J.S. Pringle and F.D. Brooks
s *Angular correlation of neutrons from spontaneous fission of ^{252}Cf*
Phys. Rev. Lett. 35 (1975) 1563-1566

20. M. Steinbock, F.D. Brooks and I.J. van Heerden
s *Polarization in n-d scattering at 16.4 and 21.6 MeV*
Proc. 4th Int. Symposium on Polarization Phenomena in Nuclear Reactions, ed. W. Gruebler and V. König (Birkhauser Verlag, Basel, 1976) 475-476

21. F.D. Brooks, S. Wynchank, P.L.M. le Roux, E.R. Hering, D.
j Shackleton, A. Wulff, H.S.T. Driver and M. Steinbock
Research and experimental work at Groote Schuur Hospital and the University of Cape Town using ^{252}Cf sources
Proc. Seminar on the Uses of Californium-252 in Teaching and Research, IAEA-SR-3/16 (IAEA, Vienna, 1976) 173-182

22. F.D. Brooks
Development of organic scintillators
Nucl. Instr. and Meth. 162 (1979) 477-505

23. D.T.L. Jones, F.D. Brooks, S. Wynchank and I.J.
s van Heerden
Differential dose measurements with T(d,n) and ^{252}Cf neutron sources
Proc. 5th Int. Conf. on Medical Physics, ed. E.H. Frei (Belinson Center, Jerusalem, 1979) p 57.1

24. C.M. Bartle, F.D. Brooks, D.T.L. Jones, W.R. McMurray and
j R. Verbruggen
A high flux associated particle neutron source
Nucl. Instr. and Meth. 180 (1981) 165-171

25. J. Whittaker, F.D. Brooks and I.J. van Heerden
s *Neutron-proton bremsstrahlung at 4.8 MeV*
Nucl. Phys. A362 (1981) 173-188

26. F.D. Brooks, P.M. Lister, J.M. Nelson and K.M. Dhuga
s *Vector analysing powers for the $^{12}C(d,\vec{n})^{13}N$, $^{9}Be(d,\vec{n})^{10}B$ and $^{28}Si(d,\vec{n})^{29}P$ reactions*
A.I.P. Conf. Proc. 69 (1981) 656-658

27. F.D. Brooks, W.A. Cilliers and M.S. Allie
s *Response of thin NE102A scintillator films to fission fragments*
Nucl. Instr. and Meth., A240 (1985) 338-342

28. F.D. Smit and F.D. Brooks
s *Angular distribution of neutrons from $^{2}H(\gamma,n)^{1}H$ at E_γ = 2.75 MeV*
Nucl. Phys. A465 (1987) 429-444

29. F.D. Brooks, J.D. Davies, G.J. Pyle, G.T.A. Squier, G.H. Eaton
j *Pulsed muons for μCF experiments at RAL*
Muon Catalyzed Fusion 2 (1988) 85-92

30. F.D. Brooks, W.A. Cilliers, B.R.S. Simpson, F.D. Smit, M.S. Allie, D.T.L. Jones, W.R.McMurray and J.V. Pilcher
s *Deuterated anthracene spectrometer for 5-30 MeV neutrons*
Nucl. Instr. and Meth. A270 (1988) 149-156

31. B.R.S. Simpson and F.D. Brooks
s *Analyzing power in neutron-proton scattering at 21.6 MeV*
Nucl. Phys. A505 (1989) 361-368

32. M.A. Paciotti, O.K. Baker, J.N. Bradbury, J.S. Cohen, M. Leon, H.R. Maltrud, L.L. Sturgess, A.N. Anderson, A.J. Caffrey, J.M. Zabriskie, F.D. Brooks, W.A. Cilliers, J.D. Davies, J.B.A. England, G.J. Pyle, G.T.A. Squier, A. Bertin, M. Bruschi, M. Piccinini, A. Vitale, A. Zoccoli, V.R. Bom, C.W.E. van Eijk, H. de Haan and G.H. Eaton
j *First direct measurement of alpha-muon sticking in d-t muon-catalyzed fusion*
A.I.P. Conf. Proc. 181 (1989) 38-51

33. J.D. Davies, F.D. Brooks, W.A. Cilliers, J.B.A. England, G.J. Pyle, G.T.A. Squier, A. Bertin, M. Bruschi, M. Piccinini, A. Vitale, A. Zoccoli, S.E. Jones, P. Li, L.M. Rees, E.V. Sheeley, J.K Shurtleff, S.F. Taylor, G.H. Eaton, B. Alper, V.R. Bom, C.W.E. van Eijk, H. de Haan, A.N. Anderson, A.J. Caffrey, J. Zabriskie, M.A. Paciotti, O.K. Baker, J.N. Bradbury, J.S. Cohen, M. Leon, H.R. Maltrud and L.N. Sturgess
j *μCF thoughts from Birmingham and the Rutherford Appleton Laboratory*
A.I.P. Conf. Proc. 181 (1989) 52-56

34. J.D. Davies, J.B.A. England, G.J. Pyle, G.T.A. Squier, F.D.Brooks, W.A. Cilliers, A. Bertin, M. Bruschi, M. Piccinini, A. Vitale, A. Zoccoli, S.E. Jones, V.R. Bom, C.W. van Eijk, H. de Haan, A.N. Anderson, M.A. Paciotti, G.H. Eaton and B. Alper
s *A direct measurement of the alpha-muon sticking coefficient in muon-catalysed d-t fusion*
J. Phys. G: Nucl. Part. Phys. 16 (1990) 1529-1537

35. C.G.L. Henderson, F.D. Brooks, W.A. Cilliers, G.J. Pyle and G.T.A. Squier
s *Simulation and emulation of direct measurements of ω_0 in dt μCF*
Muon Catalyzed Fusion 5/6 (1990/91) 405-411

36. W.A. Cilliers and F.D. Brooks
j *Tests of plastic scintillators as alpha detectors in dt μCF*
Muon Catalyzed Fusion 5/6 (1990/91) 413-419

37. D.T.L. Jones, J.E. Symons, T.J. Fulcher, F.D. Brooks,
j M.R. Nchodu, M.S. Allie, A. Buffler and M.J. Oliver
Neutron fluence and kerma spectra of a p(66)/Be(40) clinical source
Medical Physics 19 (1992) 1285-1291

38. F.D.Brooks
Developments in neutron detection
Nuclear Techniques for Analytical and Industrial Applications, ed. G. Vourvopoulos and T. Paradellis (Western Kentucky University Press, 1993) 151-170

39. M.S. Allie, F.D. Brooks, D.G. Aschman, A. Buffler, W.A.
s Cilliers, R.W. Fearick, C.G.L. Henderson, M.J. Oliver, M.R. Nchodu, S.M. Perez, D. Steyn, W.R. McMurray, B.R.S. Simpson, F.D. Smit, H.G. Miller, K. Bharuth-Ram and I.J. van Heerden
Differential cross section for n-p radiative capture at E_n = 63.4 MeV
Physics Letters B314 (1993) 173-178

40. C.G.L. Henderson, F.D. Brooks and W.A. Cilliers
s *Techniques for measuring initial sticking in d-t fusion*
Hyperfine Interactions 82 (1993) 327-335.

41. W.A. Cilliers, F.D. Brooks and J.B.A. England
j *Detection of fusion alphas from D_2-T_2 gas targets*
Hyperfine Interactions 82 (1993) 337-342

42. F.D. Brooks, C.G.L. Henderson, M.S. Allie, A. Buffler,
s M.J. Oliver and M.R. Nchodu
Element analysis by scattered neutron spectrometry
Proceedings of the 5th International Conference on Applications of Nuclear Techniques - Neutrons and their Applications, Crete, June 1994 - in press.

---

s ... senior co-author. *j* ... junior co-author.

---

7. Reprints of papers.

Reprinted from THE PHYSICAL REVIEW, Vol. 94, No. 6, 1800–1801, June 15, 1954
Printed in U. S. A.

Scintillation Response of Anthracene to Soft X-Rays

J. B. BIRKS AND F. D. BROOKS
Physics Department, Rhodes University, Grahamstown, South Africa
(Received April 20, 1954)

BIRKS[1,2] has predicted a difference between the scintillation response of organic phosphors to external electrons and to internal photoelectrons of the same energy. The scintillation response of anthracene to secondary characteristic x-rays of energies between 6 kev and 25 kev has therefore been studied. The scintillations were observed with an E.M.I. type 5060 photomultiplier, and the output pulse amplitude distribution was obtained using a "gray-wedge" pulse-height analyzer, based on the instrument originally developed by Bernstein *et al.*[3] Secondary characteristic x-rays of known energies were obtained by placing a series of scattering foils of different elements in the path of a beam of "white" x-radiation, and were detected at right angles to the primary beam direction by a 2 mm thick crystal of anthracene.

The pulse amplitude distribution photographs, obtained from the analyzer, showed that it was possible to resolve the photoelectron peaks produced by incident x-rays of energy >11 kev, when the photomultiplier was operating at room temperature (20°C). By cooling the photomultiplier to dry ice temperatures, to reduce the dark noise background, adequate resolution was obtained at lower energies from 6 kev to 11 kev.

The mean scintillation pulse height S is plotted as a function of the x-ray energy E in Fig. 1. The experimental data of Taylor *et al.*[4] on the scintillation response of anthracene to electrons of energy E, incident externally on the crystal, have been normalized to the same scale of S, and these are also plotted in Fig. 1 for comparison.

The theoretical response curve for photoelectrons, produced internally by x-rays, has been calculated from the formula[2,5]

$$\left(\frac{dS}{dr}\right)_x = \frac{A\,(dE/dr)}{1+kB\,(dE/dr)},$$

by using experimentally determined values of the constants A and kB, and the range-energy data for electrons, given by Curie.[6] The theoretical response curve for external electrons has been calculated from the formula[1,2] for particles of range r,

$$(dS/dr)_e = \phi\,(dS/dr)_x,$$

where $\phi = 1-\frac{1}{2}[\exp(-r/a_0)-(r/a_0)\,\mathrm{Ei}(r/a_0)]$, $\mathrm{Ei}(r/a_0)$ being the exponential integral. A value of $a_0 = 3$ mm air equivalent has been taken, corresponding to a mean free path for the primary photons[2] of about 3 microns.

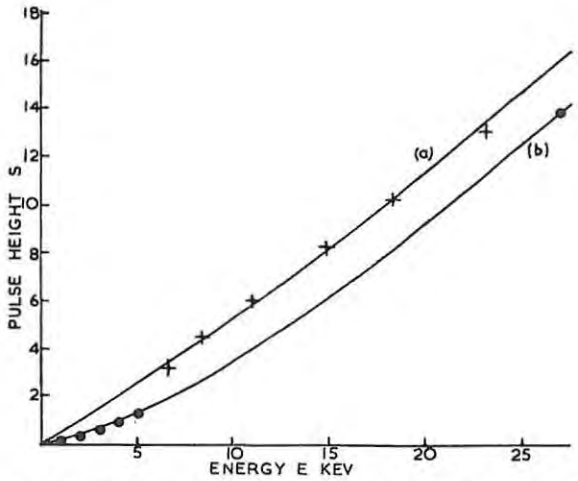

FIG. 1. Scintillation response of anthracene. (a) X-rays. Experimental +; theoretical ——. (b) Electrons. Experimental ●; theoretical ——.

The two theoretical response curves, which are plotted in Fig. 1, are in excellent agreement with the experimental data. These results provide further evidence in favor of the photon cascade theory of the scintillation process, proposed by Birks.[2,7] Further measurements are in progress on the scintillation response of anthracene and other organic phosphors to x-rays and electrons.

We are indebted to the South African Council for Scientific and Industrial Research for a grant, and for a bursary to one of us (F.D.B.).

[1] J. B. Birks, Phys. Rev. **86**, 569 (1952); **90**, 1131 (1953).
[2] J. B. Birks, *Scintillation Counters* (Pergamon Press, London; McGraw-Hill Book Company, Inc., New York, 1953).
[3] Bernstein, Chase, and Schardt, Rev. Sci. Instr. **24**, 437 (1953).
[4] Taylor, Jentschke, Remley, Eby, and Kruger, Phys. Rev. **84**, 1034 (1951).
[5] J. B. Birks, Phys. Rev. **84**, 364 (1951); Proc. Phys. Soc. (London) **A64**, 874 (1951).
[6] M. Curie, *Radioactivité* (Hermann et Cie., Paris, 1935).
[7] J. B. Birks, Phys. Rev. **94**, 1567 (1954).

REPRINTED FROM THE
PROCEEDINGS OF THE PHYSICAL SOCIETY, B, VOL. LXIX, p. 721, 1956

Scintillation Response of Anthracene to 6–30 keV Photoelectrons

BY J. B. BIRKS† AND F. D. BROOKS‡
Physics Department, Rhodes University, Grahamstown, S. Africa

MS. received 3rd August 1955, and in final form 16th February 1956

Abstract. Observations have been made of the scintillation response S of a 0·2 cm thick anthracene crystal to photoelectrons of energy $E=6$ to 30 kev produced by various characteristic K x-rays. The responses to ^{114}In and ^{137}Cs internal conversion electrons were also measured, and the results reduced to a standard scale of S, and compared with other data.

The (S, E) curve agrees closely with that predicted theoretically. The response curve at $-65°$C is identical with that at 16°C, apart from a general increase of 50% in S.

The response to internal electrons is significantly greater than that to external electrons of the same low energy. Reasons are suggested for the divergent results reported by Robinson and Jentschke. The reduced response to external electrons is attributed to the escape and/or quenching of the fluorescence excitation energy at the crystal surface. These and other surface phenomena affecting the response of organic scintillators to short-range external particles are discussed.

§ 1. INTRODUCTION

WHEN ionizing radiations impinge on anthracene or other fluorescent organic crystals, part of their incident energy is converted into light, which is emitted as normal fluorescence from the crystal. The scintillation response S depends on the nature and energy E of the incident ionizing particle, of range r within the crystal. Birks (1951) has shown that the specific fluorescence dS/dr may be expressed as a function of the specific energy loss dE/dr, and appears to be independent of the nature of the particle. The theoretical relation

$$\frac{dS}{dr} = \frac{A\,dE/dr}{1+kB\,dE/dr} \qquad \ldots\ldots(1)$$

has been obtained by considering the competitive processes of fluorescence emission and of primary quenching by molecules damaged or ionized by the incident particle.

An alternative expression has been derived by Wright (1953), who attributes the primary quenching to the combined effect of unimolecular and bimolecular processes in the primary excitation column. This leads to a relation

$$dS/dr = C\ln(1+D\,dE/dr) \qquad \ldots\ldots(2)$$

which approximates to (1), except at high dE/dr. Other relationships between dS/dr and dE/dr have been proposed by Chou (1952) and Black (1953).

† Now at British Dielectric Research Ltd., London, W.12.
‡ Now at the Atomic Energy Research Establishment, Harwell, Berks.

These expressions account satisfactorily for the scintillation response of organic crystals (and also solutions) to all types and energies of incident ionizing particles, except those of short range. For α-particles of r less than 8 mm air equivalent, the value dS/dr is, however, less than that given by (1) or (2) (Birks 1950, King and Birks 1952). A similar effect is observed with short-range electrons and protons (Taylor *et al.* 1951). Since both effects are associated with short-range particles it is suggested that they are due to surface phenomena, probably either surface escape of excitons or radiations (Birks 1952, 1953) or quenching of fluorescence excitation energy by a non-fluorescent impurity in the surface layer (King 1952). A theory of surface escape has been formulated by Birks (1952, 1953). It involves multiplying the right-hand side of (1) or (2) by a 'surface escape function'

$$\phi = 1 - \tfrac{1}{2}[\exp(-r/a_0) - (r/a_0)\mathrm{Ei}(r/a_0)] \qquad \ldots\ldots(3)$$

where $\mathrm{Ei}(r/a_0)$ is the exponential integral, and a_0 the mean free path of the escaping photons. ϕ increases from 0·5 at $r=0$, to approximately 1·0 for $r > 2a_0$. Recent observations by Wright (1955) indicate that quenching impurities are formed on the surface of anthracene crystals exposed to the atmosphere, thus causing surface quenching.

If surface effects are operative, the scintillation response of anthracene to photoelectrons produced *within* the crystal by x-rays should differ from that excited by external electrons of the same energy, since in the former case surface effects are eliminated (Birks 1952). A detailed study has therefore been made of the scintillation response of anthracene to photoelectrons of 6–30 kev energy for comparison with the external electron data of Taylor *et al.* (1951). A brief account of the preliminary results, which showed the predicted difference in response, has been published previously (Birks and Brooks 1954). Robinson and Jentschke (1954) have subsequently reported the results of a similar investigation, but showing no difference in the response to internal and external electrons. The present paper gives a fuller account of our original and later studies. These substantiate the differences in response originally reported. Similar results have recently been obtained by Fowler and Roos (1955).

§ 2. Experimental Method

2.1. *Apparatus*

A schematic diagram of the apparatus is shown in figure 1. The purpose of the experiment was to measure the scintillation response of the anthracene crystal D (0·2 cm × 0·5 cm × 0·5 cm) to photoelectrons released within it by

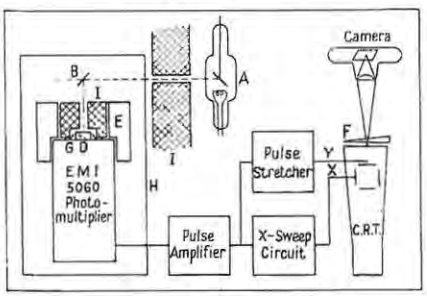

Figure 1. Schematic diagram of apparatus.
A, x-ray tube ; B, scattering foil ; D, anthracene crystal ; E, cooling jacket ; F, wedge filter ; G, aluminium reflector ; H, light-proof box ; I, lead shielding.

secondary characteristic fluorescence K x-rays of different elements. Foils of these elements were placed at B, directly above the crystal and in the path of a collimated beam of 'white' x-radiation, AB. Pure metal foils (4 $cm^2 \times 0{\cdot}01$ cm thick) of Fe, Cu, Mo, Ag and Sn were used. Powdered layers of As, I and SrO, mounted in flat black paper packets, served as 'foils' of their respective elements. With these elements an x-ray energy range of 6 kev to 32 kev was obtained. A mechanical arrangement was used, enabling the foils to be changed or radioactive sources to be substituted, without exposing the photomultiplier to external light. During the investigation, various x-ray tubes were used as sources of 'white' radiation, and the results were found to be independent of the tube used.

Other low-energy x-ray sources were also employed, as follows: (*a*) In K x-rays emitted following internal conversion in ^{114}In. Internal conversion electrons from the source were eliminated by a Perspex absorber. (*b*) Mn K x-rays emitted following K-capture in ^{55}Fe.

The scintillations were observed with an E.M.I. type 5060 photomultiplier, selected for its low dark noise and high sensitivity. The crystal D and the photocathode could be cooled by refrigerants placed in the cooling jacket E. By this means the dark noise could be virtually eliminated, and the temperature dependence of S could be studied.

Voltage pulses from the photomultiplier were fed to an A.E.R.E. Model 1049 A linear pulse amplifier. The pulse amplitude distribution was measured with a multi-channel photographic wedge pulse analyser (Maeder 1947), based on the design of Bernstein *et al.* (1953). This type of pulse analyser is particularly suitable for studying pulse sequences initiated by sources of fluctuating intensity. Provided the counting rate is not excessive, practically every pulse is counted. The only limitations on the amplitude resolution are the width of the cathode-ray tube trace and the circuit stability during the relatively short period of measurement. As described below, the characteristic response of the photographic film can be used to obtain a sharply defined pulse amplitude distribution.

2.2. *X-ray Absorption in Anthracene*

Internal photoelectrons of known energy are efficiently produced in anthracene by x-rays of energies below 20 kev since the cross section of the photoelectric absorption process in carbon (see Heitler 1949 for data) is relatively high. At x-ray energies greater than about 22 kev however, Compton scattering becomes the main absorption process, and the photoelectric absorption declines rapidly. This places an upper limit on the photoelectron energy which can be resolved against the 'Compton background', and against the background due to scattered 'white' x-rays which, though continuous and of low intensity, are efficiently absorbed at low energies. The measurements indicated 30 kev as the upper energy limit at which a photoelectric peak could be clearly resolved with the arrangement used.

2.3. *Photoelectron Energy*

The K_α and K_β components in the characteristic fluorescence were not resolved. A weighted mean photoelectron energy for each foil used was calculated from the following data: (*a*) the K_α and K_β x-ray energies (Hodgman 1954), (*b*) the $K_\alpha : K_\beta$ intensity ratio, which varies from 5 : 1 to 3 : 1 for the elements used (Compton and Allison 1946), (*c*) the photoelectric absorption coefficient. The values obtained are listed in the table.

Atomic number	25	26	29	33	38	42	47	49	50	53
Element	Mn	Fe	Cu	As	Sr	Mo	Ag	In	Sn	I
K_α energy (kev)	5·9	6·4	8·1	10·5	14·2	17·5	22·2	24·2	25·2	28·6
K_β energy (kev)	6·3	7·1	9·0	11·8	16·0	19·9	25·3	27·7	28·9	32·8
Weighted mean photo-electron energy (kev)	5·9	6·5	8·2	10·7	14·5	17·9	22·7	24·8	25·8	29·4

2.4. *Calibration and Test*

The scintillation response of the anthracene crystal to external electrons of known high energy was also measured. This enabled the photoelectron measurements to be normalized to the same scale of S as that used by other observers. Internal conversion electrons from ^{114}In (186 and 162 kev) and ^{137}Cs (624 kev) were used for this purpose. The two electron groups from ^{114}In were not clearly resolved, but the mean pulse amplitude was observed. The ratio of the observed response to ^{114}In and ^{137}Cs electrons was in agreement with the measurements of Taylor *et al.* (1951), Hopkins (1950, 1951) and other observers.

The comparative measurement of S over the interval from 6 kev to 624 kev electron energy involved accurate calibration of the pulse amplifier gain and the photomultiplier gain over a range of more than 100:1. This calibration was performed using standard scintillation sources (i.e. mono-energetic α-particles, or ^{137}Cs internal conversion electrons, on anthracene) and comparing the mean pulse amplitudes at different gain settings. For this phase of the work, in which sources of constant intensity were used, the pulse amplitude distributions were measured with a discriminator and scaler. The gain calibration was shown to be consistent by numerous cross-checks, and was found to remain stable over the whole period of the measurements. Various other instrumental tests and calibrations were also used to ensure optimum and reliable performance.

2.5. *Pulse Amplitude Distribution*

Two typical photographs of the pulse amplitude distribution records, using As K x-rays and Sn K x-rays, are shown in figure 2(*a*) and (*b*) respectively. Figure 2(*b*) shows the increase in low amplitude background at the higher x-ray energies, referred to in §2.2. The records were obtained on 35 mm Kodak 'Microfile' film, using a Zeiss Contax Camera. The enlargements were made on to high-contrast reflex document copying paper, and they are inverted and rotated through 90° relative to the presentation on the cathode-ray tube of the wedge analyser.

The use of high-contrast photographic materials gives a sharp transition from black to white, which serves as an iso-density contour or edge, from which the pulse amplitude distribution can be deduced (Maeder 1947). Since linear amplification is used, the pulse amplitude is proportional to the ordinate of the edge. N, the number of pulses per unit pulse height, is related to the abscissa x of the edge by

$$x = R \ln (N/N') \qquad \ldots\ldots (4)$$

where R and N' are constants, determined by the wedge density and the camera lens aperture respectively (Brooks 1955). Calibrations in terms of (4) were undertaken, and the abscissae in figure 2 are shown in units of N. For the present studies an accurate determination of N was not required.

2.6. *Scintillation Response*

The peak, or most probable, value of the pulse amplitude was obtained directly from the photographic records. At low particle energies this peak value is not exactly proportional to the scintillation response S, due to the asymmetry of the pulse amplitude distribution (Wright 1954 a). The peak pulse amplitude data were therefore corrected to give the true values of S, by the procedure described by Wright (1954 b).

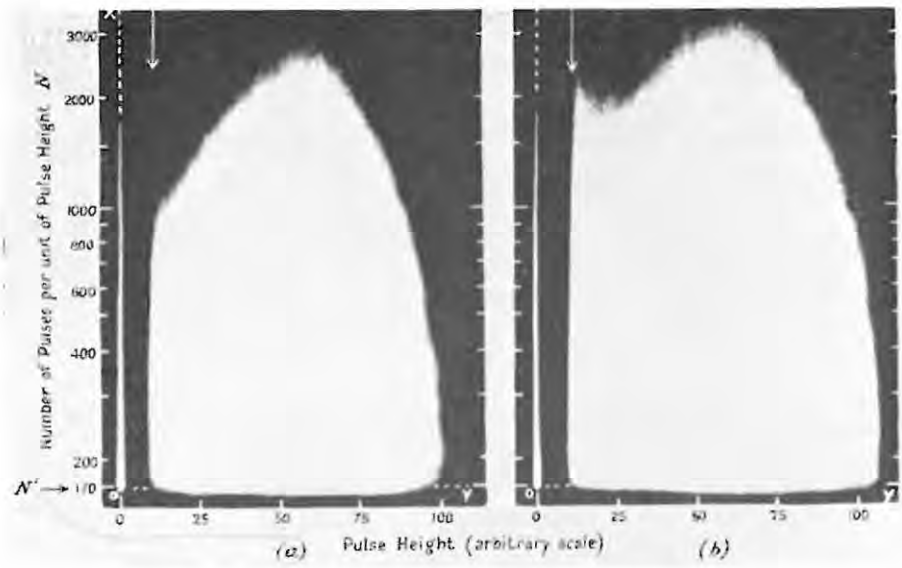

Figure 2. Pulse amplitude distribution photographs.
(*a*) As K x-rays (mean photoelectron energy = 10·7 kev)
(*b*) Sn K x-rays (mean photoelectron energy = 25·8 kev)

§ 3. Experimental Results

The observed values of the scintillation response S of the anthracene crystal to photoelectrons of energy E are plotted in figure 3 (extended points). The scale of S is the same as used by Taylor *et al.* (1951) in their measurements of the response to external electrons ($S = 6240$ units at $E = 624$ kev).

For each photoelectron energy E, three or four separate measurements were made at room temperature ($\sim 16°$c). In addition one measurement was made at a temperature of $-65°$c ($\pm 2°$c) for each energy, except for I, ^{114}In and ^{55}Fe. At $-65°$c, the scintillation response to 624 kev electrons increased by a factor of 1·50 relative to the response at room temperature. The response to photoelectrons from 6–30 kev energy increased by the same factor. Hence the low temperature photoelectron response data were normalized in terms of the 624 kev electron response, and included with the room temperature data in obtaining the mean values of S plotted in figure 3.

The error limits shown in figure 3 include the probable errors from the pulse amplitude measurements, from the instrumental calibrations, and from the normalization of the data.

§ 4. Discussion

4.1. *Present Results*

The data shown in figure 3 differ slightly from the preliminary results reported previously (Birks and Brooks 1954), and to which the statistical correction (§ 2.6) was applied by Wright (1954 b). The difference is due to the inclusion of additional observations. It will be noted that the corrected response S is not proportional to the photoelectron energy E, although it is approximately linear over the energy range considered.

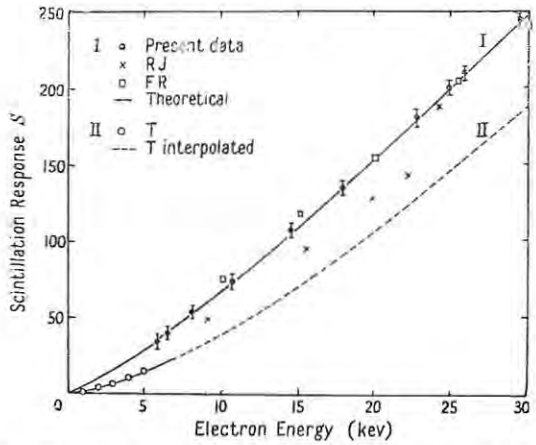

Figure 3. Scintillation response of anthracene crystal to electrons.

I, Photoelectrons: RJ, corrected data of Robinson and Jentschke (1954); FR Fowler and Roos (1955).

II, External electrons: T, Taylor *et al.* (1951); T interpolated, response curve interpolated between 5 and 80 kev by Taylor *et al.* (1951).

The increase in the scintillation response of anthracene by a factor of 1·50 in cooling from 16°C to −65°C agrees with previous observations (Sangster and Irvine 1956, Liebson 1952). The fact that the shape of the relative response curve is unaffected by the temperature reduction is significant. It indicates that the increased efficiency at low temperatures is not due to a reduction in the primary quenching processes, responsible for the non-linear response.

4.2. *Comparison with other Results*

The experimental data of Taylor *et al.* (1951) on the response of anthracene to external electrons of 1–5 kev energy are plotted in figure 3 (open circles).

Robinson and Jentschke (1954) have reported observations on the response to photoelectrons, agreeing with the external electron response data of Taylor *et al.* They did not, however, correct for the asymmetry of their pulse-height distributions (§ 2.6). The corrected values, estimated from their published observations, are plotted in figure 3 (crosses); they are significantly higher than those of Taylor *et al.*†

† In addition there appears to be a discrepancy, with regard to the response to In K x-rays, between the text of the paper by Robinson and Jentschke and their figure 5. The plotted point $S=180$ units at $E=28$ kev would appear from the text to refer to the In K_α energy which is 24·2 kev. Assuming the latter to be correct, a corrected value of $S=190$, $E=24{\cdot}2$ kev is obtained and plotted, and it is in good agreement with the present results.

The remaining discrepancies between the present results and those of Robinson and Jentschke may be attributed to differences in experimental method and arrangement, which were notably as follows: (i) Robinson and Jentschke used a single-channel pulse analyser, involving an estimated measuring period of at least 3–4 hours. This may be compared with a period of less than 30 minutes with the multi-channel wedge analyser, which thus reduces errors due to instrumental instability. (ii) They needed to subtract background counts up to pulse amplitudes equivalent to $E\sim15$ kev. In the present measurements background noise was negligible even at $E\sim6$ kev. (iii) They used a larger anthracene crystal (2 cm × 2 cm × 1 cm) and different x-ray sources, mainly excited by In K x-rays from ^{113}Sn, after the method described by Insch (1950). The various activities associated with ^{113}Sn (Hollander *et al.* 1953) probably produced a background of secondary radiations, analogous to the 'white' x-ray background described in § 2.2. The use of a larger crystal would accentuate the sensitivity to this and to the Compton background, and would also increase the number of multiple events (Compton scattering and photoelectric absorption in cascade) detected. Due to the non-linear response of anthracene, such multiple events would give a smaller scintillation response than that due to a single photoelectric event.

All such background effects tend to reduce the apparent value of S. It is thus consistent with the explanations offered that the data of Robinson and Jentschke fall below those observed in the present investigation.

The recent data of Fowler and Roos (1955) on the response of anthracene to 10–30 kev photoelectrons have been included in figure 3 (open squares) by normalizing their pulse-height scale to the present one at 20 kev. This normalization is consistent with a comparison of their proton response data with those of Taylor *et al.* (1951). The results are seen to be in satisfactory agreement with ours.

§ 5. Theory

5.1. *Specific Fluorescence and Response to Photoelectrons*

The scintillation efficiency dS/dE has been calculated as a function of E from the observed (S, E) values (figure 3) for photoelectrons. The specific energy loss dE/dr as a function of E has been similarly obtained from the range–energy data of Curie (1935) for electrons in standard air (all range data used refer to *integrated* ranges in standard air). Hence the specific fluorescence dS/dr for photoelectrons from 6–30 kev energy has been determined as a function of dE/dr.

Similar calculations have been applied to the (S, E) values for protons observed by Taylor *et al.* (1951) and Franzen *et al.* (1950), using the proton range–energy data of Livingston and Bethe (1937), and $(dS/dr, dE/dr)$ has thus been obtained for protons.

It is found that the $(dS/dr, dE/dr)$ curves are identical for electrons and protons, within the experimental error and scope of the present and quoted measurements. The original hypothesis (Birks 1951) that dS/dr is a monotonic function of dE/dr, and independent of the nature of the ionizing particle (in the absence of surface effects) is thus verified for electrons and protons.

The experimental $(dS/dr, dE/dr)$ data are equally consistent with (1), (2) and the other formulae referred to in § 1. The constants in (1) and (2) have been evaluated from the experimental response and range data, and the theoretical response curve shown in figure 3 (solid line) has been obtained by graphical integration.

At higher energies the theoretical response is also in agreement with the external electron response data of Taylor *et al.* (1951), Hopkins (1950, 1951), Robinson and Jentschke (1954) and of the present investigation (§ 2.4). These show a linear response for anthracene to electrons with E greater than 120 kev, which extrapolates to intersect the E axis at $E=20$–25 kev.

This feature of the experimental response curve is inherent in the theory. At high electron energies, where dE/dr is small, (1) or (2) may be expanded and integrated, giving

$$S = A\int_0^r (dE/dr)(1-kBdE/dr)\,dr$$
$$= A(E-E') \qquad \ldots\ldots(5)$$

where
$$E' = kB\int_0^E (dE/dr)\,dE. \qquad \ldots\ldots(6)$$

E' is practically constant for $E>200$ kev, since dE/dr is small and decreases with increasing E. A value of $E'=24$ kev has been calculated from kB and the range–energy data, and this corresponds from (5) to the intercept on the E axis of the linear portion of the (S, E) curve.

Although the response curve (figure 3) is approximately linear for low energy electrons, the scintillation efficiency is less than at higher energies. At $E=20$ kev, $dS/dE=9{\cdot}0$ units of S/kev, compared with $dS/dE=10{\cdot}4$ for $E>120$ kev. This decrease is attributed primary quenching processes as described by (1) or (2), and it is distinct from the additional surface effect encountered with externally incident electrons.

5.2. *Surface Effect for External Electrons*

The experimental results (figure 3) show a significant difference in the scintillation responses to internal photoelectrons and to external electrons. It is clear that the scintillation efficiency of anthracene is reduced for electrons absorbed near the crystal surface. This surface effect might be caused by one or more of the following processes: (*a*) back-scattering of the primary electrons; (*b*) additional quenching of the fluorescence near the crystal surface, due to chemical deterioration or other modification of the surface layer; and (*c*) surface escape of photons, emitted during the scintillation process, which would otherwise be absorbed in the crystal, leading to further fluorescence emission, and thus contributing to the scintillation response.

The effect of back-scattering has been considered by Taylor *et al.* (1951) and Butt (1952, 1953). The former estimate that less than 10% of the incident 1–5 kev electrons are scattered in a backward direction. The latter concludes that for 4–8 kev incident electrons, at least 80% of the back-scattered electrons, which constitute approximately 10% of the incident beam, dissipate half their energy in the crystal. We have made similar calculations based on the recent data of Sternglass (1954) on the back-scattering of 1–10 kev electrons from carbon, and have obtained results in agreement with Butt. It is estimated that the *maximum* effect of back-scattering of the incident electrons will be to cause a 4% reduction in the scintillation response observed by Taylor *et al.* (1951). This is quite inadequate to account for the magnitude of the observed surface effect.

Wright (1955) has recently made measurements of the photo-fluoresoence excitation spectra of anthracene crystals. These show a marked dependence of the flourescence efficiency on the depth of penetration of the exciting radiation,

the efficiency being less when the radiation is absorbed close to the surface. The magnitude of the effect depends on the state of the crystal surface, and appears to be partly due to chemical or physical deterioration of the surface, as well as to the escape of normal fluorescence radiation.

The surface effect has previously been attributed to the surface escape of radiation as described by (3) (Birks 1952, 1953). A mean free path a_0 for the escaping radiations of 3 to 8μ was found to give a reasonably consistent description of the external electron data of Taylor *et al.* (1951) and the α-particle data of King and Birks (1952). Emission and absorption processes in cascade are known to occur in anthracene in the 4000–4500 Å wavelength region (Birks and Little 1953). It has also been suggested that similar processes may occur in the 1650–1800 Å wavelength region during the scintillation process (Birks 1953, 1954a). Hence surface escape of the normal (longer wavelength) fluorescence is to be expected, while escape of the hypothetical primary (short wavelength) radiation is also possible. These alternatives cannot, however, be readily differentiated using the electron response data for anthracene, nor can the possible contribution of surface quenching be estimated without detailed knowledge of the crystal used by Taylor *et al.* (1951).

It is of interest to note that King and Birks (1952) have observed a surface effect of similar magnitude and a_0 in anthracene, *para*-terphenyl and *trans*-stilbene crystals. The overlap of the normal emission and absorption spectra in these last two materials is very much less than in anthracene (Birks and Wright 1954) and it is indeed negligible in *para*-terphenyl. Thus any surface effect associated with the escape of normal fluorescence should be much reduced in these materials, compared with anthracene, and be insignificant in the case of *para*-terphenyl.

A similar decrease in the scintillation efficiency of terphenyl solutions, when excited by short-range α-particles of r less than 10 mm (equivalent from (3) to $a_0 \sim 10\mu$) has been observed by Reynolds (1952). Such solutions are highly transparent to the normal terphenyl emission. This analogous effect in liquid scintillators, which has been previously attributed to primary photon escape (Birks 1953), might also be influenced by surface quenching due to absorbed oxygen (Pringle *et al.* 1953).

Without a fuller knowledge of the actual experimental surfaces used in the different studies, it is not possible to assess properly the relative importance of the alternative photon escape and surface quenching processes. The similar dependence of dS/dr on dE/dr, and the similar surface effect observed for each of the different organic crystalline and liquid scintillators studied, suggests, however, that common primary quenching and surface processes are operative.

§ 6. Conclusions

The present investigation has clarified several matters associated with the scintillation process in organic crystals. It has shown that:

(*a*) The scintillation response of anthracene to internal electrons can be adequately described theoretically, and that the variation of dS/dr with dE/dr for electrons and protons is independent of the nature of the particles.

(*b*) The relative scintillation response of anthracene to electrons of different energies is unaffected by a reduction in temperature from 16°C to −65°C, indicating that the 50% increase in scintillation efficiency is not due to a reduction in primary quenching processes in the excitation column.

(*c*) The scintillation response of anthracene to internal electrons is greater than that to external electrons of the same low energy. This is the result of a surface effect, probably due to the escape of photons and/or to impurity quenching of the excitation energy. The effect, which appears to be characteristic of the organic scintillators, will be encountered with any short-range externally incident particles.

The surface effects in anthracene and other organic scintillators merit further investigation. Further data are required on the scintillation response to external electrons of 5–80 kev energy, suitable for comparison with the theoretical relation (3). In future studies attention should be paid to the state of the crystal surface, to allow for any surface quenching effects.

ACKNOWLEDGMENTS

We wish to thank our colleague, Dr. G. T. Wright, for access to his unpublished results and for several interesting discussions. We are indebted to Capt. K. G. F. Collender of the Witwatersrand Native Labour Association for the loan of an X-ray tube, and to the South African Council for Scientific and Industrial Research for a research grant and for a bursary to one of us (F.D.B.).

REFERENCES

BERNSTEIN, W., CHASE, R. L., and SCHARDT, A. W., 1953, *Rev. Sci. Instrum.*, **24**, 437.
BIRKS, J. B., 1950, *Proc. Phys. Soc.* A, **63**, 1294; 1951 a, *Ibid.*, A, **64**, 874; 1951 b, *Phys. Rev.*, **84**, 364; 1952, *Ibid.*, **86**, 569; 1953, *Scintillation Counters* (London: Pergamon Press; New York: McGraw-Hill); 1954 a, *Phys. Rev.*, **94**, 1567; 1954 b, *Ibid.*, **95**, 277.
BIRKS, J. B., and BROOKS, F. D., 1954, *Phys. Rev.*, **94**, 1800.
BIRKS, J. B., and LITTLE, W. A., 1953, *Proc. Phys. Soc.* A, **66**, 921.
BIRKS, J. B., and WRIGHT, G. T., 1954, *Proc. Phys. Soc.* B, **67**, 657.
BLACK, F. A., 1953, *Phil. Mag.*, **44**, 263.
BROOKS, F. D., 1955, *M.Sc. Thesis*, Rhodes University.
BUTT, D. K., 1952, *Physica*, **18**, 242; 1953, *Proc. Phys. Soc.* A, **66**, 940.
CHOU, C. N., 1952, *Phys. Rev.*, **87**, 904.
COMPTON, A. H., and ALLISON, S. K., 1946, *X-rays in Theory and Experiment* (New York: van Nostrand), p. 641.
CURIE, M., 1935, *Radioactivité* (Paris: Hermann et Cie).
FOWLER, J. M., and ROOS, C. E., 1955, *Phys. Rev.*, **98**, 996.
FRANZEN, W., PELLE, R. W., and SCHERR, R., 1950, *Phys. Rev.*, **79**, 742.
HEITLER, W., 1949, *The Quantum Theory of Radiation* (Oxford: Clarendon Press).
HODGMAN, C. D. (Ed.), 1954, *Handbook of Chemistry and Physics* (Cleveland: Chemical Rubber Publishing Co.)
HOLLANDER, J. M., PERLMAN, I., and SEABORG, G. T., 1953, *Rev. Mod. Phys.*, **25**, 469.
HOPKINS, J. I., 1950, *Phys. Rev.*, **77**, 406; 1951, *Rev. Sci. Instrum.*, **22**, 29.
INSCH, G. M., 1950, *Phil. Mag.*, **41**, 857.
KING, J. W., 1952, *M.Sc. Thesis*, Rhodes University.
KING, J. W. and BIRKS, J. B., 1952, *Phys. Rev.*, **86**, 568.
LIEBSON, S. H., 1952, *Nucleonics*, **10**, no. 7, 41.
LIVINGSTON, M. S., and BETHE, H. A., 1937, *Rev. Mod. Phys.*, **9**, 245.
MAEDER, D., 1947, *Helv. Phys. Acta*, **20**, 139.
PRINGLE, R. W., BLACK, L. D., FUNT, B. L., and SOBERING, S., 1953, *Phys. Rev.*, **92**, 1582.
REYNOLDS, G. T., 1952, *Nucleonics*, **10**, no. 7, 46.
ROBINSON, W. H., and JENTSCHKE, W., 1954, *Phys. Rev.*, **95**, 1412.
SANGSTER, R. C., and IRVINE, J. W., 1956, *J. Chem. Phys.*, **24**, 670.
STERNGLASS, E. J., 1954, *Phys. Rev.*, **95**, 345.
TAYLOR, C. J., JENTSCHKE, W. K., REMLEY, M. E., EBY, F. S., and KRUGER, P. G., 1951, *Phys. Rev.*, **84**, 1034, and private communication.
WRIGHT, G. T. 1953, *Phys. Rev.*, **91**, 1282; 1954 a, *J. Sci. Instrum.*, **31**, 377, 462; 1954 b, *Phys. Rev.*, **96**, 569; 1955 a, *Ibid.*, **100**, 587; 1955 b, *Proc. Phys. Soc.* B, **68**, 701.

J.B. Birks and F.D. Brooks
Scintillation response of anthracene to 6-30 keV photoelectrons
Proc. Phys. Soc. B69 (1956) 721-730

F.D. Brooks
Organic scintillators
Progress in Nuclear Physics 5 (1956) 252-313

Reprinted from "PROGRESS IN NUCLEAR PHYSICS VOL 5" (1956).
Pergamon Press Limited, London

7

ORGANIC SCINTILLATORS

F. D. Brooks

CONTENTS

1. Introduction

The rapidly increasing use of scintillation counters in recent years has been greatly facilitated by the development of suitable luminescent materials. An important group among them are organic compounds, either as pure crystals or in various combinations as liquid or solid solutions. Notable advantages of the organic scintillators are their speed of response ($\sim 10^{-9}$ sec) and, in the case of solutions, the ease with which scintillators of large size and arbitrary shape can be made. Notable disadvantages are their rather low efficiencies compared with the best inorganic scintillators (Zn S (Ag), Na I (Tl) and $CdWO_4$), and the fact that the efficiency depends on ionization density; highly ionizing particles produce relatively less light and thus the relation between particle energy and light output is non-linear. These and other characteristics of different types of scintillators have been summarized, compared and discussed from time to time

in reviews and texts, notably by GARLICK (1952), JORDAN (1952), BIRKS (1953), CURRAN (1953), SWANK (1954), and BELL (1955).

In this review we shall deal chiefly with new data regarding the behaviour of organic scintillators, with new types of scintillators and with the scintillation mechanism as it is now understood. The latter has been the subject of speculation amongst authors for some time, and it is only recently that enough reliable evidence has been produced on which to base a suitably comprehensive picture.

On the practical side, a variety of new scintillators are now available as the result of intensive studies on organic liquid and plastic solutions. Factors relating to the performance of organic crystals have also been clarified. The practical data on crystals, liquids and plastics are probably of greater interest purely from the point of view of application. However, before we turn to these we consider the mechanism of the scintillation process. Apart from its own academic interest an understanding of this subject is obviously important both for interpreting the present data and for predicting or designing further applications.

2. THE SCINTILLATION PROCESS IN ORGANIC SCINTILLATORS

In a scintillation detector, energy dissipated by an ionizing particle in a scintillator is partly converted into visible light suitable for detection by a photomultiplier. Initially the particle spends its energy ionizing and exciting atoms and molecules along or near to its path. A variety of processes can follow, depending on the nature of the scintillator and the nature and energy of the particle. By various mechanisms (different in different types of scintillator) electronic excitation energy moves rapidly from initially excited atoms and molecules to others and thus travels some way through the system. Finally a portion of this energy is converted into light, the remainder being dissipated as heat or in other non-radiative processes.

For the organic scintillators it is well established that light emission is associated with electronic transitions in *molecules*, and that the energy transfer preceding emission is an inter-molecular process. This makes it convenient for us to work, as it were, backwards: to consider first the factors influencing the luminescence of organic molecules, as they emerge from the study of photoluminescence. In this way we may come to understand those factors and arrive at a description of the processes of energy absorption, energy transfer and light emission in systems of many molecules. This description then has to be extended and modified to fit the rather more complicated case of luminescence excited by ionizing particles.

We are thus led to ask the following questions:

(*a*) What are the electronic levels in an organic molecule which give rise to its luminescent characteristics;

(*b*) What are the processes of luminescence in an isolated molecule;

(*c*) How, in general, may the characteristics of the isolated molecule be modified when it is placed amongst other molecules;

Our particular interest centres on the "unchanged" p orbitals in these trigonal and digonal configurations, for it is these that eventually lead to the electronic levels responsible for the luminescence of scintillator molecules. In molecular structures three neighbour atoms bind to the trigonal configurations through the combination of their orbitals and its hybrids into three σ orbitals. Often at least one of these neighbours is another trigonal hybridized C atom, e.g. in ethylene ($H_2C = CH_2$). In this case the two p orbitals achieve maximum interaction by rotating their two nodal planes into coplanarity and combine into a π orbital, denoted π because it is mirror symmetric with respect to the common

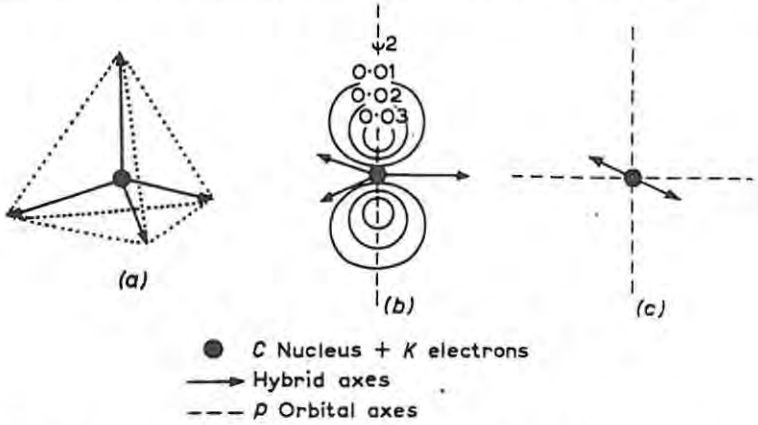

Fig. 1. Valency electron configurations for carbon. (a) In saturated structures (valency = 4). (b) In unsaturated structures (effective valency = 3). (c) In unsaturated structures (effective valency = 2).

nodal plane. The π orbital, or π-bond, corresponds to the extra link between the two C atoms in the structural formula. Similarly a combination of two digonal configurations (as in acetylene $HC \equiv CH$) produces a linear molecule with two π orbitals having mutually perpendicular nodal planes.

An extended structure of trigonal hybridized C atoms, called a "conjugated" structure, achieves planarity in the same way as did ethylene. In the conjugated structure, however, each p orbital, because it has axial symmetry, interacts, not merely with one, but with *two or three* adjacent counterparts. This is expressed in structural formulae by "non-localized" π-bonds, which are said to "resonate" between their different arbitrary positions in turn. A more accurate description is that the π electrons are non-localized and form a single stable system extending over the entire structure.

The π electron system of a molecule has, like any other electronic system, discrete energy states of its own. The energy states of the π electron system can be regarded as different possible mutual phase alignments of its p-orbital components; the state of lowest energy, or lowest π orbital, corresponds to all the p orbitals interacting in phase, and the highest π orbital to each p orbital being 180° out of phase with all its nearest neighbours. In the singlet ground state of the molecule, its π electrons, which are even in number (corresponding

energy by the *molecule* we must also bear in mind that the skeleton may contain vibrational energy, the energy differences between its vibrational states generally being significant ($\simeq$ 0·2 eV), although a good deal smaller than the π electron level spacings ($\simeq$ 4 eV). The skeleton may also contain rotational energy, but we may ignore this since the rotational energy changes are negligibly small ($<$ 0·01 eV). Furthermore the localized (inner shell and σ) electrons of the skeleton are capable of transitions of X-ray or far ultra-violet energies, but initially we may also neglect these since the photo-luminescence processes which

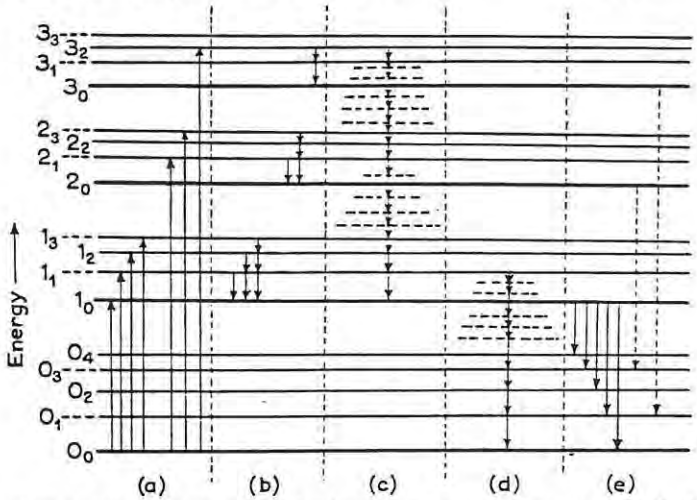

Fig. 2. Energy levels in an organic molecule and luminescence processes. (a) Excitation. (b) Internal degradation. (c) and (d) Internal conversion. (e) Fluorescence.

we shall be considering occur mostly, and have been studied, in lower energy regions.

The luminescence processes in a scintillator molecule may thus be adequately described in terms of a simplified energy level system, or diagram, comprised of singlet π electronic levels and vibrational levels. Such a diagram is shown in Fig. 2, where the electronic levels are denoted 0, 1, 2, etc., and the vibrational levels are indicated as discrete sub-levels (suffixes 0, 1, 2, etc.). It is perhaps of interest to note that the energy level systems of molecules are amenable to calculation, as, for example, DEWAR and LONGUET-HIGGINS (1954) and POPLE (1955) have recently shown for anthracene. For information on the methods of these calculations and details regarding the relation of electronic properties to molecular structure the reader is referred to the books of BOWEN (1946), PRINGSHEIM (1949), and FÖRSTER (1951).

(*b*) *Excitation and Emission of Molecular Luminescence*

Different stages of the luminescence process in a single molecule are represented in the sections (a), (b), (c), etc., of Fig. 2. At ordinary temperatures the molecule will normally occupy the state 0_0 and excitation is represented by a transition of the type shown in (a), depending on the amount of excitation

the environment of the molecule does not change, hence for a large number of mutually isolated identical molecules simultaneously excited, the emission observed has a *quantum efficiency* less than unity and an intensity which decays exponentially with a characteristic lifetime or *decay time.*

For 0–2 excitation we must consider four possible modes of de-excitation, namely 2–0 emission, 2–0 internal quenching, 2–1 emission and 2–1 internal quenching, with 1–0 de-excitation following both the latter two. However, it is found (see e.g. PRINGSHEIM, 1949), almost without exception in fluorescent organic materials and certainly in all the common scintillators, that 2–1 internal quenching has a very much higher probability than the other three processes. Neither 2–0 emission nor 2–1 emission are observed while the emission that is observed has all the characteristics (spectrum, decay time, and quantum efficiency) of that from 0–1 excitation. *Direct* 2–0 internal quenching must therefore be negligible and 2–1 internal quenching 100% efficient and rapid ($\simeq 10^{-11}$ sec) compared to the fluorescence lifetime of the 1–0 emission ($\simeq 10^{-9}$ sec). The same appears to be true for excitation to the third level and, as far as is known, for any electronic excitation up to the molecular ionization energy. In every case higher order fluorescence transitions (such as those shown by broken arrows in Fig. 2) do not occur and only 1–0 emission is observed.

The photo-luminescence process in a single molecule may thus be simply described without reference to the energy of the exciting light. In terms of Fig. 2 its stages are (a), (b), and (c) occurring within 10^{-11} seconds followed by either (d) or (e) occurring after a mean lifetime $\simeq 10^{-9}$ sec. The quantum efficiency of the molecule is the fraction of times it re-emits a photon in a large number of excitations. This quantum efficiency and the mean lifetime depend on the probabilities of stages (d) and (e), and these, in turn, depend on the environment as well as the structure of the molecule.

(c) *Luminescence Process in Scintillators*

To describe the luminescence process in any practical system such as a scintillator we must extend and modify our previous description (*b*) of the molecular luminescence process.

First of all it is important to recall that molecular luminescence characteristics depend on environment. Thus, for example, the absorption spectrum of anthracene shifts toward longer wavelengths (by about 300 Å) on changing from vapour to dilute solution to crystal (KORTUM & FINCKH, 1942); the electronic levels of the molecule are more closely spaced in the more condensed systems due to a somewhat greater average interaction of π electron systems. BOWEN (1946, 1952) has described in some detail how molecular quantum efficiency and fluorescence lifetime depend on environment. The probability of 1–0 emission (Fig. 2e) is that of the 1–0 or 0–1 transition of the molecule, which is proportional to the area of the 0–1 absorption band (see Fig. 3). The oscillator strength (proportional to ε) of this band and its frequency abcissa both depend on the environment of the molecule. BOWEN also describes how internal quenching (Fig. 2d) may be interpreted in terms of potential energy diagrams

sufficient to ensure trapping of all or most of the solvent excitation energy, the luminescence characteristics of the two component system depend entirely on the transfer process and the characteristics of the solute; the emission spectrum is that of the solute and the quantum efficiency and mean lifetime are determined by those of the solute and the efficiency of the transfer process.

Reabsorption of molecular emission is a third important effect which we have to take into account in considering the luminescence process in practical scintillation systems. This can occur in two component systems where one component

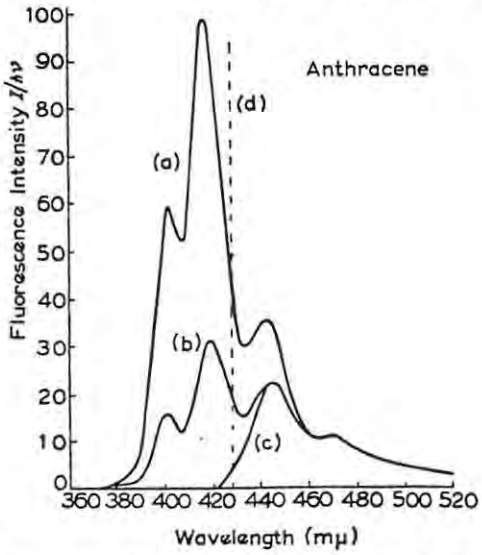

Fig. 4. Fluorescence spectra of anthracene. (a) Microcrystals. (b) Reflection (1 cm³ crystal). (c) Transmission (1 cm³ crystal). (d) Transmission limit for a 1 cm³ crystal.

emits at a wavelength lying within the absorption band of the other and also in pure crystals whose emission and absorption spectra overlap. Wherever it occurs, reabsorption has a marked effect on the luminescence characteristics of the system, the latter then being determined by several successive molecular luminescence processes, sometimes involving more than one species of molecule. Effects of spectral overlap, for example, are well demonstrated in the fluorescence spectra (2,537 Å excited) of anthracene (Fig. 4), *trans*-stilbene (Fig. 5), and *para*-terphenyl (Fig. 6) crystals measured by BIRKS & WRIGHT (1954). The different spectra (a), (b) and (c) in these figures are normalized to coincide at their longest wavelengths and represent different conditions of observation; (a) in reflection from a thin micro-crystalline layer; (b) in reflection from a thick crystal and (c) in transmission through crystal 1 cm thick. In each figure the dashed line, (d), marks the short wavelength transmission limit for the respective crystal, as subsequently measured by WRIGHT (1955d). Where overlap, indicated by comparing (d) with (a) or (b), is large a considerable portion of the molecular fluorescence spectrum is removed in the transmitted spectrum, (c). Thus overlap affects considerably the spectral distribution of

For our purposes it is convenient to describe the degree of interaction of two scintillator molecules in terms of their π electron "clouds" (Section 2(*a*)). We may define the interaction as "*negligible*" when the "clouds" are widely separated and "*strong*" when they (or in reality the respective π electron wave functions) overlap by an arbitrary appreciable amount. There may be an intermediate region of "*weak*" interaction when overlap is negligible, due to the van der Waals or polarization forces between molecules.

When two molecules possessing similar electronic levels interact strongly they reach a state where their individual π electron systems can no longer be resolved. The latter must instead be considered as a single system whose levels are similar but somewhat broader than those of its components. An arrangement of a large number of strongly interacting identical molecules similarly becomes characterized by a banded energy level system instead of a number of identical but discrete molecular systems. In these strongly interacting arrangements the π electrons of component molecules are non-localized and consequently electronic excitation energy is also non-localized over all the molecules. The term *inter-molecular* energy transfer thus loses its meaning since only the system as a whole but not its individual molecules contain excitation energy. Energy transfer between different positions of the system has a meaning, however, and here molecules serve to define different positions. Two modes of energy transfer may be distinguished. The first can occur when the excitation energy is sufficient to raise an electron from the highest broadened level, or filled band, of the system to its lowest empty band. The excited electron and its "positive hole" (left in the filled band), being non-localized and independent of one another, may move freely in their respective bands. The "*electron migration*" resulting constitutes a transfer of both excitation energy and charge. The second mode of transfer can occur when the excitation energy is insufficient to excite an electron to an empty band and arises because it is possible for the excited electron and its positive hole to exist in a series of states in which they are bound in one another's field. FRENKEL (1931) has termed an electron and positive hole bound together in this way an "*exciton*" and has described how the non-localized nature of the exciton leads to energy transfer in a system of strongly interacting atoms. *Exciton transfer* is to be distinguished from electron migration by the fact that only excitation energy, not charge, is transferred.

In outlining exciton transfer and electron migration we were concerned with a system of molecules in permanent strong interaction. What might be considered as a variation of this system is that where localized groups of two or more molecules interact strongly but only for *intermittent* periods, during collisions for example. We would, from our previous considerations, expect intermittent exciton and electron transfer to occur in this system. Transfer phenomena of the former type were in fact observed and studied (CARIO & FRANCK, 1923; KALLMANN & LONDON, 1929) in monatomic gases, prior to FRENKEL'S exciton hypothesis, and were given the name "*sensitized fluorescence.*" By analogy with the latter, intermittent exciton transfer in molecular systems can also be called sensitized fluorescence. At the same time

obscured in this region of "strong" interaction, however, because of the diffuse or non-discrete nature of the π electron cloud compared to the discrete boundaries of typical metallic antennae. We could simulate the π electron cloud more closely if we used antennae constructed from a hypothetical type of wire whose properties ranged continuously from perfect conductor along its axis to perfect insulator of unit dielectric constant at its surface. Thus the merging of two antennae surfaces into a common new medium would become the analogy of π electron cloud overlap in the strong interaction. In turn this new medium, sometimes approximated to in practice by the core of a transformer, would lead to highly efficient transfer analogous to exciton transfer. To represent electron migration we would have to attribute even more hypothetical properties to the antennae materials, but this we shall not do.

The analogy we have developed also helps to clarify some of the factors governing inter-molecular energy transfer. The resonance condition for transfer of molecular energy (Section 2(*c*)) has its analogous condition of equivalent resonant frequencies in the antennae. Also, like the analogous r.f. radiation from its equivalent flat antenna, emission from an excited molecule is polarized and has a polar diagram (of probable direction of emission) with a maximum perpendicular to its plane. Thus the efficiency of radiative transfer between two molecules is sensitive to their mutual orientations reaching a maximum when their planes are parallel and their axes (perpendicular to their planes) aligned. It is also readily seen that non-radiative modes of transfer depend on the mutual orientation of the molecules in exactly the same way.

The continuous transition between different modes of transfer makes it difficult to attribute any given observed transfer effect to a particular mode. Transfer processes have been identified in scintillators and in similar systems by studying characteristics such as efficiency, emission lifetime, spectra, polarization of emission and the dependence of these characteristics on one another and on the composition, size, temperature, etc., of the scintillator.

Radiative transfer has been indentified in many pure organic crystals by studies of spectra, decay times and efficiencies as we indicated in Section 2(*c*) when describing effects of spectral overlap. Anthracene is typical of crystals in which considerable radiative transfer occurs. However, it is now well established for all crystals including anthracene that the radiative transfer is trivial compared to the non-radiative transfer that occurs. Bowen *et al.* (1949), for example, found transfer from anthracene to naphthacene so efficient in mixed crystals with the latter as impurity, as to require explanation by a resonance transfer process. Their interpretation was subsequently questioned by Birks (1953, 1954) on the grounds that the high transfer efficiency could be due to *several* radiative exchanges in the anthracene (arising from its spectral overlap) which would multiply the chances of radiative transfer to naphthacene. However, the conclusions of Bowen *et al.* are now supported by several other independent investigations. Wright (1955d) for example, has identified non-radiative transfer in a rather special sort of "mixed" crystal, namely a surface layer ($\simeq 10^{-4}$ cm thick) of an anthracene crystal containing a non-fluorescent

Other interesting ideas are tentatively advanced by KRENZ. There is evidence noted by this author and others (e.g. HINRICHS, 1954) that some solutes such as anthracene can, during polymerization, enter into chemical bonding with polystyrene chains without significant additional effect on their π electron systems and hence fluorescence characteristics. It would appear that this increases the coupling between anthracene and polystyrene π electron systems and, therefore, the non-radiative transfer.

(e) *Luminescence Excited by Particles*

The scintillation process differs from the photo-excited luminescence process only because of the more complex excitation conditions produced by ionizing particles. In the scintillation process the excitation is instantaneously produced in a primary excitation column, perhaps only 10 to 100 molecules wide, and all possible states of the scintillator molecules are excited as well as some molecules being ionized and others dissociated or chemically damaged. We can assume that those molecules initially excited in their π electron states will initiate luminescence processes as we have described above, i.e internal conversion to their l_0 levels in $\simeq 10^{-11}$ sec, then energy transfer with partial or complete trapping in solutes and/or impurities culminated by quenching or emission. Luminescence processes may also arise from conversion of other excitation energies (e.g. of σ-bonds or K electrons) to π electron excitation or from recombination of ionized molecules and electrons into excited molecules. At all stages of these luminescence processes excited molecules are subject to the rather special and rapidly changing environment of the primary column, and this has the effect of increasing the probability of quenching relative to that of emission in the final stage, that is of producing additional *primary quenching effects*, peculiar to particle excitation. It is believed that these primary quenching effects produce the *non-linear response* properties or organic scintillators, and that they are largely responsible for the *low efficiency* of the scintillation process. They are also thought to play a part in determining the mean lifetime or decay time which characterizes the scintillation emission.

Non-linearity of response—Due to primary quenching the response L of a scintillator to a particle of energy E depends on the excitation density produced by the particle, and hence on the specific energy loss dE/dx of the particle. Now dE/dx depends on the nature of the particle and varies along the primary column, reaching a maximum near its end. Hence L is not in general proportional to E, and may only be related to E in terms of a relation between the "specific response," dL/dx, and the specific energy loss, dE/dx. Several different forms for that relation have been proposed by different authors. BIRKS (1951) relates dL/dx and dE/dx by:

$$\frac{dL}{dx} = \frac{A\, dE/dx}{1 + B\, dE/dx} \tag{1}$$

This relation describes a potential specific response, $A\, dE/dx$, which is reduced in the ratio $(1 + B\,.\,dE/dx)^{-1}$ by primary quenching. A and B are constants

Here a, p, and k are constants associated with the probabilities of bimolecular quenching, fluorescence emission and unimolecular quenching respectively.

A comparison of the available response data for anthracene with the relations (1) and (4) is shown in Fig. 7. To carry this out, dL/dx data were constructed

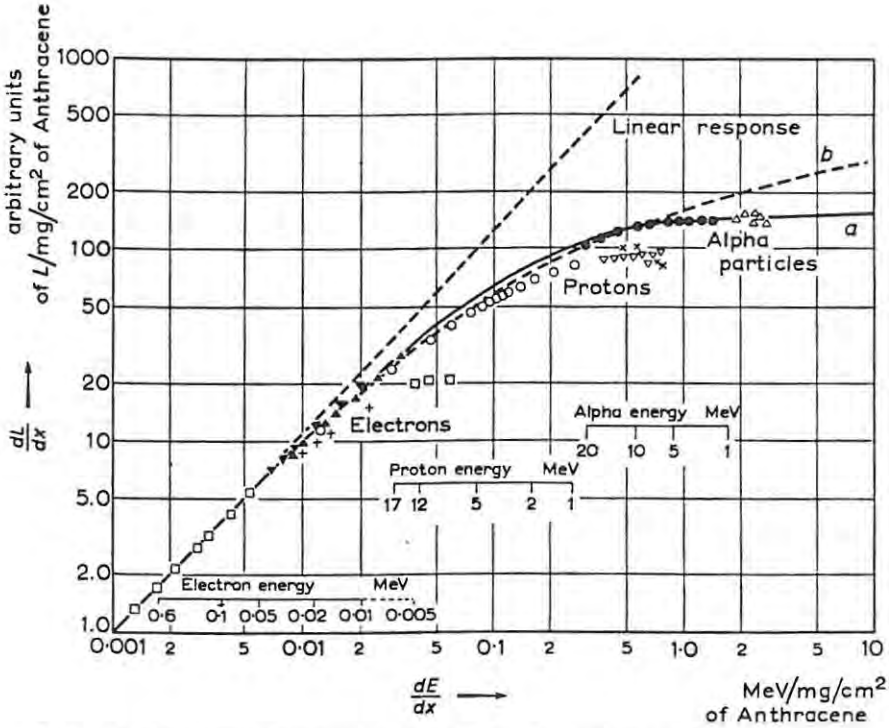

Fig. 7. Variation of specific response, dL/dx, with specific energy loss, dE/dx, for anthracene crystals.

Theoretical Curves:

(a) from eq. (1) using

A = 1040 response units/MeV

B = 6·6 mg cm^{-2}/MeV.

(b) from eq. (4) using

p/a = 52 response units/mg cm^{-2}

$\frac{a}{p+k}$ = 20 mg cm^{-2}/MeV.

Experimental Data:

(i) externally incident electrons. □ HOPKINS (1950, 1951), TAYLOR *et al.* (1951).

(ii) photoelectrons + ROBINSON & JENTSCHKE (1954)
▲ BIRKS & BROOKS (1954, 1956)
▼ FOWLER & ROOS (1955)

(iii) protons ○ FRANZEN *et al.* (1950), TAYLOR *et al.* (1951), FREY *et al.* (1951).
× FOWLER & ROOS (1955)
▽ ZIMMERMAN (1955)

(iv) alpha particles ● BIRKS (1950), TAYLOR *et al.* (1951)
BIRKS & KING (1952)
△ ZIMMERMAN (1955).

there are indications that the data for different particles (e.g. for protons and alphas in Fig. 7) do not fit a common curve. This could be due to surface effects and to other causes. Surface effects would act to make dL/dx smaller for short range protons than for longer range alpha particles of the same dE/dx, as is observed experimentally (at $dE/dx = 0{\cdot}5$ MeV/mg cm^{-2} in Fig. 7). It has also been suggested by WRIGHT (1955c) that the observed saturation of dL/dx for alpha-particles ($dE/dx \gtrsim 1$ MeV/mg cm^{-2}) might be a deviation from curve (b) produced by surface effects. This cannot be tested without proper knowledge of the surfaces used in the individual response measurements, however.

ZIMMERMAN (1955) draws attention to the uncertainties introduced in experimental dL/dx vs. dE/dx data by uncertainties in range-energy data. Present knowledge of the stopping power for both electrons and heavy particles in anthracene or similar substances is unfortunately very limited, particularly in the low energy region.

Other possible contributory causes to the differences between theoretical curves and experimental data in Fig. 7 could arise from the simplifying assumption, common to all four equations, that the excitation density produced by any particle is proportional to its energy loss per unit distance traversed in the scintillator. This is not necessarily true since;

(i) The actual density of excitation, i.e. the excitation per *unit volume* must also depend on the cross-section of the primary column, which may vary with the charge and velocity of the particle. The difference in this cross-sectional area might be small and therefore justifiably neglected for different particles of low charge but would not be negligible for heavily charged particles such as fission fragments. This might explain the observation by MILTON & FRASER (1954) that the response of stilbene to fission fragments exceeded that to be expected on the basis of the observed saturation of dL/dx for alpha-particles. Any saturation for fission fragments would be expected to occur at a higher value of dL/dx due to the broader excitation column which they produce.

(ii) The proportions of particle energy distributed to the various primary excitation processes (excitation, ionization, dissociation, damage, etc.) are known to depend both on the nature and the energy of the particles. The first is shown by the fact that alpha-particles produce far greater damage than do electrons, in anthracene and other crystals (BLACK, 1953). The latter follows from the fact that slower moving particles produce more excitations per ionization than do fast particles, but is important only at energies near or below the maximum of the Bragg ionization curve. ($\lesssim 5$ keV for electrons, $\simeq 50$ keV for protons, $\simeq 300$ keV for alpha-particles in anthracene.) ZIMMERMAN'S helium ion data fall within this range and might therefore be affected by these considerations.

These possible defects in response theories constitute a limitation to our comparison of experimental data with the theoretical curves; but more

particles (3·6 MeV) he finds that the long decay is exponential. For electrons the period of the decay is 31 mμsec, in agreement with SWANK's measurements; for alpha-particles it is, however, 53 mμsec.

Scintillation pulse shapes given by WRIGHT for anthracene are shown in

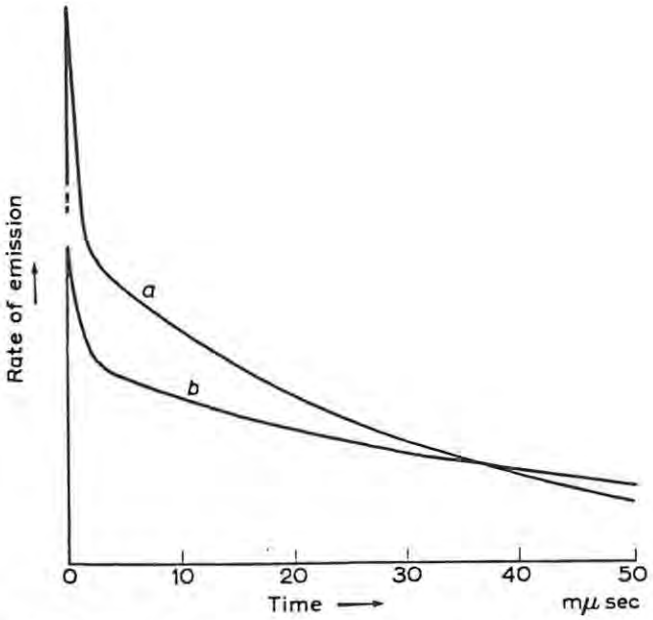

FIG. 8. Average shapes of scintillations emitted by an anthracene crystal (1 cm² × 1 mm) (a) Excited by electrons. (b) Excited by alpha-particles (3·6 MeV). Vertical scales are adjusted to equalize the areas of (a) and (b) so that these represent scintillations of equal total light output.

Fig. 8. After noting and taking into account the important reabsorption effects in this material he interprets these shapes by resolving each scintillation into:

(i) emission from primarily excited molecules

(ii) emission from excited molecules formed by recombination of electrons and primarily ionized molecules.

High excitation densities in the initial stages of the scintillation make the probability of primary quenching large. Hence the initially excited molecules are rapidly de-excited and only a small fraction of them emit (component (i)), producing the characteristic initial surge of fluorescence.

Excited molecules resulting from ion recombination are less affected by primary quenching since these are formed mainly after the excitation density has dropped appreciably. A large fraction of these emit, as a result, producing the long decay component, (ii), containing most of the emission. For alpha-particles, or, more generally, for higher initial excitation densities this fraction is smaller, since primary quenching conditions persist for longer. Apart from the reduced efficiency this results also in an increase in the apparent lifetime

particles (3·6 MeV) he finds that the long decay is exponential. For electrons the period of the decay is 31 mμsec, in agreement with SWANK's measurements; for alpha-particles it is, however, 53 mμsec.

Scintillation pulse shapes given by WRIGHT for anthracene are shown in

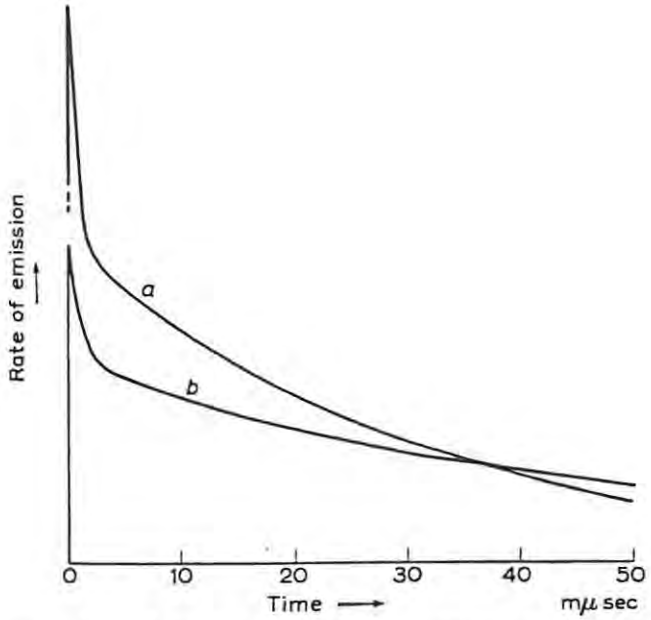

FIG. 8. Average shapes of scintillations emitted by an anthracene crystal (1 cm² × 1 mm) (a) Excited by electrons. (b) Excited by alpha-particles (3·6 MeV). Vertical scales are adjusted to equalize the areas of (a) and (b) so that these represent scintillations of equal total light output.

Fig. 8. After noting and taking into account the important reabsorption effects in this material he interprets these shapes by resolving each scintillation into:

(i) emission from primarily excited molecules

(ii) emission from excited molecules formed by recombination of electrons and primarily ionized molecules.

High excitation densities in the initial stages of the scintillation make the probability of primary quenching large. Hence the initially excited molecules are rapidly de-excited and only a small fraction of them emit (component (i)), producing the characteristic initial surge of fluorescence.

Excited molecules resulting from ion recombination are less affected by primary quenching since these are formed mainly after the excitation density has dropped appreciably. A large fraction of these emit, as a result, producing the long decay component, (ii), containing most of the emission. For alpha-particles, or, more generally, for higher initial excitation densities this fraction is smaller, since primary quenching conditions persist for longer. Apart from the reduced efficiency this results also in an increase in the apparent lifetime

electrons, while (i) and (iv) reach significant magnitudes only for heavy, highly ionizing particles.

3. Organic Crystal Scintillators

The better known and most widely used organic scintillation crystals are anthracene, *trans*-stilbene, *para*-terphenyl, and diphenylacetylene all of which are readily available from commercial sources. Many other materials such as quaterphenyl, pyrene and carbazole are also good scintillators (Sangster, 1952). These have been less widely applied and studied, however, mainly because they are not readily obtainable as suitable crystals.

For practical purposes it is convenient to classify and compare different crystals in terms of their characteristics, scintillation efficiency, degree of non-linearity of response, emission spectrum and scintillation lifetime. To interpret scintillation mechanisms, however, we require to know in addition the fluorescence characteristics of the scintillator and its molecules. In the present section we discuss the methods used to measure fluorescence and scintillation characteristics and the data obtained for the more common crystals.

(*a*) *Fluorescence and Scintillation Efficiences*

It will be recalled from Section 2(*b*) that we define the *quantum efficiency* of fluorescence as the number of quanta emitted per quantum absorbed by a material in the photo-luminescence process. This efficiency is truly characteristic of a pure material only when there is no reabsorption of fluorescence. It is then called the *molecular* quantum efficiency. Quantum efficiencies observed under practical conditions (e.g. in crystals) may be less, due to the effects of reabsorption (Section 2*c*).

By *absolute scintillation efficiency* we define the fraction of the energy dissipated by a particle which reappears as scintillation emission. In other words, its reciprocal would be the quantity of energy dissipated per photon emitted. Scintillation efficiencies of crystals may also be less than characteristic molecular scintillation efficiencies, owing to reabsorption effects. The efficiency referred to is normally that for excitation by fast electrons since it is only for these that a constant efficiency (i.e. linear response) is obtained.

Direct measurements have been made of the absolute quantum efficiencies (e.g. Gilmore *et al.*, 1952; Forster & Livingston, 1952) and absolute scintillation efficiencies (e.g. Hopkins, 1951; Harrison, 1952; Furst *et al.*, 1953; Birks & Szendrei, 1953) of crystals and liquids. Direct methods have a fundamental limitation, however, in that they require an accurate calculation of the exact fraction of fluorescence or scintillation emission collected by a detector. The latter estimation is always difficult and can be further complicated by reabsorption, by anisotropic optical properties in the crystal and even by surface effects if excitation is principally in the surface layers.

An indirect method for measuring absolute quantum efficiencies has recently been developed and applied to anthracene crystals by Wright (1955a). An effect of reabsorption in a pure crystal is to make the lifetime of its emission,

standard cannot be relied upon. SCOTT *et al.* (1952) and SANGSTER (1952) have pointed out the extreme difficulty in obtaining pure anthracene and also the tendency of purified samples to deteriorate. SANGSTER has also shown that different methods of preparation can lead to pulse height variations of 20%. HAYES *et al.* (1956) report variations of a similar magnitude amongst commercially prepared anthracene crystals. From all accounts stilbene would be a much more suitable standard than anthracene.

Numerous different observations of the scintillation efficiencies of 1 cm^3 crystals of *trans*-stilbene, *p*-terphenyl and diphenylacetylene place these all in the range 0·6 to 0·7 relative to anthracene. Thus the absolute scintillation efficiencies of these crystals are probably all about 90 eV/photon.

(*b*) *Response to different particles*

Most scintillation detectors are operated as energy spectrometers of one sort or another and for this a knowledge of the response-energy relationship of the scintillator for the particle concerned is essential. No special difficulties arise in making or interpreting response measurements, except for particles of low energy. For the latter, two important effects must be considered namely;

(i) For a small response, statistical fluctuations in photomultipliers produce a markedly asymmetric output pulse height distribution (see e.g. WRIGHT, 1954a, b; or BREITENBERGER, 1955). The mean pulse height of such a distribution may not be identified with its most probable (peak of the distribution) pulse height, which is more easily determined; it can, however, be obtained from the latter by a simple procedure described by WRIGHT (1954c). The most probable pulse height must first be reduced to a scale of equivalent number of photocathode electrons, N_c, as described by GARLICK & WRIGHT (1952). The number of photo-cathode electrons, N_m, equivalent to the true mean pulse height is then given by:

$$N_m = N_c + \Delta \tag{7}$$

where Δ is a constant which is slightly dependent on multiplier gain but whose average value is about 0·7.

(ii) Surface effects must be taken into account in interpreting response measurements for short-range surface incident particles. WRIGHT (1955c) has described a simple procedure for doing this. The crystal is excited by light of constant quantum intensity but various different wavelengths, selected, in consultation with absorption data, to give various different mean depths of penetration below the surface. Thus a measurement of fluorescence efficiency as a function of depth of excitation below the surface is obtained. It is to be hoped that measurements of this type will be undertaken simultaneously with any future response investigation in which surface effects appear to matter.

Response data for anthracene crystals are summarized in Fig. 7. For practical purposes it is useful to present these data in their original form—response L vs.

protons. Detailed response data for stilbene may be found in the papers of TAYLOR *et al.* and FOWLER & ROOS; an approximation worth noting is that in terms of the ratios given by TAYLOR *et al.* the relative responses of stilbene to different particles and energies are as in Fig. 9 except that the proton and alpha-particle responses must be multiplied by 0·7.

A convenient measure which SWANK (1954a, b) adopts to describe non-linearity is the "alpha-to-beta ratio." This is defined by comparing the ratio of pulse height to energy for polonium alpha-particles (5·3 MeV) with that of a high energy electron ($>$ 1 MeV). It is 0·10 for anthracene as can be seen from Fig. 9, while the measurements of TAYLOR *et al.* show that it is about 0·07 for stilbene. Various other measurements have indicated that the alpha-to-beta ratios of terphenyl (HOFSTADTER, 1950) and diphenylacetylene crystals and other organic scintillators are very close to those of anthracene and stilbene.

(c) *Emission Spectra*

To achieve an efficient scintillation counter the scintillator must transmit a maximum proportion of its emission directly to the photomultiplier cathode and the emission which it transmits must be of a wavelength which matches the spectral sensitivity curve of the latter. The extent of reabsorption (the effect which determines the former factor) can be evaluated from emission spectra measurements for different conditions of excitation (see Section 2*c*); at the same time emission spectra observed in transmission through the scintillator can be used to determine the degree of matching with the photomultiplier cathode.

Emission spectra measurements are, for the most part, straightforward. Ultra-violet light is the most convenient means of excitation to use, due precautions being necessary, of course, to eliminate "background" fluorescence emission from the excitation source, crystal holder, etc. Where a quantitative knowledge is required of the spectral characteristic, the light detector used (photomultiplier or photographic plate) must be calibrated in units of relative energy, or of relative quantum intensity and the variation of bandwidth and transmission coefficient of the dispersive apparatus used (spectrophotelometer, spectograph, etc.) with wavelength must be known. KING (1954) and BIRKS & WRIGHT (1954) have given full details of fluorescence spectra determinations. Spectra obtained by the latter authors for anthracene, stilbene, and terphenyl crystals are shown in Figs. 4, 5 and 6. It should be recalled that the scintillation emission for each of these crystals has the spectral distribution of the transmitted spectra (curves (c)) in these figures.

Fluorescence spectra for diphenylacetylene crystals are also given by BIRKS & WRIGHT (1954) and by KING (1954).

(d) *Fluorescence and Scintillation Lifetimes*

Modern methods that have been used to measure *fluorescence lifetimes* of scintillators are based on the method originally due to GAVIOLA in 1927, subsequently extended by other authors (see e.g. FÖRSTER, 1951) and lately especially by BAILEY & ROLLEFSON (1953). In this method the intensity, I_E,

Table 2. Mean Fluorescence Lifetimes of Crystals (at room temperature)

Crystal	*Molecular emission lifetime,* τ_m (mμsec)	*Crystal emission‡ lifetime,* τ_c (mμsec)
Anthracene	3·5 ± 1·0 (2) 6·4 ± 0·2 (3)	17 (1) 14 ± 2 (2) 12·6 (3)* 24·2 (3)†
trans-Stilbene	1·7 ± 0·6 (2)	3·1 (1) 3·0 ± 0·8 (2) 4·8 (3)
para-Terphenyl	3·5 ± 1·0 (2)	11 (1) 3·8 ± 1·0 (2) 5·2 (3)
Diphenylacetylene		2·5 (1) 3·0 ± 0·8 (2) 4·7 (3)

Data references (1) LIEBSON *et al.* (1950)
(2) BIRKS & LITTLE (1953)
(3) HAMILTON (1955)

* Mean of 60 measurements for average aged surfaces.
† Mean of 70 measurements for freshly-cleaved, glass-smooth, surfaces.
‡ Crystal size > 2 mm thick.

anode pulses must be made large enough to record directly on more conventional oscillographs. POST & SHIREN (1950) (see also POST, 1952) and SINGER *et al.* (1956) obtained large anode pulses by operating the photomultiplier at a very high voltage (~5 kV) for short periods lasting about one microsecond; this method has the advantage that the high voltage also reduces the transit time spread in the photomultiplier and thus improves the time resolution obtainable. PHILLIPS & SWANK (1953) obtained large anode pulses by using artificial pulsed X-rays instead of single nuclear radiations to excite large scintillations. A notable advantage of their method was that successive scintillations were of the same size and occurred at a controlled time; hence they could be accurately superimposed and averaged in a single recording. By experiment and calculation including factors such as the finite X-ray pulse width, PHILLIPS & SWANK determined that the time dispersion of their experimental system was 3 to 4 millimicroseconds. They showed that scintillation lifetimes greater than this value could be accurately determined by plotting the co-ordinates of recordings on semi-logarithmic paper (Fig. 10) and measuring slopes. The slow components evident towards the ends of the decay curves in Fig. 10 have also been studied by a direct pulsed X-ray method. HARRISON (1954) has described how these components are enhanced by employing a long pulse of X-ray excitation.

Indirect methods, although more complicated in principle, are often simpler

WRIGHT (1956) has developed a novel indirect method which utilizes the fact that the power, W, generated by scintillation pulses in the photomultiplier anode load, R, depends on their shape. For exponential anode pulses of decay time, τ, mean pulse height, $\bar{V}$, recurring at a frequency z, he shows

$$W = \left[1 + \frac{\text{var}\,(V)}{\bar{V}^2}\right] \frac{i^2 R}{2z(\tau + RC)} \tag{10}$$

where i is the mean current and C the capacitance to earth at the anode. WRIGHT uses a thermistor bridge in the anode load to determine W. A check of W^{-1} as a function of R^{-1} in terms of eq. (10) serves to determine whether the mean *anode* pulse shape is exponential and if so determines τ. For anthracene crystals excited by gamma-rays and alpha-particles WRIGHT obtained that the mean anode pulse shapes were exponential giving $\tau = 31$ mμsec and 53 mμsec respectively. From this he calculated that when photomultiplier transit time spread effects were taken into account, the mean *scintillation* pulse shapes must be as illustrated in Fig. 8.

Scintillation lifetime data reported by various authors for anthracene, stilbene, terphenyl, and diphenylacetylene crystals excited by gamma- or x-rays are listed in Table 3. SWANK & BUCK (1955) have pointed out that the scintillation lifetime is very sensitive to impurities. Similarities are evident in Table 3

Table 3. Mean Scintillation Lifetimes of Organic Crystals ($\geqslant$ 1 mm thick), for γ-ray or x-ray Excitation

Lifetimes are given in units of 10^{-9} sec and refer to room temperature $\sim$ 20°C to 25°C

Crystal \ Source of preparation	SANGSTER[a] (1952)	*Larco Instrument Company*	*Harshaw Chemical Company*	*National Radiac Inc.*	*Miscellaneous or Unknown*
Anthracene	30 (7) 29·9 (10)	33·2(10)[b] 31 (11)[c]	24 (4) 34 (5) 38·4(10)[b]	35·3(10)[b]	34 (1) 30 (3) 29·4 (8) 23 (2) 23 (6) 26 (9)
trans-Stilbene	8 (7) < 3·0 (10)			6·4(10)[b]	12 (1) 5·7 (4) 8·2 (8) 6 (2) 13 (5) 4 (12) 8 (3) 6·9 (6)
para-Terphenyl	12 (7) 4·5 (10)			5·0(10)[b]	6 (3)
Diphenylacetylene	7 (7) 3·5 (10)	5·4 (10)[b]			4 (3) 6·9 (8)

[a], [b], [c] Crystal Sizes: [a] $\frac{1}{2}$" diam. × $\frac{1}{4}$"; [b] $\frac{13}{16}$" diam. × $\frac{1}{2}$"; [c] 1 cm² × 1 mm

References

(1) HOFSTADTER *et al.* (1950)
(2) POST & SHIREN (1950)
(3) LIEBSON *et al.* (1950)
(4) LUNDBY (1950)
(5) ELLIOT *et al.* (1950a)
(6) BITTMAN *et al.* (1952)
(7) SANGSTER (1952)
(8) PHILLIPS & SWANK (1953)
(9) HANLE & JANSEN (1954)
(10) SWANK & BUCK (1955)
(11) WRIGHT (1956)
(12) SINGER *et al.* (1956)

(i) excitation of solvent molecules;

(ii) transfer of excitation energy between solvent molecules together with primary quenching;

(iii) trapping of excitation energy by the solute molecules;

(iv) emission or quenching in the solute.

The concentration dependence of liquid scintillator characteristics (especially efficiency) arises from the concentration dependence of stages (iii) and (iv).

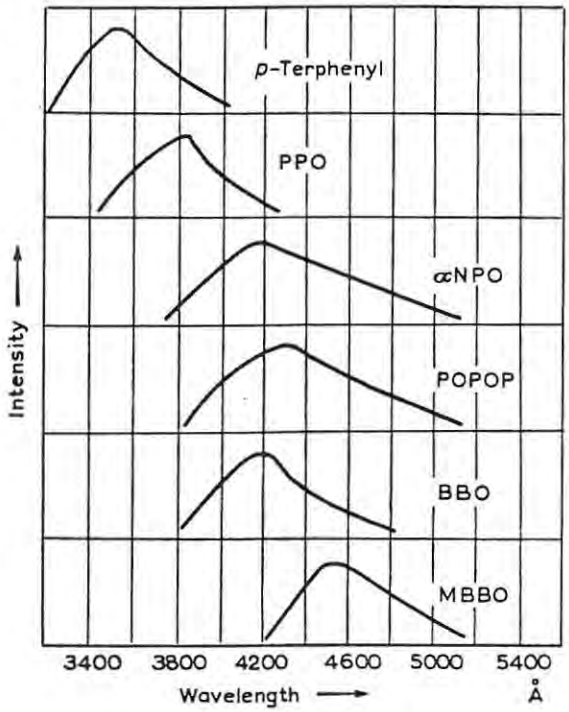

Fig. 11. Emission spectra of scintillator solutions in toluene (excited by gamma rays).

Because the trapping probability, (iii), increases with solute concentration, c, the efficiency, η, also increases with c, at low concentrations. At higher concentrations the quenching in (iv) generally increases due to "self-quenching" (KALLMANN & FURST, 1951b); hence η generally reaches a maximum and decreases again as c is further increased. KALLMANN & FURST showed experimentally that this type of η vs. c relationship held for a wide variety of solutions. They also showed, by consideration of the competition between trapping, emission, internal quenching, self-quenching, etc., that η could be expressed (FURST & KALLMANN, 1952);

$$\eta = \frac{Pc}{(Q + c)(R + c)} \tag{11}$$

Table 4. "Phenyloxazole" and "Phenyloxadiazole" Solutes
(after HAYES *et al.*, 1954)

Designation	*Structure*	*Relative* pulse height*	*Solubility in toluene at 25°C (g/litre)*
p-Terphenyl		1·00†	8
PPO	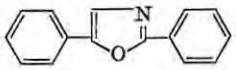	1·06†	270
αNPO	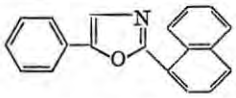	0·96†	75
PBD	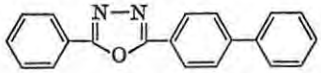	1·28†	> 20
POPOP	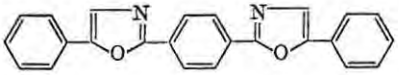	0·86‡	1·2
BBO	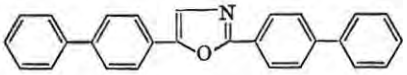	0·86‡	1·4
MBBO	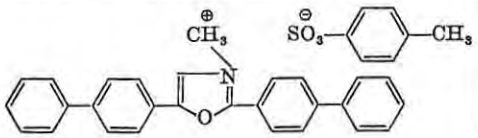		

Designations: PPO, 2, 5 diphenyloxazole;
αNPO, 2-(1-naphthyl)-5-phenyloxazole;
PBD, 2-phenyl-5-(4-biphenylyl)-1, 3, 4-oxadiazole;
POPOP, 1, 4-bis 2-(5-phenyloxazolyl)-benzene;
BBO, 2, 5-di-(4-biphenylyl)-oxazole;
MBBO, 2, 5-di-(4-biphenylyl)-3 methyloxazolium p-toluenesulphonate.

* *Conditions:* (1) Volume 1 ml; (2) Aluminium reflector; (3) DuMont 6292 Photomultiplier; (4) For Cs^{137} electrons.
† For 3 g/litre solution in toluene.
‡ For 1 g/litre solution in toluene.

can be used to best advantage where the energy transfer from primary solvent to solute would otherwise be inefficient and that the main conditions for their effective use are that there should be efficient transfer of energy to and from themselves. Naphthalene appears to be the most useful of the secondary solvents

1953), PPO (PRINGLE *et al.*, 1953), BBO, MBBO (HAYES *et al.*, 1954) and POPOP (OTT *et al.*, 1955). Complete shifting of the scintillation spectrum to

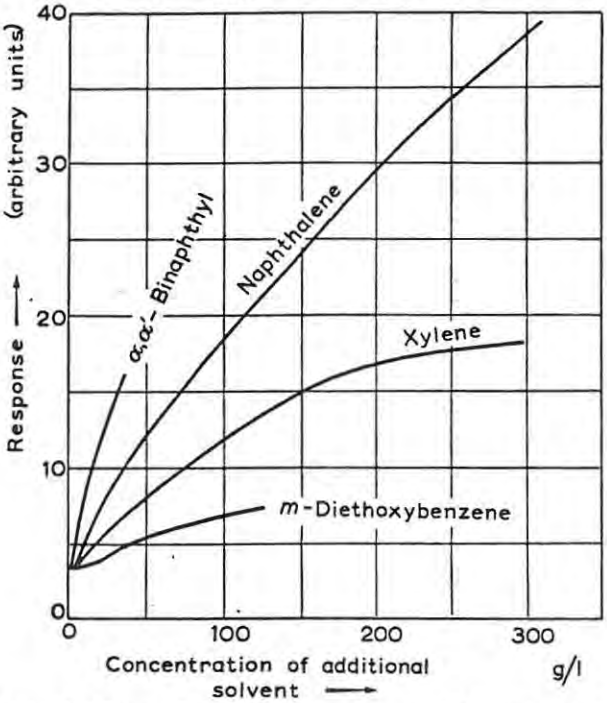

Fig. 13. Effects of additional "solvents" on the response of the system *n*-butylphosphate + 9, 10-diphenylanthracene (0·5 g/litre) to gamma-rays.

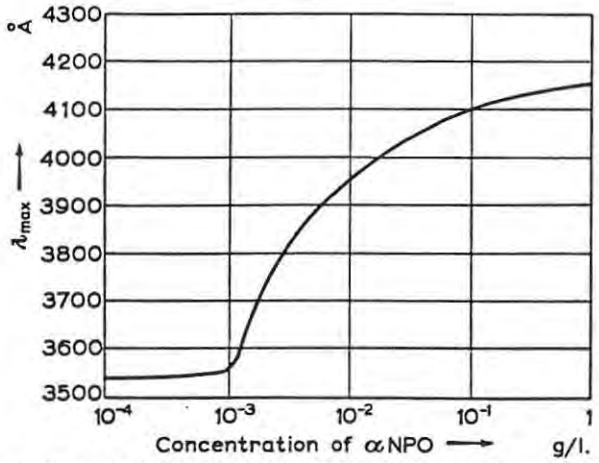

Fig. 14. Wavelength shifting with α NPO in 6 g/litre terphenyl in toluene.

that of the secondary solute is accomplished with very small secondary solute concentrations ($\simeq$ 0·1 g/litre) as, for example, HAYES *et al.* (1954) have demonstrated for α NPO in 6 g/litre terphenyl in toluene (Fig. 14); thus the low

To conclude this discussion of the efficiencies of liquid scintillators it is perhaps of interest to recall a very useful paper by GARWIN (1952) on the design of liquid scintillator cells. GARWIN notes especially that phenylcyclohexane + terphenyl + diphenylhexatriene solutions can be used without risk of poisoning in lucite containers (cemented by acetic acid) and also gives details regarding the design and construction of "light pipes" to give both efficient and *uniform* light collection.

Non-linearity of response—Little detailed information is available on the non-linearity characteristics of liquid scintillators. However, REYNOLDS (1952) has

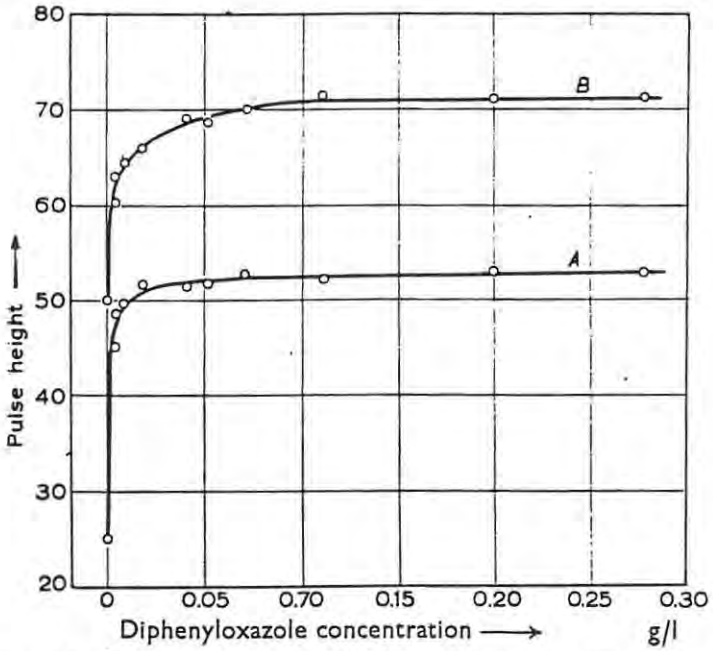

Fig. 15. Pulse height vs. PPO concentration curves for xylene + *p*-terphenyl (3 g/litre) + PPO solutions, showing effects of oxygen quenching. Curve A: unbubbled solutions. Curve B: solution through which nitrogen was bubbled. Pulse heights are for Cs^{137} gamma rays.

determined that the alpha-to-beta ratio for solutions of terphenyl in toluene decreases with decreasing terphenyl concentration, from 0·09 at 5 g/litre to 0·06 at 0·2 g/litre. Most liquid scintillators would appear to show similar non-linearity characteristics according to FURST & KALLMANN (1952) and HARRISON (1952); hence their relative responses to different particles and energies are probably similar to that of anthracene crystals, shown in Fig. 9.

Scintillation lifetimes—The scintillation lifetimes of liquid scintillators for gamma-ray excitation are mostly of the order 3 mμsec or less, close to the lower limit of measurement, set by the transit time spreads of the fastest modern photomultipliers. Pulsed photomultiplier techniques (Section 3*d*) are probably the most suitable for measuring lifetimes of this order. Two independent

Useful methyl borate loaded liquid scintillators have been described by MUEHLHAUSE & THOMAS (1953) and BOLLINGER (1955); both used equal volumes of methyl borate and scintillator solvent (phenylcyclohexane and toluene respectively) and the former used a solute combination of either terphenyl (4 g/litre) + diphenylhexatriene (8 mg/litre) or PPO (4 g/litre) + diphenylhexatriene (16 mg/litre), while the latter used PBD (4 g/litre) + POPOP (20 mg/litre). For an enriched methyl borate (70% B^{10}) loading and a 2·5 cm scintillator thickness, BOLLINGER (1955) quotes a mean neutron capture time of 0·4 μsec and a detection efficiency $\simeq$ 40% for 1 keV neutrons. Practical limitations which affect the detector arise from the small response of the

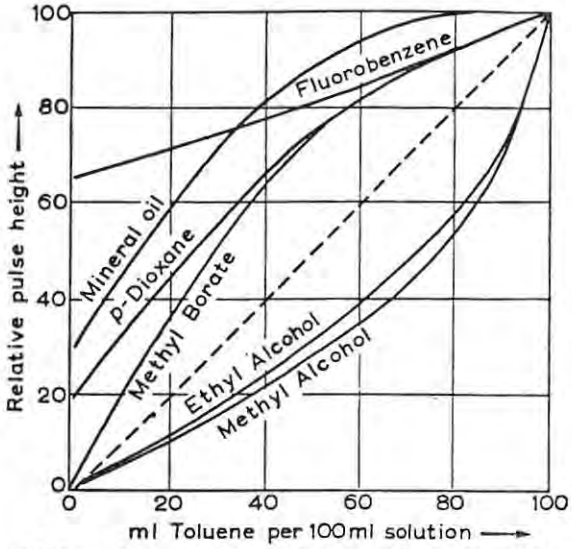

Fig. 16. Relative pulse heights (for Cs^{137} electrons) for 3 g/litre PPO solutions in toluene mixed with various less efficient solvents.

scintillator to the "heavy" Li^7 and alpha particles; for scintillators a few cm thick all or most of the 0·48 MeV gamma-ray energy will generally escape so that the neutron is detected by a pulse equivalent to $\sim$ 0·2 MeV of electron energy. This demands effective discrimination against photomultiplier noise pulses and makes pulse height discrimination against gamma-ray background difficult.

Boron has also been successfully loaded into liquid scintillators in the form of triborine-triamine ($B_3N_3H_6$), or borazole, by KIRKBRIDE (1953) and HOOVER & DOHNE (1954). The striking fact about this compound is its similarity to benzene in structure (a hexagon of alternate B and N atoms instead of 6 C atoms) and absorption spectrum (PLATT *et al.*, 1947). However, the hope that it would be as efficient a scintillator solvent as benzene was not fulfilled. KIRKBRIDE (1955) has suggested that this failure is due to inefficient energy transfer from borazole to solutes such as terphenyl and that it might be overcome by using a suitable secondary solvent.

activities of loaded isotopes, notably the β emitters C^{14} and H^3 whose spectral end points are 155 and 18 keV respectively. Quick and reliable techniques for estimating C^{14} and H^3 activities are demanded by the widespread use of these isotopes as labelling atoms in the tracer chemistry of organic compounds and the use of C^{14} in radiocarbon dating.

Particular advantages to liquid scintillation techniques are their 4π detection properties (see above) and the fact that solid samples may frequently be dissolved directly in the detecting medium; thus the inconvenience of preliminary processing (e.g. to CO_2 or H_2 for gas counting) and the hazards of contamination during such processing are often avoided and time is saved.

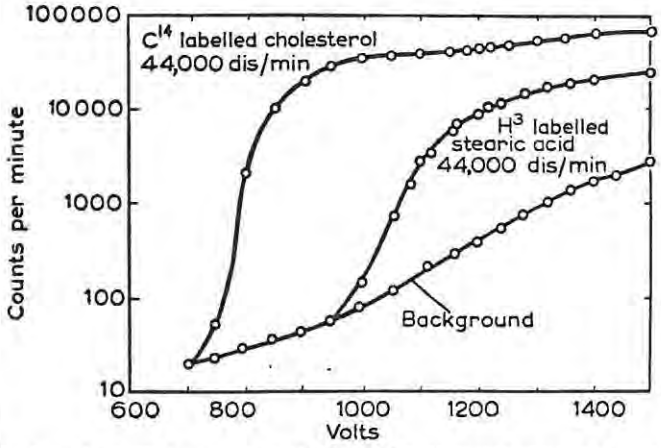

Fig. 18. Liquid scintillator counting of C^{14} and H^3. Counting rates as a function of photomultiplier voltage.

Various methods have been employed to load C^{14} and H^3 labelled compounds into liquid scintillators. The loading is most ideally accomplished when the labelled compound is soluble in an efficient scintillator such as terphenyl-xylene or PPO-toluene and is a diluter rather than a quencher. Many compounds among the steroids and fatty acids fulfil these requirements and fairly large samples of them can be dissolved and counted with high efficiency, e.g. caproic acid (Raben & Bloembergen, 1951), stearic acid and cholesterol (Hayes & Gould, 1952; Rosenthal & Anger, 1954). Results obtained by Rosenthal & Anger, using a DuMont type K-1177 photomultiplier and a xylene-terphenyl (1·9 g/litre)-diphenylhexatriene (0·02 g/litre) scintillator operating at $-10°C$, are shown in Fig. 18; they estimated that their apparatus could resolve $1{\cdot}8 \times 10^{-11}$ curie of C^{14} in cholesterol and $4{\cdot}3 \times 10^{-10}$ curie of H^3 in stearic acid.

Labelled compounds which are insoluble in the most efficient solvents (xylene, toluene, or phenylcyclohexane) present a bigger loading problem. Sometimes these may be dissolved in a diluter which *is* soluble in the efficient solvents. Hayes & Gould (1952), for example, determined H^3 activities in tritium water by making a diluter of 95% ethyl alcohol (5% HTO) and adding this (1 part

series of collisions to recoil protons or electrons respectively and thus eventually to the scintillation process. A scintillation pulse height proportional to energy may thus be obtained for photons but not, in general, for neutrons, due to the non-linear response of the scintillator to protons.

Probably one of the first large liquid scintillators designed to operate on the total energy absorption principle outlined above was the high-energy gamma-ray spectrometer described by CLELAND and KOCH (1952); they used a solution of xylene-terphenyl 48 in. long × 7 in. diameter viewed by sixteen RCA 5819 photomultipliers. FOOTE and KOCH (1954) have recently given further information about this instrument. Using the Monte Carlo sampling method they calculated that escape of secondary energy from the counter would limit its resolution, for photons entering along its axis, to about 10% at 5 MeV and 7% or less from 15 to 35 MeV. The resolution obtained in practice was about 10% above 15 MeV and became rapidly poorer below this energy; this appeared to be largely due to non-uniform light collection. FOOTE and KOCH suggest that their liquid counter could be improved in design and that it may prove useful above 15 MeV or where its inherent fast response is desired; for the lower energy region (to $\gtrsim$ 100 keV) it does not compare with the NaI (Tl) crystal spectrometer (5 in. diameter × 8 in. long) described by them (see also KOCH and FOOTE, 1954).

Large liquid scintillators for counting photons in the higher energy range ($>$ 50 MeV) have been described by PUGH *et al.* (1954), and THRESHER *et al.* (1955). PUGH *et al.* have described a counter for 50 to 150 MeV photons which uses a liquid scintillator (16 in. diameter × 30 in. long) to detect electron pairs produced in a lead converter (0·26 cm thick); for their applications they found it necessary to locate and identify photons by means of a telescope, the liquid scintillator then serving to provide an estimate of the photon energy. THRESHER *et al.* (1955) have described a detector of benzene + terphenyl + diphenyl-hexatriene solution, 12·7 cm square × 76 cm long and viewed by six DuMont 6292 photomultipliers. Based on the shower production data of KANTZ and HOFSTADTER (1954) for electrons in carbon they calculate that this counter should give a light output proportional to gamma-ray energy for energies less than 180 MeV; they also quote an efficiency of about 50% and a line width of about 10% for 100 MeV photons.

Scintillators for fast neutron counting have been described by MUEHLHAUSE (1953) and THRESHER *et al.* (1955). MUEHLHAUSE uses a cylinder (16 in. diameter × 16 in. long) of methyl borate + toluene (1:1) + PPO + αNPO, viewed by twenty-five 5819 photomultipliers. A fast neutron ($\sim$ 0·1 to 10 MeV) is identified by the "double-pulse method" (MUEHLHAUSE and THOMAS, 1953), that is by a recoil proton scintillation followed, within a few microseconds, by a second scintillation, associated with the reaction of the moderated neutron with a B^{10} nucleus. THRESHER *et al.*, have described two large scintillators for counting neutrons of $\sim$ 100 MeV; one, of dimensions 7·6 × 14 × 44·5 cm for neutron-scattering experiments and the other, 25 cm diameter × 25 cm long, for bad geometry attenuation experiments. Both counters achieve

Carlo calculations of the neutron capture rate in scintillators containing different amounts of Cd. The theoretical distribution obtained for a solution containing 0·003 Cd atoms per H atom is shown in Fig. 19 together with experimental data for such a solution. Of primary importance in the development of the large Cd loaded scintillator was its application to the detection of the free neutrino, presumed to interact with a proton to produce a positron of a few MeV and a neutron of a few keV energy. Such a decay would produce delayed coincidences with a time-delay and second pulse size similar to those produced by fast neutrons. Further large scintillators which COWAN, REINES *et al.*, have developed for neutrino detection are described elsewhere in this volume.*

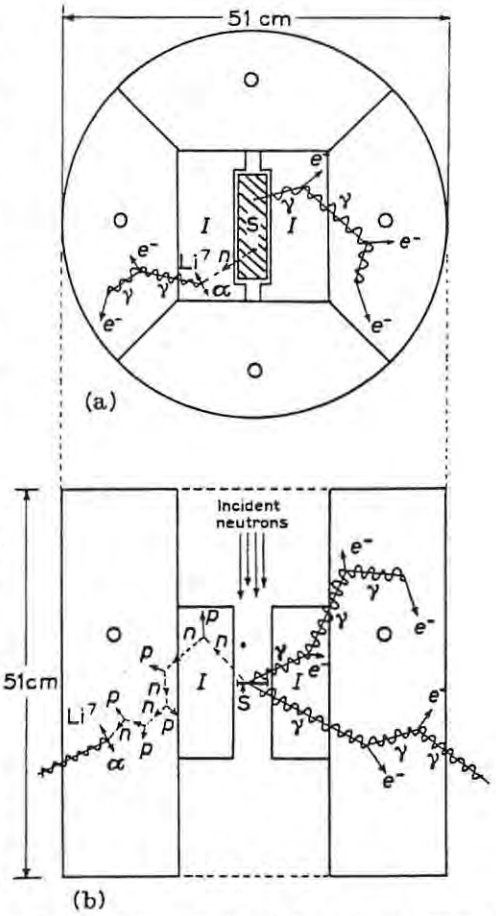

Fig. 20. Schematic diagram of the "Argonne counter" (BOLLINGER, 1955):
(*a*) End view. (*b*) Top (or side) view.
I = "inner" counters containing 3·5% B^{10}
O = "outer" counters containing 0·25% B^{10}
S = sample

Cadmium-loaded scintillators of similar design to the above, have also been employed in studies of neutrons from spontaneous and neutron-induced fission (HICKS *et al.*, 1955; see also BOLLINGER, 1955). In these experiments the fission source is a conventional gas ionization fission counter placed at the centre of the scintillator in an open axial channel. Pulses from the fission counter trigger an oscilloscope sweep on which the random capture pulses of individual fission neutrons in the scintillator are displayed.

BOLLINGER (1955) has described a system of large liquid scintillators used in measurements of partial neutron cross-sections for slow neutrons in a time-of-flight spectrometer at Argonne National Laboratory. The arrangement used is shown in plan in Fig. 20, i.e. two inner (I) scintillators containing 3·5% B^{10} and four outer (O) scintillators containing 0·25% B^{10}; eight DuMont 6292 photomultipliers view each O and six view each I scintillator. Different events (i.e. scattering, capture or fission) in the

* Article by B. W. RIDLEY.

some of the special applications of plastic scintillators after discussing their characteristics.

(*a*) *Characteristics*

Efficiencies and scintillation spectra—As with liquid solutions a principal aim in the development of plastic solutions has been to obtain scintillators of high efficiency. From the earliest studies it was evident that plastic solutions showed an efficiency, η vs. concencentration, c, dependence similar to that found in liquids (Koski, 1951). It was also evident that η depended on the method of preparation of the scintillator as well as its contents. Schorr & Torney (1950) tested three different methods for preparing plastic solutions of *p*-terphenyl in polystyrene, namely: (1) mixing the terphenyl in molten polystyrene; (2) polymerizing a solution of terphenyl in styrene with a benzoyl peroxide catalyst (0·1% to 1%) and (3) polymerizing without the catalyst. Useful products were obtained by all three methods, but the solution prepared by method (2) was the best scintillator; Schorr & Torney suggested that the other solutions might have suffered from the rather prolonged heating which methods (1) and (3) involved.

Methods that have subsequently been used to prepare plastic scintillators are essentially variations, modifications or extensions of one or other of the three methods described above. Method (2) has proved very popular, especially since Pitchat *et al.* (1951, 1953) showed it could be used to prepare scintillators from 1,1,4,4-tetraphenyl-1,3-butadiene (TPB) which they found to be very efficient. Bulk polymerization methods (i.e. (2) and (3)) are, however, unsatisfactory for preparing solutions of some other potentially useful solutes such as 1,6-diphenylhexatriene (DPH) and 1,4-diphenylbutadiene (DPB). This is due to mutual interference between these solutes and the polymerization process. Carlson & Koski (1952) have reported that DPH reacts with styrene during polymerization; they found that it slowed down the polymerization process, that its emission spectrum shifted to shorter wavelengths and that the efficiency of the solid scintillator was very small. Similar, though less marked, effects were observed by Pitchat *et al.* (1953) in DPB-polystyrene. DPH and DPB solutions prepared by type (1) methods, e.g. by pressure moulding (Eichholz & Horwood, 1952) or by "slow" injection moulding (de Waard *et al.*, 1954) are much more efficient than those prepared by bulk polymerization. de Waard *et al.* (1954) have reported that moulded DPB-polystyrene has an efficiency $\simeq$ 93% that of the polystyrene solution of TPB, the most efficient plastic scintillator solute known.

Buck & Swank (1953) have described techniques and methods for preparing plastic scintillators from styrene and vinyltoluene solutions (by method (3) above). They have also carried out extensive tests and comparisons on a variety of scintillators; these are described in the above paper and in another paper by Swank & Buck (1953). Some of their data are reproduced in Figs. 21 and 22. Fig. 21 shows the dependence of pulse height (i.e. efficiency) on solute concentration for different solutes in polystyrene and polyvinyltoluene; the pulse

comparatively low efficiency of DPB is presumably due to decomposition of DPB molecules during the polymerization of the solution, as described above. Based on similar considerations to those which led FURST & KALLMANN (1952) to formulate eq. (11), SWANK & BUCK (1953) have derived a relation between η and c for plastic scintillators, namely:

$$\eta = \eta_0 \frac{(q_0 + \sigma c)}{(1 + \sigma c)} \frac{(1)}{(1 + mc)} \tag{13}$$

Here σ is a constant determined by the properties of the solute and solvent, $(1 + mc)^{-1}$ describes the "self-quenching" of the solute and q_0 is the quantum

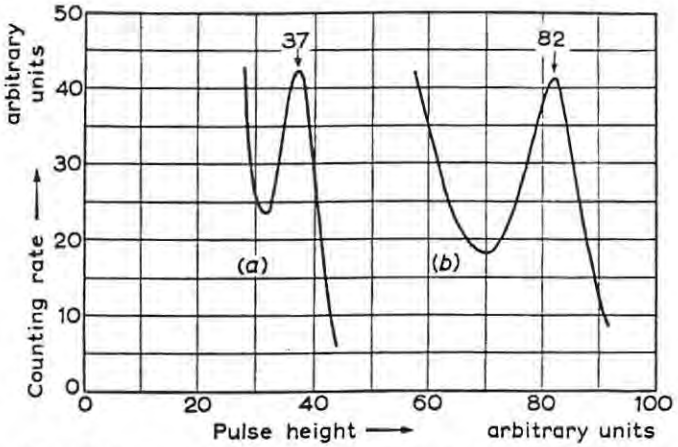

Fig. 23. Differential pulse height distributions obtained with a Cs^{137} source, RCA 5819 photomultiplier and: (a) A plastic scintillator (4% p-terphenyl + 0·02% TPB in polyvinyltoluene). (b) An anthracene crystal. Both scintillators were cylinders $\frac{13}{16}$" in diameter and $\frac{1}{2}$" long.

efficiency of the solvent. η_0 denotes the theoretical limiting efficiency at high c, in the absence of self-quenching ($m = 0$). Except for the addition of the term q_0, (13) is identical to (11); the reason for this difference is of course that q_0 is much larger for polystyrene than for liquid solvents, hence radiative transfer cannot be neglected in plastics whereas it may be in liquids.

SWANK & BUCK found that by proper adjustment of parameters eq. (13) could be made to fit all their experimental curves (Fig. 21); they also noted agreement with the theory in that this adjustment gave the same value for q_0 for all systems having the same solvent; $q_0 = 0{\cdot}16$ for polystyrene and 0·21 for polyvinyltoluene. It is also of interest to note that THORNTON (1954) has pointed out that eq. (13) may be derived from the theory of JOHNSON & WILLIAMS (1950) (cf. eq. (12)).

Secondary solutes or spectrum shifters have as important applications in plastic solutions as they have in liquids. Diphenylhexatriene has rather limited uses in plastics because of its instability during polymerization; however, EICHHOLZ & HORWOOD (1952) have noted that it is a useful spectrum shifter in scintillators prepared by pressure moulding. TPB has been widely applied as a

efficient plastic solutions, such as those listed in Table 7. BORELI and GRIMELAND (1955) have studied the response of a TPB-polystyrene plastic to gamma-rays, alpha-particles and 2·5 MeV neutrons; they found the plastic slightly more nonlinear than an anthracene crystal. Evidence of variation of the alpha-to-beta ratio with solute concentration may be found in the efficiency, η, vs. concentration, c, data of SWANK and BUCK (1954). They have given η vs. c curves for several solutes excited by electrons (Fig. 21) and by alpha-particles; for any given solute, different shaped curves were obtained for the two types of particle and, in general, the difference indicated that the alpha-to-beta ratio decreased with decreasing c, as in liquid solutions. Within a reasonable degree of accuracy, however, the relative responses of the more efficient plastic solutions to different particles and energies may be taken to be the same as for anthracene crystals, that is as in Fig. 9.

Scintillation Lifetimes

The scintillation lifetimes of plastic scintillators, excited by gamma-rays, tend, like those of liquid scintillators, towards the present lower limit of measurement of a few mμsec. Some values which SWANK and BUCK (1955) have given for solutions of 4% terphenyl in polyvinyltoluene ($\frac{1}{16}$ in. diam. × $\frac{1}{2}$ in. long) are; $\leqslant$ 3·0 mμsec for this solution alone; 4·0 mμsec for the solution incorporating, in addition, 0·02% TPB as secondary solute; 3·0 mμsec with 0·1% diphenylstilbene. SINGER *et al.* (1956) determined a scintillation lifetime of 2·2 $\pm$ 0·3 mμsec for a plastic of polystyrene + terphenyl (1%) + αNPO (0·3%) + zinc stearate (0·01%). It is also of interest to note that the plastics, like crystals and unlike liquids, emit a small proportion of their light with decay times of microseconds or more (HARRISON, 1954); furthermore this proportion increases with decreasing temperature and is smaller for more heavily ionizing particles (ROZMAN, 1955).

Stability under Ionizing Radiations

HINRICHS (1954) has reported studies of the light outputs of various polystyrene solutions under continuous electron irradiation. He found a range of effects in different solutions, e.g. for a 2% anthracene solution he found that the light output increased and correlated this with changes in its spectral distribution. In other solutions there were no significant spectral changes and a decrease in output occurred (Fig. 24), such that the output intensity, I, was related to the total number of electrons absorbed per cm^2, N, by:

$$I = (I_0 - I') \exp.(-\alpha N) + I' \qquad (14)$$

where I_0 represents an initial intensity, I' a limiting intensity reached after considerable irradiation and α is a "damage-coefficient" characteristic of the solute and its concentration. The behaviour of the DPB solution (Fig. 24) is interesting in that its I vs. N relationship has two distinct phases with different values of α. Although no generalization may yet be accepted, the common plastic scintillators might be expected to behave like the solutions represented

combination which he recommends is terphenyl (2·5%) + TPB (0·03%) + zinc stearate (0·01%) (mould release agent). WOUTERS suggests that this technique might, in its limit, produce a scintillator some 6 ft × 2·5 ft × 1 ft.

The chief advantages of the plastic scintillators would appear to be their general ruggedness, ease to machine to desired shapes and their short scintillation lifetimes. Their ease to shape makes them especially suitable for devices such as the "phoswich," or phosphor sandwich (see WILKINSON, 1952), and the multiple scintillator arrangement designed by MCCRARY *et al.* (1954) to reduce gamma-ray sensitivity when counting fast neutrons. In the latter device,

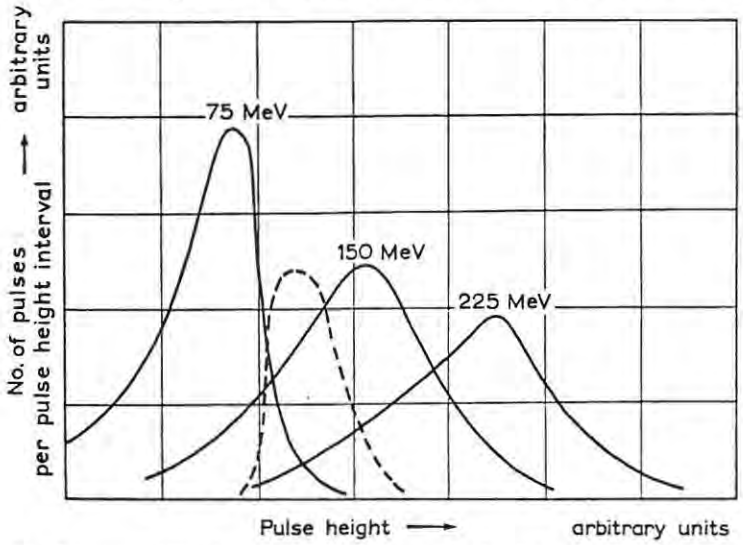

Fig. 25. Response of "laminated counter" (PUGH *et al.*, 1954) to monoenergetic electrons and to μ mesons.
—— monoenergetic electrons
– – – cosmic ray μ mesons.

which is also discussed by BOLLINGER (1955), a number of spherical scintillators (plastic or crystal) are immersed in a non-hydrogeneous, optically inert material, such as glass or trifluorochloroethylene. The sphere diameters and spacings are so chosen that the secondary electrons from gamma-rays dissipate most of their energy in the inert medium whereas recoil protons are generated and mainly stopped in the spheres and therefore give larger pulses. A high efficiency is obtained which is also strongly dependent on neutron energy and the sphere diameter.

PUGH *et al.* (1954) have described a high energy (>50 MeV) gamma-ray counter which uses plastic scintillators machined to discs of 8 in. diameter × 0·100 in. thick. The counter, which is 8 in. long, consists of fifty of these discs separated by forty-nine 0·047 in. discs of lead; the lead is used to develop a shower which is sampled by the scintillator. Light collection depends on total internal reflections in the scintillator discs, the light being collected, integrated and piped to photomultipliers from plastic corner pieces attached to their perimeters.

BREITENBERGER, E.	1955	*Progr. Nucl. Phys.* **4**, 56.
BUCK, W. L. and SWANK, R. K. . .	1953	*Nucleonics* **11**, No. 11, 48.
CARIO, G. and FRANCK, J. . . .	1923	*Z. Physik* **17**, 202.
CARLSON, T. and KOSKI, W. S. . .	1952	*Phys. Rev.* **85**, 697.
CHOU, C. N.	1952a	*Phys. Rev.* **87**, 904.
	1952b	*Phys. Rev.* **87**, 376.
CLELAND, M. R. and KOCH, H. W. .	1952	*Nucleonics* **10**, No. 3, 41.
COHEN, S. G. and WEINRIB, A. . .	1954	*Phys. Rev.* **93**, 1117.
COLGATE, S. A.	1951	*Rev. Sci. Instr.* **22**, 346.
COLLINS, G. B.	1948	*Phys. Rev.* **74**, 1542.
COWAN, C. L., REINES, F., HARRISON, F. B., ANDERSON, E. C. and HAYES, F. N.	1953	*Phys. Rev.* **90**, 493.
CURRAN, S. C.	1953	*Luminescence and the Scintillation Counter* (London).
DE WAARD, H. and MARTINI, J. E. P. .	1952	*Physica* **18**, 647.
DE WAARD, H., PRINS, W. and PRINS, A.	1954	*Appl. Sci. Res.* B, **3**, 372.
DEWAR, M. J. S. and LONGUET-HIGGINS, H. C.	1954	*Proc. Phys. Soc.* A, **67**, 795.
DEXTER, D. L.	1953	*J. Chem. Phys.* **21**, 836.
EICHHOLZ, G. G. and HORWOOD, J. L. .	1952	*Rev. Sci. Instr.* **23**, 305.
ELLIOT, J. O., LIEBSON, S. H., MYERS, R. D. and RAVILIOUS, C. F. . .	1950a	*Rev. Sci. Instr.* **21**, 631.
ELLIOT, J. O., LIEBSON, S. H. and RAVILIOUS, C. F.	1950b	*Phys. Rev.* **79**, 393.
FARMER, E. C. and BERSTEIN, I. A. .	1952	*Science* **115**, 460.
FOOTE, R. S. and KOCH, H. W. . .	1954	*Rev. Sci. Instr.* **25**, 746.
FORSTER, L. S. and LIVINGSTON, R. .	1952	*J. Chem. Phys.* **20**, 1315.
FÖRSTER, T.	1947	*Ann. Physik* **2**, 55.
	1949	*Z. Electrochem.* **53**, 93.
	1951	*Fluoreszenz Organischer Verbindungen* (Göttingen).
FOWLER, J. M. and ROOS, C. E. . .	1955	*Phys. Rev.* **98**, 996.
FRANCK, J. and LIVINGSTON, R. . .	1949	*Rev. Mod. Phys.* **21**, 505.
FRANZEN, W., PELLE, R. W. and SHERR, R.	1950	*Phys. Rev.* **79**, 742.
FREY, H. B., GRIM, W. M., PRESTON, W. M. and GRAY, T. S. . . .	1951	*Phys. Rev.* **82**, 372.
FRENKEL, J. I.	1931	*Phys. Rev.* **37**, 17 & 1276.
FRIEDEL, R. A. and ORCHIN, M. . .	1951	Ultraviolet Spectra of Aromatic Compounds (New York).
FURST, M. and KALLMANN, H. . .	1952	*Phys. Rev.* **85**, 816.
	1953	*Phys. Rev.* **89**, 912.
	1954a	*Phys. Rev.* **94**, 503.
	1954b	*Phys. Rev.* **96**, 902.
	1955a	*J. Chem. Phys.* **23**, 607.
	1955b	*Phys. Rev.* **97**, 583.
FURST, M., KALLMANN, H. and BROWN, F. H.	1955	*Nucleonics* **13**, No. 4, 58.
FURST, M., KALLMANN, H. and KRAMER, B.	1953	*Phys. Rev.* **89**, 416.
GARLICK, G. F. J.	1952	*Progr. Nucl. Phys.* **2**, 51.
GARLICK, G. F. J. and WRIGHT, G. T. .	1952	*Proc. Phys. Soc.*, B, **65**, 415.
GARWIN, R. L.	1952	*Rev. Sci. Instr.* **23**, 755.

LIEBSON, S. H., BISHOP, M. E. and ELLIOT, J. O.	1950	*Phys. Rev.* **80**, 907.
LUNDBY, A.	1950	*Phys. Rev.* **80**, 477.
MCCRARY, J. H., TAYLOR, H. L. and BONNER, T. W.	1954	*Phys. Rev.* **94**, 808.
MILTON, J. C. D. and FRASER, H. S.	1954	*Phys. Rev.* **96**, 1508.
MUEHLHAUSE, C. O.	1950	*Phys. Rev.* **79**, 277.
	1953	BNL Report 242 (T-38).
MUEHLHAUSE, C. O. and THOMAS, G. E.	1952	*Phys. Rev.* **85**, 926.
	1953	*Nucleonics* **11**, No. 1, 44.
OTT, D. G., HAYES, F. N., HAMMEL, J. E. and KEPHART, J. F.	1955	*Nucleonics* **13**, No. 5, 62.
PHILLIPS, H. B. and SWANK, R. K.	1953	*Rev. Sci. Instr.* **24**, 611.
PITCHAT, L. and KOECHLIN, Y. J.	1951	*J. Chim. Phys.* **48**, 225.
PITCHAT, L., PESTEIL, P. and CLEMENT, J.	1953	*J. Chim. Phys.* **50**, 26.
PLATT, J. R., KLEVENS, H. B. and SCHAEFFER, G. W.	1947	*J. Chem. Phys.* **15**, 598.
POPLE, J. A.	1955	*Proc. Phys. Soc.*, A, **68**, 81.
POST, R. F.	1950	*Phys. Rev.* **79**, 735.
	1952	*Nucleonics* **10**, No. 6, 56.
POST, R. F. and SHIREN, N. S.	1950	*Phys. Rev.* **78**, 81.
PRINGSHEIM, P.	1949	*Fluorescence and Phosphorescence* (New York).
PRINGLE, R. W., BLACK, L. D., FUNT, B. L. and SOBERING, S.	1953	*Phys. Rev.* **92**, 1582.
PRINGLE, R. W., TURCHINETZ, W. and FUNT, B. L.	1955	*Rev. Sci. Instr.* **26**, 859.
PUGH, G. E., FRISCH, D. H. and GOMEZ, R.	1954	*Rev. Sci. Instr.* **25**, 1124.
RABEN, M. S. and BLOEMBERGEN, N.	1951	*Science* **114**, 363.
REINES, F., COWAN, C. L., HARRISON, F. B. and CARTER, D. S.	1954	*Rev. Sci. Instr.* **25**, 1061.
REYNOLDS, G. T.	1952	*Nucleonics* **10**, No. 7, 46.
REYNOLDS, G. T., HARRISON, F. B. and SALVANI, G.	1950	*Phys. Rev.* **78**, 488.
ROBINSON, W. H. and JENTSCHKE, W.	1954	*Phys. Rev.* **95**, 1412.
ROSENTHAL, D. J. and ANGER, H. O.	1954	*Rev. Sci. Instr.* **25**, 670.
ROZMAN, I. M.	1955	Soviet Physics JETP **1**, 185.
SANGSTER, R. C.	1952	*M.I.T. Technical Report*, No. 55.
SCHMILLEN, A.	1953	*Z. Physik*, **135**, 294.
SCOTT, K. T. B., HUTCHINSON, S. K. and LAPAGE, R.	1952	A.W.R.E. Report, No. 0-4/53.
SCHORR, M. G. and TORNEY, F. L.	1950	*Phys. Rev.* **80**, 474.
SINGER, S., NEHER, L. K. and RUEHLE, R. A.	1956	*Rev. Sci. Instr.* **27**, 40.
SWANK, R. K.	1954a	*Ann. Rev. Nucl. Sci.* **4**, 111.
	1954b	*Nucleonics* **12**, No. 3, 14.
SWANK, R. K. and BUCK, W. L.	1953	*Phys. Rev.* **91**, 927.
	1955	*Rev. Sci. Instr.* **26**, 15.
TAYLOR, C. J., JENTSCHKE, W. K., REMLEY, M. E., EBY, F. S. and KRUGER, P. G.	1951	*Phys. Rev.* **84**, 1034.

FIGURE REFERENCES

FIG. 18. From ROSENTHAL, D. J. and ANGER, H. O., *Rev. Sci. Instr.* **25,** 670 (1954).

FIG. 19. From HARRISON, F. B., COWAN, C. L. and REINES, F., *Nucleonics* **12,** No. 3, 24 (1954).

FIG. 20. Composed from data given by L. M. BOLLINGER, International Conference on the Peaceful Uses of Atomic Energy, Geneva, 1955; A/CONF. 8/P/580.

FIGS. 21, 22, 23. From BUCK, W. L. and SWANK, R. K., *Nucleonics* **11,** No. 11, 48 (1953).

FIG. 24. From HINRICHS, H., *Zeit. Naturforsch.* **9a,** 625 (1954).

FIG. 25. From PUGH, G. H. *et al.*, *Rev. Sci. Instr.* **25,** 1124 (1954).

F.D. Brooks
Scintillation counters with pulse shape selection to distinguish neutrons from gamma-rays
Liquid Scintillation Counting, ed. C.G. Bell and F.N. Hayes (Pergamon, New York, 1958) 268-269

Reprinted from "Liquid Scintillation Counting" 1958
PERGAMON PRESS: NEW YORK · LONDON · PARIS · LOS ANGELES

SCINTILLATION COUNTERS WITH PULSE SHAPE SELECTION TO DISTINGUISH NEUTRONS FROM GAMMA-RAYS

F. D. BROOKS
Atomic Energy Research Establishment, Harwell, England

FOLLOWING a paper by G. T. WRIGHT[1] concerning scintillation pulse shapes and decay times of organic crystals, scintillation counters have been developed which distinguish alpha-particles or neutrons from gamma-rays by pulse shape selection. Wright reported that the shapes of anthracene scintillation pulses are different when excited by alpha-particles and gamma-rays respectively. A similar property has been found in other organic scintillators and when fast neutrons (i.e. recoil protons) are substituted for alpha-particles; the counters developed here use this property to discriminate promptly between different types of particle. Efficient discrimination is obtained using anthracene, stilbene or quaterphenyl crystals and various liquid scintillators.

The pulse shape selection is effected by deriving two output pulses per scintillation from the last dynodes in the photomultiplier. In one channel the scintillation current pulse is integrated to produce a pulse height, h, proportional to the total light output. In the other channel the scintillation current is passed through a network of non-linear response and then integrated; consequently the pulse height, h_c, produced in this channel depends on the scintillation pulse shape as well as on the total light output. For a given h, h_c is smaller when the decay time of the scintillation pulse is longer.

Differences in pulse shape may be demonstrated by applying the h and h_c pulses to the X and Y plates respectively of a cathode-ray tube. The CRT-trace is brightened only while the applied pulses are at their peak values, hence each scintillation registers as a point (h, h_c) on the CRT screen. Similarly a series of scintillations of different light outputs (e.g. a Compton distribution) form a locus on the screen. For example with a Co^{60} gamma source and a 1 in^3 stilbene crystal a single continuous locus is obtained (Fig. 1). Using the same crystal and a Po–Be (gamma + neutron) source two distinct loci are obtained (Fig. 2), the upper locus coincides with that in Fig. 1 and the lower one is attributed to recoil proton scintillations. In practical applications one requires to select pulses on either the 'neutron locus' or the 'gamma locus' only; this may be done by using a simple electronic circuit which operates directly from the h and h_c information.

Crystal, liquid and plastic scintillators have been investigated with respect to their suitability for pulse shape discriminators of this type. The dependence

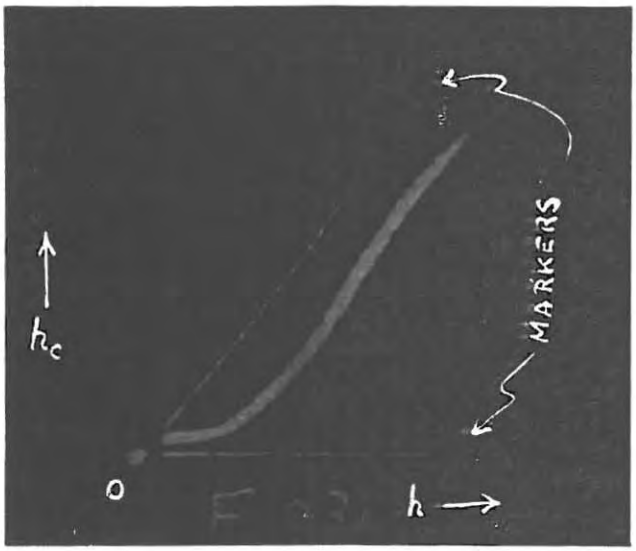

Fig. 1. Co^{60} source γ-rays.

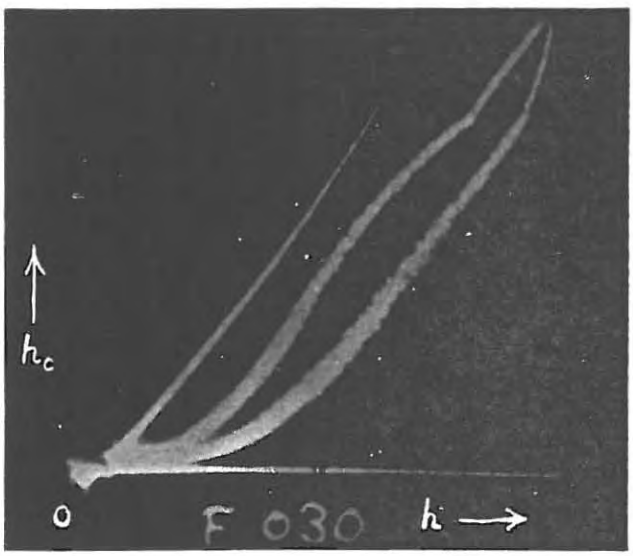

Fig. 2. Po–Be source γ-rays and neutrons.

facing page 268

F.D. Brooks
A scintillation counter with neutron and gamma-ray discriminators
Nucl. Instr. and Meth. 4 (1959) 151-163

NUCLEAR INSTRUMENTS AND METHODS 4 (1959) 151–163; NORTH-HOLLAND PUBLISHING CO.

A SCINTILLATION COUNTER WITH NEUTRON AND GAMMA-RAY DISCRIMINATORS

F. D. BROOKS

U.K.A.E.A. *Research Group, Harwell, Didcot, Berks.*

Received 16 February 1959

Certain organic scintillators, notably anthracene, stilbene and quaterphenyl crystals and oxygen-free liquid scintillators, show an effectively longer scintillation decay time for heavily ionizing particles such as alpha-particles or protons than for electrons. A scintillation counter is described which distinguishes fast neutrons from gamma-rays by means of the different decay times of recoil proton and Compton electron scintillations respectively. Measurements of the proton-electron resolution for different scintillators are described. It is found, for example, that using a one inch thick stilbene crystal, 2 MeV neutrons may be detected with 9.5% efficiency while the detection efficiency for 2 MeV gamma-rays is reduced by decay time discrimination to less than 0.007%. An application of the counter for fission cross section measurements by fission neutron detection is described. The decay time properties of the scintillators are discussed and the longer decay time for protons (or alpha-particles) is interpreted in terms of slow (10^{-7} sec) ion recombination processes in the scintillators; these processes produce a slow component in the scintillation decay and in a proton scintillation the proportion of slow component is more than in an electron scintillation[4]).

1. Introduction

In a scintillation detector the mode of decay and the decay time of the light emission from the scintillator may sometimes be of particular interest; for example when the timing resolution of the instrument is estimated or when the physical processes in the scintillator are the subject of study. These characteristics have recently achieved new prominence following the report by Wright[1]) that scintillations produced by alpha-particles and electrons in anthracene crystals showed decay times of 53 mμsec and 31 mμsec respectively. It was subsequently reported[2]) that other organic scintillators, notably stilbene and quaterphenyl crystals and some liquid scintillators, showed decay time properties similar to those observed in anthracene; although the scintillation decay itself was not studied in detail it was found that the decay times of these scintillators were effectively longer for heavily ionizing particles, such as alpha-particles or protons than for electrons.

This effect has since become the basis of a new type of scintillation counter[2,3,4]) which discriminates promptly and efficiently between protons (or alpha-particles) and electrons and is thus particularly useful for detecting fast neutrons in the presence of gamma-rays. The present paper describes such a counter and its application to nuclear physics experiments. Studies of various scintillators with respect to their suitability for use in the counter are also described and the physical processes responsible for the decay time differences are discussed.

2. Description of the Counter

To achieve a simple practical instrument a photomultiplier circuit is used which delivers an output pulse whose amplitude, h, depends on the *decay time* of the scintillation. The circuit may be adjusted to give zero, or very small, h for one particular decay time, e.g. that for gamma-ray scintillations; in this condition neutron (i.e. recoil proton) scintillations, having a different decay time, each produce a pulse of large h and may be selected by an amplitude discriminator.

[1]) G. T. Wright, Proc. Phys. Soc. B **49** (1956) 358.
[2]) F. D. Brooks, Progress in Nuclear Physics, Ed. O. R. Frisch 5 (Pergamon, London, 1956) 284; Liquid Scintillation Counting, (Pergamon London, 1958), p. 268.
[3]) M. Forte, International Conference on the Peaceful Uses of Atomic Energy, A/CONF. 15/P/1514, Geneva (1958)
[4]) R. B. Owen, I. R. E. Transactions on Nuclear Science, NS-5, No. 3 (1958) 198.

amplitudes which would be obtained at the dynode and anode respectively if R_dC and R_aC were much greater than T_γ. Assuming that the gain, k, between the last dynode and the anode is constant, we may write:

$$V_{oa} = kV_{od} . \quad (4)$$

The shapes and times of maxima of the dynode and anode pulses are different according to eqs. (1) and (2) respectively. However each pulse is stretched by a circuit consisting of a crystal diode and condenser (0.001 μF) so that two pulses of similar shape but opposite polarity are fed to the output terminal, A, of the counter (fig. 1). Ideally the amplitudes of these components are respectively $\phi_d V_{\gamma d}$ and $\phi_a V_{\gamma a}$, where ϕ_d is the constant fraction by which the positive pulse amplitude is reduced between the dynode and A and ϕ_a is that by which the negative pulse amplitude is reduced between the anode and A. The amplitude, h, of the resultant pulse at A is:

$$h = \phi_d V_d - \phi_a V_a . \quad (5)$$

Thus for a gamma-ray scintillation,

$$h_\gamma = \phi_d V_{\gamma d} - \phi_a V_{\gamma a} = \phi_d [0.96 - 0.50 (k\phi_a/\phi_d)] V_{od} . \quad (6)$$

Now ϕ_d is controlled by the potentiometers PR1 and PR3 in fig. 1 and ϕ_a is controlled by PR2 and PR4. We may adjust these potentiometers to make $k\phi_a/\phi_d = 1.92$ thereby making h_γ always zero, irrespective of the value of V_{od}, or the total light in the scintillation. In other words the circuit may be "balanced" to give zero pulse height output at A for all gamma-ray scintillations.

Now consider the response of the balanced circuit to a neutron scintillation of decay time, T_n, where for example, $T_n = 2T_\gamma$. As before we obtain from fig. 2 that $V_{nd} = 0.92\ V_{od}$ and that $V_{na} = 0.37\ kV_{od}$. Thus for a neutron the resultant pulse amplitude, h_n, at A is:

$$h_n = \phi_d (0.92 - 1.92 \times 0.37) V_{od} = 0.21\ \phi_d V_{od} . \quad (7)$$

That is for a neutron a positive output pulse is obtained of amplitude proportional to V_{od} and hence to the total light in the scintillation. This is true in general provided T_n is greater than T_γ.

In practice the circuit behaviour is not exactly, but only qualitatively described by the above analysis, for a number of reasons. Firstly, it is an approximation to describe the scintillation decay as a single exponential (refs.[1,4-7]); this is not true in general for the organic scintillators. Secondly, the photomultiplier current pulse shape will generally vary from the scintillation pulse shape[1]) due to statistical effects, transit time spread and space charge saturation in the multiplier. Thirdly, because space charge saturation may occur between the last dynode and the anode, k is not as assumed in eq. (4), constant but depends on V_{od}. Fourthly, ϕ_d and ϕ_a also depend on V_{od} because the two diodes in the output circuit are characteristically non-linear impedances. However the non-linear effects from the two diodes may be made to cancel one-another out to some extent by selecting a pair with similar resistance-voltage characteristics and adjusting PR1 or PR2 to equalise the pulse amplitudes fed to them. Furthermore, remaining diode non-linearity may be part compensated for by the space charge saturation effect, for whereas ϕ_d and ϕ_a increase as V_{od} increases, k decreases. A dynode voltage distribution may be obtained for which the variation of k compensates that of ϕ_a/ϕ_d so that the product $k\phi_a/\phi_d$ remains constant. The circuit may thus be balanced in terms of eq. (6) over a wide range of V_{od}.

The counter is adjusted to balance with the aid of a cathode ray tube display, obtained as indicated in fig. 3. For this display, an additional output pulse of amplitude, h_0, is obtained from the second last dynode of the photomultiplier, via B in fig. 1. The load time constant at this dynode is long compared with T_γ or T_n hence h_0 is proportional to the total light in the scintillation or to V_{od} in eqs. (6) and (7). The two coincident output pulses from A and B in fig. 1

[5]) H. B. Phillips and R. K. Swank, Rev. Sci. Instr. 24 (1953) 611; R. K. Swank and W. L. Buck, Rev. Sci. Instr. 26 (1955) 15.

[6]) H. Kallmann and G. J. Brucker, Phys. Rev. 108 (1957) 1122.

[7]) F. B. Harrison, Nucleonics 12, No. 3 (1954) 24; Phys. Rev. 89 (1953) 322.

The photomultipliers tested include the types RCA 5819 and 6810, Du Mont 6292, and EMI 6260, 6097, 6099 and 9530. Using neutron and gamma-ray sources and a stilbene crystal all tubes gave loci similar to those in fig. 4; that is no particular type appeared to be superior for this application. The same was true when a liquid scintillator was used. This result is interesting because the transit time spreads claimed for the selection of multipliers range from 2 to 20 mμsec and are thus comparable with the decay times generally quoted[5,6]) for stilbene and liquid scintillators, which are both less than 10 mμsec. However, scintillations from these scintillators actually contain a proportion ($\lesssim$20%) of slow components[4,7]) of decay times $\gtrsim$ 100 mμsec in addition to the more familiar fast component of decay time < 10 mμsec. Owen[4]) has shown that it is these slow components which are responsible for the effective difference in decay time for protons and electrons; a proton scintillation contains more slow component emission and less fast component emission than an electron scintillation. Since the transit time spreads of all the multipliers are much less than the slow component decay times, all are equally capable of resolving the difference between proton and electron scintillations.

Loci were also photographed using anthracene, quaterphenyl and diphenylacetylene crystals respectively. Anthracene and quaterphenyl gave resolved proton and electron loci very similar to those shown for stilbene in fig. 4. Diphenylacetylene crystals did not resolve proton and electron loci however and thus do not appear to show different decay times for protons and electrons. Loci were also observed for 1 cm^3 anthracene and stilbene cyrstals at different temperatures, ranging from + 25° C to — 70° C and no change in the loci with crystal temperature was found for either crystal.

It was found that liquid scintillators do not in general resolve proton and electron loci unless dissolved oxygen has previously been removed from them; e.g. by flushing with dry nitrogen to displace the dissolved oxygen or by removing all

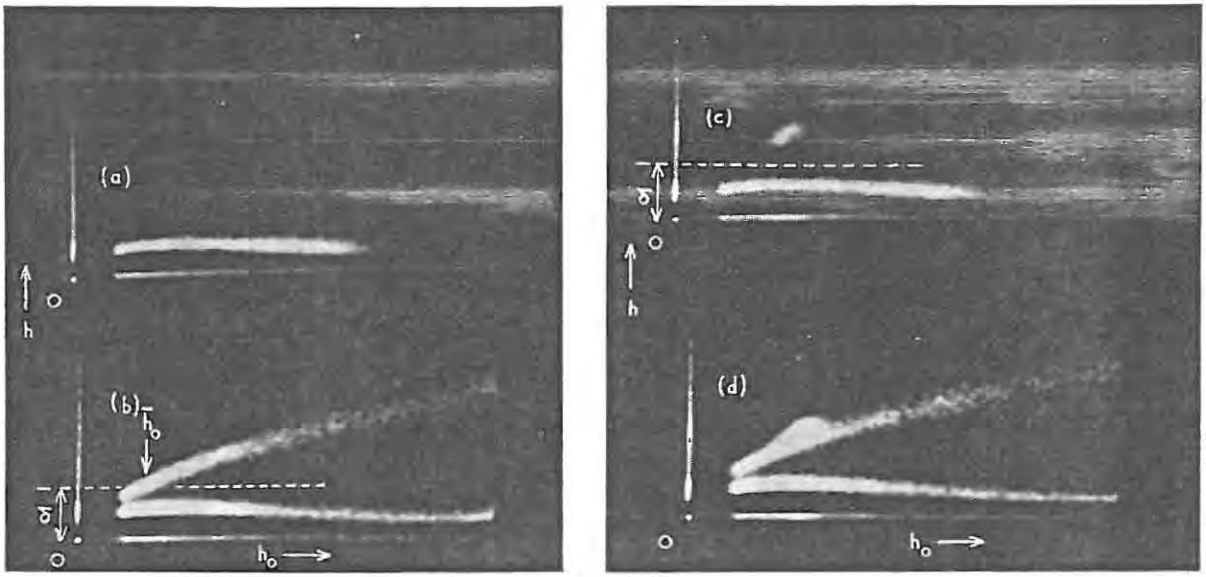

Fig. 4. Distributions of the pulse amplitude h, (which depends on scintillation decay time), versus the pulse amplitude h_0 (proportional to total light in the scintillation), for stilbene and; (a) Co^{60} source (1.3 MeV gamma-rays); (b) Po^{210}-Be source ($\lesssim$ 12 MeV neutrons + 4.5 MeV gamma rays); (c) Co^{60} source + Am^{241} source (5.5 MeV alpha-particles); (d) Po^{210}-Be source + Am^{241} source.

The h pulses corresponding to these events were fed via a gate, opened by the single-channel analyser, to the 100-channel analyser which then gave their pulse height distribution. The pulse height distribution obtained is thus equivalent to the pulse density as a function of ordinate

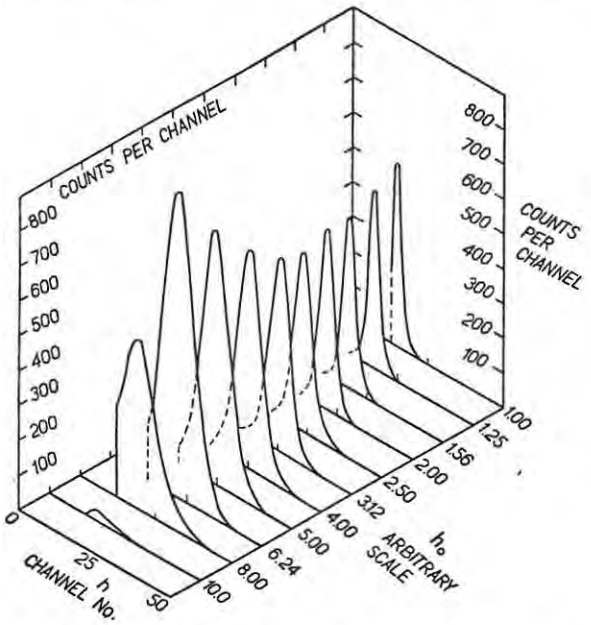

Fig. 7. A series of pulse height distributions obtained using stilbene and a Co^{60} source. Each component distribution shows the number of scintillations recorded per channel per ten minutes as a function of h for a particular value of h_0.

along a particular abcissa in figs. 4, 5 or 6. A series of such measurements gives a complete three-dimensional picture of the loci, of pulse density versus h versus h_0.

Figs. 7 and 8 show two series of pulse height distributions obtained using a stilbene crystal and an EMI 6097 photomultiplier; fig. 7 with the Co^{60} source and fig. 8 with the Po^{210}-Be source. A channel width 0.1 × the mean pulse height of the channel was used in the single-channel analyser.

For each component run (i.e. value of h_0) in fig. 8 the proton-electron resolution may be defined, arbitrarily, as the ratio, R, of the distance between the (mean pulse heights of the) proton and electron groups to the full width at half-maximum of the electron group. R has been evaluated as a function of h_0 from figs. 7 and 8 and is plotted in fig. 9. The scale of h_0 was calibrated in terms of electron energy from the Compton edge observed for Co^{60} 1.3 MeV gamma-rays (fig. 7). The scale of proton

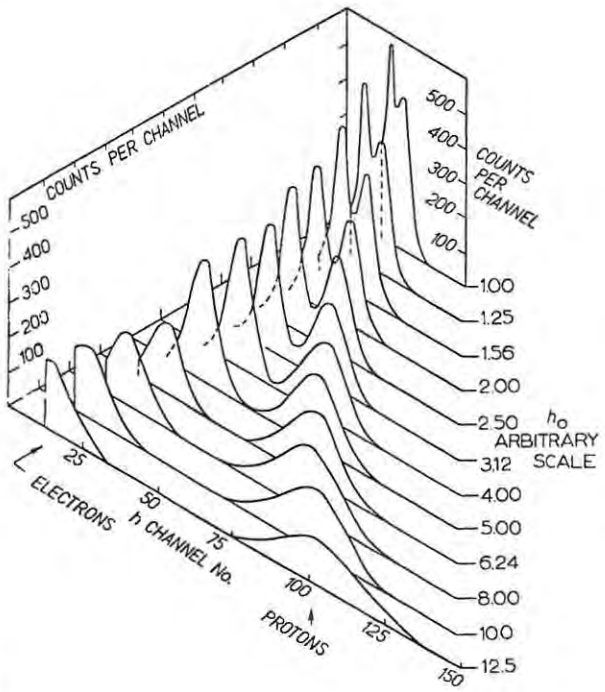

Fig. 8. A series of pulse height distributions obtained as for fig. 7 but using stilbene and a Po^{210}-Be source.

energy also shown in fig. 9 is based on the known relative response of stilbene to protons and electrons[11]).

Additional measurements of R were made for other scintillators, namely anthracene and quaterphenyl crystals and a solution of 4 g/litre PPO + 0.1 g/litre POPOP in toluene. The data obtained are included in fig. 9. If we adopt the criterion that R must exceed unity for effective resolution, then, from fig. 9 we see that the three crystals resolve above a proton energy of 0.5 MeV (and electron energy of 0.13 MeV) while the liquid scintillator resolves above proton and electron energies of 0.6 MeV and 0.16 MeV respectively.

[11]) Taylor, Jentschke, Remley, Eby and Kruger, Phys. Rev. 84 (1951) 1034.

Suppose we choose $\delta = 40$, then by integrating the appropriate curve in fig. 10 from 0 to 2 MeV we obtain that the fraction of the recoil proton distribution counted is 0.35; thus the absolute neutron counting efficiency is $0.35 \times 27 = 9.5\%$. Similarly, 14% of the gamma-rays are Compton scattered in the crystal producing recoil electrons with a Compton energy distribution from 0 to 1.8 MeV. From the curve for $\delta = 40$ in fig. 11 we obtain that a fraction, 0.0005, or less, of this Compton distribution is counted; thus the absolute gamma-ray counting efficiency is less than 0.0005×14 i.e. less than 0.007%.

5. Timing Resolution and Dead Time

The output pulse, h, from the counter is necessarily relatively "slow" (≈ 5 μsec wide) due to the long integrating times used in the output circuit (fig. 1). Thus the counter has an effective dead time of about 5 μsec, or at count rates exceeding about 10^4 (neutrons + gamma-rays) per second, neutron counts will be lost. The timing resolution of the counter is not limited by the slow rise time (≈ 0.5 μsec) of the h pulse however. For fast timing or coincidence applications an independent "fast" output pulse is derived from one of the photomultiplier dynodes, as the h_0 pulse is derived via B in fig. 1. This pulse is then delayed and gated by the discriminator triggered by the h pulse. In this system the timing resolution depends only on the photomultiplier transit time spread and the scintillator decay time and can be 5 mμsec or less for stilbene or liquid scintillators.

6. An Application of the Counter

This type of scintillation counter obviously has many possible applications for discrimination between alpha-particles, protons and electrons. A typical application for fission neutron detection will be described as an example.

To determine the fission cross section of uranium-235 for 6 eV to 60 eV neutrons two experiments were carried out as follows, using 3.1 inch diameter discs of U^{235} of 0.425 g/cm^2 and 9.0 g/cm^2 respectively. In each experiment the disc, or sample, was placed in a neutron beam produced by the Harwell 15 MeV linear electron accelerator, 10 metres from the accelerator target or pulsed neutron source. The stilbene crystal of the counter was placed close to the sample but outside the incident neutron beam. A fraction of the incident neutrons produced U^{235} fission in the sample and a fraction of the fission neutrons emitted were detected in the crystal. Using a neutron discriminator setting corresponding to $\delta = 40$ in fig. 10, the counter was adjusted to respond only to neutrons of energy greater than 1 MeV. Thus, as shown by the curve for $\delta = 40$ in fig. 11, at least 99.9% of any gamma-rays detected by the crystal (e.g. from radiative capture in the sample) were discarded by the discriminator. Counts from the discriminator were fed to a 100-channel time-sorter to be time analysed with respect to the accelerator neutron pulse. The duration of the neutron pulse at the accelerator target was less than 0.5 μsec and the width of each timing channel was 1.0 μsec. The fission neutron yield per timing channel, y, was thus determined as a function of incident neutron time-of-flight (from target to sample) that is as a function of incident neutron energy. This was done for the same total number of incident neutrons for the thick and thin samples respectively.

Now for U^{235} the number of neutrons emitted per fission and the fission neutron energy spectrum do not vary significantly with incident neutron energy from 6 eV to 60 eV[14]). We may thus assume that the measured fission neutron yield, y, is proportional to the number of fissions in the sample or, in other words, that the fission detection efficiency of the counter, ϵ, is constant over this incident neutron energy range. Now suppose we have N neutrons incident on the sample during the total time that a particular timing channel is open in the experiment and that only a small fraction ($< 2\%$) of these neutrons are scattered or stopped in the sample. Then the fission cross section, σ_f, averaged over the incident neutron energy range defined by

[14]) L. M. Bollinger, Conference on Neutron Physics by Time of Flight, Gatlinburg, ORNL 2309 (1956) p. 167.

from equation (8) and are plotted in fig. 12; solid points and open circles indicate data derived from the thin sample experiment and triangles indicate data derived from the thick sample experiment. At the incident neutron energies corresponding to the solid points the thin sample satisfied the condition for equation (8) (i.e. transmitted more than 98% of the incident neutrons). The open circles correspond to neutron energies for which this condition was not satisfied and these data include a correction for the effective thickness of the thin sample. In some regions between resonances where the thick sample satisfied the condition for eq. (8), the thick sample data (triangles) were preferred, since this sample gave a higher fission yield and hence a more accurate result. The cross section data shown in fig. 12 are in good agreement with those listed by Hughes and Schwartz[12]).

For fission cross section measurements the fission neutron detection method has some advantages over fission fragment detection, where a thin sample, itself enclosed in a fission chamber or gas scintillation counter, is essential. In the neutron detection method thick samples may be used, alpha-activity in the sample is no problem and millimicrosecond time-of-flight resolution is possible assuming that an organic scintillator is the neutron detector. However, it is essential that only neutrons are counted and, in particular, that gamma-rays are not counted; the neutron discriminating scintillation counter fulfils this requirement ideally.

7. The Nature of the Decay Time Differences

The physical effects behind the decay time differences are a subject of interest in their own right. For our purposes they are of particular interest in so far as they explain the scintillator behaviour observed and reported in section 3; that is, that diphenylacetylene crystals, unlike anthracene, stilbene and quaterphenyl, do not show an effective decay time difference; that liquid scintillators show such a difference only provided they do not contain dissolved oxygen; that plastic scintillators show, if anything, only a very small difference.

Scintillation decay shapes have been studied by Harrison[7]), Swank[5]), Wright[1]), Kallmann and Brucker[6]) and Owen[4]). From their data one might conclude that in general for organic scintillators, the scintillation decay may be described as the sum of several exponential components, one millimicrosecond "fast" component, responsible for 80% or more of the total emission, and one or more "slow" components of periods between 0.1 μsec and 100 μsec. Harrison[7]) originally showed that these slow components were appreciable in scintillations produced by X-rays in anthracene and stilbene, though they were not observed in liquid scintillators (presumably containing dissolved oxygen). Kallmann and Brucker[6]) determined that the fast component periods were virtually identical for alpha-particle and electron scintillations respectively in a wide range of crystal, liquid and plastic scintillators, including anthracene and stilbene. Owen[4]) showed that the slow component periods were the same for proton and electron scintillations respectively in anthracene, stilbene and quaterphenyl crystals and also in oxygen-free liquid scintillators but that the proportion of slow component emission was higher (and that of fast component lower) in proton scintillations. In other words, the nett, or effective, decay time for protons is longer than that for electrons in these scintillators because proton scintillations contain a higher proportion of slow components.

After Owen's conclusions we might presume that those scintillators which do not show a decay time difference for protons and electrons must either: (1) emit little slow component or; (2) emit similar proportions of slow component for both protons and electrons. Liquid scintillators containing dissolved oxygen and plastic scintillators would seem to fall into category (1), from Harrison's observation[7]) that slow components are negligible in the former and responsible for only 10% or less of the light emitted by the latter. Diphenylacetylene crystals might fall into either category, for although it has been reported that these emit slow components[5]) it is not established whether the proportion of slow

molecule to another[17]) we should, to be exact, consider energy transfer as an alternative mode of decay in equations (A). In the case of stilbene however, this would not affect the qualitative result, since energy transfer generally leads to other stilbene molecules being excited and these must eventually decay by either (i) or (ii) in equations (A). Energy transfer is more important in liquid and solid solution scintillators for in these it is the solvent (e.g. toluene or polystyrene) which is initially excited and excitation energy is transferred to a relatively small proportion (1 to 10%) of solute (e.g. p-terphenyl, PPO or POPOP) which emits. However the above qualitative description may still be valid for solution scintillators provided it is read that the processes in (A) and (B) apply to the solvent and that branch (i) of (A) describes, not solvent emission, but the solvent to solute energy transfer which leads eventually to emission from the solute.

The basis of the above interpretation, namely that the slow components may be attributed, indirectly, to slow recombination processes, would perhaps require more justification than can at present be provided. An alternative explanation, suggested by Harrison[7]), is that some molecules are initially excited to long-lived ($\approx 10^{-7}$ sec) triplet states and that these decay by acquiring sufficient vibrational energy to reach the singlet first excited electronic state, from which they decay according to (A). However, the fact that the decay time difference in anthracene and stilbene does not depend on crystal temperature (section 3) does not favour this explanation; one would expect that the triplet-singlet transition and hence the proportion of slow component in the scintillation would depend on the crystal temperature.

The fact that dissolved oxygen removes, or reduces, the slow components from liquid scintillators also seems to favour recombination processes rather than long-lived triplet states. We might infer that the effects produced by the oxygen are associated with the unpaired electrons in the O_2 molecule which lead to its high electron affinity. The threshold energy for electron capture by O_2 is about 3 eV[18]) and is thus within the expected range of energy of the ionization electrons produced in the scintillators. It is thus feasible that O_2 molecules in the scintillator might compete with ionized scintillator molecules for the ionization electrons, thus reducing the number of recombinations and hence the proportion of slow component which these eventually produce. On the other hand radiation chemistry studies[19]) have suggested that for a given incident particle and energy more triplet states are excited in organic solutions containing dissolved oxygen than in those that are oxygen-free; so in scintillators we should expect to see any slow component from long-lived triplet states increase in proportion when oxygen is dissolved in the scintillator. In fact the opposite is observed; the addition of oxygen removes or reduces the proportion of slow component, thus favouring the recombination processes rather than the long-lived triplet states.

Acknowledgements

The author is indebted to Dr. E. Bretscher for his support and interest in this work. He also wishes to thank Mr. J. E. Jolly for valuable assistance, the A.E.R.E. Linear Accelerator Group for their co-operation and Drs. S. K. Hutchinson and R. A. Lapage (A.W.R.E.) and Nuclear Enterprises (G.B.) Ltd., for providing scintillators for the experiments. The results of this paper were discussed with Drs. E. B. Paul, W. M. Lomer, E. R. Rae, R. B. Schwartz and Mr. F. W. K. Firk and the author is indebted to them for many helpful suggestions and criticisms.

[17]) T. Förster, Fluoreszenz Organischer Verbindungen (Gottingen, 1951);
H. Kallmann and M. Furst, Phys. Rev. **81** (1951) 853; Phys. Rev. **94** (1954) 503; Phys. Rev. **96** (1954) 902;
J. B. Birks, Phys. Rev. **94** (1954) 1567.

[18]) F. H. Field and J. L. Franklin, Electron Impact Phenomena (Academic Press Inc., 1957) p. 313.

[19]) C. R. Reid, Excited States in Chemistry and Biology (Pergamon, London, 1957) p. 180.

Pulse Shape Discrimination in a Plastic Scintillator

F. D. BROOKS,† R. W. PRINGLE,‡ SENIOR MEMBER, IRE,
AND B. L. FUNT§

Summary—A plastic scintillator has been developed which shows a decay time dependent upon energy loss per unit distance, and hence is suitable for use with pulse shape discrimination methods. This scintillator was employed in conjunction with an improved discrimination system and the data were analyzed on a two-dimensional analyzer which provided a matrix of 72×64 channels. At a bias level where 99 per cent of the electron scintillations were eliminated, it was possible to obtain almost 100 per cent counting efficiency for recoil protons of 2 mev, and the scintillator was useful for protons down to 0.5 mev.

The influence of various monomers, polymerization conditions, scintillating solutes, and secondary solvents was investigated, and a preliminary survey of the effects of these variables on pulse shape discrimination is presented.

INTRODUCTION

The technique of discriminating between different types of particle by means of different scintillation pulse shapes[1-3] is now well known and is finding increasing application in nuclear physics experiments. This method requires firstly that the scintillation decay should depend on the energy loss per unit distance, dE/dx, of the particle in the scintillator. Secondly, it requires a circuit (usually connected directly to the photomultiplier output) which is sensitive to the scintillation decay rather than to the total light in the scintillation and which signals the nature of the particle, *e.g.*, by a negative output pulse for low dE/dx and a positive pulse for high dE/dx.

Among the organic scintillators in particular, the first requirement is well fulfilled by crystals such as stilbene, anthracene and quaterphenyl, and by a wide range of oxygen-free liquid scintillators. Organic crystals and liquids in general make good discriminators using any type of discriminating circuit. On the other hand, with plastic scintillators the experience, until recently, has been that the discrimination is much poorer than that obtained using crys-

†Atomic Energy Research Establishment, Harwell, England.
‡Nuclear Enterprises (G. B.) Ltd., Edinburgh, Scotland.
§University of Manitoba, Winnipeg, Canada.

[1] F. D. Brooks, "Organic scintillators," in "Progress in Nuclear Physics," O. R. Frisch, Ed., Pergamon Press, Inc., London, England, vol. 5, pp. 252–313, 1956; and in "Liquid Scintillation Counting," C. B. Bell and F. N. Hayes Eds., Pergamon Press, Inc., p. 268, 1958. "A scintillation counter with neutron and gamma-ray discriminators," *Nuclear Instruments and Methods*, vol. 4, pp. 151–163; April, 1959. This work is the subject of patent applications in the U.S.A. and other countries.

[2] R. B. Owen, "The decay time of organic scintillators and their application to the discrimination between particles of differing specific ionization," IRE TRANS. ON NUCLEAR SCIENCE, vol. NS-5, pp. 198-201; December, 1958.

[3] M. Forte, "Possibilities of discrimination between particles of different kind by means of organic scintillator decay curves," International Conf. on the Peaceful Uses of Atomic Energy, ALCONF. 15/P/1514, Geneva; September, 1958.

tals or liquids. The present studies were initiated with the aim of producing a useful discriminating counter incorporating a plastic scintillator. A plastic in which the pulse shape is particularly sensitive to dE/dx has been produced and an improved discrimination system has been developed. The discrimination obtained with this combination of plastic and circuit is comparable with that obtained using the best crystal and liquid scintillators.

DISCRIMINATION SYSTEM

The discrimination system, shown in Fig. 1, is based on the discrimination circuit described in a a previous paper.[1] Its operation in distinguishing between, *e.g.*, a Compton electron scintillation and a recoil proton scintillation may be described briefly as follows. Fig. 1(a) shows schematically an electron scintillation and a proton scintillation as observed, for example, in stilbene.[2] These pulses are drawn to have the same *area*, corresponding to equal total light in the respective scintillations. The difference between them is that the proton scintillation contains relatively less light in the main (fast) component (decay time $\lesssim 10^{-8}$ second) and relatively more light in the slow component or tail (decay times $\gtrsim 10^{-7}$ second). In the photomultiplier output circuit the anode time constant is $\sim 10^{-8}$ second, hence the amplitude of the negative pulse which is generated across the anode load is proportional (approximately) to the amount of fast component in the scintillation. At the last dynode the time constant is somewhat larger, $\gtrsim 10^{-7}$ second, hence the positive pulse amplitude produced there is proportional to the sum of the fast and slow components. The anode and dynode pulses are stretched by diode-capacitor networks and are passed via variable attenuators, PR1 and PR2 respectively, to the output terminal A where they are mixed. PR1 and PR2 may be adjusted to "balance" the negative and positive amplitudes fed to A in such a way that an electron scintillation produces zero output or a negative pulse at A, whereas a proton scintillation produces a positive pulse.

In practice, it is easy to balance the circuit so that the output pulse [Fig. 1(b)] is negative going for electrons and positive going for protons. However, unless the *shapes* of the two stretched pulses fed to A are perfectly matched, the electron output pulse may exhibit a positive overshoot as illustrated in Fig. 1(b). This overshoot becomes a serious nuisance when the difference between electron and proton scintillation shapes is marginal, as was the case for some of the plastics studied in the early stages of this work. It proved expedient to eliminate the overshoot by using a linear gate, as in Fig. 1, to select only the front portion of the output circuit pulse h as illustrated in Fig. 1(c). By this means, the condition of balance is judged in terms of the front portion of the output pulse alone and balancing is considerably facilitated.

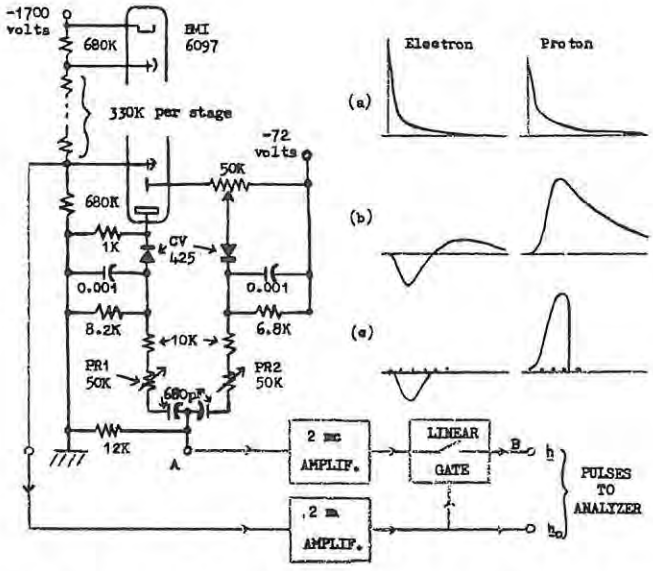

Fig. 1—Discriminating system and schematic illustrations of: (a) scintillations in stilbene; (b) output pulse at A; (c) h output pulse at B.

DISCRIMINATION TESTS

For the discrimination tests, an integrated pulse was obtained from the next to the last dynode of the photomultiplier (Fig. 1). The amplitude h_0 of this pulse is proportional to the total light in the scintillation, which, in turn, is a function of the energy and nature of the primary ionizing particle. In the tests, the amplitude h_0 is analysed coincidentally with the discrimination pulse amplitude h. This is done either by display on a CRT or by using a two-dimensional pulse height analyzer.

The CRT method has the advantages of being quick and electronically simple, but, on the other hand, it is only a qualitative test. The pulses h_0 and h are stretched at their peak amplitudes and fed to the X and Y plates respectively, of the CRT. Thus, each scintillation plots a point (h_0, h) on the CRT screen and we obtain the loci defined by many events by taking a time exposure photograph of the screen. Fig. 2 shows results obtained using a) a stilbene crystal; b) NE 213 liquid scintillator; and c) the new plastic scintillator, "plastic 77." In each case, the upper

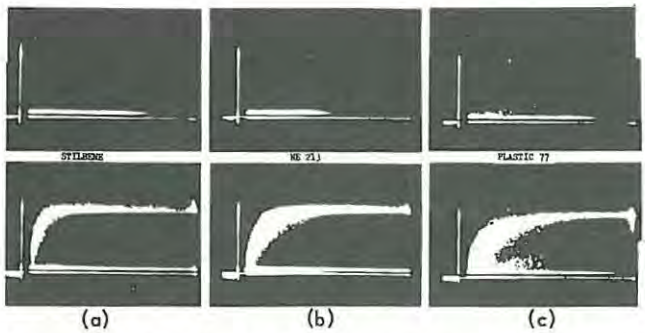

Fig. 2—CRT displays of the discrimination pulse height h (ordinate) vs the integrated pulse height h_o (abcissa) obtained using a Co^{60} source (upper photograph) and a Po-Be source (lower photograph). (a) stilbene; (b) NE 213 liquid scintillator; and (c) plastic 77.

photograph was obtained using a Co^{60} gamma-ray source and the lower photograph, a Po^{210}-Be (neutron + gamma-ray) source. As demonstrated by the Compton electron distributions obtained using Co^{60}, the electron scintillations define a locus of small and constant h; the amplitude h measured for electrons is in fact the pedestal introduced by the linear gate in Fig. 1 and indicated by the dotted line drawn in Fig. 1(c). For all of the scintillators, recoil proton scintillations define a locus (shown in the Po^{210}-Be photograph) which is higher in h and clearly separated from the electron locus. Fig. 2(c) in particular is a qualitative indication that the pulse shape discrimination obtained using plastic 77 is comparable with that obtained from stilbene or NE 213.

The tests undertaken using the two-dimensional pulse height analyzer give quantitative, and hence, more useful, results at the expense of extra time spent on data handling and analysis. The analyzer, a magnetic tape recording system with a total capacity of 2^{16} channels, has been described elsewhere.[4,5] For the present tests, it provided a matrix of 72 channels × 64 channels, which were used to analyze the integrated pulse h_0, and the discriminator pulse h, respectively. The results obtained for plastic 77 are displayed in Fig. 3 as three-dimensional models of number of counts h_0, vs h. The model on the left of Fig. 3 refers to data obtained using a Co^{60} source and the right-hand model refers to a Po-Be source. It will be seen that these models are analogous, respectively,

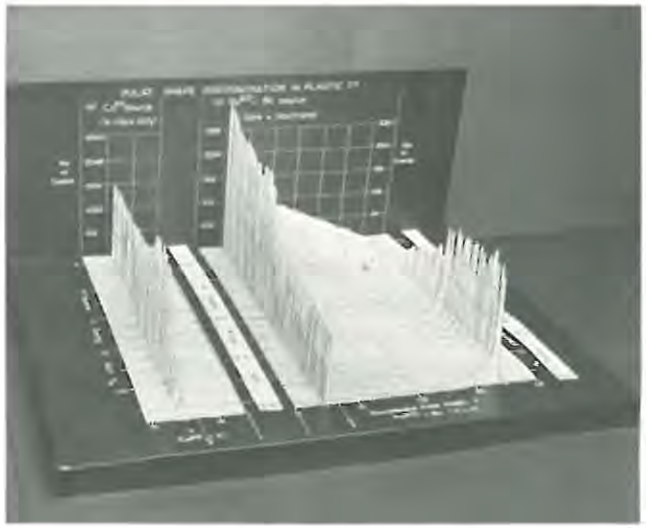

Fig. 3—Data from the coincident pulse-height analysis of the integrated pulse h_0, and the discrimination pulse h, obtained using Plastic 77 and; (a) Co^{60} source; (b) Po-Be source. The scale of h_0 is calibrated in electron energy and in equivalent porton energy. The level δ indicates the bias required on h to eliminate ≥ 99 per cent of the electron scintillations, irrespective of electron energy.

to the upper and lower photographs of Fig. 2(c). However, whereas in Fig. 2(c) pulse density must be inferred from photographic density, the equivalent in Fig. 3, number of counts per channel, is actually measured. The latter data are thus amenable to a further analysis in which, section by section in h_0, the distribution in h is resolved into proton and electron components and the proton-electron resolution is measured. For example, we may select a bias δ (see Fig. 3) on the pulse height h, defined so as to elim-

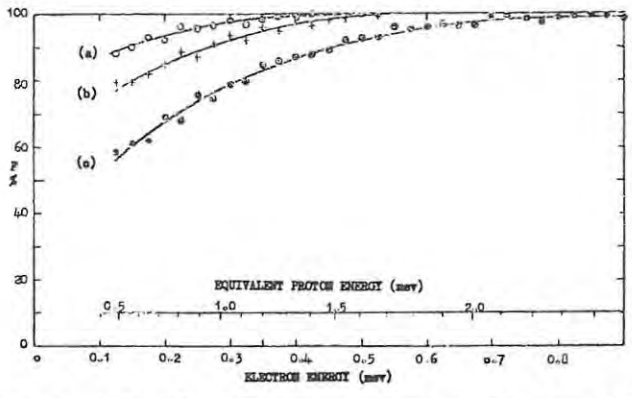

Fig. 4—A bias δ on the pulse h is set to eliminate ≥ 99 per cent of the electron scintillations of any energy. This figure shows the percentage F of proton scintillations counted above δ as a function of proton and electron energy for: (a) stilbene; (b) NE 213 liquid scintillator; and (c) plastic 77.

[4] F. H. Wells, "Uses of magnetic tapes and cores for nuclear data storage and computation," *Nuclear Instruments and Methods*, vol. 2, pp. 165–168; February, 1958.

[5] J. R. Bird and J. R. Waters, "The use of digital recording on magnetic tape for the study of γ-rays from resonant neutron capture in platinum," *Nuclear Phys.*, vol. 14, pp. 212–221; December, 1959.

inate at least 99 per cent of the electron h pulses of any energy (*i.e.*, any h_0). Then we measure, as a function of proton energy (*i.e.*, h_0), the percentage of protons F for which h exceeds δ. Fig. 4 shows the percentage F as a function of electron energy and equivalent proton energy, for a) stilbene, b) NE 213 and c) plastic 77. At proton energies above ~ 2 Mev there is little to choose between the three scintillators in terms of proton-electron discrimination. At lower energies, the plastic is inferior to NE 213 and stilbene but it still shows useful discrimination down to proton energies of ~ 0.5 Mev.

DISCRIMINATION AS A FUNCTION OF PLASTIC COMPOSITION AND PREPARATION

Plastic 77 is the product of a systematic study of discrimination vs plastic composition. The variables in this study were:

1) The bulk solvent (monomers styrene, methyl styrene and vinyl toluene were studied);
2) Polymerization conditions;
3) Secondary solvents including naphthalene and mono-isopropyl-biphenyl (IP);
4) Inclusion of compounds (divinyl benzene, allyl methacrylate) which induce cross-linking in the polymer; and
5) The scintillation solutes, p-terphenyl, PPO, PBD and POPOP and their concentrations.

The results of this study can be summarized as follows:

1) The choice of monomer does not influence the degree of pulse shape discrimination but, on the other hand, it is important to purify the monomer and, in particular, to remove inhibitors and dissolved oxygen before polymerization. The vinyltoluene monomer used in plastic 77 was vacuum-distilled in the first stage of preparation.

2) Oxygen-free conditions should be maintained throughout the preparation until polymerization is completed. In the case of plastic 77, polymerization took place in a nitrogen atmosphere for seven days at 135°C. Catalysts and mold-release agents were not incorporated in the monomer solution because there is evidence that these tend to poison the pulse shape discrimination property.

3) The inclusion of naphthalene or IP as secondary solvents has a marked beneficial effect on the pulse shape discrimination. In the case of naphthalene, discrimination is improved at the expense of light output but with IP light output as well as discrimination is improved. Plastic 77 contains 10 per cent by weight of IP and has a pulse height efficiency relative to anthracene of 70 per cent.

4) Cross-linking in the polymer produces a slight increase in the pulse shape discrimination. No cross-linking compounds are included in plastic 77.

5) Of the three primary solutes tested, p-terphenyl proved the best, and the highest concentration studied, 35 gm/liter, proved optimum. Plastic 77 contains this amount of p-terphenyl together with 0.5 gm/liter POPOP.

DISCUSSION

Of the factors which contribute to the improved pulse shape discrimination of plastic 77, we should emphasise the oxygen-free preparation and the inclusion of IP. The need for extremely pure components and oxygen-free conditions is really no surprise in view of previous experience with liquid scintillators.[1] The effect of IP is particularly interesting and merits further investigations to determine whether, for example, the IP acts as a secondary solvent in the sense established by Furst and Kallmann[6] and/or whether it has a more subtle and important role during or after polymerization.

On the practical side, the advent of a discriminating plastic should particularly simplify those experiments which require organic detectors either big or in precise or awkward shapes. It is hoped that plastic scintillators which compete rather than compare (in discrimination) with stilbene will eventually be produced. Meanwhile, however, it should be stressed that although plastic 77 is markedly better than regular plastics (*e.g.*, NE 102), very careful balancing of the discrimination system (Fig. 2) is required to obtain the optimum performance demonstrated in Figs. 2, 3 and 4.

---

[6] M. Furst and H. Kallmann, "Energy transfer by means of collision in liquid organic solutions under high energy and ultraviolet excitations," *Phys. Rev.*, vol. 94, pp. 503–507, May, 1954; "Magnitude of excitation energy and energy transfer by collision," *Phys. Rev.*, vol. 96, pp. 902–903, November, 1954; and "Enhancement of fluorescence in solutions under high-energy irradiation," *Phys. Rev.*, vol. 97, pp. 583–587, February, 1955.

F.D. Brooks, R.W. Pringle and B.L. Funt
Pulse shape discrimination in a plastic scintillator
I.R.E. Trans. on Nucl. Sci. NS7 (1960) 35-38

GENERAL SURVEY ON CHOICE OF THE DETECTOR FOR A TIME-OF-FLIGHT EXPERIMENT

F. D. BROOKS

Atomic Energy Research Establishment, Harwell, U.K.

Abstract

Different kinds of neutron detectors are reviewed, attention being paid to such characteristics as time resolution, efficiency, background discrimination and dimensions. The special requirements of detectors for transmission and scattering measurements, fission experiments and capture studies, are considered. In the case of scattering and transmission measurements several detectors are surveyed and their suitability for various neutron energy regions is discussed.

I. INTRODUCTION

When we are faced with the problem of selecting a detector for a time-of-flight experiment four rather obvious criteria will usually suggest themselves. These are:

(1) time resolution, which should be compatible with, if not slightly better than, the width of the neutron burst;

(2) detection efficiency, which should be as near to 100% as possible;

(3) discrimination against backgrounds, e.g. from unwanted neutrons or other radiations; and

(4) physical considerations, e.g. as to thickness and/or area.

How we weigh the importance of these and other possible criteria depends very much on the particular experiment. In this survey we aim to cover detectors for total and partial cross section experiments in the neutron energy range 0 to 0.1 MeV. We do this under three headings, which cover, respectively, neutron detectors, detectors for fission experiments, and detectors for capture experiments.

II. NEUTRON DETECTORS FOR TRANSMISSION AND SCATTERING EXPERIMENTS

In Table 1 we consider a selection of slow-neutron detectors and list some of their properties. The first column of the table lists the name of the detector; some details are given in the footnotes, others can be found in the references listed in columns (9) and (10). In columns (2) and (3) we list a typical

TABLE I

Properties of Slow Neutron Detectors

Detector *	Typical thickness		Timing resolution	Neutron Peak			Discriminat. against gammas*	References	
	cm	atom/barn B^{10} or Li^6	μs	Full Width at Half Max.	Eqv. Electr. Ener. (MeV)	Relative Pulse Height		Specific	General
(1) $B^{10}F_3$ Counter (at 150 cm Hg)	10	0.0004	$\geqslant 0.5$	$\sim 5\,\%$	2.3	—	P.H.S.		
(2) B^{10}-plug and NaI(Tl) cryst.	2(B^{10}) 3(NaI)	0.14	0.05	$\sim 10\,\%$	0.48	480	P.H.S.	6	
(3) Li^6I(Eu) cryst.	2.5	0.046	~ 0.1	12 %	4.1	1400	P.H.S.	54	55
(4) B^{10}-loaded liq. scint.	1.0	0.006	~ 0.4	60 %	0.10	10 - 20	P.H.S. & P.S.D.	11	56, 57
(5) B^{10}-loaded glass	1.0	0.016	0.05	50 %	0.18	(10)	P.H.S.	12, 13	3, 58, 59 60, 61,
(6) Li^6-loaded glass	3.8	0.045	0.005	25 %	1.6	200	P.H.S.	62	
(7) B^{10}-ZnS(Ag) mixture	0.05	0.0004	~ 0.1	No peak			P.H.D. & P.S.D.	17	1, 3, 16
(8) Proton recoil	3	—	~ 0.01	No peak			T.O.F.	8, 9	
(9) Self-Indication	—	—	~ 0.01	No peak			(P.H.D.)	10	

Notes

* Detector compositions in percentage weight:
(4) Toluene (50), Methyl borate (50) + 4 g/l PBD + 0.02 g/l.POPOP (ref. 11). For other recipes see ref. 56.
(5) Na_2O (14.4), $B^{10}_2O_3$ (47.3), Al_2O_3 (30.7), Ce_2O_3 (7.6) (ref. 13).
(6) Li^6_2O (11.7), Al_2O_3 (8.8), Ce_2O_3 (3.8), SiO_2 (75.7) (ref. 62).
(7) ZnS(Ag) (65) + Boron Plastic (35), prepared from ethylene glycol, n-butanol and boric acid in ratio 3.7 : 2.65 : 10 (ref. 17).

* Method of Discrimination against γ-rays.
P.H.S. = Pulse Height Selection (i.e. single channel).
P.H.D. = Pulse Height Discrimination.
P.S.D. = Pulse Shape Discrimination.
T.O.F. = Time-of-Flight.

operating thickness for each detector, this, in most cases, being the thickness used by the author(s) referred to in column (9). In Figure 1 we show curves of neutron detection efficiency, ε_n, versus neutron energy for detectors (1) to (8) of the table.

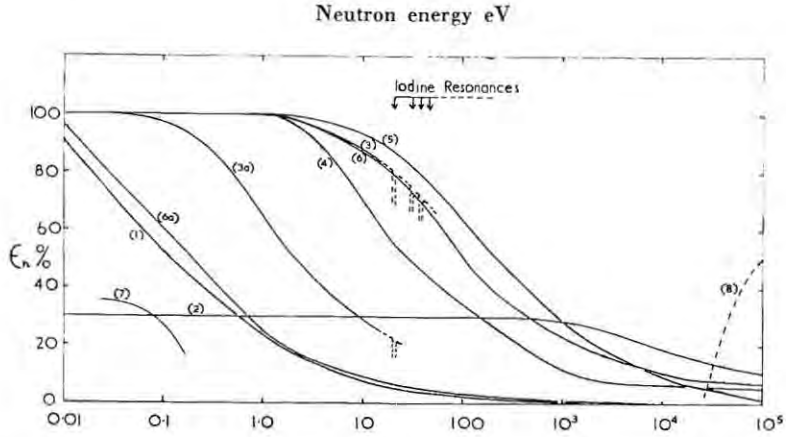

Figure 1

Neutron detection efficiency, ε_n, versus neutron energy for detectors (1) to (8) of Table 1. Curves (1) to (8) refer to the respective detectors at the thicknesses listed in the table. Curve (3a) refers to a 0.4 cm thick $Li^6I(Eu)$ crystal; curve (6a) refers to a 0.17 cm thick Li^6-loaded glass scintillator.

All of the detectors in Table 1, except (8) and (9), utilise the (n,α) reactions on either B^{10} or Li^6 as a means of neutron detection. In the first six detectors, (n,α) events are identified by a peak in the pulse height distribution. Columns (5), (6) and (7) of Table I list the characteristics of this neutron peak. Detector number (7), the B^{10}-ZnS(Ag) mixture, does not give a peak because the (n,α) reaction products can lose a variable amount of energy in the boron compound before they reach a ZnS(Ag) crystal.

In Table I and Figure 1 we have most of the data upon which we shall presently base our discussion of the different neutron detectors. Before doing this, however, it is interesting and relevant to see how they compare in discrimination against γ-rays. The $B^{10}F_3$ counter is, of course, ideal in this respect, since it is very thin to electron energies comparable with the heavy particle energy release (2.3 MeV) in the (n,α) reaction. Detector number (7) achieves γ-insensitivity in an analogous way. It is thin in order to achieve reasonable light collection, and, besides this, ZnS(Ag) is a very efficient scintillator for heavy particles. Thus a bias curve for γ-rays shows a sharp cut-off compared with one taken for neutrons, which extends to large pulse heights. In general a bias can be found which reduces γ-sensitivity to a tolerable level without

undue sacrifice of neutron efficiency [1]. Pulse shape discrimination techniques may also be applied to reduce γ-sensitivity [2,3].

For detectors (2) to (6) the properties which determine γ-sensitivity are composition (through Z), density and the properties listed in columns (5) and (6) of Table 1, i.e. the width and equivalent electron energy of the neutron peak. Assuming pulse height selection in a channel of this width and mean electron energy, γ-sensitivity is due only to those photoelectric, Compton and pair interactions which release a total electron energy within the limits defined by the channel. Figure 2 shows, for each detector, the calculated detection efficiency, ε_γ, versus γ-energy, for normally incident γ-rays. Only the Compton effect is significant for detectors (4), (5) and (6). Thus for these three detectors, ε_γ varies in a simple manner with γ-energy, rising sharply as the Compton edge enters the channel, reaching a maximum as the edge reaches the

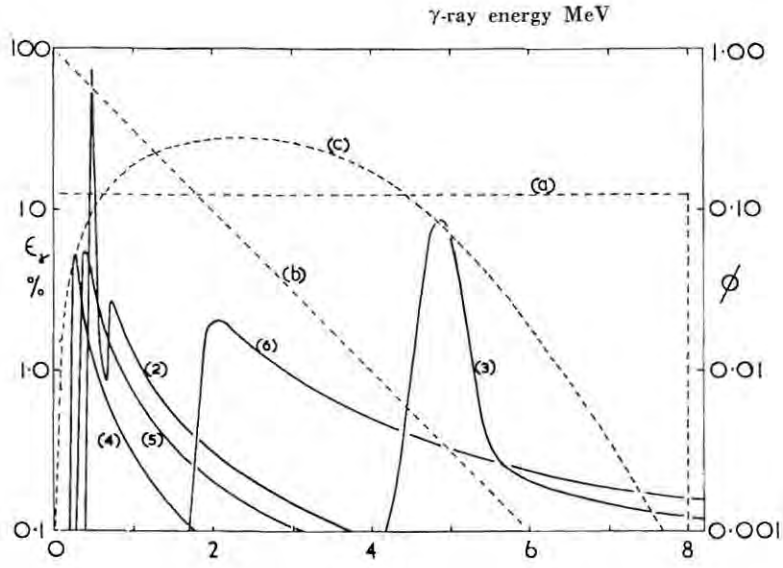

Figure 2

γ-ray detection efficiency, ε_γ, versus γ-energy for detectors (2) to (6) of Table I (solid curves) and γ-ray spectra, $\Phi(E)$; (a) flat spectrum; (b) exponential spectrum; (c) "capture" spectrum (broken curves).

top of the channel, and declining at higher energies as the Compton distribution spreads over an energy range which is broad compared with the channel width. Photoelectric and pair interactions are taken into account for detectors (2) and (3) respectively, and these account for the prominent peaks of curves (2) and (3) in Figure 2.

To completely assess the γ-sensitivity of detectors (2) to (6) we require to know the shape of the γ-ray spectrum. For a spectrum, $\phi(E)$, the total γ-sensitivity is proportional to the integral :

$$\int_0^\infty \phi(E)\,\varepsilon_\gamma(E)\,dE$$

As examples we show, in Table 2, the total γ-ray detection efficiencies calculated for the three spectra illustrated by the broken curves, (a), (b) and (c) in Figure 2. Curve (a) is the simplest spectrum, flat from 0 to 8 MeV, and zero above 8 MeV. Curve (b), the exponential, corresponds very approximately to the spectrum of prompt γ-rays accompanying fission [4]. Curve (c) is an "average" neutron capture γ-ray spectrum [5]. The efficiencies calculated for the three spectra are listed in Table 2, columns (a), (b) and (c) respectively. Not surprisingly, the relative detection efficiencies are quite sensitive to the γ-spectrum, the $Li^6I(Eu)$ crystal showing marked superiority for a "soft" spectrum (b), while the B^{10}-loaded liquid and B^{10}-loaded glass are superior for the "capture" spectrum, (c). It should be noted, however, that these calculations

TABLE II

γ-Ray Detection Efficiencies of Slow-Neutron Scintillation Detectors for Various γ-ray Spectra

		Percentage of γ'-s detected		
γ-ray spectrum →		(a) Flat	(b) Exponential	(c) "Capture"
Detector	Thickness cm			
(2) B^{10}-plug and NaI (Tl)	3 (NaI)	0.66	2.76	0.65
(3) $Li^6I(Eu)$ crystal	2.5	0.55	0.02	0.33
(4) B^{10}-loaded liquid	1.0	0.17	0.82	0.12
(5) B^{10}-loaded glass	1.0	0.28	1.00	0.25
(6) Li^6-loaded glass	3.8	0.44	0.17	0.70

apply to γ-rays incident along the direction of the neutron beam and assume that the detector is entirely in the beam. For detector (2) in particular, the NaI(Tl) crystal is assumed to be immediately behind the B^{10}-plug, in the neutron beam. In the geometry more commonly used with this detector [6], i.e. with the NaI(Tl) placed outside the beam and well shielded from all γ-rays except those coming from the B^{10}-plug, the data given for detector (2) in Table 2 should be reduced by a factor of about ten or more.

The data in Table 2 reflect the discrimination achieved against γ-rays by pulse height selection alone. In the case of the B^{10}-loaded liquid, detector (4), pulse shape discrimination (P.S.D.) can be utilised to reduce γ-sensitivity by a further factor of 12, at the expense of 40% loss of neutron detection efficiency. For details see Figure 3. In the case of detector (2) P.S.D. is obviously impos-

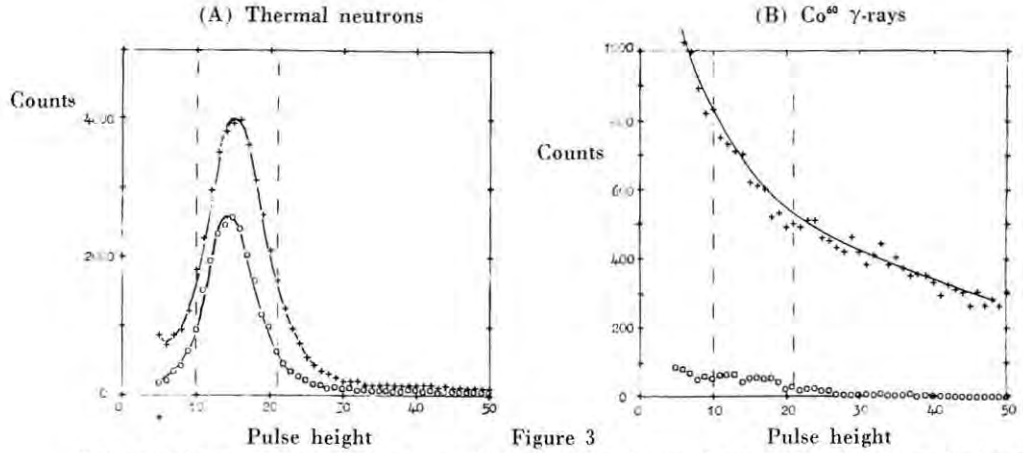

Figure 3

Pulse height spectra obtained using a B^{10}-loaded liquid scintillator, with (circles), and without (crosses), pulse shape discrimination[34,36]. Spectra (A) refer to thermal neutrons, spectra (B) refer to a Co^{60} γ-source. The ratios of the areas between 10 and 21 pulse height units, (with P.S.D.) : (without P.S.D.), are 0.61 for (A) and 0.08 for (B).

sible because detection is via the 0.48 MeV γ-ray which accompanies 93% of the $B^{10}(n,\alpha)Li^7$ reactions. Neither, unfortunately is P.S.D. applicable to the remaining three scintillation detectors, i.e. the $Li^6I(Eu)$ crystal, the B^{10}-loaded glass and the Li^6-loaded glass. None of these show significantly different pulse shapes for (n,α) and electron scintillations respectively. However the glass scintillators do show very slight pulse shape differences [7] and it would seem worthwhile to experiment further with glass compositions with the aim of enhancing these differences.

The (n,α) pulse heights in the $Li^6I(Eu)$ crystal and the Li^6-loaded glass scintillator are equivalent to the relatively high electron energies of 4.1 and

1.6 MeV respectively. For these it is therefore not unrealistic to consider γ-discrimination by the method of reducing the scintillator thickness to less than the range of a 3.5 MeV or 1.2 MeV electron, respectively. This criterion would allow a 0.4 cm thick $Li^6I(Eu)$ crystal or a 0.17 cm thick Li^6-loaded glass. The neutron efficiencies of these "γ-insensitive" scintillators would be as shown by curves (3a) and (6a) respectively, in Figure 1.

The proton recoil detector (number (8)) is designed for use with monoenergetic neutrons from a pulsed Van de Graaff accelerator. Time-of-flight is used to discriminate against γ-rays and also to discriminate against unwanted neutrons, but not as the primary means of neutron energy measurement [8,9].

In the self-indication method [10], which we have labelled detector number (9), detection is via neutron capture γ-rays from a sample similar to the transmission sample under study. However the γ-detecting scintillators, as in the usual geometry for detector (2), are placed outside the incident neutron beam and shielded to minimize sensitivity to all γ-rays except those from the detecting sample.

For the remainder of this section our purpose is to emphasize the merits and weaknesses of each of the detectors considered and to assess their suitability for transmission and/or scattering experiments.

(1) The $B^{10}F_3$ counter has the merit of extremely low sensitivity to γ-rays. It is generally most useful for work at energies below $\sim$ 10 eV. At higher energies it suffers the disadvantages of low efficiency and modest time resolution.

(2) The chief advantages of the B^{10}-plug and NaI(Tl) detector are *(i)* time resolution and *(ii)* potentially high efficiency and a flat response characteristic through the use of a thick B^{10}-plug. Disadvantages are the need for a high solid angle of NaI(Tl) to obtain high efficiency, and, in consequence, *(i)* the need for very thorough shielding against γ-rays, and *(ii)* backgrounds from β- and γ-decays following neutron capture in iodine.

(3) The $Li^6I(Eu)$ crystal offers the advantages of high neutron efficiency and low γ-sensitivity provided that the γ-spectrum is "soft". It has, however, one very serious drawback, namely neutron capture by iodine rather than by Li^6 at iodine resonance energies, with the result that the response characteristic (curve (3) in Figure 1) shows sharp dips. It is, in consequence, unsuitable for high resolution work above $\sim$ 19 eV. For work below this energy however, the thin ($\leqslant$ 0.4 cm) $Li^6I(Eu)$ crystal might be very useful.

(4) Advantages of the B^{10}-loaded liquid scintillator are high neutron efficiency and low γ-sensitivity, the latter assuming that pulse shape discrimination is used. Disadvantages are: *(i)* low scintillation pulse height; *(ii)* sensiti-

vity to fast neutron backgrounds through proton recoils; *(iii)* modest timing resolution; and *(iv)* that the liquid system is awkward to handle—containment allowing good light collection is essential and great care is necessary to avoid "poisoning" the liquid. However, despite this formidable list of drawbacks, B^{10}-loaded liquids have functioned very successfully as transmission detectors at A.N.L. [11].

(5) Advantages of the B^{10}-loaded glass scintillator are: *(i)* high neutron efficiency; (*ii*) timing resolution; and (*iii*) insensitivity to fast neutrons. Low scintillation pulse height is a potential disadvantage but not a limitation, since the (n,α) peak is clearly separated from photomultiplier noise [12,13].

(6) The Li^6-loaded glass scintillator repeats the advantages *(i)* to *(iii)* of the B^{10}-loaded glass. In addition it has a good pulse height and is insensitive to γ-rays of less than $\sim$ 1.6 MeV. On the other hand it is γ-sensitive over a broad energy range extending upwards from 1.7 MeV. As in the case of the Li^6I(Eu) crystal, however, we can obtain general γ-insensitivity (at the expense of neutron efficiency) by using a thin ($\leqslant$0.17 cm) glass.

(7) Under the heading, detector (7), we can include both B^{10}-ZnS (Ag) detectors and the essentially similar Li^6F-ZnS(Ag) detector [14]. These have the merit that they can be rendered γ-insensitive simply by increasing a bias level. This simplicity, however, is achieved at the expense of neutron efficiency. They also have the advantage of being relatively simple to fabricate, an advantage which has promoted their use in large area detectors [15,16,17].

(8) The proton recoil detector has the advantage of an efficiency which increases with neutron energy in the region $\sim$ 50$-$100 keV where the (n,α) detectors are losing efficiency. On the other hand, in order to operate below 100 keV the detecting system needs to be fairly elaborate, with cooling and coincidence discrimination to reduce the effect of photomultiplier noise [8].

(9) In the self-indication method [10] the fact that the detector is operative only at, and near to, resonance energies can be an advantage or a disadvantage. It could be an advantage, for example, in reducing neutron backgrounds such as those due to delayed fission neutrons from the Harwell "Booster" [18]. Disadvantages of the self-indication method are that it is necessarily inaccurate on the wings of resonances and at resonances where capture is weak compared with scattering. Nevertheless the Columbia group have proved its value for transmission work [19,20].

To complete this section we attempt to summarize the way in which a transmission or scattering detector might be selected under various circumstances.

(a) Transmission or Scattering Detector for Neutron Energies $\leqslant$ 10 eV.

The $B^{10}F_3$ counter might still be chosen on the grounds of simplicity and γ-insensitivity. Alternatively the B^{10}-ZnS(Ag) or Li^6-ZnS(Ag) systems or the thin Li^6-loaded glass might be preferred for better time resolution and reduced detecting thickness. The thin Li^6I(Eu) crystal might be favoured for high neutron detection efficiency.

(b) Transmission Detector for Neutron Energies up to $\sim$ 10 keV.

The B^{10}-loaded glass, the Li^6-loaded glass or the B^{10}-plug & NaI (Tl) would be favoured for the requirements of neutron efficiency, timing resolution, and insensitivity to fast neutrons. If the two latter requirements were relaxed and insensitivity to γ-rays was important, the B^{10}-loaded liquid scintillator (with P.S.D.) might be preferred.

(c) Scattering Detector for Neutron Energies up to $\sim$ 1 keV.

Insensitivity to γ-rays is the main requirement here and this limits the choice to the $B^{10}F_3$ counter, the B^{10}-loaded liquid (with P.S.D.) or the *thin* Li^6-loaded glass. The former and the latter win on the grounds of simplicity but lose to the B^{10}-loaded liquid in respect of neutron efficiency.

(d) Transmission Detector for Neutron Energies from $\sim$ 10 to 100 keV.

In this energy region we have two types of experiment to consider, depending on whether time-of-flight is used for neutron energy measurement or as a means of neutron-γ discrimination. For the former the Li^6-loaded glass, the B^{10}-loaded glass or the B^{10}-plug & NaI(Tl) might be favoured on the grounds of timing resolution and simplicity. At energies above $\sim$ 50 keV, the higher efficiency afforded by the proton recoil detector is probably not worth the complexity involved with this detector. For the second, or pulsed Van de Graaff, type of experiment however, there is usually an interest in going to energies above 100 keV, hence the proton recoil detector might be favoured for neutron efficiency.

III. DETECTORS FOR FISSION EXPERIMENTS

Our treatment in this section will be brief since the subject has already been covered in another paper at this symposium [21]. We wish to compare the detection techniques available for three types of fission experiment which utilize the neutron time-of-flight method. These are (a) fission cross section measurements, (b) measurements of η, the number of prompt fission neutrons emitted per neutron absorbed, and (c) measurements of fission fragment mass distributions as a function of neutron energy.

(a) Detectors for fission cross section measurements.

A fission can be identified by the detection of fission fragments or by the detection of prompt (fast) fission neutrons. In the former method the fissile sample must of course be thin to fission fragments; however the fission detection efficiency will generally approach 100%. In the second method the sample can be thick but fission detection efficiency is limited to $\leqslant 10\%$ by the solid angle and efficiency of the fast neutron detector. The two methods are complementary from the viewpoint that $\exp(-n\sigma_T)$ must be small for accurate fission cross section measurement (n is the sample thickness in atoms per cm^2, σ_T is the total cross section). Thus where σ_T is large, i.e. on resonance peaks, n should be small and fragment detection is favoured. Off resonances, however, n can be large, thus fission neutron detection may be favoured.

(i) Fission fragment detectors.

For fragment detection we can choose between an ion chamber [22,23,24], a gas scintillation counter [25,26] or a solid state detector [27,28]. The first two have the merit that they can handle large area ($\sim$ 100 cm^2) samples. Solid state detectors, though simpler, are, in contrast, considerably smaller units (typically $\leqslant 3$ cm^2). On the other hand, the rise time of fission pulses from the ion chamber is ~ 0.3 μs, compared with a few ns for the other two detectors. The ion chamber is thus much more susceptible to "α pile-up", e.g. for a highly α-active nuclide, like Pu^{239}, the maximum amount of material which an ion chamber can handle is about 10 mg, compared with $\sim$ 120 mg which a gas scintillator has handled comfortably [25].

(ii) Fission neutron detectors.

Fission cross section measurements via fission neutron detection depend on the assumption that $\bar{\nu}$, the average number of prompt neutrons per fission, is constant over the incident neutron energy range under study. For Pu^{239} this assumption has been verified experimentally [29] up to a neutron energy of $\sim$ 1.7 keV. The properties required of the fission neutron detector are timing resolution, efficiency, and good discrimination against neutron capture γ-rays. Neutron detectors which have been used include: (*i*) the Hornyak Button [30,31,32]; (*ii*) a high pressure methane ion chamber [33]; (*iii*) a pair of large liquid scintillators operated in coincidence [29,25]; and (*iv*) crystal or liquid organic scintillators with pulse shape discriminators [34,35]. The last two detecting systems offer the best in fission detection efficiency ($\sim$ 5—10%), in discrimination against γ-rays ($\leqslant 0.01\%$) and in timing resolution ($\leqslant 0.05$ μs). A "fast-slow" system is required in detector (*iv*), to attain this timing resolution, if one of the older type P. S. D. circuits [34,36,37] is used. This requirement could be removed through the use of fast, jitter-free, P. S. D. circuits which have recently been developed [38,39].

(b) Detectors for η-measurements.

The fission neutron detector requirements here are the same as those considered in the previous paragraph. However, the condition that $\bar{\nu}$ be constant can be relaxed if the detection efficiency for a single fission neutron is small.

(c) Detectors for fission fragment mass distribution measurements.

Fission fragment mass distributions can be measured (*i*) by radiochemical methods and (*ii*) by using back-to-back fission fragment detectors. The use of the former technique in a time-of-flight experiment was demonstrated by the Los Alamos experiment [40], in which the neutron source was a single burst from a nuclear explosion. The detector in this experiment was the U^{235}-covered periphery of a spinning wheel, the U^{235} being radiochemically analysed afterwards.

In method (*ii*) two fragment detectors measure the energies, E_1 and E_2 of the two fission fragments respectively, and their mass ratio is obtained from the relation:

$$m_1/(m_1+m_2) = E_2/(E_1+E_2).$$

The first and foremost property required of the fragment detectors is good energy resolution. The gas scintillation detector is unsatisfactory in this respect. The ion chamber [41] and the solid state detector [27,42] achieve satisfactory energy resolution but compromise on one or other of the remaining two desirable properties, namely rise-time and large sample area respectively (see paragraph (a) above).

IV. DETECTORS FOR CAPTURE EXPERIMENTS

We may conveniently divide capture experiments into two types, capture cross section measurements and studies of neutron capture γ-ray spectra respectively.

(a) Detectors for capture cross section measurements.

The detector requirements here are the usual ones of timing resolution and efficiency and also that the detector be insensitive to scattered neutrons and that the capture detection efficiency be independent of capture γ-ray spectrum. The last is the most critical requirement and the one which limits the use of the most popular and obvious γ-ray detector, namely the NaI(Tl) crystal. NaI(Tl) detectors have been used nevertheless [43], but only under special conditions where (*i*) γ-spectra were the same from resonance to resonance and (*ii*) a suitable ($\Gamma\gamma >> \Gamma_n$) low energy resonance was available for calibrating the detector efficiency.

One method of achieving independence of the capture spectrum is to use a 4π and totally absorbing γ-detector consisting of a large liquid scintillator [44,45,46]. With timing resolution $\sim$ 0.03 μs and $\sim$ 100% capture detection efficiency, this detector is ideally suited for high resolution capture cross section measurements using thin samples. The neutron sensitivity of such a tank is primarily through the 2.2 MeV γ-ray which follows neutron capture in hydrogen. This sensitivity is reduced to a low level by loading the scintillator with methylborate, the boron serving to capture neutrons with the emission of a lower energy γ-ray (0.48 MeV).

Another approach toward achieving independence of the capture spectrum is that used in the detector to be described by Moxon and Rae [47] later in this session. Their detector consists of a calculated thickness ($\sim$ 4 cm) of graphite, which acts as a γ-ray to electron convertor, and thin plastic scintillators ($\sim$ 0.03 cm) to detect electrons. The detector efficiency, like that of a thick-walled Geiger counter, is proportional (approximately) to the total energy in the γ-ray cascade, and essentially independent of γ-ray multiplicity.

(b) Detectors for the study of capture γ-ray spectra.

The principal, and sometimes conflicting, properties required of the detector in this type of experiment are: (*i*) good γ-ray energy resolution (i.e. "line-shape"); (*ii*) small probability of summing the energies of two or more γ-rays and detecting them as one γ-ray; (*iii*) timing resolution; and (*iv*) detection efficiency. Requirements (*i*) and (*iv*), together with the low neutron intensities available when neutron energy is simultaneously being measured by time-of-flight, inevitably dictate that the detector must consist of one or more NaI(Tl) crystals.

Single NaI(Tl) crystals have been used [48] in sizes up to $\sim$ 25 cm diam. $\times$ 15 cm, the advantage in going to large crystals being better line-shape rather than higher overall detection efficiency; the need to avoid summing requires that the solid angle of detection be kept small. Arrangements of two or more crystals have been used to improve line shape and/or to increase solid angle while avoiding summing. For example, the Brookhaven group [49] have used six crystals (10 cm $\times$ 10 cm) connected in parallel to a single pulse height analyser, but with an anticoincidence gate to eliminate summing of events in two or more crystals. A two-crystal pair spectrometer has been used at Harwell [50] to improve line-shape. The sum-coincidence method [51] has been considered at Yale [52] as a means of selecting and studying two-step capture γ-ray cascades. The Argonne group [53] have used two crystals in coincidence, with one biased just below the binding energy, so that the other records transitions from the first few excited states of the compound nucleus. By this technique the transitions feeding the low-lying states are studied (indirectly) under much higher resolution than would have been possible by observing them directly.

The last two coincidence techniques mentioned suffer the limitation that they do not permit observation of the single transition direct from the capturing state to the ground state, a transition which is often of particular interest in neutron capture γ-ray work. In the other γ-spectrometers the main requirement is a good line shape. A single large crystal (or several anticoincidence-gated large crystals) has the advantage that it improves line-shape without sacrificing γ-efficiency. Two- or three-crystal pair spectrometers, in contrast, are capable of better line-shapes, but at the expense of γ-efficiency.

Acknowledgements.

I am indebted to all the authors who have allowed me to quote their results prior to publication.

REFERENCES

(1) SUN, K.H., MALMBERG, P.R., PECJAK, F.A., *Nucleonics* **14**, No. 7, 46 (1956).
(2) WRAIGHT, L.A., Harwell Memo, AERE M 833.
(3) EGELSTAFF, P.A., HARRIS, D.H.C. and WRAIGHT, L.A., to be published in *Nucl. Instr.*
(4) MAIENSCHEIN, F.C., PEELLE, R.W., ZOBEL, W. and LOVE, T.A., 2nd Int. Conf. on the Peaceful Uses of Atomic Energy, **15**, 368, Geneva (1958).
(5) GROSHEV, L.V., DEMIDOV, A.M., LUTSENKO, V.N. and PELEKOV, V.I., "Atlas of Gamma-Ray Spectra from Radiative Capture of Thermal Neutrons", Pergamon Press (London) (1959).
(6) RAE, E.R. and BOWEY, E.M., *Proc. Phys. Soc.* A**66**, 1073 (1953).
(7) BOLLINGER, L.M. and THOMAS, G.E., to be published in *Rev. Sci. Instr.*
(8) CRANBERG, L. et al., Oak Ridge Report, ORNL-2309, p. 148 (1956).
(9) CRANBERG, L., BEAUCHAMP, R.K. and LEVIN, J.S., *Rev. Sci. Instr.* **28**, 89 (1957).
(10) RAINWATER, J., HAVENS, W.W. Jr., DESJARDINS, J.S. and ROSEN, J.L., *Rev. Sci. Instr.* **31**, 481 (1960).
(11) BOLLINGER, L.M. and THOMAS, G.E., *Rev. Sci. Instr.* **28**, 489 (1957).
(12) BOLLINGER, L.M., THOMAS, G.E. and GINTHER, R.G., *Rev. Sci. Instr.* **30**, 1135 (1959).
(13) BISHAY, A.M., *J. Am. Ceramics Soc.*, 231, May 1961.
(14) STEDMAN, R., A.E.C.L. Report, CRRP 931.
(15) SEIDL, F.G.P., PALEVSKY, H., HUGHES, D.J., and ZIMMERMAN, R.L., Brookhaven Report, BNL 2947 and *Nucl. Instr.* **1**, 92 (1957).
(16) RAFFLE, J.F. and HALL, J.W., Harwell Report, AERE-M 461 (1959).
(17) HARRIS, D.H.C., Harwell Report, AERE - R 3688 (1961).
(18) POOLE, M.J. and WIBLIN, E.R., 2nd Int. Conf. on the Peaceful Uses of Atomic Energy, **14**, 266, Geneva (1958).
(19) ROSEN, J.L., DESJARDINS, J.S., RAINWATER, J. and HAVENS, W.W. Jr., *Phys. Rev.* **118**, 687 (1960).
(20) DESJARDINS, J.S., ROSEN, J.L., HAVENS, W.W. Jr. and RAINWATER, J., *Phys. Rev.* **120**, 2214 (1960).
(21) RAE, E.R., Contribution to this Symposium, Session II, 119.
(22) YEATER, M.L., MILLS, W.R. and GAERTTNER, E.R., *Phys. Rev.* **104**, 479 (1956).
(23) MICHAUDON, A., GENIN, R., JOLY, R. and VENDRYES, G., Saclay Report, CEA - 1093 (1958).
(24) MOORE, M.S., MILLER, L.G. and SIMPSON, O.D., *Phys. Rev.* **118**, 714 (1960).
(25) BOLLINGER, L.M., COTE, R.E. and THOMAS, G.E., Proc. 2nd Int. Conf. on the Peaceful Uses of Atomic Energy, **15**, 127, Geneva (1958).
(26) HAVENS, W.W. Jr., MELKONIAN, E., RAINWATER, L.J. and ROSEN, J.L., *Phys. Rev.* **116**, 1538 (1959).

(27) MELKONIAN, E., Harwell Report, AERE-R 3524 (1960).
(28) JAMES, G.D. and UTTLEY, C.A., Contribution to this Symposium, Session II, 115 and 109.
(29) BOLLINGER, L.M., Oak Ridge Report, ORNL-2309, 167 (1956).
(30) HORNYAK, W.F., *Rev. Sci. Instr.* **23**, 264 (1952).
(31) PALEVSKY, H., HUGHES, D.J., ZIMMERMAN, R.L. and EISBERG, R.M., *J. Nucl. Energy* **3**, 177 (1956).
(32) YEATER, M.L., HOCKENBURY, R.W. and FULLWOOD, R.R., *Nucl. Sci. Eng.* **9**, 105 (1961).
(33) FARLEY, F.J.M., *J. Sci. Instr.* **33**, 276 and *J. Nucl. Energy* **3**, 33 (1956).
(34) BROOKS, F.D., *Nucl. Instr.* 4, 151 (1959).
(35) BROOKS, F.D., Contribution to this Symposium, Session II, 131.
(36) BROOKS, F.D., PRINGLE, R.W. and FUNT, B.L., *I.R.E. Trans. on Nucl. Sci.*, Vol. NS-7, No. 2-3, p. 35 (1960).
(37) OWEN, R.B., *Nucleonics* **17**, No. 9, 92 (1959).
(38) RETHMEIER, J., BOERSMA, H.J., JONKER, C.C., *Nucl. Instr.* **10**, 240 (1961).
(39) DAEHNICK, W. and SHERR, R., to be published in *Rev. Sci. Instr.*
(40) COWAN, G.A., TURKEVICH, A., BROWNE, C.I. et al., *Phys. Rev.* **122**, 1286 (1961).
(41) ROELAND, L.W., BOLLINGER, L.M., THOMAS, G.E., Proc. 2nd Int. Conf. on the Peaceful Uses of Atomic Energy, **15**, 440, Geneva (1958).
(42) GOODING, T.J., *Proc. Phys. Soc.* **77**, 1097 (1961).
(43) RAE, E.R. and BOWEY, E.M., *J. Nucl. Energy* **4**, 179 (1957).
(44) DIVEN, B.C., TERRELL, J. and HEMMENDINGER, A., *Phys. Rev.* **120**, 556 (1960).
(45) BLOCK, R.C., Oak Ridge Reports, ORNL-2910, 35 (1960) and ORNL-3085, 48 (1961).
(46) GIBBONS, J.H., MACKLIN, R.L., MILLER, P.D. and NEILER, J.H., *Phys. Rev.* **122**, 182 (1961).
(47) MOXON, M.C. and RAE, E.R., Contribution to this Symposium, Session IV, 443.
(48) BOLLINGER, L.M., COTE, R.E. and MARION, J.P., *Bull. A.P.S.*, Series II, **6**, 274 (1961).
(49) HUGHES, D.J., PALEVSKY, H., BOLOTIN, H. and CHRIEN, R., Proc. Int. Conf. on Nucl. Structure, Kingston, p. 771 (1960).
(50) BIRD, J.R., R.P.I. Neutron Physics Symposium, May 1961, to be published in *Nucl. Sci. Eng.*
(51) HOOGENBOOM, A.M., *Nucl. Instr.* **3**, 57 (1958).
(52) DRAPER, J.E. and FLEISCHER, A.A., *Nucl. Instr.* **9**, 67 (1960).
(53) KENNETT, T.J., BOLLINGER, L.M. and CARPENTER, R.T., *Phys. Rev. Letters*, **1**, 76 (1958).
(54) NICHOLSON, K.P. and SNELLING, G.F., Harwell Report, AERE EL/R 1350 (1954).
(55) SCHENK, J. and HEATH, R.L., *Phys. Rev.* **85**, 923 (1952).
(56) MUEHLHAUSE, C.O. and THOMAS, G.E., *Phys. Rev.* **85**, 926 (1952) and *Nucleonics* **11**, 44, No. 1 (1953).
(57) FURST, M., KALLMANN, H. and BROWN, F.H., *Nucleonics* **13**, No. 4, 58 (1955).
(58) EGELSTAFF, P.A., *Nucl. Instr.* 1, 197 (1957).
(59) GINTHER, R.J. and SCHULMAN, J.H., *I.R.E. Trans. on Nucl. Sci.*, NS-5, No. 3, 92 (1958).
(60) VOITOVETSKII, V.K., TOLMACHEVA, N.S. and ARSAEV, M.I., *Atomn. Energ.*, **6**, 321 (1960).
VOITOVETSKII, V.K. and TOLMACHEVA, N.S., *Atomn. Energ.*, **6**, 472 (1960).
(61) GINTHER, R.J., *I.R.E. Trans. on Nucl. Sci.*, NS-7, No. 2-3, 28 (1960).
(62) FIRK, F.W.K., SLAUGHTER, G.G. and GINTHER, R.J. to be published in *Nucl. Instr.*

DISCUSSION

Chrien:

I want to point out that there has been a large amount of information produced using BF_3 detectors from 10 eV up to 1 keV and I think there will still be plenty of use for them in this energy region.

Brooks replied:

I accept your statement, of course. Perhaps it should even have been included in my survey. However, my aim has been to show how one might choose a neutron detector from those currently available. I think that it is fair to say that the detector choice for transmission work above 10 eV would now be the B^{10}-plug - NaI, B^{10} liquid, or one of the B^{10} or Li^6-glasses, rather than $B^{10}F_3$ counters.

Comment by *Egelstaff*:

I would like to make a brief remark at this point on the question of thickness of Li^6-glass. This will be in lieu of giving a paper later in the session.

We have made a number of measurements on the resolution and the amount of overlap with γ-rays for Li-glass as a function of thickness. The results of this are given in Table I.

TABLE I

Thickness of glass (inches)	Resolution (in %)	% neutron peak overlap
1/16	10.3	1
1/8	11.0	7
1/4	13.7	20
3/8	15.5	50

For the resolution, we have taken the full width at half maximum amplitude. We see that the width is increasing with the glass thickness, but in particular for the very thin piece of glass, the resolution is rather good.

The γ-ray source used for determining the percentage overlap was a Co^{60}-source giving a flux of 5 mR/h. This Co^{60}-spectrum overlaps the neutron spectrum to some extent (Figure 1) and if we take a vertical line passing through the end-point of the γ-spectrum, we can determine the fraction of the neutron peak lying to the left of that line. This fraction, which we call the percentage overlap, varies very sharply with thickness as can be seen from Table I, and this confirms the point Dr. Brooks was making about the relative insensitivity of the thin glass to γ-rays as well as the fact that it has good resolution.

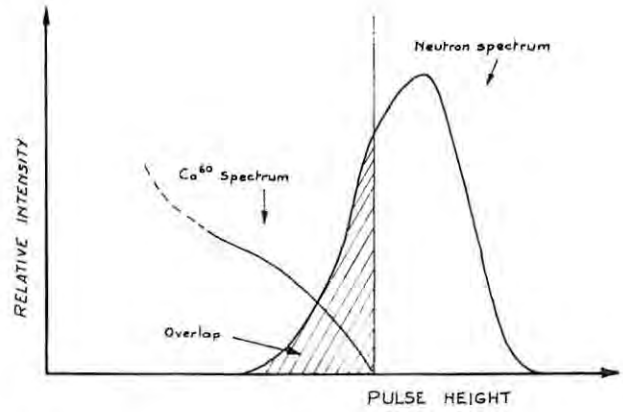

Figure 1
Curve showing the definition of the amount of overlap between neutron pulse spectrum and Co^{60} γ-ray spectrum for Li^6-glass detectors.

Comment by *Cranberg:*

A Li^6H detector would have exceptional usefulness as a detector, covering a wide range of neutron energy at high efficiency. The low energy neutrons would be detected by $Li^6(n,\alpha)T$ and the higher energy neutrons by proton recoil. It is hoped that those interested in such a broad-range detector would stimulate the development work necessary to produce Li^6H in the form of a scintillating crystal.

Cocking:

I should like to ask if anyone has any experience of using an idea tried out in a different context by myself and others, which is relevant to the point made by Dr. Brooks about using thin Lithium Iodide crystals, thinner than the range of recoil electrons in the crystal, the point here being if one wishes to use a very large crystal, one can make it up of several smaller ones and separate these optically with very thin aluminium so that the photomultiplier still sees the whole crystal optically but a recoil electron is stopped in one of these different regions. Has anyone any experience of applying this method ?

Bollinger:

I see that Dr. Cocking is getting very close to an idea that we at Argonne have been working on, so I must hurry to get the idea on the record. We are attempting to make a detector that is very insensitive to γ-rays by using small *balls* of either a B- or a Li-glass scintillator. The scintillating balls are embedded in a transparent medium that does not scintillate. It is hoped that, because of the difference in the ranges of electrons and the reaction products, we will be able to find a ball size for which the medium will be sensitive to neutrons, but insensitive to γ-rays. It is also hoped that, by a proper adjustment of refractive indices, it will be possible to extract most of the light. These ideas

are, of course, merely an extension of the technique already used by Dr. Bonner for fast neutrons. The work at Argonne is being done by Dr. Thomas.

Brooks:

I should like to make a comment on the suggestion of using multiple scintillators. What we thought we could do was to use several slabs viewed by two P.M. in an arrangement such as given in Figure 2. Assuming that the radiation is falling in along a direction indicated on the figure, we only need an anticoincidence arrangement in order to distinguish between neutrons and γ-rays.

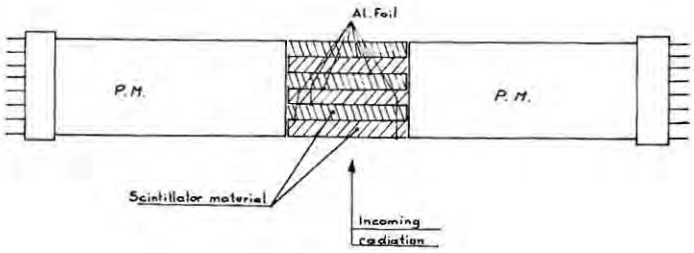

Figure 2
Anti-coincidence arrangement for neutron detector using multiple scintillator slabs.

F.D. Brooks
General survey on choice of the detector for a time-of-flight experiment
Neutron Time-of-Flight Methods, ed. A. Spaepen (EANDC, Brussels, 1961) 389-405

A measurement of eta versus energy for U235

by F.D. BROOKS

Reprinted from Proceedings of the Symposium on neutron time-of-flight methods,
organized by the European-American Nuclear Data Committee
(Saclay, France, 24-27 July, 1961),
Session II, pp. 131-137.

A MEASUREMENT OF ETA VERSUS ENERGY FOR U^{235}

F.D. BROOKS
Atomic Energy Research Establishment, Harwell, UK.

Abstract

Eta, the number of prompt fission neutrons emitted per neutron absorbed, has been measured for U^{235} + n as a function of neutron energy from 0.7 eV to 50 eV. Fission neutrons were detected by liquid scintillation counters with pulse shape discriminating circuits to minimize sensitivity to capture γ-rays. This detector served to measure the fission neutron yield and also, by a "self-indication" method, to measure the transmission of the U^{235} sample. Four different samples were used and the energy range 0.7 - 10 eV was covered with 44 ns/m resolution, while the energy range 10 - 50 eV was covered with 11 ns/m resolution.

This experiment to measure eta (the number of prompt fission neutrons emitted per neutron absorbed) versus neutron energy for U^{235} + n differed only in detail from other direct measurements [1,2,3,4] on U^{235}, U^{233} and Pu^{239}.

Figure 1(a) shows the experimental arrangement, a flight path with sample positions, (1) at 22.3 metres, and (2) at 19 metres, from the Harwell pulsed

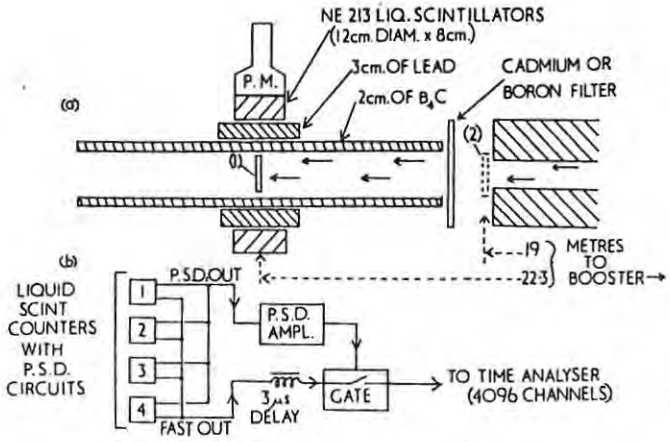

Figure 1
(a) Experimental arrangement for the measurement of eta.
(b) Block diagram of pulse shape discriminating system.

neutron source, the "Booster". The fission neutron detector was at 22.3 metres and consisted of four liquid scintillators (NE 213 scintillator, 12 cm diam. × 8 cm) in parallel. Each scintillation counter had a fast ($\lesssim 0.05$ μs) output for timing as well as a pulse shape discrimination (P.S.D.) output to bias out γ-ray scintillations. The "fast-slow" system illustrated in figure 1(b) was used to overcome the time jitter ($\lesssim 0.5$ μs) of the P.S.D. circuits. The fast output was delayed for 3 μs while the P.S.D. amplifier decided whether to gate it through to the time analyser as a neutron scintillation. This P.S.D. system [5] enabled us to gate out more than 99.9% of the γ-rays detected by the scintillators, irrespective of γ-energy. At the same time the detection efficiency for fission neutrons, as measured using a calibrated Pu^{240} spontaneous fission source, was $\sim$ 5%. The time-of-flight analyser used was the 4096 channel digital tape recording system recently described by Waters and Bird [6].

Four uranium metal samples (93% U^{235}, 6% U^{238}, 1% U^{234}) were used in the measurement of eta for U^{235}. In this paper we present data obtained from 0.9 to 50 eV using the thickest sample, "Sample A". Sample A was a disc 7.9 cm in diameter with 8.95 g/cm² U^{235}. Sample B, 7.9 cm diam. and 8.95 g/cm² U^{235}, fulfilled an important auxiliary role in the eta measurement using A.

The experiment was divided at 10 eV into two broad energy regions. Below 10 eV a cadmium filter was used (see Figure 1(a)) and the timing channels were 1.00 μs, so that the nominal resolution was 44 ns/m. Above 10 eV a boron filter and 0.25 μs channels (11 ns/m) were used. Three time-of-flight runs were made in each energy region, to measure:

(*i*) the count rate, Y, with A at position (1) in figure (a):

(*ii*) the count rate with B at position (1): and

(*iii*) the count rate with B at (1) and A at (2).

Examples of raw data obtained in runs (*i*), (*ii*) and (*iii*) are shown in Figure 2(a). Run (*iii*) divided by run (*ii*) gave the fraction, I, of neutrons transmitted by A (example in Figure 2(b)). By using this "self-indication" method we have ensured that the yield, Y, and the transmission, T, were measured with essentially identical resolution. Eta, η, can thus be related to Y and T by the formula:

$$= \frac{\phi Y}{kN(E)(1-T)} \qquad (1)$$

where k is the detector efficiency, which can be assumed to be constant provided that the average number of neutrons per fission, $\bar{\nu}$, is constant, $N(E)$ is the number of incident neutrons as a function of energy and ϕ is a scattering correction factor.

Additional time-of-flight runs were made to determine relative values of $N(E)$ and to normalize the relative values of η thus obtained to the thermal

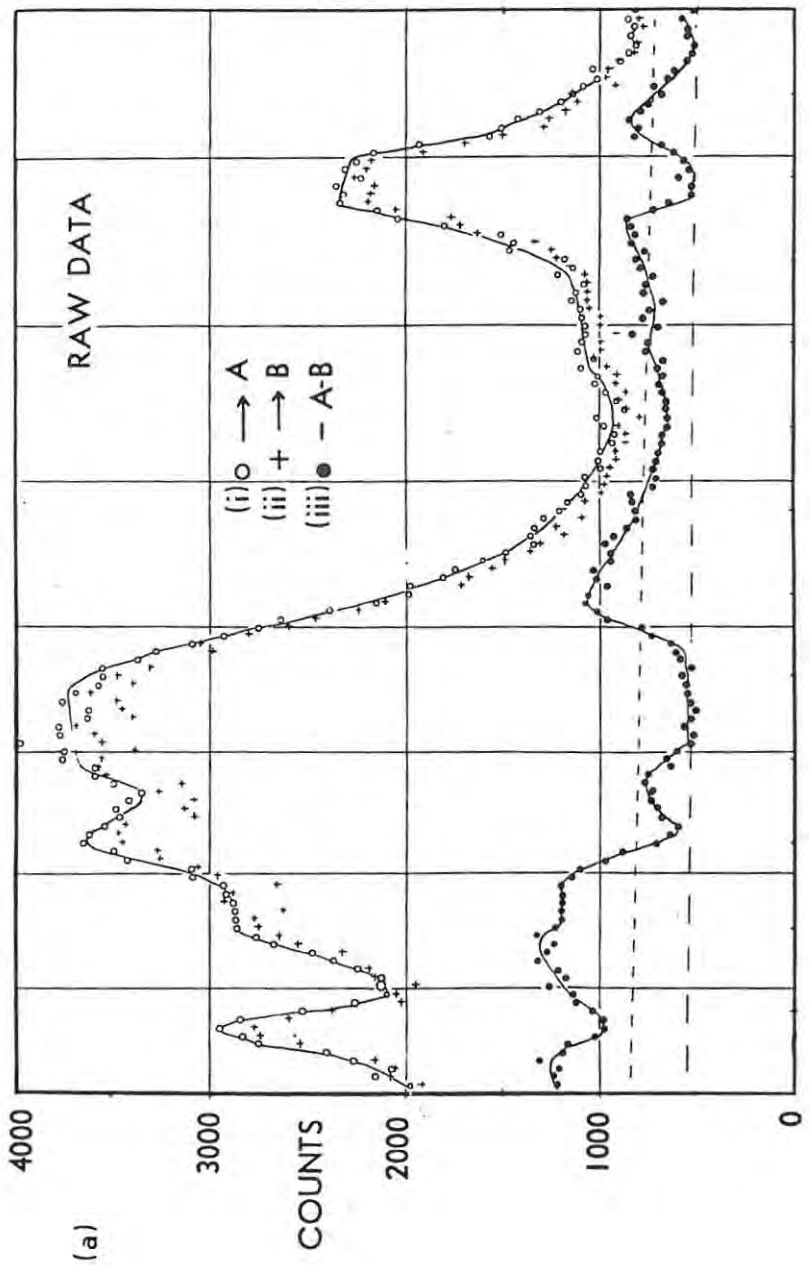

Figure 2
(a) Raw data. Counting rate versus neutron energy:
(*i*) with sample A at position (1) in figure 1 (a)
(*ii*) with sample B at (1)
(*iii*) with B at (1) and A at (2).

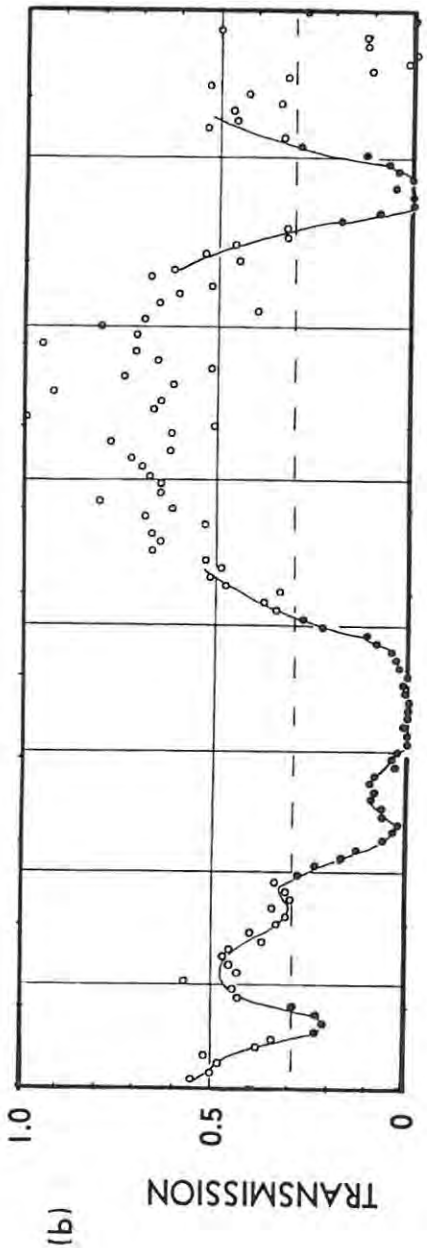

Figure 2
(b) Transmission of sample A.

value, $\eta = 2077$ [7]. $N(E)$ was measured using a thin BF_3 counter detector known to have an efficiency which varied as $(E)^{-1/2}$. The data were normalized to the thermal η-value by a cadmium difference method.

The scattering correction ϕ is difficult to measure or calculate. A simple analysis, covering only the possibilities of scattering out of the sample or absorption after one scattering, and neglecting the small energy shift in scattering gives for ϕ:

$$\phi = \left[1 - \left(\frac{\sigma_S}{\sigma_T}\right)^2 - T'\frac{\sigma_S}{\sigma_T}\left(1 - \frac{\sigma_S}{\sigma_T}\right)\right]^{-1} \qquad (2)$$

when σ_S and σ_T are the scattering and total cross sections and T' is the sample transmission averaged over the paths of the scattered neutrons. As yet we have not attempted to measure or calculate ϕ exactly. Instead we present, in Figure 2 (c), (d), (e) and in Figure 3, results of η/ϕ versus energy, and indicate by solid, rather than open, circles, data for which we estimate $1.00 \lesssim \phi < 1.05$. In other words the solid circles represent measurements of η $(= \eta/\phi)$ at energies where we estimate that neglect of scattering corrections causes less than 5% error.

The condition that $1.00 \leqslant \phi < 1.05$ was determined as follows. We know that for U^{235} neutron resonances below 50 eV, $\Gamma_n << \Gamma_F + \Gamma_\gamma$ i.e. that *resonance* scattering is small compared with capture and fission. Thus we have neglected resonance scattering and have required only that the total cross section, σ_T, should be sufficiently greater than the potential scattering cross section σ_P, to make ϕ, as given by equation (2), less than 1.05. Taking $\sigma_P = 12$ barns, the condition becomes that σ_T should exceed 75 barns or that the transmission, T, of sample A, should be less than 0.3. The data, $\eta/\phi(\sim \eta)$, are thus presented as solid circles where $T < 0.3$. The only exceptions to this procedure are at the energies 5.2, 6.7, 21 and 36.7 eV where transmissions of < 0.3 are attributed to the resonances of U^{234}- and U^{238}-impurities in sample A.

The errors shown on the η/ϕ data in Figures 2 and 3 are the standard statistical errors calculated from the primary time-of-flight data, that is runs (*i*), (*ii*) and (*iii*) and the backgrounds associated with these runs. U^{235} resonance energies are indicated by solid arrows, impurity resonance energies by broken arrows. In Figure 2(e), showing η/ϕ from 0.9 to 2.8 eV, resolution has been sacrificed in order to improve statistical accuracy by grouping into 8 μs channels.

Figures 2 and 3 illustrate that the approximation $\phi = 1.0$ is met, and hence that η is measured at, and near to, most of the U^{235} resonance energies. In several cases the data are sufficiently accurate to define a slope or variation of η through the resonance energy. This result is consistent with much recent evidence for U^{235} and other fissile nuclides which has indicated resonance-resonance interference in the fission cross section.

The principal features of the method which was used in this experiment are the pulse shape discriminating neutron detector and the transmission measurement by the "self-indication" method. The latter leads to the advantage that resolution effects are minimized when yield, Y, and transmission, T, are combined to evaluate η. On the other hand the transmission measurement is necessarily inaccurate between resonances or, in general, where the fission cross section is small. This disadvantage was not felt in the present measurements in which η could not be determined between resonances because the scattering correction factor, ϕ, was not known.

REFERENCES

(1) PALEVSKY, H., HUGHES, D.J., ZIMMERMAN, R.L. and EISBERG, R.M., *J. Nucl. Energy* **3**, 177.
(2) FARLEY, F.J.M., *J. Nucl. Energy* **3**, 33.
(3) BOLLINGER, L.M., Oak Ridge Report, ORNL.2309, 167.
(4) BOLLINGER, L.M., COTE, R.E. and THOMAS, G.E., Proc. 2nd Int. Conf. on the Peaceful Uses of Atomic Energy **15**, 127.
(5) BROOKS, F.D., PRINGLE, R.W. and FUNT, B.L., I.R.E., Trans. on Nuclear Sci. Vol NS-7, n° 2-3, 35.
(6) WATERS, J.R. and BIRD, J.R., *Nucleonics* **19**, n° 4, 17.
YEATER, M.L., MOCKENBURG, R.W. and FULLWOOD, R.R., *Nucl. Sci. and Eng.*, **9**, 105.
(7) MACKLIN, R.L., and al., O.R.N.L. Report.

DISCUSSION

Fluharty to Rae:

How do you propose to use the η-data to determine average reactor cross sections?

Rae replied:

We are not trying to obtain average cross sections from the η measurements, but rather to determine level parameters, in particular Γ_f to insert in multilevel analysis of the cross section data. Our reactor physicists feel that obtaining good multilevel fits is the only way to know how the cross section varies, for example, with reactor temperature.

Fluharty to Rae:

How do the data compare with the Saclay fission cross section measurements?

Rae replied:

We have not yet completed the analysis of the present data, but a table of Γ_f values obtained from an earlier run with lower resolution and more uncertainty in spectrum and background was in good agreement with the Saclay results.

Fluharty to Rae:

Why did you not take simultaneous total cross section data with a 1/v detector?

Rae replied:

We do intend to make total cross section measurements on U^{235}, but we have not yet got round to doing it.

Comment of Sher:

We have looked at different measurements of η of U^{233} in the region between 2 and 10 eV and find that these agree neither with each other nor with values calculated from the cross sections. We are, therefore, anxious to encourage further measurements using the new improved techniques. This is of importance in the design of intermediate breeders.

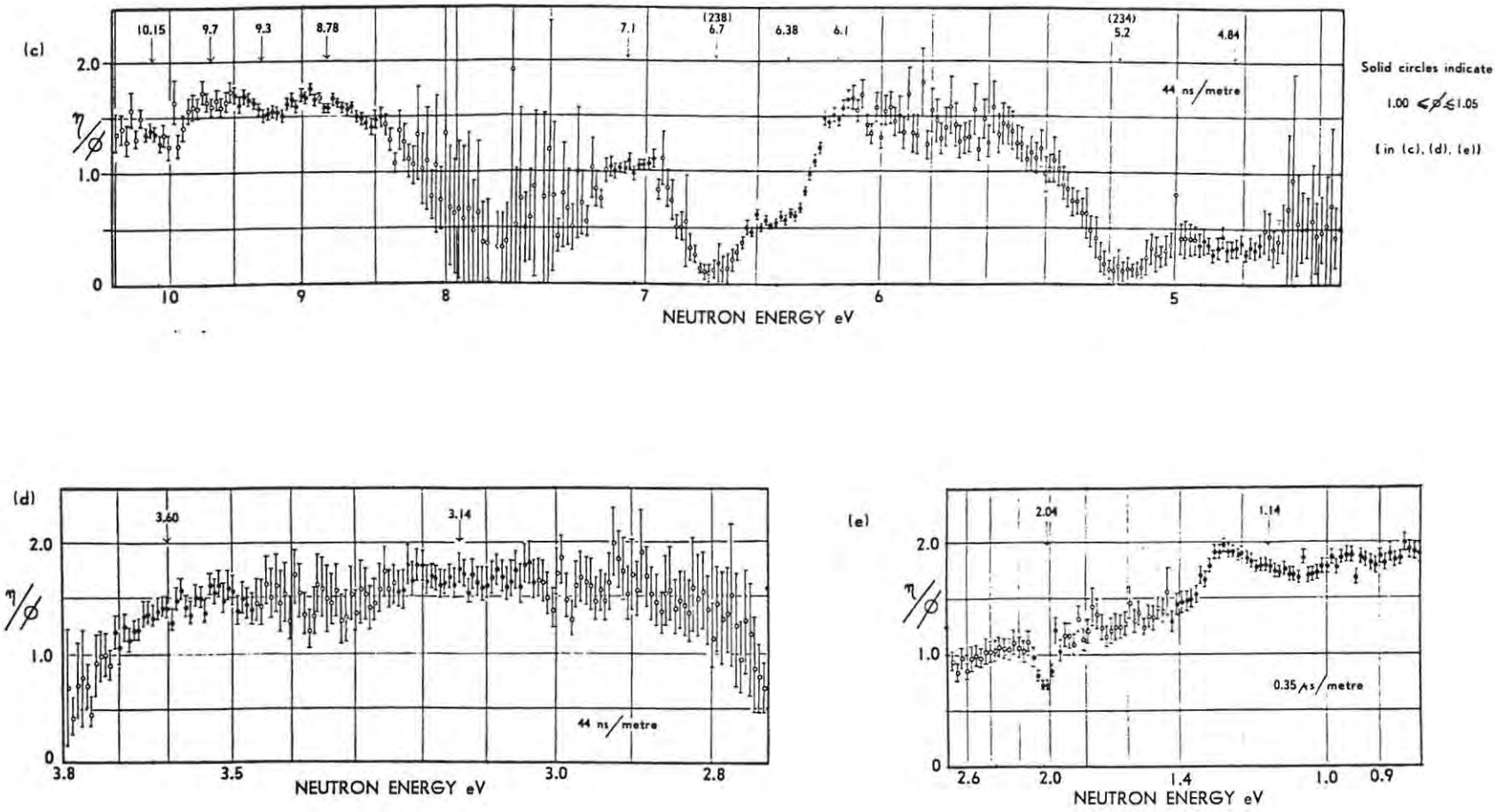

Figure 2
(c), (d), (e), η/ϕ versus neutron energy.
Solid points represent $1.00 \leqslant \phi < 1.05$ ϕ = scattering correction factor.

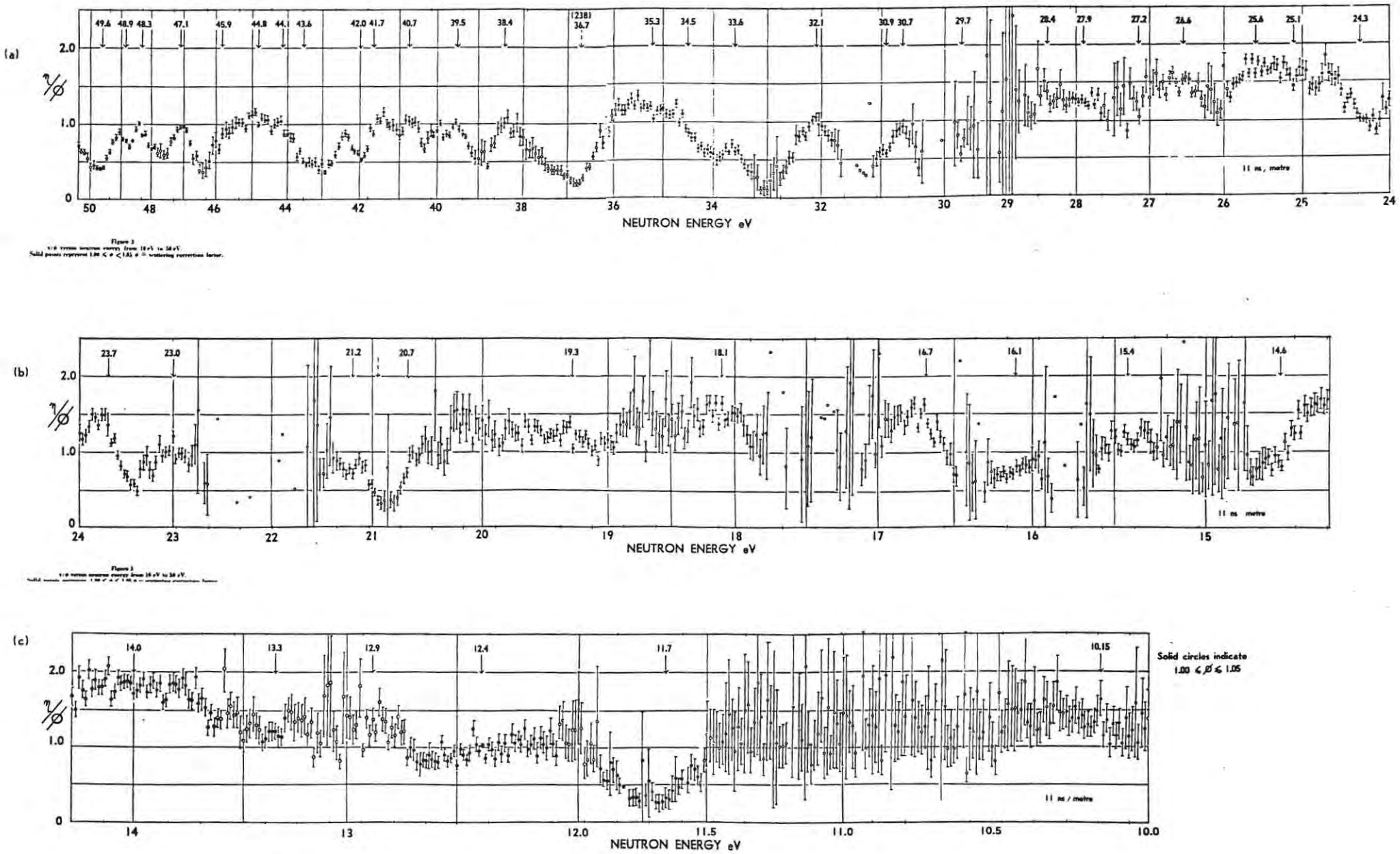

Figure 3

η/ϕ versus neutron energy from 10 eV to 50 eV.
Solid points represent $1.00 \leqslant \phi < 1.05$ ϕ = scattering correction factor.

NEUTRON PHYSICS

Proceedings of the Symposium held at Rensselaer Polytechnic Institute, May 5-6, 1961

Edited by M. L. Yeater

Department of Nuclear Engineering and Science, Rensselaer Polytechnic Institute Troy, New York

ACADEMIC PRESS

New York and London 1962

F.D. Brooks and J.R. Bird
Partial cross section measurements with the Harwell 28 Mev linear accelerator
Neutron Physics, ed. M.L. Yeater (Academic Press, New York, 1962) 109-123

Partial Cross Section Measurements with the Harwell 28-Mev Linear Accelerator

F. D. BROOKS and J. R. BIRD
Atomic Energy Research Establishment, Harwell, England

1. The Linac Facilities

The Harwell 28-Mev electron linac[1] running into the "booster" target is, for our purposes, a pulsed neutron source with the following properties. The pulse repetition frequency is 200 per second, the pulse width is 0.25 μsec (minimum), and the neutron intensity during the pulse is $\sim 10^{17}$ neutrons/second.

Figure 1 indicates how 10 flight paths are at present disposed about the booster for various cross section measurements. The longest path (200 meters) is used for total cross section work. Other paths are used for fission, scattering, and capture cross sections, respectively, while another is used for measurements of eta versus energy. The shorter flight paths, 13 and 6 meters, respectively, are used for studies of capture γ-ray spectra for different resonances, and fission mass distributions for different resonances, respectively. The total cross section facility at 15 meters is designed for small-sample work, and we are hoping that this will put us into competition with choppers for measurements on separated isotopes and fission products.

Signals from the 10 detector stations are cabled back to a central laboratory, housed in the same building as the accelerator, for time-of-flight analysis. For this analysis we have seven 100-channel units, one 1000-channel unit, and a digital magnetic tape recording system[2] which is equivalent to four 4096-channel time analyzers.

For the remainder of this paper we will confine ourselves to two of the partial cross section experiments mentioned above. These are (i) a measurement of eta versus neutron energy for U^{235}, and (ii) an investigation of capture γ-ray spectra for different resonances in Pt^{195}.

2. Measurement of Eta Versus Neutron Energy

The experiment to measure η, the number of prompt fission neutrons emitted per neutron absorbed, as a function of incident neutron

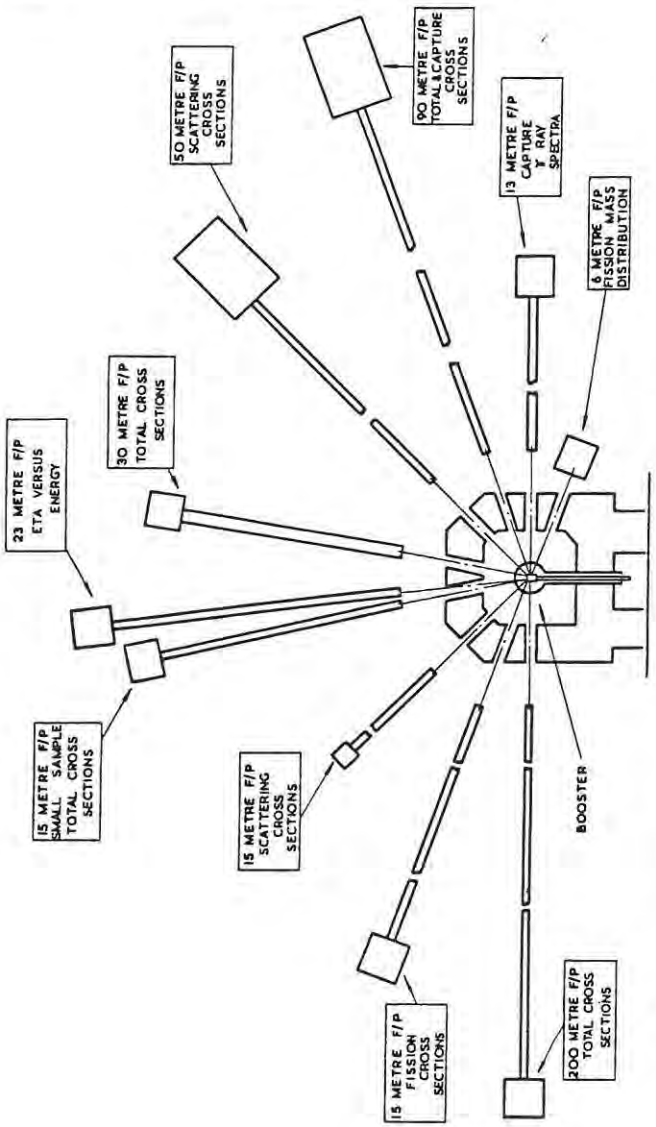

FIG. 1. Layout of neutron cross section experiments utilizing the Harwell "booster" pulsed neutron source.

energy, E, is similar, in principle, to several other "direct" measurements [3-7] on the three most abundant fissile nuclei. Figure 2(a) shows the experimental arrangement, a flight path with sample positions, (1) at 22.3 meters and (2), at 19 meters from the pulsed neutron source. The fission neutron detector, which is at 22.3 meters, consists of four liquid scintillation counters (NE 213 liquid*) in parallel. Each counter has a fast output for timing and a pulse shape discriminator to bias out γ-ray scintillations. These outputs

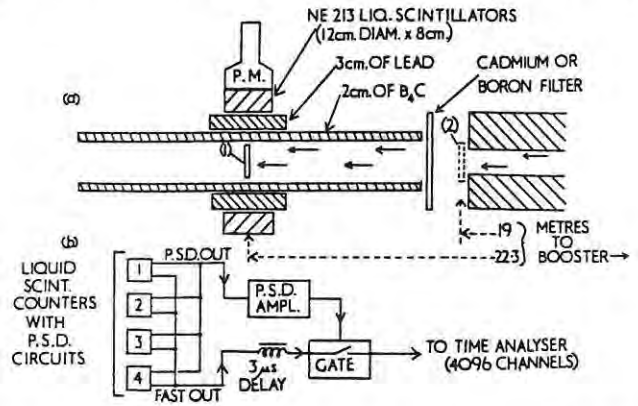

FIG. 2. *a*, Experimental arrangement for the measurement of eta; *b*, block diagram of pulse shape discrimination system.

are coupled as shown in Fig. 2(b); the fast output is delayed 3 μsec while the P.S.D. amplifier decides whether to gate it through to the time analyzer as a neutron scintillation. This P.S.D. system[8] enables us to gate out more than 99.9% of the γ-rays detected in the scintillator, irrespective of γ-energy. At the same time, the detection efficiency for fission neutrons, as measured using a calibrated Pu^{240} spontaneous fission source, is $\sim 5\%$.

Four uranium metal samples (93% U^{235}, 6% U^{238}, 1% U^{234}) were used for the measurement of η for U^{235}. In this paper we present some of the data obtained using the thickest sample, "sample A," which was a disk of 3.1-inch diameter and 8.95 gm/cm^2 U^{235}. Sample

* Supplied by Nuclear Enterprises (G.B.) Ltd., Edinburgh, Scotland.

B, of 8.59 gm/cm² U^{235}, but otherwise similar to A, fulfilled an important auxiliary role in this measurement on "sample A."

The η measurement using A was divided into two broad energy regions, 0.7-11 and 5-300 ev, respectively. In the lower energy region the cadmium filter was used [see Fig. 2(a)] and the time-of-flight resolution was 44 nsec/meter. The boron filter was used in the upper region and the resolution there was 11 nsec/meter. Three time-of-flight runs were made in each region to measure:

(a) the count rate Y, with A at position (1) [Fig. 2(a)];

(b) the count rate with B at (1); and

(c) the count rate with B at (1) and A in transmission, at (2).

Run (c) divided by run (b) thus gave T, the fraction of neutrons transmitted by A. By using this "self-detection" method we have ensured that Y and T are measured with essentially identical resolution. Eta was calculated from the formula

$$\eta = \frac{\phi \cdot Y}{k \cdot N(E) \cdot (1 - T)} \tag{1}$$

where k is the detector efficiency, which may be assumed to be constant provided that $\bar{\nu}$ the average number of neutrons per fission is constant, $N(E)$ is the number of incident neutrons as a function of energy, and ϕ is the scattering correction factor.

Additional time-of-flight runs were made to determine relative values of $N(E)$ and to normalize the relative values of η thus obtained to the thermal value $\eta = 2.077$.[9] The spectrum $N(E)$ was measured using a thin BF_3 counter detector known to have an efficiency which varied as $(E)^{-1/2}$. The data were normalized to the thermal η value by a cadmium difference method.

The scattering factor, ϕ, is difficult to measure or calculate. A simple analysis covering only the possibilities of scattering out of the sample or absorption after one scattering, and neglecting the small energy shift in scattering, gives for ϕ:

$$\phi = [1 - (\sigma_S/\sigma_T)^2 - T' \cdot \sigma_S/\sigma_T(1 - \sigma_S/\sigma_T)]^{-1} \tag{2}$$

where σ_S and σ_T are the scattering and total cross sections, respectively, of the sample, and T' is the sample transmission averaged over the paths of the scattered neutrons. As yet we have not attempted

to measure or calculate ϕ exactly. Instead we have calculated η only at energies where we could reasonably assume that $1.00 \leq \phi < 1.05$. For sample A this meant, in practice, that we calculated η only where the transmission, T, was measured to be less than ~ 0.3.

Figures 3 and 4 show the measurements of transmission, T, and eta from 0.7 to 33 ev incident neutron energy. There are many gaps in the eta data due to the lack of information on ϕ. However, we are able to present data at most of the resonance energies and also, in several cases, to determine the behavior of η over resonances. In many of these cases the result is that η varies through the resonance, a result which is similar to that which Bollinger[5,6] observed in several Pu^{239} resonances and which suggests resonance-resonance interference in the fission process. Such interference implies of course, that we cannot analyze resonance fission cross sections in terms of the single level Breit-Wigner formula. However, if following Teichmann[10] we assume that the single level formula is a good approximation (i.e., that interference is a minimum and can be neglected) at the resonance energy, we can write[4] for values, η_R, of eta at resonance energies:

$$\eta_R = \frac{\bar{\nu}\,\Gamma_f}{\Gamma_\gamma + \Gamma_f},$$

i. e.,

$$\Gamma_f = \frac{\Gamma_\gamma}{(\bar{\nu}/\eta_R) - 1} \tag{3}$$

where Γ_γ and Γ_f are radiation and fission widths, respectively. Thus, if we know, or can assume, values for $\bar{\nu}$ and Γ_γ, we can arrive at values for Γ_f. Some fission widths obtained by taking[11] $\bar{\nu} = 2.43$ and assuming a constant radiation width[12] $\Gamma_\gamma = 33$ Mev are shown and compared with recent BNL-325 data[11] (u) in Table I. The agreement between the two sets of data is quite good. A useful by-product of the direct eta measurement might therefore be that it affords a simple, and perhaps reliable, method of determining fission widths.

3. Gamma-Rays from Platinum Resonances

In the study of the intensities of individual γ-rays following resonance neutron capture, it is desirable to have the best available γ-ray resolution. All measurements to date have been made with

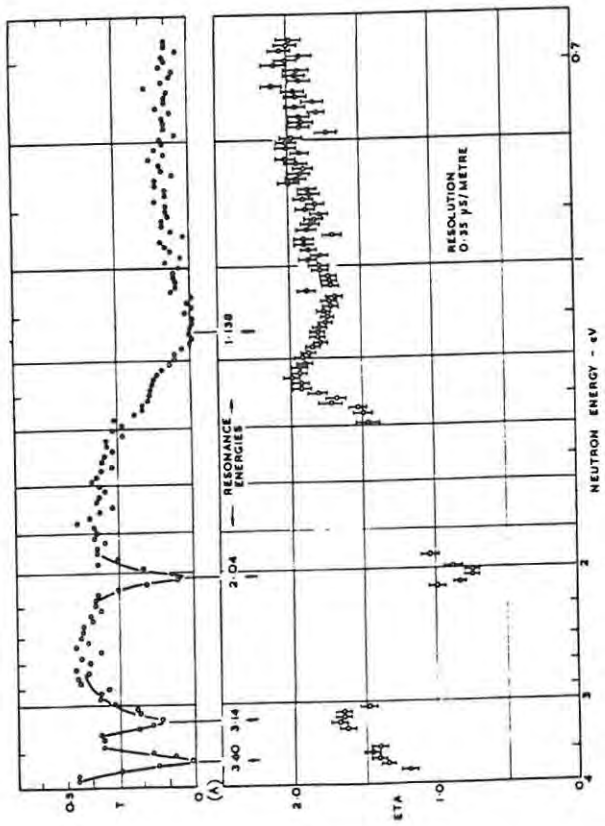

FIG. 3. Transmission, T, of sample A (above) and Eta of U^{235} (below) versus incident neutron energy; *a*, from 0.7 to 4.0 ev at 0.35 μsec/meter resolution; *b*, from 2.8 to 3.7 ev and from 4.6 to 11.0 ev at 44 nsec/meter resolution.

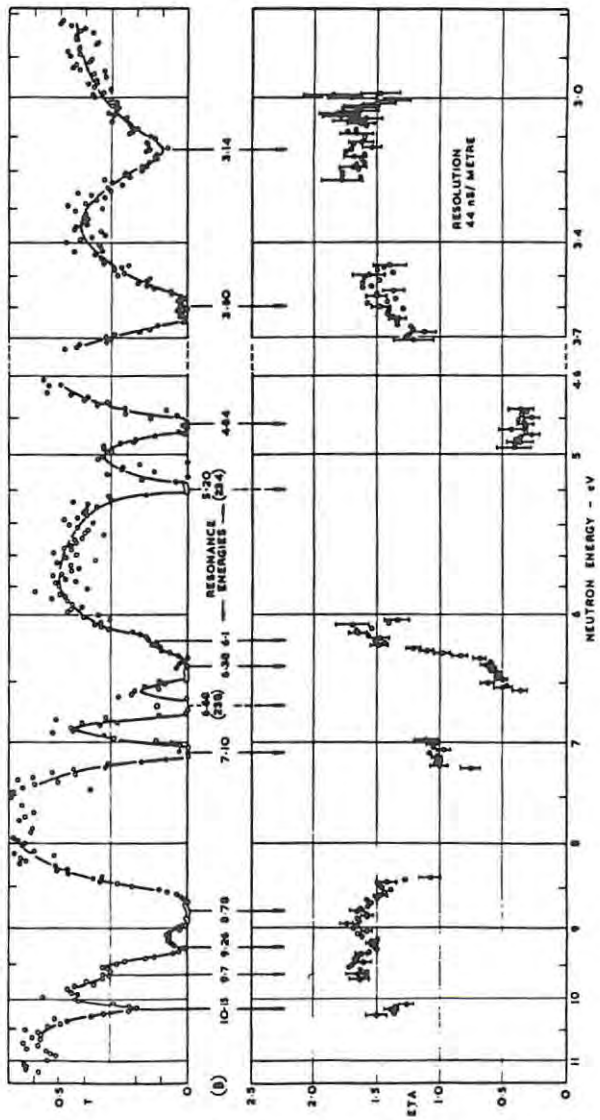

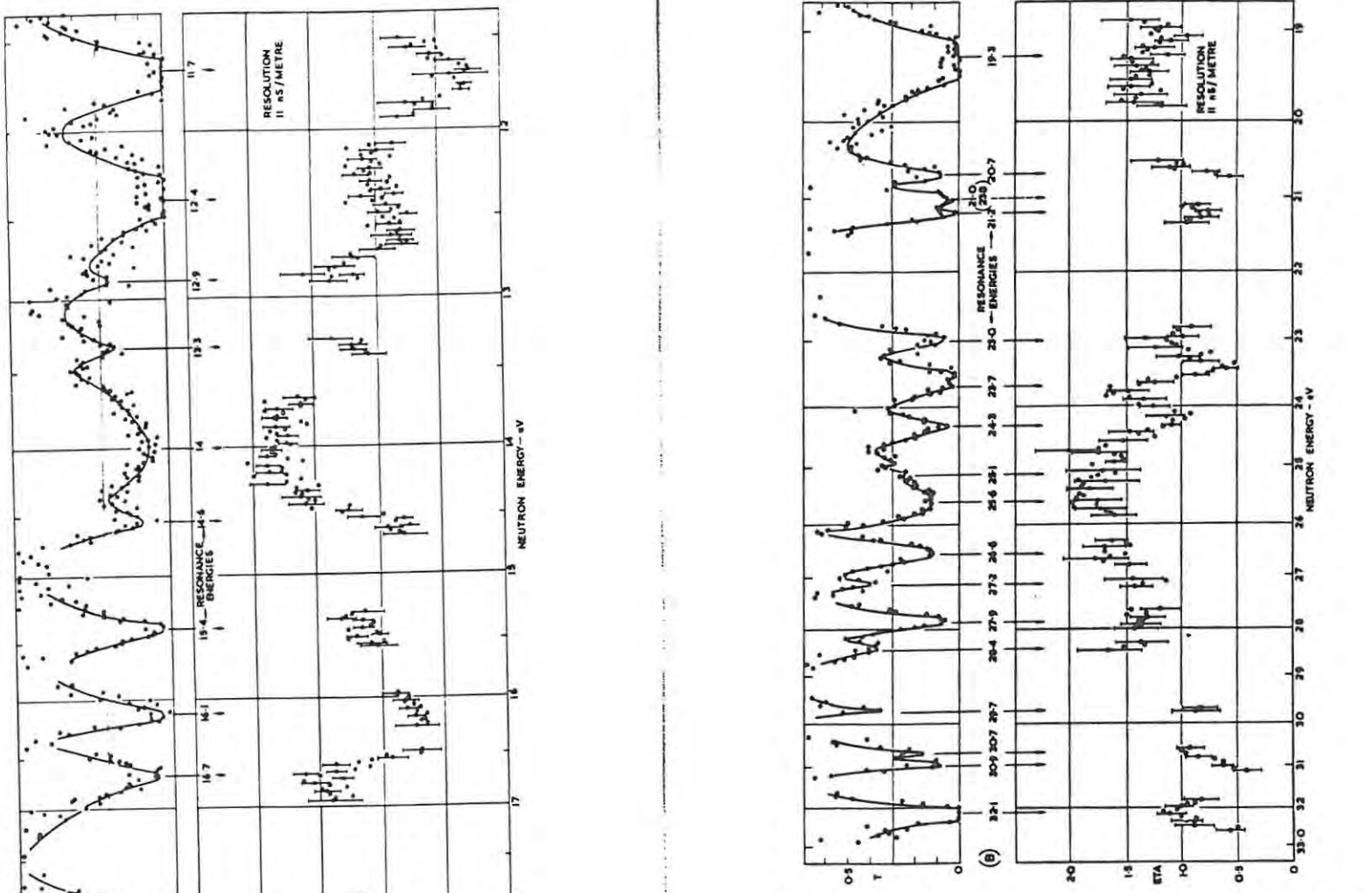

FIG. 4. Transmission, T, of sample A (above) and eta of U^{235} (below) versus incident neutron energy; *a* from 11.5 to 18.5 ev; *b* from 19.0 to 33.0 ev. Resolution = 11 nsec/meter.

TABLE I

FISSION WIDTHS OF U^{235} NEUTRON RESONANCES

Resonance energy (ev)		1.14	2.04	3.14	3.60	4.84	6.1	6.38	7.1	8.78	9.26
Fission Widths (Mev)	(a)	94	14	76	46	5.1	56	10.8	24	65	56
	(b)	106 ± 11	12 ± 3	115 ± 44	45 ± 4	4 ± 3	—	9 ± 1	23 ± 18	60 ± 6	—

(a) Calculated from the value η_R of eta at resonance energy assuming $\bar{\nu} = 2.43$, $\Gamma_\gamma = 33$ Mev.
(b) Value given in Hughes and Schwartz.[11]

single sodium iodide crystals of as large a size as possible in order to reduce the effect of pair escape events. By using an additional crystal to detect escaping 0.51-Mev γ-rays in coincidence with a primary event an appreciable improvement in line shape can be achieved. This technique has been used to measure the intensity of the three highest energy γ-rays from the first three resonances in Pt^{195}.

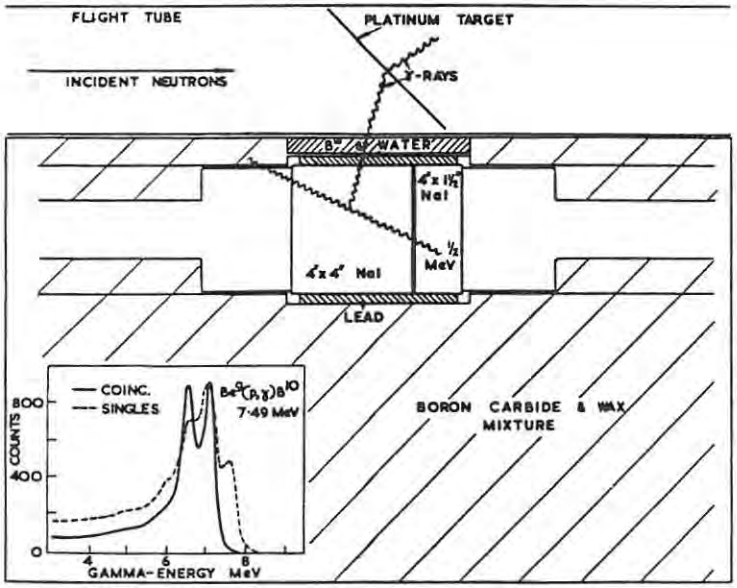

FIG. 5. Experimental layout for the measurement of γ-ray spectra from resonant neutron capture in platinum. Inset shows pulse-height spectra obtained from the 4 × 4 inch NaI (Tl) crystal using the 7.49 Mev γ-ray from Be^9 (p, γ) B^{10}; (i) broken curve, no coincidence required; (ii) solid curve, requiring a coincident 0.5-Mev γ-ray detected in the 4 × 1.5 inch NaI (Tl) crystal. Curves (i) and (ii) are normalized to equal count rate at the first escape peak. The actual count rate with coincidence is 15 times less than without coincidence.

The experimental layout is shown in Fig. 5. The target of 250 gm of platinum is at 13.5 meters from the neutron booster and the time

of detection of γ-rays defines the time-of-flight of the captured neutrons with a resolution of 25 nsec/meter. The primary γ-ray detector is a 4 by 4 inch NaI crystal beside which is a 4 by 1.5 inch crystal. The line shape obtained with this method is shown in Fig. 5 (inset) for the 7.49-Mev γ-ray from Be^9 (p, γ) B^{10}. The coincidence requirement removes the total energy peak and many Compton events.

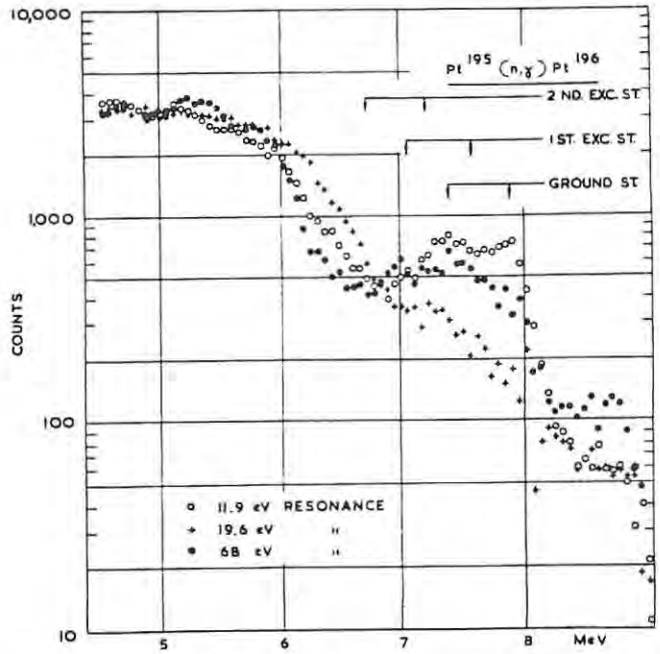

FIG. 6. Coincidence pulse-height spectra obtained for the 11.9 ev (open circles), 19.6 ev (crosses) and 68 ev (solid circles) neutron resonances in Pt^{195}. The energy calibration of the abcissa indicates electron pulse height in Mev plus 0.5 Mev.

It also reduces the counting rate in the first escape peak by a factor of 15. The first and second escape peaks are resolved much better than usual, partly because of the removal of Compton events, but chiefly because the primary events that are favoured by the technique,

occur in a slab of the main crystal parallel to the photomultiplier so that the optical efficiency is more uniform than normal. The line shape has been measured for a number of γ-rays in the energy range 4 to 10 Mev and analyzed in terms of Gaussian peaks plus a Compton tail. The width of the peaks are found to increase only slowly with energy.

In order to measure the spectra from resonances, the neutron time-of-flight and the pulse height from the large crystal were recorded digitally on magnetic tape. This method allows the resonance area to be determined for each pulse-height channel so that the background is determined and removed from the one set of data without requiring repeated runs. The spectra thus obtained for the first three resonances in Pt^{195} are shown in Fig. 6. The ordinate is the actual number of counts for the 11.9-ev resonance, the other curves having been normalized to equal areas. The arrows show the positions at which peaks are expected for the transitions from the capturing state to the ground state of Pt^{196} and to the first and second excited states. The known line shapes for these three γ-rays have been used in a least squares program to determine the intensity of each transition at each resonance.

The spectra do not show zero counts above the ground state peaks indicating that there is some contribution having a resonance shape which can be attributed to chance coincidences. This has been corrected for, by using the shape of the spectrum for the 96-ev resonance (which involves capture in Pt^{198}) for energies above the binding energy which is 6.5 Mev. This shape was normalized to the observed count rate above the ground state peaks for each Pt^{195} resonance spectrum. The normalizing factor was found to be approximately equal to the ratios of the total count rates for the respective resonances. This correction changes the individual γ-ray intensities by the order of 10% but gives a notable improvement in the least squares fitting.

The relative intensities of the various γ-rays are given in Table II normalized to unity for the ground state transition of the 68.5-ev resonance. The errors quoted include contributions from both the statistical errors and systematic errors. The latter were estimated from the effect of various changes on the assumptions involved in the process of fitting line shapes.

The results are also given in Table II of measurements made with thermal neutrons using a cadmium difference technique, but

TABLE II

RELATIVE INTENSITIES OF CAPTURE GAMMA RAYS FOR RESONANCES IN $Pt^{195} - n$

Neutron energy (ev)	Gamma ray[a]	Relative intensities			
		Singles	Singles	Coinc.	Bollinger *et al.*[13]
11.9	γ_0	1.00	1.00	1.00	1.00
	γ_1	0.29 ± 0.1	0.53 ± 0.1	0.40 ± 0.1	< 0.05
	γ_2			< 0.02	
19.6	γ_0	0.29 ± 0.05	0.20 ± 0.05	0.16 ± 0.03	0.25 ± 0.03
	γ_1	0.19 ± 0.05	0.23 ± 0.05	0.23 ± 0.05	0.10 ± 0.02
	γ_2			0.25 ± 0.03	
68.5	γ_0	0.48 ± 0.1	0.67 ± 0.15	0.45 ± 0.08	0.43 ± 0.04
	γ_1	0.52 ± 0.1	0.67 ± 0.15	0.51 ± 0.1	0.24 ± 0.06
	γ_2			0.12 ± 0.03	
			Groshev *et al.*[14]	Kinsey *et al.*[14]	
Thermal (not normalized)	γ_0	0.4	0.4	0.3	
	γ_1	0.4	0.2		
	γ_2	0.35	0.6	0.2	

[a] γ_0, γ_1, γ_2—transitions from capturing state to ground state, 1st, and 2nd excited states, respectively.

these are on an arbitrary intensity scale not normalized to the values in the rest of the table. The relative intensities of the three γ-rays agree reasonably well with the results of previous experiments considering the poor accuracy involved in the difference measurements. The first two sets of results for resonances given in Table II are the results of earlier measurements made with a single sodium iodide crystal as the γ-ray detector. These show quite satisfactory agreement for the intensities deduced for the ground and first excited state transitions. However, a comparison with the results of Bollinger *et al.*[13] show rather poor agreement unless larger systematic errors are assumed to dominate this type of measurement.

ACKNOWLEDGMENTS

We would like to express our thanks to Dr. Alexander Langsdorf, visitor to us from Argonne National Laboratory, who collaborated in the early stages of the capture γ-ray experiment. We are also indebted to Miss M. R. Avery for assistance in that experiment and to Mr. J. E. Jolly and Miss G. Holman for assistance in the measurement of eta versus energy for U^{235}.

REFERENCES

1. M. J. Poole and E. R. Wiblin, *Proc. 2nd. Intern. Conf. Peaceful Uses of Atomic Energy, Geneva, 1957* **14**, 266 (1958).
2. J. R. Waters and J. R. Bird, *Nucleonics* **19**, 17 (1961).
3. H. Palevsky, D. J. Hughes, R. L. Zimmerman, and R. M. Eisberg, *J. Nuclear Energy* **3**, 177 (1956).
4. F. J. M. Farley, *J. Nuclear Energy* **3**, 33 (1956).
5. L. M. Bollinger, O.R.N.L. Rept. ORNL-2309, p. 167 (1956).
6. L. M. Bollinger, R. E. Cote, and G. E. Thomas, *Proc. 2nd. Intern. Conf. Peaceful Uses of Atomic Energy, Geneva, 1957* **15**, 127 (1958).
7. M. L. Yeater, R. W. Hockenbury, and R. R. Fullwood, *Nuclear Sci. & Engr.* **9**, 105 (1961).
8. F. D. Brooks, R. W. Pringle, and B. L. Funt, *I.R.E. Trans. on Nuclear Sci.* NS-7, 35 (1960).
9. R. L. Macklin *et al.*, O.R.N.L. 60-2-84 (1960).
10. T. Teichmann, *Phys. Rev.* **77**, 506 (1950).
11. D. J. Hughes and R. B. Schwartz, "Neutron Cross Sections," BNL 325, 2nd. ed. 1958.
12. W. W. Havens and E. Melkonian, *Proc. 2nd. Intern. Conf. Peaceful Uses of Atomic Energy, Geneva, 1957* **15**, 99 (1958).
13. L. M. Bollinger, R. E. Cote, and T. J. Kennett, *Phys. Rev. Letters* **3**, 376 (1959).

NUCLEAR INSTRUMENTS AND METHODS 39 (1966) 68–76; © NORTH-HOLLAND PUBLISHING CO.

NEUTRON RESONANCE SCATTERING MEASUREMENTS WITH ^{6}Li GLASS DETECTORS

M. ASGHAR* and F. D. BROOKS+

Nuclear physics Division, U.K.A.E.A. Research group, Atomic Energy Research Establishment, Harwell

Received 20 July 1965

A detector for the measurement of neutron elastic scattering cross sections in the resonance region is described. The detector consists of five lithium-loaded glass scintillators assembled into two groups, the scintillators in the first group having a ^{6}Li content 46 times greater than those in the second. The response of the two groups to gamma-rays is matched as closely as possible so that when the output of the second group is subtracted from that of the first, the effective sensitivity of the system to gamma-rays is close to zero. Measurements on ^{169}Tm, ^{197}Au and ^{232}Th demonstrate that scattering cross section data accurate enough to determine resonance spins may readily be obtained.

1. Introduction

The resonances observed in the low energy ($\lesssim 1$ keV) neutron cross sections of most medium and heavy nuclei (i.e. $A \gtrsim 50$) are mainly due to s-wave (i.e. $l = 0$) interactions between the neutron and the nucleus. Each resonance can therefore be described in terms of the parameters, E_0, J, Γ, Γ_n, Γ_γ and Γ_f, which represent respectively, the resonance energy, the total angular momentum of the corresponding compound nucleus state, the total resonance width and the partial widths for decay by neutron emission, by emission of gamma rays, or by fission, these being the principal modes of decay. The resonance parameters are important on the one hand for the development of nuclear theory and for testing the results of theoretical predictions[1]). Practical applications, on the other hand, are concerned with computations of reactor temperature coefficients, neutron reaction yields, self protection effects, etc.[2]).

An accurate and elegant way of determining resonance parameters is to combine the results of several different types of neutron cross section measurements, as described by Lynn and Rae[3]). Assuming a non-fissile nucleus, the measurements required are: a. the neutron transmission vs energy for several samples of different thickness; and b. the cross sections vs energy for neutron capture and neutron elastic scattering respectively. Capture data of high quality[4]) have recently become available for several nuclei. Correspondingly accurate transmission data are also available[5]) or can always be measured with relative ease. In contrast, very few scattering data are available which are of a quality suitable for combination with the transmission and capture data to determine resonance parameters

This lack of neutron scattering data in the resonance region stems largely from the fact that no neutron detector has been available which combines a high detection efficiency with certain other characteristics considered to be essential, or desirable, for low energy neutron scattering measurements by the time-of-flight method. These characteristics relate to the energy resolution of the experiment and to the need to differentiate (experimentally) between neutron scattering and radiative capture. They may be summarised as follows. An ideal detector should:

a. have a time resolution which is better (i.e. less) than the width of the neutron burst;

b. have an active thickness which is less than the rms variation in the neutron flight path from the source to to the detector;

c. be insensitive to neutron capture gamma-rays. Alternatively it should incorporate a means of discriminating against these gamma rays.

With regard to requirements a. and b. it should be noted that the energy resolution, $\Delta E/E$, of a time-of-flight spectrometer, at an energy, E, is given by the formula:

$$\Delta E/E = (2/L)\,\{\sum(\Delta L)^2 + v^2\sum(\Delta T)^2\}^{\frac{1}{2}}, \qquad (1)$$

where L is the flight path length and v is the neutron velocity. The two sums are to be taken over all factors which contribute to the flight path spread, ΔL and to the timing uncertainty, ΔT, respectively. The fulfilment of both requirements a. and b. thus ensures that the detector itself is responsible for only a small or negligible part of the resolution width, ΔE.

The detector which has been most widely used in the past, for resonance neutron scattering work, is the boron trifluoride proportional counter. The BF_3-counter is very satisfactory as regards requirement c. However BF_3-counter systems generally suffer from a low detection efficiency ($\lesssim 2\%$) for neutron energies

* Attached from the Department of Nuclear Physics, University of Oxford.

+ Present address: Physics Department, University of Cape Town, Rondebosch, C.P., South Africa.

exceeding 10 eV and this efficiency can be increased only at the expense of requirements a. and b. In contrast to this, scintillation detectors, such as the ^{10}B-loaded liquid[6]) and the ^{6}Li-loaded glass[7]), can achieve considerably higher efficiencies without sacrifice of requirements a. and b. However, the satisfaction of requirement c. generally presents a problem with scintillators.

The scattering detector which is the subject of this paper is based on lithium-loaded glass scintillators[7]). Two or more glass scintillators of widely different ^{6}Li content are used simultaneously so that, under suitable conditions, taking the difference between their responses results in a high efficiency for neutrons and an effective zero efficiency for gamma-rays. The method of operation is closely analagous to that long since devised and used by Peirson[8]) to remove Compton continua from the pulse height spectra produced by gamma-rays irradiating a NaI(Tl) crystal. To do this Peirson subtracted from the NaI(Tl) spectrum, a pulse height spectrum observed simultaneously in a suitably matched organic crystal. In the same way a pair of lithium loaded glass scintillators, similar to one another in all respects except their ^{6}Li content, can be matched very closely in respect of their efficiency and pulse height response to gamma-rays. The effective response to gamma-rays is thus reduced to zero, when one spectrum is subtracted from the other.

2. Description of the detector

In the studies relating to this detection system and in the early measurements made with it, a single pair of glass scintillation detectors was used. The number of scintillators was later increased to five. We will describe the principle of operation in terms of the prototype, or two-glass, detection system.

Fig. 1a shows the prototype scattering detector. The two glass scintillators were each 4.4 cm in dia. and 2 cm thick and were similar in all respects except their lithium content. One scintillator, hereafter denoted "glass A", contained 6 per cent by weight of lithium[7]), enriched to 95 per cent in ^{6}Li. The other scintillator, denoted "glass B", contained 2.5 per cent by weight of natural lithium (hence about 0.185 per cent by weight of ^{6}Li). The scintillators, together with their photomultiplier tubes (type EMI 6097B), were shielded against neutron backgrounds by placing them in boron carbide cylinders and surrounding the whole detector by slabs of boric acid and wax mixture. The sample of scattering material, in the form of a disc, was placed normal to the incident neutron beam, while the two scintillation etectors were placed in the plane of the sample at equal distances ($\sim$ 5 cm) from the centre of the sample.

Fig. 1b shows the electronics used with the detector. The signals from the photomultipliers were fed into

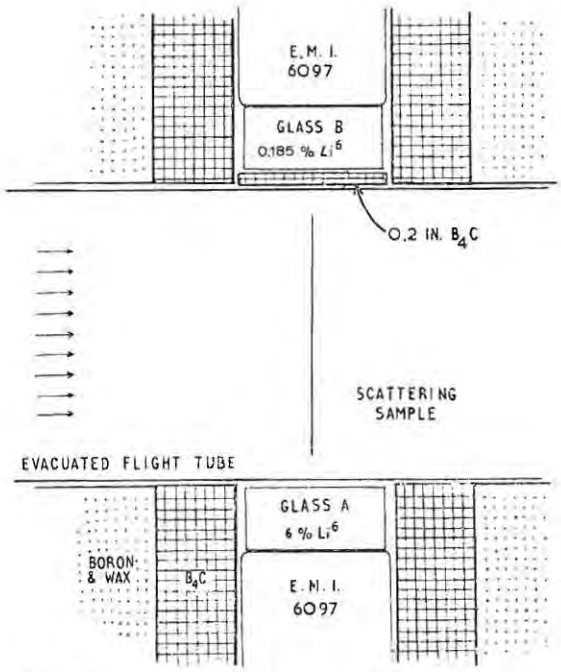

Fig. 1. a. The prototype neutron scattering detector using two glass scintillators.

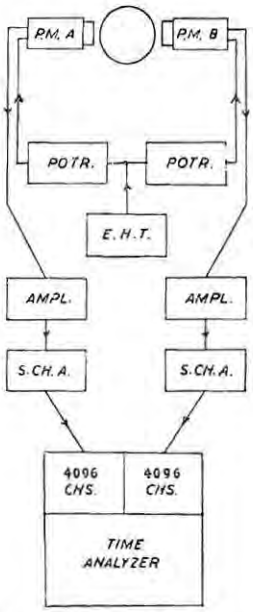

Fig. 1. b. Block diagram of electronics.

linear amplifiers, from there into single channel pulse height analysers and then to the time analyser. The pulse height distribution obtained from glass A, using a source of moderated Po-Be neutrons is shown in fig. 2a; the peak corresponds to ^{6}Li(n,α)T events in which the reaction products share a total energy of 4.8 MeV. Compton pulse height distributions obtained using a source of ThC″ (2.66 MeV) gamma-rays are also shown in fig. 2; for glass A in fig. 2b and for glass B in fig. 2c. The gain of the B-detector was first set so as to match the Compton edges of glasses A and B. Identical pulse height windows were then set on the two spectra at a mean pulse height corresponding to the neutron peak of glass A. A generous window width (1.3 to 1.9 MeV Compton electron energy) was used, as illustrated in fig. 2 and great care was exercised in order to achieve and maintain identical windows for the two glasses.

The operation of the detector may readily be followed by considering its response to an "ideal" neutron and gamma-ray source placed at the sample-centre position. Suppose that the source emits N monoenergetic, low-energy, neutrons and G monoenergetic gamma-rays (> 1.5 MeV), every second. Then the counting rates, N_A and N_B, observed in the pulse height windows A and B respectively, will be given by the following equations:

$$N_A = \alpha_n N + \alpha_\gamma G \text{ and } N_B = \beta_n N + \beta_\gamma G.$$

In these equations α_n and β_n denote the efficiencies for counting neutrons in windows A and B respectively; α_γ and β_γ denote the efficiencies of the respective windows for counting gamma-rays.

By eliminating G from these equations we obtain the following equation:

$$N = Y/\varepsilon \tag{2}$$

where

$$Y = N_A - KN_B, \tag{3}$$

$$K = \alpha_\gamma/\beta_\gamma, \tag{4}$$

$$\varepsilon = \alpha_n - K\beta_n. \tag{5}$$

The "net counting rate", Y, given by eq. (3), may be interpreted as the counting rate which would be observed using a gamma-insensitive detector of neutron detection efficiency, ε, given by eq. (5). The elimination, or compensation, of gamma-sensitivity therefore depends on an accurate knowledge and understanding of the behaviour of K, the ratio of gamma efficiencies, given by eq. (4). Now it should be noted that K will be: a. close to unity; and b. *independent of the energy* of the gamma-rays. These properties are the result of two

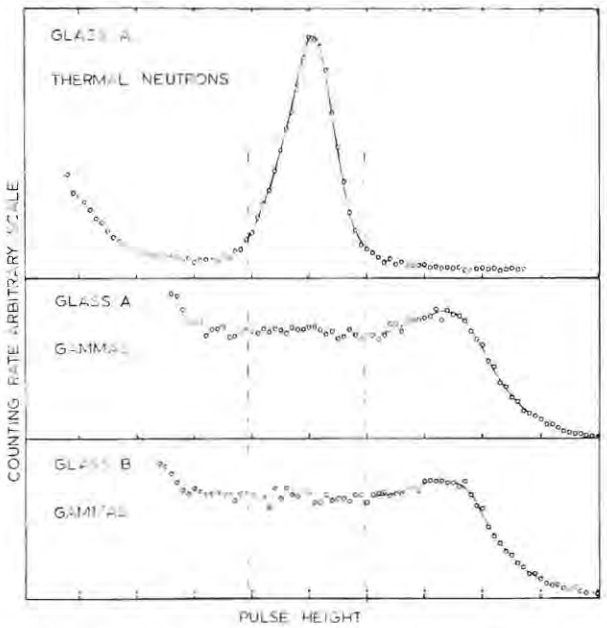

Fig. 2. Pulse height distributions: a. thermal neutrons on glass A [the peak is due to ^{6}Li(n,α)^{3}H events]; b. ThC″ gamma-rays (2.66 MeV) on glass A; c. ThC″ gamma-rays on glass B.

facts, namely: (i) the fact that the glasses are virtually identical in their response to gamma-rays; and (ii) the fact that the pulse-height windows, A and B, are identical. It therefore follows that the ratio, K, applying to a spectrum containing several gamma-rays (e.g. from neutron capture) will be the same as that observed for a monoenergetic gamma-ray source. An experimental verification of this assumption is described in section 4. It will be demonstrated in section 4 that an accurate measure of K is obtained simply by placing a gamma-ray source (e.g. ThC″) in the sample position (fig. 1) and taking the ratio of counting rates observed (after subtracting backgrounds) in windows A and B respectively.

The operation of the detector in a scattering experiment is virtually identical to the operation described above, it being noted that all quantities in eqs. (2) to (5), except K are, in general, a function of incident neutron energy. The experiment consists of measuring the counting rates per timing channel, $N_A(E)$ and $N_B(E)$ for glasses A and B respectively, as a function of incident neutron time of flight. The net counting rate or yield per channel, $Y(E)$, may then be obtained and, provided the scattering sample is "thin", $Y(E)$ may be related to the scattering cross section, $\sigma_s(E)$, of the sample by the following equation:

$$Y(E) = N_A(E) - KN_B(E) = \varepsilon(E) \cdot N_0(E) n \sigma_s(E). \tag{6}$$

In eq. (6) $N_0(E)$ represents the number of neutrons incident on the sample per timing channel at the energy E and n equals the thickness of the sample, expressed in atoms/barn. The practice normally adopted for scattering measurements in the resonance energy region is to measure $Y(E)$ both for the sample of the element of interest and for a sample of an element whose scattering cross section varies slowly with neutron energy and is well known, e.g. lead. The two measurements are made under identical conditions so that the factors $\varepsilon(E)$ and $N_0(E)$ may be eliminated by taking the ratio of the scattering yields $Y(E)$ for the two measurements. In this way $\sigma_s(E)$ is obtained for the element of interest from eq. (6).

While it is not actually necessary to measure the neutron detection efficiency, $\varepsilon(E)$, it is clearly desirable to have as high an efficiency as possible. From eq. (5) it can be seen that $\varepsilon(E)$ will have a maximum value approximately equal to $\alpha_n(E)$ provided that the ratio $\alpha_n(E):\beta_n(E) \gg K$. At high neutron energies this ratio is equal to the ratio of ^{6}Li concentrations in glasses A and B respectively, i.e. is about 31. At lower energies, as the individual neutron efficiencies, $\alpha_n(E)$ and $\beta_n(E)$, increase, self screening (exponential neutron absorption) becomes progressively more severe in glass A than in glass B, and the ratio drops toward the value K. This effect is easily counteracted by placing a neutron absorber (0.2″ of B_4C) between the sample and glass B, as shown in fig. 1a. The boron absorber screens glass B to an extent which more than compensates for the self-screening in glass A, hence a high ratio $\alpha_n(E)/\beta_n(E)$ is maintained at all neutron energies. It should be noted, firstly that the boron absorber has negligible effect on the gamma-ray detection characteristics of glass B and secondly that the 0.48 MeV gamma-ray resulting from neutron capture in ^{10}B will have no effect either, because it falls below the threshold of the pulse height windows.

The prototype (two-glass) detector was used for studying elastic neutron scattering from ^{169}Tm. Subsequently two more ^{6}Li glasses and one more natural lithium glass, were added to make the more efficient detector which is illustrated in fig. 3. The five scintillation counters are surrounded by a shield of boric oxide contained in the hexagonal box seen in the centre of the picture. The signal and photomultiplier voltage supply leads to three of the five photomultipliers inside the hexagon can be seen. Part of the evacuated flight path can also be seen on the left of the picture. Minor modifications were made to the electronics to obtain two outputs, namely a single "A" output from the three ^{6}Li-glasses connected in parallel, and a single "B" output from the two natural lithium glasses. The mode of operation from this point onwards was identical to that described for the prototype detector.

3. Scattering measurements

Fig. 4, 5 and 6 show some scattering data obtained using a flight path of 50 m associated with the neutron time of flight spectrometer based on the Harwell 45 MeV electron linac[9]). The width of the neutron burst from the "neutron booster" target[9]) was 0.25 μs and 0.25 μs timing channels were used, giving a neutron time of flight resolution of about 5 ns/m at high neutron energies. The data shown were accumulated over periods of running lasting up to 72 h each.

Fig. 4 shows data obtained using the prototype detector. The quantities, $N_A(E)$ and $KN_B(E)$, observed using a thulium scattering sample of 3.2×10^{-4} atoms/barn, are plotted against neutron energy. Figs. 5 and 6 show data obtained using the five-glass detector. In these figures the net counts, $Y(E)$, are plotted vs neutron energy for: a. a gold sample of thickness 7.67×10^{-4} atoms/barn (fig. 5); and b. a ^{232}Th sample of thickness 1.32×10^{-4} atoms/barn (fig. 6). In the case of fig. 6 it is particularly worth noting that the quality of the data was not impaired by the high activity ($\sim 10^5$ gamma-rays/min) of the thorium sample used.

It may readily be confirmed that the scattering data shown in figs. 4–6 are of a quality which is comparable

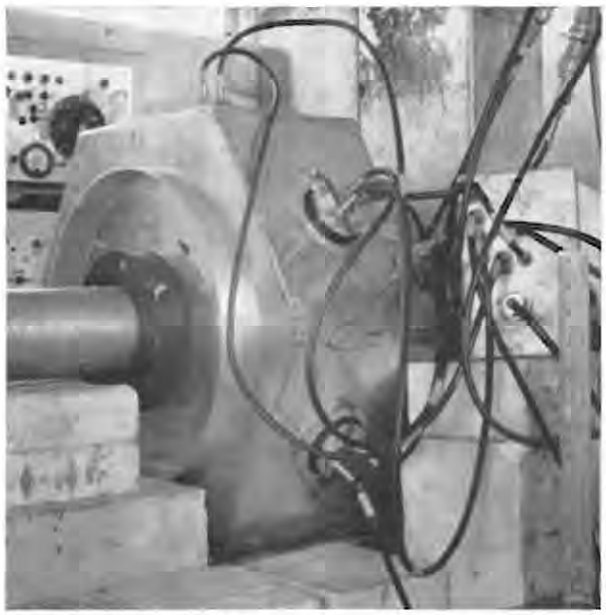

Fig. 3. A photograph of the five-glass neutron scattering detector. The glass scintillators with their photomultipliers are inside the "hexagon", surrounded by boric oxide. Part of the evacuated incident neutron flight path can be seen at the left.

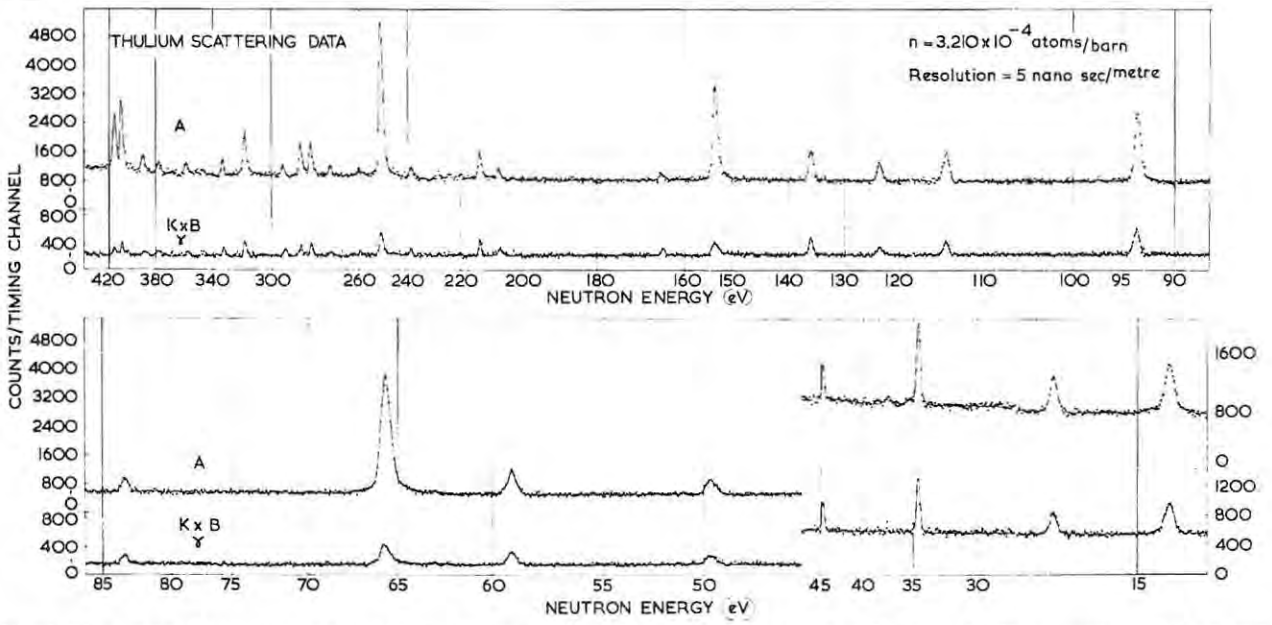

Fig. 4. The number of counts per timing channel plotted against the neutron energy for a ^{169}Tm sample. The quantity kN_B is plotted against the energy for glass B. The yield, $Y = N_A - kN_B$, eq. (2) is proportional to the number of scattered neutrons per timing channel. These data were obtained using the two-glass detector.

with the best capture cross section data[4]) and transmission data[5]) now available for the nuclides ^{169}Tm, ^{197}Au and ^{232}Th respectively. These scattering data have been[10]) and are being, combined with the capture and transmission data to deduce responance parameters. By way of example we illustrate in fig. 7 the analysis of the 17.4 eV level in ^{169}Tm, following the method described by Lynn and Rae[3]). Fig. 7 shows two sets of curves of Γ_n vs Γ, corresponding to the formation of the compound nucleus, ^{170}Tm, in a state of total angular momentum, $J = 0$, or a state of $J = 1$, respectively. Each set consists of: (i) three curves (T_1, T_2 and T_3) based on transmission data; (ii) one curve based on capture data[4]), c; and (iii) one curve based on the scattering data, s, (fig. 4). The scattering curves were derived from the following relation[3]):

$$\sigma_0 \Gamma_n = 4\pi\lambda\!\!\!^{-2} g \Gamma_n^2 / \Gamma. \quad (7)$$

In this equation $\lambda\!\!\!^{-}$ is the reduced neutron wavelength in the neutron-nucleus system and σ_0 represents the total cross section at exact resonance. The statistical weight factor, g, is given by the following equation:

$$g = \tfrac{1}{2}(2J+1)/(2I+1), \quad (8)$$

where I is the spin of the target nucleus ($I = \frac{1}{2}$ for ^{169}Tm) and $J = I \pm \frac{1}{2}$. A value for $\sigma_0\Gamma_n$ was obtained from the area of the resonance observed in the scattering data (fig. 4) in order to construct the curves labelled s in fig. 7 from eq. (7).

Taking into account the standard deviations for the various experimental data shown in fig. 7, it can be seen that a solution (i.e. values of Γ_n and Γ) in reasonable agreement with all of the experimental data is only possible for the $J = 1$ set. A detailed statistical analysis[12]) indicates that the solution $J = 1$, $\Gamma = 57$ MeV, $\Gamma_n = 2.6$ MeV (and hence $\Gamma_\gamma = 54.4$ MeV), is about 95 per cent probable on the basis of the results shown, whereas all solutions based on $J = 0$ are less than 1 per cent probable. It should be noted that the accuracy of the scattering data is, to a large extent responsible for eliminating the possibility of a solution based on $J = 0$. In this example and in many others, the scattering data are indispensable for purpose of assigning the J-value and thereby enabling the resonance analysis to be completed.

4. Measurement of the ratio of gamma-ray efficiencies

The satisfactory operation of this scattering detector obviously depends sensitively on the accuracy to which the ratio of gamma-ray efficiencies, K given by eq. (3), is known, and the stability to which the electronics maintains a constant value of K during an experiment. The choice of fairly wide pulse height windows on the two glasses, as illustrated in fig. 2, is related to the need for high stability.

Because of the importance of the ratio K to the detector operation, an auxiliary experiment was under-

taken whose aims were: a. to obtain an accurate value of K and b. to test the assumption that K is independent of the spectrum of gamma-rays emitted following neutron capture. Samples of five different elements were selected on the basis of two criteria; firstly that the selection should cover as wide a range of different (thermal) neutron capture spectra[11]) as possible; and secondly that each element should have at least one neutron resonance below about 5 eV for which $\Gamma_\gamma \gg \Gamma_n$. The resonances and the elements chosen were respectively, 4.9 eV in Au; 1.5 eV in In; 3.9 eV in Tm; 4.3 eV in Ta; and 1.2 eV in Rh. The capture gamma-ray spectrum[11]) of Au (for thermal neutrons) shows a much higher proportion of high energy ($\gtrsim 4$ MeV) transitions than do those of Ta, In, Tm and Rh. For the experiment a 0.2″ thick sleeve of boron carbide was inserted in the flight path between the sample and the scintillators of the five-glass detector, it having been confirmed in a previous experiment that this sleeve would absorb more than 99 per cent of neutrons of energy less than 5 eV. By this means it was ensured that the resonance maxima in the counting yields (N_A or N_B) vs incident neutron energy observed for the selected samples could be attributed entirely to neutron capture gamma-rays. A value of K was thus determined for each element (or resonance) simply by taking a ratio of the resonance areas observed (after subtracting background) using "bank A" and "bank B" respectively. The results of these measurements are listed in table 1. A value of K obtained using a source of ThC″ (2.66 MeV) gamma-rays in the form of disc of the same diameter (7.9 cm) as the scattering samples is also given in table 1. These results verify that the ratio of gamma-ray efficiencies, K, is independent of gamma-ray spectrum, and give the best value, $K = 1.64 \pm 0.03$. It should in particular be noted that the most convenient method of calibration, namely by means of the ThC″ source, gives a result which is in agreement with the "direct" method, using resonance capture gamma-rays.

TABLE 1

Nucleus	Resonance energy (eV)	Gamma ratio K
Au	4.9	1.66 ± 0.07
In	1.5	1.64 ± 0.06
Tm	3.9	1.72 ± 0.05
Ta	4.3	1.60 ± 0.06
Rh	1.2	1.55 ± 0.06
ThC″ gamma rays		1.70 ± 0.02

5. Discussion

5.1. Detection efficiency and timing resolution

It is of interest to compare the new scintillation scattering detector with the assembly of BF_3 proportional counters previously used at Harwell for resonance scattering work[12–14]). In the latter detector 18 BF_3 counters (5 cm in dia.) containing a total of 45 g of ^{10}B were assembled to make an annulus 60 cm long

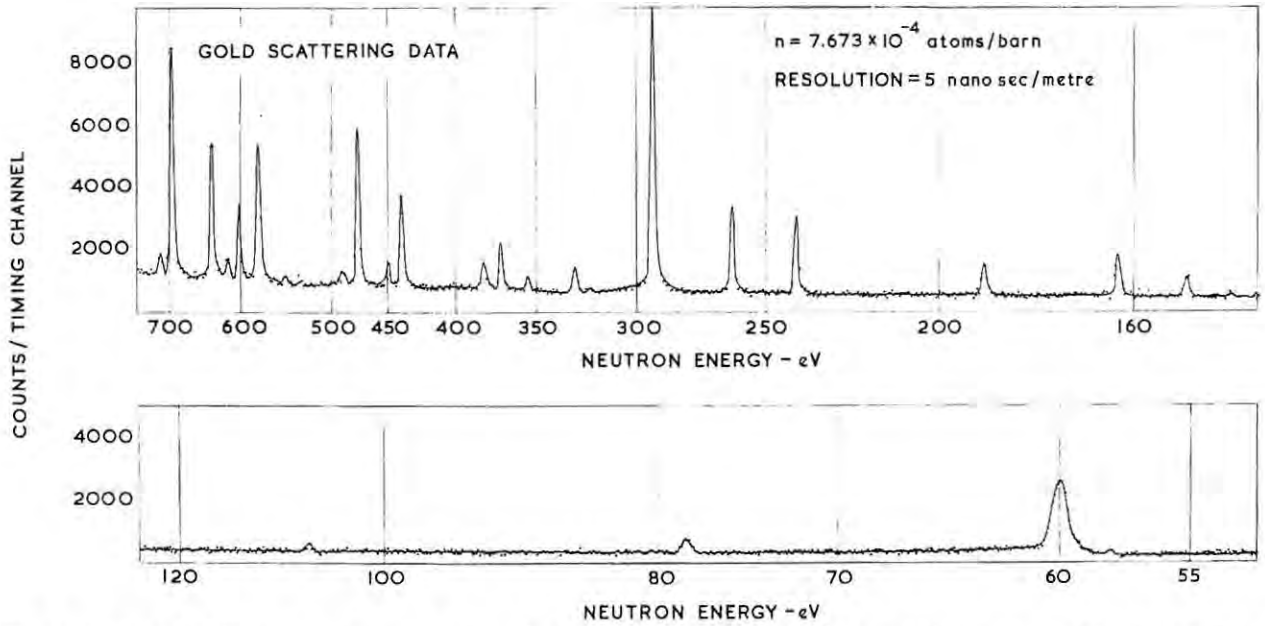

Fig. 5. The yield, Y, plotted against neutron energy, for a sample of ^{197}Au. These data were obtained using a five-glass detector.

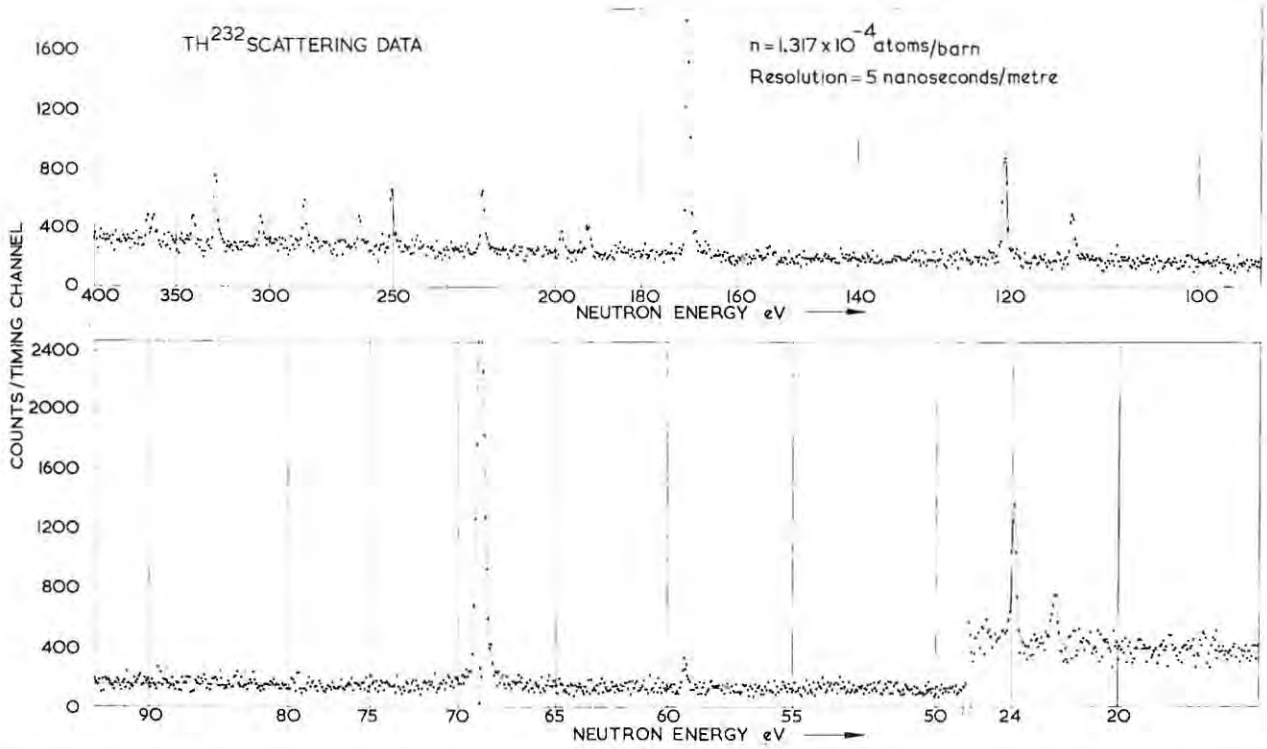

Fig. 6. The yield, Y, plotted against neutron energy, for a sample of ^{232}Th. The data were obtained using the five-glass detector.

by 13 cm i.d. and 30 cm o.d.[15]). The solid angle of this system was therefore nearly 4π; however, a distance uncertainty of about 30 cm was introduced by the extended counting volume and a timing uncertainty of 0.5 μs or more was introduced by the characteristic "jitter" of the proportional counters.

Fig. 8 shows as a function of neutron energy: a. the calculated efficiency; and b. the calculated energy resolution, $\Delta E/E$, for both the BF_3 detector assembly and the five-glass scintillation detector. The energy resolution calculations were based on eq. (1) and took into account both the distance uncertainty of 6 cm introduced by the neutron source and the timing uncertainties introduced by both the source (0.25 μs) and the timing channels (0.25 μs) of the time of flight spectrometer. It is clear from fig. 8 that the efficiency and energy resolution of the scintillation detector are each better by about a factor of three than the corresponding values for the BF_3 counter assembly. Moreover while the efficiency of the BF_3 assembly could only be increased at the expense of its energy resolution, the efficiency of the scintillation detector could immediately be increased by a large factor without affecting its energy resolution, simply by increasing the solid angle.

5.2. Effects of gamma-ray sensitivity

The main drawback of the scintillation detector system arises from its sensitivity to gamma-rays, notwithstanding the fact that the effective gamma-sensitivity is, in principle, zero. For a resonance of very small neutron width, i.e. $\Gamma_n \ll \Gamma_\gamma$, a very high statistical accuracy is required of the primary measurements, N_A and N_B and the ratio of gamma-ray efficiencies, K must also be known to a very high accuracy, in order to achieve even modest accuracy in the net counting rate, $Y=(N_A - KN_B)$. These considerations will generally set a lower limit on the value of $\sigma_0\Gamma_n$, in eq. (7) which can be measured with useful accuracy, say to 20 per cent or better. It has been found that measurements of this accuracy are feasible for $\sigma_0\Gamma_n \gtrsim 5$ eV·barn. It is difficult however to generalise since the limit is also a function of several other factors, e.g. incident neutron energy and intensity, duration of the experiment, actual ratio of Γ_n to Γ, etc.

The above limitation will not exist for a neutron detector for which the gamma-sensitivity approaches zero, (as in the BF_3 proportional counter), or is otherwise effectively suppressed, rather than compensated. Two important conclusions emerge from this consideration. In the first place the BF_3 detector assembly

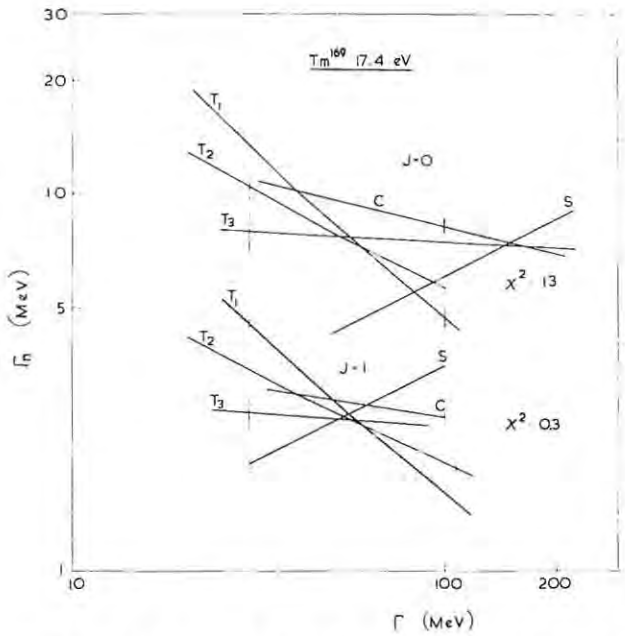

Fig. 7. A plot of neutron width, Γ_n, vs total width, Γ, for the 17.4 eV neutron resonance of ^{169}Tm. The two sets of curves correspond to the two possible total angular momenta, $J = 0$ or $J = 1$ respectively, with which the compound nucleus (^{170}Tm) can be formed. The curves in each set were derived as follows: (i) curves T_1, T_2 and T_3 from transmission measurements made using samples of thickness 6.97×10^{-3}, 2.04×10^{-3} and 3.16×10^{-4} atoms/barn, respectively; (ii) curve c, ref. 4) from capture measurements; (iii) curves s, from the scattering data.

remains a better detection system than the ^{6}Li-glass scintillator assembly for scattering measurements below about 10 eV neutron energy. Below 10 eV $\Gamma_n \ll \Gamma_\gamma$, in general, and the BF_3 detector is reasonably satisfactory in respect of both efficiency and time resolution. In the second place the technique of compensation employed in the ^{6}Li-glass system is *potentially* less advantageous than discrimination against capture by a method which actually reduces the gamma-sensitivity of the detector, e.g. by time-of-flight differentiation or by pulse shape discrimination. The use of time-of-flight to distinguish neutron scattering in the resonance region from both capture and fission (i.e. fast neutrons) has been, and is being, attempted at a number of laboratories including Harwell[16]). Pulse shape discrimination against gamma-rays has been demonstrated both for ^{10}B loaded liquids[17]) and for ^{6}Li-glass scintillators[18]) of composition somewhat different from those used in the present detector. However in both of these systems operation appears to be near to the limit of the pulse shape discrimination technique, and the best results obtained are typically 50 per cent loss of neutrons for 90 per cent rejection of gamma-rays. This factor, in contrast to the simplicity and ease of operation of ^{6}Li-glass scintillators (without pulse shape discrimination), works in favour of the latter. The position may change in the future, for example when more experience is available on time-of-flight discrimination methods, or if a better means of pulse shape discrimination becomes available*. In the meanwhile, however, the simple ^{6}Li-glass detection system may provide an answer to many of the experimental problems associated with neutron scattering measurements between about 10 eV and 1 keV.

We are indebted to Drs. E. Bretscher and E. R. Rae for the interest they have shown in this work and for the support they have given it. We are also grateful for for the interest shown by several members of the Linac group in particular to Mr. F. W. K. Firk for providing the first ^{6}Li-glass scintillator. We also wish to thank Messrs. M. G. Schomberg and J. E. Jolly for their assistance and one of us (M.A.) would like to thank the Pakistan Atomic Energy Commission for their sponsorship and financial support at Oxford University for the duration of these studies.

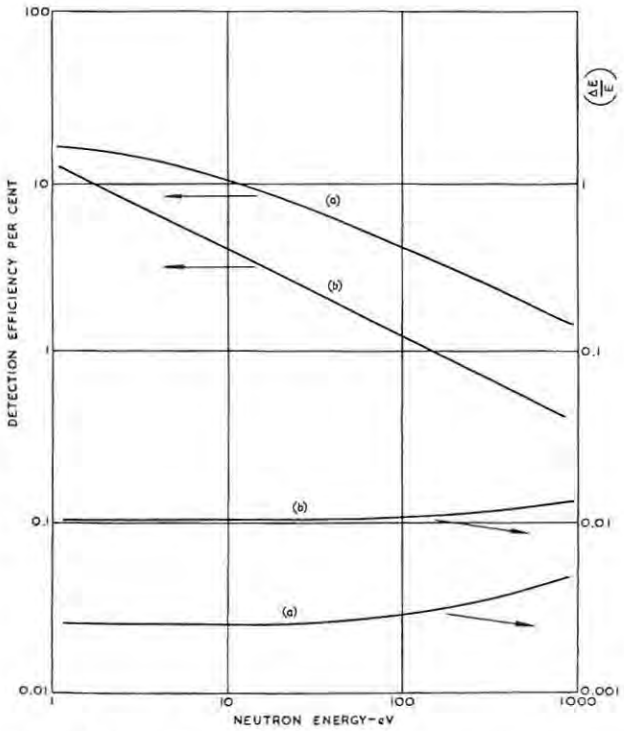

Fig. 8. Calculated detection efficiency and calculated energy resolution, $\Delta E/E$, vs neutron energy for (a) the five-glass scintillation detector; and (b) a $4\pi BF_3$-counter assembly[15]). The calculations apply to the 50 m flight path of the Harwell 45 MeV Linac time-of-flight spectrometer.

References

1) J. A. Harvey, Proc. Symp. Neutron time-of-flight methods, (ed. J. Spaepen, EAEC, Brussels, 1961) 23.
2) E. R. Rae, R. Batchelor, P. A. Egelstaff and A. T. G. Ferguson, Proc. Third Intern. Conf. Peaceful uses of Atomic Energy, Geneva (1964) to be published.
3) J. E. Lynn and E. R. Rae, J. Nucl. Energy **1** (1957) 418.
4) M. C. Moxon and E. R. Rae, Nucl. Instr. and Meth. **24** (1963) 445.
5) D. J. Hughes and R. B. Schwartz, Neutron cross sections, Brookhaven National Laboratory Report BNL-325 (2nd ed.) 1958.
6) L. M. Bollinger and G. E. Thomas, Rev. Sci. Instr. **28** (1957) 489.
7) F. W. K. Firk, R. J. Ginther and G. C. Slaughter, Nucl. Instr. and Meth. **13** (1961) 313.
8) D. H. Peirson, Nature **173** (1954) 990.
9) M. J. Poole and E. R. Wilbin, Proc. Sec. Intern. Conf. Peaceful Uses of Atomic Energy, 1958, Geneva **14** (1958) 266.
10) M. Asghar, F. D. Brooks, J. E. Jolly and M. G. Schomberg, in Harwell Report AERE-PR/NP5 (ed. D. L. Allan, 1963) p. 13.
11) L. V. Groshev, A. M. Demidov, V. N. Lutsenko and V. I. Pelenkov, *Atlas of gamma-ray spectra from radiative capture of thermal neutrons*, (Pergamon Press, London, 1959).
12) E. R. Rae, E. R. Collins, B. B. Kinsey, J. E. Lynn and E. R. Wiblin, Nucl. Phys. **5** (1958) 89.
J. E. Evans, B. B. Kinsey, J. R. Waters and G. H. Williams, Nucl. Phys. **9** (1958) 205.
13) J. R. Waters, Phys. Rev. **120** (1960) 2090.
J. R. Waters, J. E. Evans, B. B. Kinsey and G. H. Williams, Nucl. Phys. **12** (1959) 563.
14) J. R. Fraser and R. B. Schwartz, Nucl. Phys. **30** (1962) 269.
15) E. R. Collins, private communication.
16) F. D. Brooks, J. E. Jolly and M. G. Schomberg, in Harwell Report AERE-PR/NP6 (ed. D. L. Allan, 1964) p. 14.
17) F. D. Brooks, Proc. Symp. Neutron time of flight methods (ed. J. Spaepen, EAEC, Brussels, 1961) p. 389.
18) C. Coceva, Nucl. Instr. and Meth. **21** (1963) 93.

Note added in proof:* Jackson and Thomas have recently reported [H. E. Jackson and G. E. Thomas, Rev. Sci. Instr., **36 (1965) 419] major improvements in the pulse shape discrimination performance of boron-loaded liquid scintillators. These developments were not known to us at the time this paper was submitted for publication.

M. Asghar and F.D. Brooks
Neutron resonance scattering measurements with ^{6}Li-glass detectors
Nucl. Instr. and Meth. 39 (1966) 68-76

VOLUME II
RESONANCE ABSORPTION

REACTOR PHYSICS
in the Resonance and Thermal Regions

Proceedings of The National Topical Meeting of the American Nuclear Society San Diego, February 7–9, 1966

Edited by
A. J. Goodjohn and G. C. Pomraning

THE M.I.T. PRESS
Massachusetts Institute of Technology
Cambridge, Massachusetts and London, England

F.D. Brooks
Measurements of alpha and eta in the intermediate energy range
Reactor Physics in the Resonance and Thermal Regions, ed. A.J. Goodjohn and G.C. Pomraning (M.I.T. Press, 1966) Vol. 2, 193-222

MEASUREMENTS OF ALPHA AND ETA IN THE INTERMEDIATE ENERGY RANGE

F. D. Brooks
University of Cape Town
South Africa

Introduction

Alpha and eta are fission parameters which are of particular interest to the reactor physicist. For a given nuclide and for neutrons of energy E, alpha, $\alpha(E)$, is the ratio of the capture cross section, $\sigma_c(E)$, to the fission cross section, $\sigma_f(E)$:

$$\alpha(E) = \sigma_c(E)/\sigma_f(E) \qquad (1)$$

Eta, $\eta(E)$, is the number of fission neutrons emitted per neutron (of energy E) absorbed, and can also be defined in terms of $\alpha(E)$ and the average number of neutrons per fission, $\bar{\nu}$:

$$\eta(E) = \frac{\bar{\nu}}{(1+\alpha(E))} \qquad (2)$$

Over the restricted energy range considered in this paper ($E \leq 30$ keV), it appears reasonable to assume that $\bar{\nu}$ is independent of E.

For the nuclides U^{233}, U^{235}, and Pu^{239}, some accurate values of eta and alpha have been available at low energy and at high energy for about three years. Leonard[1] summarized the low-energy data, which gave $\alpha(E)$ and $\eta(E)$ to 2% or better for $E \leq 1$ eV; and Hopkins and Diven[2] measured the ratio of the average capture cross section to the average fission cross section, i.e., the ratio $\langle\sigma_c(E)\rangle/\langle\sigma_f(E)\rangle$, at nine incident neutron energies between 30 keV and 1 MeV. The latter measurements gave the quantity $(1+(\langle\sigma_c(E)\rangle/\langle\sigma_f(E)\rangle))$ to an accuracy of about 2% or better.

In contrast to these accurate high- and low-energy values, the data available three years ago for neutrons with energies between 1 eV and 30 keV were sparse and often very rough. Since that time, this "intermediate" energy range has become the object of intense research. Methods for measuring $\eta(E)$ have improved,[3] and $\alpha(E)$ has been directly measured in the resonance region for the first time.[4] These developments have been motivated largely by the demands of reactor physicists for nuclear data in this energy region. Interest in the resonance cross sections of the fissile nuclides has also increased as a result of recent developments[5] in the theory of fission processes induced by resonance-energy neutrons.

On the practical side, much of the progress that has occurred has been made possible by technical developments common to the whole field of slow-neutron spectroscopy, notably developments in pulsed-neutron sources, radiation detectors, and data-collecting and data-processing systems. This would thus seem to be a very suitable moment to review the methods presently being used to measure $\alpha(E)$ and $\eta(E)$, to consider the problems concerning the future development of these measurements, and to discuss and compare some of the data obtained so far.

Measurement of Eta and Alpha: General Considerations

Energy Resolution

In any experiment which utilizes a neutron spectrometer it is most important to bear in mind that the spectrometer does not perfectly define the neutron energy. The quantities measured in an experiment, or in any part of an experiment, are averages over the resolution function of the spectrometer. Equations 1 and 2 and other equations which relate individual fission parameters and cross sections will not necessarily be valid for averages of these parameters and cross sections. However, when the resolution width of the spectrometer is small compared with the average resonance width, the effects of finite resolution are small and can be ignored.

In the following discussion, the effects of finite energy resolution will first be ignored completely. How and at what energies these effects become important will then be considered.

Direct Methods

Both alpha and eta can, with some restrictions, be measured directly, that is, without actually measuring the cross sections

which are basic to their definitions. Alpha can be measured by placing a thin sample of fissile material in a beam of neutrons of energy E, and observing the rates of capture and of fission in the sample. The ratio of the capture rate to the fission rate then gives $\alpha(E)$.

If a thick sample of fissile material is placed in the neutron beam of energy E, and the rate at which fission neutrons are produced by the sample is observed, $\eta(E)$ can be obtained. If the fraction of incident neutrons scattered within the sample is small, then, by definition, $\eta(E)$ is proportional to the fission-neutron count rate divided by $N(E) \cdot F(E)$, where $N(E)$ is the rate at which neutrons are incident on the sample and $F(E)$ is the fraction of incident neutrons absorbed by the sample. The eta experiment must therefore include measurements of both $N(E)$ and $F(E)$. Ideally, $F(E)$ should be made to approach unity by using a thick sample. If an appreciable fraction of the incident neutrons scatter within the sample, a correction to allow for the effects of this scattering must be included in the calculation of $\eta(E)$.

Calculations from Other Data

Since $\bar{\nu}$ is known to high accuracy,[1] Equation 2 can be used to calculate $\eta(E)$ from measurements of $\alpha(E)$, and vice versa. In this connection it should be noted that if $\alpha(E)$ is small, a rough measurement of $\alpha(E)$ will give a relatively accurate value of $\eta(E)$. To compete with the alpha experiment, the eta experiment must therefore be simpler to carry out and give a more accurate result.

Values of $\alpha(E)$ and $\eta(E)$ can obviously also be derived from cross-section data, for example, from capture- and fission-cross-section data. Alternatively, if the scattering cross section, $\sigma_s(E)$, is known with sufficient accuracy and the total and fission cross sections are then measured, $\eta(E)$, for example, can be derived from the following equation:

$$\eta(E) = \frac{\bar{\nu} \cdot \sigma_f(E)}{\sigma_t(E) - \sigma_s(E)} \qquad (3)$$

However, like the direct measurement of $\eta(E)$ itself, this method is subject to greater uncertainty when the scattering cross section constitutes an appreciable fraction of the total cross section.

Energy Measurement

For neutron energies less than a few eV, it is possible to obtain "monoenergetic" neutron beams by using a crystal spectrometer. For energies exceeding about 30 keV, "monoenergetic" beams may be obtained by using a Van de Graaff Accelerator in conjunction with the (p, n) reaction on Li^7 or tritium. The neutron sources available for experiments in the intermediate energy region[6] produce a broad and continuous spectrum of neutron energies and are pulsed or chopped so as to allow measurement of the neutron energy by the time-of-flight method. These sources include neutron choppers (operating in conjunction with high-flux reactors), the pulsed reactor, pulsed accelerators, and nuclear detonations. Since this paper is concerned with measurements of alpha and eta in the intermediate energy region, attention will be focused for the most part on experiments involving pulsed, continuous-energy sources, rather than those involving the "monoenergetic" type of source.

Direct Measurement of $\eta(E)$

Outline of the Method

The direct measurement of eta using a pulsed, continuous-energy neutron source consists of three basic experimental measurements. It is desirable that each measurement should be carried out with the same energy resolution for incident neutrons, i.e., the same flight-path length, same compound timing uncertainty in the time-of-flight measurement, etc.

Suppose that the experiment is carried out using a uniform slab of pure fissile metal as a sample, and let the thickness of the slab be n atoms per barn. First, the spectrum of incident neutrons (i.e., the relative number per energy (or timing) interval versus energy) at the sample position (see Figure 1) is measured. Second, the yield of fission neutrons from the sample is measured as a function of incident neutron energy. Dividing the second measurement by the first gives Y(E, n), the corrected relative yield of fission neutrons per incident neutron.

Finally, the neutron transmission, T(E, n), of the sample is measured. If the neutron energy is such that scattering of incident neutrons is negligible, i.e., $\sigma_s(E) << \sigma_t(E)$, then (1 - T(E, n)) closely approximates the fraction of incident

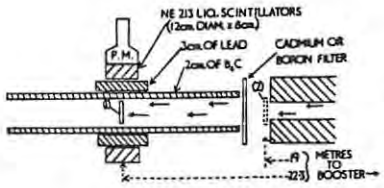

Figure 1. Fission-neutron detector for the measurement[3] of $\eta(E)$. The position of the fissile sample is at (1). Four liquid scintillators were used.

neutrons absorbed by the sample. Hence, $\eta(E)$ is given by the equation

$$\eta(E) = \frac{k \cdot Y(E, n)}{(1 - T(E, n))} \qquad (4)$$

and where k is a constant which is independent of incident neutron energy and depends on the detection efficiency of the fission-neutron detector. A value for k can be obtained by referring to some standard value of $\eta(E)$, e.g., the value obtained from the absolute measurement of eta at thermal energy.[7] The relative values of $\eta(E)$ are thus normalized to the standard value.

The necessity of using a "thick" sample in the eta experiment is illustrated by Equation 4. For a "thin" sample, T(E, n) tends to unity, so small errors on the transmission measurement lead to overwhelming large errors in $\eta(E)$. It is easily shown, in fact, that the yield Y(E, n) is proportional to the fission cross section $\sigma_f(E)$ in the thin-sample limit, so the "eta-experiment" measures $\sigma_f(E)$ rather than $\eta(E)$ in this limit. Conversely, for T(E, n) tending to zero ("thick" sample), the result obtained for $\eta(E)$ is insensitive to T(E, n) and the measured yield Y(E, n) is directly proportional to $\eta(E)$. Provided that $\sigma_s(E) << \sigma_t(E)$, the measurement of $\eta(E)$ then becomes very simple. The detector requirements, for example, may be no more than a "1/v-detector" for the spectrum measurement and a gamma-insensitive fast-neutron detector for the fission-yield measurement. The use of the thick sample also ensures that a good count rate is obtained in the yield measurement, thus allowing high accuracy to be obtained.

Unfortunately, the condition $\sigma_s(E) << \sigma_t(E)$ is seldom satisfied outside the thermal region. When this condition is not

satisfied, Equation 4 is suspect or invalid for two reasons:

1. Because (1 - T(E, n)) is an overestimate of the fraction of incident neutrons absorbed.
2. Because the yield Y(E, n) also includes fast neutrons from fissions caused indirectly by incident neutrons, i.e., after the incident neutrons have first suffered one or more scatterings within the sample.

The second effect would be of no consequence were it not for the fact that a neutron loses energy in the process of scattering. If A is the mass number of the target nucleus (assuming $A \geq 30$) and E is the energy of the incident neutron, then the average energy loss per scattering, ΔE, is given approximately by the following equation:

$$\Delta E = \frac{2E}{(A+2)} \tag{5}$$

Thus, for $A \sim 240$, $\Delta E/E$ is slightly less than 1%.

Fissions observed for a particular incident energy, E, may therefore include some fissions produced by scattered neutrons with energies between E and $(E - 2 \cdot \Delta E)$. Unless eta happens to be constant throughout this energy range, some allowance must be made for the energy spread of the neutrons actually responsible for the observed fissions; otherwise, a wrong value of $\eta(E)$ will be obtained.

Except where scattering is small, the quantity given by Equation 4 is not $\eta(E)$ but depends on such factors as sample thickness and shape, $\sigma_t(E)$, $\sigma_s(E)$, ΔE, etc. Thus, for a given sample of thickness n, a quantity $\eta_m(E, n)$ can be defined as follows:

$$\eta_m(E, n) = \frac{k \cdot Y(E, n)}{(1 - T(E, n))} \tag{6}$$

The calculation of $\eta(E)$ from $\eta_m(E, n)$ can become a very complicated operation. In fact, it is probably true that the calculation of scattering corrections constitutes the major part of the effort required to measure $\eta(E)$ directly for $E \geq 10$ eV.

For the transmission and spectrum measurements in the eta experiment, it is possible to use methods and techniques that have been developed for total and partial cross-section measurements. Therefore, the two main points of interest in the various methods that have so far been used to measure $\eta(E)$ are perhaps the type of detector used in the fission-yield measurement, on the one hand, and, on the other hand, the method used to calculate scattering corrections.

Fission-Neutron Detection Systems

The fission-neutron detector for the eta experiment must discriminate effectively against gamma rays in order not to be sensitive to neutron-capture events. While a high detection efficiency for fission neutrons is also desirable, it should be noted that an efficiency of less than about 10% makes the eta experiment approximately independent of the assumption that $\bar{\nu}$ is constant. For a neutron detector of low efficiency the probability of simultaneously detecting two neutrons from the same fission, and registering them as one neutron, is very small. The experiment therefore always measures the number of neutrons per neutron absorbed, i.e., eta. If the efficiency for detecting a fission neutron approaches unity, the experiment measures the number of fissions per neutron absorbed, and this is proportional to eta only if the number of neutrons per fission, $\bar{\nu}$, is constant.

Hornyak[8] fast-neutron detectors were used in many of the early measurements[9-11] of $\eta(E)$, a notable exception being the measurements of Farley[12] for Pu^{239}, for which a methane-filled ion-chamber was used. In all of these experiments, the efficiency for detecting a fission neutron was a very small fraction of 1%. Bollinger, et al.,[13] were the first to take advantage of the higher detection efficiency to be obtained by using large liquid-scintillator detectors. For some time previous to their experiments, the use of such detectors had seemed prohibited by their sensitivity to gamma rays. However, Bollinger, et al.,[13] were able to discriminate effectively against capture gamma rays by the judicious use of lead shielding together with coincidence circuitry.

More recently, organic-scintillator detectors have been used, and the pulse-shape-discrimination method has been applied to discriminate against gamma rays.[3,14,15] Fission-neutron detection efficiencies of a few percent have been obtained using liquid scintillators. Sowerby, et al.,[16] have recently demonstrated that an efficiency of about 40% for detecting a fission neutron can be obtained by using a system of liquid-scintillator detectors with pulse-shape discrimination.

Calculation of Scattering Corrections

The calculation of scattering corrections for incident-neutron energies below about 10 eV presents few problems because the average energy loss per scattering, ΔE, is generally considerably less than the average level spacing, D, and because the neutron width, Γ_n, is generally a very small fraction of the total width, Γ, for neutron resonances at energies below 10 eV

in the fissile nuclides. It is therefore correct to say that scattering is a small effect compared with absorption at energies in the vicinity of the larger resonances. In the vicinity of the weaker resonances and at off-resonance energies, the scattering cross section $\sigma_s(E)$ may be taken as equal to the potential scattering cross section. At these energies, therefore, $\sigma_s(E)$ will constitute an appreciable fraction of the total cross section and the scattering correction will be appreciable. However, since $\Delta E << D$, the variation of $\sigma_t(E)$ over the energy range $2\Delta E$ will often not be large.

It is thus reasonable to calculate scattering corrections neglecting the energy loss in scattering, ΔE, for $E << 10$ eV. The correction is essentially a correction for the fact that the term $(1 - T(E, n))$ in Equation 3 overestimates the fraction of incident neutrons absorbed by the sample. To calculate this correction, $\sigma_s(E)$ must be known and the probability that a scattered neutron will escape from the sample must be calculated. Various methods have been used[3,9,11] which appear to permit calculation of the scattering correction to an accuracy such that it contributes less than about 3% uncertainty to the uncertainty in $\eta(E)$.

For incident neutron energies exceeding 10 eV, account must be taken of the energy loss in scattering when calculating the scattering correction. Yeater, et al.,[11] have described a method of calculation which is based on the Monte Carlo technique. An alternative approach has been evolved at Harwell,[3,15] and a brief description of this method may be of interest here. By taking account of scattering to the first order, the following equation can be derived:

$$\eta_m(E, n) = \eta(E) \cdot W(E) + \frac{\sigma_s(E)}{\sigma_t(E)} \cdot < P(E', \theta, n) \cdot \eta(E') \cdot W(E') > \quad (7)$$

In this equation $W(E) = 1 - (\sigma_s(E)/\sigma_t(E))$. The term $P(E', \theta, n)$ denotes the probability that a neutron scattered through an angle θ and having an energy E' after scattering will not escape from the sample. The triangular brackets, $< \ldots >$, indicate that the product enclosed must be averaged over $\theta = 0$ to 2π, over the energy range from $E' = E$ to $E' = E - 2\Delta E$, and over the spatial distribution of scattering centers in the sample. The second term on the right-hand side of Equation 7 represents the effect of fissions caused by neutrons which have previously been scattered once. Terms corresponding to neutrons which have undergone two or more scatterings have been neglected since this appears to be a reasonable approximation provided that resonance scattering is small (i.e., $\Gamma_n < 0.1\Gamma$).

If the sample should contain a significant proportion of material of mass number very different from that of the fissile material, then the term $< \ldots >$ in Equation 7 must be replaced by a sum of such terms, including one term for each component in the sample. This would apply, for example, for oxide or alloy samples, or for samples clad in aluminum or copper cans.

If unclad samples of pure metal are used and $\eta_m(E, n)$ is measured for a series of samples of different thickness, n, then a fairly simple method may be used to correct for scattering effects. By using total-cross-section data $\sigma_t(E)$ calculated from the transmission measurements, the quantity $<P(E', \theta, n)>$ can be calculated for each sample at each incident energy. Furthermore, since it is reasonable to assume that the quantities $P(E', \theta, n)$ and $\eta(E') \cdot W(E')$ will be uncorrelated, the following approximation can be made:

$$<P(E', \theta, n) \cdot \eta(E') \cdot W(E')> = <P(E', \theta, n)> \cdot <\eta(E')\ W(E')> \quad (8)$$

Equation 6 can therefore be rewritten in the following form:

$$\eta_m(E, n) = \eta(E) \cdot W(E) + \chi \cdot < P(E', \theta, n) >$$

where χ is a factor which is independent of sample thickness.

At each incident energy, E, a straight line can therefore be fit to the $\eta_m(E, n)$ and $<P(E', \theta, n)>$ data for the set of samples. This gives $\eta(E) \cdot W(E)$, and provided that $\sigma_s(E)$ is known, $\eta(E)$ can be obtained.

This method cannot readily be employed to correct data obtained using oxide, alloy, or canned samples because Equation 8 will contain one or more additional terms of the form $\chi \cdot <P(E', \theta, n)>$, but with χ different from the range of the average, $2 \cdot \Delta E$. For such samples, however, the calculation of $\eta(E)$ can be programmed to run from low to high incident neutron energy and thus to provide, as it proceeds, data which can be used to calculate the terms of the form $<P(E', \theta, n) \cdot \eta(E') \cdot W(E')>$. Thus, as before, $\eta(E)$ can be obtained provided that $\sigma_s(E)$ is known with sufficient accuracy.

The calculation of scattering corrections for $E \gtrsim 10$ eV would obviously be far too tedious to attempt by hand calculation. However, these are very trivial calculations for a large digital computer to perform. For example, using the Harwell method, about five minutes of IBM-7030 time is sufficient to calculate $\eta(E)$ and also $\sigma_t(E)$, $\sigma_f(E)$, $\sigma_c(E)$, and $\alpha(E)$ starting from the raw data (counts per channel versus channel number) for five samples (12 runs) and 2000 channels per run.

Limitations of the Eta Experiment

Measurements of $\eta(E)$ using the methods and techniques outlined above may be expected to be valid for neutron energies of up to a few tens of eV, assuming that the neutron-energy resolution for the measurement is good. As the experiment is extended to higher neutron energies, the validity of the methods used and the assumptions made become more open to doubt. In particular, the effects of energy resolution on the measurements must be carefully considered, and it must also be noted that scattering effects will become more important because the average neutron width increases with neutron energy.

The effect of poor energy resolution on the eta experiment depends on the thickness of the sample used and on the extent to which scattering occurs in the sample. If scattering is small compared with absorption and if the transmission, $T(E, n)$, of the sample tends to zero over the energy range spanned by the resolution function, then $\langle\eta(E)\rangle$, i.e., the average of $\eta(E)$ over the resolution function, is measured. If scattering is small and the average transmission, $\langle T(E, n)\rangle$, approaches unity, then the experiment measures the quantity $(\bar{\nu} \cdot \langle\sigma_f(E)\rangle / \langle\sigma_t(E)\rangle)$, i.e., the ratio of average fission and average total cross sections. The two quantities measured in these two limiting cases will not necessarily be equal, even if $\sigma_t(E) \gg \sigma_s(E)$ over the resolution function.

If scattering effects are appreciable, there is the further complication that the calculation of the scattering correction will also be subject to errors introduced by poor resolution. This, and the fact that the scattering correction will increase in magnitude at higher neutron energies, effectively limits the usefulness of eta measurements at low energies. Even with the best energy resolution likely to be obtainable in the next few years, it would probably not be worthwhile to attempt to extend the measurement of eta to neutron energies exceeding about 1 keV.

Direct Measurement of $\alpha(E)$

Outline of the Method

In contrast to the measurement of $\eta(E)$, the measurement of $\alpha(E)$ makes great demands on the detection techniques available at the present time but can always be carried out in a manner designed to keep scattering corrections small. As mentioned earlier, the direct alpha experiment consists of two basic measurements. The rate of capture in the fissile sample is

observed in one measurement, and the rate of fission in the same sample is observed in the other measurement. The ratio of the two measurements is proportional to $\alpha(E)$ provided that secondary (i.e., post-scattering) captures and fissions do not constitute more than a small proportion of all the captures and fissions observed. If the detection efficiencies for both capture and fission are known, absolute values of $\alpha(E)$ are obtained. Furthermore, if a measurement of the incident neutron spectrum is also made, capture- and fission-cross-section data can be obtained. However, this is not necessary for the determination of $\alpha(E)$.

The alpha experiment poses the same difficulty as would an experiment designed to measure the capture cross section of a fissile nuclide for resonance-energy neutrons. The capture of a neutron results in the prompt emission of gamma radiation, and the obvious way to detect capture is by means of this radiation. However, fission also results in the prompt emission of gamma rays; hence, some method must be found to discriminate against the fission gamma rays or to correct for their presence. Fission gamma rays can be gated out if the fission itself is detected and identified with high efficiency, e.g., by using fission-fragment or fission-neutron detectors. An alternative which is more difficult with the techniques available today is to exploit the different properties of the gamma radiation from fission and capture, e.g., spectrum, total energy, and/or multiplicity, in order to discriminate between the two types of event.

A further requirement which is imposed on the capture detector used in an alpha experiment is that its efficiency for detecting a capture must not depend on the spectrum of the capture gamma radiation. This spectrum may vary with incident-neutron energy although the total gamma-ray energy in the cascade following each neutron capture will be effectively constant for neutrons with energies of less than about 30 keV.

The equipment required for the alpha experiment therefore includes capture and fission detectors with characteristics or specifications which are by no means easy to satisfy. On the other hand, relatively thin samples can be used, so in contrast to the eta experiment, the calculation of scattering corrections is not necessarily a major problem.

Detection Techniques for $\alpha(E)$ Measurements

Hopkins and Diven[2] have demonstrated that the use of large liquid-scintillator detectors offers a solution to some of the problems encountered in measuring alpha. A spherical liquid scintillator with a diameter of 1 meter or greater will absorb

more than 90% of the energies of neutrons and/or gamma rays released in a fission or capture which occurs at the center of scintillator. The efficiency for detecting either process is therefore close to unity. In order to distinguish fission from capture, a scintillator solution containing about 1%(by weight) of cadmium can be used. A capture event is then characterized by a single prompt pulse, whereas a fission event is characterized by a prompt pulse followed, within a few microseconds, by one or more delayed pulses. These delayed pulses correspond to capture of the fission neutrons by the cadmium after they have slowed down to thermal energy in the liquid.

This detection system was used by Hopkins and Diven to obtain values of $\langle\sigma_c(E)\rangle/\langle\sigma_f(E)\rangle$, i.e., the ratio of the average capture cross section to the average fission cross section for neutron energies exceeding 30 keV. They used a pulsed "monoenergetic" neutron beam with a spread in neutron energy of a few keV and a beam pulse length of 60 nanosec. Using such a beam permits a simple method of discriminating against scattered neutrons. The "prompt" time, i.e., time of arrival of incident neutrons at the sample, is uniquely defined with respect to the beam pulse, and either a capture or a fission will result in a large scintillation pulse at this time. A scattered neutron will cause only a very small pulse at the "prompt" time, followed by a large pulse a few microseconds later, when it is captured. If a continuous beam or a beam with a very broad spread in neutron energy were used, the prompt time would not be uniquely defined and scattering events would be indistinguishable from capture events.

Despite the problem of having to cope with sensitivity to scattered neutrons, the detection system of Hopkins and Diven can be used with a continuous-energy neutron source. This has been demonstrated by Van Shi-di, et al.,[17] who have used a very similar detection system to measure the capture and fission cross sections of U^{235}, and their ratio, for neutrons with energies from thermal up to 30 keV.

The most detailed measurements of alpha yet published for any fissile nuclide are those of de Saussure, et al.,[4] for U^{235}. The detection system used for these measurements is shown in Figure 2. A multiplate fission ionization chamber containing about 4 g of U^{235} was placed at the center of a large tank (effective diameter, 1.25 meters) containing liquid scintillator. Considerable effort was made to maintain an efficiency close to unity for detection of fission fragments by the fission chamber. Essentially all of the gamma rays emitted by the U^{235} following a neutron absorption were detected by the scintillator. After experimental-background and a few other small corrections were made, the ratio of scintillator pulses in

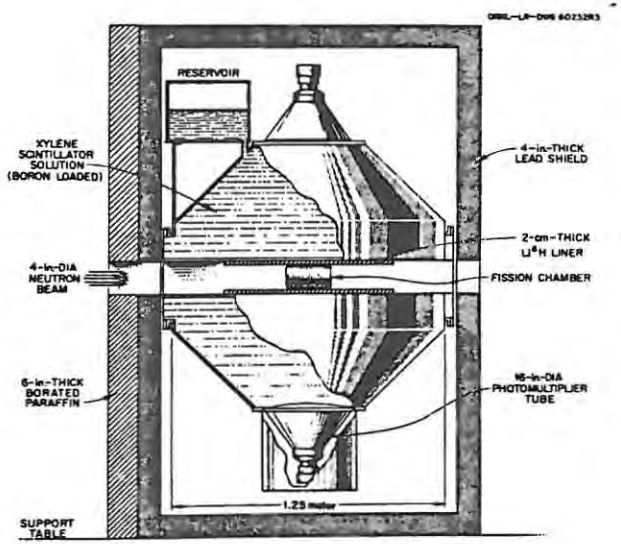

Figure 2. Liquid-scintillator tank used for the measurement[4] of $\alpha(E)$.

anticoincidence with the fission chamber to those in coincidence with the fission chamber gave $\alpha(E)$.

It would seem very difficult, if not impossible, to use the detection system of de Saussure, et al,[4] to measure $\alpha(E)$ for fissile nuclides other than U^{235}. The difficulty arises primarily because the fission detector must accommodate a minimum quantity of a few grams of fissile material in order to be able to carry out a measurement of $\alpha(E)$ using any of the pulsed-accelerator neutron sources available today. Even with semiconductor detectors or gaseous scintillation counters instead of an ionization chamber, it would be impossible to accommodate more than a few tenths of one gram of U^{233} or Pu^{239}, for example, because of "pile-up" difficulties associated with the high alpha activity of these nuclides.

Sowerby, et al.,[16] have recently constructed a detection system which incorporates liquid-scintillator counters for detecting fission neutrons and a Moxon-Rae[18] detector for detecting capture events. Pulse-shape discrimination is used in the neutron detectors. Although the efficiency for detecting a single fission neutron is only about 40%, the fact that two or three neutrons are emitted per fission makes it possible to

detect fission with an efficiency of about 80%. The alpha activity of the samples is of no consequence in this case. The limit is set by the "pile-up" of rejected gamma-ray scintillations in the pulse-shape-discrimination system. Samples of Pu^{239} weighing up to a few tens of grams can be handled by this detector. The Moxon-Rae detector is well known for its application to capture-cross-section measurements [18,19] for nonfissile nuclides.

A method for measuring alpha which utilizes the differences in gamma-ray spectra to distinguish capture from fission has been described and discussed by Diven and Hopkins[2] and by de Saussure, et al.[4] A large liquid-scintillator tank like that shown in Figure 2 is used; the fissile sample is placed at the center of the tank and bombarded with neutrons (preferably "monoenergetic"), and the pulse-height spectrum of scintillations from the tank is observed. Since the pulse-height spectra associated with fission and capture have different shapes and the fission pulse-height spectrum can be determined independently using a fission chamber in place of the sample, it should be possible to subtract the fission spectrum and hence to obtain the capture spectrum and the ratio of capture to fission, or alpha. The fission spectrum to be subtracted from the absorption spectrum must be normalized at high pulse heights corresponding to gamma-ray energies of more than 10 MeV, where no contribution from the capture spectrum is possible.

This method would be convenient if alpha were about unity. For low values of alpha, however, it is rather inaccurate because the capture spectrum is determined as a difference.

Hemmendinger[20] has recently described the measurement of neutron resonance cross sections using a nuclear detonation as the neutron source. A notable feature of these experiments is that the detonation delivers in a single pulse as many neutrons as it would take a pulsed accelerator about one hundred years to produce. Accurate measurements of cross sections are therefore possible using extremely small quantities of sample in conjunction with detectors of low efficiency. The short duration of each measurement also makes it possible to experiment with highly radioactive materials. Special Moxon-Rae detectors have been constructed[20] using semiconductor counters for capture-cross-section measurements, and it seems very likely that the nuclear-detonation experiments will soon become a very important source of $\alpha(E)$ data as well as other neutron-cross-section data.

Effect of Energy Resolution on Alpha Measurements

When the energy resolution for incident neutrons is poor, the direct alpha experiment measures the ratio of average cross sections, $\langle\sigma_c(E)\rangle / \langle\sigma_f(E)\rangle$, the cross sections being averaged over the resolution function of the neutron spectrometer. This ratio of averages is not necessarily the same as the average of the ratio, i.e., $\langle\alpha(E)\rangle$. However, the ratio of average cross sections appears to be of more value to reactor physicists than $\langle\alpha(E)\rangle$. There is therefore no serious limitation or restriction which affects the alpha experiment when it is carried out at high energies or with poor energy resolution.

Results of Eta and Alpha Measurements

U^{235}

Since U^{235} is, in many ways, the easiest fissile nuclide with which to experiment, it has received a good deal more attention than other fissile nuclides. In Figures 3 through 10, some examples of data that have been obtained for this nuclide are presented. Measurements[3] of eta for energies up to 100 eV are shown in Figures 3 through 6. Below 5 eV these data are in very good agreement with values of $\eta(E)$ calculated from fission- and total-cross-section measurements by Shore and Sailor.[25] The data shown in Figures 3 through 6 were obtained with good energy resolution up to an energy of about 20 to 30 eV.

The cross-section and $\alpha(E)$ measurements of de Saussure, et al.,[4] from 3 to 25 eV are shown in Figures 7 and 8. A comparison may be made between their $\alpha(E)$ values, shown in Figure 7, and $\alpha(E)$ values calculated from $\eta(E)$ data,[3] shown in Figure 9. The two sets of data agree fairly well at the resonance energies (which can be identified from the plot of $\sigma_t(E)$ given in Figure 4), but not so well at energies for which the absorption cross section is small. However, this is not surprising, since at these energies both measurements are prone to systematic errors due to experimental backgrounds; in addition, the scattering correction in the $\eta(E)$ measurement is largest at these energies.

Various compilations and evaluations of U^{235} cross-section data have been carried out from time to time. Freemantle[21] recently described an evaluation which includes data for energies up to 100 keV. In Figure 10, a summary given by Freemantle[21] of the ratio $\langle\sigma_c(E)\rangle / \langle\sigma_f(E)\rangle$ from 10 eV to 100 keV is shown. The combined data define a fairly consistent pattern for the gross variation of the ratio with energy, although there are some large differences among the various sets of data.

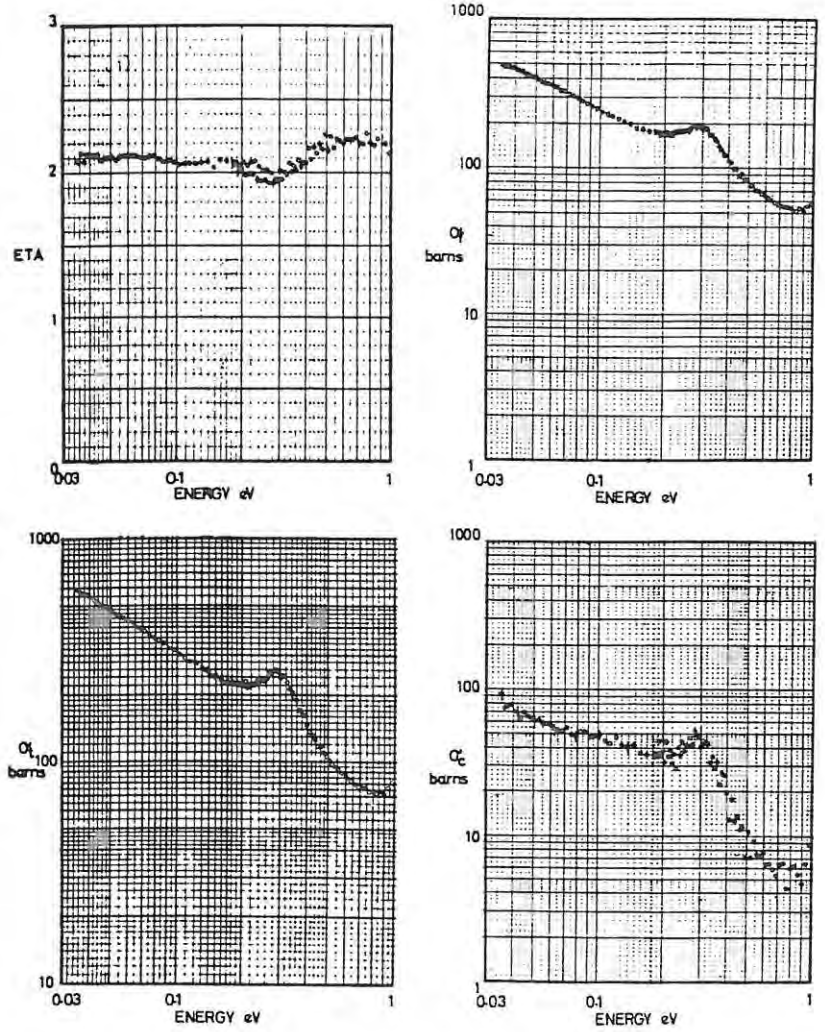

Figure 3. Measurements[3] of eta and cross sections for U^{235} in the energy region 0.03 to 1 eV. The fission data are normalized[7] so as to make $\eta(E) = 2.084$ (average) for $E = 0.06 \pm 0.01$ eV.

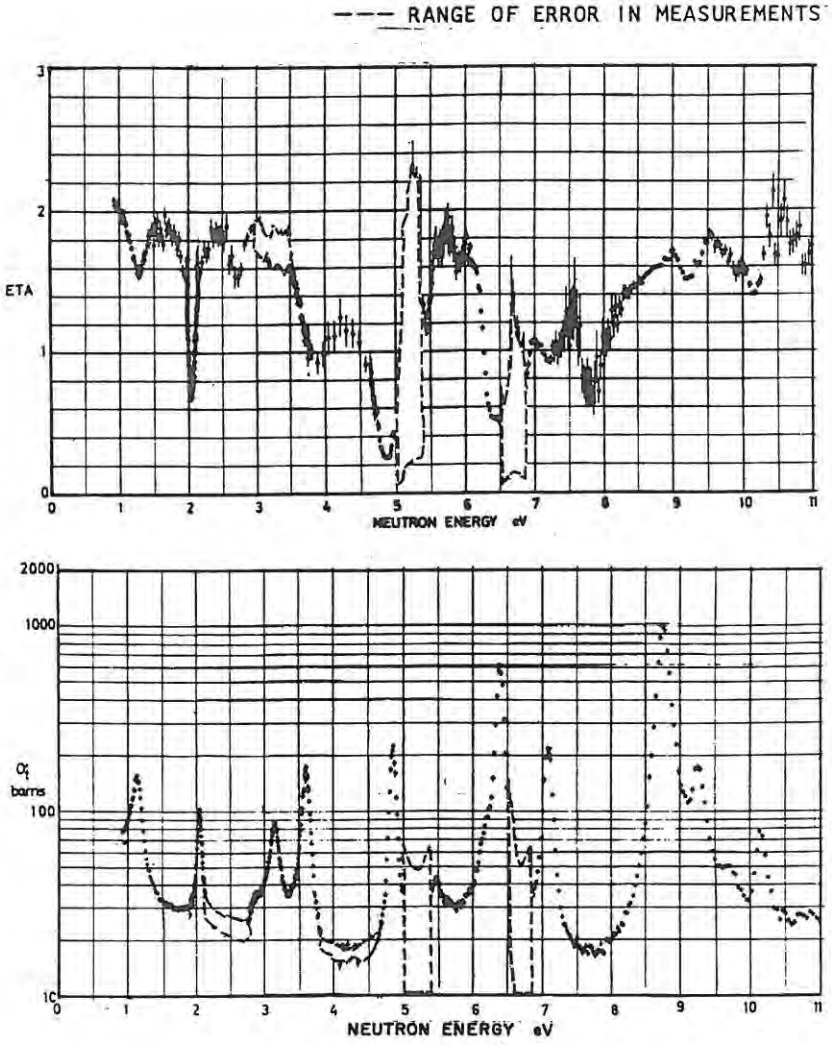

Figure 4. Measurements[3] of $\eta(E)$ and $\sigma_t(E)$ for U^{235} in the energy region 1 to 11 eV. The large errors in the regions 5.2 eV and 6.7 eV are assigned arbitrarily and indicate that corrections have been made for resonances of the U^{234} and U^{238} impurities in the U^{235} samples used. The energy loss in scattering was ignored when these eta data were corrected for scattering effects.

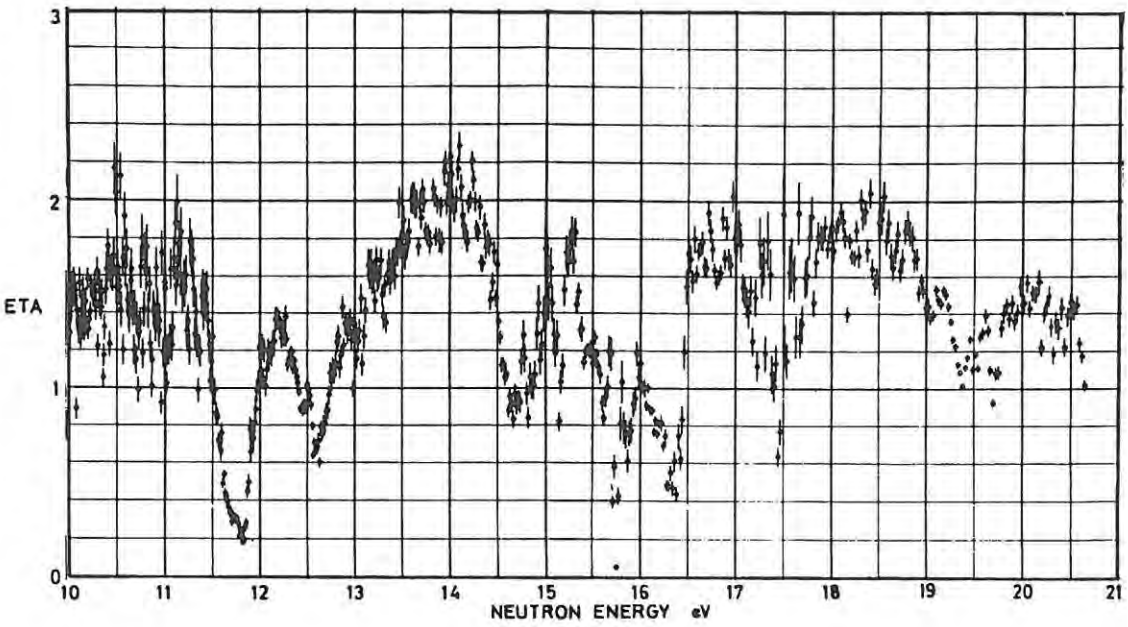

Figure 5. Values[3] of $\eta(E)$ for U^{235} in the energy range 10 to 21 eV. The energy loss in scattering was taken into account when these data were corrected for scattering effects.

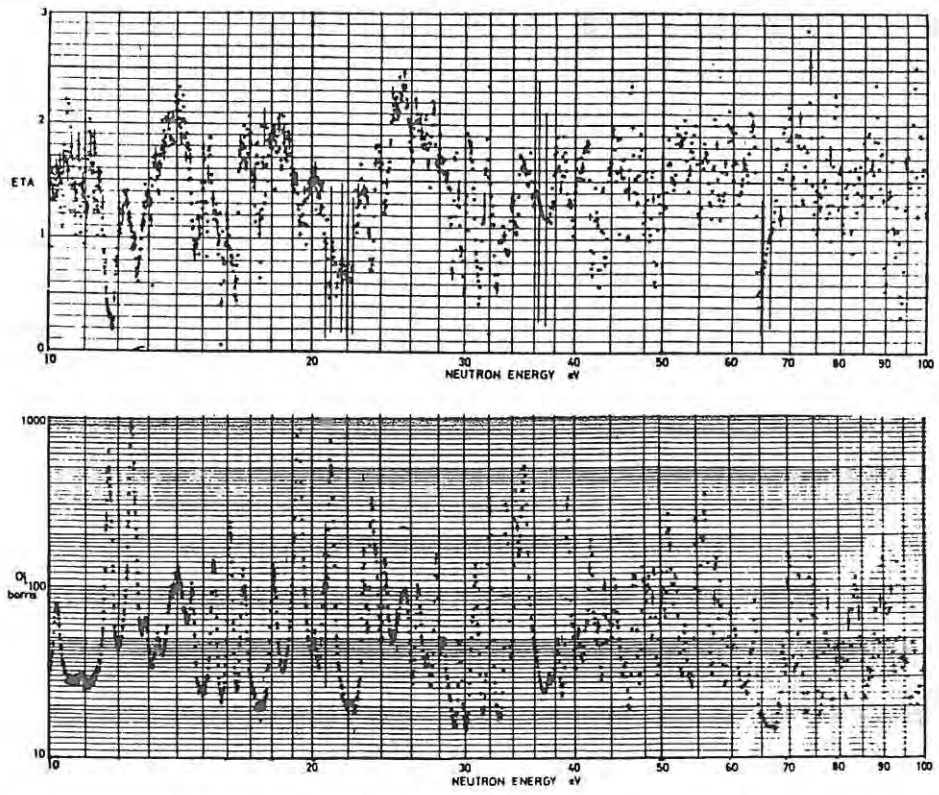

Figure 6. Measurements[3] of $\eta(E)$ and $\sigma_t(E)$ for U^{235} in the energy region 10 to 100 eV. The energy loss in scattering was taken into account when these data were corrected for scattering effects. Corrections have been made to the data for impurity resonances at 20.8, 22.0, 31.3, 37.0, and 66.5 eV.

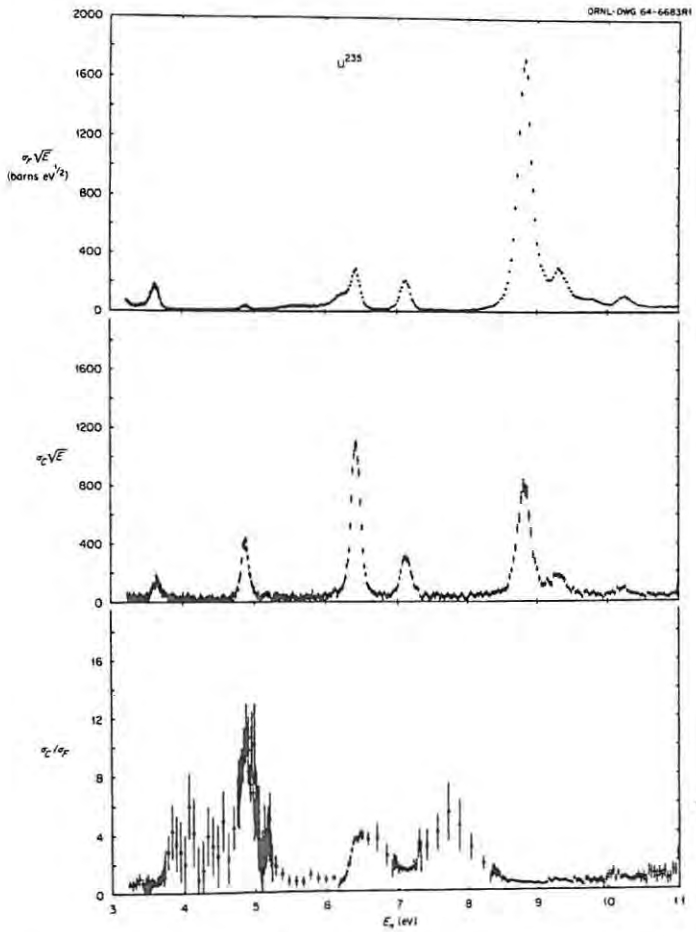

Figure 7. Capture and fission cross sections[4] for U^{235} (multiplied by the square root of the neutron energy) and their ratios (α) from 3 to 11 eV. Where the capture and fission cross sections are low, introducing large errors in α, the values of α are averaged over the approximate neutron-resolution width. These averages are denoted by the circular points.

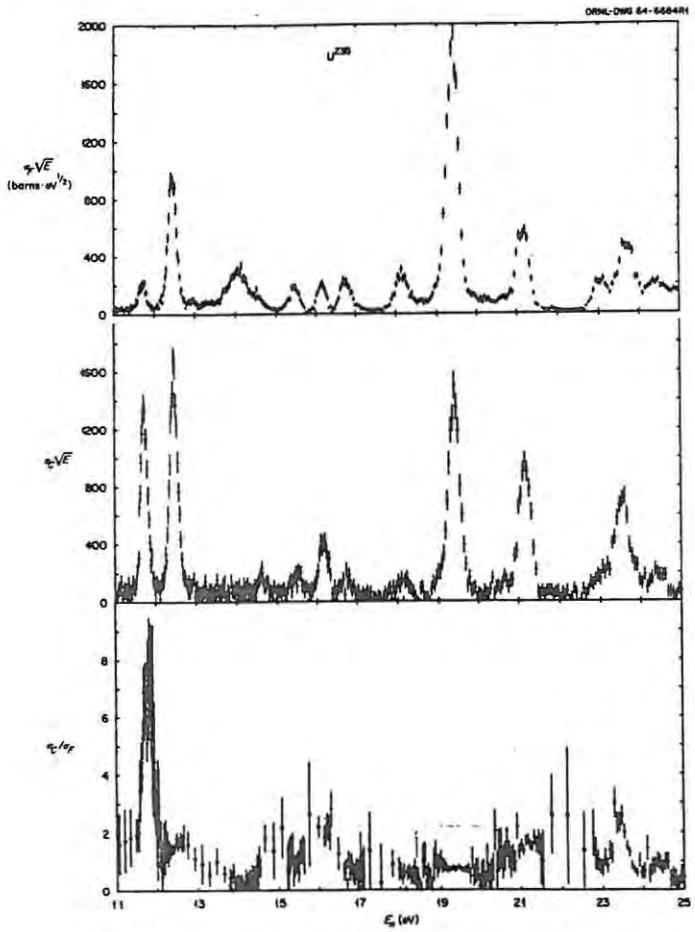

Figure 8. Capture and fission cross sections[4] for U^{235} (multiplied by the square root of the neutron energy) and their ratios (α) from 11 to 25 eV. Where the capture and fission cross sections are low, introducing large errors in α, the values of α are averaged over the approximate neutron resolution width. These averages are denoted by the circular points.

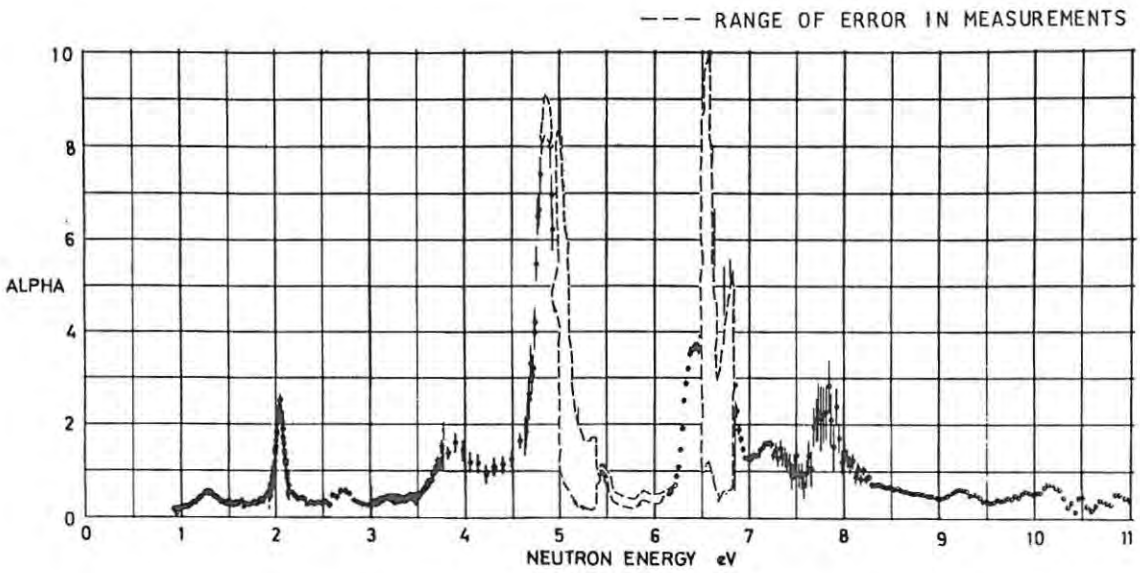

Figure 9. Values of $\alpha(E)$ for U^{235} in the energy region 1 to 11 eV. These values were calculated from the $\eta(E)$ data[3] shown in Figure 3, using Equation 2 and assuming $\overline{\nu} = 2.42$.

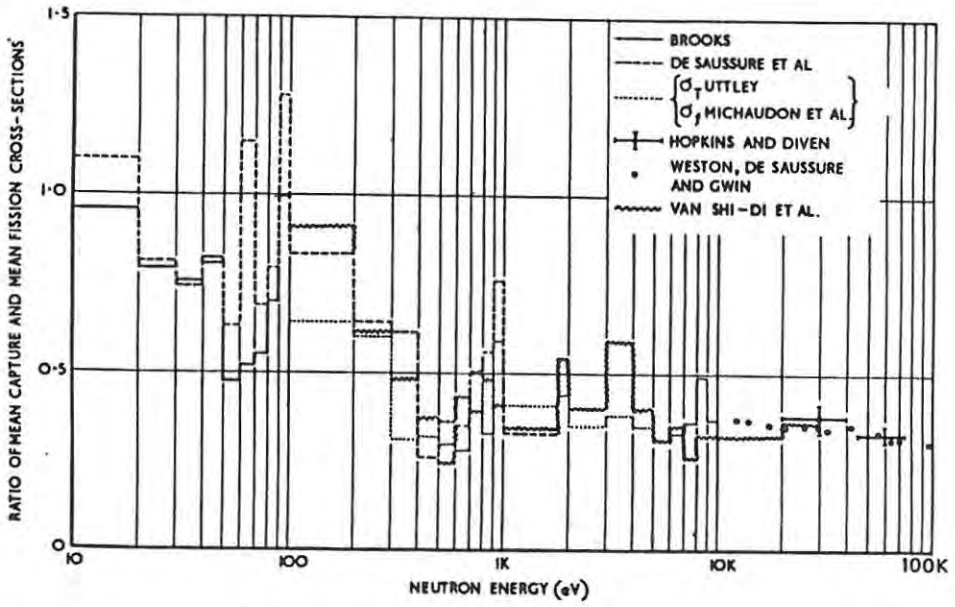

Figure 10. Capture to fission ratio for U^{235}, as given by Freemantle.[21] References to the various data listed are as follows: Brooks;[3] de Saussure, et al.;[4] Uttley;[22] Michaudon, et al.;[23] Hopkins and Diven;[2] Weston, et al.;[24] Van Shi-Di, et al.[17]

U^{233} and Pu^{239}

Measurements of $\eta(E)$ for U^{233} for energies above 1 eV have been reported by Fluharty, et al.,[26] and Yeater, et al.[11] Measurements of $\eta(E)$ for Pu^{239} for energies above 1 eV have been reported by Farley[12] and by Bollinger, et al.[13] All of these measurements were published prior to 1961 and by now have received wide circulation. No measurements of $\alpha(E)$ for neutron energies below 30 keV appear to have been reported for U^{233} or Pu^{239}. However, much attention is now being devoted to the special problems associated with measuring $\alpha(E)$ for these two nuclides, so this position may perhaps improve fairly soon. Further detailed measurements of $\eta(E)$ for U^{233} and Pu^{239} have been made at Harwell. The data obtained[27] for neutron energies below 11 eV are shown in Figures 11 and 12 for U^{233} and Pu^{239}, respectively. These data are in agreement with the earlier data for U^{233} and Pu^{239}.

Cross-Section Data Obtained in Conjunction with Eta and Alpha Measurements

When alpha or eta is measured, useful cross-section data may also be obtained at the cost of very little extra experimental effort. If the incident-neutron spectrum obtaining in the alpha experiment is measured, capture- and fission-cross-section data may be obtained as well as alpha. Capture- and fission-cross-section data obtained by de Saussure, et al.,[4] are shown in Figures 7 and 8.

If the eta experiment is repeated for a series of samples of different thickness, both total- and fission-cross-section data may be obtained in addition to eta.[3] The measurement of $\sigma_f(E)$ is subject to the assumption that the average number of neutrons per fission, $\bar{\nu}$, is independent of incident-neutron energy. The capture cross section $\sigma_c(E)$ may also be derived from these measurements, provided that the scattering cross section is known.

Total-cross-section data obtained in conjunction with $\eta(E)$ measurements[3] are shown for U^{235} in Figures 3, 4, and 6. Fission- and capture-cross-section data are shown in Figures 3 and 13. For the purpose of resonance analysis, it is very useful to have a set of partial-cross-section data measured with the same energy resolution, plus a set of transmission data for several samples of different thickness.

Cross-section data such as those shown in Figures 3 and 13 may also be used to calculate resonance fission and capture integrals, as given in Table 1. By using the Harwell data[3] for the energy range 0.45 to 100 eV with the data of Uttley[22] and Michaudon[23] for the range 100 eV to 10 keV and the data of Hanna and Walker[28] for the range 10 keV to 1 MeV, the values given in the second row of Table 1 are obtained. The ratio of

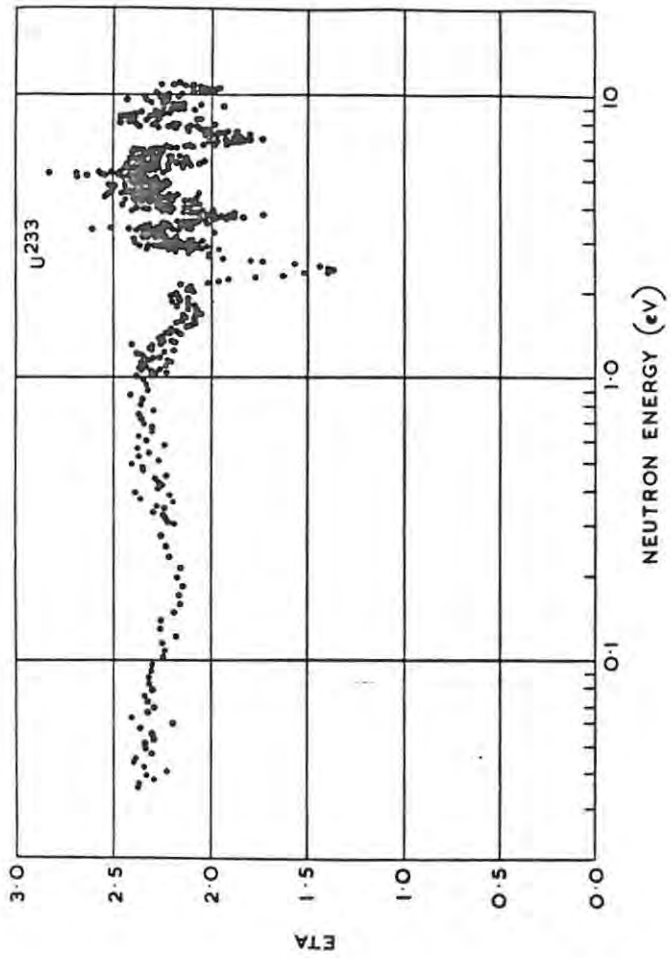

Figure 11. Values[27] of $\eta(E)$ for U^{233} in the energy region 0.03 to 11 eV.

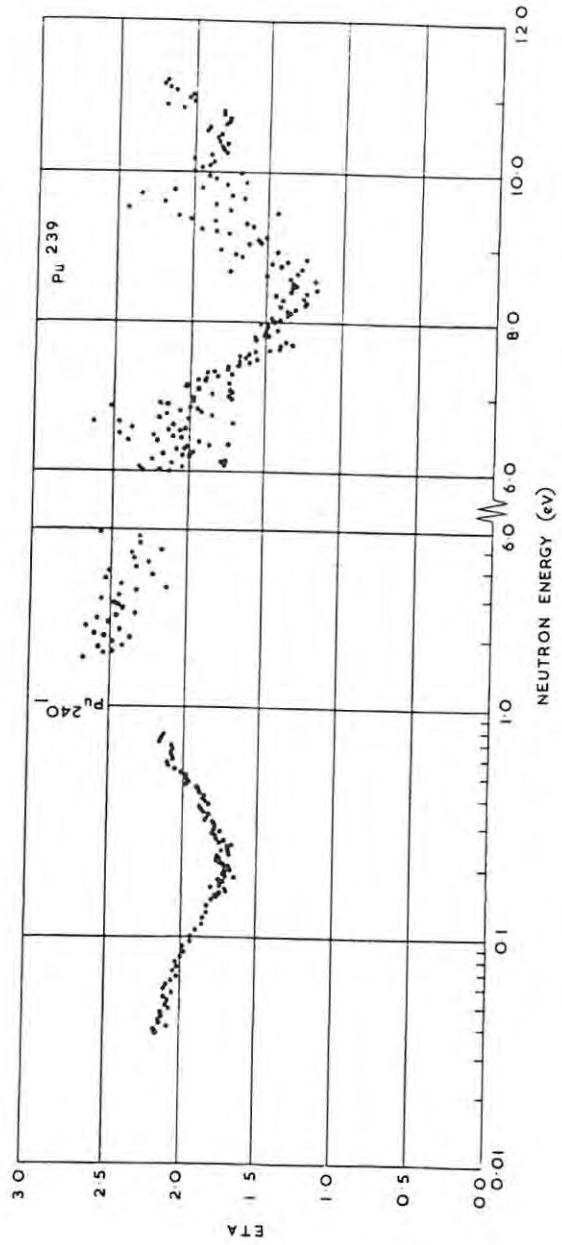

Figure 12. Values[27] of $\eta(E)$ for Pu^{239} in the energy region 0.03 to 11 eV.

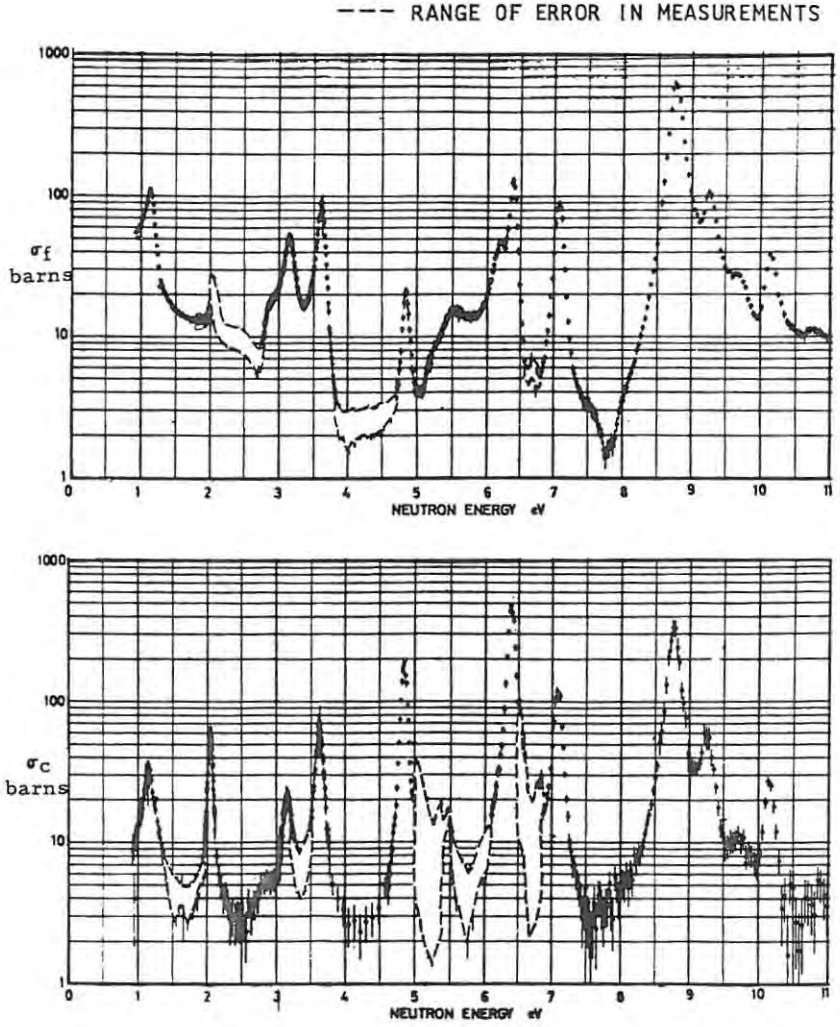

Figure 13. Values[3] of $\sigma_f(E)$ and derived values of $\sigma_c(E)$ for U^{235} in the energy region 1 to 11 eV. These data were obtained at the same time as the data shown in Figure 3.

Table 1. Fission and Capture Integrals

	$I_f = \int_{0.45\ eV}^{E} \frac{\sigma_f \cdot dE}{E}$ (barns)	$I_c = \int_{0.45\ eV}^{E} \frac{\sigma_c \cdot dE}{E}$ (barns)	$\frac{I_c}{I_f}$
E = 100 eV Ref. 3	208.5	125.3	
E = 1 MeV Refs. 3, 22, 23, 28	268	152	0.57 ±0.06
E = 1 MeV Ref. 29	274 ±10	144 ±5	0.526 ±0.027

the capture integral to the fission integral thus obtained is 0.57 ±0.06. The recommended values from integral measurements of the fission and capture resonance integrals given by Stehn, et al.,[29] are listed in the third row of Table. 1. These data give a value of 0.526 ±0.027 for the ratio of capture to fission. The values obtained from the differential and integral measurements are therefore consistent.

Conclusions

The situation regarding alpha and eta measurements might be summarized as follows. At low energies, i.e., provided that good energy resolution is available, the eta experiment is reliable and has the advantage of experimental simplicity. However, the eta data obtained from the eta experiment are difficult to interpret if the energy resolution is not good. The value of this experiment is increased considerably if it is repeated using a series of samples of different thickness, so that total-, fission-, and capture-cross-section data can also be derived from the basic measurements.

The alpha experiment requires the use of fission and capture detectors which must meet very stringent specifications. It is therefore considerably more difficult, from the experimental viewpoint, than the eta experiment. However, the data obtained are easy to interpret and the experiment may readily be extended to provide fission- and capture-cross-section data as well as alpha data. At low energies $\alpha(E)$ is measured, but at high energies $\langle\alpha_c(E)\rangle / \langle\alpha_f(E)\rangle$ is obtained.

It is to be hoped that in the near future, accurate data for $\eta(E)$ and $\alpha(E)$ for U^{233}, U^{235}, and Pu^{239} will be available for neutron energies up to a few tens of eV. It is perhaps even possible that a comparison of accurate $\alpha(E)$ and $\eta(E)$ measurements in the low-energy region (up to a few eV) will provide a test of the assumption that $\bar{\nu}$ is constant. The future of measurements above a few tens of eV, and particularly of measurements in the kilovolt-energy region, would appear to lie with the alpha experiment. In both types of experiments, it seems likely that the capability to provide auxiliary cross-section data will receive increasing attention and emphasis.

References

1. Leonard, B. R., Neutron Physics, M. L. Yeater (ed.), Vol. 2, 1962, p. 3.
2. Hopkins, J. C., and B. C. Diven, Nucl. Sci. Eng. 12, 169 (1962); and EANDC Symposium on Neutron Time of Flight Methods, J. Spaepen (ed.), Euratom, Brussels, 1961, p. 407.
3. Brooks, F. D., et al., United Kingdom Atomic Energy Reports AERE-M1670, 1966, and AERE-NP/GEN 35 (to be published).
4. de Saussure, C., Oak Ridge National Laboratory Report ORNL-3738, 1965; and Nucl. Sci. Eng. 23, 45 (1965); see also Oak Ridge National Laboratory Report ORNL-3360, (1963), p. 51.
5. Lynn, J. E., Phys. Rev. Letters 13, 412 (1964).
6. Good, W. M. and Rae, E. R., United Kingdom Atomic Energy Authority UKAEA Report AERE-NP/GEN 21.
7. Macklin, R. L., et al., Nucl. Sci. Eng. 8, 210 (1960).
8. Hornyak, W. F., Rev. Sci. Instr. 23, 264 (1952).
9. Palevsky H., et al., J. Nucl. Energy 3, 177 (1956).
10. Leonard, B. R., Proceedings of the Tripartite Conference on Cross-Sections of Fissile Nuclei, N. J. Pattenden (ed.), United Kingdom Atomic Energy Authority Report AERE-NP/R2076, 1958.
11. Yeater, M. L. R. W. Hockenbury, R. W. and R. R. Fullwood, Nucl. Sci. Eng. 9, 105 (1961).
12. Farley, F. J. M., J. Nucl. Energy 3, 33 (1956).
13. Bollinger, L. M., R. E. Coté, and G. E. Thomas, Second Geneva Conference, Proceedings, Vol. 15, United Nations, Geneva, 1958, 127.
14. Ignat'ev, K. G., I. V. Kirpichnikov, and S. I. Sukoruchkin, Atomnaya Energiya 16, 110 (1964).

15. Brooks, F. D., EANDC Symposium on Neutron Time-of-Flight Methods, J. Spaepen (ed.), Euratom, Brussels, 1961, p. 131.
16. Sowerby, M. G., private communication.
17. Van Shi-Di., et al., Symposium on the Physics and Chemistry of Fission, Salzburg, 1965, Paper SM-60/86.
18. Moxon, M. C., and E. R. Rae, Nucl. Instr. Methods 24, 445 (1964).
19. Macklin, R. L., J. H. Gibbons and T. Inada, Nucl. Phys. 43, 353 (1963).
20. Hemmendinger, A., Phys. Today 18, No. 8, 17 (1965).
21. Freemantle, R. G., United Kingdom Atomic Energy Authority Report AEEW-M502, 1965.
22. Uttley, C. A., United Kingdom Atomic Energy Authority Report AERE-M1272, 1963.
23. Michaudon, A., et al., French Atomic Energy Commission Report CEA-1093, 1960.
24. Weston, L. W., G. de Saussure, and R. Gwin, Oak Ridge National Laboratory ORNL-3499 Vol. 1, 1963, p. 11.
25. Shore, F. J., and V. L. Sailor, Phys. Rev. 112, 191 (1958).
26. Fluharty, R. G., M. S. Moore, and J. E. Evans, Second Geneva Conference, Proceedings, Vol. 15, United Nations, Geneva, 1958, p. 111.
27. Brooks, F. D., et al., United Kingdom Atomic Energy Authority Report AERE-M1709, 1966.
28. Hanna, G. C., and W. H. Walker, unpublished data.
29. Stehn, J. R., et al., in Brookhaven National Laboratory Report BNL-325, (2d ed., Suppl. 2, Vol. III), 1965.

Reprinted from:

NUCLEAR PHYSICS, VOLUME A121 (1968) No. 3

L. M. SPITZ
Physics Department, University of Cape Town

E. BARNARD
South African Atomic Energy Board, Pretoria

and

F. D. BROOKS
Physics Dept., University of Cape Town

NEUTRON CAPTURE CROSS SECTIONS OF Cr, Mn, Ni, Nb, Ag, In, Sb AND Au IN THE 8 TO 120 keV REGION

NORTH-HOLLAND PUBLISHING COMPANY - AMSTERDAM

4.A.1 *Nuclear Physics* A121 (1968) 655—672;

NEUTRON CAPTURE CROSS SECTIONS OF Cr, Mn, Ni, Nb, Ag, In, Sb AND Au IN THE 8 TO 120 keV REGION

L. M. SPITZ
Physics Department, University of Cape Town

E. BARNARD
South African Atomic Energy Board, Pretoria

and

F. D. BROOKS
Physics Dept., University of Cape Town

Received 26 August 1968

Abstract: Moxon-Rae detectors were used to measure ratios of the radiative capture cross section of elemental Cr, Mn, Ni, Nb, Ag, Sb and Au to that of In for neutrons of energy 8 to 120 keV. Relative capture cross sections of In for 8 to 30 keV neutrons were also measured. These were converted to absolute cross sections by using the In capture cross sections determined by Gibbons *et al.* The data were analysed to determine p-wave strength functions for Nb, Ag, Sb and Au, and average radiation widths for Cr, Mn and Ni.

E NUCLEAR REACTIONS Cr, Mn, Ni, Ag, In, Sb, Au(n,γ). E = 8–120 keV; measured $\sigma_{n\gamma}(E)$. Deduced $\Gamma_n^1/D, \Gamma_\gamma$.

1. Introduction

Studies of radiative capture of keV neutrons have in the past been conducted with a variety of aims in mind. Some investigations have been motivated by interest in the properties of the compound states formed by neutron capture. Strength functions and resonance parameters have been determined [1-3]) from capture cross-section measurements and compared with theoretical predictions [3,4]) based on compound nucleus theory. In addition the capture data are sometimes of interest to the theory of stellar nucleosynthesis [5,6]), and they are often of considerable importance [7]) in reactor physics and reactor design studies.

The work reported in this paper deals with three groups of elements. The elements Cr, Mn and Ni, which form the first group, are important from the reactor data viewpoint and possibly also from the stellar nucleosynthesis viewpoint, yet few capture cross-section data are available for them. In addition to this, the capture cross sections of these elements in the keV region are of such a nature that an analysis to determine average radiation widths is possible.

The second group includes the elements Nb, Ag, In and Sb. The capture cross sections of these elements were studied with the aim of determining values of the p-wave strength function S_1 in the mass number $\approx$ 100 region. Theories have predicted and experiments have confirmed that S_1 reaches a maximum in this mass region, but there has been controversy [8,9]) as to whether the data indicate a single maximum or two maxima.

The capture cross section of Au is of interest as a standard cross section [6,7]), particularly since this element may be investigated by all of the main methods of capture cross-section measurement in use at the present time. Most of the capture cross-section data available for Au have been summarised and reviewed by Pönitz [7]), and he notes in particular that there are significant discrepancies between different measurements of the shape of the cross section in the 1–1000 keV region.

2. Experimental method

The present experiments consisted of two parts. In one part, the relative capture cross section of In was measured in the 8–30 keV region using a long counter [10]) to measure the relative incident neutron flux. In the second and major part, ratios of the capture cross sections of the remaining elements to that of In were measured at a number of neutron energies in the 8 to 120 keV region.

In order to measure the capture ratios, similar sized samples of indium and of the different elements were bombarded by neutrons and the relative yields of capture gamma rays were measured with the aid of Moxon-Rae [11,12]) detectors. Neutrons were obtained from the ^{7}Li(p, n)^{7}Be reaction, the protons being provided either by the 3 MV pulsed Van de Graaff of the South African Atomic Energy Board at Pelindaba, Transvaal or by the 5.5 MV pulsed Van de Graaff of the Southern Universities Nuclear Institute at Faure, Cape Province. The neutron flux was monitored both by integrating the proton charge deposited on the target and also by means of a long counter.

The samples used for the measurements on Cr, Mn, Ni, Ag, In and Au were metal discs of either 2.5 cm or 5.1 cm diam. The Nb and Sb samples consisted of powdered metal packed into thin-walled aluminium containers. The thickness n of the samples expressed in atoms per b ranged from 0.005 to 0.027, and samples of two or more different thicknesses were studied in the cases of Ni, Ag, In and Sb. Details of the samples are given in table 1.

The Moxon-Rae detectors were based on the design of Macklin *et al.* [12]) and consisted of 3.4 g/cm^2 thick Compton converters (80 % graphite plus 20 % Bi_2O_3) backed by scintillation detectors utilizing 0.5 mm thick NE 102A plastic scintillators. Two alternative detection systems A and B were used. The A-system consisted of a single 12.5 cm diam. photomultiplier tube with matching scintillator and converter. The B-system consisted of four 5 cm diam. photomultipliers (with matching scintillators and converters) connected in parallel. Each detector provided output

pulses suitable for operating a conventional "fast-slow" electronic system, i.e. a "fast" output for nsec time-of-flight measurement and a "slow" output for selecting events in the "Moxon-Rae peak" of the pulse-height spectrum.

TABLE 1
Sample parameters

Element	ε (MeV)	M_s	Thickness n (atom/mb)
Cr	8.12	0.831	26.0
Mn	7.27	0.928	12.7
Ni	8.23	0.820	6.7 13.4 26.8
Nb	7.23	0.934	6.14
Ag	7.07	0.955	8.26 14.8
In	6.75	1.00	5.53 7.89
Sb	6.64	1.017	6.50 9.19
Au	6.50	1.038	5.78

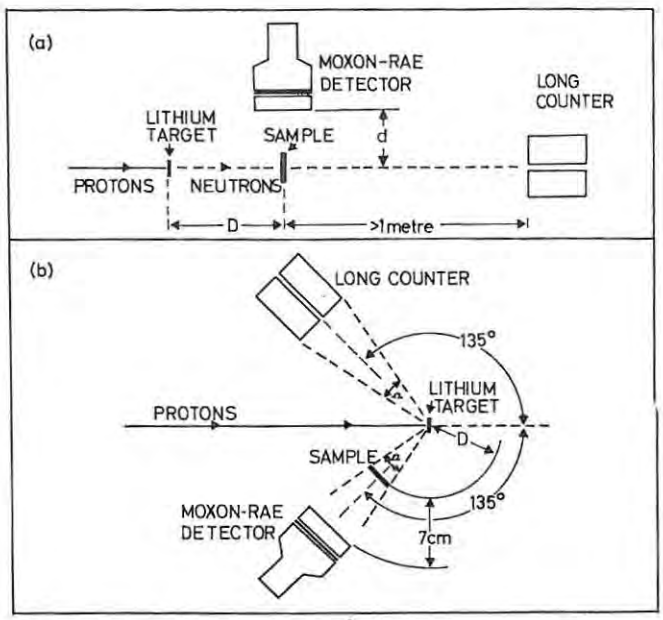

Fig. 1. Experimental arrangements for capture yield measurements: (a) in geometries I and III; and (b) in geometry II. The distance d was 8 and 10 cm in geometries I and III, respectively. The distance D was 8.1 cm in geometry III, 7 cm in geometry II and varied between 12 and 26 cm for different measurements in geometry I.

Neutron time-of-flight analysis was used to separate the neutron capture gamma rays from background gamma rays, particularly those originating at the (p, n) source. In some phases of the work, time of flight also served to measure the neutron energy. Three alternative detection geometries (I, II and III) were employed. In geometry I, thin ($\approx$ 2 keV) lithium targets were used in order to obtain "mono-energetic" neutrons and the target, sample and detector were disposed as shown in fig. 1(a). The neutron energy was calculated from the proton energy assuming a Q-value of -1.6433 MeV for the ^{7}Li(p, n)^{7}Be reaction [13]). The neutron energy resolution (FWHM) in this geometry varied from about 10 keV at 30 keV to 6 keV at 100 keV. A typical time-of-flight spectrum obtained in geometry I using a 5.1 cm diam. silver sample is shown in fig. 2(a). Besides the gamma-ray peak (channel 80) and the major neutron peak (channel 62) corresponding in this example to capture of 58-keV neutrons, there is a minor peak (channel 45) corresponding to capture of 7 keV neutrons from the associated kinematic group emitted at 180° (c.m.). The background data [indicated by crosses in fig. 2(a)] show the results of a run taken without a sample. After correcting for background and for the contribution of the low-energy group, the area of the 58 keV peak was obtained and compared with the area obtained under the same conditions using an indium sample. The ratio of these areas gave the yield ratio $Y_z(E)$ for silver at $E = 58$ keV. This procedure was repeated for the remaining samples at the same energy, and then the whole procedure was repeated for the full set of samples at a series of neutron energies in the 30–100 keV region. The results of these measurements were thus a set of yield ratios for different samples at different neutron energies.

In geometry II, a thin ($\lesssim$ 10 keV) lithium target was used and the capture sample was placed 7 cm from this target at an angle of 135° to the proton beam direction, as shown in fig. 1(b). The Moxon-Rae detector A was placed 7 cm behind the sample, and the neutron energy was determined from the time-of-flight measurement. Data were taken at several neutron energies in the range 10 to 40 keV. The neutron energy resolution (FWHM) varied from 3 keV at 10 keV to 8 keV at 40 keV. A typical time-of-flight spectrum obtained using a 5.1 cm diam. indium sample is shown in fig. 2(b). The neutron capture peak is again clearly resolved (channel 72), and the additional peak observed in the vicinity of channels 30 to 40 is attributed to capture of neutrons in the detector itself. A set of capture yield ratios was measured as in geometry I. In geometry II, however the incident neutron fluxes for runs at different energies were monitored using the long counter placed at the same angle and solid angle with respect to the target as the sample [see fig. 1(b)].

In geometry III, a thick ($\approx$ 25 keV) lithium target was used and the capture sample and Moxon-Rae detector were placed as shown in fig. 1(a). Using detector B, the capture yield was then measured as a function of time of flight and thus as a function of neutron energy in each run. The proton energy was held at 1.891 ± 0.001 MeV so as to maintain a stable continuous neutron spectrum for all of the runs carried out in this geometry. Three typical runs are shown in fig. 2(c); these are a background run

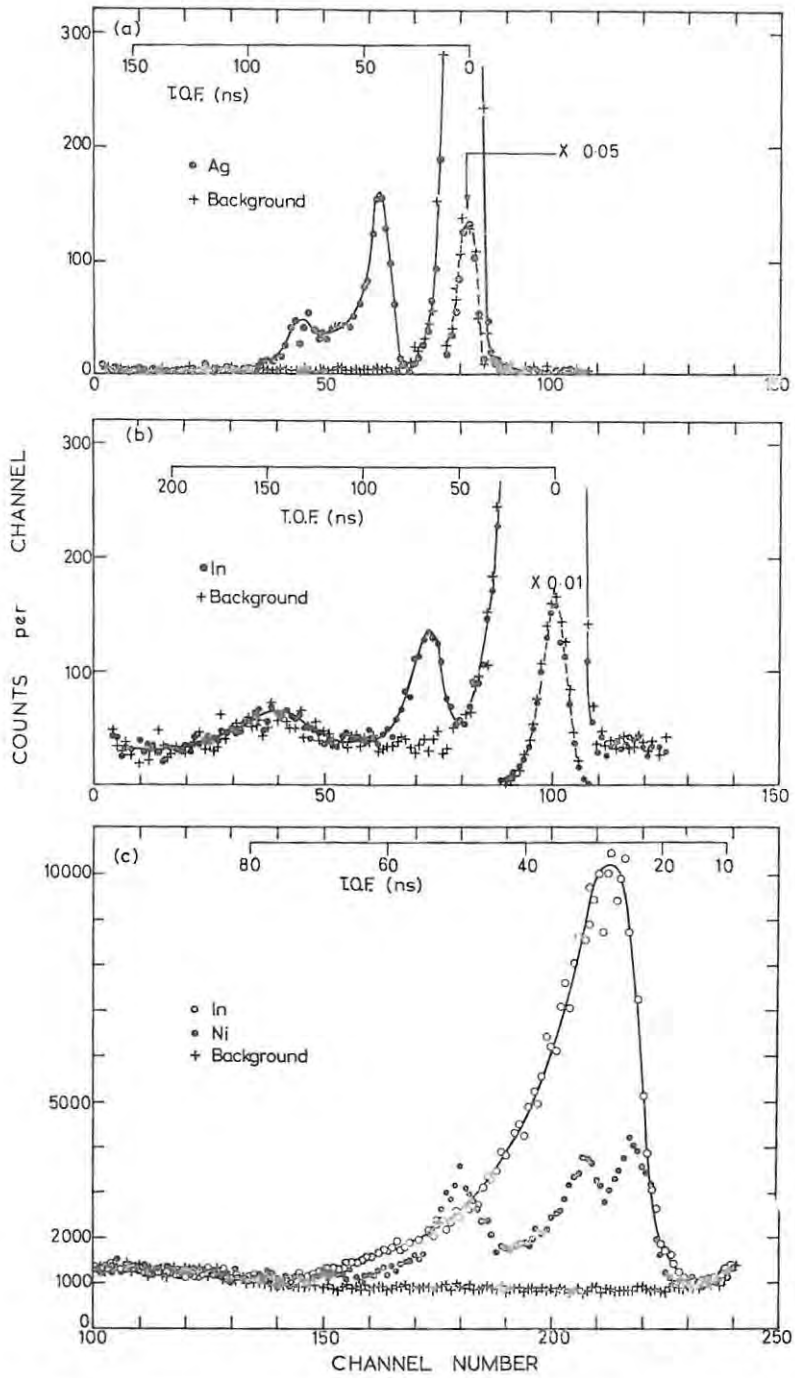

Fig. 2. Time-of-flight spectra observed (a) in geometry I using a silver sample ($n = 0.0082$ atom/b); (b) in geometry II using an indium sample ($n = 0.00789$ atom/b); and (c) in geometry III using indium (open circles) and nickel samples (closed circles) of thickness $n = 0.00553$ and 0.0268 atom/b respectively.

The crosses indicate spectra observed under the same conditions (a)–(c), respectively, but with no sample in position.

(no sample) and two runs obtained using 5.1 cm diam. samples of In and Ni, respectively. Capture yield ratios were obtained by dividing the yield for each sample (channel by channel) by the yield for indium. The energy resolution was determined mainly by the time resolution (3.6 ns FWHM) of the system and varied from about 7 % at 8 keV neutron energy to 23 % at 50 keV.

3. Reduction of cross-section ratios

The ratio $R_z(E)$ of the capture cross section of the element z to that of indium at the neutron energy E was obtained by multiplying the measured yield ratio $Y_z(E)$ by three factors as follows:

$$R_z(E) = Y_z(E)M_z\phi_z(n, E)/\phi_0(n, E). \tag{1}$$

The factors ϕ_z and ϕ_0 are introduced to correct for the effects of self-screening and multiple scattering of neutrons in the element z sample and indium sample, respectively. Each factor ϕ is a product of two other factors ϕ' and ϕ'', the correction factors for self-screening and multiple scattering, respectively. For the measurements on Nb, Ag, In, Sb and Au the self-screening factor ϕ' was calculated using the method described by Macklin [14]) and the multiple scattering factor ϕ'' was calculated using the method described by Gibbons *et al.* [1]). The factors ϕ' and ϕ'' were found to lie within 5 % of unity for all of the samples, and the final ratio ϕ_z/ϕ_0 was never found to differ from unity by more than 2 %.

These methods were not readily adaptable for calculating the multiple scattering and self-screening corrections for Cr, Mn and Ni owing to the resonance structure in the neutron cross sections of these elements in the 8 to 100 keV region. The factor ϕ_z/ϕ_0 has been assumed equal to unity in calculating the cross-section ratios for these elements.

The factor M_z is introduced into eq. (1) to account for the variation of the detection efficiency of the Moxon-Rae detector from element to element. An essential feature [11]) of this type of detector is that the probability of detecting neutron capture is proportional to the total energy of the gamma-ray cascade which follows a capture event. The neutron separation energies ε of compound nuclei formed by neutron capture are typically 7 MeV, thus for radiative capture of neutrons of energy less than 120 keV the efficiency of the detector will to a good approximation be proportional to ε.

In the present measurements elemental samples were used, with each element typically containing several isotopes. The weighted average value of ε applicable in this case is given by

$$\varepsilon = \sum_{i=1}^{m} a_i\sigma_i\varepsilon_i / \sum_{i=1}^{m} a_i\sigma_i, \tag{2}$$

where a_i, σ_i and ε_i denote the fractional abundance, the relative capture cross section and the neutron separation energy respectively of the ith isotope and m the number

of isotopes in the elemental mixture. Since the relative cross sections σ_i are generally not known, we make the approximation that they are equal and eq. (2) reduces to the following:

$$\varepsilon = \sum_{i=1}^{m} a_i \varepsilon_i . \tag{3}$$

The values ε used in this work are summarised in table 1. The values of ε_i used in the calculations were taken from the data given by Maples *et al.* [15]). The factors M_x were obtained by dividing the value of ε for indium by the value of ε for the corresponding element.

4. Results

The results of the cross-section-ratio measurements $R_x(E)$ are shown in figs. 3 and 4. The solid circles in these figures represent data obtained using either geometry I or geometry II, while the open circles represent data obtained using geometry III. In the data shown for Ni in fig. 4, the triangles also represent data obtained using geometry III. The open circles, the open triangles and the solid triangles show the results of three independent measurements using Ni samples of different thickness. The general consistency of the three sets of data suggests that the neglect of self-screening and multiple scattering corrections has probably not led to very serious errors.

Capture cross sections have been calculated by multiplying the ratio data shown in figs. 3 and 4 by assumed values for the radiative capture cross section of indium. The indium cross sections used were based on an empirical fit to the data of Gibbons *et al.* [1]); it should be noted that the latter data were normalized to the absolute measurement of Schmitt and Cook [16]) at a neutron energy of 24 keV. The fitting led to the following empirical expressions for the indium cross section as a function of energy:

(i) for 7 keV $< E <$ 18 keV

$$\sigma(E) = 1820 - 39.1\, E; \tag{4}$$

(ii) for 18 keV $< E <$ 120 keV

$$\sigma(E) = 44000/\{\sqrt{E}(1+4E^{0.25})\}, \tag{5}$$

where E is in keV and $\sigma(E)$ in mb.

The cross sections obtained are shown in figs. 5–7. The solid circles show data obtained using either geometry I or geometry II, while the open circles show data obtained using geometry III. In the case of Ni (fig. 7), the open circle cross sections were calculated from weighted mean values of the three sets of ratios at each energy (fig. 4).

The solid circles for In in fig. 5 represent the measurements for which the relative neutron flux at different energies was determined by means of the long counter.

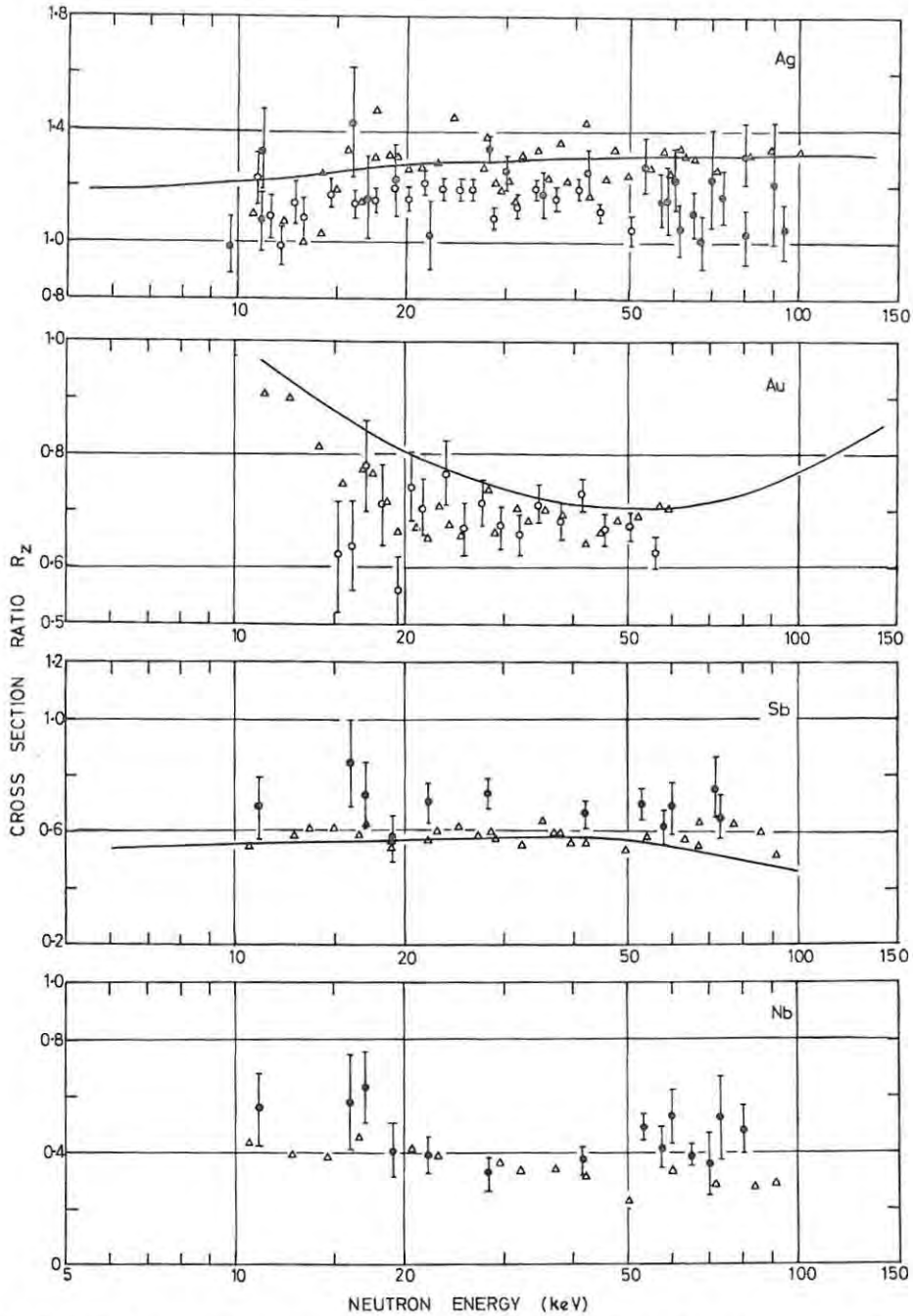

Fig. 3. Ratios R_z of capture cross sections of Ag, Au, Sb and Nb to the capture cross section of indium as a function of neutron energy: ●-geometries I and II; ○-geometry III; △-calculated from ref. [1]); solid curve calculated from ref. [7]).

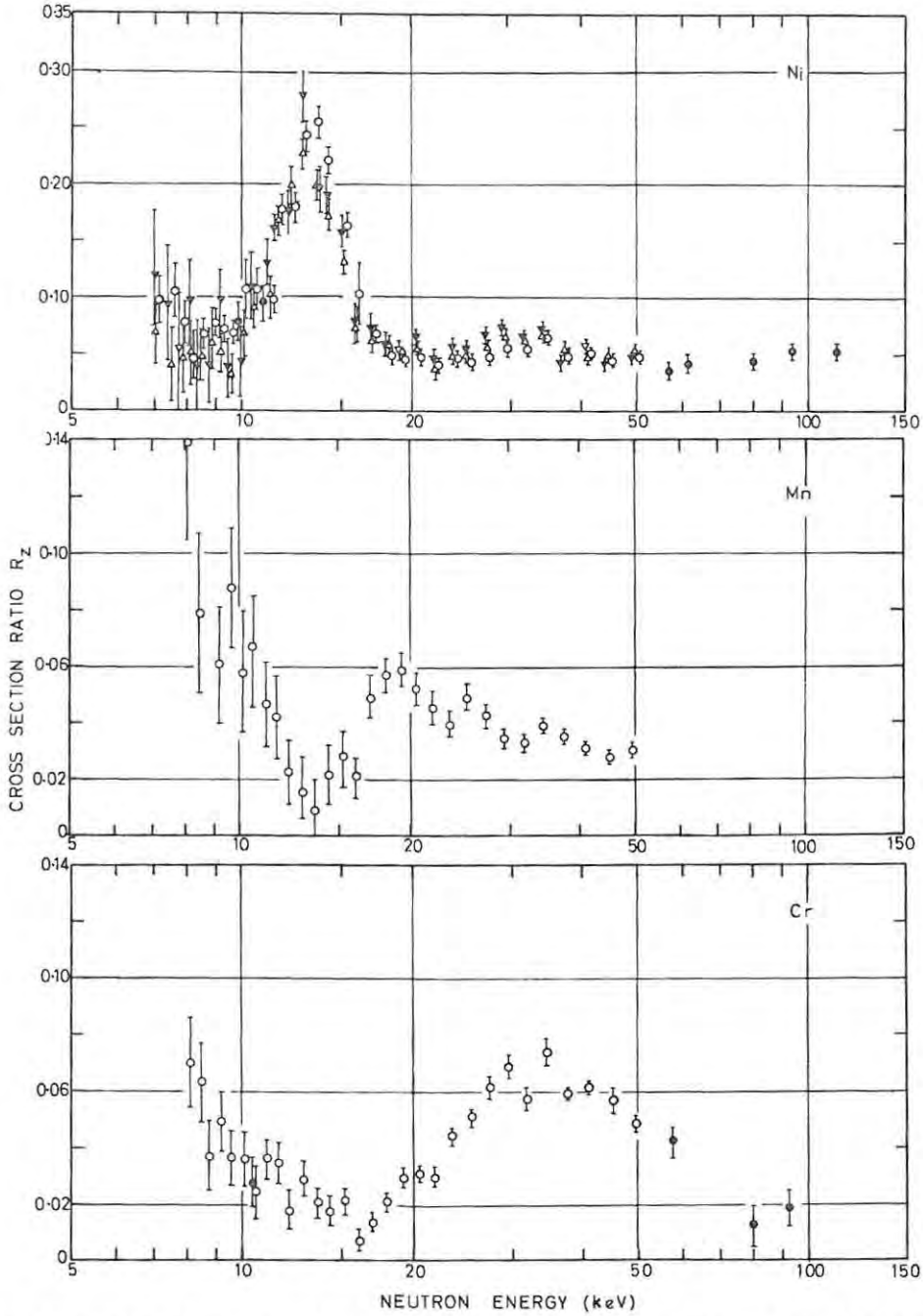

Fig. 4. Ratios R_z of capture cross sections of Ni, Mn and Cr to the capture cross section of In as a function of neutron energy: ●-geometry I; ○-geometry III. The geometry III data for Ni were obtained using samples of thickness (in atom/b) as follows: ▼-0.0067; △-0.0134 and ○-0.0268.

These measurements used geometry II, in which the long counter and capture sample received the same neutron flux from the (p, n) source [see fig. 1(b)]. The cross sections were normalized to $\sigma = 760$ mb at $E = 30$ keV, which is the indium capture cross section given by eq. (5) at this energy. The dotted line in the plot for In (fig. 5) shows the energy dependence of the empirical fit [eqs. (4) and (5)] to the In capture cross section of Gibbons *et al.* [1]).

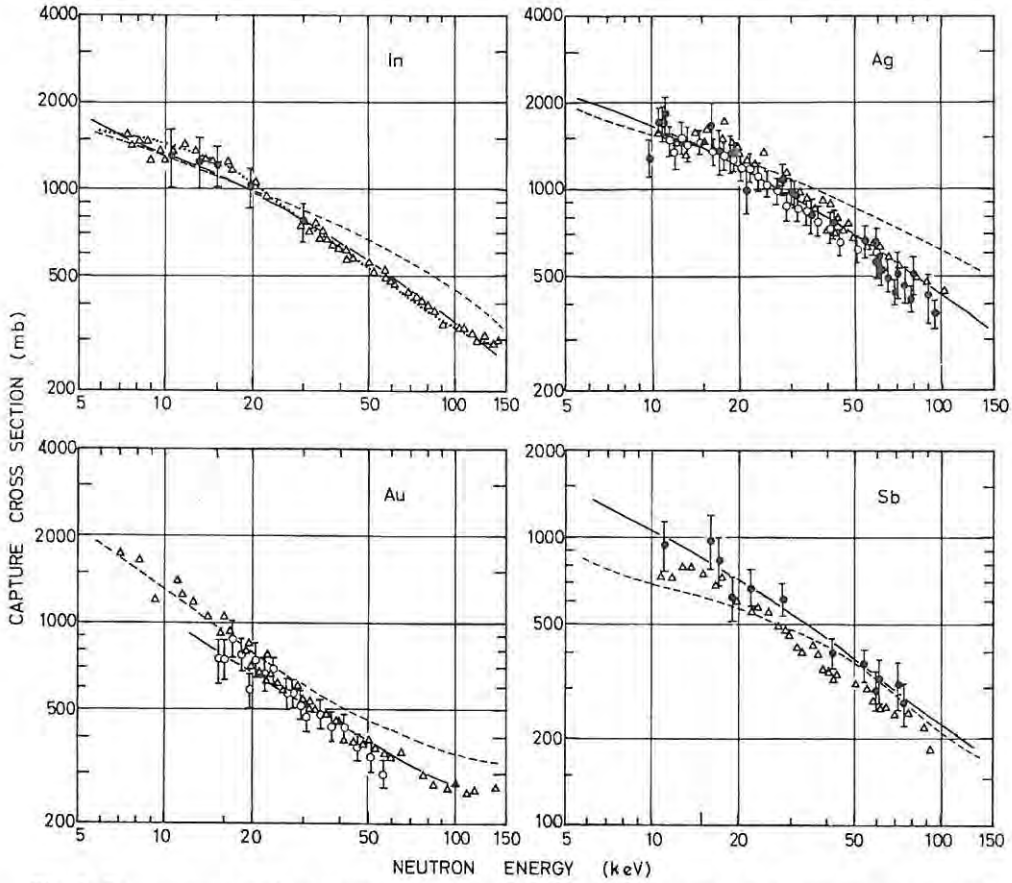

Fig. 5. Capture cross sections versus neutron energy for In, Ag, Au and Sb. ●-geometries I and II; ○-geometry III; △-ref. [1]). The solid curves show cross sections calculated using the parameters listed in table 2. The dashed curves are taken from ref. [7]), the dotted curve (for In only) shows the empirical fit [eqs. (4) and (5)] to the data of ref. [1]).

5. Analysis

5.1. THE p-WAVE STRENGTH FUNCTION S_1

The theory of neutron capture has been developed by several authors, notably Margolis [17]) Dresner [18]), Lane and Lynn [19]) and Cameron [3]). By making some approximations and assumptions, we can apply this theory to derive values for the

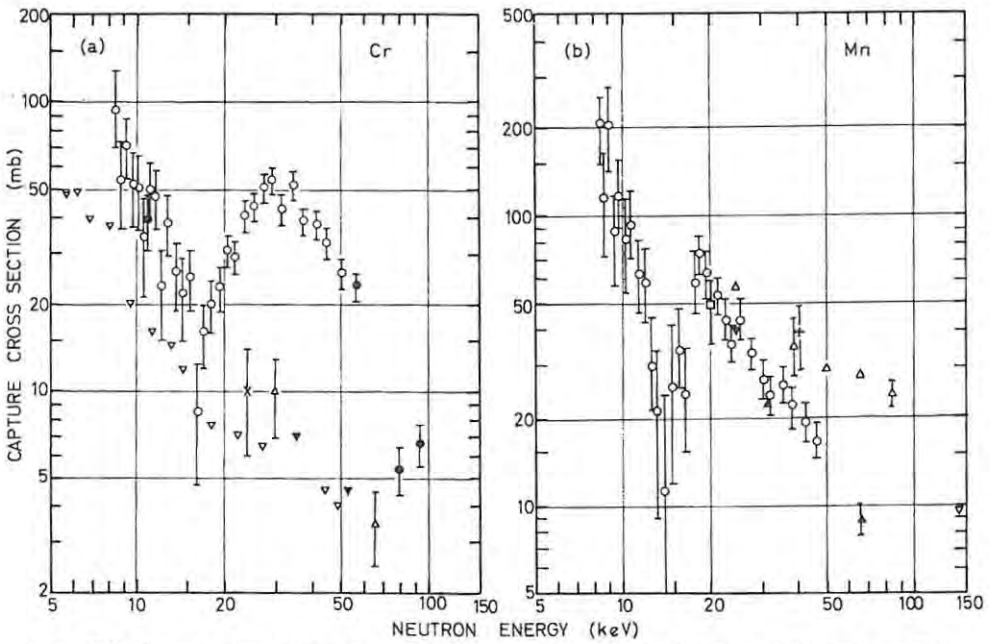

Fig. 6(a). Capture cross section versus neutron energy for Cr ●-geometry I; ○-geometry III; △-, ref. [1]); ×-ref. [25]); ▽-ref. [24]); ▼-ref. [25]). (b) Capture cross section versus neutron energy for Mn ⊙-geometry III; □-ref. [26]); ▲-ref. [27]); △-ref. [28]); ▼-ref. [29]); +-ref. [30]); ▽-ref. [31]).

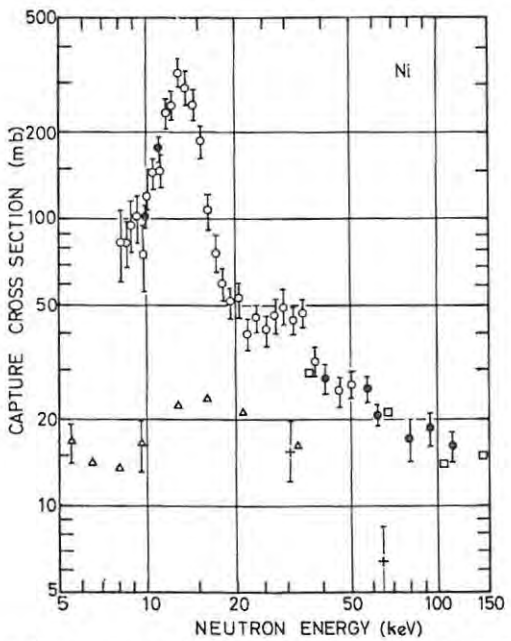

Fig. 7. Capture cross section versus neutron energy for Ni ●-geometry I; ⊙-geometry III; △-ref. [32]); □-ref. [33]); +-ref. [1]).

p-wave strength function from capture cross sections. The method is similar to that used by Gibbons *et al.* [1]).

The average capture cross section $\langle\sigma\rangle$ for a given neutron energy may be expressed as the sum of average partial cross sections for different incident neutron partial waves l. For each l-value, the partial cross section is summed over the allowed values of compound nucleus total angular momentum J

$$\langle\sigma\rangle = \sum_l \sum_J \langle\sigma(Jl)\rangle. \tag{6}$$

The neutron strength function $S_l(J)$ for compound states of angular momentum J formed by capture of neutrons of energy E and orbital angular momentum l is defined as follows:

$$S_l(J) = \langle\Gamma_n^l(J)\rangle/\langle D(J)\rangle, \tag{7}$$

where

$$\Gamma_n^l(J) = \Gamma_n(Jl)/p_l\sqrt{E}, \tag{8}$$

and $\langle D(J)\rangle$ denotes the average spacing for these states, while for individual states $\Gamma_n(Jl)$ denotes the neutron width and p_l the neutron penetrability. For s-wave neutrons p_0 is unity, while for p-wave neutrons

$$p_1 = x^2/(1+x^2),$$

where $x = kR$ and k and R denote the neutron wave number and the nuclear radius, respectively.

We now assume (i) that the neutron strength function S_l is the same for all allowed values of J; (ii) that $\langle D(J)\rangle = \langle D\rangle/g(J)$, where $\langle D\rangle$ is the observed spacing for all values of J and $g(J)$ the statistical weight for levels of angular momentum J; and (iii) that inelastic neutron scattering, where present may be neglected and hence that the average total width may be expressed as:

$$\langle\Gamma(Jl)\rangle = \xi(IJl)\langle\Gamma_n(Jl)\rangle + \langle\Gamma_\gamma(Jl)\rangle, \tag{9}$$

where $\xi(IJl)$ is the number of contributing channel spins for a target nucleus spin I and a given combination of J and l and $\langle\Gamma_\gamma(Jl)\rangle$ the average radiation width for levels of given J and l.

The average partial cross sections for s- and p-wave capture at neutron energy E are then reduced to

$$\langle\sigma(0)\rangle = \frac{2\pi^2}{k^2} S_0\sqrt{E} \sum_J \frac{g(J)\langle\Gamma_\gamma(Jl)\rangle F(\alpha J)}{\langle\Gamma_\gamma(Jl)\rangle + \{S_0\langle D\rangle\sqrt{E}/g(J)\}}, \tag{10}$$

$$\langle\sigma(1)\rangle = \frac{2\pi^2}{k^2} S_1 p_1\sqrt{E} \sum_J \frac{g(J)\langle\Gamma_\gamma(Jl)\rangle F(\alpha J)}{\langle\Gamma_\gamma(Jl)\rangle + \{\xi(IJl)S_1 p_1\langle D\rangle\sqrt{E}/g(J)\}}, \tag{11}$$

where $F(\alpha J)$ denotes the correction factor [3,19]) required when the ratio of averages is used in place of an average of ratios.

For neutron energies less than 30 keV, the penetrabilities p_l for partial waves of order $l > 1$ are very much smaller than the penetrabilities p_0 and p_1. We therefore neglect these higher-order components and assume that the observed average cross section may be regarded as a sum of s- and p-wave components given by eqs. (10) and (11), respectively. The p-wave strength function S_1 can then be determined from this analysis if the s-wave strength function S_0, the level spacing $\langle D \rangle$ and the average radiation widths $\langle \Gamma_\gamma(Jl) \rangle$ are known.

Values of S_l were determined for Nb, Ag, In, Sb and Au by fitting a sum of s- and p-wave components to the present measurements of the respective capture cross sections in the 8 to 30 keV region. The fitting was carried out by computer using a method of least-squares. The values S_0, $\langle D \rangle$ and $\langle \Gamma_\gamma(Jl) \rangle$ used in the analysis are listed in table 2. In all cases it was assumed that $\langle \Gamma_\gamma \rangle$ was the same for all values of J. For Nb, different values of $\Gamma_\gamma(Jl)$ were assumed for $l = 0$ and $l = 1$, respectively, in accordance with the results reported in ref. [21]). For the remaining elements, the radiation width for p-waves was assumed to be the same as that for s-waves. The values of S_1 obtained from the analysis are given in table 2. The solid curves in fig. 5 show the fitted cross sections calculated using the parameters summarised in table 2.

TABLE 2
Strength functions

Element	$\langle \Gamma_\gamma \rangle$ [a]) (eV)	$\langle D \rangle$ [a]) (eV)	S_0 [a]) ($\times 10^4$)	S_1 ($\times 10^4$)
Nb	0.150 ($l = 0$) 0.230 ($l = 1$)	73.5 ($l = 0$) 65 ($l = 1$)	0.35	3.3 ±1.8
Ag	0.137	23	0.85	5.6 ±2.3
In	0.079	8.7	0.6	3.9 ±1.5
Sb	0.115	24	1.0	3.7 ±1.5
Au	0.115	17	1.5	0.69±0.40

[a]) Based on data given in refs. [9, 20, 21, 22]).

5.2. RADIATION WIDTHS Γ_γ

The capture cross sections of Cr, Mn and Ni (figs. 6 and 7) show maxima and minima which can be attributed to partially resolved resonances. This structure indicates regions where the cross sections are dominated by a few levels and makes it possible to determine average radiation widths.

The capture cross section may be written as the sum of capture cross sections σ_i for the m members of the elemental mixture

$$\sigma = \sum_{i=1}^{m} a_i \sigma_i , \tag{12}$$

where a_i denotes the fractional abundance of the ith isotope. We assume that each cross section σ_i may be described as a sum of isolated Breit-Wigner single level

resonance components, that $\Gamma_n \approx \Gamma$ for all resonances, and that Γ_γ does not vary much from resonance to resonance. The integral of the cross section under the jth resonance of the ith isotope is then given by

$$\int_{-\infty}^{\infty} \sigma_{ij} \mathrm{d}E = 2\pi^2 \lambda\!\!\!^{-2}_{ij} g_{ij} \langle \Gamma_\gamma \rangle, \tag{13}$$

where $\lambda\!\!\!^{-}_{ij}$ is the reduced neutron wavelength corresponding to the resonance energy and g_{ij} the statistical weight.

The integral of the capture cross section over an energy range E_1 to E_2 may now be expressed as a sum $\alpha+\beta$, where β represents the contributions from distant levels, and α is obtained by combining eqs. (12) and (13):

$$\alpha = \int_{E_1}^{E_2} \sigma \mathrm{d}E = 2\pi^2 \langle \Gamma_\gamma \rangle \sum_{i=1}^{m} a_i \sum_{j=1}^{r_i} g_{ij} \lambda\!\!\!^{-2}_{ij}, \tag{14}$$

where r_i is the number of resonances involving the ith isotope in the energy range E_1 to E_2.

We now approximate the wavelength $\lambda\!\!\!^{-}_{ij}$ by a constant effective wavelength $\lambda\!\!\!^{-}$ corresponding to an energy $\langle E \rangle$, which is the mean of E_1 and E_2. We also assume an effective average $\langle g_i \rangle$ for each isotope and express r_i in terms of the average level spacing $\langle D_i \rangle$ as

$$r_i = (E_2 - E_1)/\langle D_i \rangle. \tag{15}$$

Then from eqs. (14) and (15)

$$\langle \Gamma_\gamma \rangle \approx \frac{\langle E \rangle \alpha}{2\pi^2 \lambda\!\!\!^{-2} (E_2 - E_1) \sum_{i=1}^{m} \{a_i \langle g_i \rangle / \langle D_i \rangle\}}, \tag{16}$$

Eq. (16) has been used to calculate values of $\langle \Gamma_\gamma \rangle$ for Cr, Mn and Ni. The choice of the limits E_1 and E_2 was determined in each case by the structure of the capture cross section (figs. 6 and 7). The contribution β of distant levels to the cross section in the region E_1 to E_2 was estimated by inspection, and an important criterion in the choice of E_1 and E_2 was that β should be as small a fraction as possible of the total integrated cross section $(\alpha+\beta)$. The parameters used in calculating $\langle \Gamma_\gamma \rangle$ are shown in table 3 with the results of the calculations.

6. Discussion

The cross-section ratios shown in figs. 3 and 4 are the basic results of the present experiments, hence it is useful to compare them with independent measurements. Although other authors do not present their data as cross-section ratios to indium, such ratios may readily be calculated from the cross-sections reported by Gibbons *et al.* [1]) and by Pönitz [7]). Thus the cross-section data reported by Gibbons *et al.* [1]) for Ag, Au Sb and Nb have been divided by the empirical fit [eqs. (4) and (5)] to

the indium cross sections reported by these authors, and the resulting ratios are shown as triangles in fig. 3. The solid curves in fig. 3 indicate ratios calculated from the average cross sections reported by Pönitz [7]; these data are averages of many independent sets of data (including those of Gibbons *et al.* [1]) at (approximately) the same energy.

TABLE 3
Radiation widths

Z	Element	E_1 (keV)	E_2 (keV)	Isotope [a]) A	$\langle D \rangle$ (keV)	$\langle \Gamma_\gamma \rangle$ (eV)
24	Cr	16	80	52	10.4 [b])	2.3 ±1.0
				53	2.8 [c])	
25	Mn	14	50	55	2.9 [d])	0.67±0.25
28	Ni	8	20	58	1.1 [e])	0.29±0.13
				60	0.7 [e])	
		20	50	58	3.9 [e])	0.34±0.14
				60	3.5 [e])	

[a]) The less abundant isotopes of Cr and Ni have been omitted from the calculations. The effect on the results is insignificant.
[b]) Based on data in range $E < 600$ keV from refs. [20,34]).
[c]) Based on data in range $E < 30$ keV from refs. [20,35]).
[d]) Based on data in range $E < 100$ keV from ref. [36]).
[e]) Based on data in range E_1 to E_2 from ref. [37]).

Comparison (see fig. 3) shows that the present cross-section ratios for Ag and Au are about 10 % lower than the ratios derived from the data of Pönitz. The present ratios for Sb on the other hand are about 10 % higher than the Pönitz values. The data for Au agree satisfactorily with the ratios obtained from the data of Gibbons *et al.* Allowing for standard deviations of about 10 % on the ratios obtained by both Pönitz and Gibbons *et al.*, we conclude that the three sets of data for the elements Ag, Au, Sb and Nb are consistent. There are no data available for similar comparisons for Ni, Mn and Cr shown in fig. 4.

The present cross sections for Ag, Au and Sb (fig. 5) were obtained by multiplying the corresponding cross-section ratios shown in fig. 3 by a smooth function [eqs. (4) and (5)] fitted to the indium cross-sections obtained by Gibbons *et al.* [1]) (triangles in fig. 5). Therefore, as can be seen in fig. 5 the present cross sections agree with those reported by Gibbons *et al.* where the cross-section ratios agree and vice versa. The discrepancies between these two sets of cross sections on the one hand and the average cross sections obtained by Pönitz on the other hand, contrast with the general agreement between the three sets of ratios shown in fig. 3. Since the various ratios and cross sections shown in figs. 3 and 5 were obtained using a variety of methods and techniques for the capture yield measurement, the cross-section discrepancies must originate from systematic errors in other phases of the experiments, e.g., normalization or the relative measurements of incident neutron intensity.

Bogart † for example has drawn attention to the fact that inconsistencies arise between relative neutron flux measurements based on the $^{6}Li(n, \alpha)^{3}H$ and $^{10}B(n, \alpha\gamma)^{7}Li$ reactions, respectively, and that these inconsistencies can lead to significant discrepancies when a comparison is made between capture cross-section measurements which are referred to the different reactions.

Some independent capture cross-section measurements [1,23-33]) for Cr, Mn and Ni are compared with the present data for these elements in figs. 6 and 7. The present data for Cr and Ni are systematically higher than most other measurements. In the case of Ni, the present data are in good agreement with the data of Staviskii and Shapar [33]) in the energy region 30 keV to 120 keV. The present data for Ni are also in agreement with the capture cross sections predicted by Schmidt [38]) on the basis of thermal capture cross-section values and resonance capture integral data. The maximum at $E \approx 15$ keV in the present data for Ni is consistent with the high-resolution capture-yield measurements reported by Block *et al.* [37]), provided allowance is made for the much poorer energy resolution of the present measurements.

The p-wave strength functions obtained for Nb, Ag, In and Sb (table 2) lie in the range 3×10^{-4} to 6×10^{-4} and agree with several recent measurements for different nucleides in the mass number range 90 to 120. The results are also consistent with the values predicted by Buck and Perey [4]) for the 3P size-resonance of S_1 in the $A \approx 100$ region. On the other hand, the analysis used to derive S_1 is subject to some basic limitations. It depends on the use of assumed values for parameters such as S_0, $\langle \Gamma_\gamma \rangle$ and $\langle D \rangle$. The results are sensitive to uncertainties in these parameters, in normalization of the cross-sections (in the case of In), and in the In cross sections reported by Gibbons *et al.* [1]) (in the cases of Ag, Au and Sb). The analysis is particularly sensitive to the ratio $\langle \Gamma_\gamma \rangle / \langle D \rangle$ and also therefore (except in the case of Nb) to the assumption that this ratio has the same value for s- and p-wave resonances. The precision of S_1 is low ($\approx 50\,\%$ standard deviations) because of these uncertainties. However, the results indicate a lower limit of $S_1 \gtrapprox 2 \times 10^{-4}$ for the nucleides Nb, Ag, In and Sb.

The radiation widths $\langle \Gamma_\gamma \rangle$ obtained for Cr, Mn and Ni (table 3) follow a trend previously noted [3]) in this mass region showing $\langle \Gamma_\gamma \rangle$ decreasing with increasing atomic number. Similar values of $\langle \Gamma_\gamma \rangle$ are obtained for Ni when the data are analysed in the 8 to 20 keV and 20 to 50 keV regions. From the capture measurements of Block *et al.* [37]) and the total cross-section data of Garg *et al.* [39]) it appears that p-wave resonances contribute most of the capture cross section of Ni in the 20 to 50 keV region, whereas the s-wave resonances at 12.7 keV and 15 keV contribute a significant fraction of the capture cross section in the 8 to 20 keV region. Therefore the average radiation widths for these s- and p-wave resonances in Ni are probably not very different from one another.

The radiation width observed for Cr is considerably higher than that observed for the neighbouring elements Mn and Ni (table 3) and is also significantly higher than

† See discussion in ref. [7]).

might be expected from the theoretical predictions of Cameron [3]). The result is nevertheless consistent with the value $\langle \Gamma_\gamma \rangle = 2.9 \pm 0.9$ eV reported by Coté *et al.* [40]) for Cr. Despite this agreement, the present value of $\langle \Gamma_\gamma \rangle$ would be high if the average level spacing of 10.4 keV assumed (table 3) for the most abundant isotope of Cr, namely ^{52}Cr, is an overestimate. This is a real possibility since the level spacings assumed for Cr are based on Van de Graaff measurements [34, 35]) taken with energy resolution of about 1 keV, whereas the spacings assumed for both Mn and Ni are based on higher-resolution measurements [36, 37]) using electron linacs. In view of this possibility, it would be interesting to study the capture cross section of Cr with the high resolution which Block *et al.* have used for Ni. The capture measurements of Block *et al.* showed about three times as many levels as had previously been noted in total cross-section measurements on Ni. A similar increase in the number of Cr levels would bring about a proportionate decrease in the present value of $\langle \Gamma_\gamma \rangle$, which would thus be consistent with expectations based on theory [3]) and $\langle \Gamma_\gamma \rangle$ values observed for neighbouring nucleides.

We are indebted to the technical and operating staffs of the Van de Graaff accelerators at the A.E.B. laboratories, Pelindaba, and the Southern Universities Nuclear Institute, Faure for their assistance in carrying out these experiments. We also express our thanks to the South African Council for Scientific and Industrial Research for the support which they have granted to this project and for a bursary to one of us (LMS). The support and hospitality granted to two of us (LMS and FDB) by the South African Atomic Energy Board is also gratefully acknowledged.

References

1) J. H. Gibbons, R. L. Macklin, P. D. Miller and J. H. Neiler, Phys. Rev. **122** (1961) 182
2) N. Starfelt, in Nuclear structure study with neutrons (North-Holland Publ. Co., Amsterdam, 1966) p. 318
3) A. G. W. Cameron, N. H. Lazar and H. W. Schmitt, in Fast neutron physics, Part II, ed. by J. B. Marion and J. L. Fowler (Interscience, New York, 1963) p. 1699
4) B. Buck and F. Perey, Phys. Rev. Lett. **8** (1962) 444
5) R. L. Macklin and J. H. Gibbons, Revs. Mod. Phys. **37** (1965) 166
6) J. H. Gibbons, in Progress in fast neutron physics (University of Chicago Press, 1963) p. 193
7) W. P. Pönitz, in Nuclear data for reactors, Vol. I (IAEA, Vienna, 1967) p. 277
8) H. W. Newson, in Nuclear structure study with neutrons (North-Holland Publ. Co., Amsterdam, 1966) p. 195
9) C. A. Uttley, C. M. Newstead and K. M. Diment, in Nuclear data for reactors (IAEA, Vienna, 1967) p. 165
10) A. O. Hanson and J. L. McKibben, Phys. Rev. **72** (1947) 673
11) M. C. Moxon and E. R. Rae, Nucl. Instr. **24** (1963) 445
12) R. L. Macklin, J. H. Gibbons and T. Inada, Nucl. Phys. **43** (1963) 353
13) F. Everling, L. A. Koenig, J. H. E. Mattauch and A. H. Wapstra, Nuclear Data Tables Part I (U.S.A.E.C., 1961)
14) R. L. Macklin, Nucl. Instr. **26** (1964) 213
15) C. Maples, G. W. Goth and J. Cerny, Nucl. Data **2** (1966) 429
16) H. W. Schmitt and C. W. Cook, Nucl. Phys. **20** (1960) 202

17) B. Margolis, Phys. Rev. **88** (1952) 327
18) L. Dresner, Nucl. Sci. Eng. **1** (1956) 103
19) A. L. Lane and J. E. Lynn, Proc. Phys. Soc. **70A** (1957) 557
20) M. D. Goldberg, S. F. Mughabghab, S. N. Purohit, B. A. Magurno and V. M. May, BNL-325, Vol. IIB, Suppl. No. 2 (1966)
21) G. Le Poittevin, S. de Barros, V. D. Huynh, J. Julien, J. Morgenstern and C. Samour, in Nuclear structure study with neutrons (North-Holland Publ. Co., Amsterdam, 1966) p. 530
22) J. B. Garg, J. Rainwater and W. W. Havens, Phys. Rev. **137** (1965) B547
23) T. S. Belanova, A. A. Van'kov, F. F. Mikhailus and Yu. Ya. Stavisskii, Atom. Energ. **19** (1965) 3
24) S. P. Kapchigashev and Yu. P. Popov, Atomn. Energ. **16** (1964) 256
25) Yu. Ya Stavisskii and A. V. Shapar, Atomn. Energ. **12** (1962) 514
26) R. Booth, W. P. Ball and M. H. MacGregor, Phys. Rev. **112** (1958) 226
27) R. L. Macklin, J. H. Gibbons and T. Inada, Phys. Rev. **129** (1963) 2695
28) Yu. Ya. Stavisskii and V. A. Tolstikov, Atomn. Energ. **10** (1961) 508
29) R. L. Macklin, N. H. Lazar and W. S. Lyon, Phys. Rev. **107** (1957) 504
30) N. A. Bostrom, I. L. Morgan, J. T. Prud-homme, P. L. Okhuysen and O. M. Hudson, Texas, Nuclear Report WADC-TN-59-107 (1959)
31) A. E. Johnsrud, M. G. Silbert and H. H. Barschall, Phys. Rev. **116** (1959) 927
32) S. V. Kapchigashev and Yu. P. Popov, Atomn. Energ. **15** (1963) 120
33) Yu. Ya. Stavisskii and A. V. Shapar, Atomn. Energ. **10** (1961) 264
34) C. D. Bowman, E. G. Bilpuch and H. W. Newson, Ann. of Phys. **17** (1962) 319
35) R. Wagner, W. M. Good and D. Paya, in Nuclear structure with neutrons (North-Holland Publ. Co., Amsterdam, 1966) p. 536
36) J. Morgenstern, S. de Barros, G. Bianchi, C. Corge, V. D. Huynh, J. Julien, G. Le Poittevin, E. Netter and C. Samour, *ibid*, p. 531
37) R. C. Block, R. W. Hockenbury, Z. Bartolome and R. R. Fullwood, in Nuclear data for reactors, Vol. 1 (IEAA, Vienna, 1967) p. 565
38) J. J. Schmidt, Kernforschungszentrum Karlsruhe Report KFK-120 (EANDC-E-35 U) (1962)
39) J. B. Garg, J. Rainwater and W. W. Havens, Columbia University Report CR-1860 (1964)
40) R. E. Cote, L. M. Bollinger and J. M. Le Blanc, Phys. Rev. **111** (1958) 288

L.M. Spitz, E. Barnard and F.D. Brooks
Neutron capture cross sections of Cr, Mn, Ni, Nb, Ag, In, Sb and Au in the 8 to 120 keV region
Nucl. Phys. A121 (1968) 655-672

Reprinted from:

NUCLEAR PHYSICS, VOLUME A125 (1969) No. 2

C. A. R. BAIN and F. D. BROOKS

Department of Physics, University of Cape Town

INELASTIC SCATTERING OF NEUTRONS TO THE 59 keV LEVEL OF ^{127}I

NORTH-HOLLAND PUBLISHING COMPANY - AMSTERDAM

2.L: 3.A *Nuclear Physics* **A125** (1969) 312—320;

INELASTIC SCATTERING OF NEUTRONS TO THE 59 keV LEVEL OF ^{127}I

C. A. R. BAIN † and F. D. BROOKS
Department of Physics, University of Cape Town

Received 12 November 1968

Abstract: The excitation of the 59 keV level of ^{127}I by neutron inelastic scattering was studied using a small NaI scintillation crystal as both target and detector. Measurements were carried out in the incident neutron energy range 50–500 keV, and the neutron flux incident on the crystal was monitored with a ^{6}Li loaded glass scintillator. The cross sections obtained are compared with those calculated from Hauser-Feshbach theory.

E NUCLEAR REACTIONS ^{127}I(n, n′γ), E = 50–500 keV; measured $\sigma_{nn'}(E)$.

1. Introduction

The statistical theory of Hauser and Feshbach [1]) has been widely used [2]) to interpret experimental measurements of neutron inelastic scattering. Subsequent developments in the theory of nuclear reactions [3]) have emphasized the effects of compound nucleus level structure on average reaction cross sections. In particular, for the case of inelastic neutron scattering it has been shown [2,4,5]) that when the distribution of level widths in the compound nucleus is taken into consideration, the reaction cross section may be reduced by up to about 50 %. This reduction in the cross section is greatest at neutron energies close to the inelastic threshold and much smaller, in general, at higher energies.

The study of inelastic neutron scattering at neutron energies close to the threshold is therefore of particular interest. Measurements based on conventional techniques may be hampered in this region by the low reaction yield and the low energy of the inelastically scattered neutrons. In the study of inelastic scattering to the 59 keV level of ^{127}I, however, the use [6,7]) of a small NaI crystal as both target and detector minimizes the first of these difficulties and avoids the second difficulty. With this arrangement, it is possible to detect the de-excitation radiations (59 keV gamma rays or internal conversion electrons plus X-rays) resulting from inelastic scattering in the crystal with high efficiency. In this paper, we report measurements using this technique for neutrons in the energy range 50 to 500 keV.

† Present address: A.E.B. Isotope Unit, Southern Universities Nuclear Institute, Faure, C.P.

2. Experimental method

A schematic diagram of the experimental arrangement used for the measurements is shown in fig. 1. The neutron source was the $^{7}Li(p, n)^{7}Be$ reaction produced by protons from the 5.5 MV pulsed Van de Graaff accelerator of the Southern Universities Nuclear Institute, Faure, Cape Province. Thin Li metal targets were used to obtain neutrons of well-defined energy; the neutron energy was calculated from the proton energy assuming a Q-value of -1.6433 MeV for the $^{7}Li(p, n)^{7}Be$ reaction [8]). The NaI crystal used in the experiment was 3.8 cm diam. and 0.16 cm thick.

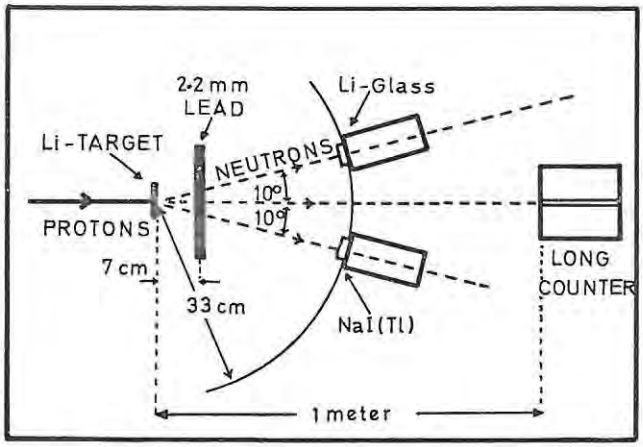

Fig. 1. Schematic diagram of the experimental arrangement.

The neutron flux incident on the NaI crystal was monitored by a ^{6}Li loaded glass scintillator [9]). The two scintillators were mounted on EMI-6097B photomultiplier tubes, which were placed symmetrically about the 0° (proton beam) direction (fig. 1) so as to receive the same mean incident neutron energy and flux from the (p, n) source. The pulsed-beam time-of-flight technique was used to discriminate against background, particularly gamma rays originating in the Li target. A 2.2 mm thick lead sheet was placed between the target and the scintillators in order to shield the scintillators from an intense flux of low-energy gamma rays, which originated from the target. A long counter [10]) placed at 0° at 1 m from the ^{7}Li target was used as an auxiliary neutron monitor.

A standard "fast-slow" electronic system was used to obtain time-of-flight spectra from the two detectors. The fast outputs from the two photomultipliers were coupled and fed to the start input of a common time-to-pulse-amplitude converter. The slow outputs from the photomultipliers were fed to separate single-channel pulse-height analysers; the outputs of these analysers were used to coincidence-gate the multi-channel analyser, which recorded the time spectra. The two pulse-height windows also operated the routing control of the multi-channel analyser so that

the two time spectra were recorded simultaneously in different segments of the analyser memory. This arrangement ensured that the counting losses (due to analyser deadtime) were exactly the same for the two spectra, so that no deadtime correction was necessary when a ratio of count rates was determined from the two spectra.

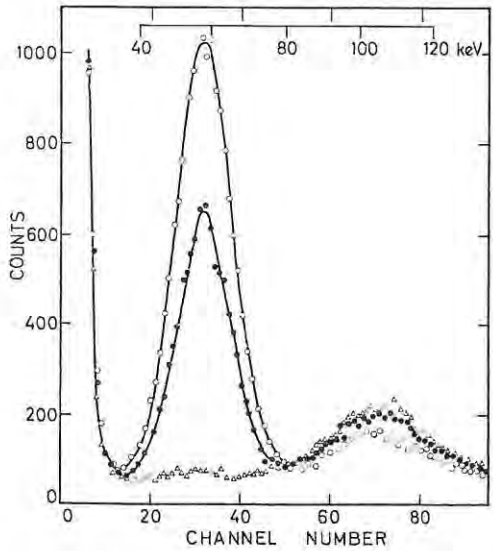

Fig. 2. Pulse-height spectra obtained from the NaI crystal using different neutron energies; △-45 keV, ●-75 keV, o-90 keV. The peaks centred at the 59 keV pulse-height are attributed to decay of the 59 keV level of ^{127}I after neutron inelastic scattering. The pulse-height scale is calibrated in terms of the 61 keV γ-ray emitted by ^{241}Am.

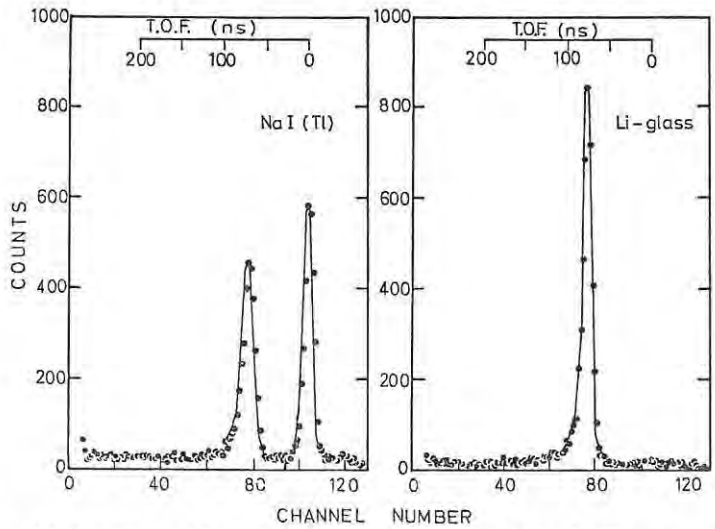

Fig. 3. Time-of-flight spectra obtained using neutrons of energy 110 keV. The spectra were obtained simultaneously from the NaI and the Li glass detectors, respectively.

A preliminary investigation was carried out of the pulse-height spectra obtained from the NaI crystal for different incident neutron energies of 40–90 keV. The results (see fig. 2) demonstrated that a peak centred at a pulse-height corresponding to an electron energy of 59 keV appeared when the incident neutron energy exceeded this value. Thus for the time-of-flight measurements, the single-channel analyser as scciated with the NaI crystal was set to select pulse amplitudes corresponding to the electron energy range 59 ± 15 keV. Assuming an internal conversion coefficient [11]) of 1.95, we estimate the efficiency ε for detecting depopulation of the 59 keV level of ^{127}I as 0.97 ± 0.02.

The experiment was divided into two measurements. In one set, a small Li glass I (diam. 2.9 cm and thickness 0.25 cm) was used and in the other set a larger glass II (diam. 3.8 cm and thickness 1.27 cm) was used. The glasses were type NE-905 (supplied by Nuclear Enterprises Ltd., Edinburgh) with a nominal ^{6}Li content of 7.0 % (by weight). In each set of measurements, the single-channel analyser associated with the Li loaded glass detector was set so as to select pulses corresponding to ^{6}Li(n, α)^{3}H reactions in the scintillator [9]). The efficiency of the glass for detecting such reactions is essentially unity.

The time-of-flight measurements were carried out using a 33 cm flight path. The time resolution obtained was about 10 ns (FWHM) for both detectors. Two typical time-of-flight spectra for a mean neutron energy of 110 keV are shown in fig. 3. In each time spectrum, the peak in the region of channel 76 is attributed to neutron interactions in the corresponding scintillator, i.e. (n, n′γ) in the NaI crystal and (n, α) in the Li glass, respectively. Similar pairs of spectra were obtained at a series of neutron energies; at each energy, the areas of the neutron peaks in the two spectra and the ratio R of these areas (NaI: Li) were measured.

Since the geometry was chosen so as to equalize the neutron fluxes incident on the two detectors, in first approximation for each detector the count rate in the neutron peak is proportional to three factors. These are

(i) the solid angle Ω subtended by the scintillator at the neutron source,

(ii) the thickness n of the scintillator expressed in nuclei (of ^{127}I or ^{6}Li, respectively) per cm^2 and

(iii) the cross section σ for the appropriate reaction.

We now introduce a factor ϕ to take account of the combined effects of self-screening and multiple scattering of the incident neutrons in the scintillator. For a given neutron energy

$$\sigma_1 = (\Omega_2 n_2 \phi_2 / \Omega_1 n_1 \phi_1)(R/\varepsilon)\sigma_2, \tag{1}$$

where the subscripts 1 and 2 denote the NaI crystal and the Li glass, respectively. The cross section σ_1 for population of the 59 keV level is thus obtained from the known cross section σ_2 for the ^{6}Li(n, α) reaction [12]), the observed count rate ratio R and direct calculations of Ω_1, Ω_2, n_1, n_2, ϕ_1, ϕ_2 and ε.

The factors ϕ_1 and ϕ_2 were calculated using cross-section data obtained from ref.[12]). The values obtained for ϕ_1 were in the range 1.03–1.05, while the values obtained for ϕ_2 ranged from 1.10 to 1.20 for glass I and 1.22 to 1.56 for glass II. A correction was also applied for the contribution of neutron radiative capture events to the neutron peak recorded by the NaI detector. This correction amounted to about 25 % for 70 keV neutrons, 10 % for 90 keV neutrons and less than 5 % for neutrons of energy exceeding 120 keV.

3. Results and calculations

The results of the cross-section measurements for the 59 keV level are shown in fig. 4. The open circles denote the measurements using the thin Li glass (glass I)

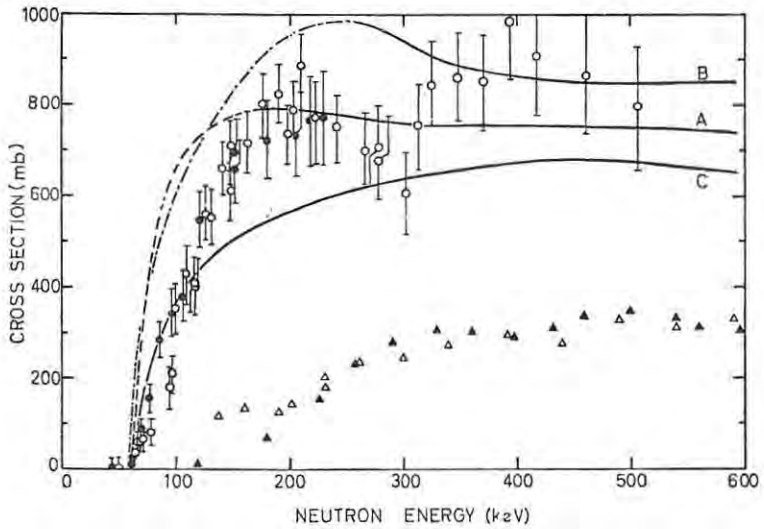

Fig. 4. Cross section for population of the 59 keV level of ^{127}I by neutron inelastic scattering; ○-present data (based on glass I), ●-present data (based on glass II), △-ref. [6]), ▲-ref. [7]). Curves A and B show the cross sections calculated from the Hauser-Feshbach theory using transmission coefficients based on the potentials of Bjorklund and Fernbach [17]) and Perey and Buck [20]), respectively. The dashed sections of these curves indicate energy regions in which the calculations are based on extrapolated values for the neutron transmission coefficients. Curve C shows results of the calculation reported by Sharma and Nath [21]).

and the solid circles the data obtained using glass II. The two sets of data are consistent. The open and closed triangles in fig. 4 show the results of the earlier measurements reported by van Loef and Lind [6]) and by Guernsey and Wattenberg [7]), respectively. The present results are in marked disagreement with these data.

The nucleus ^{127}I has excited states at 59, 203, 375 and 417 keV, respectively; as far as we know, there are no additional excited states below 417 keV [ref. [13])]. The cross sections observed for the 59 keV level (fig. 4) in the energy range 59–203 keV

will therefore correspond unambiguously to the cross sections for inelastic neutron scattering to the 59 keV level. The cross sections observed at energies above 203 keV may be partly due to inelastic scattering to the 203 keV level with de-excitation by cascade through the 59 keV level. However, the contribution of such events to the NaI count rate is likely to be small because the branching probability for transitions between the 203 keV and 59 keV levels has been reported [14]) to be 7.5 %. The cross sections observed between 203 keV and 375 keV are therefore expected to represent a good approximation to the cross sections for inelastic scattering to the 59 keV level at these incident energies. The information available about the decay properties of the 375 keV and higher levels is very limited. However since the 375 keV level is believed [13]) to have angular momentum $\frac{1}{2}$, it is unlikely to decay via the 59 keV level ($J = \frac{7}{2}$). The cross-section data obtained at neutron energies up to at least 417 keV are therefore expected to be those for inelastic scattering to the 59 keV level.

It is of interest to compare the cross-section data shown in fig. 4 with inelastic scattering cross sections calculated on the basis of a statistical model of the type proposed by Hauser and Feshbach [1]). Calculations have been performed using the modified Hauser-Feshbach theory formulated by Auerbach and Moore [15]). Assuming that inelastic neutron scattering dominates all other modes of decay of the compound nucleus, we obtain [15]) for the cross section $\sigma(E, E_n)$ for inelastic scattering of neutrons of incident energy E and final energy E_n

$$\sigma(E, E_n) = \frac{\pi\lambda\!\!\!^{-2}}{2(2I+1)} \frac{\sum_{lj}\{T(ljE)\sum_{J}\{(2J+1)\sum_{l_n j_n} T(l_n j_n E_n)\}\}}{\sum_{i=1}^{m}\sum_{l_i j_i} T(l_i j_i E_i)}, \qquad (2)$$

where m denotes the number of final states which can be reached with the incident energy E and the subscripts i and n the final states reached with emergent energies E_i and E_n, respectively. The reduced incident neutron wavelength is denoted by $\lambda\!\!\!^{-}$ and the total angular momentum of the ground state of the target nucleus by I. The transmission coefficients for incoming and outgcing neutrons are denoted by T; incoming neutrons are implied by the absence of subscripts in the parameters l, j and E. The coefficients T are summed over all combinations of neutron orbital angular momentum l, channel spin j and compound nucleus angular momentum J allowed by conservation of angular momentum and parity. The ranges over which the quantum numbers J, l and j are allowed to vary therefore depend on the angular momenta and parities of both the initial state and the appropriate final state of the target nucleus.

The cross sections for inelastic scattering of neutrons to the first four excited states of ^{127}I have been calculated from eq. (2) assuming that the ground state and the states at 59, 203, 375 and 417 keV have total angular momenta and parities $\frac{5}{2}^+$, $\frac{7}{2}^+$, $\frac{3}{2}^+$, $\frac{1}{2}^+$ and $\frac{5}{2}^+$, respectively [13]). The neutron transmission coefficients used in the calculations are based on values calculated by Auerbach and Perey [16]) for $A = 128$. These authors have fitted elastic-scattering data for a range of nuclei using the

Bjorklund and Fernbach [17]) potential; they give tables of neutron transmission coefficients $T(ljE)$ for neutron energies down to 100 keV. In order to extend the present calculations to incident and final neutron energies less than 100 keV, the transmission coefficient data have been extrapolated to lower energies. For s-wave neutrons, the transmission coefficients were extrapolated to reach a limiting value $T(0, \frac{1}{2}, E) = 4k^2R^2$ for neutron energies $E \lesssim 10$ keV, where k is the neutron wave number and R the nuclear radius. For the partial waves $l \geqq 1$, the extrapolations were arbitrary; however this did not seriously affect the final result, since these components contributed less than 10 % of the cross section below 100 keV.

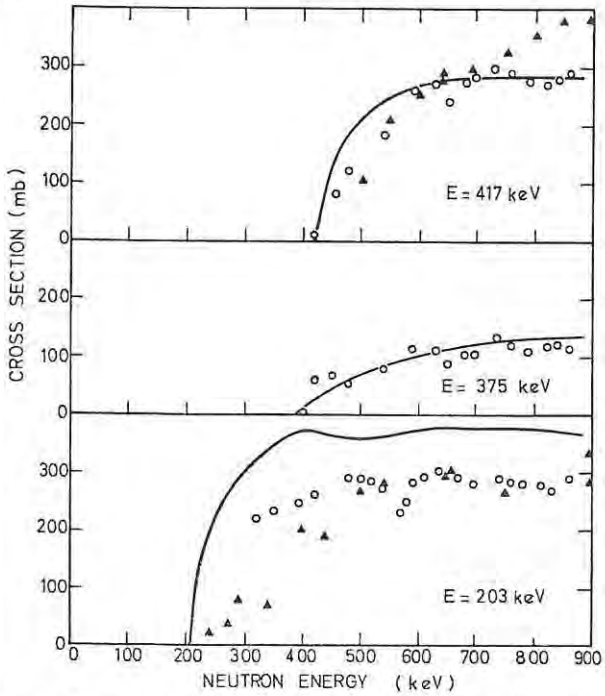

Fig. 5. Cross sections for neutron inelastic scattering to the 203 keV, 375 keV and 417 keV levels of ^{127}I, respectively; ▲-ref. [6]), o-ref. [18]). The curves show cross sections calculated from the Hauser-Feshbach theory using the same transmission-coefficient data as used for curve A of fig. 4.

The inelastic scattering cross sections calculated for the 59 keV level are shown by curve A in fig. 4. For neutron energies exceeding 160 keV (indicated by the solid portion of the curve), the calculations are essentially independent of any assumptions made in extrapolating the transmission-coefficient data. The results obtained in the 60–160 keV region (dashed part of curve A) are subject to uncertainties arising from these assumptions.

The inelastic scattering cross sections calculated for the 203, 375 and 417 keV levels are shown in fig. 5 with the measurements reported by van Loef and Lind [6]) (triangles) and Day and Lind [18]) (circles), respectively.

4. Discussion

The discrepancy (see fig. 4) between the present results and earlier data [6,7]) for the 59 keV level is disturbing. The data obtained from the NaI crystal are very unlikely to have appreciable systematic errors, and corrections for multiple neutron scattering in this scintillator were only a few per cent. Larger multiple-scattering corrections were necessary for both Li glasses; however, consistent results were obtained for glasses I and II, respectively, for which the multiple-scattering corrections differed considerably.

In view of the fact that the present results depend on assumptions regarding the chemical composition of the Li glass scintillators, the composition of glass II was checked by measuring the neutron transmission of the glass at several energies between 40 and 500 keV. The results were consistent with transmissions calculated from total cross sections [12]) and the composition supplied by the manufacturer of the glass scintillators. The present results depend on the assumed $^6Li(n, \alpha)^3H$ cross section [12]). If, as has been suggested by Fort and Leroy [19]), the latter cross sections were about 10 % higher than reported in ref. [12]), the present cross sections (fig. 4) would have to be increased correspondingly, and the discrepancy with the earlier data [6,7]) would be increased.

The symmetry of the experimental arrangement (fig. 1) was checked by carrying out runs with the detectors interchanged; it was demonstrated that the assumption of symmetry did not lead to significant errors. The discrepancy with the earlier measurements therefore remains and is not understood.

The present data are in good agreement with the cross sections for inelastic scattering calculated from the theory of Auerbach and Moore [15]) for incident neutron energies above 160 keV (curve A of fig. 4). The calculated cross sections are very dependent upon the assumed neutron transmission coefficients. The cross sections for inelastic scattering to the 203, 375 and 417 keV levels were based on the same transmission coefficient data as used for the 59 keV level; the results of the calculations for these three levels agree well with the data reported by Day and Lind [18]) and van Loef and Lind [6]) (see fig. 5). Calculations performed for the 59 keV level using an alternative set of transmission coefficients [16]) based on the potential of Perey and Buck [20]) led to higher cross sections (curve B of fig. 4) for 150–500 keV neutrons. The results of independent calculations recently reported by Sharma and Nath [21]) using transmission coefficients quoted by Beyster *et al.* [22]) are also shown in fig. 4 (curve C). The present experimental values agree to within about 20 % with the calculations (curves A-C of fig. 4) in the 160–500 keV region.

For incident neutron energies below 160 keV, the present experimental values for the 59 keV level are significantly lower than the cross sections obtained from the present calculations (curves A and B of fig. 4). These discrepancies are significant, notwithstanding the fact that the cross sections calculated in this energy region depend sensitively on the extrapolated values of the s-wave neutron transmission

coefficients. However, the validity of the model used in the calculations is questionable at energies close to the inelastic threshold. The discrepancies would probably be reduced if a theory incorporating a level width fluctuation correction [2-5]) were used. For further calculations in the threshold region, it would also be desirable to have reliable values for the neutron transmission coefficients for neutron energies down to a few keV. In the case of ^{127}I in particular, this implies a need for neutron elastic scattering cross-section data in the keV energy region.

It is a pleasure to acknowledge the assistance and cooperation of the staff of the Southern Universities Nuclear Institute during this experiment. We also express our thanks to the South African Council for Scientific and Industrial Research for financial support.

References

1) W. Hauser and H. Feshbach, Phys. Rev. **87** (1952) 366
2) L. Cranberg, Progress fast neutron physics (University of Chicago Press, 1963) p. 89;
R. B. Day in Progress, Progress in fast neutron physics (University of Chicago Press, 1963) p. 111;
A. T. G. Ferguson, Nuclear structure study with neutrons (North-Holland Publ. Co., Amsterdam, 1966) p. 63
3) A. M. Lane and J. E. Lynn, Proc. Phys. Soc. **A70** (1957) 557;
P. A. Moldauer, Phys. Rev. **123** (1961) 968; **129** (1963) 754
4) A. B. Tucker, J. T. Wells and W. E. Meyerhof, in Comp. Rend. Congr. Int. de physique nucléaire, Paris (1964) p. 671
5) A. B. Smith and P. T. Guenther, Nuclear structure study with neutrons (North-Holland Publ. Co., Amsterdam, 1966) p. 89;
D. Wilmore, *ibid*, p. 510
6) J. J. van Loef and D. A. Lind, Phys. Rev. **101** (1956) 103
7) J. D. Guernsey and A. Wattenberg, Phys. Rev. **101** (1956) 1516
8) F. Everling, L. A. Koenig, J. H. E. Mattauch and A. H. Wapstra, Nuclear Data Tables, Part I (1961)
9) F. W. K. Firk, R. J. Ginther and G. C. Slaughter, Nucl. Instr. **13** (1961) 313
10) A. O. Hanson and J. L. McKibben, Phys. Rev. **72** (1947) 673
11) L. A. Sliv and I. M. Bland, Alpha-, beta- and gamma-ray spectroscopy, Vol. 1 (North-Holland Publ. Co., Amsterdam, 1965) p. 1639
12) D. J. Hughes and R. B. Schwartz, BNL-325, 2nd ed. (1958)
13) Nuclear Data Sheets, compiled by K. Way *et al.* (Printing and Publ. Office, National Academy of Sciences-National Research Council, Washington 25, D.C., 1959–66)
14) J. Kownacki, J. Ludziejewski and M. Moszynski, Nucl. Phys. **A107** (1968) 476
15) E. H. Auerbach and S. O. Moore, Phys. Rev. **135** (1964) B895
16) E. H. Auerbach and F. G. Perey, BNL-765 (T-286) (1962)
17) F. Bjorklund and S. Fernbach, Phys. Rev. **109** (1958) 1295
18) R. B. Day and D. A. Lind, Ann. of Phys. **12** (1961) 485
19) E. Fort and J. L. Leroy, Nuclear data for reactors, Vol. 1 (IAEA, Vienna, 1967) p. 267
20) F. G. Perey and B. Buck, Nucl. Phys. **32** (1962) 353
21) H. C. Sharma and N. Nath, Nucl. Phys. **A106** (1968) 241
22) J. R. Beyster, R. G. Schrandt, M. Walt and E. Salmi, Los Alamos Scientific Laboratory Report LA-2099 (1957).

C.A.R. Bain and F.D. Brooks
Inelastic scattering of neutrons to the 59 keV level of ^{127}I
Nucl. Phys. A125 (1969) 312-320

F.D. Brooks and D.T.L. Jones
Polarization in n-p scattering at 21.6 MeV
Proc. 3rd Int. Symposium on Polarization Phenomena in Nuclear Reactions, ed. H.H. Barschall and W. Haeberli (Univ. of Wisconsin Press, 1971) 430-432

Polarization in Neutron-Proton Scattering at 21.6 MeV

F. D. BROOKS and D. T. L. JONES, University of Cape Town, South Africa

The polarizations observed [1, 2] and predicted [3] in neutron-proton scattering at $E_n < 30$ MeV are of the order of a few percent and are therefore difficult to measure accurately. In this paper we present some polarization data obtained by a new method which may have advantages in the study of n-p scattering.

The new method utilizes the directional dependence of scintillation pulse shapes from an anthracene crystal [4] to determine the left-right asymmetry of proton recoils within the crystal. The pulse shape is characterized by the output S of a pulse shape discrimination circuit [5]. This output S and also the total light output L from a scintillation depend on the proton direction in the crystal; L and S pass through a minimum, a maximum, and a shallow saddle as the proton direction is scanned through the three mutually perpendicular axes (1, 2, and 3; see fig. 1) of the crystal. The amplitude L is a maximum for the direction which corresponds to a minimum in S and vice-versa.

Two-parameter analyses of (L,S) are shown in fig. 2 for monoenergetic neutrons incident in the 12-plane of the crystal at different angles θ to axis 1: (a) $\theta = 0°$; (b) $\theta = 60°$; and (c) $\theta = 90°$. The variation in S for a change of 90° in proton direction is seen by comparing S values at the points of maximum L (corresponding to forward recoiling protons) in fig. 2(a, c). Different L values along the proton locus correspond to unique proton energies E_p and recoil angles ϕ related by $E_p = E_n \cos^2\phi$. At $\theta = 0$ (fig. 2a) the proton locus is relatively narrow

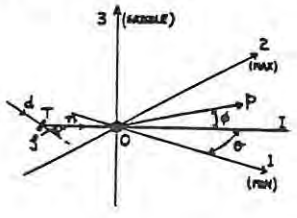

Fig. 1.

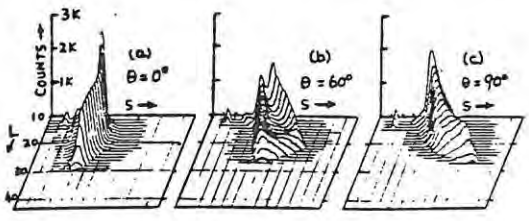

Fig. 2. Two-parameter spectra.

fit. Previous measurements [1, 2] at E_n = 16 MeV and 24 MeV have favored [3] the YLAN3M' fit.

The present technique could clearly be improved by adding a solenoid to rotate the spin of the incident neutrons, and we hope to do this soon. In other respects the technique should compare favorably with the conventional coincidence geometry used to determine P_{np}. Since all scatterings are detected, a range of scattering angles can be studied simultaneously and electronic requirements are simple.

REFERENCES

[1] W. Benenson, R. L. Walter, and T. H. May, Phys. Rev. Lett. 8 (1962) 66.
[2] R. B. Perkins and J. E. Simmons, Phys. Rev. 130 (1963) 272.
[3] M. H. Hull, F. A. McDonald, H. M. Ruppel, and G. Breit, Phys. Rev. Lett. 8 (1962) 68.
[4] K. Tsukada and S. Kikuchi, Nucl. Instr. 17 (1962) 286.
[5] F. D. Brooks, R. W. Pringle, and B. L. Funt, I.R.E. Trans. on Nucl. Sci. NS7 (1960) 35.
[6] W. Busse et al., Nucl. Phys. A100 (1967) 490.

NUCLEAR INSTRUMENTS AND METHODS 121 (1974) 69–76; © NORTH-HOLLAND PUBLISHING CO.

DIRECTIONAL ANISOTROPY IN ORGANIC SCINTILLATION CRYSTALS

F. D. BROOKS and D. T. L. JONES*

Physics Department, University of Cape Town, Rondebosch, C.P., South Africa

Received 29 October 1973

The scintillation pulse height responses and scintillation pulse shape discrimination (PSD) properties of anthracene crystals have been investigated for protons at six different energies in the range 1–22 MeV. Similar investigations were made for stilbene, terphenyl and quaterphenyl crystals at 8 MeV and for stilbene and naphthalene crystals at 22 MeV. The pulse height and PSD responses were investigated as a function of proton direction using recoil protons released within the crystals by monoenergetic incident neutrons. The pulse height anisotropy of anthracene crystals varies from 33% at 1 MeV to 8% at 22 MeV. The pulse height anisotropies of the other crystals are similar to that of anthracene at the same energy. The PSD anisotropy of anthracene expressed as a percentage of the PSD dispersion between Compton electrons and recoil protons varies from 3% at 1 MeV to 92% at 22 MeV. The PSD anisotropy of naphthalene is about half that of anthracene at 22 MeV and the PSD anisotropies of the other crystals are 3–7 times smaller than that of anthracene at 8 MeV. The pulse height and PSD anisotropies of anthracene are consistent with a model which assumes that the transfer of excitation energy during the scintillation process occurs preferentially in directions lying within the *ab*-planes of the crystal lattice.

1. Introduction

The scintillation pulse height responses of organic crystals to protons and heavier ions are known[1–6]) to depend on the direction of the ion relative to the axes of the crystal. The directional phenomena have been studied using alpha particle beams[2]) and using recoil protons released in crystals by fast neutrons[3–6]). It has been suggested[1,2,5]) that there may be preferred directions of exciton propagation in the crystal lattice which affect the dynamics of the scintillation mechanism in such a way as to render the scintillation response direction-dependent.

Most previous investigations of the directional phenomena have concentrated exclusively on the scintillation pulse height response, that is on the integral of the light output over the full scintillation decay. The form of this decay[7]) is also of fundamental interest and practical importance. Tsukada and Kikuchi[4]) showed in 1962 that the scintillation decay of anthracene, excited by 3.7 MeV protons, was direction-dependent. Thereafter it was shown[8]) that the directional anisotropy of scintillation properties provided a means for determining the directions of recoil protons in an anthracene crystal. No other investigations of the directional dependence of scintillation pulse shapes appear to have been reported for anthracene or for other organic crystals in the meantime.

The scintillation decay of an organic crystal may be described[1,7]) in terms of two components, a "fast" exponential component of lifetime typically 4–80 ns, depending on the crystal, and a "slow", non-exponential "tail". The integrated intensity of the fast component is typically four or more times larger than that of the slow component. Pulse shape discrimination (PSD) techniques for particle identification rely on the fact that for many organic scintillators the relative intensities of the fast and slow components differ for different types of particle.

In their studies of directional effects in anthracene Tsukada and Kikuchi[4]) investigated the individual direction dependences of the integrated fast component and the integrated slow component for proton scintillations. They found that both components were direction-dependent and that the fast component was significantly more so than the slow one. This implied that the scintillation decay of anthracene was direction-dependent and it therefore seemed possible that PSD techniques might be used for direction-sensing as well as for particle identification. The present work was initiated with such an application in mind and it has already led to a new method for measuring the left–right asymmetry of proton recoils from n–p scattering within an anthracene crystal[8]). In association with the development of this method directional effects were investigated in five different types of organic crystal, all of which were known[9]) to be effective pulse shape discriminators. The aims of the investigation were, firstly, to study the direction dependences of the scintillation pulse height responses of the crystals, and secondly, to determine to what extent their scintillation

* Present address: Physics Department, University of Wisconsin, Madison, Wisc. 53706, U.S.A.

TABLE 1
Details of crystals.

Crystal	Molecular formula	Shape and dimensions
Anthracene-A	$C_{14}H_{10}$	irregular: volume = 1.5 cm^3
Anthracene-B	$C_{14}H_{10}$	cylinder : 2 cm diam. × 2 cm
Naphthalene	$C_{10}H_8$	cylinder : 3.5 cm diam. × 2.5 cm
trans-Stilbene	$C_{14}H_{12}$	cylinder : 4 cm diam. × 1 cm
p-Terphenyl	$C_{18}H_{14}$	cube : 1 cm side
p-p′-Quaterphenyl	$C_{24}H_{18}$	irregular: volume = 2 cm^3

decay characteristics, as indicated by a PSD system, were direction-dependent.

2. Experimental

The crystals studied were monocrystals of anthracene, trans-stilbene, p-p′-quaterphenyl, p-terphenyl and naphthalene (see table 1). The studies were carried out at room temperature, (20 ± 5)°C, using monoenergetic neutron beams from the ^{7}Li(p,n), D(d,n) and T(d,n) reactions. The reactions were induced by protons or deuterons from the 5.5 MV Van de Graaff accelerator of the Southern Universities Nuclear Institute, Faure, C.P., and gave neutron energies in the range 1–22 MeV. Pulsed beams and time-of-flight gating were used in some of the measurements to define the neutron energy precisely and to suppress backgrounds.

For each crystal studied a particular face of the crystal was chosen as a reference face and was optically coupled to the photomultiplier cathode by means of paraffin oil. A coordinate system was then defined in which the polar axis ($\theta = 0°$) was perpendicular to the reference face and coincided with the photomultiplier axis, as shown in fig. 1a, and the azimuthal axis ($\phi = 0°$) was arbitrarily defined by characteristic physical features (or marks scratched) on the reference face. A horizontal neutron beam was used and the photomultiplier was mounted with its axis horizontal and free to rotate about a vertical axis OC (fig. 1a) which was fixed in the laboratory frame and passed through the centre of the crystal. The photomultiplier assembly could also be rotated independently about its own axis. Thus the polar coordinates θ and ϕ of the neutron beam were varied by rotating the crystal about the axis OC and the photomultiplier axis respectively. For convenience we shall sometimes refer to the

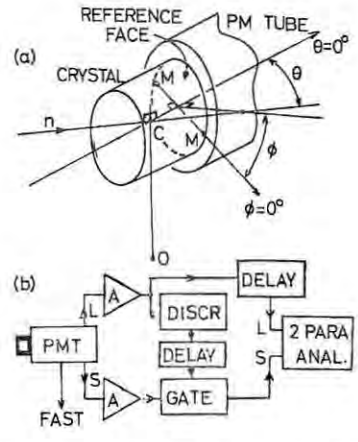

Fig. 1. (a) Definition of coordinate axes. The neutron beam n and the photomultiplier axis ($\theta = 0°$) are coplanar and horizontal. The reference face of the crystal is normal to the photomultiplier axis and the marks M on this face define the azimuthal axis ($\phi = 0°$). (b) Block diagram of the electronic system.

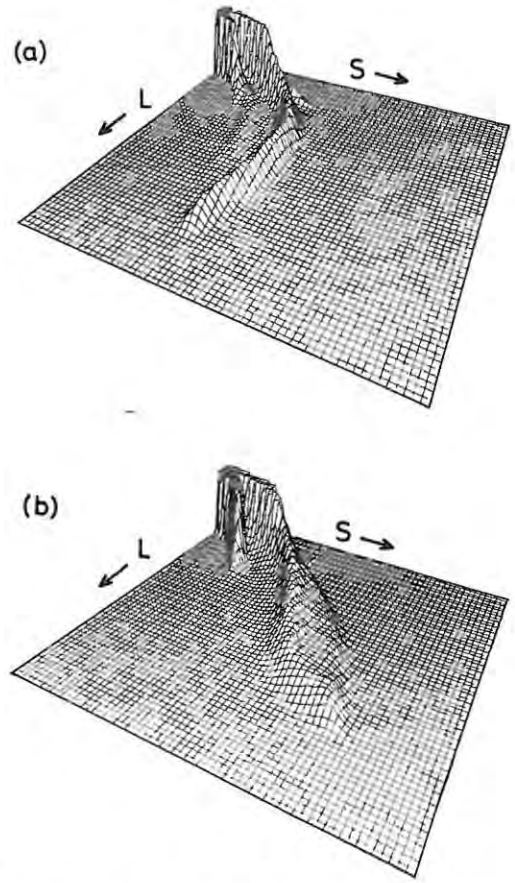

Fig. 2. Isometric plots of *LS* spectra (counts vs *L* vs *S*) obtained for 21.6 MeV neutrons incident on anthracene crystal A: (a) for $(\theta,\phi) = (0°, 40°)$; and (b) for $(\theta,\phi) = (90°, 40°)$. The upper limit of the counts scale is 1500 in (a) and 800 in (b).

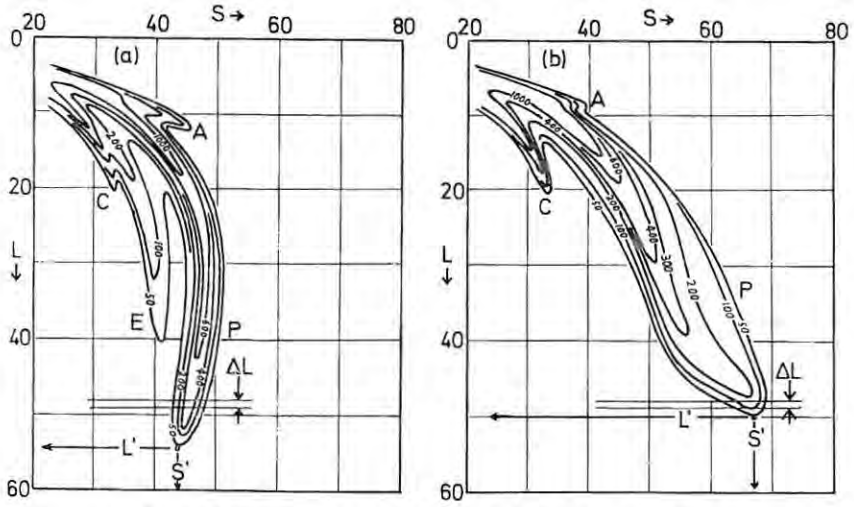

Fig. 3. Contours of equal count rate for the LS spectra (a) and (b) shown in fig. 2. The ridges in the spectra are attributed to: Compton electrons (C); recoil protons (P); escaping recoil protons (E) and alpha particles (A). The point (L', S') indicates the limit of the proton ridge in each spectrum. The position of the pulse height window ΔL used in the subsequent analysis is also shown.

coordinates (θ,ϕ) defined in this way as the "crystal orientation".

The experiments were conducted using two types of photomultiplier tube, namely EMI 6097B and Philips 56AVP. The 56AVP tube was fitted with a mu-metal shield and both tubes were tested to check that their responses were not affected by movement in the earth's magnetic field. Three outputs were taken from the photomultiplier circuit. These were: a fast signal for timing; a pulse height output L proportional to the total light in the scintillation; and a PSD output S. The PSD output was obtained from a circuit similar to that of ref. 9 and was a non-linear measure of the proportion of slow component in the scintillation. After processing in the electronic system[9]) shown in fig. 1b the L and S outputs were fed to the two inputs of a 4096-channel two parameter analyser (Northern Scientific type NS625/630).

3. Direction dependences of L and S

The direction dependences of the scintillation response and the scintillation decay of anthracene are illustrated by two-parameter analyses of the photomultiplier outputs, L and S, for monoenergetic neutrons. A pair of LS spectra obtained using neutrons of energy $E_n = 21.6$ MeV incident on the anthracene crystal A at $(\theta, \phi) = (0°, 40°)$ and $(90°, 40°)$ respectively are shown in fig. 2. Contour plots of the same two spectra are shown in fig. 3.

The most prominent feature in each spectrum is the "proton ridge" P, which extends from the origin up to a well-defined limit (L', S'). As the crystal rotates the proton ridge sweeps across the L–S plane between the limiting positions shown in figs. 2 and 3. In the process the limit (L', S') moves in such a way that S' increases as L' decreases. The ridge observed at the orientation giving maximum L' (fig. 2a) is narrower (i.e. sharper) with respect to S than that observed at the orientation giving minimum L' (fig. 2b).

Other features of interest in the LS spectra (figs. 2 and 3) are the ridges attributed to Compton recoil electrons (C), escaping recoil protons (E) and alpha particles (A). The alpha particles are attributed to $^{12}C(n,\alpha)^9Be$ and $^{12}C(n,n')3\alpha$ reactions within the crystal. The Compton ridge, unlike the proton ridge P, does not change position with crystal orientation. This is to be expected since Compton electrons undergo multiple large-angle scattering as they slow down and therefore do not maintain a unique direction.

The escaping protons responsible for E are presumed to be mainly high energy protons (> 10 MeV) whose ranges in anthracene are comparable with the linear dimensions of the crystal. Consider two protons, one which escapes from the crystal after depositing sufficient energy to produce a pulse height L and one of lower initial energy which produces the same pulse height after coming to rest in the crystal. In the former case the average excitation density along the proton track within the crystal will be smaller, so the escaping proton will have the appearance of a particle of mass intermediate between that of a proton and an electron. This explains why the ridge E lies between P and C and

why E lies close to P near the limit $L \approx L'$ and close to C at low L. The escape ridge is obscured in the spectrum taken at $(\theta, \phi) = (90°, 40°)$ (figs. 2b and 3b) because the ridges E and P are both broader at this orientation of the crystal.

For a proton recoiling at angle θ_p relative to the neutron beam the proton energy E_p is equal to $E_n \cos^2 \theta_p$. Thus all protons with directions lying within the surface of a cone of half-angle θ_p about the neutron beam will have the same energy. The proton energy E_p will therefore not uniquely characterise the proton direction except in the limit $E_p = E_n$ corresponding to $\theta_p = 0°$, i.e. to protons recoiling forward. Our interest is therefore focussed on the regions $L \approx L'$ of the LS spectra (figs. 2 and 3) since these are the regions for which $E_p \approx E_n$ and for which we can therefore assume that the proton direction lies close to that of the neutron beam, namely the direction (θ, ϕ) in the crystal coordinate frame.

The direction dependence of the pulse height $L(\theta, \phi)$ was studied by observing the limit L' for different orientations (θ, ϕ) of the crystal. After erasing the gamma ridge C the remainder of each LS spectrum was projected onto the L axis and L' was estimated from the resulting pulse height distributions (fig. 4a) by extrapolating the region of maximum slope of each distribution to the abscissa.

The direction dependence of the PSD amplitude $S(\theta, \phi)$ was studied by comparing PSD amplitudes S at a constant pulse height, L, the latter pulse height being in fact a small range ΔL of L close to the minimum observed limit L', as shown in fig. 3. The selected region was projected onto the S-axis to give a PSD amplitude distribution as shown in fig. 4b and the PSD amplitude $S(\theta, \phi)$ was taken as the median value of this distribution.

The direction dependences of L and S were also investigated by simpler methods which avoided the need for full-scale two-parameter analysis. The pulse height dependence $L(\theta, \phi)$ was determined by pulse height analysis, leading directly to spectra as in fig. 4a. In these measurements the PSD output was used merely to discriminate against gamma background. The PSD amplitude $S(\theta, \phi)$ was studied by electronically selecting events in the range ΔL (fig. 3) of L and pulse amplitude analysing S for these events. This was done either using a gated multichannel analyser, which gave spectra of the type shown in fig. 4b or, more conveniently, by using two amplitude discriminators and scalers. The discriminators were biased at suitable levels within the range S_2 to S_1 (see fig. 4b), such that the scaler count rates each provided a non-linear measure of S. The count rate scales were calibrated in terms of S by comparison with results obtained by means of the first method.

Comparative studies of $L(\theta, \phi)$ were made for four of the crystals listed in table 1 (anthracene-A, stilbene, terphenyl and quaterphenyl) using 8 MeV neutrons. Then $L(\theta, \phi)$ and $S(\theta, \phi)$ were studied for anthracene (both crystals) at different neutron energies in the range 1–22 MeV. The maxima and minima of the L and S responses of anthracene, stilbene and naphthalene were also compared at $E_n = 22$ MeV.

Data obtained for anthracene at $E_n = 8$ MeV are summarized in contour plots of $L(\theta, \phi)$ and $S(\theta, \phi)$ in fig. 5. These plots are based on observations at 80 (fig. 5a) and 240 (fig. 5b) different settings of (θ, ϕ), covering in each case a solid angle range of slightly more than 2π. The measurements included several complementary pairs which confirmed that results obtained for the opposing directions (θ, ϕ) and $(\pi - \theta, \phi + \pi)$ were identical. This identity was then assumed for the remaining data and used to extend the contour plots over the full 4π solid angle range, as shown in fig. 5.

For anthracene at 8 MeV, as can be seen in fig. 5, L and S vary smoothly (approximately sinusoidally) with θ or ϕ. This is also the case at other proton energies and for all the crystals studied. The directions

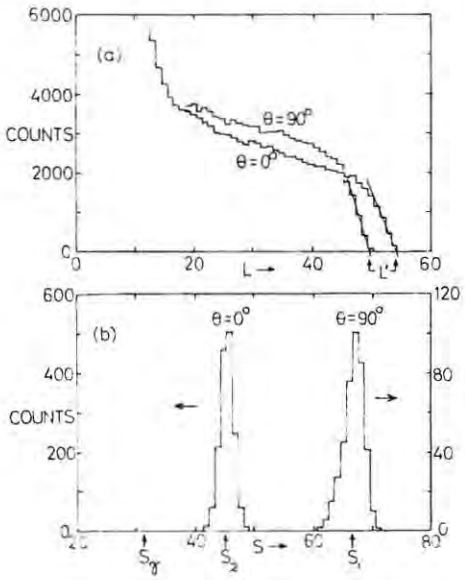

Fig. 4. Projections of selected regions of the LS spectra of figs. 2 and 3: (a) projections of the proton ridges onto the L axis; and (b) projections of segments within the window ΔL (see fig. 3) onto the S axis. The arrow S_p, in (b), indicates the position at which a gamma peak is observed in the projected spectrum obtained using high energy gamma rays.

corresponding to the maxima or minima of L or S are found to be independent of proton energy in all the crystals studied. The directional properties of the crystals are therefore defined in terms of these maxima and minima. We define the pulse height anisotropy A_L by the equation

$$A_L = 2(L_2 - L_1)/(L_1 + L_2),$$

where the L_1 and L_2 are the minimum and maximum observed values of $L(\theta, \phi)$. The PSD anisotropy A_S is defined by the equation

$$A_S = 2(S_2 - S_1)/(S_1 + S_2 - 2S_\gamma),$$

where S_1 and S_2 are the proton PSD amplitudes at the orientations corresponding to the pulse heights L_1 and L_2 and S_γ is the gamma-ray PSD amplitude, that is the median value of the Compton electron group in the projected S spectra.

Thus A_L is a measure of directional variation of the pulse height relative to the average pulse height and

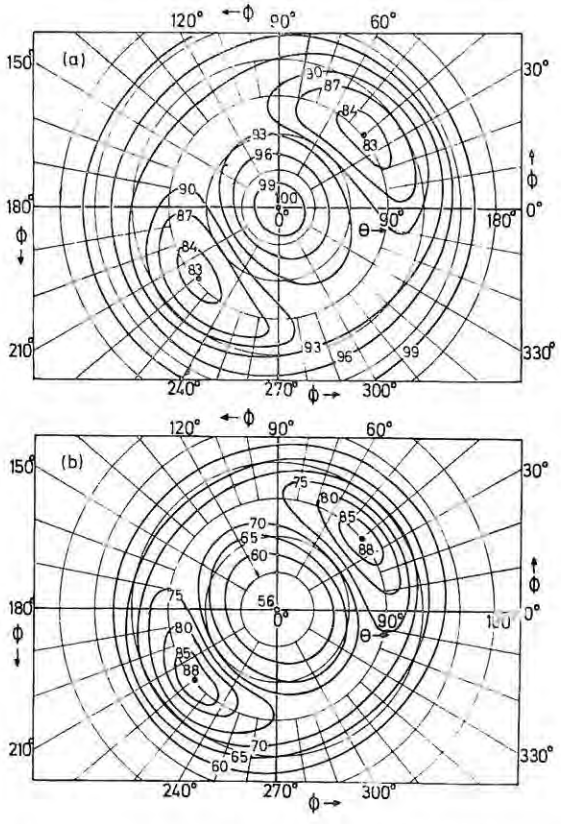

Fig. 5. Contours of: (a) equal pulse height $L(\theta,\phi)$; and (b) equal PSD output $S(\theta,\phi)$, as a function of proton direction (θ,ϕ) for 8 MeV protons in anthracene crystal A. The scales of L and S are arbitrary.

TABLE 2

Anisotropies at 8 MeV and 21.6 MeV.

Crystal	8 MeV A_L	8 MeV A_S	8 MeV R	21.6 MeV A_L	21.6 MeV A_S	21.6 MeV R
Anthracene	0.19	−0.42	4.0	0.08	−0.88	7.2
Naphthalene	–	–	–	0.11	−0.43	1.6
Stilbene	0.22	0.12	0.5	0.09	0.29	1.2
Terphenyl	0.20	0.06	0.1	–	–	–
Quaterphenyl	0.20	0.12	0.5	–	–	–

TABLE 3

Anisotropies versus proton energy for anthracene.

E_p (MeV)	1	3	5	8	16	21.6
A_L	0.33	0.29	0.23	0.19	0.11	0.08
A_S	−0.03	−0.10	−0.36	−0.42	−0.84	−0.88
R	0.1	0.5	2.8	4.0	6.1	7.2

A_S is a measure of the directional variation of the PSD amplitude relative to the PSD separation of protons and electrons. We also define a directional resolving power R as follows:

$$R = 2|S_2 - S_1|/(\Delta S_1 + \Delta S_2)$$

where ΔS_1 and ΔS_2 represent the full widths at half-maxima of the groups S_1 and S_2 in the projected PSD spectra (fig. 4b). Using Rayleigh's criterion therefore, a value of R exceeding unity indicates that the PSD anisotropy is sufficient to distinguish protons recoiling in the mutually perpendicular directions corresponding to the minimum and maximum PSD outputs.

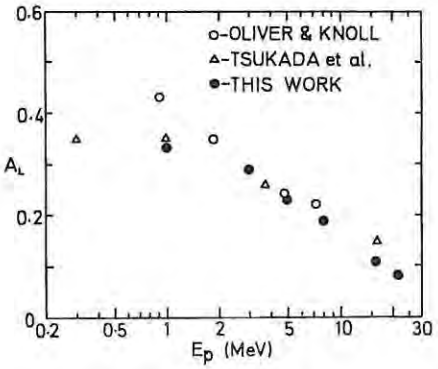

Fig. 6. Pulse height anisotropy A_L of anthracene as a function of proton energy: (a) this work (solid circles); (b) from ref. 6 (open circles); and (c) from ref. 5 (triangles).

The values of A_L, A_S and R obtained from the comparative studies of different crystals at $E_n = 8$ MeV and $E_n = 21.6$ MeV are summarised in table 2. The results obtained from studies on anthracene crystals at different energies in the range $E_n = 1$–22 MeV are shown in table 3 and in fig. 6.

The anisotropy properties of the other crystals were not studied as extensively as were those of anthracene. However, the PSD anisotropies of stilbene, terphenyl and quaterphenyl were also investigated at the proton energies 1 and 3 MeV and found to be less than at 8 MeV. The PSD anisotropy of terphenyl was similarly found to be small at 21.6 MeV.

The parameters A_S and R are of limited quantitative significance because the non-linear response of the PSD system makes the PSD output S sensitive to the circuit settings and photomultiplier operating conditions as well as to the scintillation pulse shapes. The circuit and photomultiplier settings were constant within each set of data shown in table 2, i.e. for 8 and 22 MeV respectively, hence comparisons within each of these sets are meaningful. However, the data shown in table 3 were obtained under different experimental conditions owing to the large dynamic range (22:1) of neutron energy covered. The PSD anisotropies A_S listed in this table may partially reflect these changes in operating conditions.

4. Discussion

We previously noted that the proton ridge (fig. 2) is narrower with respect to S in the LS spectrum observed at $(\theta, \phi) = (0°, 40°)$ than in that observed at $(\theta, \phi) = (90°, 40°)$. This can be explained with reference to the PSD contours shown in fig. 5b. The near-circular form of the lower contour levels (60–70) indicates that, for recoil angles less than 60°, the direction $\theta = 0°$ is an approximate axis of symmetry for S. For neutrons incident at $\theta = 0°$ the PSD outputs resulting from recoils at a given angle $\theta_p (< 60°)$ are approximately independent of the azimuthal angle of recoil ϕ_p. For example, for $\theta_p = 45°$, S varies from 59 to 62 units for different values of ϕ_p. The direction $(\theta, \phi) = (90°, 45°)$, on the other hand, is clearly not an axis of symmetry for S. For example, in the case of recoils in the directions $(\theta, \phi) = (45°, 40°)$ and $(90°, 85°)$, both of which make an angle of 45° with the direction $(\theta, \phi) = (90°, 40°)$, $S = 62$ and 76 units respectively. Thus for neutrons incident at $(\theta, \phi) = (90°, 40°)$ there is a much larger variation of S with ϕ_p, for a given θ_p, and the proton ridge is consequently broader than that observed at $(\theta, \phi) = (0°, 40°)$.

The pulse height anisotropy data for anthracene are compared with values based on the data reported by Tsukada et al.[5]) and Oliver and Knoll[6]) in fig. 6. There is general agreement on the trend of decreasing anisotropy with increasing proton energy. It is also noticeable from the present measurements at 8 MeV (table 2) that the different crystals show similar pulse height anisotropies A_L at the same energy.

The PSD anisotropies, in contrast, vary considerably from crystal to crystal at the same energy (table 2). In the case of anthracene the large negative PSD anisotropy A_S observed for protons of energy greater than 5 MeV (table 3) may be interpreted as an indication that the fast component is significantly more anisotropic than the slow component in this crystal. This is consistent with the observations of Tsukada and Kikuchi[4]) for 3.7 MeV protons, which showed that the pulse height anisotropy of anthracene was almost entirely due to the anisotropy of the fast component and that the anisotropy of the slow component was relatively small in this crystal.

Since the fast component is known to be responsible for most of the pulse height in all of the crystals studied[1,7]) we infer that the pulse height anisotropies of naphthalene, stilbene, terphenyl and quaterphenyl may similarly be attributed mostly to the anisotropies of their respective fast components. Since the pulse height anisotropies of these crystals are similar to those of anthracene at the same proton energy we infer that the anisotropies of their respective fast components are similar to that of anthracene. Furthermore, from the relatively small PSD anisotropies observed for stilbene, terphenyl and quaterphenyl

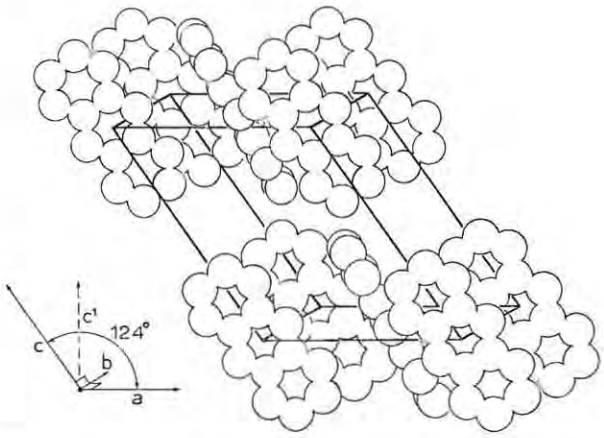

Fig. 7. Arrangement of molecules in the unit cell of the anthracene crystal[10]). The lengths (in Å) of the sides of the unit cell are $a = 8.56$, $b = 6.04$ and $c = 11.16$. The artificial c'-axis is the direction normal to the ab-plane.

(table 2) we infer that in each of these crystals the anisotropies of the slow and fast components must be similar. The PSD anisotropy observed for naphthalene on the other hand, being similar to that observed for anthracene, suggests that the anisotropy of the slow component is relatively small in this crystal, as appears to be the case in anthracene.

In previous studies[1-6]) the pulse height anisotropy has been related to the crystallographic axes which were independently located by means of X-ray analysis. The dispositions of the *a*-, *b*- and *c*-axes of the anthracene lattice and the orientations of molecules in this lattice[10]) are shown in fig. 7. For anthracene and naphthalene crystals the direction of minimum L coincided with the crystal *b*-axis and that of maximum L coincided with the artificial c'-axis, defined as the direction perpendicular to the *ab*-plane of the crystal. This correspondence was found to be reversed in stilbene crystals, while for terphenyl crystals L was found to be a minimum along the c'-axis and maximum along the *a*-axis. It has been pointed out[1]) that differences in molecular orientations and spacings in the respective crystal lattices could be responsible for these effects. However, it is interesting and possibly significant that the PSD anisotropy is large and negative and the anisotropy of the slow component is correspondingly small, in those crystals, i.e. anthracene and naphthalene, for which the c'-axis corresponds to a maximum in L.

The possibility that proton channelling may play a role in producing the directional anisotropies of the pulse height and PSD outputs must be considered. The sinusoidal variation of L and S with θ and ϕ contrasts with the multiple sharp variations that would be expected from channelling. While it remains possible that such sharp structure may be present to some degree, but not resolved by the experiments, it seems more likely that the gross features of the L and S anisotropies are caused by effects related to the molecular properties or the inter-molecular coupling within the crystals.

The pulse height anisotropy observed in anthracene, for example, may be related to the crystal structure if one postulates that energy transfer by exciton migration or other means occurs more rapidly within *ab*-planes than between different *ab*-planes. The molecular orientations and spacings in the anthracene lattice (fig. 7) are such that this would be a reasonable assumption. A proton moving parallel to the c'-axis of an anthracene crystal will excite molecules in the maximum number of *ab*-planes whereas a proton of the same energy moving perpendicular to the c'-axis will excite molecules in the minimum number of *ab*-planes. The excitation energy will disperse away from the proton track more rapidly in the former case than in the latter and the average excitation *density* at any given instant after the initial excitation will therefore be less. The scintillation response is higher for a lower time-average excitation density[1]) hence a maximum pulse height will be expected for protons moving parallel to the c'-axis, as is observed in practice. In terms of this picture we also expect the pulse height anisotropy to be larger for higher excitation densities, i.e. for lower energies. This is also consistent with the experimental observations on anthracene crystals as shown in fig. 6.

The pulse height anisotropies of stilbene and terphenyl could be interpreted along similar lines provided we assumed that the preferred directions of energy transfer were within the ac'-plane in stilbene and the bc'-plane in terphenyl. While the molecular orientations in these crystals[10]) are indeed different from those in the anthracene crystal, it is not clear from the information available which directions, if any, should be preferred for energy transfer.

The interpretation of PSD anisotropies, or more fundamentally, of the slow-component anisotropies, is complicated by the indirect and semi-quantitative nature of the experimental data and by the fact that the origin of the slow component in the scintillation decay is itself uncertain. According to the model of the scintillation process proposed by Birks[1]) the scintillation emission originates from the fluorescence decay of scintillator molecules in their lowest excited π-singlet states. The fast component is associated with the decay of those π-singlet states which are populated during or very shortly after the passage of the primary particle. The slow component is associated with excited π-singlet states which are populated over a much longer time scale via slower secondary processes which occur in the wake of the particle; for example, ion recombination, dimer formation, or triplet–triplet interactions. This latter process, which is currently the favoured candidate for the slow component in anthracene, refers to interactions of adjacent molecules both of which are initially excited to their (long-lived) lowest excited π-triplet states[1]). Since the probability of triplet–triplet interactions will depend on the density of π-triplet excited molecules, anisotropy in the energy transfer processes which control this density could lead to anisotropy in the resulting slow scintillation component. It is also conceivable that the proportion of π-triplet excitations formed in the initial excitation stage might depend directly on the direction of the exciting particle relative to the crystal axes as

well as on the excitation density immediately after its passage. The experimental data available at present are insufficient to decide which, if any, of these processes determine the PSD anisotropy properties of the different crystals studied. It would clearly be worthwhile in future work to study the directional dependence of the scintillation decay itself in detail, or at least to study the anisotropies of individual integrated fast and slow components, as was done by Tsukada and Kikuchi[4]) for anthracene at 3.7 MeV.

The appreciable magnitude of the PSD anisotropy of anthracene for proton energies exceeding 5 MeV (see A_S and R in table 3) is useful from the practical viewpoint. The utilization of the PSD anisotropy for the purpose of neutron polarization measurements is the subject of a companion paper[11]). Other applications relating to neutron spectroscopy and neutron direction sensing may also be feasible and are now being explored.

We are indebted to several colleagues who have assisted in this work, especially Dr L. M. Spitz, Mr G. Pauletta and Mr D. Shackleton, to the staff of the Southern Universities Nuclear Institute, and to Mr P. A. Back for constructing much of the equipment used. We also thank the South African Council for Scientific and Industrial Research for financial support and for the award of a bursary to one of us (D.T.L.J.).

References

1) J. B. Birks, *The theory and practice of scintillation counting* (Pergamon Press Ltd., London, 1967).

2) P. H. Heckmann, Z. Phys. **157** (1959) 139; P. H. Heckmann, H. Hanson and A. Flammersfeld, Z. Phys. **162** (1961) 84; P. H. Heckmann, W. Sander and A. Flammersfeld, Z. Phys. **165** (1961) 12; W. F. Kienzle and A. Flammersfeld, Z. Phys. **165** (1961) 1.

3) J. H. Coon (unpublished) quoted by C. D. Swartz and G. E. Owen, *Fast neutron physics*, part I (eds. J. B. Marion and J. L. Fowler; Interscience, New York, 1960) p. 211.

4) K. Tsukada and S. Kikuchi, Nucl. Instr. and Meth. **17** (1962) 286.

5) K. Tsukada, S. Kikuchi and Y. Mijagawa, Nucl. Instr. and Meth. **37** (1965) 69.

6) D. B. Oliver and G. F. Knoll, IEEE Trans. Nucl. Sci. **NS-15** (1968) 122.

7) L. M. Bollinger and G. E. Thomas, Rev. Sci. Instr. **32** (1961) 1044.

8) F. D. Brooks and D. T. L. Jones, Proc. 3rd Intern. Symp. on *Polarization phenomena in nuclear reactions* (eds. H. H. Barshall and W. Haeberli; The University of Wisconsin Press, 1971) p. 430.

9) F. D. Brooks, Nucl. Instr. and Meth. **4** (1959) 151; F. D. Brooks, R. W. Pringle and B. L. Funt, IEEE Trans. Nucl. Sci. **NS-7** (1960) 35.

10) A. I. Kitaigorodskii, *Organic chemical crystallography* (translated from the Russian; Consultants Bureau Enterprises Inc., New York, 1961) p. 420.

11) F. D. Brooks and D. T. L. Jones, Nucl. Instr. and Meth. **121** (1974) 77.

F.D. Brooks and D.T.L. Jones
Directional anisotropy in organic scintillation crystals
Nucl. Instr. and Meth. 121 (1974) 69-76

NUCLEAR INSTRUMENTS AND METHODS 121 (1974) 77–85; © NORTH-HOLLAND PUBLISHING CO.

A SCINTILLATION POLARIMETER FOR n–p SCATTERING STUDIES

F. D. BROOKS and D. T. L. JONES*

Physics Department, University of Cape Town, Rondebosch, C.P., South Africa

Received 29 October 1973

A neutron polarization analyser is described in which the direction dependence of the scintillation pulse shape discrimination (PSD) properties of an anthracene crystal provide the basis for observing the left–right asymmetry of recoil protons associated with the n–p scattering of monoenergetic neutrons within the crystal. The polarimeter consists of a single anthracene crystal mounted on a magnetically shielded photomultiplier tube which is fitted with a PSD circuit. The pulse height and PSD outputs from the photomultiplier are analysed in two parameter mode and a set of observations consisting of a pair of two-parameter spectra leads to a measurement of the recoil proton asymmetry as a function of recoil angle. The polarization in n–p scattering is then deduced as a function of centre-of-mass scattering angle θ_{cm} for values of θ_{cm} in the range 50°–180°.

1. Introduction

In a companion paper[1]) we described an investigation of the scintillation pulse height responses and scintillation pulse shape discrimination (PSD) properties of some organic crystals. The direction dependence of these properties was studied for recoil protons from incident neutrons with energies in the range 1–22 MeV. In anthracene crystals in particular the scintillation pulse shape was found to be markedly direction dependent over most of this energy range. It was apparent that the PSD properties of anthracene, besides providing the familiar means for discriminating against gamma-ray backgrounds, could also provide a means for sensing the directions of recoil protons released within the crystal. An obvious application occurred in the study of the neutron polarization in n–p scattering[2]). A scintillation polarimeter was developed in which the direction dependence of the PSD output provided the means for determining the left–right asymmetry of the proton recoils from n–p scattering. The design and operation of this polarimeter are described in this paper and its suitability for the study of the polarization in n–p scattering is discussed.

2. Outline of the method

The equipment used is identical to that described in ref. 1 and consists of a single anthracene crystal mounted on a magnetically shielded photomultiplier tube fitted with a PSD circuit[3]). The photomultiplier provides three output pulses, namely: a fast output signal for time-of-flight spectroscopy; a linear output L which is proportional to the total light in the scintillation; and a PSD output S which depends non-linearly on the proportion of slow component in the scintillation decay. The L and S outputs are processed by the same electronic system and two-parameter analyser as in ref. 1 to give two-parameter spectra of counts versus L versus S. We refer to these spectra as LS spectra.

The laboratory arrangement for polarization measurements is shown schematically in fig. 1a. A monoenergetic neutron beam is taken at angle ζ from for example, the T(d,n) reaction. The monoenergetic beam is selected by time-of-flight gating unless the choice of beam and target makes this unnecessary. The neutron and deuteron beams define a horizontal plane and the anthracene crystal is oriented at (α, β) to

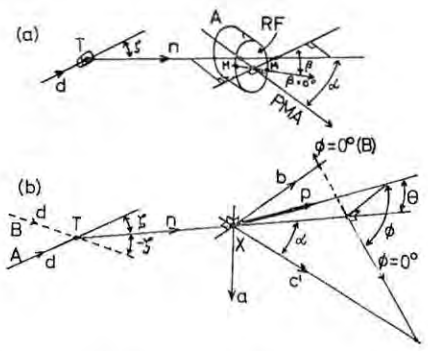

Fig. 1. Schematic diagrams of experimental geometry showing deuteron beam d, neutron beam n and tritium target T. (a) Diagram showing reference face RF of anthracene crystal A, photomultiplier axis PMA, and $\beta = 0°$ axis, defined by marks M. (b) Diagram showing centre X of crystal, mutually perpendicular crystal axes, a, b and c', and recoil proton p. The azimuthal axis $\phi = 0°$ is defined by projecting the deuteron beam onto a plane normal to the neutron beam. The dashed lines illustrate changes implied by a switch from position A to position B.

* Present address: Physics Department, University of Wisconsin, Madison, Wisc. 53706, U.S.A.

the neutron beam where α and β correspond to the angles referred to as θ and ϕ in ref. 1. The angle α is the angle between the photomultiplier axis and the neutron beam. The angle β is the angle between the projection of the neutron beam on the reference face of the crystal and the azimuthal axis of the crystal. The reference face is that face of the crystal which is optically coupled to the photomultiplier cathode and the azimuthal axis, $\beta = 0$ in fig. 1a, is a line which is arbitrarily defined in this face. To simplify the present discussion we shall restrict ourselves to the anthracene crystal A of ref. 1, for which the reference plane was an *ab*-plane and for which the photomultiplier axis therefore coincided with artificial *c'*-axis of the crystal[1]). For this crystal or for any other anthracene crystal therefore, the angle α could equally well be defined as the angle between the neutron beam and the *c'*-axis of the crystal.

The pulse height anisotropy properties of anthracene for protons are such that, for a given proton energy, L is a minimum for protons moving parallel to the *b*-axis of the crystal and a maximum for protons moving parallel to the artificial c'-axis[4]). The PSD anisotropy characteristics[1]) are such that S is maximum when L is minimum and vice versa, as can be seen in fig. 2 of ref. 1. An optimum orientation for asymmetry measurements is one in which there is maximum variation of S for proton recoils to left and right of the neutron beam direction.

This is achieved if the *a*-axis of the crystal is aligned vertical (so that the *bc'*-plane is horizontal) and the neutron beam direction is intermediate between the *b*- and *c'*-axis so as to make the angle $\alpha = 60°$, as shown in fig. 1b. We define two positions A and B (fig. 1b) at this orientation, depending whether a proton recoil from the neutron beam towards the *c'*-axis is in the same sense (A) or the opposite sense (B) as the deflection from the deuteron beam to the neutron beam. We can change from position A to position B by changing ζ to $-\zeta$, as shown in fig. 1b or by rotating the crystal through 180° about the neutron beam or by rotating the crystal about the *a*-axis until the *c'*-axis makes an angle $(2\pi - \alpha)$ with the neutron beam. The photomultiplier is mounted in such a way that any one of these angles may be adjusted without affecting the other two.

An *LS* spectrum obtained at the orientation $(\alpha,\beta) = (60°, 40°)$ and with other conditions identical to those used for fig. 2 of ref. 1 is shown in isometric projection in fig. 2. A contour plot of the same spectrum is shown in fig. 3. The structure in this spectrum is similar to that in the spectra shown in ref. 1 except that the proton ridge P now splits into two ridges P_1 and P_2 (see fig. 3) over most of its length. We can show that these ridges correspond to protons recoiling into the forward quadrants on either side of a vertical plane through the neutron beam. The ridge P_1 corresponds to recoils into the quadrant containing the *c'*-axis and P_2 to recoils into the quadrant containing the *b*-axis. By comparing the numbers of counts under each ridge

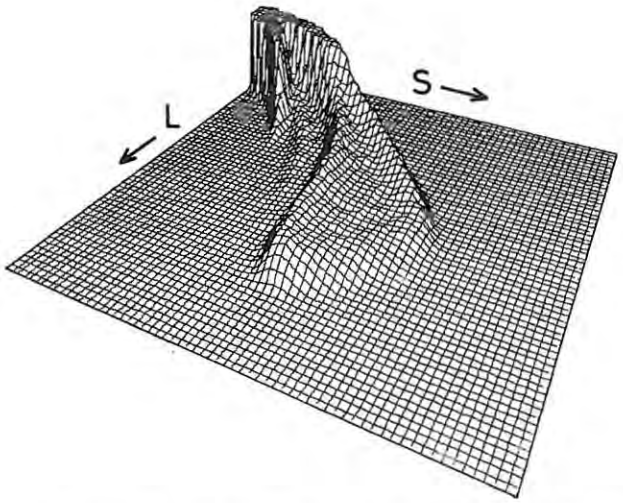

Fig. 2. Isometric plot of an *LS* spectrum obtained for 21.6 MeV neutrons incident on the anthracene crystal A. The spectrum shows counts (vertical) vs pulse height L vs PSD output S. The upper limit of the count scale is 500.

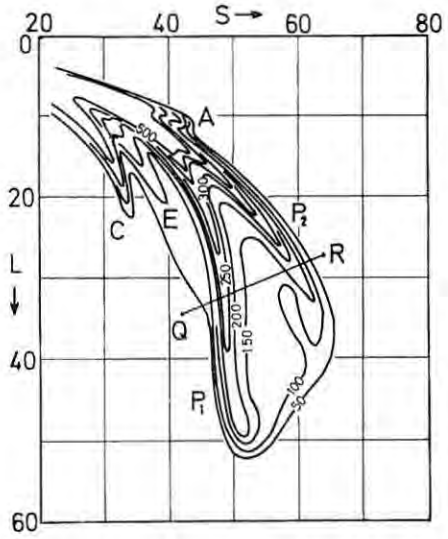

Fig. 3. Contour plot of the *LS* spectrum shown in fig. 2. The ridges in the spectrum are identified as follows: Compton electrons, C; recoil protons P_1 and P_2; escaping recoil protons E; and alpha particles, A. The line QR represents the locus of a constant recoil angle θ.

we can determine the left–right asymmetry of the proton recoils within the crystal.

The proton component of the LS spectrum includes recoils at laboratory angles ranging from 0° to almost 90° relative to the neutron beam. The pulse height L depends on the energy E_p and on the direction of the recoil proton. The proton direction is specified by the angle of recoil θ relative to the neutron beam and the azimuthal angle of recoil ϕ. The azimuthal axis is defined by projecting the deuteron beam onto a plane perpendicular to the neutron beam, as illustrated in fig. 1b. The energy E_p is related to the angle θ and the incident neutron energy E_n by

$$E_p = E_n \cos^2 \theta. \quad (1)$$

From measurements[1]) of the L and S anisotropies we know that the loci of constant E_p and hence of constant recoil angle θ approximate to straight lines across the LS-plane, such as the line QR in fig. 3. By defining a series of such lines we can therefore divide the proton region of the LS spectrum into angle bins corresponding to different recoil angles. In principle therefore a single LS spectrum contains sufficient information to determine the left–right asymmetry as a function of recoil angle over a wide range of recoil angles.

3. Operation for a particular proton recoil angle

The operation of the asymmetry analyser is best described by first showing how the left–right asymmetry would be calculated if the LS spectrum contained only proton recoils at a particular recoil angle and then showing how the LS spectrum is sub-divided into a set of recoil angle bins for a series of such calculations. We therefore confine the initial discussion to a specific proton recoil angle $\theta = 30°$ and to a specific neutron energy $E_n = 11$ MeV for which the recoil proton energy at $\theta = 30°$ is $E_p = 8.3$ MeV, from eq. (1). The direction dependence of S at this energy may be deduced from the data given in fig. 5 of ref. 1 for the nearby neutron energy of 8 MeV. These data are referred to the crystal coordinate frame defined in ref. 1, so we must transform them to the present laboratory frame in which the crystal is oriented at $(\alpha, \beta) = (60°, 40°)$. The transformed data for position A of this orientation in the laboratory frame are shown in fig. 4. The laboratory recoil directions corresponding to minimum and maximum PSD output, S_{min} and S_{max} are $(\theta, \phi) = (60°, 0°)$ and $(30°, 180°)$ respectively. From fig. 4 we can read the variation of $S(\theta, \phi)$ with ϕ for the recoil angle $\theta = 30°$ and we obtain a curve of the form shown in fig. 5a, in which S ranges between the values S_- (at $\phi = 0°$) and S_+ (at $\phi = 180°$). We define the fractional dispersion $F(\theta)$ of S with ϕ for recoil angle θ by

$$F(\theta) = (S_+ - S_-)/(S_{max} - S_{min}). \quad (2)$$

Thus from the data shown in fig. 4, $F(\theta) = 0.9$ at $\theta = 30°$. These data also indicate that for any value of θ within the range $\theta \lesssim 70°$ the PSD outputs at $\phi = 90°$ and 270° are very nearly equal. Assuming that in the ideal case these outputs for $\phi = 90°$ and 270° are the

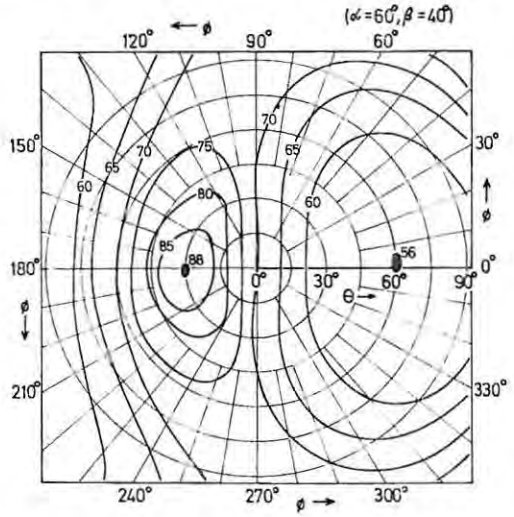

Fig. 4. Contours of equal PSD output S for 8 MeV protons as a function of proton direction (θ,ϕ). The plot is for the crystal orientation $(\alpha,\beta) = (60°, 40°)$ and was obtained by transforming the data shown in fig. 5 of ref. 1 to this orientation. The latter figure is equivalent to a contour plot of $S(\theta,\phi)$ for the crystal orientation $(\alpha,\beta) = (0°, 40°)$.

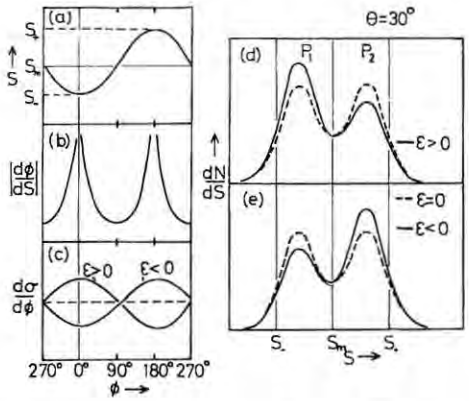

Fig. 5. PSD responses and spectra (schematic) for 8 MeV proton recoils at $\theta = 30°$: (a) PSD output S vs recoil azimuth ϕ; (b) $|d\phi/dS|$ vs ϕ; (c) $d\sigma/d\phi$ vs ϕ from eq. (3); (d) projected and resolution-broadened spectra dN/dS vs S for $\varepsilon > 0$ (solid curve) and $\varepsilon = 0$ (dashed curve); and (e), as (d) but for $\varepsilon < 0$ (solid curve).

same and equal to $S_m(\theta)$ for recoils at angle θ, we note further that $S<S_m(\theta)$ for ϕ in the range $0°\pm90°$ and $S>S_m(\theta)$ for ϕ in the range $180°\pm90°$. Thus the PSD output S indicates whether the associated proton recoil direction is to the "left" or the "right" of the neutron beam. For equal numbers of left and right recoils $S_m(\theta)$ should correspond to the median of the number distribution with respect to S.

The left–right asymmetry $\varepsilon(\theta)$ of proton recoils from n–p scattering may therefore be deduced from the amplitude distribution of the S output as follows. The partial differential cross section $(d\sigma/d\phi)_{\theta\phi}$ for elastic proton recoil in direction (θ, ϕ) in the laboratory frame is given by

$$(d\sigma/d\phi)_{\theta\phi} = [\sigma(\theta)/2\pi]\,[1+P_0\,P(\theta)\cos\phi] = [\sigma(\theta)/2\pi]\,[1+\varepsilon(\theta)\cos\phi], \quad (3)$$

where $\sigma(\theta)$ is the total differential cross section for elastic recoil at angle θ, P_0 denotes the polarization of the incident neutron beam, and $P(\theta)$ denotes the analysing power for proton recoils at angle θ in n–p scattering.

The number of proton recoils per unit S at angle θ and leading to a PSD output S may now be written

$$(dN/dS)_{\theta S} = k\sum_{\phi}(d\sigma/d\phi)_{\theta\phi}\,|d\phi/dS|_{\theta\phi}, \quad (4)$$

where k depends on the incident neutron intensity and the crystal thickness and the sum is taken over all values of ϕ which correspond to the value S (see fig. 5a). The modulus $|d\phi/dS|_{\theta\phi}$ is derived as a function of ϕ from fig. 5a and has the form shown in fig. 5b while $(d\sigma/d\phi)_{\theta\phi}$ is given by eq. (3) and has one of the three forms shown in fig. 5c, depending whether $\varepsilon(\theta)$ is zero, positive or negative.

The S amplitude distribution for a constant recoil angle θ is thus obtained by taking the product, as in eq. (4), of the functions shown in figs. 5b and 5c and convoluting with the resolution function of the PSD output measurement. Figs. 5d and 5e illustrate schematically the types of distribution that will result for either zero, positive or negative values of $\varepsilon(\theta)$.

Projecting the LS spectrum associated with proton recoils at a particular angle θ, e.g. $\theta = 30°$, onto the S axis therefore leads to a distribution of the form shown in fig. 5d or 5e. The peaks P_1 and P_2 in this distribution correspond to the ridges P_1 and P_2 in the LS spectrum. If the proton asymmetry $\varepsilon(\theta)$ increases the peak P_1 increases in height and the peak P_2 decreases. The opposite happens if $\varepsilon(\theta)$ decreases.

In changing from position A to position B (fig. 1b) we either change ζ to $-\zeta$, or we change α to $(2\pi-\alpha)$ or we rotate the crystal through 180° about the neutron beam. The first method reverses the sign of the incident polarization P_0 and hence also that of $\varepsilon(\theta)$. The second and third methods produce an equivalent effect since they shift the phase of figs. 5a and 5b by 180° relative to that of fig. 5c. The effect on the projected S spectrum is therefore the same whatever the method used to change from position A to position B. If the S spectrum for position A resembles the solid curve in fig. 5d then that for position B will resemble the solid curve in fig. 5e and vice-versa.

In principle the asymmetry $\varepsilon(\theta)$ can be determined by comparing the integrals under the peaks P_1 and P_2 observed in either position A or position B. For position A the integral under the lower part $[S<S_m(\theta)]$ corresponds to recoils with ϕ in the range $0°\pm90°$. Thus the integral $N_<$ under this part is given by

$$N_< = [k\sigma(\theta)/2\pi]\int_{-\frac{1}{2}\pi}^{+\frac{1}{2}\pi}[1+\varepsilon(\theta)\cos\phi]\,d\phi = [k\sigma(\theta)/2\pi]\,[\pi+2\varepsilon(\theta)]. \quad (5)$$

Similarly the integral $N_>$ under the upper part of the A spectrum corresponding to recoils with ϕ in the range $180°\pm90°$, is given by

$$N_> = [k\sigma(\theta)/2\pi]\,[\pi-2\varepsilon(\theta)]. \quad (6)$$

The asymmetry $\varepsilon(\theta)$ is therefore obtained from eqs. (5) and (6):

$$\varepsilon(\theta) = \tfrac{1}{2}\pi(N_<-N_>)/(N_<+N_>) = \tfrac{1}{2}\pi\,\Delta N_A/N_A, \quad (7)$$

where ΔN_A therefore represents the difference between the integrals under the lower and upper parts of the spectrum obtained at position A and N_A represents the integral of the full spectrum.

The corresponding result obtained using the position B spectrum instead of the position A spectrum is

$$\varepsilon(\theta) = -\tfrac{1}{2}\pi\,\Delta N_B/N_B, \quad (8)$$

where ΔN_B and N_B are defined in the same way as ΔN_A and N_A. The minus sign arises in this case because the lower and upper regions of the spectrum correspond to recoils with ϕ in the ranges $180°\pm90°$ and $0°\pm90°$ respectively, which is the reverse of the situation applying for the position A spectrum.

Asymmetries determined directly from either eq. (7) or eq. (8) will clearly depend sensitively on the value of $S_m(\theta)$ used, through the effect this has on the difference ΔN_A or ΔN_B. However, for small errors in $S_m(\theta)$ the effect on ΔN_A is nearly exactly equal to that

on ΔN_B. The asymmetry term in eq. (3) contains $\cos\phi$ as a multiplicative factor and therefore has very little influence on the value of dN/dS at $S \approx S_m(\theta)$ where $\phi \approx 90°$ or 270°. The errors arising from a slightly incorrect choice of $S_m(\theta)$ will therefore cancel in the difference $(\Delta N_A - \Delta N_B)$ and may be eliminated as follows. Summing eqs. (7) and (8) we obtain

$$\varepsilon(\theta) = (\pi/4N_A)\,[\Delta N_A - (N_A/N_B)\,\Delta N_B]\,.$$

Thus if we normalize the A and B spectra so as to make $N_A = N_B = N$ we obtain

$$\varepsilon(\theta) = (\pi/4N)\,(\Delta N_A - \Delta N_B)\,. \qquad (9)$$

A suitable method for determining the limit $S_m(\theta)$ is to take the median S value of the sum of normalized projected A and B spectra. The summed spectrum should contain equal numbers of left and right recoils hence the median value should correspond to $S_m(\theta)$ as noted earlier. We must also note, however, that both this assumption and the assumption that small errors will cancel in the difference $(\Delta N_A - \Delta N_B)$ depend on the A and B positions of the experiment being perfectly symmetric about the neutron beam. A monitor of this symmetry is provided by the points of inflection in the projected A and B spectra illustrated in figs. 5d and 5e. We identify these points of inflection with the limits S_- and S_+ defined in eq. (2). Small experimental asymmetries shift the projected spectra slightly along the S axis or produce small changes in the dispersions $(S_+ - S_-)$ of the spectra without otherwise altering the form of the spectra significantly. The presence of such asymmetries is thus revealed by differences between the S_- limits or the S_+ limits of the A and B spectra respectively. Provided the shifts are small, however, they can effectively be eliminated and false asymmetries thereby avoided by shifting and redispersing one spectrum or both spectra with respect to S until the S_- and S_+ boundaries of the two spectra coincide.

In practice therefore the proton recoil asymmetry $\varepsilon(\theta)$ given by eq. (9) can be rendered insensitive to the choice of $S_m(\theta)$ and to small asymmetries in the experimental geometry if the limits S_- and S_+ of the projected LS spectra are aligned before $S_m(\theta)$ is determined or any other calculations are made.

4. Determination of asymmetry as a function of recoil angle

To calculate proton asymmetries from a pair of LS spectra we divide the proton regions of the spectra into angle bins, each corresponding to a finite range of recoil angle θ, and calculate the asymmetry for each bin in the manner outlined in section 3. The preferred procedure is to determine beforehand the limits or points of inflection S_- and S_+ at each value of L in each spectrum. The LS spectra (not the projected S spectra) are then redispersed so as to bring their S_- and S_+ limits into line. Furthermore, the final values of S_- and S_+ are chosen so as to simplify the next step in the data reduction, namely the definition angle bins. The limits of the angle bins are defined by straight lines (such as QR in fig. 3) in the L–S plane. The widths $\Delta\theta$ of these bins are chosen with reference to the pulse height resolution of the crystal at the appropriate energy. Widths of $\Delta\theta = 5°$ or more in the laboratory frame (i.e. 10° or more in the cm frame) have been used for the incident neutron energies 16 MeV or 22 MeV. The A and B data within each angle bin are then projected onto the S-axis and $\varepsilon(\theta)$ is calculated from the projected spectra as previously described.

The LS spectra are redispersed and the angle bins are defined in the following way. Each spectrum is presented as a data matrix in which the elements are counts and the row and column numbers correspond to L and S respectively. Assume that the number of columns is $4n$ and that the points of inflection S_- and S_+ are specified for each row of both the A and B data matrices. Each row of each data matrix is transformed so that the counts within the region S_- and S_+ are linearly redispersed over a region extending from column $[2n - n\,F(\theta)]$ to column $[2n + nF(\theta)]$, where $F(\theta)$ is the fractional dispersion given by eq. (2) for

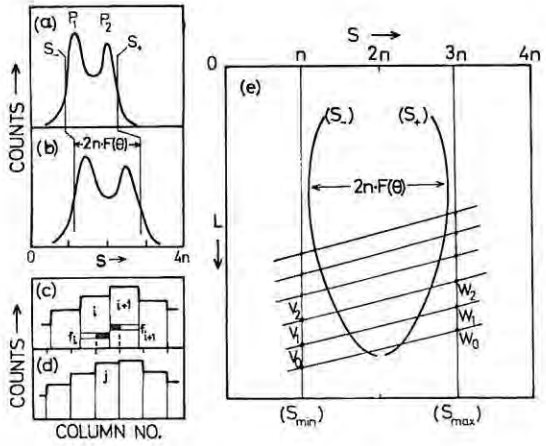

Fig. 6. Redispersion of LS spectra (schematic) and definition of angle bins: (a) spectrum of counts vs S for a single row (L value) of the original LS data matrix; (b) spectrum (a) after redispersion; (c) a portion of spectrum (a); (d) the corresponding portion of spectrum (b); and (e) definition of angle bins in the redispersed LS spectrum.

the mean recoil angle θ corresponding to the pulse height L. The angle θ is determined by using the known[4]) relative pulse height versus energy response of anthracene to protons to determine the mean recoil proton energy E_p corresponding to L and using eq. (1) to determine θ from E_p.

The redispersion process is schematically illustrated in fig. 6. Figs. 6a and 6b illustrate the transformation of a single row of the LS spectrum. The transformation may be pictured if we imagine firstly, the distribution shown in fig. 6a shifted along the S axis until its centre corresponds to $S = 2n$ in fig. 6b and secondly, the S scale of fig. 6b multiplied by a factor $(S_+ - S_-)/[2n\,F(\theta)]$. The forms of the two distributions will then be identical and the distributions will only differ in their count scales and in the number of points or histogram steps along their S axes, as illustrated for a small portion of the two distributions in figs. 6c and 6d. The number of counts N_j in channel j of the redispersed distribution is given by

$$N_j = \sum_{i=1}^{4n} f_i N_i , \qquad (10)$$

where N_i represents the number of counts in channel i of the original distribution and f_i is the fraction of this channel which is overlapped by channel j of the redispersed distribution, as illustrated in figs. 6c and 6d.

Since the interval $(S_+ - S_-)$ in the original distribution corresponds to an interval $2nF(\theta)$ in the redispersed distribution we see from eq. (2) that the interval $(S_{max} - S_{min})$ in the former will correspond to an interval $2n$ in the latter. From the data of fig. 4 we can also show that the values $S = n$ and $3n$ in the redispersed distribution will correspond to the limits S_{min} and S_{max} in the original distribution. In the redispersed LS spectrum, therefore, we assume that the S values n and $3n$ correspond to S_{min} and S_{max} for every row or L value as illustrated in fig. 6e. The limits S_- and S_+ which vary with L are illustrated by the lines S_- and S_+ in fig. 6e. These limits vary smoothly from row to row, but always lie symmetrically about $S = 2n$ and within the region $S = n$ to $3n$.

The proton region is now subdivided into angle bins by defining boundaries as illustrated by the lines $V_m W_m$ in fig. 6e. Each such line corresponds to a specific recoil angle and hence to a specific proton energy E_p, given by eq. (1). The pulse height anisotropy[1]) at proton energy E_p is a measure of the amount that L varies as S varies from S_{min} to S_{max}. The angle boundaries are therefore defined with reference to the ordinates $S = n$ and $S = 3n$ as follows. From a calibration run such as fig. 2a of ref. 1, for which the crystal c'-axis was aligned with the neutron beam, we determine the maximum pulse height that could be observed for a proton energy $E_p = E_n$ and mark this point V_0 on the ordinate $S = n$ as shown in fig. 6e. From a similar calibration run such as fig. 2b of ref. 1, for which the crystal b-axis was aligned with the neutron beam, or from the pulse height anisotropy data for anthracene[1]) we obtain the minimum pulse height that could be observed at this proton energy and mark this pulse height W_0 on the ordinate $S = 3n$ as shown in fig. 6e. These points define the bin boundary line $V_0 W_0$ corresponding to the bin limit $\theta = 0°$. The boundaries $V_1 W_1$, $V_2 W_2$ etc. corresponding to successively increasing boundary recoil angles θ are determined by calculating the recoil proton energy from eq. (1), using the relative pulse height versus energy data[4]) for anthracene to determine V_1, V_2 etc. and using the pulse height anisotropy data shown in fig. 6 of ref. 1 to determine W_1 from V_1, W_2 from V_2 and so on.

The first angle bin is thus defined by the lines $V_0 W_0$ and $V_1 W_1$ in fig. 6e, the second by the lines $V_1 W_1$ and $V_2 W_2$ and so on. The boundary lines are extrapolated across the LS plane as shown in fig. 6c and the counts between each pair of boundaries are projected onto the S axis to give the projected spectrum (A or B) for the corresponding angle bin. The counts in those channels which are cut by the boundary lines are distributed proportionally between the bins on either side of the boundary. The asymmetry $\varepsilon(\theta)$ is determined by comparing the projected A and B spectra as outlined in section 3. The median limit $S_m(\theta)$ is specified as outlined in that section. The other limits used in calculating the integrals N_A and N_B and the differences ΔN_A and ΔN_B are specified far away from the proton ridges provided these ridges are well resolved from other significant structure in the projected spectrum. If significant other structure lies close by the ridge, for example that due to alpha particles or escape protons at the low L values (figs. 2 and 3), then limits lying between this structure and the proton ridges are used.

The analysing power $P(\theta)$ for proton recoils at recoil angle θ is equal to $\varepsilon(\theta)/P_0$. Thus, with negligible error we obtain the polarization in n–p scattering $P_{np}(\theta_{cm})$ at the associated centre-of-mass neutron scattering angle $\theta_{cm} = \pi - 2\theta$ from

$$P_{np}(\theta_{cm}) = -P(\theta) = -\varepsilon(\theta)/P_0 . \qquad (11)$$

The calculation of n–p polarization values from pairs (A and B) of LS spectra is accomplished with the aid of a Fortran IV programme POLYANA. The LS spectra from the multiparameter analyzer are provided

either on magnetic tape or punched cards. These are read in together with other data required for the calculation and the complete data reduction is carried out leading directly to a table and plot of $P_{np}(\theta_{cm})$, with errors, as a function of θ_{cm}. The time required for calculation is typically 1 s of c.p.u. time per angle bin on a Univac-1106 computer.

An example of a measurement of $P_{np}(\theta_{cm})$ for 21.6 MeV incident neutrons is shown in fig. 7a. The data shown in this figure are discussed in another publication[5]).

5. Limitations and uncertainties

Although *LS* spectra (figs. 2 and 3) may be obtained which include proton recoils at angles extending over most of the kinematically allowed recoil angle range, $\theta < 90°$, only the data at laboratory recoil angles less than about 70° are suitable for analysis. Recoils at larger angles lead to events in the lower pulse height region of the spectrum and cannot be resolved from other components in this region, notably the protons and alpha particles from neutron-induced reactions on carbon. Furthermore, the fractional dispersion $F(\theta)$ given by eq. (2) drops off at $\theta > 70°$, as can be appreciated from fig. 4, and the resolution of the left–right asymmetry determination is consequently impaired. This latter difficulty could be partially overcome by using a different crystal orientation e.g. $(\alpha, \beta) = (45°, 40°)$ instead of $(60°, 40°)$, but then $F(\theta)$ would be smaller at small recoil angles ($\theta \lesssim 40°$) and the sensitivity for asymmetry measurements at these angles would be reduced.

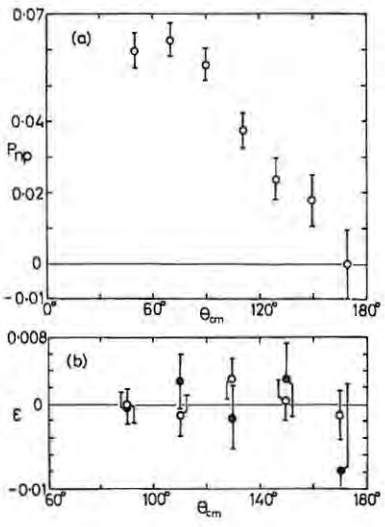

Fig. 7. Polarization P_{np} and asymmetry ε vs neutron cm scattering angle θ_{cm} for incident neutrons of energy 21.6 MeV: (a) polarization measurements; and (b) null asymmetries determined either by using an unpolarized incident neutron beam (solid circles) or from analysis of a pair of A spectra (open circles). The error bars in (a) were calculated from eq. (13). The error bars in (b) are statistical only and were calculated from eq. (12).

Multiple neutron scattering in the anthracene crystal could lead to errors in the polarization measurement, especially if the primary scattering was on carbon, for which the energy loss is small and the analysing power can be high. This problem could be serious with larger crystals, but it appears to be unimportant at the neutron energies ($E_n > 10$ MeV) and for the small crystals used to date. The linear dimensions of these crystals are about 2 cm or less and therefore correspond to less than one-tenth of the incident neutron mean free path at these energies.

On the other hand, for small crystals and for neutrons of energy greater than 10 MeV, the fraction of recoil protons escaping from the crystal is appreciable. However, problems that could arise from this effect are largely avoided by the fact that the escaped protons form a separate ridge in the *LS* spectrum (E in fig. 3) and can therefore be excluded to a large extent by proper choice of the integration limits for the asymmetry calculations. The effect of any residual escape component is to dilute the observed asymmetry without introducing spurious asymmetries. This dilution can be estimated and corrected for by using the data obtained in calibration runs, such as that shown in fig. 2a of ref. 1, in which the escape ridge is clearly resolved from the main proton structure.

The fact that virtually every recoil proton is detected has an important consequence when we estimate the statistical uncertainty on an asymmetry measurement within a particular angle bin. The experimental method assigns *every* recoil within a given bin as either "low", if $S < S_m(\theta)$, or "high" if $S > S_m(\theta)$, where θ is the mean recoil angle for the bin. Each recoil either adds one count to, or subtracts one count from, the difference ΔN between the number of low-S and high-S recoils in the bin θ. Therefore, since the difference ΔN is in principle determined directly, ΔN_A and ΔN_B may be regarded as primary observations in the experiment and we can in consequence show that the statistical error $\Delta\varepsilon(\theta)$ may be estimated from

$$\Delta\varepsilon(\theta) = (\pi/4N)\left[|\Delta N_A| + |\Delta N_B| + N^{-1}(\Delta N_A^2 + \Delta N_B^2)\right]^{\frac{1}{2}}. \quad (12)$$

From eqs. (9) and (12) it can be seen that for a given N and a given $\varepsilon(\theta)$ the statistical error $\Delta\varepsilon(\theta)$ will be a minimum if $\Delta N_A = -\Delta N_B$. The definition of $S_m(\theta)$

as the median value of the summed A and B spectra in fact ensures this equality and thereby helps to minimize the statistical error.

The systematic errors to which the polarization measurements are also subject include firstly those caused by imprecise knowledge of the incident neutron polarization P_0 and secondly those which may arise from experimental asymmetries or errors which pass undetected and therefore uncorrected in the measurement. Making allowance for these we can express the error $P_{np}(\theta_{cm})$ on the neutron polarization measurement by

$$\Delta P_{np}(\theta_{cm}) = |P_0^{-1}| \{[\Delta\varepsilon(\theta)]^2 + + (\Delta\varepsilon_{sys})^2 + [P_{np}(\theta_{cm})\, \Delta P_0]^2\}^{\frac{1}{2}}, \quad (13)$$

where $\Delta\varepsilon_{sys}$ represents the undetected false asymmetry and ΔP_0 the uncertainty on the polarization of the incident neutron beam.

We may estimate an upper limit for the systematic error $\Delta\varepsilon_{sys}$ by measuring a known null asymmetry under conditions simulating those of the actual asymmetry measurement. One way of carrying out a null test is to measure recoil proton asymmetries in the scattering of an unpolarized incident neutron beam, such as that obtained at the angle $\zeta = 0°$ from the T(d,n) reaction. The results of such a test are shown in fig. 7b. Alternatively a null asymmetry should be obtained if like runs are paired (i.e. A and A, or B and B, instead of A and B) and this can be checked using runs obtained at different angle settings. For example suppose that we have a set of four runs consisting of two A runs at (ζ, α) and $(-\zeta, 2\pi-\alpha)$ respectively and two B runs at $(-\zeta, \alpha)$ and $(\zeta, 2\pi-\alpha)$ respectively. From this set we can obtain two independent null checks, based on the A pair and B pair respectively, as well as two independent asymmetry measurements based on AB pairings. The results of a null check of this type are shown in fig. 7b. The error bars shown in fig. 7b represent the statistical errors only. Both null checks are seen to give asymmetries which are consistent with zero. From such checks an upper limit of $\Delta\varepsilon_{sys} = 0.0011$ was deduced and was then used in eq. (13) to calculate the total polarization errors shown in fig. 7a.

6. Discussion

A comparison of the statistical precisions of polarization values obtained by the present method with those obtained in experiments based on conventional double-scattering geometry is of interest. The two methods are similar up to the point that a polarized incident neutron beam is sampled by n–p scattering in an hydrogenous scatterer. In the present method the recoil proton associated with each scattering is observed and analysed as to recoil angle and direction (left or right) without further statistical sampling. In the double scattering method, however, further statistical sampling occurs in the detection of scattered neutrons by two identical detectors which are disposed at equal angles θ on either side of the incident neutron beam. The primary observations in the double scattering geometry are therefore the counts N_1 and N_2 recorded by these detectors for a given number of scatterings in the scatterer. The asymmetry is given by

$$\varepsilon(\theta) = (N_1 - N_2)/(N_1 + N_2), \quad (14)$$

and the standard deviation $\Delta\varepsilon(\theta)$ is estimated from

$$\Delta\varepsilon(\theta) = [4N_1 N_2/(N_1 + N_2)^2]. \quad (15)$$

A comparison of eqs. (12) and (15) for small asymmetries, $|\varepsilon| < 0.1$, and for the same total number of neutrons detected, namely $N_1 + N_2 = N_A + N_B = 10^4$, is shown in fig. 8. Curve (a) shows the standard deviation given by eq. (12) and curve (b) shows the standard deviation given by eq. (15). The comparison in fig. 8 shows that even for asymmetries as large as 10% the statistical errors obtained using the present method should be lower by at least a factor of two than those obtained using the double scattering method. For very small asymmetries in particular the statistical precision of the present method exceeds that of the double scattering method by a much larger factor, more than an order of magnitude for example for $\varepsilon < 0.01$.

The present method is therefore well suited to the

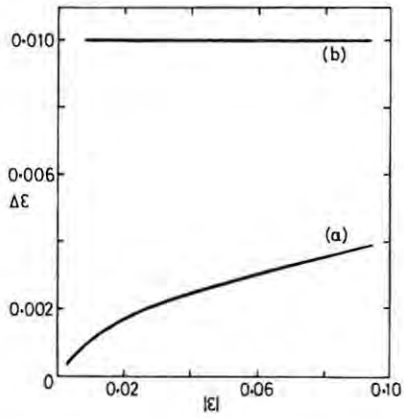

Fig. 8. The statistical error $\Delta\varepsilon$ on the asymmetry ε as a function of $|\varepsilon|$ for a total of 10^4 neutrons detected: (a) by the present method [from eq. (12)]; and (b) if the scattered neutrons are detected [from eq. (15)].

measurement of small asymmetries and should offer advantages in studies of the small polarizations in n–p scattering at neutron energies less than 30 MeV. It is a single-scattering method and is therefore less demanding of neutron beam intensity than double-scattering experiments. Background levels should, in consequence, also be lower than in the double scattering method. The ability to make simultaneous polarization measurements over a range of neutron scattering angles ($\theta_{cm} \approx 50°$–$170°$) is also an advantage. A limitation on the other hand is the resolution on the centre-of-mass scattering angle, which is about 10° for 16 MeV neutrons and is expected to be larger (i.e. worse) at lower energies. This resolution is tolerable in the case of n–p scattering, however, because the polarization P_{np} is expected to be a slowly varying function of θ_{cm}.

The method also has advantages of experimental simplicity. In particular the electronic system required (fig. 1b of ref. 1) is simple and the capacity to tolerate small mechanical misalignments, the effects of which are eliminated in the redispersion stage of the data reduction, is also an advantage. The data reduction process itself, although complex in principle, is simple and straightforward in practice.

The anthracene polarimeter has been used to date with two different crystals, A and B of ref. 1, to study the polarizations in n–p scattering at 16 and 22 MeV. The results will be published elsewhere[5]). Further studies are now being made at other neutron energies in the range 8–30 MeV. It appears that the method will become less effective at neutron energies lower than 8 MeV because the directional resolution of anthracene as indicated by the parameter R in table 3 of ref. 1, drops off with recoil proton energy. On the other hand the polarimeter should be suitable for work at higher neutron energies than 30 MeV and may well prove more effective at these energies than at lower energies, provided crystals large enough to avoid excessive proton escape are used.

We thank Mr P.A. Back for construction of much of the equipment used, the staff of the Southern Universities Nuclear Institute for their cooperation and our colleague Mr G. Pauletta for his assistance in these experiments. We also thank the South African Council for Scientific and Industrial Research for financial support and for a bursary to one of us (D.T.L.J.).

References

1) F. D. Brooks and D. T. L. Jones, Nucl. Instr. and Meth. **121** (1974) 69.

2) F. D. Brooks and D. T. L. Jones, Proc. 3rd Intern. Symp. on *Polarization phenomena in nuclear reactions* (eds. H. H. Barschall and W. Haeberli; Univ. of Wisconsin Press, Madison, 1971) p. 430.

3) F. D. Brooks, Nucl. Instr. and Meth. **4** (1959) 151; F. D. Brooks, R. W. Pringle and B. L. Funt, IEEE Trans. Nucl. Sci. **NS-7** (1960) 35.

4) J. B. Birks, *The theory and practice of scintillation counting* (Pergamon Press Ltd., London, 1967).

5) D. T. L. Jones and F. D. Brooks, Nucl. Phys. **A222** (1974) 79.

A scintillation polarimeter for n-p scattering studies
Nucl. Instr. and Meth. 121 (1974) 77-85

1.B: 2.B

Nuclear Physics A222 (1974) 79—92; © *North-Holland Publishing Co., Amsterdam*

POLARIZATION IN NEUTRON-PROTON SCATTERING AT 16.4 AND 21.6 MeV

D. T. L. JONES † and F. D. BROOKS

Physics Department, University of Cape Town, Rondebosch, C.P., South Africa

Received 4 January 1974

Abstract: The polarization in neutron-proton scattering was studied using polarized neutron beams obtained from the ^{3}H(d, n) reaction, scattering these beams in monocrystalline anthracene scintillators and observing the asymmetry of the associated recoil protons. The technique used is a new one which utilizes the direction dependence of the scintillation properties in order to determine the left-right asymmetry of the proton recoils within the scintillation crystal. The measurements led to polarization values at neutron c.m. scattering angles from 90° to 150° at 16.4 MeV and from 50° to 170° at 21.6 MeV, in 20° steps in both cases. The Δ^{P}_{LS} and Δ^{D}_{LS} spin-orbit splitting phase parameters derived from the measurements are: $0.52° \pm 0.06°$ and $0.02° \pm 0.05°$ respectively at 16.4 MeV; and $0.93° \pm 0.04°$ and $0.11° \pm 0.02°$ respectively at 21.6 MeV. The data are compared with the predictions of the Yale-Buffalo and Livermore phase parameter fits.

E NUCLEAR REACTIONS H($\vec{n}$, n), $E = 16.4, 21.6$ MeV; measured polarization $(P)\theta$; deduced spin-orbit splitting parameters. Natural target.

1. Introduction

The phenomenological knowledge of the nucleon-nucleon interaction as determined by the energy dependent Livermore [1]) and Yale-Buffalo [2]) phase parameter analyses is now reasonably unambiguous above 30 MeV. These analyses are based essentially on all the p-p and n-p scattering data up to several hundred MeV.

The $T = 1$ phase parameter determinations agree fairly well below 30 MeV. These parameters can be determined solely from the p-p scattering data, which have reached an advanced level of accuracy. The situation is less favourable for the $T = 0$ case, however, where the parameters must be determined from the sparser and less precise n-p scattering data. More accurate n-p data are needed, particularly in order to determine the behaviour of the S-D coupling parameter and the $^1\mathrm{P}_1$ phase shift. Further data on the polarization in n-p scattering are also of immediate interest because they lead directly to values for the phase parameters Δ^{P}_{LS} and Δ^{D}_{LS}, representing the expectation values in Born approximation of the spin-orbit interaction in the P- and D-states.

Polarizations in n-p scattering below 30 MeV are of the order of a few percent and are therefore difficult to measure with the precision required for the phase parameter

† Present address: Physics Department, University of Wisconsin, Madison, Wisc. 53706, USA.

analyses. The present work is an attempt to make more accurate measurements of the n-p polarization in the 10 to 30 MeV region using a new technique which reduces some of the technical difficulties involved. The method utilizes the directional effects associated with the scintillation properties of anthracene crystals [3]). The potential advantages of this method in comparison with the usual double scattering technique lie in its experimental simplicity. A single scintillation crystal provides the means to detect and identify both left and right scatterings, all scatterings are detected and a range of scattering angles can be studied simultaneously. In addition, since it is the associated recoil protons which are detected, no further sampling is required and consequently the statistical accuracy is improved.

2. Experimental method

The polarization in n-p scattering was studied at 16.4 and 21.6 MeV using polarized monoenergetic neutron beams obtained from the ^{3}H(d, n)^{4}He reaction. The deuteron beam was provided by the 5.5 MV Van de Graaff accelerator of the Southern Universities Nuclear Institute, Faure, C.P. Seven sets of measurements were made with minor variations in the tritium target, the anthracene crystal and other details. The experimental conditions for the seven sets of measurements are summarized in table 1. The tritium gas target referred to in table 1 was 3 cm long and was operated at a pressure of 0.7 atm. The solid targets were tritiated titanium (2.5 mg/cm^2), gold-backed and cooled by means of a cold finger immersed in liquid nitrogen. The anthracene crystal A was of irregular shape and mass 1.5 g and the crystal B was approximately cylindrical with height and diameter both 2.1 cm. In three of the seven sets of measurements the primary component in the neutron spectrum from the ^{3}H(d, n) source was selected by time of flight gating. The neutron flight path for these runs was 0.5 m and the timing resolution (FWHM) was 1.5 ns.

The anthracene crystal was mounted on a magnetically shielded photomultiplier tube fitted with a pulse shape discrimination (PSD) circuit [4]). The photomultiplier provided a fast output for time-of-flight analysis, a linear output L, which was pro-

TABLE 1
Experimental details

Set	A	B	C	D	E	F	G
E_d (MeV)	5.0	4.0	4.0	5.0	5.0	5.0	5.35
ζ (deg)	80	80	85	20	20	20	30
E_n (MeV)	16.9	16.2	16.0	21.6	21.6	21.6	21.4
P_0	−0.42	−0.31	−0.31	0.21	0.21	0.21	0.30
ΔP_0	0.02	0.02	0.02	0.01	0.01	0.01	0.02
Target	solid	gas	solid	gas	solid	solid	solid
Crystal	A	A	A	B	A	A	A
TOF	no	no	yes	no	yes	no	yes

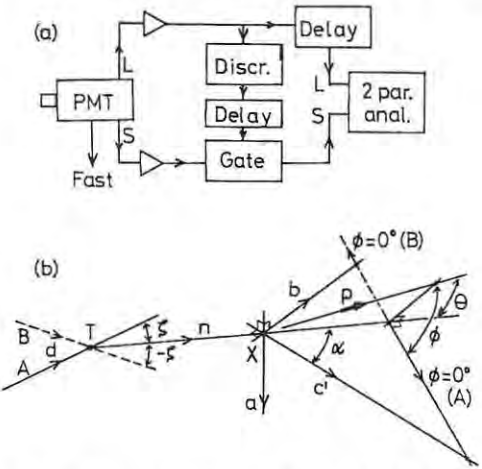

Fig. 1. (a) Block diagram of electronic system. (b) Schematic diagram of experimental geometry showing: tritium target T; centre X of anthracene crystal; mutually perpendicular crystal axes *a*, *b* and *c'*; deuteron and neutron beams d and n; and recoil proton p. The dashed lines indicate the changes implied by a switch from position A to position B. The ϕ-axis is defined by projecting the deuteron beam onto the plane normal to the neutron beam.

portional to the total light in the scintillation, and a PSD output S which depended non-linearly on the proportion of slow component in the scintillation decay. The outputs L and S were processed by the electronic system shown in fig. 1a and fed into a two-parameter analyser. The raw data from each experimental run therefore consisted of a two-parameter spectrum of counts versus L versus S. We refer to these spectra as LS spectra.

The laboratory geometry is shown schematically in fig. 1b. A monoenergetic neutron beam was taken at angle ζ from the ^{3}H(d, n) reaction, with the neutron and deuteron beams both in the horizontal plane. The orientation of the anthracene crystal to the neutron beam was determined with reference to the crystal axes in the manner outlined below.

The pulse height anisotropy properties of anthracene for protons are such [3]) that L is a minimum for protons moving in directions parallel to the b-axis of the crystal and a maximum for directions parallel to the artificial c' axis. The c' axis is defined as the direction perpendicular to the mutually perpendicular a- and b-axes of the crystal. The PSD anisotropy characteristics [3]) of the crystal are such that S is a maximum when L is minimum and *vice versa*. In order to observe the left-right asymmetry of proton recoils the crystal is oriented so that its a-axis is vertical and so that the neutron beam makes an angle $\alpha = 60°$ with the c' axis, as shown in fig. 1b. The angle α is adjusted by rotating the crystal about its a-axis. At the setting $\alpha = 60°$ the S-output for a recoil at a given angle in the horizontal plane differs according to whether the recoil is to left or to right of the neutron beam. The output is lower for recoil directions which tend towards the c' axis. We define two positions A and B

(fig. 1b) at this asymmetry orientation depending whether a proton recoil from the neutron beam towards the c' axis is in the same sense (A) or the opposite sense (B) as the deflection from the deuteron beam to the neutron beam. We can change from position A to position B by changing ζ to $-\zeta$, as indicated in fig. 1b or by rotating the crystal through 180° about the neutron beam or by rotating the crystal about the (vertical) a-axis until the c' axis makes an angle $(2\pi - \alpha)$ with the neutron beam. The photomultiplier is mounted in such a way that any one of these angles may be adjusted without affecting the other two.

An LS spectrum obtained with an anthracene crystal oriented as shown in fig. 1b and a neutron energy of 21.6 MeV is shown as an isometric plot in fig. 2 and as a contour plot in fig. 3. The structure in this spectrum is attributed [3]) to (see fig. 3): Compton electrons (C): recoil protons (P_1 and P_2); escaped recoil protons (E); and α-particles (A) from neutron reactions on the carbon in the crystal. The recoil proton component splits into two ridges P_1 and P_2 over most of the L-range shown in the spectrum. We associate these two ridges with protons recoiling into the forward quadrants on either side of a vertical plane through the neutron beam. The ridge P_1 corresponds to recoils into the quadrant containing the c' axis and P_2 to recoils into the quadrant containing the b-axis. By comparing the number of counts under each ridge we can determine the left-right asymmetry of the proton recoils within the crystal.

The proton component of the LS spectrum includes recoils at lab angles ranging from 0° to almost 90°. The pulse height L depends on the energy E_p and on the

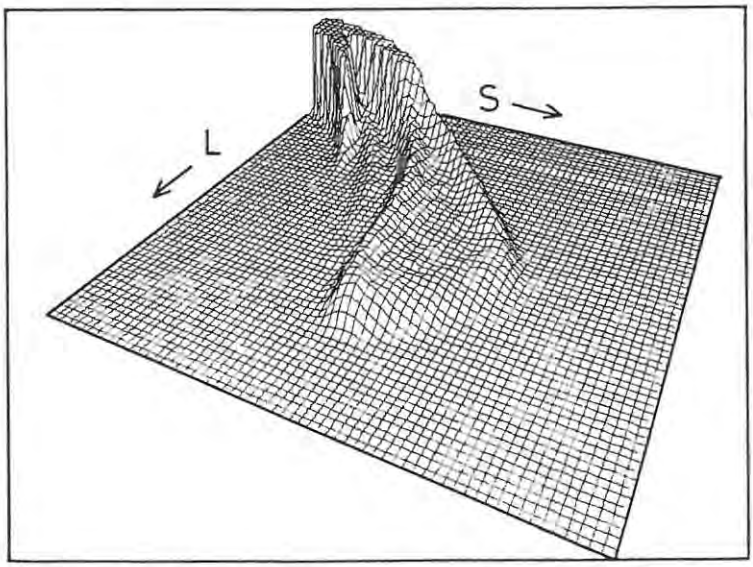

Fig. 2. Isometric plot of an LS spectrum obtained for 21.6 MeV neutrons incident on the anthracene crystal. The spectrum shows counts (vertical) versus pulse height L versus PSD output S. The limiting value of the count scale is 500.

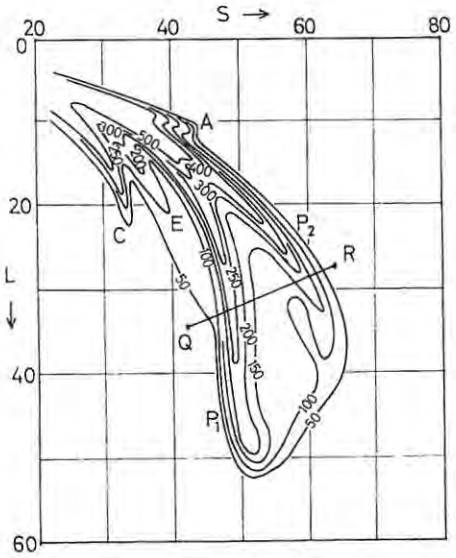

Fig. 3. Contour plot of the LS spectrum shown in fig. 2. The ridges in the spectrum are identified as follows: Compton electrons, C; recoil protons, P_1 and P_2; escaping recoil protons, E; and α-particles, A. The line QR represents the locus of a constant recoil angle θ.

direction of the recoil proton. The proton direction is specified by the angle of recoil θ relative to the neutron beam and the azimuthal angle of recoil ϕ, as illustrated in fig. 1b. The energy E_p is related to the angle θ and the incident neutron energy E_n by

$$E_p = E_n \cos^2 \theta. \tag{1}$$

From measurements [3]) of the L- and S-anisotropies we know that the loci of constant E_p and hence of constant recoil angle θ approximate to straight lines across the LS plane, such as the line QR in fig. 3. By defining a series of such lines we can therefore divide the proton region of the LS spectrum into angle bins corresponding to different recoil angles. In principle therefore a single LS spectrum contains sufficient information to determine the left-right asymmetry as a function of recoil angle over a wide range of recoil angles. At the crystal orientation used the S-outputs S_m for recoils at azimuths $\phi = 90°$ and 270° should ideally be identical. Recoils having azimuths in the range $\phi = 0° \pm 90°$ should therefore have $S < S_m$ and those with azimuths in the range $\phi = 180° \pm 90°$ should have $S > S_m$ in position A, and *vice versa* in position B. Thus a comparison of counts below and above S_m, within each bin, should measure the recoil asymmetry averaged over ϕ, for the recoil angle corresponding to the bin.

In practice it is not possible to determine asymmetries from a single LS spectrum because it is impossible to specify S_m sufficiently accurately. However this difficulty is avoided if, instead of analysing single LS spectra, we determine the asymmetry by comparing two spectra, one taken in position A and the other in position B. The recoils which contributed to ridge P_1 in position A contribute to ridge P_2 in position B and

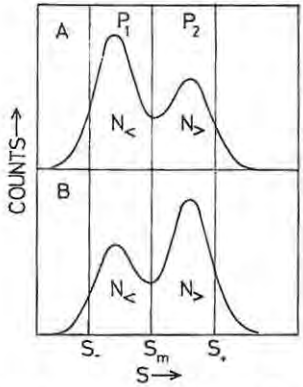

Fig. 4. Schematic illustration of projected A and B spectra for a single angle bin. Here S_- and S_+ are points of inflection in the spectra. The spectra are normalized to equal total proton counts N. Also, S_m is the median of the summed A and B spectra.

vice versa, hence the *change* in the relative intensities of P_1 and P_2 on changing positions is a measure of the left-right asymmetry of the proton recoils. The asymmetry in thus determined as a function of recoil angle from a comparison within each angle bin of the relative number of counts under ridges P_1 and P_2 in the A and B spectra.

The methods used to define the angle bins and to calculate the recoil proton asymmetry within each bin are described in detail in ref. [3]). In brief outline the main steps in this process involve: firstly, transforming or redispersing the *LS* spectra with respect to *S*, into a form convenient for defining angle bins; secondly, defining the angle bins; and thirdly, projecting the A spectrum and the B spectrum within each bin onto the *S*-axis and calculating the asymmetry.

The projected A and B spectra for a single angle bin are illustrated schematically in fig. 4. Ideally the points of inflection S_- and S_+ should coincide for the two spectra. This is not always true in practice, due for example to small mechanical misalignment of the apparatus. However the linear transformation of the spectra in the process of redispersion ensures that these points of inflection are so aligned after this transformation has been made. The A and B spectra are normalized to the same total number N of proton counts and the value S_m corresponding to $\phi = 90°$ or $270°$ is taken as the median of the sum of these spectra, i.e. the median of the spectrum, (A+B).

In the A spectrum the integrated counts $N_<$ and $N_>$ in the regions below and above S_m correspond to recoils having ϕ in the ranges $0°\pm90°$ and $180°\pm90°$ respectively. In the B spectrum this correspondence is reversed. Defining ΔN as the difference $(N_< - N_>)$ between the proton counts below and above S_m, we can show that the proton recoil asymmetry is given by [3]):

$$\varepsilon(\theta) = \frac{\pi}{4N}(\Delta N_A - \Delta N_B), \tag{2}$$

/here the suffixes A and B refer to the A and B spectra respectively. The asymmetry iven by eq. (2) is insensitive to small errors in S_m because systematic errors cancel in he difference $(\Delta N_A - \Delta N_B)$ and because $\cos\phi$, which is a multiplicative factor in the olarization term in the n-p scattering cross section, is zero at $\phi = 90°$ or 270°, the zimuthal recoil angles which are associated with a PSD output S_m.

The analysing power for proton recoils at the mean recoil angle θ is given by

$$P(\theta) = \varepsilon(\theta)/P_0, \tag{3}$$

/here P_0 is the polarization of the incident neutron beam. With negligible error we an assume that the polarization in n-p scattering P_{np} at the associated neutron c.m. cattering angle $\theta_{c.m.} = \pi - 2\theta$ is given by

$$P_{np}(\theta_{c.m.}) = -P(\theta). \tag{4}$$

The standard deviation ΔP_{np} of the polarization P_{np} has a statistical component, a ystematic component and a component contributed by the uncertainty ΔP_0 on the ncident neutron polarization. The expression for ΔP_{np} is [3])

$$\Delta P_{np} = |1/P_0|((\Delta\varepsilon)^2 + (\Delta\varepsilon_{sys})^2 + (P_{np}\Delta P_0)^2)^{\frac{1}{2}}. \tag{5}$$

he component $\Delta\varepsilon$, representing the statistical error on the asymmetry measurement, s estimated from [3])

$$\Delta\varepsilon = (\pi/4N)(|\Delta N_A| + |\Delta N_B| + (1/N)(\Delta N_A^2 + \Delta N_B^2))^{\frac{1}{2}}. \tag{6}$$

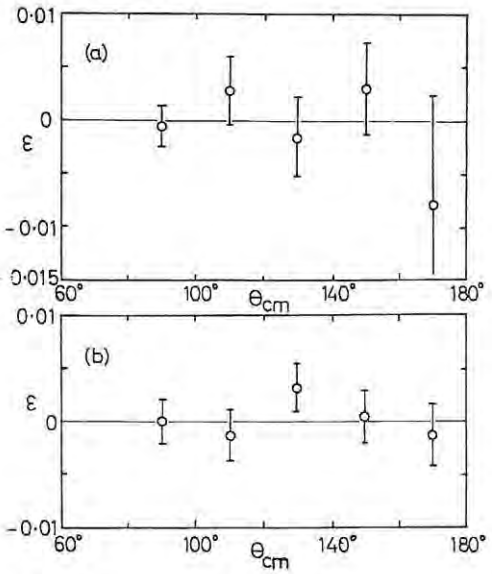

ig. 5. Measurements of null asymmetries obtained: (a) using an unpolarized 22 MeV incident eutron beam (at $\zeta = 0°$); and (b) from the analysis of a pair of A spectra obtained at , α) = (30°, 60°) and (−30°, 300°) respectively in the G series of runs (see table 1).

The systematic error component $\Delta\varepsilon_{sys}$ in eq. (5) was estimated by means of two different kinds of experiments. In the first method the proton asymmetry was measured for unpolarized incident neutrons emitted at the angle $\zeta = 0°$ from the ^{3}H(d, n) source. The results of such a measurement are shown in fig. 5a. In the second method the asymmetries obtained by pairing like runs (i.e. A and A or B and B instead of A and B) at different angle settings, e.g. (ζ, α) and $(-\zeta, 2\pi-\alpha)$, were studied. The results of such a test are shown in fig. 5b and are seen to be consistent with zero asymmetry at every recoil angle. The null measurements and tests gave an upper limit of $\Delta\varepsilon_{sys} = 0.0011$. This value was used in the calculation of standard errors $\Delta P_{np}(\theta)$ from eq. (5).

Two points should be mentioned which relate to the standard errors obtained. Firstly the fact that the recoil protons associated with neutron scatterings are detected leads to smaller statistical errors than would be obtained under equivalent conditions using neutron detection. Secondly the redispersion of the *LS* spectra in the data reduction process helps to eliminate small systematic errors that might otherwise be introduced, for example errors arising from imperfect alignment of the anthracene crystal with respect to the neutron beam. These two points are more fully discussed in ref. [3]).

3. Results and discussion

The detailed results obtained in the seven sets of measurements denoted A-G in table 1 are listed in table 2. Measurements A-C are grouped into one set corresponding to an incident energy of 16.4 MeV and measurements D-G into a second set corresponding to an incident energy of 21.6 MeV. The small energy variations within each set are neglected in view of the fact that the polarization P_{np} varies slowly and smoothly with neutron energy. The polarization values were calculated for c.m. angle bins of width 20°, a width which comfortably exceeds that corresponding to the pulse height resolution of the anthracene crystal over the proton energy range of interest.

The different sets of measurements shown in table 2 span different ranges of c.m. scattering angle because experimental conditions varied from one set to another. Polarization values were obtained for mean c.m. scattering angles ranging from 90° to 150° for the 16.4 MeV data and from 50° to 170° for the 21.6 MeV data. Background effects, especially those resulting from reactions on the carbon within the scintillator limit the measuring technique [3]) to c.m. scattering angles larger than 50°. The use of time-of-flight gating helped to suppress backgrounds from low-energy neutrons in some of the measurements. However tests showed that such gating was not essential provided that well-focussed deuteron beams and clean tritium targets were used in the ^{2}H(d, n) neutron source.

The results shown in table 2 supersede the preliminary values reported by us [5]) at the Madison symposium in 1970.

TABLE 2
Results of polarization measurements

E_n (MeV)	$\theta_{c.m.}$ (deg)	$P_{np}(\theta_{c.m.})$ [a]				ΔP_{stats}	Average $P_{np}(\theta_{c.m.})$ [b]
		set A	set B	set C			
16.4	90	0.031±0.003	0.029±0.004	0.031±0.003		0.002	0.030±0.004
	110		0.027±0.007			0.007	0.027±0.008
	130		0.020±0.009			0.009	0.020±0.010
	150		0.009±0.012			0.012	0.009±0.013
		set D	set E	set F	set G		
21.6	50	0.060±0.002				0.002	0.060±0.005
	70	0.067±0.003	0.064±0.011	0.061±0.002		0.002	0.063±0.005
	90	0.057±0.002	0.052±0.014	0.054±0.003	0.056±0.002	0.001	0.056±0.005
	110	0.032±0.003	0.037±0.015	0.050±0.007	0.057±0.006	0.002	0.038±0.005
	130	0.022±0.005	0.023±0.018	0.026±0.007	0.028±0.007	0.003	0.024±0.006
	150	0.020±0.009		0.014±0.007	0.022±0.009	0.005	0.018±0.007
	170	−0.006±0.018		0.002±0.011		0.009	0.000±0.010

[a]) Errors are statistical only.
[b]) Errors are statistical plus systematic.

The incident polarization values assumed for the polarization calculation (see table 1) were based on data quoted in the review article by Walter [6]). The standard errors quoted for the individual measurements A–G in table 2 are statistical only, i.e. those given by the first term of eq. (5). The data at each energy and angle were weighted in proportion to the inverse squares of their statistical errors to calculate the average polarization for that energy and angle. The resulting average polarization values are shown in the last column of table 2 and their associated statistical error components in the second last column of this table. The standard errors quoted together with the polarization values in the last column of table 2 include systematic error components corresponding to the second and third terms of eq. (5). The combined uncertainties contributed by these terms were $\Delta P = 0.004$ for the 16.4 MeV data and $\Delta P = 0.005$ for the 21.6 MeV data, at all scattering angles.

It should be noted that multiple neutron scattering effects in the anthracene crystals are presumed to have been small owing to the small size of the crystals used. Therefore no corrections have been made for such effects. The escape of recoil protons from the crystals on the other hand, was known to be appreciable. However as pointed out in ref. [3]),the pulse shape discrimination technique effectively discriminates against escaping protons by placing them on a separate ridge, E in fig. 3, in the LS spectrum. Therefore, since advantage was taken of this discrimination, no corrections were required for the effects of proton escape.

The polarization values are plotted against neutron c.m. scattering angle in fig. 6 (16 MeV data) and fig. 7 (22 MeV data) together with published data [7–11]) at or

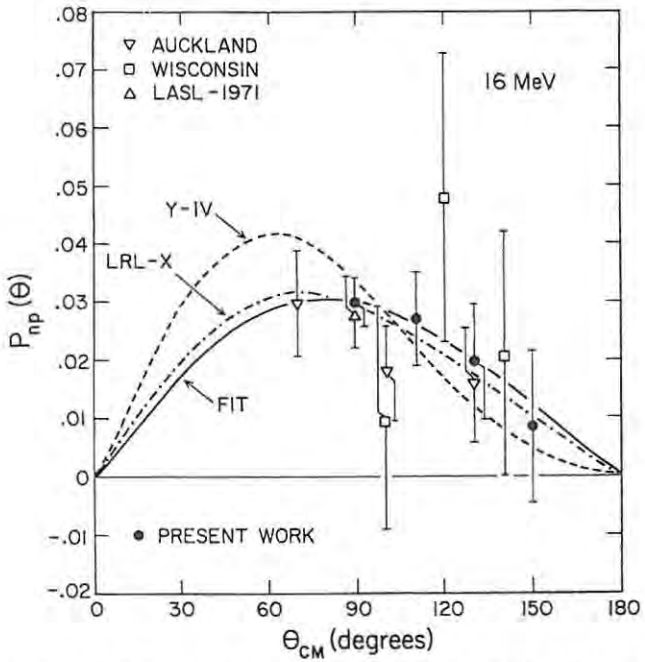

Fig. 6. Polarization versus neutron c.m. scattering angle for incident neutron energies near to 16 MeV. The data shown are: □ – ref. [7]) (16.4 MeV); △ – ref. [10]) (16.8 MeV); ▽ – ref. [11]) (16.2 MeV); ● – present work (16.4 MeV). The solid curve shows the fit based on eq. (7). The broken curves show the predictions of the $(\text{Y-IV})_{pp+np}$ and LRL-X (ε_1 constrained) phase parameter solutions at 16 MeV.

near to these energies. Some of the earlier data have been adjusted to take account of the more accurate source polarization values that have become available since these data were first published. The effects of these adjustments were to decrease the data of Benenson *et al.* [7]) by 10 % at 16.4 MeV and 26 % at 23.7 MeV and to increase the data of Perkins and Simmons [8]) at 23.1 MeV by 4 %. The present data are consistent with the previous values but are slightly and systematically higher than the other data near to 22 MeV.

Theoretical curves based on the Yale-Buffalo [2]) and the Livermore [1]) phase parameter solutions are also shown in figs. 6 and 7. The Yale-Buffalo curve corresponds to the $(\text{Y-IV})_{pp+np}$ solution using the n-p $T = 1$ phases and was calculated for the case of recoil protons detected. The Livermore curve corresponds to the LRL-X (ε_1 constrained) phase parameter solution and was calculated for the case of neutrons detected. The present data at 16 MeV are consistent with both theoretical curves but if all the data at this energy are taken into account the LRL-X solution appears to be favoured. At 22 MeV the present data are better fitted by the Yale-IV solution whereas the other measurements tend to favour the LRL-X solution.

In the 10 to 30 MeV region the polarization in n-p scattering is related in a simple way to the triplet P and triplet D phase shifts. If the phase shifts are assumed to be

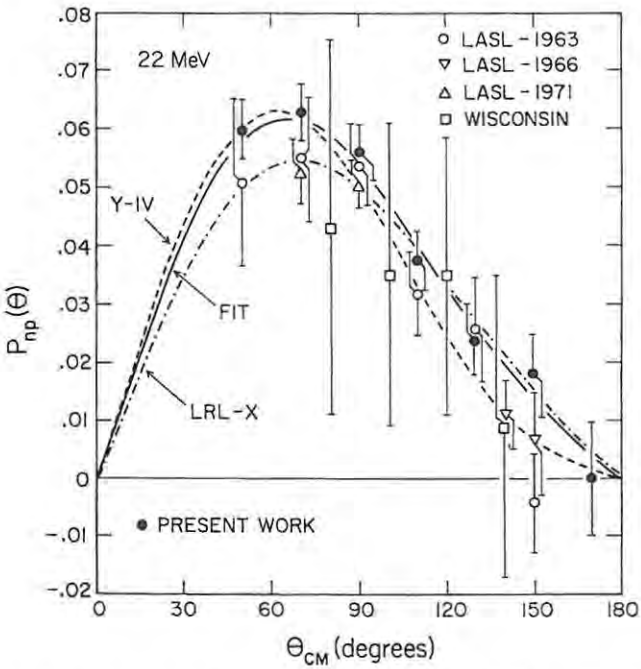

Fig. 7. Polarization versus neutron c.m. scattering angle for incident neutron energies near to 22 MeV. The data shown are : □ – ref. [6]) (23.7 MeV); ○ – ref. [8]) (23.1 MeV); ▽ – ref. [9]) (23.1 MeV); △ – ref. [10]) (23.1 MeV); ● – present work (21.6 MeV). The solid curve shows the fit based on eq. (7). The broken curves show the predictions of the $(\text{Y-IV})_{pp+np}$ and LRL-X (ε_1 constrained) phase parameter solutions at 22 MeV.

small, as indeed they are, the n-p polarization is approximately represented by the expression [10])

$$P_{np}(\theta_{c.m.}) = \sin^2 \delta_{01} \sin \theta_{c.m.}(12\Delta_{LS}^{P}+60\Delta_{LS}^{D} \cos \theta_{c.m.})/4k^2\sigma(\theta_{c.m.}), \qquad (7)$$

where k is the c.m. wave number of the incident neutron, Δ_{LS}^{P} and Δ_{LS}^{D} are expectation values in the Born approximation of the spin-orbit interaction in the P- and D- states, and δ_{01} is the triplet S-wave phase shift. The parameters Δ_{LS}^{P} and Δ_{LS}^{D} are related to the phase shifts δ_{LJ} for orbital and total angular momenta L and J respectively by the expressions [10])

$$\Delta_{LS}^{P} = \tfrac{1}{12}(-2\delta_{10}-3\delta_{11}+5\delta_{12}), \qquad (8)$$

$$\Delta_{LS}^{D} = \tfrac{1}{60}(-9\delta_{21}-5\delta_{22}+14\delta_{23}). \qquad (9)$$

Thus at the level of approximation used in eq. (7) the magnitude of the polarization angular distribution relates to the spin-orbit splitting of $T = 1$ triplet P waves, whereas the shape of this distribution relates to the spin-orbit splitting in the $T = 0$ triplet D waves.

The Δ_{LS} parameters were determined by fitting experimental data to eq. (7). For this purpose the S-wave phase shift was calculated from the effective range formula using Houk's parameters [12]) and values $\delta_{01} = 91.9°$ and 84.5° were obtained at 16 and 22 MeV respectively. The differential elastic cross section was obtained from the expression [13])

$$\sigma(\theta_{c.m.}) = (\sigma_T/4\pi)(1 + b\cos\theta_{c.m.} + b\cos^2\theta_{c.m.})/(1+\tfrac{1}{3}b), \qquad (10)$$

where $b = (E_n/90)^2$ for E_n in MeV and the total n-p scattering cross section σ_T, which was obtained from Gammel's formula [13]), was 609 mb at 16 MeV and 438 mb at 22 MeV.

Fits were made to eq. (7) for thee combinations of the experimental data: firstly the present data alone; secondly all other data known to us [7-11]); and thirdly all data, i.e. other plus present. In each case each datum was weighted in proportion to the inverse square of the total error quoted for it. The Δ_{LS} parameters resulting from the fitting are shown in table 3 (for the 16 MeV data) and table 4 (for the 22 MeV data). The solid curves drawn in figs. 6 and 7 indicate the fits to the present data alone, at 16 and 22 MeV respectively. Values of the Δ_{LS} parameters given by the Yale-Buffalo and the Livermore phase solutions are also shown in tables 3 and 4.

The value of Δ^P_{LS} obtained from the fit to the present data at 22 MeV (see table 4) is significantly higher than the values obtained from the fit to previous measurements or from either of the phase analyses mentioned. However the fits to all three combina-

TABLE 3

Δ_{LS} phases at 16 MeV

Source	Δ^P_{LS} (deg)	Δ^D_{LS} (deg)
present data	0.52±0.06	0.02±0.05
refs. [7,10,11])	0.46±0.06	0.03±0.05
all data	0.50±0.05	0.02±0.04
$(Y-IV)_{pp+np}$ n-p	0.58	0.09
$(Y-IV)_{pp+np}$ p-p	0.54	
$(LRL-X)_{constrained}$	0.50	0.03

TABLE 4

Δ_{LS} phases at 22 MeV

Source	Δ^P_{LS} (deg)	Δ^D_{LS} (deg)
present data	0.93±0.04	0.11±0.02
refs. [7-10,14])	0.83±0.04	0.13±0.02
all data	0.88±0.03	0.12±0.02
$(Y-IV)_{pp+np}$ n-p	0.83	0.13
$(Y-IV)_{pp+np}$ p-p	0.76	
$(LRL-X)_{constrained}$	0.81	0.06

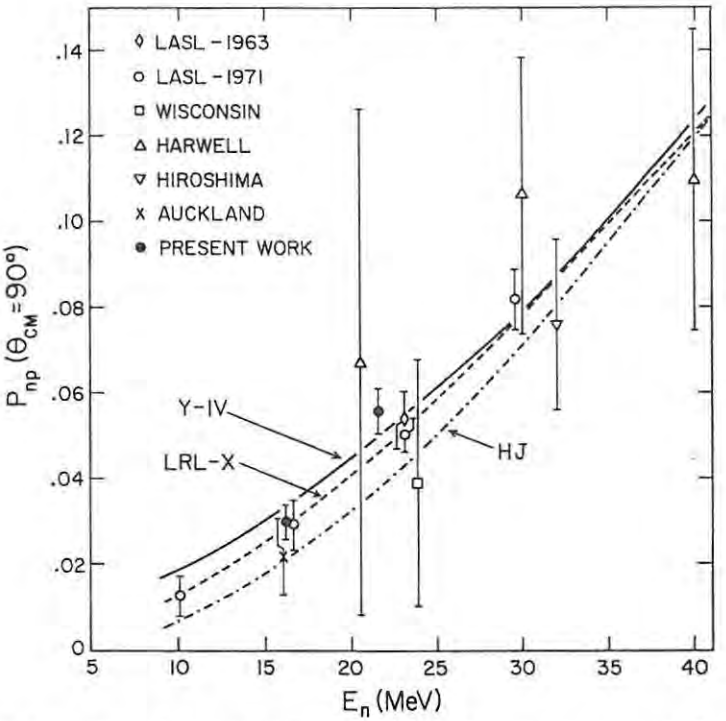

Fig. 8. Polarization at $\theta_{c.m.} = 90°$ as a function of incident neutron energy. The data shown are: □ – ref. [7]); ◇ – ref. [8]); ○ – ref. [10]); × – ref. [11]); △ – ref. [14]); ▽ – ref. [15]); ● – present work. The data of refs. [7,11,14]) have been linearly interpolated from measurements at neighbouring angles. The associated errors in these cases are those of a single measurement. The curves shown are based on the $(Y\text{-}IV)_{pp+np}$ and LRL-X (ε_1 constrained) phase parameter solutions and the Hamada Johnston (HJ) potential model.

tions of the 22 MeV data give values of Δ^{D}_{LS} which are consistent with the (Y-IV) phase solution but differ significantly from the (LRL-X) phase solution (table 4). The same is true for the Δ^{D}_{LS} values obtained at 16 MeV (table 3) except that the (LRL-X) phase solution is favoured rather than the (Y-IV) solution at this energy. The different Δ^{P}_{LS} values obtained at 16 MeV (table 3) are consistent with one another and with the predictions of both phase analyses.

From eq. (7) it can be seen that the polarization $P_{np}(\theta_{c.m.})$ for the scattering angle $\theta_{c.m.} = 90°$ is a measure of the phase parameter Δ^{P}_{LS}. Fig. 8 shows a plot of polarization measurements [7,11,14,15]) at this angle as a function of neutron energy. Theoretical curves based on the Yale-Buffalo and Livermore phase parameter solutions and on the Hamada-Johnston potential model [10,16]) are also shown. The data are significantly higher than the latter prediction but do not appear to favour either of the other solutions, which themselves diverge significantly below 20 MeV.

The Δ^{P}_{LS} parameter is of particular interest since the Yale-Buffalo phase analysis predicts isospin splitting of this parameter. The magnitude of the predicted splitting

is about 9 % at both 16 and 22 MeV as can be seen from tables 3 and 4. A comparison of the Δ^{P}_{LS} parameters determined independently from n-p and p-p data should indicate the presence and magnitude of the isospin splitting. Such a test has not proved meaningful in the past however, owing to the accuracy of the n-p data being insufficient. With the additional n-p data now available it might be possible to discern the isospin splitting. Further phase analyses based on all the n-p and p-p data now available should in any case be worthwhile and interesting.

We are grateful to Professor G. Breit, Dr. G. Pappas and Dr. M. Tischler for supplying the results of the (Y-IV) phase parameter calculations and to Professor M. H. MacGregor for supplying the results of the (LRL-X) phase parameter calculations. We are also indebted to Mr. P. A. Back for construction of the equipment used and to Mr. G. Pauletta and the staff of the Southern Universities Nuclear Institute for their assistance in running the experiments. We also wish to thank the South African Council for Scientific and Industrial Research for financial support and for a bursary to one of us (DTLJ).

References

1) M. H. MacGregor, R. A. Arndt and R. M. Wright, Phys. Rev. **182** (1969) 1714
2) R. E. Seamon, K. A. Friedman, G. Breit, R. D. Haracz, J. M. Holt and A. Prakash, Phys. Rev. **165** (1968) 1579
3) F. D. Brooks and D. T. L. Jones, Nucl. Instr., to be published
4) F. D. Brooks, Nucl. Instr. **4** (1959) 151
F. D. Brooks, R. W. Pringle and B. L. Funt, IRE Trans. Nucl. Sci. **NS-7** (1960) 35
5) F. D. Brooks and D. T. L. Jones, Proc. 3rd Int. Symp. on polarization phenomena in nuclear reactions, ed. H. H. Barschall and W. Haeberli (The University of Wisconsin Press, 1971) p. 430
6) R. L. Walter, Proc. 3rd Int. Symp. on polarization phenomena in nuclear reactions, ed. H. H. Barschall and W. Haeberli (The University of Wisconsin Press, 1971) p. 317
7) W. Benenson, R. L. Walter and T. H. May, Phys. Rev. Lett. **8** (1962) 66
8) R. B. Perkins and J. E. Simmons, Phys. Rev. **130** (1963) 272
9) J. J. Malanify, P. J. Bendt, T. R. Roberts and J. E. Simmons, Phys. Rev. Lett. **17** (1966) 481
10) G. S. Mutchler and J. E. Simmons, Phys. Rev. **C4** (1971) 67
11) R. Garrett, A. Chisholm, D. Brown, J. C. Duder and H. N. Bürgisser, Nucl. Phys. **A196** (1972) 421
12) T. L. Houk, Phys. Rev. **C5** (1971) 1886
13) J. L. Gammel, Fast neutron physics, part 2, ed. J. B. Marion and J. L. Fowler (Interscience, New York, 1963) p. 2185
14) A. Langsford, P. H. Bowen, G. C. Cox, G. B. Huxtable and R. A. J. Riddle, Nucl. Phys. **74** (1965) 241
15) N. Ryu, J. Sanada, H. Hasai, D. C. Worth, M. Nishi, T. Hasegawa, H. Ueno, M. Seki, K. Iwatani, Y. Nojira and K. Kondo, Nucl. Phys. **A180** (1972) 657
16) T. Hamada and I. D. Johnston, Nucl. Phys. **34** (1962) 382

D.T.L. Jones and F.D. Brooks

Polarization in neutron-proton scattering at 16.4 and 21.6 MeV

Nucl. Phys. A222 (1974) 79-92

1.B:2.A.1 *Nuclear Physics* A255 (1975) 267—274;

CROSS SECTIONS FOR THE n+d BREAKUP REACTION

G. PAULETTA † and F. D. BROOKS
Physics Department, University of Cape Town, Rondebosch 7700, South Africa

Received 5 September 1975

Abstract: The n+d breakup cross section has been measured between 8 and 22 MeV by integrating the energy distributions of breakup protons and recoil deuterons observed in a deuterated scintillator. The results obtained deviate from the trend suggested by recent measurements of the cross section for proton-induced breakup and favour predictions based on a local N-N potential having a hard core in the singlet state.

E NUCLEAR REACTIONS ^{2}H(n, 2n), E = 8.2–22 MeV; measured cross section. Enriched target.

1. Introduction

At energies between 100 eV and the threshold for pion production, deuteron breakup is the only significant process, other than elastic scattering, in the neutron-deuteron interaction. Consequently, it is important that calculations and phase analyses reproduce the total breakup cross section σ_b. Such calculations have indicated [1]) that the doublet state contributes significantly to this cross section. It is also well known that the doublet phases are sensitive to the details of the nuclear force, hence the same is expected to be true of the breakup cross section.

Recent theoretical predictions [1–5]) of σ_b at incident neutron energies exceeding 12 MeV have in fact proved sensitive to the nature of the N-N potential and invite comparison with experiment. Direct measurements of σ_b have been made at energies below 14.1 MeV [refs. [6–8])]. The only data available above this energy are those obtained indirectly [9–11]) by subtracting the cross section for neutron elastic scattering σ_e from the total neutron cross section of deuterium σ_t. However the accuracy of the indirect method is limited by the fact that σ_e is about twice as large as σ_b at these energies. The present work was motivated by the need for more direct measurements of σ_b, especially at energies above 12 MeV.

2. Experimental technique

In the present work a ratio proportional to σ_b/σ_e was obtained by bombarding deuterated liquid scintillators (NE230) with monoenergetic neutrons and observing the energy spectra of the protons and recoil deuterons produced. Neutrons were

† Present address: Institut de Physique, Université de Neuchâtel, 2000 Neuchâtel, Switzerland.

obtained from the ^{2}H(d, n) and ^{3}H(d, n) reactions using the pulsed deuteron beam from the 5.5 MV Van de Graaff accelerator of the Southern Universities Nuclear Institute, Faure, CP, South Africa. The scintillators were encapsulated in cylindrical glass cells. Cells of different size were used to test sensitivity to multiple neutron scattering in the scintillator and sensitivity to escape of protons and deuterons from the detecting volume. The cells were all of diameter 27 mm and their lengths were 12, 25 and 37 mm respectively.

A block diagram of the experimental arrangement is shown in fig. 1. Pulse shape discrimination (PSD) was used to identify and distinguish the recoil deuterons and breakup protons. The scintillation pulse height L and the PSD output S were recorded in two-parameter mode and a time-of-flight gate was used to select the primary component of the incident neutron spectrum. The resulting two-parameter LS spectra, of which an example is shown in fig. 2, were resolved into electron, proton, deuteron and alpha-particle "ridges". Each row L of the LS spectrum was analysed independently and considered as the sum of four Gaussian components corresponding to sections of the e-, p-, d- and α-ridges respectively. A least squares

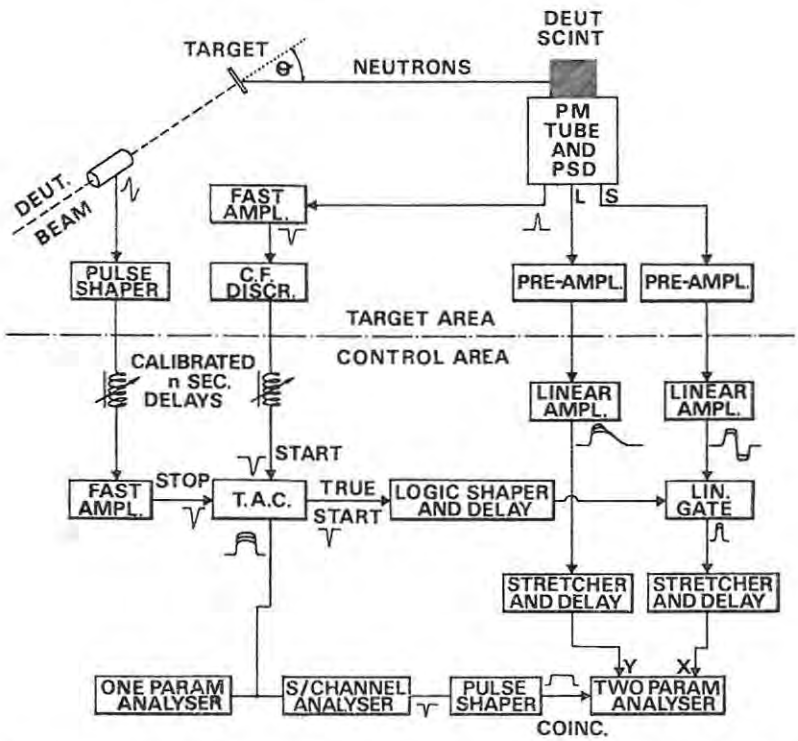

Fig. 1. Schematic representation of the experimental arrangement. The time-of-flight system on the left is used to reject background and secondary neutrons originating from breakup reactions in the target. The linear system on the right is used to obtain the biparametric LS spectrum.

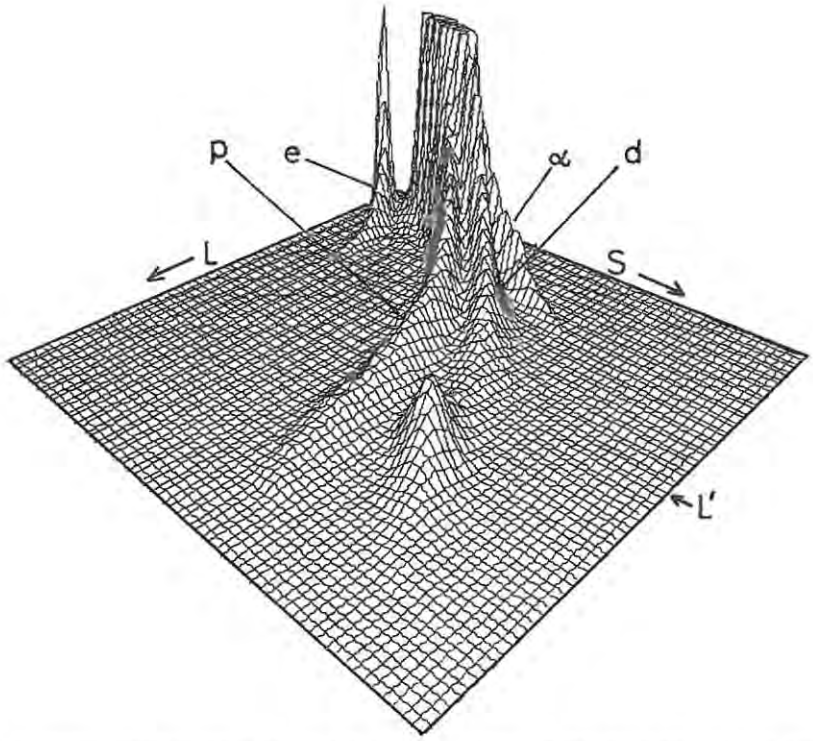

Fig. 2. Isometric representation of an LS spectrum obtained for 22 MeV neutrons incident on deuterated NE230 scintillator. The ridges labelled e, p, d and α are attributed to electrons, protons, deuterons and alphas respectively. The pulse height L' indicates the position of the minimum in the deuteron ridge. The (vertical) counts scale is arbitrarily truncated at the value 500 in this plot.

method was used to fit the data and the proton and deuteron components were then projected onto the L-axis and converted from pulse height spectra to energy spectra. The response of the detector to deuterons was determined by measuring the endpoint of the projected deuteron ridge as a function of incident neutron energy and correcting for the effects of finite resolution. The response L_p of the scintillator to protons is related to its response L_d to deuterons by [12]) $L_p(E) = \frac{1}{2}L_d(2E)$.

An example of a proton spectrum obtained using 22.0 MeV incident neutrons is shown in fig. 3. The separation of protons and deuterons by PSD was effective down to proton energies of about 3 MeV.

3. Analysis of data

Assume for the moment that there is no multiple neutron scattering in the scintillator, that no deuterons or protons escape and that no reactions other than those on deuterium occur. If the integrals of the proton and deuteron spectra are

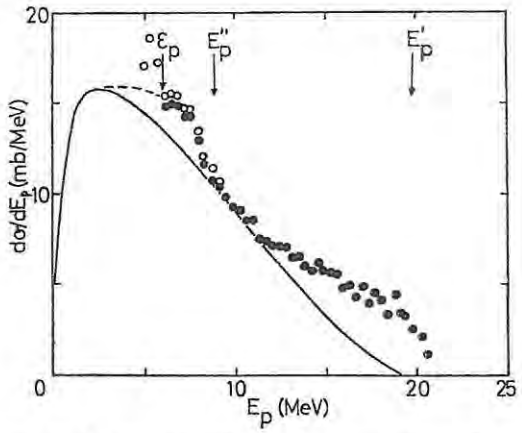

Fig. 3. Energy spectrum (solid circles) of breakup protons observed at 22 MeV incident energy. The open circles at low proton energy indicate values before correcting for the contribution from the $^{12}C(n, p)^{12}B$ reaction. The energy ε_p is the lower energy limit used in calculating the integral of the proton spectrum and the energies E_p' and E_p'' indicate upper limits of the regions where contributions from n-n FSI and n-p FSI are expected (see text). The solid curve shows the phase space distribution which was normalized to the data as described in the text and used to extrapolate the spectrum to zero energy (dashed curve) in order to calculate the fraction ϕ_p.

taken with lower energy limits ε_p and ε_d respectively then the ratio of these integrals is given by

$$R = \phi_p \sigma_b / \phi_d \sigma_e, \tag{1}$$

where ϕ_p and ϕ_d represent the fractions of protons and deuterons with energies exceeding ε_p and ε_d respectively. In the case of the deuteron spectrum it is convenient to set ε_d at the recoil energy corresponding to the minimum in the differential elastic cross section at $\theta_{c.m.} \approx 120°$. A corresponding minimum is clearly seen in the L-spectrum for deuterons, for example at $L \approx L'$ on the deuteron ridge in fig. 2. The deuteron integral is then relatively insensitive to small variations in ε_d and the fraction ϕ_d can be accurately estimated by integrating the differential elastic scattering cross-section data. At the incident energies used the differential cross sections for n-d and p-d elastic scattering at backward angles are essentially equal and Coulomb effects in the p-d scattering at forward angles may be corrected for [9]). Hence p-d as well as n-d data may be used to determine ϕ_d. In the present work values of ϕ_d obtained from p-d and n-d elastic data in the energy range 5–50 MeV were plotted as a function of energy. A smooth curve was drawn through these points and values of ϕ_d were read from this curve.

The fraction ϕ_p was estimated by extrapolating the measured part of the proton spectrum to zero energy. For this purpose the spectrum was considered to be a phase-space distribution with enhancements corresponding to those kinematic configurations which favour either final-state interactions (FSI) or quasi-free scattering (QFS). Configurations favouring n-n QFS are localised close to zero proton energy,

whereas those favouring n-p QFS are distributed over all proton energies isotropically. Both n-n and n-p FSI effects are distributed over a range of proton energies. The dependences of the FSI amplitudes on the production angle of the interacting pair have been investigated [13-21]). They are found to be strongly peaked at production angles corresponding to a proton being emitted in the forward direction, but relatively featureless at intermediate angles. Consequently, one expects enhancements due to FSI to be observable near the maximum proton energies for n-n and n-p FSI, that is, near E_p' and E_p'' where E_p' is the maximum breakup proton energy and $E_p'' \approx \frac{4}{9}E_p'$. The shape of the distribution at intermediate energies should be dominated by the phase-space distribution.

Our measurements support these conclusions (see fig. 3). Pronounced enhancements are seen near E_p' and E_p'' and these can be attributed to the n-n and n-p FSI respectively. The intermediate region contains no pronounced features. A further enhancement is expected near zero proton energy, due to the n-n QFS mechanism, but this enhancement is expected [22]) to be of the same order as that due to n-n FSI at high proton energy. The extrapolation of the spectrum to zero proton energy was therefore based on a phase-space distribution normalized to the data in the intermediate region $E_p \approx 0.5\,E_p'$ (see fig. 3). The uncertainties introduced by this approximation were estimated by taking the n-n FSI component as an upper limit measure of the n-n QFS component.

Having thus determined the fractions ϕ_d and ϕ_p, two methods were used to determine the breakup cross section σ_b from the observed ratio R. The first method was based on the fact that the quantity $\phi_d\sigma_e$ represents the integrated elastic cross section corresponding to the forward recoil peak in the deuteron spectrum. Thus using the elastic data to obtain $\phi_d\sigma_e$ the breakup cross section was calculated from

$$\sigma_b = (R/\phi_p)\phi_d\sigma_e. \tag{2}$$

The second method was based on the fact that the total neutron cross section σ_t of deuterium is equal to $\sigma_e+\sigma_b$ in the energy range under consideration. Thus σ_b was obtained in terms of the accurately known σ_t from

$$\sigma_b = \sigma_t/\{1+(\phi_p/\phi_d R)\}. \tag{3}$$

4. Results and discussion

The cross-section data obtained by the two methods are in good agreement. The mean values obtained at each incident neutron energy are summarised in table 1 and plotted in fig. 4. The integrals used to calculate the ratio R were corrected for multiple neutron scattering in the scintillator and for the effects of proton and deuteron escape from the scintillator. Corrections to the deuteron integral are facilitated by the fact that the energy distributions are known. For the proton integral, it was assumed that the breakup products are distributed according to the

TABLE 1
Values of the cross section σ_b

E_n (MeV)	8.2	12.17	13.66	14.00	14.80	16.05
σ_b (mb)	103±10	176±14	181±13	172±12	176±14	181±12
E_n (MeV)	17.40	18.80	20.02	21.07	22.00	
σ_b (mb)	172±12	180±17	179±16	180±17	176±16	

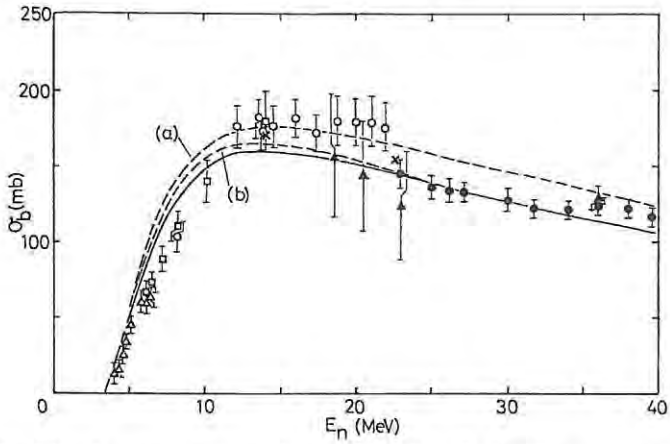

Fig. 4. The N+d breakup cross section. Experimental data for incident neutrons are: open circles, present work; squares, ref. [6]); and open triangles, ref. [8]). Experimental data for incident protons are: solid circles, ref. [25]). Values derived from neutron elastic scattering data are: solid triangles, ref. [10]). Data from theoretical calculations are: solid curve, ref. [1]); dashed curves, refs. [3,4]); and crosses, ref. [5]).

phase-space distribution. In view of the similarity of the measured distributions to the phase-space distribution (see fig. 3) this is expected to be a reasonable approximation. The proton integral was also corrected for small contributions from: (i) the ^{12}C(n, p)^{12}B reaction, using the data of Rimmer and Fisher [23]); and (ii) n-p scattering on the small (1.39 %) hydrogen impurity in the scintillator. Another potential contributor to the proton integral is the reaction ^{12}C(n, np)^{11}B ($Q_{g.s.} = -16$ MeV). Cross sections for this reaction are not known hence the lower limit ε_p was set sufficiently high to eliminate errors from this source (e.g. $\varepsilon_p \gtrapprox 6$ MeV for $E_n = 22$ MeV). The magnitudes of the corrections to the proton and deuteron integrals never exceeded 15 %.

The uncertainties quoted in table 1 and plotted in fig. 4 include contributions from statistical uncertainties, from uncertainties in the corrections to the integrals and from uncertainties in σ_e, σ_t, ϕ_d and ϕ_p. Of these the last was usually the major contributor to the total uncertainty. The uncertainty in ϕ_p could probably be reduced substantially by using a realistic breakup proton energy spectrum [24]) to extrapolate the observed distribution to zero energy.

The present data at 8 and 14 MeV agree with the data of Catron *et al.* [6]) at these energies (fig. 4). At higher energies the present data are systematically higher than the "indirect" values of σ_b calculated by Seagrave *et al.* [10]) from elastic scattering data. The data above 14 MeV also deviate from the trend suggested by the measurements by Carlson *et al.* [25]) of the cross section for proton-induced breakup.

For comparison, some calculated values of σ_b are also shown in fig. 4. The calculations of Sloan [1]) and Doleschall [5]) were based on separable potentials. Those of Kloet and Tjon [3, 4]) were based on local potentials of the Yukawa type, incorporating hard cores. Curve (a) in fig. 4 was obtained [3]) using a hard core in the singlet N-N potential only [potential I-IV of ref. [4])] whereas curve (b) was obtained using a potential with hard cores in both singlet and triplet states [potential I-III of ref. [4])]. Pure S-wave potentials were used in all the calculations except those of Doleschall [5]) which included separable P-wave interactions exactly in the Faddeev formalism. Calculations performed by Bruinsma *et al.* [2]) using S-wave N-N potentials yield results similar to those of Sloan [1]).

Although the experimental uncertainties are too large to admit of any conclusive comparison with theory, the present results seem to favour the calculations [3, 4]) made using a local potential having a hard core in the singlet state (curve (a) of fig. 4). However the inclusion of higher partial waves [5]) in calculations made using separable potentials could also lead to higher values of σ_b as can be seen in fig. 4.

We are indebted to Prof. I. Slaus for helpful comments and to Drs. P. Doleschall, I. H. Sloan, W. M. Kloet and J. A. Tjon for providing details and results of their calculations. We also thank the staff of the Southern Universities Nuclear Institute for their assistance and the South African Council for Scientific and Industrial Research for financial support and for a bursary to one of us (G.P.).

References

1) I. H. Sloan, Nucl. Phys. **A168** (1971) 211
2) J. Bruinsma, W. Ebenhöh, J. H. Stuivenberg and R. van Wageningen, Nucl. Phys. **A228** (1974) 52
3) W. M. Kloet and J. A. Tjon, private communication
4) W. M. Kloet and J. A. Tjon, Nucl. Phys. **A210** (1973) 380
5) P. Doleschall, private communication
6) H. C. Catron, M. D. Goldberg, P. W. Hill, J. M. Le Blanc, J. C. Stoering, C. J. Taylor and M. A. Williamson, Phys. Rev. **123** (1961) 218
7) V. J. Ashby, H. C. Catron, L. L. Newkirk and C. J. Taylor, Phys. Rev. **111** (1958) 616
8) M. Holmberg, Nucl. Phys. **A129** (1969) 329
9) A. Horsley, Nucl. Data Tables **A4** (1968) 327
10) J. D. Seagrave, J. C. Hopkins, D. R. Dixon, P. W. Keaton, Jr., E. C. Kerr, A. Niiler, R. H. Sherman and R. K. Walker, Ann. of Phys. **74** (1972) 250
11) W. T. H. van Oers and K. W. Brockman, Jr., Nucl. Phys. **A92** (1967) 561
12) G. Pauletta, Ph.D. thesis, University of Cape Town, 1973, unpublished
13) J. P. Burg, J. C. Cabrillat, M. Chemarin, D. Ille and G. Nicolai, Nucl. Phys. **A179** (1972) 377
14) H. Brückmann, W. Kluge, H. Mathäy, L. Schänzler and K. Wick, Nucl. Phys. **A157** (1970) 209

15) J. C. Van der Weerd, T. R. Canada, C. L. Fink and B. I. Cohen, Phys. Rev. **C3** (1971) 66
16) B. J. Wielinga, G. J. F. Blommestijn, R. van Dantzig, K. Mulder, A. D. Ijpenberg, I. Slaus, W. M. Kloet and J. A. Tjon, Proc. Int. Conf. on few-particle problems in the nuclear interaction, Los Angeles, 1972, ed. I. Slaus, S. A. Moszkowski, R. P. Haddock and W. T. H. van Oers (North-Holland, Amsterdam, New York) p. 515
17) I. Basar, I. Slaus, J. Hudomalj and P. Tomas, Proc. 1st Int. Conf. on the three-body problem in nuclear and particle physics, Birmingham, 1969, ed. J. S. C. McKee and P. M. Rolph (North-Holland, Amsterdam, 1970) p. 349
18) K. Ilakovac, L. G. Kuo, M. Petravic, I. Slaus and P. Tomas, Nucl. Phys. **43** (1963) 254
19) V. K. Voitovetskii, I. L. Korsunskii and Yu. F. Paekin, Nucl. Phys. **69** (1965) 531
20) K. Debertin, K. Hoffman and E. Rössle, Nucl. Phys. **41** (1969) 497
21) A. Bond, Nucl. Phys. **A120** (1969) 183
22) I. Slaus, Acta Phys. Acad. Sci. Hung. **33** (1973) 191
23) E. M. Rimmer and P. S. Fisher, Nucl. Phys. **A108** (1968) 567
24) W. Ebenhöh, Nucl. Phys. **A191** (1972) 97
25) R. F. Carlson, I. Slaus, S. Y. Tin, W. T. H. van Oers, P. Doherty and D. J. Margaziotis, Proc. Int. Conf. on few-particle problems in the nuclear interaction, Los Angeles, 1972, ed. I. Slaus, S. A. Moszkowski, R. P. Haddock and W. T. H. van Oers (North-Holland, Amsterdam, New York) p. 476

G. Pauletta and F.D. Brooks
Cross sections for the n+d breakup reaction
Nucl. Phys. A255 (1975) 287-274

Angular Correlation of Neutrons from Spontaneous Fission of ^{252}Cf

J. S. Pringle and F. D. Brooks
Physics Department, University of Cape Town, Rondebosch, 7700, South Africa
(Received 18 August 1975)

The n-n angular correlation for neutrons emitted in spontaneous fission of ^{252}Cf has been measured. Discrepancies are observed when these and other experimental observations are compared with Monte Carlo calculations based on the evaporation model. It is suggested that the discrepancies could be attributed to enhanced neutron emission along the fission axis.

It is well established[1,2] that a large fraction 5–90%) of the neutrons emitted promptly in ontaneous or thermal-neutron fission can be counted for in terms of evaporation from the ly accelerated fission fragments. However the igin of the remaining 10–25% of the neutron ission remains in question and it has been sug- sted that these neutrons may be emitted at the stant of scission[1,2] or during the acceleration riod of the fragments.[3] Models of the neutron ission rest mainly on experimental observa- ns of the velocity and angular distributions of prompt neutrons, the angular distributions ing referred to the axis defined by the direc- n of the light fragment.

Another observable in the neutron emission ocess is the neutron-neutron angular correla- n, that is the n-n coincidence rate as a func- n of angle between emitted neutrons. Such a easurement was reported for thermal-neutron fission of ^{235}U by De Benedetti *et al.*[4] in 1948. However no further measurement of this observable appears to have been reported since then. The n-n angular correlation experiment does not require the detection of fission fragments, and hence stronger and thicker sources may be used than in angular distribution measurements. On the other hand, the observations are automatically averaged over all orientations of the fission axis, which implies some loss of detail. The correlation is nevertheless sensitive to the characteristics of neutron emission and provides a useful additional method for testing models of emission process. We have measured the n-n angular correlation of prompt neutrons from the spontaneous fission of ^{252}Cf. In order to compare results with predictions based on the evaporation model we have also made Monte Carlo calculations simulating our experiment and the measurement of the neutron angular distribution.[1]

The n-n angular correlation was measured using a source consisting of 2 μg of ^{252}Cf in the form of four 15-mm-long rods, each sealed in a 1-mm-diam platinum-iridium container. The neutron detectors were an NE213 liquid scintillator (38 mm diam×25 mm length) and an anthracene crystal (25 mm diam×25 mm length) each mounted on a magnetically shielded photomultiplier tube. Pulse-shape discrimination was used to reject γ events and the detectors were operated at a proton detection threshold of 0.7 MeV. The pulse-shape discrimination rejection efficiencies of both detectors, as measured for Compton electrons from ^{60}Co γ rays, were better than 99.9%. The proton detection thresholds were calibrated using monoenergetic neutron beams obtained from the reaction ^{7}Li$(p,n)^{7}$Be. One detector and the source were fixed in the horizontal plane and the other detector was rotated about a vertical axis through the source to vary the n-n correlation angle θ. The time-delay spectrum was recorded and the true coincidence rate was determined from the peak in this spectrum. The accidental coincidence rate, estimated from the remainder of the time spectrum, never exceeded 10% of the true rate.

The distances from the source to the two scintillators were 30 cm for the measurements made at $\theta \geq 45°$. For $\theta < 45°$ one detector was moved back to 40–50 cm and a shadow shield was inserted between the two detectors to attenuate spurious coincidences arising from neutron scattering from one detector to the other. This scattering background was carefully investigated and the geometry and length of the shield were chosen to limit it to a negligible level.

The singles count rates N_1 and N_2 of the two detectors and the coincidence rate $N_c(\theta)$ at angle θ were determined in the experiment. Let N_f be the fission rate of the source, $\bar{\nu}$ the average neutron yield per fission, and Ω_1 and Ω_2 the solid angles subtended by the two detectors. Then, since Ω_1 and Ω_2 are small,

$$N_1 = \Omega_1 \epsilon_1 \bar{\nu} N_f / 4\pi \text{ and } N_2 = \Omega_2 \epsilon_2 \bar{\nu} N_f / 4\pi ,$$

where ϵ_1 and ϵ_2 are the average efficiencies of the detectors for detecting a fission neutron. The coincidence rate is given by

$$N_c(\theta) = \Omega_1 \Omega_2 \epsilon_1 \epsilon_2 \bar{\nu} N_f P(\theta) / 4\pi ,$$

where $P(\theta)$ represents the number of fission neutrons emitted per unit solid angle at angle θ to, and in coincidence with, the νth fission neutron. We define a ratio

$$R(\theta) = N_c(\theta)/N_1 N_2 = 4\pi P(\theta)/\bar{\nu} N_f .$$

Thus $R(\theta)$ is proportional to the angular correlation $P(\theta)$, independent of the experimental geometry (Ω_1 and Ω_2), and insensitive to small variations in instrumental stability insofar as these affect ϵ_1 and ϵ_2.

The experimental results are plotted in Fig. 1 together with a prediction of $R(\theta)$ based on an evaporation model including a 10% scission neutron component. The prediction was generated by a Monte Carlo calculation for 4×10^4 simulated fissions. The first stage of the calculation simulated the neutron emission from the source as follows. In each fission, pre-emission fragment masses were selected by sampling a mass distribution based on two sets of experimental data.[5,6] The (fully accelerated) velocities of the fragments in the laboratory frame were determined from the data of Whetstone.[6] For each fragment, the average neutron yield $\bar{\nu}$ and the variance σ_ν^2 were determined from the data of Signarbieux *et al.*[7] The actual number of neutrons emitted by each fragment was chosen by sampling a Gaussian $(\bar{\nu}, \sigma_\nu^2)$ distribution. A fraction[1] (10%) of the neutrons, randomly chosen, was designated as scission neutrons. It was assumed[1] that this component was emitted isotropically from a source stationary in the laboratory frame, while the remaining 90% of the fission neutrons were emitted isotropically in the frames of the fully accelerated fragments. The angles of emission of both scission and fragment neutrons in the respective emitting frames were assumed to be uncorrelated. Neutron emission energies were sam-

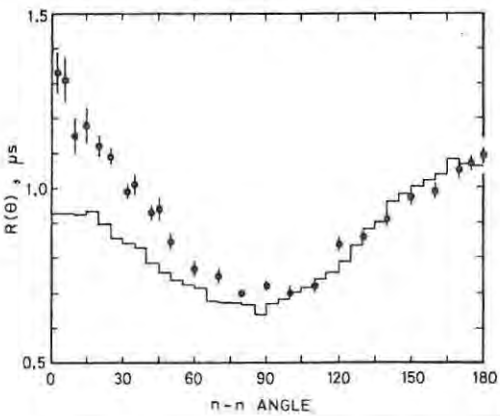

FIG. 1. The n-n angular correlation $R(\theta)$ for ^{252}Cf fission, showing experimental measurements (points) and Monte Carlo simulation (histogram).

led from evaporation spectra of the form

$$N(E) = (E/T^2)\exp(-E/T),$$

'here T is the nuclear temperature of the fragıent emitting the neutron and E is the neutron nergy in the appropriate frame. Fragment temeratures were determined from the data of Kluge nd Lajtai.[8] An evaporation temperature $T = 1.3$ leV was used in the case of scission neutrons.[1] ı accordance with recent experimental evidence,[9] nergies of evaporation neutrons were assumed ɔ be uncorrelated. The Monte Carlo calculation 'as checked by computing various parameters of ıe simulated fission source. For example, the imulation gave $\bar{\nu} = 3.73$, and a ratio $\bar{\nu}_L/\bar{\nu}_H$, for ıe light and heavy fragments, of 1.15. Both vales are in good agreement with experiment. The imulated neutron spectrum was also consistent 'ith an experimental measurement.[10]

The final stages of the Monte Carlo calculation imulated the present experiment and the angular istribution measurement of Bowman *et al.*[1] The imulated angular correlation was normalized to ıe experimental data in the range $\theta = 80°$–$180°$ nd is plotted in Fig. 1. The sensitivity of the imulation to the proton detection threshold was ıvestigated by repeating the Monte Carlo calcuıtion using thresholds 0.2 MeV lower and higher ıan the experimental value of 0.7 MeV. No sigificant change was observed in the form of the orrelation. From Fig. 1 it may be seen that the imulation reproduces the form of the experiıental data reasonably well at angles in the range $=100°$–$180°$ but not smaller angles.

The angular distribution measurement of Bowıan *et al.*[1] was simulated using a *neutron* detecion threshold of 0.55 MeV (velocity 1.025 cm/ sec) as used in their experiment. The simulated istribution was normalized to their data in the ngle range $\theta = 40°$–$140°$ and is shown (histogram) ɔgether with the data in Fig. 2. A curve by Bowıan *et al.*[1] based on an analytical formula in 'hich average values, independent of the fragıent mass ratio, were used for the velocities, ɛmperatures, and neutron yields of the fission ragments is also shown in Fig. 2. Whereas the urve fits the data well, the prediction of the Ionte Carlo calculation is too low both at small ngles, $\theta \lesssim 30°$, and large angles, $\theta \gtrsim 150°$. This iscrepancy between the two calculations was inestigated by modifying the Monte Carlo calculaon so as to use the fixed values used by Bowman *t al.*[1] for the fragment velocities, temperatures, nd neutron yields. The modified calculation gave

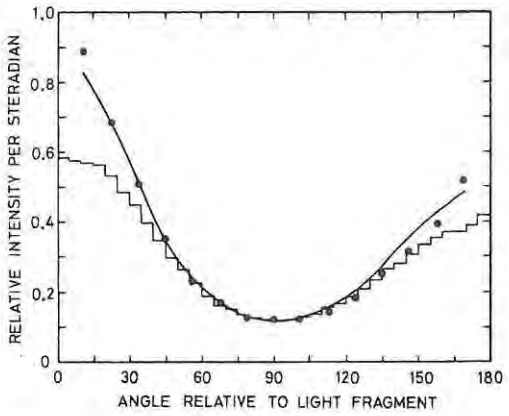

FIG. 2. Simulated angular distribution of neutrons from ^{252}Cf fission (histogram). The points show experimental data (Ref. 1) and the curve shows the fit obtained by using an analytical model (Ref. 1). The standard deviations of the data are smaller than the point size.

results in close agreement with the curve shown in Fig. 2, indicating that the discrepancy between curve and histogram may be attributed to the different assumptions made in the two calculations. The present simulation (histogram) is more realistic insofar as it takes account of the dependence of neutron emission characteristics on the fragment masses. For this reason and notwithstanding the poorer agreement with experiment, we consider it a better representation of the angular distribution of the evaporation model.

Further calculations were made to test the sensitivity of the simulations to the scission neutron fraction. For fractions less than 10% there is little change in the distributions, while larger fractions increase the discrepancies between experiment and theory. It is also evident that the fits would not be improved by attributing[3] a fraction of the neutron emission to evaporation during the fragment acceleration period. Such a model leads to results intermediate between those with and without a scission component.

We therefore conclude that the evaporation model in the form considered here cannot explain the results of the neutron angular correlation and angular distribution measurements, and that some mechanism must operate which enhances neutron emission along the fission axis. Ericson and Strutinski[11] have considered the effect of fragment angular momentum and have shown that this might cause such an enhancement. However Gavron and Fraenkel[9] consider that this effect must be small for the case of ^{252}Cf fission. Anoth-

r possibility is that neutrons emitted at the scis-
ion stage may be directed preferentially along
ıe fission axis. Recent studies[12] of the analo-
ous[13] process of light charged particle emission
ı ternary fission have indicated an unexpectedly
ırge axial component and it would therefore not
e surprising if the same were true for scission
eutrons. On the evidence now available however
is not possible to do more than speculate as to
ıe origin of the enhanced axial emission of neu-
·ons.

We thank the International Atomic Energy Agen-
y, Vienna, for the loan of the ^{252}Cf source and
ıe South African Council for Scientific and In-
ustrial Research for financial support and a
ursary to one of us (J.S.P.).

[1]H. R. Bowman, S. G. Thompson, J. C. D. Milton, and
'. J. Swiatecki, Phys. Rev. 126, 2120 (1962), and 129,
133 (1963).

[2]K. Skarsvåg and K. Bergheim, Nucl. Phys. 45, 72
963); S. S. Kapoor, R. Ramanna, and P. N. Rama
ao, Phys. Rev. 131, 283 (1963); M. V. Blinov, N. M.
azarinov, and I. T. Krisyuk, Yad. Fiz. 16, 1155 (1973)
[Sov. J. Nucl. Phys. 16, 634 (1973)].

[3]K. Skarsvåg, Phys. Scr. 7, 160 (1973); G. A. Pik-
Pichak, Yad. Fiz. 10, 321 (1970) [Sov. J. Nucl. Phys.
10, 185 (1970)].

[4]S. De Benedetti, J. E. Francis, W. M. Preston, and
T. W. Bonner, Phys. Rev. 74, 1645 (1948).

[5]H. W. Schmitt, J. H. Neiler, and F. J. Walter, Phys.
Rev. 141, 1146 (1966).

[6]S. L. Whetstone, Phys. Rev. 131, 1232 (1963).

[7]C. Signarbieux, J. Poitou, M. Ribrag, and J. Matu-
szek, Phys. Lett. 39B, 503 (1972).

[8]Gy. Kluge and A. Lajtai, Phys. Lett. 27B, 65 (1968).

[9]A. Gavron and Z. Fraenkel, Phys. Rev. C 9, 632
(1974).

[10]J. W. Meadows, Phys. Rev. 157, 1076 (1967).

[11]T. Ericson and V. Strutinski, Nucl. Phys. 8, 284
(1958), and 9, 689 (1959).

[12]E. Piasecki, M. Dakowski, and A. Kordyasz, in *Proceedings of the Symposium on the Physics and Chemistry of Fission, Rochester, New York, 1973* (International Atomic Energy Agency, Vienna, Austria, 1974), p. 383; V. M. Adamov, L. V. Drapchinsky, S. S. Kovalenko, K. A. Petrzhak, L. A. Pleskachevsky, and I. T. Tyutyugin, Phys. Lett. 48B, 311 (1974).

[13]N. Feather, in *Proceedings of the Symposium on the Physics and Chemistry of Fission, Vienna, Austria, 1969* (International Atomic Energy Agency, Vienna, Austria, 1969), p. 83.

J.S. Pringle and F.D. Brooks
Angular correlation of neutrons from spontaneous fission of ^{252}Cf
Phys. Rev. Lett. 35 (1975) 1563-1566

M. Steinbock, F.D. Brooks and I.J. van Heerden
Polarization in n-d scattering at 16.4 and 21.6 MeV
Proc. 4th Int. Symposium on Polarization Phenomena in Nuclear Reactions, ed. W. Gruebler and V. Konig (Birkhauser Verlag, Basel, 1978) 475-478

POLARIZATION IN n-d SCATTERING AT 16.4 AND 21.6 MeV

M. Steinbock, F.D. Brooks and I.J. van Heerden
Department of Physics, University of Cape Town, Rondebosch, Cape, South Africa.

A comparison of the polarization asymmetries observed in n-d and p-d elastic scattering provides a test of the charge symmetry of nuclear forces. Discrepancies have been observed between the p-d and n-d polarizations measured at incident energies near to 22 MeV [1-3]) and 35 MeV [1,4]) respectively. However Morris *et al.*[5]) have recently measured P_{nd} at incident neutron energies of 16.8 and 21.1 MeV and have obtained results in good agreement with the p-d polarization data. The present work has been motivated by the need for further n-d data in this region.

The measurements were made using a ^{3}H(d,n) source with pulsed 5.0 MeV deuterons from the Van de Graaff accelerator of SUNI, Faure, C.P. South Africa. Neutrons emitted at angles 20° and 80° respectively, with energies 21.6 and 16.4 MeV and polarizations +0.21 and -0.42 respectively were used. Time-of-flight gating was used to select the primary component in the neutron spectrum.

The polarization analyser was a deuterated anthracene scintillation crystal. Recoil deuterons from n-d elastic scattering within the crystal were studied and pulse shape discrimination (PSD) was used to determine the left-right asymmetry of the recoils. The experimental method is similar to that used previously [6,7]) to study the polarization in n-p scattering and depends on the fact that the PSD response of the crystal is sensitive to the direction of the recoil deuteron relative to the crystal axes. The scintillation detector provides a fast output for timing, a pulse height output L, from which the deuteron energy may be deduced, and a PSD output S. Fig.1 shows an LS spectrum from dual-parameter analysis of data obtained using 21.6 MeV neutrons entering the crystal in a direction parallel to its artificial *c'*-axis. The forward recoil deuteron peak F which lies at a relatively low S value in fig.1 would move to the position F' in the LS plane for neutrons entering parallel to the *b* - axis. Thus for neutrons entering in a direction lying within the *bc'*-plane and making an angle of 50° with the *c'*-axis recoils to the right (towards the *b*-axis) and to the left (towards the

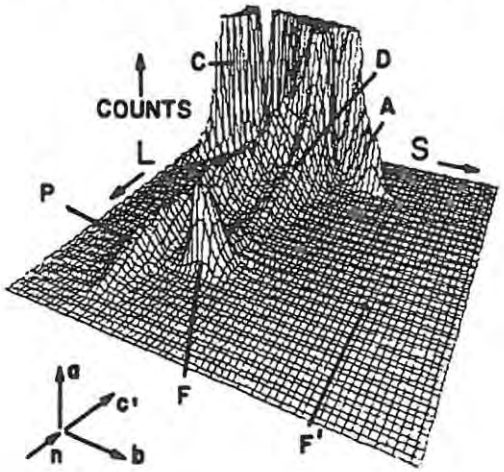

Fig. 1 LS spectrum for 21.6 MeV neutrons directed parallel to the *c'*-axis, showing ridges due to: Compton electrons (C); breakup protons (P); recoil deuterons (D); and α-particles (A) from reactions on carbon. The peak F corresponds to forward recoiling deuterons. The point F' shows the position of this peak in the spectrum obtained for neutrons directed parallel to the *b*-axis.

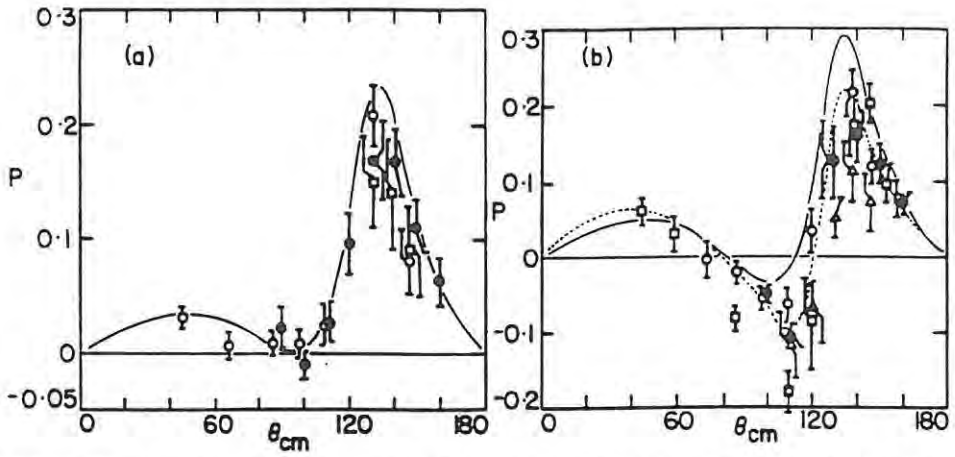

Fig.2 Polarization data at energies near to (a) 16.4 and (b) 21.6 MeV. Solid circles show present work; squares ref.[2]); triangles ref.[3]); open circles, ref.[5]). See text for curves.

c'-axis) produce higher and lower S outputs respectively. The dispersion of the deuteron component over the LS plane at this orientation of the crystal provides a basis for determining the asymmetry.

The recoil deuteron energy deduced from L is correlated with the associated neutron centre-of-mass scattering angle θ_{cm} hence the asymmetry may be determined as a function of θ_{cm}. Methods based on those developed for the natural anthracene analyser [6,7]) have been used, with modifications to correct for the partial overlap of the proton and deuteron components in the LS spectra.

The results of the measurements are shown in fig.2 together with other data [2,3,5]) at nearby energies. The solid curves are based on the work of Pieper [8]) and were adjusted to 16.4 and 21.6 MeV by interpolating his results. The dashed curve in fig. 2b shows the trend of the p-d polarization data [1]) at 20.2 MeV. The trend of the p-d data [1]) at 17.5 MeV lies close to the solid curve in fig.2a. The data obtained at 16.4 MeV (fig.2a) are consistent with the other data at nearby energies, except possibly in the region near $\theta_{cm} = 130^{o}$. The data obtained at 21.6 MeV (fig.2b) are consistent with the recent measurements of Morris *et al.*[5]) and confirm that the negative dip observed between $\theta_{cm} = 80^{o}$ - 120^{o} is shallower than indicated by the earlier n-d measurements [2,3]) and consistent with the p-d data at these angles. We conclude therefore that there is no discrepancy between the n-d and p-d polarizations at these energies.

References

1) J.C. Faivre,Garreta,Jungerman,Papineau,Sura and Tarrata,Nucl.Phys. A127 (1969) 169
2) J.J.Malanify,Simmons,Perkins and Walter,Phys.Rev. 146 (1966) 632
3) R.L.Walter and Kelsey, Nucl. Phys. 46 (1963) 66
4) J. Zamudio-Cristi,Bonner, Brady,Jungerman and Wang,Phys.Rev.Letts. 31 (1973) 1009
5) C.L. Morris,Rotter,Dean and Thornton,Phys.Rev.C,9(1974) 1687
6) F.D.Brooks and Jones,Nucl.Instr. & Meth.,121 (1974) 69 & 77
7) D.T.L. Jones and Brooks,Nucl. Phys. A222 (1974) 79
8) S.C. Pieper, Nucl. Phys. A193 (1972) 529

F.D. Brooks, S. Wynchank, P.L.M. le Roux, E.R. Hering, D. Shackleton, A. Wulff, H.S.T. Driver and M. Steinbock
Research and experimental work at Groote Schuur Hospital and the University of Cape Town using ^{252}Cf sources
Proc. Seminar on the Uses of Californium-252 in Teaching and Research, IAEA-SR-3/16 (IAEA, Vienna, 1976) 173-182

PANEL PROCEEDINGS SERIES

SOME PHYSICAL, DOSIMETRY AND BIOMEDICAL ASPECTS OF CALIFORNIUM-252

PROCEEDINGS OF AN EDUCATIONAL SEMINAR
ON THE USES OF CALIFORNIUM-252
IN TEACHING AND RESEARCH
HELD BY THE
INTERNATIONAL ATOMIC ENERGY AGENCY
IN KARLSRUHE, 14–18 APRIL 1975

INTERNATIONAL ATOMIC ENERGY AGENCY
VIENNA, 1976

RESEARCH AND EXPERIMENTAL WORK AT GROOTE SCHUUR HOSPITAL AND THE UNIVERSITY OF CAPE TOWN USING CALIFORNIUM-252 SOURCES

F.D. BROOKS, S. WYNCHANK, P.L.M. Le ROUX, E.R. HERING, D. SHACKLETON, A. WULFF, H.S.T. DRIVER, M. STEINBOCK
Groote Schuur Hospital and
The University of Cape Town,
Cape Town,
South Africa

Abstract

RESEARCH AND EXPERIMENTAL WORK AT GROOTE SCHUUR HOSPITAL AND THE UNIVERSITY OF CAPE TOWN USING CALIFORNIUM-252 SOURCES.

Experiments have been undertaken to determine the high-LET and low-LET components of the absorbed dose from neutron beams. This is achieved by measuring the fluxes of the high-LET and low-LET radiations in a tissue-equivalent phantom individually and simultaneously using a scintillation probe fitted with a pulse shape discriminator. This system was successfully used with a 22 MeV neutron beam from the T(d,n) reaction and has been employed with ^{252}Cf sources. Results obtained in the low-energy ranges (up to 3 MeV) indicate that the electron counts exceed the high-LET counts by a factor of 2 to 3. These results are related to the absorbed dose. Calculations have also been undertaken to establish whether the Paterson-Parker system could be used for the design of ^{252}Cf treatments and the optimum needle activities to yield the desired dose. Experiments are under way to determine the variation of RBE and OER for ^{252}Cf radiations around the source. The inhibition of root growth in Vicia Faba is being used to determine any such effects. Dose rates comparable to that employed in interstitial radiotherapy are being aimed at. A study of dose fractionation effects is also being undertaken.

The selection and nature of the projects was dictated largely by the relatively low activity of the sources supplied by the International Atomic Energy Agency, the facilities and staff available to undertake the work and the past experience gained in these fields of measurement using other sources of radiation.

The research projects initiated cover the fields of energy deposition by neutrons in a tissue-equivalent medium and a series of radiobiological studies on root systems. To do this efficiently some dosimetric measurements were initiated using ionization chambers, TLD systems and chemica dosimetry. Calculations were also undertaken to determine the feasibility of using differently loaded ^{252}Cf sources in interstitial radiotherapy.

1. HIGH AND LOW-LET PARTICLE COUNTING

A good deal of experience had been gained in the detection and measurement of the high-LET and low-LET components of the dose absorbed in a tissue-equivalent liquid phantom from neutron beams generated at 8 MeV and 22 MeV in a 5.5 MeV Van de Graaff accelerator operated jointly by the

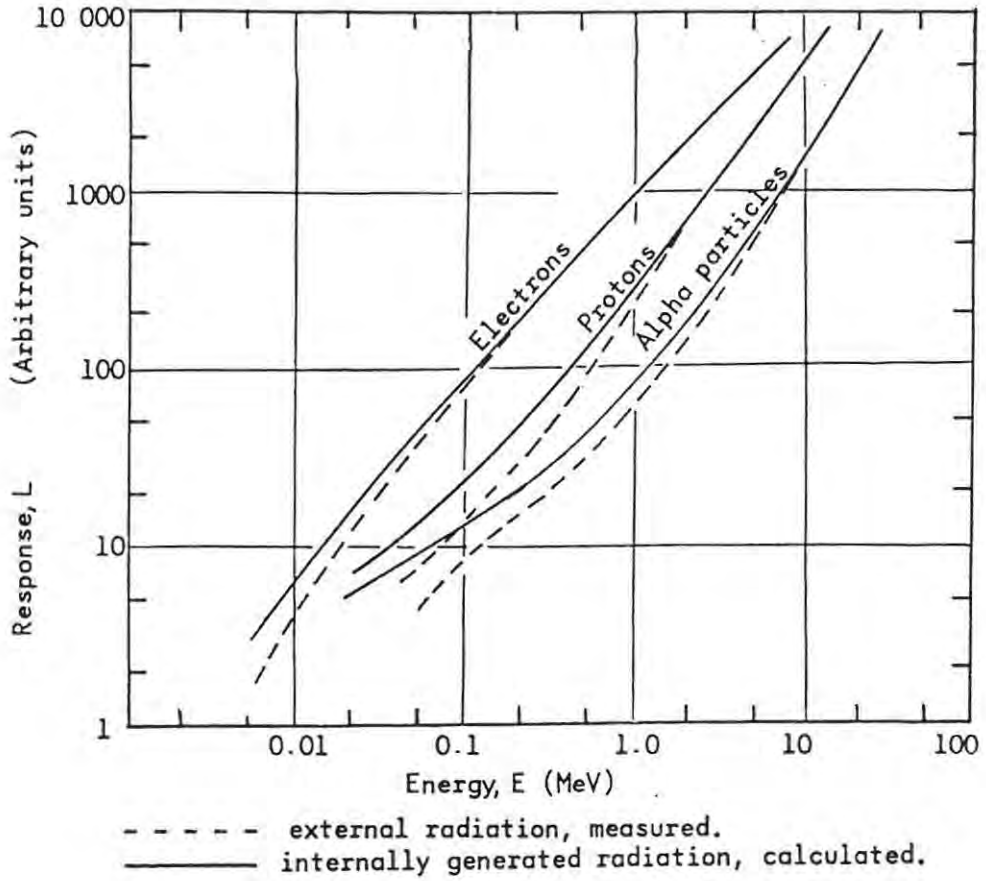

FIG.1. Response of an anthracene crystal to electrons, protons and alpha particles (– – – external radiation, measured; ——— internally generated radiation, calculated).

Universities of Cape Town and Stellenbosch (Southern Universities Nuclear Institute). This work was done as part of a feasibility study of using cyclotron generated neutron beams in radiotherapy – hence the high energies involved. It was considered possible to extend this to ^{252}Cf.

The basis of the method used is the technique of pulse shape discrimination (PSD) by means of which an organic phosphor, placed within the phantom, is in effect able to distinguish between high-LET radiations (recoil protons and alpha particles) and low-LET radiations (Compton scattered electrons from gamma photons).

In certain phosphors a particle-induced scintillation is composed of an intense fast decaying and a low-intensity slowly decaying component, so that the light output may be approximated by the expression:

$$L = A \cdot e^{-t/\tau_1} + B \cdot e^{-t/\tau_2} \quad \text{for} \quad \tau_2 \gg \tau_1$$

For example, in anthracene, τ_1 = 33 ns and τ_2 = 370 ns.

The importance of this lies in the fact that the ratio B/A is a function of the LET, or dE/dx, which in turn is determined by the nature of the ionizing particle. In anthracene, B/A for a proton is about twice that for an electron. An alpha particle induces an even higher slow-to-fast component ratio. The theory of the operation of the electronic circuits

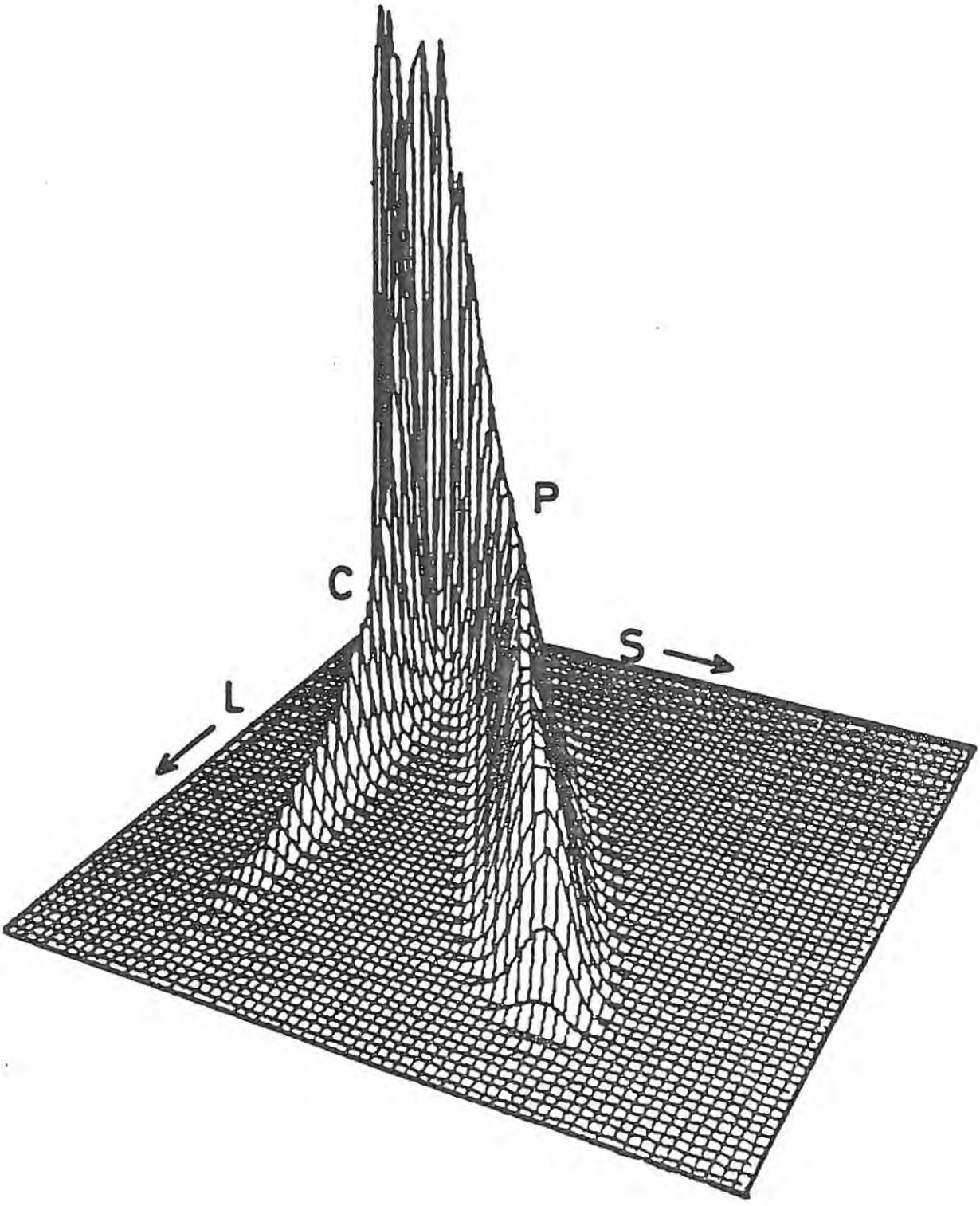

FIG.2. Two-parameter plot of L (measure of light output) and S (non-linear measure of LET) against number of counts (vertical scale) for 8 MeV Van de Graaff neutrons.

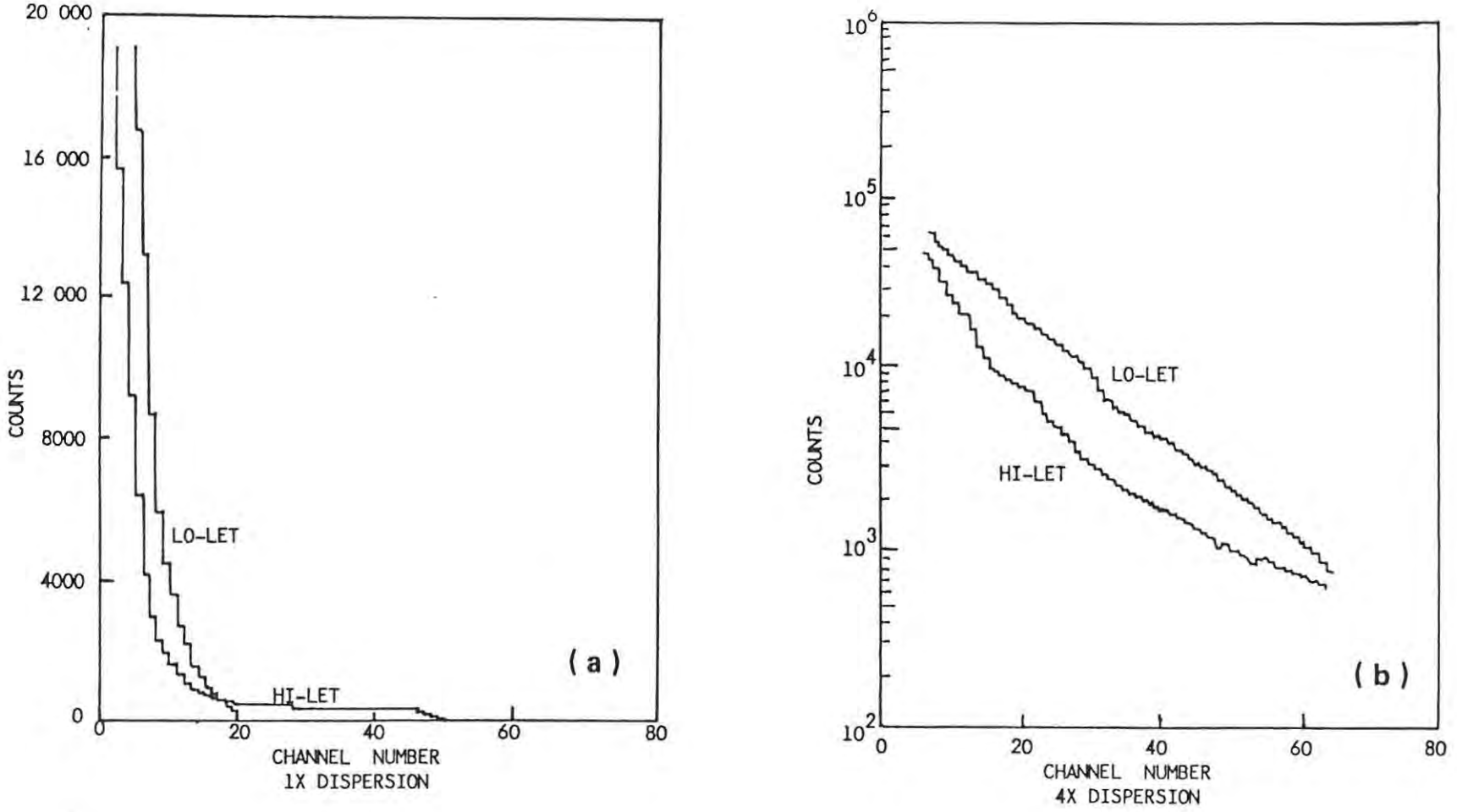

FIG.3. Processed results for a 22 MeV neutron beam: (a) 1 × dispersion; (b) 4 × dispersion.

employed to mix the outputs from the last dynode and the anode of the photomultiplier, to which the phosphor is coupled, has been described by Brooks [1]. The mixed output has greater amplitude if induced by a recoiling proton than if arising from an electron recoil for equivalent integrated light outputs of the phosphor.

This PSD technique has been successfully applied to plastic and liquid scintillators, too. For the liquid scintillator NE213 Henchoz and Joseph[2] have found τ_1 = 2.5 ns and τ_2 = 150 ns with B/A = 0.007 for electrons and B/A = 0.014 for protons. In the work undertaken to date, an anthracene crystal has been used because of its high light output and, consequently, high resolution. There are two possible disadvantages associated with the use of anthracene. These are that the atomic composition differs rather markedly from that of tissue and the fact that it has an asymmetry effect associated with the crystal axes, i.e. the height and shape of a scintillation pulse each depend on the direction of the charged particle trajectory with respect to the crystal axes.

In the present studies the crystal was placed at the optimum orientation with respect to the primary neutron beam for the PSD outputs deriving from the proton and electron crystal excitations to be as markedly separated as possible. Due to the asymmetry effect, the crystal response to events induced by radiation scattered in the phantom was inevitably somewhat different to that for events induced by the primary beam.

Efforts will, therefore, be directed towards acquiring a liquid or plastic phosphor which approximates the atomic composition of tissue more closely than anthracene, and which does not exhibit the directional effects associated with crystal phosphors. It will be difficult to achieve exact tissue equivalence, since the oxygen content has to be limited because of its effect on pulse shape. However, at the relatively low average neutron energy of ^{252}Cf neutrons, this lack of oxygen will be of negligible practical significance.

The relationship between the energy of the particles and the response (luminous intensity) produced in the anthracene obtained by Brooks, as reported by Birks [3], is shown in Fig. 1.

The results of measurements undertaken on an 8 MeV neutron beam generated on the Van de Graaff accelerator are shown as a two-parameter plot in Fig. 2. This shows the number of counts (vertical) versus parameters L and S; L is a measure of light output from each scintillation and, therefore, of the energy of the proton or electron causing the scintillation, and the parameter S is a non-linear measure of the LET. The proton recoils from neutron-proton scattering in the phosphor form a characteristic ridge P in the L-S plane, and the electrons from Compton scattering of gamma rays form another distinct ridge C.

By projecting each ridge onto the L-axis one obtains the pulse-height distribution and, hence, the energy spectrum for the corresponding particles (protons and electrons, respectively). By integrating each spectrum, taking due account of the energy, one can then obtain the integrated high-LET and low-LET doses respectively.

Similar measurements have been undertaken around ^{252}Cf sources in a tissue-equivalent medium. The final processed results are not available yet but will be presented and processed in the same way as described above for the 8 MeV neutron beam measurements. Processed results for a 22 MeV neutron beam are shown in Figs 3a, b.

Figure 3a shows pulse-height spectra observed for electrons and for high-LET radiation (protons and alpha particles) with the probe placed in a water phantom at a depth of 4 cm on the central axis of the beam. Figure 3b shows the low pulse-height regions of the same two spectra with the pulse-height dispersion increased fourfold. The characteristic edge in the region of channel 45 in Fig. 3a provides an energy calibration corresponding to forward recoiling 22 MeV protons. The electron energy corresponding to this pulse height is obtained from tables of the relative pulse-height response of the probe to electrons and protons, and is 16 MeV. Figure 3a indicates that the ratio of electron intensity to proton intensity drops off rapidly at large pulse heights. However, the high-energy protons in this region of the spectrum contribute significantly to the low-LET dose (while they are degraded to ~ 3 MeV) as well as to the high-LET dose (at the end of their range). These protons are therefore less effective than low-energy protons in increasing the high-LET component of the total dose, which is the aim of neutron therapy.

The low-energy or low pulse-height regions (Fig. 3b) of the spectra are of particular interest in view of this consideration, and the fact that this is the energy region of interest in ^{252}Cf neutron radiation. It will be noted that the electron counts exceed high-LET counts by a factor of 2 to 3 in this region. This is offset, however, by the fact that the energy per unit pulse height from the probe is higher for high-LET radiations than electrons by a factor of about 4 for protons.

Making allowance for these effects one obtains, as a rough estimate, that the low-LET and high-LET components contribute 30% and 70% of the total dose, respectively. The relative contributions are expected to be somewhat different for ^{252}Cf, however, due to the characteristic spectra of neutrons and γ-rays arising from ^{252}Cf fission events.

2. RADIOBIOLOGICAL STUDIES

The radiobiological studies being undertaken at present involve the inhibition of root growth in Vicia faba to measure the Oxygen Enhancement Ratio (OER) and Relative Biological Effectiveness (RBE) of ^{252}Cf radiation. Due to the low activity of the available sources the studies will be confined to chronic low-dose-rate exposures of up to 2 rad $\cdot h^{-1}$ for 7 days or more. The irradiations will be done at 3.5°C, since cell division at this temperature is almost completely arrested; hence, the effect of the dose is not affected by cell proliferation, though repair of sublethal damage does proceed at this low temperature. The effects of different dose rates at different distances from the source will be investigated. These will be obtained by positioning the roots on a jig as shown in Fig. 4. The sources will be placed on the bottom Perspex ring; different distances from the roots confined to the centre can be achieved by using rings of various diameters.

The four SALC ^{252}Cf sources are arranged symmetrically on this ring. The irradiation jig is placed in water at 3.5°C in a tank (30 cm × 20 cm × 30 cm) and the water is stirred vigorously by a Braun thermostatically-controlled heater used in conjunction with a cooling unit. This stirring prevent de-oxygenation of the water. To irradiate the roots under hypoxic conditions oxygen is bubbled through the water; for anoxic irradiations nitrogen is bubbled through.

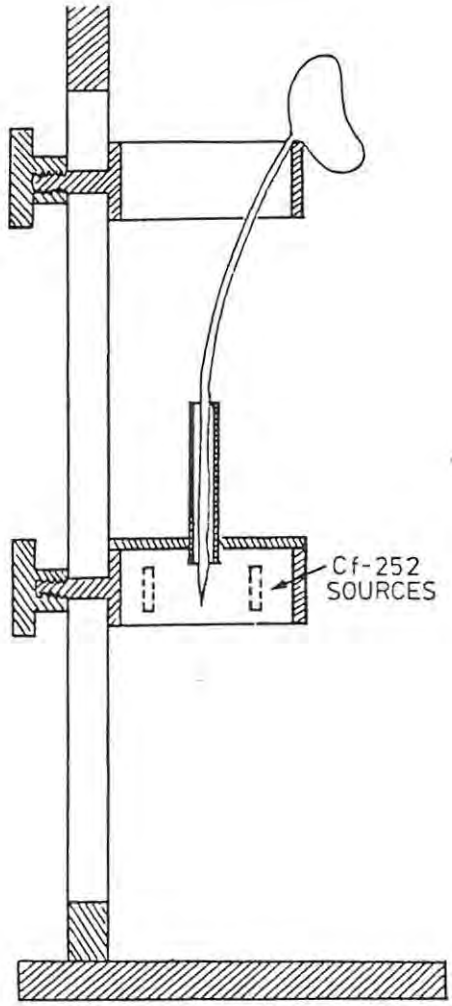

FIG.4. Jig for positioning roots of Vicia faba for irradiation.

To determine the RBE of ^{252}Cf relative to that of radium and iodine-125, the seedlings will be irradiated with radium and iodine gamma radiation at about the same dose rates and under the same experimental conditions. Although the dose rates for the ^{252}Cf sources are at present calculated from published data, measurements will be made using ^{6}LiF and ^{7}LiF thermoluminescent powder. After irradiation the roots will be grown at 19°C for 10 days and the minimum growth rate or G_{10} (growth in ten days after irradiation as a fraction of control of equal age) used to assess radiation damage.

An attempt will be made to interpret the results in terms of the different LET components arising from ^{252}Cf radiation. In conjunction with these studies with ^{252}Cf, experiments will be done at a range of neutron dose rates available on the Van de Graaff accelerator. Here the gamma-ray component will be less. Initial experiments have been run on this unit with dose rates of the order of 100 rad $\cdot h^{-1}$. To measure the dose rates in these experiments a disc-type ionization chamber was constructed and measurements were made with a continuous flow of ethylene gas through the chamber. The chamber was made up of conducting tissue-equivalent plastic, as produced by Shonka.

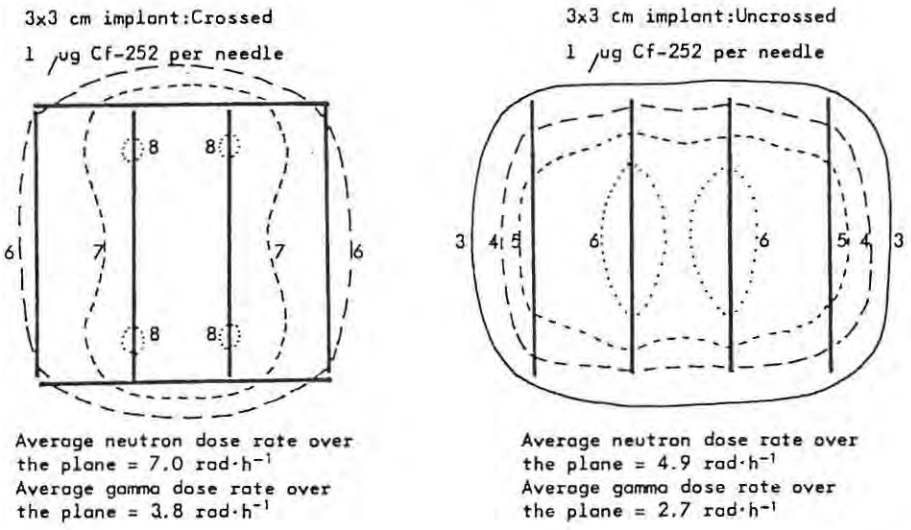

FIG.5. Neutron isodoses in rad·h^{-1} over an implanted area of 3 cm x 2 cm using 1 μg ^{252}Cf needles.

3. INTERSTITIAL RADIOTHERAPY

Californium-252 medical neutron sources have been available for some time for therapeutic evaluation programmes. These sources are of such a nature that afterloading procedures have to be adopted during implantation. When we were considering the acquisition of commercially-produced sources, prospective suppliers requested details of the required source activities and physical dimensions. An attempt was consequently made to determine optimum source loadings and active lengths which would allow of treatment planning according to the Paterson-Parker rules if these should be applicable for ^{252}Cf sources. In view of the relatively short half-life and relatively high cost of ^{252}Cf sources, it was decided to ascertain to what extent the required range of needles for direct implantation could be limited and yet have sufficient flexibility to cover adequately the specified implant areas and volumes encountered in clinical situations.

From a radiation protection point of view, afterloading techniques are indicated where at all feasible. In such cases tubes could be used. Radiotherapists felt, however, that there are certain sites, such as the tongue and buccal cavity, where needles would be technically more convenient to use. In order to calculate the dose rates arising from such implants the calculated dosage data of Krishnaswamy [4] was used, since this was available in the most convenient tabular form. These tables give the neutron and gamma dose distribution around sources of 1.5, 2.0 and 3.0 cm active lengths. By graphical analysis it was possible to derive from this data reasonably accurate dosage distributions of linearly loaded, indian club and dumb-bell type sources, such as are used in radium therapy.

Initial calculations were confined to rows of sources of 3 cm active length spaced one centimetre apart. Because of the uncertainty of the RBE factor for ^{252}Cf neutrons, it was thought advisable to calculate the neutron and gamma dose components separately.

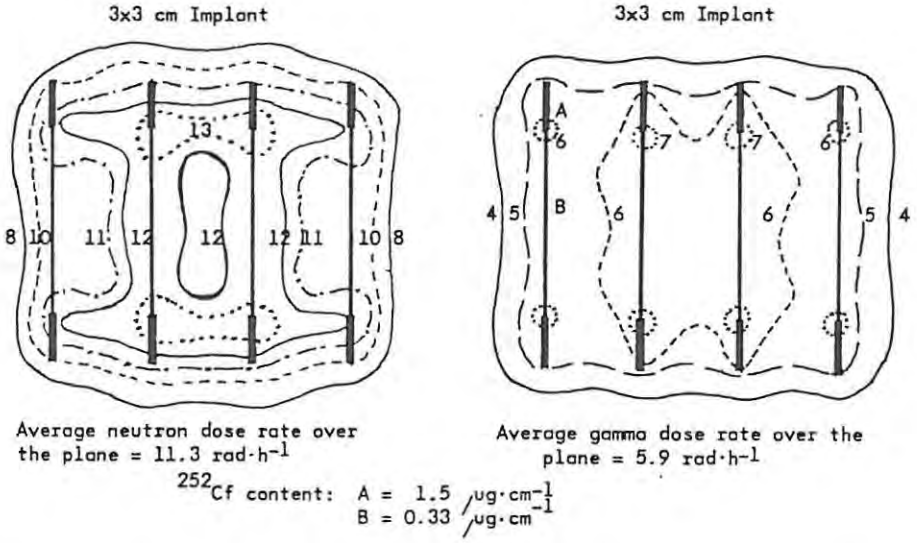

FIG.6. Neutron and gamma-ray isodoses over an implanted area of 3 cm x 3 cm using differentially loaded dumb-bell type needles.

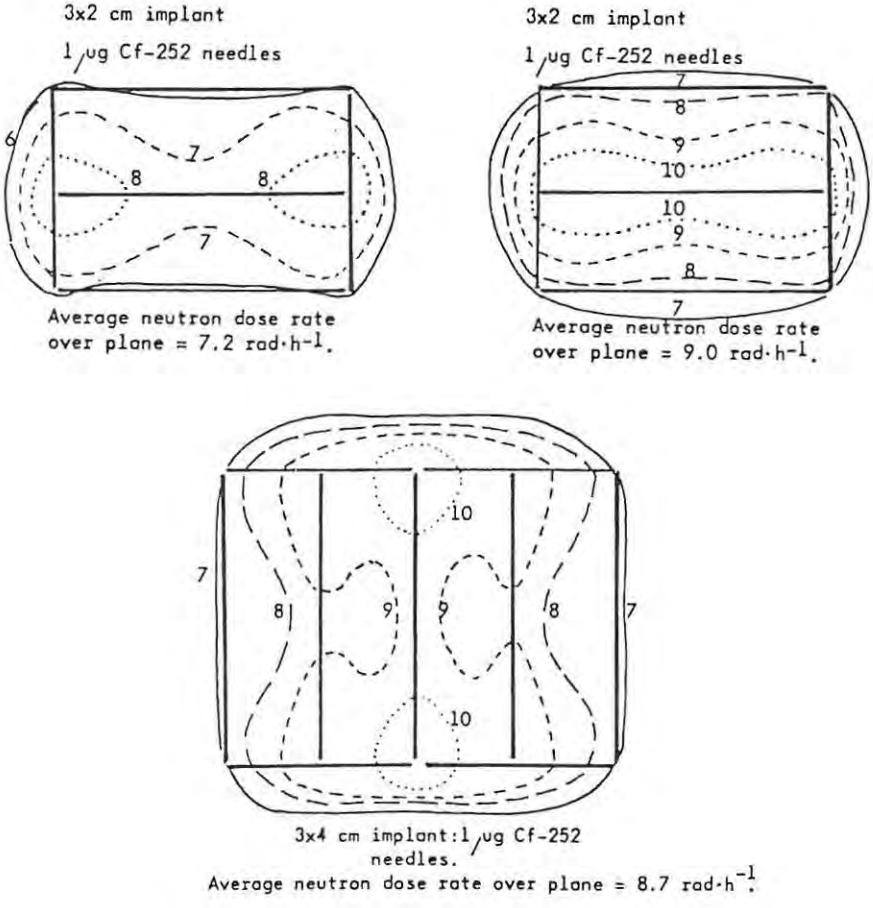

FIG.7. Neutron isodoses over different implanted areas. All sources are of 1 µg ^{252}Cf content except the central source on the right-hand top which has an activity of 2 µg ^{252}Cf.

Following the convention adopted by Paterson and Parker, the doses were calculated on a 0.5 cm square grid on a plane 0.5 cm from the plane of the implant. Similar computer calculations have been undertaken by Bloch et al. [5] for linearly loaded sources and the results obtained show exceptional agreement with our calculations for linear sources. Their conclusions were verified by our calculations. They suggested that in order to achieve dose uniformity to within the accepted ± 10% limits over the implanted area, the inner sources should be removed earlier than the outer sources. We extended these investigations by deriving dose distributions around linear sources of different activities and differentially loaded sources and then evaluating the dose rates deriving from source distributions according to the Paterson-Parker rules.

The results of our calculations are shown in Figs 5 to 7. A study of these dose distributions indicates that the use of the Paterson-Parker system is justified if it is assumed that the RBE and OER do not vary with distance from the source. Experiments have been planned to determine whether any such variation does in fact occur.

REFERENCES

[1] BROOKS, F.D., Nucl. Instrum. Methods 4 (1959) 151.
[2] HENCHOZ, A., JOSEPH, C., Helv. Phys. Acta. 38 (1965) 663.
[3] BIRKS, J.B., The Theory and Practice of Scintillation Counting, Pergamon Press (1964).
[4] KRISHNASWAMY, V., Calculated depth dose tables for californium-252 sources in tissue, Phys. Med. Biol. 17 (1972) 56.
[5] BLOCH, P., KRISHNASWAMY, V., HALE, J., Dose tables for californium-252 implants, Am. J. Roentgenol. 115 4 (1972) 822.

NUCLEAR INSTRUMENTS AND METHODS 162 (1979) 477-505 ; © NORTH-HOLLAND PUBLISHING CO.

DEVELOPMENT OF ORGANIC SCINTILLATORS

F. D. BROOKS

Physics Department, University of Cape Town, Rondebosch, Cape, 7700, South Africa

The development of organic scintillators is reviewed with emphasis on work that has been reported since 1964. The scintillation process is discussed. Measurements of scintillator properties such as response-energy dependence, energy resolution, timing characteristics, pulse shape discrimination and scintillation anisotropy are reviewed. Some recent and novel applications of organic scintillators are noted.

1. Introduction

Organic scintillators have a history which extends back to one of the earliest photomultiplier scintillation detectors[1]). This first organic detector, which was described by Kallmann and Broser[1]) in 1947, incorporated a naphthalene crystal scintillator selected for its large size and its transparency to its own fluorescence emission. Several more suitable and more efficient organic scintillators were introduced within the next few years, among them other crystals such as anthracene[2]) and stilbene[3]), crystal solutions such as anthracene in naphthalene[4]), liquid solutions[5–7]) and plastic solutions[8]). An important general characteristic of the organic scintillators, their short response time (<10 ns), was also noted[9]) at a very early stage in their history.

The organic scintillator scene some thirty years later is dominated by the liquid and plastic scintillators. These classes now offer the fastest response times and the simplest and most economical ways of obtaining large efficient detecting volumes. However, fast response in the present-day context implies a time resolution of <200 ps and large size may be reckoned in volumes of kiloliters in contrast to the several cm^3 which this description implied in the nineteen forties.

This technical progress has been led by advances in the understanding of the organic scintillation mechanism[10–14]). So also has the development of practical applications, such as neutron detection and liquid scintillation counting, with which the organic detectors are particularly closely associated. The advent of n–γ discrimination by the pulse shape technique[15]) for example has established the organic scintillator as the standard detector of MeV neutrons and the development of methods for loading active samples into liquid scintillators[16]) has led to many applications of 4π liquid scintillation counting[16,17]) in the medical, biological and environmental fields.

These and other developments of organic scintillators have been reviewed from time to time (for example see refs. 10, 18–25) and especially in the authoritative text on the theory and practice of scintillation counting published by Birks[11]) in 1964. In the present review, therefore, we set out with the intention of emphasising developments in the post-1964 period. We review first the scintillation process in organic materials as it is now understood, then the characteristics of organic scintillators, brought up to date as far as possible by recent measurements, and finally we consider some recent applications of these detectors.

2. The scintillation process in organic scintillators

Practical scintillators can be formed by combining suitable organic compounds in many different ways. We can classify different combinations as unitary, binary, ternary or higher order, according to the number of compounds they contain. The ideal unitary system is a pure monocrystal scintillator such as anthracene or stilbene. Typical binary systems might be the liquid scintillator consisting of 3 g/l of p-terphenyl (solute) dissolved in xylene or toluene (solvent) or the plastic scintillator consisting of 10 g/l of p-terphenyl (solute) in polystyrene or polyvinyltoluene (solvent). By including a small concentration (0.01–0.1 g/l) of secondary solute, such as 1,4-bis-[2-(5-phenyloxazolyl)]benzene, better known as POPOP, these binary systems are transformed into typical ternary scintillators.

In the scintillation process in an efficient binary system the incident ionizing particle deposits energy essentially entirely in the bulk constituent or

TABLE 1
Organic scintillator compounds.

Compound	Formula	Application[a]
1. Benzene	C_6H_6	S
2. Toluene	$C_6H_5 \cdot CH_3$	S
3. p-Xylene	$C_6H_4 \cdot (CH_3)_2$	S
4. 1, 2, 4, Trimethylbenzene (pseudo-cumene)	$C_6H_3 \cdot (CH_3)_3$	S
5. Hexamethylbenzene	$C_6 \cdot (CH_3)_6$	S
6. Styrene monomer	$C_6H_5 \cdot C_2H_3$	S
7. Vinyltoluene monomer	$C_6H_4 \cdot CH_3 \cdot C_2H_3$	S
8. Naphthalene	$C_{10}H_8$	S', C
9. Anthracene	$C_{14}H_{10}$	C
10. Biphenyl	$C_{12}H_{10}$	S'
11. p-Terphenyl	$C_{18}H_{14}$	C, PS
12. p-Quaterphenyl	$C_{24}H_{18}$	C
13. trans-Stilbene	$C_{14}H_{12}$	C
14. Diphenylacetylene	$C_{14}H_{10}$	C
15. 1, 1', 4, 4'-tetraphenylbutadiene	$C_{28}H_{22}$	SS
16. Diphenylstilbene	$C_{26}H_{20}$	SS
17. PPO [2,5-diphenyloxazole]	$C_{15}H_{11}NO$	PS
18. α-NPO[2-(1-Naphthyl), 5-phenyloxazole]	$C_{19}H_{13}NO$	PS
19. PBD[2-Phenyl, 5-(4-biphenylyl)-1,3,4-oxadiazole]	$C_{20}H_{14}N_2O$	PS
20. BBO[2,5-Di(4-biphenylyl)-oxazole]	$C_{27}H_{19}NO$	SS
21. POPOP[1,4-Bis-{2-(5-phenyloxazolyl)}-benzene]	$C_{24}H_{16}N_2O_2$	SS
22. TOPOT[1,4-Di-{2-(5-*p*-tolyloxazolyl)}-benzene]	$C_{26}H_{20}N_2O_2$	SS
23. DiMePOPOP[1,4-Di-{2-(4-methyl-5-phenyloxazolyl)}-benzene]	$C_{26}H_{20}N_2O_2$	SS

[a] S–primary solvent; S'–secondary solvent; PS–primary solute; SS–secondary solute; C–crystal scintillator.

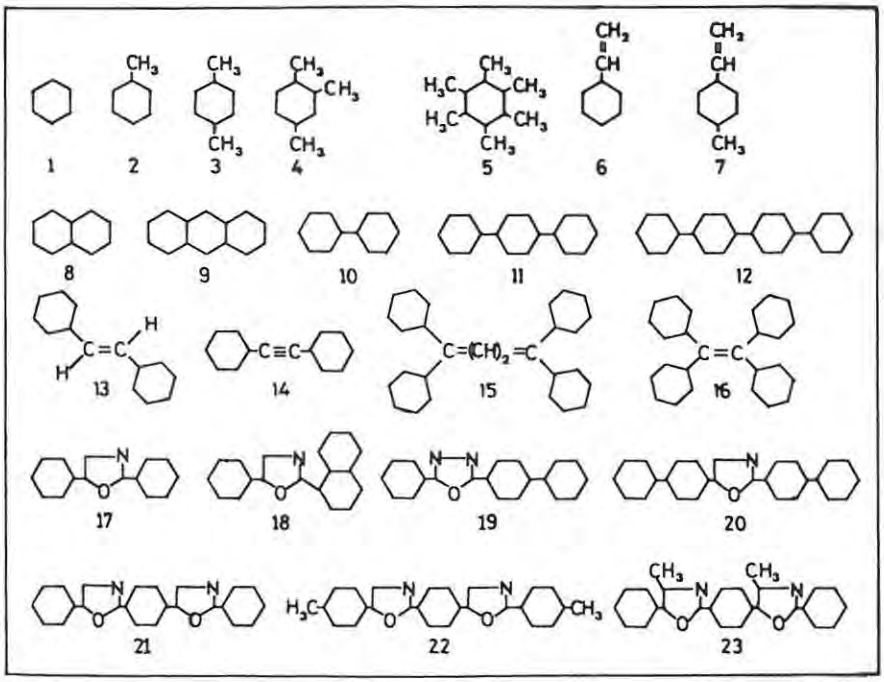

Fig. 1. Molecular structures of some organic scintillator compounds. The compounds are numbered as in table 1.

solvent but the final scintillation emission originates almost entirely from the solute showing that an efficient transfer of excitation energy occurs from solvent to solute. In a ternary system there is a further transfer of energy from solute to secondary solute.

At the outset, therefore, we can distinguish three aspects which are basic to the scintillation mechanism in organic systems. One aspect has to do with the molecular energy states which carry, transfer and finally radiate the scintillation energy. A second aspect relates to the manner in which these states are populated when an ionizing particle deposits energy in the scintillator. The third aspect deals with the processes and interactions which take place between excitation and light emission and which determine characteristics such as the scintillation decay and response which may be particularly important from the practical viewpoint.

2.1. Molecular structure and π-electronic states

Some of the better known organic scintillator compounds are listed in table 1 with their chemical formulae. Some molecular structures are shown in fig. 1. The scintillators are aromatic compounds with planar molecules built up mainly from condensed or linked benzenoid rings[11,12]). A key feature of the molecular structure is the presence of extended groupings of conjugated double bonds, based largely on linkages between unsaturated carbon atoms. In simplified terms this nonsaturation implies that only two or three of the four valence electrons of carbon are strongly localized within the molecular structure. They occupy so-called σ-orbits positioned between the atoms which they bind. The remaining valence electrons are delocalized within the molecule and are not associated with any one particular atom. They occupy π-molecular orbitals which extend over the conjugated region, above and below the molecular plane containing the σ-orbitals. The π-electronic states are of particular interest because transitions between these states lead to the luminescence observed in the scintillation process[11,22]).

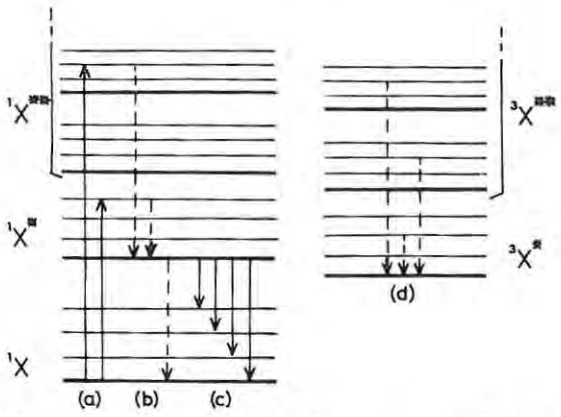

Fig. 2. Schematic energy level diagram for a scintillator molecule X. Vertical lines (a)–(d) indicate radiative (solid lines) and radiationless (broken lines) transitions.

To be specific we first consider an ideal pure monocrystal unitary scintillator of the compound X. The organic scintillator compounds form molecular crystals in which inter-molecular binding is due to van der Waals forces. Since this binding is weak the crystal may be approximated as a system of oriented but non-interacting molecules. Fig. 2 shows a schematic energy level sequence for the π-electronic levels of a scintillator molecule. The ground state configuration is a singlet denoted ^1X in which the π-electron spins are fully paired. The excited π-electronic states include the first excited singlet state denoted $^1X^*$ and higher excited singlets $^1X^{**}$. Other π-electronic configurations with unpaired π-electron spins give rise to excited states such as the lowest triplet state $^3X^*$ and the higher triplet states $^3X^{**}$ shown in fig. 2. Associated with each π-electronic level is a vibrational band of substates as shown in fig. 2.

The properties and transitions of π-electronic systems have been widely investigated in studies of photo-excited luminescence[22]). Photon absorption is constrained by the multiplicity selection rule for electric dipole transitions, which inhibits transitions between singlet and triplet states by a large factor, typically of the order of 10^8, for the $^1X \rightarrow {}^3X^{**}$ transition in fig. 2. Thus photon absorption at wavelengths between those corresponding to the $^1X \rightarrow {}^1X^*$ transition and the molecular ionization threshold effectively excites only the singlet states $^1X^*$ and $^1X^{**}$. Absorption occurs by vibronic transitions, such as (a) in fig. 2, in which vibrational as well as electronic modes are excited. For normal or low excitation densities, implying a negligible probability of interaction between excited molecules, all higher singlet excitations decay rapidly ($<10^{-11}$ s), non-radiatively and with near to 100% efficiency to the lowest state of the $^1X^*$ vibrational band [see (b) in fig. 2]. In this process of internal degradation the excess excitation energy is taken up by vibrational phonons through the

vibrational coupling of the electronic states to the molecule. Many organic compounds besides the efficient scintillators exhibit this property of efficient internal degradation of excitations from higher states to the $^1X^*$ state[22]).

Before and after degradation to the $^1X^*$ state the interaction of an excited molecule with an unexcited molecule can lead to transfer[26]) of the excitation energy either radiatively or non-radiatively. Intermolecular coupling in organic crystals facilitates non-radiative transfer by processes such as excitation migration[27,28]). In this way the electronic excitation energy is effectively delocalized over many molecules in the crystal.

The $^1X^*$ state is observed to decay exponentially, with lifetime in the range 1–80 ns, depending on the scintillator, and with a high probability of radiative decay or 'fluorescence'. For scintillation crystals such as anthracene or stilbene the radiative branching probability, or quantum efficiency, exceeds 80%. The decay proceeds to the vibrational substates of the ground state ^1X, as shown by (c) in fig. 2, hence the fluorescence spectrum lies predominantly at wavelengths longer than the singlet absorption threshold corresponding to the $^1X \rightarrow {}^1X^*$ transition. The crystal is therefore highly transparent to its own scintillation emission.

Triplet states have been studied using high intensity photo-excitation. For example, the $^3X^*$ state of anthracene has been excited using a laser source of wavelength longer than that corresponding to the singlet absorption threshold[29]) and higher triplet states $^3X^{**}$ have been populated by double photon absorption[29–30]) and inter-system crossing $^1X^{**} \rightarrow {}^3X^{**}$. Like the $^1X^{**}$ states, the $^3X^{**}$ states are found[22]) to decay rapidly, non-radiatively and efficiently to the lowest triplet state $^3X^*$ as depicted by (d) in fig. 2. The decay of the $^3X^*$ state to the ground state ^1X is strongly forbidden by the multiplicity selection rule and the associated longer wavelength emission called phosphorescence is very weak in comparison with the fluorescence emission and does not appear to play a significant role in the scintillation process. The $^3X^*$ state decays instead by the process of triplet annihilation[31–36]),

$$^3X^* + {}^3X^* \rightarrow {}^1X^* + {}^1X + \text{phonons}, \qquad (1)$$

in which two triplet excitons interact to form one singlet excited $^1X^*$. The time scale of this process is determined by the kinetics of the triplet exciton diffusion process preceding the triplet–triplet interaction and can be many orders of magnitude longer than the $^1X^*$ fluorescence lifetime. The subsequent decay of the $^1X^*$ states populated according to eq. (1) therefore generates an additional delayed fluorescence component[34–36]) with the same spectral distribution as the prompt fluorescence but emitted non-exponentially and over a much longer time scale.

Another type of bimolecular process which can be important in photoluminescence phenomena is that leading to complex formation between an excited molecule and an unexcited molecule[22,37,38]), for example

$$^1X^* + {}^1X \rightarrow {}^1D^* \qquad (2)$$

where the product $^1D^*$ is an excited dimer, known as an excimer if formed from two molecules of the same species as in eq. (2), or as an exciplex if formed from two different species. Excimers and exciplexes behave like distinct molecular species and exhibit their own characteristic fluorescence[38,39]). They do not appear to play an important part in the scintillation process except possibly in certain dilute liquid and plastic solutions.

2.2. Primary excitation by ionizing particles

The model proposed by Meyer and Murray[40]) of the scintillation process in inorganic crystals drew a distinction betxeen the roles of primary excitations induced directly by the incident particle and those induced by secondary electrons produced by the particle. The same distinction is a key feature of the model of Voltz et al.[12–14,41,42]) which has been very successful in describing the organic scintillation mechanism. Fig. 3 taken from the paper of Laustriat[43]) represents a portion of the wake

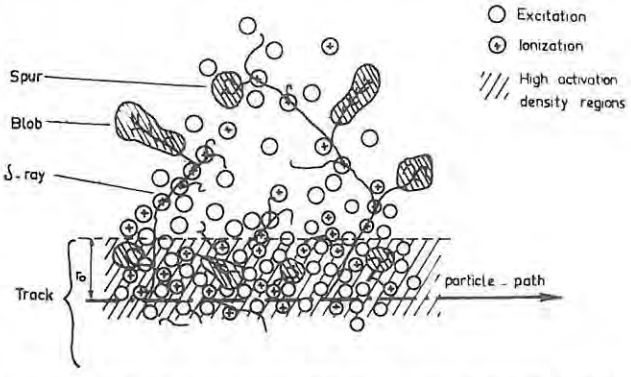

Fig. 3. Schematic representation[43]) of the spatial distribution of excitations induced by a charged particle in an organic scintillator (fig. from ref. 43).

of a medium energy heavily ionizing particle (e.g. 10 MeV p, d or α) in a scintillator medium, immediately after passage of the particle. The primary excitation includes molecules ionized or excited by the direct Coulomb interaction at distances up to several molecular diameters from the particle path. In addition, secondary electrons released in close encounters with the particle cause further excitations as they are brought to rest in the medium. The average density of excitation drops off away from the particle path but for heavily ionizing particles we can define a core or track consisting of a region of very high excitation density, extending to a radius r_0 measured from the path as shown in fig. 3.

The escape of fast secondary electrons (δ-rays) from the track leads to further excitation and ionization outside the track, including additional regions of localized high excitation density, as illustrated by the 'blobs' and 'spurs' in fig. 3. Incident beta rays or other high energy electrons behave like extremely high energy δ-rays and so produce no track of the type defined in fig. 3 and no high excitation density regions other than the blobs and spurs. At the opposite extreme, for a very heavily ionizing particle which produces a high density of δ-rays, the blobs and spurs outside the track merge to form a more or less uniform annular region of high excitation density.

For a section of the particle path (as in fig. 3) the distribution of primary energy between the track and beyond it and the densities of primary excitation in each of these regions depend on the specific energy loss dE/dx, the charge z and the velocity of the particle. The two regions each make their own distinct contribution to the scintillation process and these contributions must each be integrated along the finite path length of the particle in the scintillator.

2.3. The scintillation decay of organic crystals

The scintillation emission is associated with the decay of π-electronic states excited by the incident particle, by secondary electrons produced by the particle, by ion recombination, or by X-ray or ultra-violet photons emitted following ion recombination. For excitations in regions of low excitation density the decay proceeds as in the photoluminescence process, that is by efficient internal degradation to the lowest excited singlet and triplet states $^1X^*$ and $^3X^*$ in the first instance. However, for excitations within the track the final yield of fluorescence emission is reduced because additional non-radiative decay paths are accessible through mutual interactions of excited molecules or transfer of excitation energy to transient or permanent quenching agents created by the incident particle. It is assumed[12–14]) that these ionization quenching processes compete strongly with the rapid ($\sim 10^{-11}$ to 10^{-10} s) and otherwise efficient processes of internal degradation of excitation energy from the higher π-electronic states $^1X^{**}$ and $^3X^{**}$ to the $^1X^*$ and $^3X^*$ states.

The $^1X^*$ state is therefore populated promptly from unquenched decays of $^1X^{**}$ excitations both within and outside the track and the decay of this state leads to the prompt component of the scintillation emission which decays exponentially, as in the photofluorescence process, and with the same quantum efficiency and lifetime. However, whereas in the photofluorescence process essentially all the $^1X^{**}$ excitations decay to the $^1X^*$ state, in the scintillation process only a fraction do so, and this fraction decreases with increase of the specific energy loss of the incident particle in the scintillator. The assumption that ionization quenching operates prior to the population of the $^1X^*$ state and not after, is supported by observations on many scintillators, which indicate that the lifetime of the prompt decay component is independent of mode of excitation, whether by photoexcitation or by electrons, protons or alpha particles. In some crystals however the lifetime of the prompt emission is sensitive to crystal-thickness and the depth below the surface at which excitation occurs[11]). This effect is important for anthracene crystals at depths or thickness of $<100\,\mu$m and it can be understood as a boundary phenomenon which affects the energy transfer processes in the crystal or the absorption and re-emission of fluorescence photons[44]).

In addition to the prompt emission the scintillation decay exhibits a delayed, non-exponential component of mean life typically >300 ns[11]). Like the analogous delayed component observed in photoluminescence under high excitation density, the delayed scintillation component is attributed[12]) to triplet annihilation processes as described by eq. (1). Ion recombination provides a mechanism for populating higher triplet states $^3X^{**}$ in the scintillation process, and is expected to favour triplet states over singlet states in the ratio of their multiplicities, that is 3 : 1. The triplet annihilation processes, being bimolecular and therefore dependent

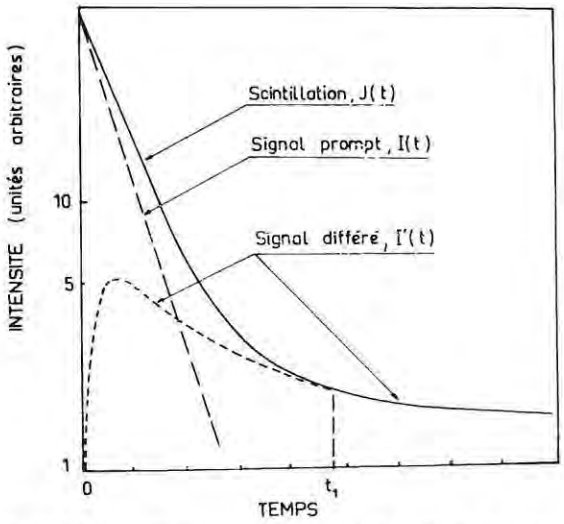

Fig. 4. Schematic representation[41]) of the scintillation decay, $J(t)$ of an organic scintillator showing the prompt component $I(t)$ and delayed component $I'(t)$ (fig. from ref. 41).

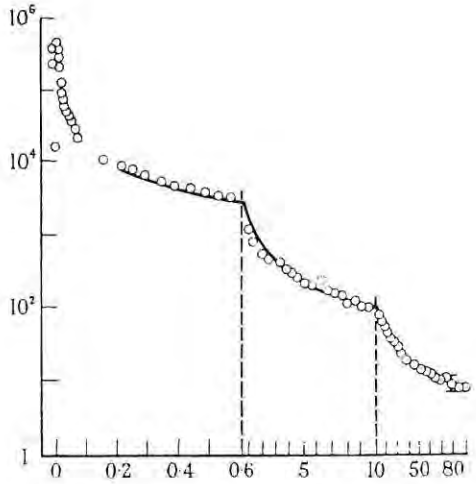

Fig. 5. Experimental points[45]) and theoretical curve fit[12]), normalized at 0.2 μs, for the delayed component decay resulting from excitation of a trans-stilbene crystal by α-particles (fig. from ref. 12).

on excitation density, are concentrated in the particle track and in the spurs and blobs of high secondary excitation density. Excitations resulting from ion recombination in the track should be less sensitive to ionization quenching than the corresponding prompt excitations because the density of excited molecules and quenching agents in the track must drop appreciably during the finite time ($<10^{-10}$ s) required for ion recombination. Thus the delayed component originating from ion recombination and triplet annihilation is less sensitive to specific energy loss than the prompt component. The relative integrated intensities of the prompt and delayed components therefore depend on $\mathrm{d}E/\mathrm{d}x$ and hence on the type of particle responsible for the scintillation, thereby providing the basis for the technique of particle identification by pulse shape discrimination.

Models describing the kinetics of the prompt and delayed components have been formulated by King and Voltz[12]) and by Voltz et al.[14,41]). These authors have obtained good theoretical fits to experimental measurements of the scintillation decays of stilbene and anthracene crystals and of some liquid scintillators. By fitting these observations they determine various parameters characteristic of triplet excitations in the scintillators concerned and the values they obtain are in good agreement with independent estimates of these parameters based on photofluorescence or photoconductivity studies.

Fig. 4. taken from Voltz et al.[41]) illustrates schematically the resolution of a scintillation decay into a prompt exponential component and a delayed non-exponential component. Fig. 5 shows the fit obtained by King and Voltz[12]) to the delayed component decay of stilbene for 5 MeV α-particles, as observed by Bollinger and Thomas[45]).

2.4. Ionization quenching and specific fluorescence

The response $L(E)$ of organic scintillators to heavily ionizing particles is a non-linear function of the particle energy E and is smaller for the more heavily ionizing particle when different types of particle are compared at the same energy. A very successful semi-empirical model was formulated by Birks[46]) in 1951 to describe this phenomenon. Recognizing that the non-linear response is caused by quenching processes governed by the specific energy loss, or energy deposited per unit distance $\mathrm{d}E/\mathrm{d}x$ along the particle path, Birks proposed a relation between the specific fluorescence $\mathrm{d}L/\mathrm{d}x$, representing the scintillation photons emitted per unit distance, and $\mathrm{d}E/\mathrm{d}x$:

$$\mathrm{d}L/\mathrm{d}x = A\ \mathrm{d}E/\mathrm{d}x\ (1+kB'\ \mathrm{d}E/\mathrm{d}x)^{-1}$$

$$= A\ \mathrm{d}E/\mathrm{d}x\ (1+B\ \mathrm{d}E/\mathrm{d}x)^{-1}, \qquad (3)$$

where $B'\mathrm{d}E/\mathrm{d}x$ represents the density of quenching centres produced per unit distance by the incident particle and the specific fluorescence is reduced by a factor $(1+kB'\mathrm{d}E/\mathrm{d}x)$ due to quenching processes characterised by a quenching parameter k.

A modified relation, including quenching effects to the next order in dE/dx was proposed by Chou[47]):

$$dL/dx = A\, dE/dx\, [1 + B\, dE/dx + C(dE/dx)^2]^{-1}, \quad (4)$$

and a different treatment by Wright[48]) which also included second order effects led to a third relation of the form

$$dL/dx = (A/2B)\ln(1 + 2B\, dE/dx). \quad (5)$$

The similar behaviour of eqs. (3)–(5) in the limit of small dE/dx may be demonstrated by putting $C = \frac{1}{2}B^2$ in eq. (4) and expanding in powers of $(B\, dE/dx)$, which gives the same expansion to second order for the three relations. In agreement with experiment the three relations predict a linear response $L(E) = AE + L_0$ in this limit. In the limit of high dE/dx the relations predict different behaviours. For $B\,dE/dx \gg 1$ eq. (3) predicts saturation of the specific fluorescence, $dL/dx = A/B$, which implies a response proportional to the range $R(E)$ of the particle in the scintillator, that is $L(E) = (A/B)\,R(E)$. Eq. (5) predicts a continuing rise of dL/dx with increasing dE/dx and eq. (4) predicts that dL/dx will pass through a maximum if the coefficient C is assumed to be positive. These three models and a later and more general model proposed by Blanc et al.[49]) share a common assumption – that the specific fluorescence dL/dx can be expressed as a function of the specific energy loss dE/dx alone, implying that data from different types of particle should all lie on the same curve in a plot of dL/dx versus dE/dx.

Prior to 1964 most of the attempts made to test the dL/dx versus dE/dx models were based on response measurements on anthracene crystals. The general trends predicted by eqs. (3)–(5) were confirmed by these early investigations[11]) but some evidence was reported which suggested that dL/dx depended on particle type as well as on dE/dx. However, the significance of this evidence was and remains doubtful, in view of the susceptibility of anthracene crystals to surface effects[11]) which can distort observations made using low-energy surface-incident charged particles. In the meanwhile the dependence of dL/dx on particle type as well as on dE/dx has been established from measurements on plastic scintillators using heavy ion beams as well as electrons, protons and α-particles. In addition Voltz et al.[13,14]) have formulated a theory of the scintillation response which takes account of the spatial distribution of primary excitations (see section 2.2) and of the kinetics of the prompt and delayed scintillation components (see section 2.3). They obtain the following expressions for the specific fluorescences $(dL/dx)_p$ and $(dL/dx)_d$ of the two components

$$(dL/dx)_p = C_p\{(1 - F_s)\,(dE/dx)\exp[-B_s(1 - F_s) \times (dE/dx)] + F_s(dE/dx)\}, \quad (6)$$

$$(dL/dx)_d = C_d\{\phi_1(dE/dx)\exp[-B_t\,\phi_1(dE/dx)] + \phi_2(dE/dx)\}, \quad (7)$$

where the first term in each equation represents the integrated (over time) intensity of the scintillation emission resulting from primary excitations within the particle track and the second term represents the integrated intensity of the emission resulting from excitations outside the track by fast secondary electrons. The exponential damping factors in the first terms represent the effects of primary ionization quenching in the track and B_s and B_t are parameters which characterize the quenching of singlet $^1X^{**}$ and triplet $^3X^{**}$ states respectively. The factors C_p and C_d are constants of proportionality which depend on the quantum efficiency of the final emitting state (the $^1X^*$ state in the case of a crystal scintillator) and the average energy which must be deposited in the scintillator (assuming no primary quenching) to populate the $^1X^*$ or $^3X^*$ state respectively. The parameter F_s is a function[13]) of the quantity $z^2(dE/dx)^{-1}$ where z is the charge of the incident particle. The parameters ϕ_1 and ϕ_2 in eq. (7) depend on the relative numbers of triplet states populated within and outside the track respectively and on the number of $^1X^*$ states fromed per triplet $^3X^*$ that decays or annihilates. Like the fraction F_s in eq. (6), the ratio ϕ_1/ϕ_2 depends on z.

The components $(dL/dx)_p$ and $(dL/dx)_d$ given by eqs. (6) and (7) therefore depend on particle charge z as well as on the specific energy loss dE/dx. Like eqs. (3)–(5) these relations predict a linear variation of response with energy in the limit of small dE/dx. For increasing values of dE/dx the behaviour of dL/dx depends on z and different forms of variation may occur, depending on the values of F_s, B_s, B_t, ϕ_1 and ϕ_2. For small values of F_s or of ϕ_2/ϕ_1 the first terms in eqs. (6) and (7) will produce maxima in the dependences of $(dL/dx)_p$ and $(dL/dx)_d$ on dE/dx. For appreciable values of F_s or ϕ_2/ϕ_1 the second terms in these equations will

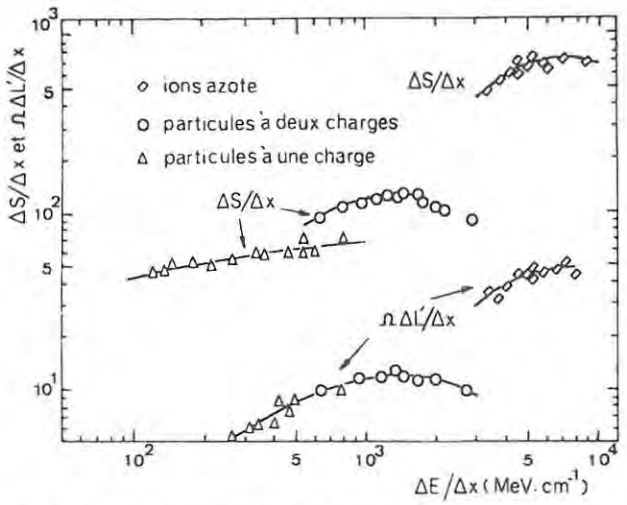

Fig. 6. Specific fluorescence, $\Delta S/\Delta x$ or $\Omega \Delta L'/\Delta x$ (arbitrary units), vs specific energy loss $\Delta E/\Delta x$ observed[42]) using thin foils of plastic scintillator NE102. The quantities $\Delta S/\Delta x$ and $\Omega \Delta L'/\Delta x$ correspond to (dL/dx) and $(dL/dx)_d$ [eqs. (6) and (7)] respectively. Data shown are for: nitrogen ions (squares); protons and deuterons (triangles); and $^3He^{++}$ and $^4He^{++}$ ions (circles) (fig. from ref. 42).

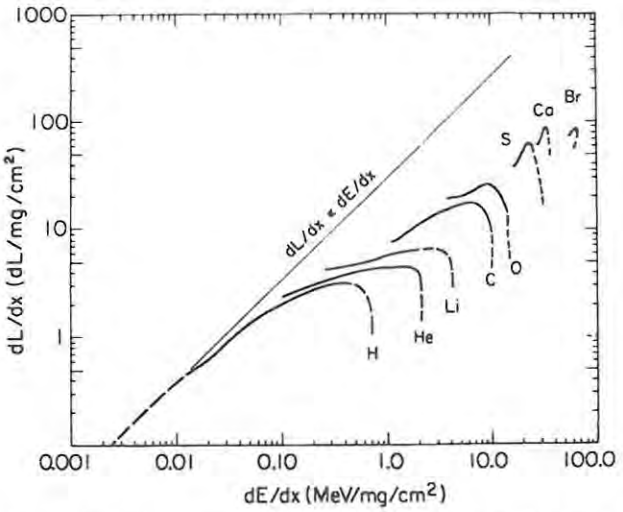

Fig. 7. Specific fluorescence dL/dx vs calculated specific energy loss dE/dx in NE102 for different incident ions[50]). The solid and dashed curves are based on response measurements with uncertainties ±5% and ca. ±20% or greater respectively (fig. from ref. 50).

ultimately cause an increase of $(dL/dx)_p$ or $(dL/dx)_d$ with dE/dx at high dE/dx. If F_s or ϕ_2/ϕ_1 are appreciable and constant in the limit of high dE/dx then the linear relationship between response and energy will be restored in this limit but with the constant of proportionality reduced from C_p to $F_s C_p$ in the case of the prompt component $L_p(E)$ and from $(\phi_1+\phi_2)C_d$ to $\phi_2 C_d$ in the case of the delayed component.

Some of the distinctive characteristics predicted by eqs. (6) and (7) have been verified experimentally. For example, Lopes da Silva and Voltz[42]) have measured specific fluorescences for thin foils of plastic scintillator (NE102) using protons (0.3–4 MeV), deuterons (0.3–1 MeV), tritons (0.3–1 MeV), $^3He^{++}$ ions (1–3 MeV), α particles (1–9 MeV) and nitrogen ions (10–80 MeV). Fig. 6 taken from their paper shows the pronounced dependence of the total specific fluorescence dL/dx [equivalent to the sum of eqs. (6) and (7)] on ion charge, the absence of dependence of dL/dx and $(dL/dx)_d$ on ion mass (for a given z) and the predicted maxima in dL/dx and $(dL/dx)_d$ for light doubly charged ions. Fig. 7 shows the values of dL/dx versus dE/dx derived by Bechetti et al.[50]) from their response measurements for a range of different ions (from H to Br) incident on NE102. The curves for individual ions show distinct maxima in dL/dx and give different values of dL/dx at the same dE/dx. Fig. 8 shows measurements of dL/dx obtained by Muga and Bridges[51]) for ^4He ions transiting a NE102 foil. By measuring the foil response at successively lower ion energies the variation of dL/dx with dE/dx was followed down through and below the maximum of the Bragg dE/dx versus E curve. The specific fluorescence was found to double back (fig. 8) showing lower values of dL/dx at energies below the Bragg maximum than for the energies, above that of the maximum, corresponding to the same value of

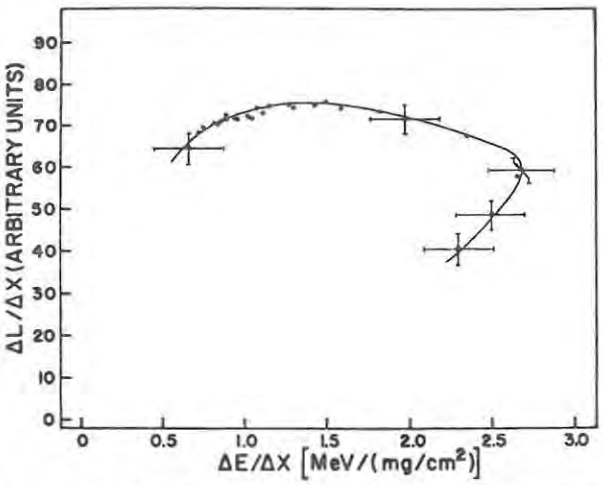

Fig. 8. Specific fluorescence $\Delta L/\Delta x$ vs specific energy loss $\Delta E/\Delta x$ for $^4He^{++}$ ions transiting a 112 μg/cm^2 NE102 scintillator foil[51]) (fig. from ref. 51).

dE/dx. The effect can probably be understood in terms of the changes that must occur in parameters such as F_s, B_s, B_t, ϕ_1 and ϕ_2 as the Bragg maximum is passed.

Ahlen et al.[52]) have studied the responses of Pilot Y (0.984 g/cm^2) and Pilot F (0.328 g/cm^2) plastic scintillator sheets to relativistic ^{20}Ne ion beams; to cosmic-ray iron ions and to atmospheric muons and have discussed their results with reference to the model of Voltz et al.[14,41]). They use a form of F_s which is suitable for relativistic energies

$$F_s = \frac{\ln(\varepsilon_{max}/T_0) - \beta^2}{2\ln(\varepsilon_{max}/I_0) - \beta^2}, \tag{8}$$

where T_0 is the minimum kinetic energy required for a secondary electron to escape from the primary ionization track, I_0 is the adjusted ionization potential of the scintillator material (63 eV) and $\varepsilon_{max} = 2m_e c^2\beta^2\gamma^2$ with Lorentz parameters γ and β for the incident particle. Using their neon data to fit the parameters B_s in eq. (5) and T_0 in eq. (8). Ahlen et al. are able to make accurate predictions of the scintillator responses to muons and iron ions. Their results also confirm the predicted linear response to relativistic but highly ionizing iron ions as shown in fig. 9 which is taken from their paper.

The model of Voltz et al.[14,41]) has therefore already achieved some notable successes and it represents a significant step forward in the description of the specific fluorescence dL/dx. However, more data are required to check the validity of the model over a wider range of incident particle energy and charge state.

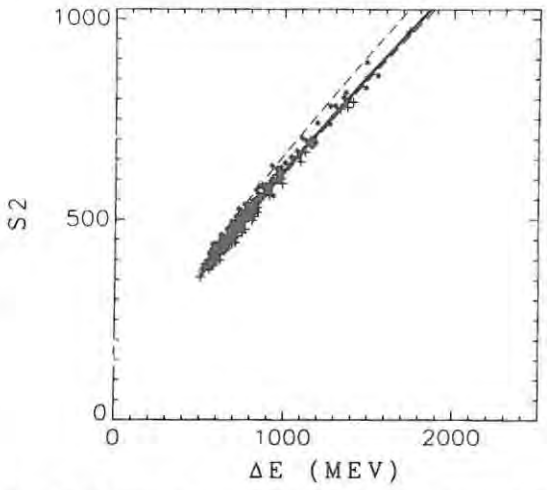

Fig. 9. Response S2 of a Pilot F plastic scintillator sheet (0.328 g/cm^2) to transiting iron ($Z=26$) ions as a function of the energy ΔE deposited in the scintillator[52]). The energy at exit from the scintillator, of the event with the greatest ΔE shown here is 47.5 MeV per nucleon (fig. from ref. 52).

2.5. Liquid and plastic scintillator solutions

A binary solution scintillator[11,53]) contains two molecular species X and Y such that the lowest π-electronic excited states of the solute Y, the singlet $^1Y^*$ and triplet $^3Y^{**}$, lie at lower excitation energies than the corresponding states $^1X^*$ and $^3X^{**}$ of the solvent X. In an efficient binary system the early stages of the scintillation process are similar to those in a unitary scintillator. The only major systematic differences are in the mechanisms of intermolecular energy transfer, which depend on the physical form – crystal, liquid or plastic – of the solvent. Primary excitation, ionization quenching and internal degradation of excitation energy take place as in a unitary system and excitation energy is rapidly fed to the $^1X^*$ and $^3X^*$ states of the bulk component, the solvent X. In an efficient scintillator the process of energy transfer from solvent to solute then competes strongly with other modes of de-excitation (fluorescence or quenching) of $^1C^*$ and $^3X^*$. The energy transfers from X^* to Y are represented by

$$^1X^* + {}^1Y \rightarrow {}^1X + {}^1Y^*, \tag{9}$$

$$^3X^* + {}^1Y \rightarrow {}^1X + {}^3Y^*. \tag{10}$$

The transfer processes are accompanied or followed by internal degradation of the excess vibrational energy in $^1Y^*$ or $^3Y^*$ thus leaving the excitation trapped in these, the lowest excited states of the system. The fluorescence decays of the $^1Y^*$ states from eq. (9) lead to the prompt scintillation emission. Triplet annihilation [eq. (1)] of the $^3Y^*$ states from eq. (10) populates $^1Y^*$ states over a relatively long period and thus produces a delayed scintillation component.

In liquid or plastic solutions the energy transfer process implied by eq. (9) can be radiative or non-radiative[54]) and the importance of non–radiative transfer increases with increasing solute concentration. The transfer of triplet excitation energy [eq. (10)] requires a non-radiative mechanism. Two limiting cases of non-radiative transfer (in solutions) are identified by Birks[54]). One is the situation in which complete statistical mixing of X^* and Y occurs owing to molecular diffusion and/or migration of excitation energy X^* through the solvent system. This collisional type of process appears to

dominate the energy transfer in typical binary liquid scintillators based on low-viscosity solvents (e.g. benzene, xylene or toluene) and containing appreciable concentrations of solutes[55]).

The other limiting situation[54]) is that in which X^* and Y remain effectively stationary, apart from possible Brownian rotation, and transfer occurs by a long-range, radiationless, dipole–dipole interaction process, the theory of which has been developed by Förster[56]). This type of nonradiative transfer occurs in typical plastic scintillators in which the π-electron systems which carry the solvent excitation energy are localized in individual aromatic segmers coupled to polymer chains[11]).

The time dependence of the prompt scintillation component in binary solutions is discussed by Birks[54]) and Birks and Pringle[57]). The prompt component in liquid scintillators can be written in the form[57])

$$P_Y(T) = [K/(K-1)]\,(e^{-T} - e^{-KT}), \qquad (11)$$

where $P_Y(T)$ is proportional to the rate of photon emission, $T(=t/\tau_{0Y})$ is the time measured in units of the decay time τ_{0Y} of the solute $^1Y^*$ fluorescence and t = time in seconds. The parameter $K = k_X\tau_{0Y} = \tau_{0Y}/\tau_X$ represents the ratio of lifetimes of the excitation in the solute and solvent and k_X is given by

$$k_X = 1/\tau_X = (1/\tau_{0X}) + k_{YX}[^1Y], \qquad (12)$$

where τ_{0X} is the $^1X^*$ fluorescence decay time, $[^1Y]$ is the molar concentration of the solute and the product $k_{YX}[^1Y]$ is the rate of the energy transfer process represented by eq. (9).

In a unitary scintillator the rise time of the prompt emission is negligible compared with the fluorescence decay time because the emitting state $^1X^*$ is populated by very rapid decay from the primary $^1X^{**}$ excitations. In contrast, the prompt decay [eq. (11)] of the emitting $^1Y^*$ state in a binary liquid scintillator has a rise time determined mainly by the smaller of the lifetimes τ_{0Y} and τ_X. The lifetime τ_X depends on the solute concentration [eq. (12)]. By increasing this concentration the ratio K of the two lifetimes is increased and the scintillation rise time is reduced. The function $P_Y(T)$ of eq. (11) is plotted in fig. 10 for values of K from 1.5 to ∞.

The time dependence of the prompt component in binary plastic scintillators has a different form to eq. (11) due to the different energy transfer pro-

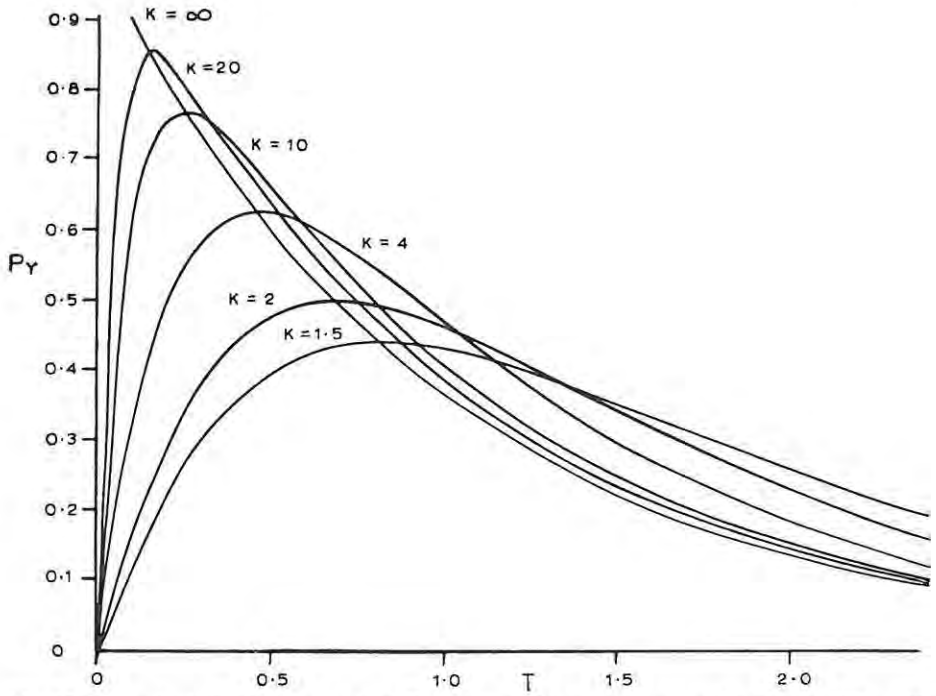

Fig. 10. General scintillation pulse shapes[57]) P_Y vs T of binary liquid solutions [eq. (11)] for different values of the parameter K. The time T is expressed in units of the decay time τ_{0Y} of the solute fluorescence (fig. from ref. 57).

cesses which occur in liquid and plastic solutions[54]). The time dependence is proportional to the function[54,57])

$$p_Y(t) \propto \{\exp(-t/\tau_{0Y}) - \exp[-(t/\tau_{0X}) - 2\gamma(t/\tau_{0X})^{\frac{1}{2}}]\}, \quad (13)$$

in which the parameter $\gamma = [^1Y]/[^1Y]_0$ is the ratio of the molar solute concentration $[^1Y]$ to a critical molar concentration $[^1Y]_0$ which is defined in terms of the critical radius[56]) for the dipole–dipole transfer process. Thus in plastic scintillators, as in liquids, a higher concentration of solute will lead to a faster scintillation rise time.

The time dependence of the delayed scintillation component in binary systems is discussed and analysed by Voltz et al.[14,41]). Their model predicts[14]) and their experiments verify[51]) that the time-dependence of the delayed component in binary liquid scintillators is determined by the properties of the solvent and is independent of the scintillation solute, as illustrated in fig. 11. This observation is consistent with triplet annihilation, in terms of which the annihilation rate which governs the time distribution of the delayed component is itself governed by the rate of triplet $^3Y^*$ diffusion through the solvent. The effect whereby dissolved oxygen reduces the delayed component in liquid scintillators[58]) is explained[14]) in terms of oxygen quenching of triplet excitations and good agreement is obtained[41]) with experimental measurements.

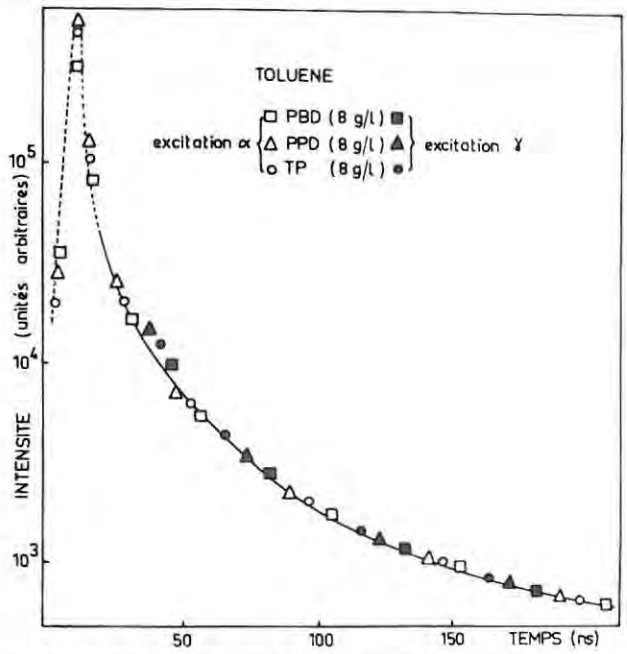

Fig. 11. Experimental points and theoretical curve fit[41]), normalized at 180 ns, for the delayed scintillation component resulting from excitation of binary liquid scintillators by α-particles (open points) and γ-rays (solid points). The solutions contained 8 g/l of PBD (squares), PPO (triangles) or terphenyl (circles) in toluene and were degassed (fig. from ref. 41).

The addition of a secondary solute to convert from a binary to a ternary solution extends the scintillation process by a further energy transfer stage [eqs. (9) and (10)] between the solute Y and the secondary solute Z. The $^1Y^* \rightarrow {}^1Z^*$ transfer occurs both radiatively and non-radiatively, in the latter case by the long range dipole–dipole interaction[56]). The use of secondary solutes has advantages if the longer wavelengths of their emission spectra are more efficiently transmitted through the scintillator to the photomultiplier, for example in large liquid scintillators. However, where the light transmission is already very good, as is often the case for small scintillators, for example, the addition of a secondary solute will be no advantage in this respect. It may in fact be a disadvantage in another respect because the additional energy transfer which is involved can degrade the timing response of the scintillator[54,57]).

Another type of three-component scintillator, not usually referred to as ternary, is that obtained by adding a suitable secondary solvent[59]), for example naphthalene, in fairly high concentration (e.g. 300 g/l) to a binary solution. The role of the secondary solvent appears to be [59]) to facilitate the solvent to solute energy transfer [eqs. (9) and (10)] by acting as an intermediary in the transfer process[59,60]). The effect is particularly important for the triplet energy transfer [eq. (10)] and therefore for applications such as pulse shape discrimination which depend on the associated delayed scintillation component. On the other hand, secondary solvents, like secondary solutes, degrade the timing resolution of the system.

2.6. Directional effects in crystal scintillators

In addition to ion channelling effects and blocking effects the characteristics of organic crystal scintillators exhibit a direction-dependence in their response to protons and heavier particles. Investigations with α-particle beams[62-66]) and with recoil protons[67-71]) have shown that the scintillation responses of crystals are generally anisotropic and pass through maxima or minima for α-particle or proton directions parallel or nearly parallel to one or other of the crystal axes. Fig. 12, taken from

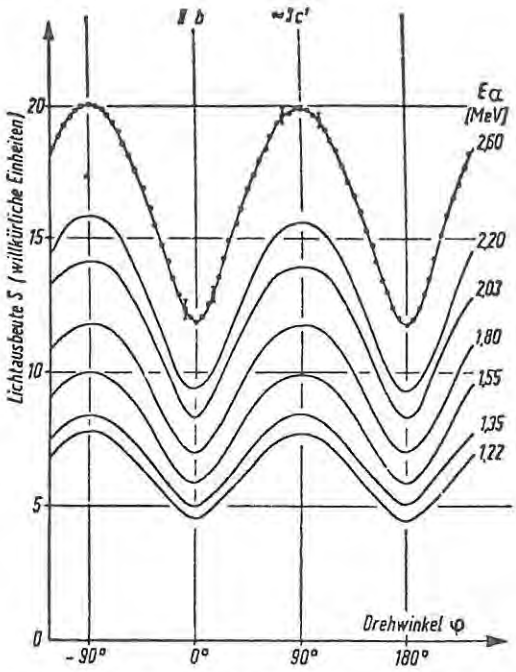

Fig. 12. Response S of an anthracene crystal to α-particles of different energy as a function of α-particle direction in the bc'-plane[63]). The angle ϕ indicates the α direction relative to the crystal b-axis (fig. from ref. 63).

the paper of Kratochwill[63]), shows the response of an anthracene crystal as a function of α-particle energy and direction, for directions in the bc'-plane of the crystal. The artificial c'-axis of the crystal is defined as the normal to the crystal ab-plane, as illustrated with reference to the anthracene unit cell in fig. 13. For anthracene the direction of maximum response (fig. 12) coincides approximately with the c'-axis and the direction of minimum response coincides with the b-axis[63]).

A response anisotropy A_L may be defined[71]) as the variation in response divided by the average response, that is

$$A_L = 2(L_{max} - L_{min})/(L_{max} + L_{min}), \qquad (14)$$

where L_{max} and L_{min} are the maximum and minimum responses. Fig. 14 shows measurements of A_L as a function of energy for recoil protons in anthracene. Like ionization quenching and the associated non-linear energy responses, the anisotropy is larger at low proton energies. The magnitude of the directional effect seriously limits the usefulness of crystal scintillators for neutron detection, as pointed out by Coon[67]). On the other hand there are also useful applications of the anisotropy effect in the field of direction sensing[71]).

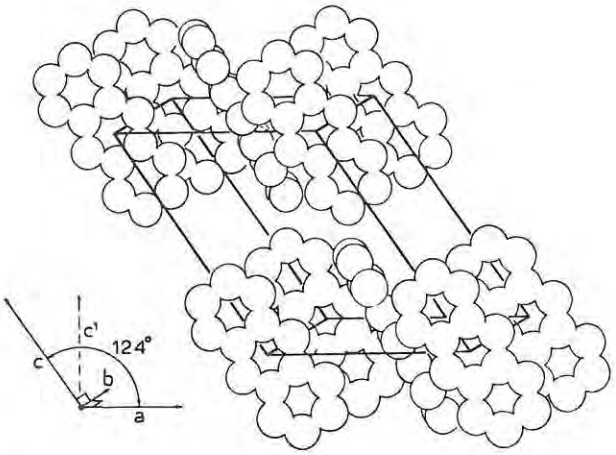

Fig. 13. Arrangement of molecules in the unit cell of the anthracene crystal. The lengths (in Å) of the sides of the unit cell are $a=8.56$, $b=6.04$ and $c=11.16$. The artificial c'-axis is the direction normal to the ab-plane fig. from ref. 71).

The investigations by Tsukada and Kikuchi[68,69]) of the scintillation anisotropy of anthracene for 3.7 MeV recoil protons are of particular interest because the direction dependences of the prompt and delayed scintillation components were separately measured. A similar form of the direction dependence was found for the two components (with maxima close to the c'-direction and minima parallel to the b-direction) but the magnitude of the anisotropy was significantly larger for the prompt component. The direction-dependence of the scintillation pulse shape implied by this result was later confirmed by pulse shape discrimination studies[71]) using recoil protons of energies 8–22 MeV and similar effects were found in a naphthalene crystal[71]) and in a deuterated anthracene crystal[72]). Pulse shape discrimination studies

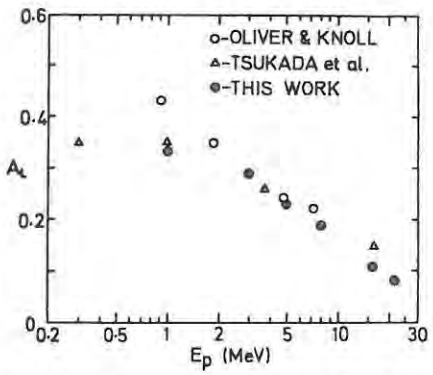

Fig. 14. Response anisotropy A_L of anthracene as a function of proton energy E_p [71]). Data are from ref. 69 (triangles), ref. 70 (open circles) and ref. 71 (solid circles) (fig. from ref. 71).

on stilbene, terphenyl and quaterphenyl crystals[71]) showed pulse shape anisotropies considerably smaller than those for anthracene.

Ion channeling effects and blocking effects have been observed and studied[65,73]) in anthracene and other crystals and their relationship to the response anisotropy effect has been discussed. Wille[73]) shows that for a given specific energy loss dE/dx in anthracene the specific fluorescence dL/dx is the same for channelled 6–9 MeV α-particles as for those incident in random directions. Kratochwill[63]) compared anisotropy measurements for 1–9 MeV α-particles with calculations based on quenching models[13,66]). He finds that the anisotropy of the prompt component cannot be explained by assuming only that the quenching parameter B_S in eq. (6) is direction–dependent. The pulse shape anisotropy characteristics of anthracene may be qualitatively understood[71]) in terms of a competition between transfer and quenching processes with the transfer process being anisotropic and occurring preferentially within the *ab*-plane of the crystal.

At the moment a complete quantitative explanation of the direction dependent characteristics of crystal scintillators appears to be lacking. It seems likely that the origins of the phenomena are related to those of the ionization quenching effect but it is not clear whether the Voltz model[13,14]) for ionization quenching will provide a suitable basis for understanding the scintillation anisotropy effects.

3. Characteristics of organic scintillators

The main characteristics which we use to describe the performance and properties of an organic scintillator may be summarized as:

a) the scintillation emission spectrum and the transmission of this spectrum through the scintillator;
b) the variation of response with energy for different types of charged particle;
c) the absolute scintillation efficiency, the response resolution and the associated energy resolution;
d) the fast timing characteristics, including the time resolution and the parameters which describe the prompt component of the scintillation decay [eqs. (11) and (13)];
e) the pulse shape characteristics, including the relative intensities of the prompt and delayed scintillation components (fig. 4) for different types of particle, and the suitability of these characteristics for particle identification by pulse shape discrimination; and
f) the direction-dependence (for crystal scintillators only) of the response and scintillation pulse shape.

The mean free paths for interactions of γ rays and neutrons in the scintillator and the associated detection efficiencies for these radiations are also of interest and importance. Further information on these subjects may be found in refs. 74–78. The scintillation emission spectrum (a) is usually assumed to be the same as that observed under photo-excitation (see e.g. refs. 11, 22) as is verified for example by Langenschiedt[79]) for a number of liquid scintillators.

Measurements of the characteristics (b)–(f) require the use of a photomultiplier tube and may therefore be sensitive to the photomultiplier characteristics which must be subtracted in order to obtain the true intrinsic scintillator characteristic. On the other hand uncorrected measurements which include the photomultiplier contribution may be at least as useful in assessing overall detector performance in a practical situation.

3.1. Response versus energy for different particles

Response measurements should ideally be carried out under strictly controlled conditions in order to facilitate comparisons between different scintillators and measurements. The size and shape of scintillator should be standardized together with the light collection geometry, including the shape and material of the light reflector used. Dissolved oxygen should be removed from liquid scintillators or displaced by nitrogen or argon for example. For crystals and plastic scintillators it is important that the scintillator surface should be clean and pure if externally incident charged particles are used. For crystals the orientation of crystal axes relative to the incident particle direction should be known or specified. The scintillation emission spectrum $F(\lambda)$ and the absolute spectral sensitivity $\phi(\lambda)$ of the photomultiplier cathode should be known in order to calculate the photocathode response factor η of the photomultiplier-scintillator combination.

$$\eta = \int \phi(\lambda)\, F(\lambda)\, d\lambda \Big/ \int F(\lambda)\, d\lambda , \qquad (15)$$

where the integrations are taken over the spectrum $F(\lambda)$. The photocathode response should be

TABLE 2
Response data reported 1965–1976.

First author name	Year	Scintillators	Particle and energy (MeV)	Ref.
1) Miller	1965	Pilot B	e, p	80
2) Schoett	1966	anthracene, terphenyl, NE102	d(10–28), α(8–55)	81
3) Dietzsch	1967	NE213	p	82
4) Maier	1968	NE213	p	83
5) Smith	1968	anthracene, stilbene, NE213, NE102, NE230	e(0.2–1), p(0.3–15)	84
6) Craun	1970	as (5)	as (5)	85
7) Masterson	1970	NE218	e, p(1–30)	86
8) Titus	1970	anthracene, plastics	e(0.25–1.25)	87
9) Webb	1970	liquid	p and d(30–200)	88
10) Bertin	1971	NE213	e(0–3), n(1–6)	89
11) Katz	1972	NE213	p	90
12) Knox	1972	NE213	e(0.3–1)	91
13) Bertl	1972	NE230, NE231	p	92
14) Madey	1972	NE102, NE228	p(3.5–10.5)	93
15) Buenard	1976	Pilot-U	HI($Z = 2$–18, $E = 20$–300)	94
16) Bechetti	1976	NE102, Pilot B	HI($Z = 1$–35, $E = 2$–160)	50
17) Lockwood	1976	NE213	p(3–75)	95

uniform over the full area used and the photomultiplier response should be linear over the full range of intensity studied. The integration time constant of the photomultiplier output and succeeding amplifier should be specified since a short time constant (<30 ns) will lead to an output pulse amplitude which is proportional to the prompt component only whereas a long time constant (>0.5 μs) may be necessary to obtain an output proportional to the total light in the scintillation.

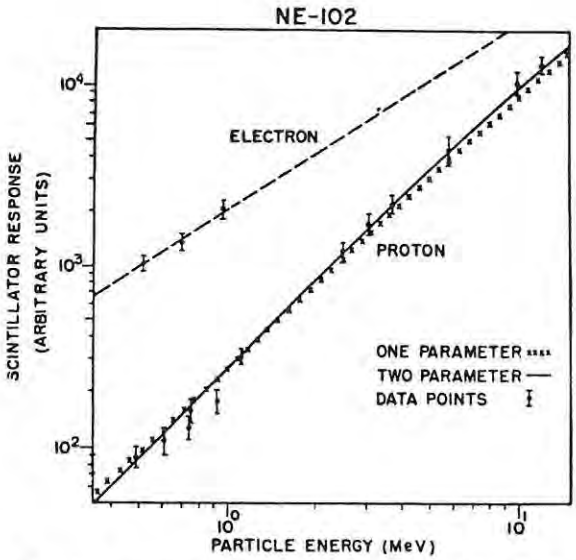

Fig. 15. Response as a function of energy for electrons and protons in plastic scintillator NE102. Data points are taken from ref. 84. Theoretical fits[85]) to the proton data are based on eqs. (3) (crosses) and (4) (solid curve) (fig. from ref. 85).

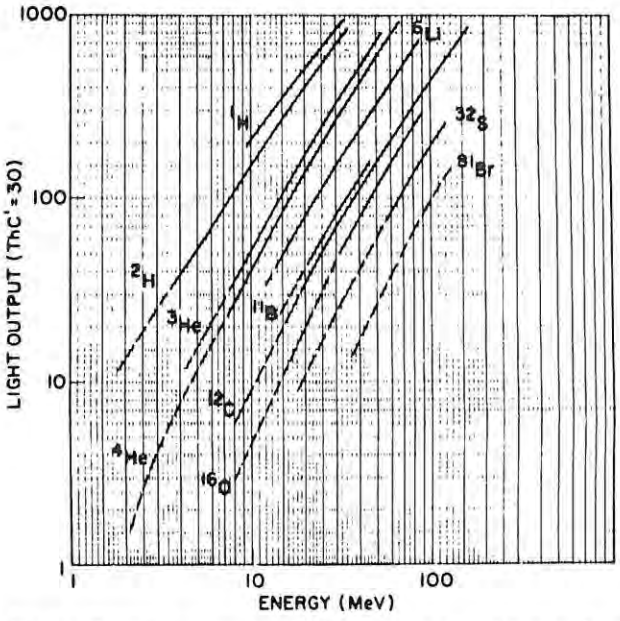

Fig. 16. Response vs energy of typical plastic scintillators such as NE102 to near-normal incident heavy ions[50]). Estimated uncertainty is ±5% except for dashed curves which are likely lower limits to the intrinsic response and have ±20% or greater uncertainty[50]) (fig. from ref. 50).

Most response measurements that have been reported for the organic scintillators are uncertain or unspecific in regard to one or more of the important factors mentioned above. Many of the response data for crystals are now of limited value because they were taken before the response anisotropy of crystal scintillators was known or appreciated. Some response measurements for liquid or crystal scintillators which have appreciable delayed components are also of limited value because no output integration time constant is given. This type of uncertainty is small for plastic scintillators because the delayed component is much weaker in these systems.

A summary of some response measurements reported since 1965 is[50,80-95]) presented in table 2. Measurements reported up to 1964 are summarized by Birks[11]). Fig 15, taken from Craun and Smith[85]) shows the response measurements reported by Smith et al.[84]) for electrons and protons incident on the plastic scintillator NE102. Fig. 16 shows response measurements reported by Bechetti et al.[50]) for protons and some heavier ions on the plastic scintillators NE102 and Pilot B. They find that these plastics when prepared under similar conditions produce relative light outputs equal to within 10% for ions $Z = 1$–16.

The theoretical fits to the proton data in fig. 15 were obtained[85]) by integrating the specific fluorescence dL/dx given by eqs. (3) and (4) over the range of the particle in the scintillator. As illustrated by this example, the simpler approximations for dL/dx [eqs. (3)–(5)] are suitable for describing the response to light ions of medium or high energy. However for heavy ions or low energy light ions the more detailed eqs. (6) and (7) of the Voltz model[13,14]) should be used. Alternatively, Bechetti et al.[50]) describe four simple empirical parameterizations which fit the response data for heavy ions (fig. 16) in the range $0.5 < E/A < 15$ MeV/nucleon to ±20% or better. One example is

$$L = 1.58 Z^{1.22}(R - 0.042Z), \qquad (16)$$

where R is the ion range in mg/cm^2 and L is given in the units of fig. 16.

3.2. Response resolution

The energy resolution attainable using a particular photomultiplier–scintillator combination depends on the matching [eq. (15)] of the scintillator emission spectrum with the photomultiplier photocathode response function, on the efficiency of light transmission to the photocathode and on the absolute efficiency of the scintillator. The combined effect of these factors can be expressed in terms of a practical efficiency ε which reflects the number of photocathode electrons emitted per keV of incident electron energy deposited in the scintillator. Values of $\varepsilon = 1$–2.5 electrons/keV have been reported[96,97]) for the organic scintillators. The yield of photocathode electrons and hence the pulse height resolution for any particle and energy may be obtained by determining the equivalent incident electron energy which corresponds to the same scintillation response using the data of figs. 15 and 16.

An example of the quality of pulse height resolution achieved in practice is shown in fig. 17, taken from the work of St. Onge et al.[78]). The spectrum is a Compton distribution for ^{60}Co γ-rays (1.17 and 1.33 MeV) obtained using a cell of liquid scintillator (NE213, 44.4 mm diam. × 19.1 mm deep) which was carefully coupled to a selected RCA 8575 photomultiplier. The two Compton edges are clearly resolved and the response resolution ($\delta L/L$) is ~7% (fwhm). Based on $\sqrt{n}$ statistics this performance would correspond to a response resolution $\delta L/L < 3\%$ (fwhm) for protons of energy >15 MeV. Bechetti et al.[50]) report a comparable performance for plastic scintillators for which they observed $\delta L/L < 3\%$ (fwhm), relatively independent of ion species for $L > 500$ units on the scale of fig. 16. They point out that the resolution of semiconductor detectors degrades rapidly with increasing ion mass, due to nuclear stopping, and speculate that the intrinsic scintillator energy resolution $\delta E/E$

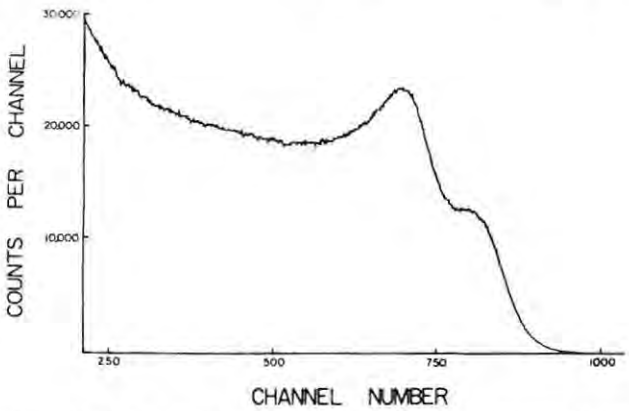

Fig. 17. Pulse height spectrum[78]) of ^{60}Co γ-rays in an NE213 scintillation detector of volume 44.4 mm diam. × 19.1 mm depth (fig. from ref. 78).

TABLE 3
Comparison of measured prompt component lifetimes [a].

Scintillator	Kirkbride[98])	Lynch[96])	Kunze[100])	Birks[57])	Binkert[100])	Kelly[101])
Pilot B	1.90	1.6		2.4		1.69
Naton 136	1.87	1.6		2.3		1.70
NE111			2.3	1.7	1.75	1.66, 2.27
Pilot U						1.36

[a] Values are quoted in ns.

($< \delta L/L$) for very heavy ions ($Z > 35$) may approach that possible with existing semiconductor detectors.

3.3. TIMING CHARACTERISTICS AND TIME RESOLUTION

The basic limitations of scintillation detectors in time measurements are reviewed by Lynch[96]). The time resolution of a scintillation detector depends on the scintillation pulse shape and intensity and on the timing characteristics of the photomultiplier. The relevant time characteristics in the organic scintillators are those which describe the prompt component in the scintillation decay. The factors which determine these characteristics are discussed by Birks[54]) and Birks and Pringle[57]).

The single photon sampling technique developed by Bollinger and Thomas[45]) provides a direct method for observing scintillation pulse shapes and has been used[43,57,96,102]) to measure the time characteristics of prompt and delayed scintillation components. Table 3, taken from Lynch[96]), shows a comparison of measurements of the prompt component lifetimes τ_{0Y} in eqs. (11) and (13), for four different commercial plastic scintillators. The measuring technique should give results reproducible to within 0.1 ns between different observers. The much larger spread in values could be partly due to variation in scintillator constitution from one production batch to another, as reported by Kelly et al.[101]) for NE111. However, there are also indications of systematic effects between different observers. For example individual experimenters observe very similar life-times for Pilot B and Naton 136, but the highest value is 50% greater than the lowest value reported. These differences and their possible causes are further discussed by Lynch[96]).

Birks[54]) has pointed out that the scintillation decay time, which is commonly used to categorize the time characteristics of an organic scintillator does so adequately only for a unitary (pure crystal) system for which the scintillation rise time is negligible in comparison with the decay time. A more suitable timing characteristic is perhaps the full width at half maximum Δt of the scintillation pulse shape. Thus for a pure crystal scintillator of decay time τ, $\Delta t = 0.693\tau$ while for a binary scintillator Δt depends on the scintillation rise time as well as on the lifetime τ_{0Y} [eqs. (11) and (13)] which governs the decay of the prompt component. The scintillator time resolution is governed by the rate of photon emission and therefore de-

TABLE 4
Figures of merit for fast timing.

Scintillator	Crystal		Liquid		Plastic						
	anthracene	stilbene	PBD[a] (10)	PPO[a] (4)	NE238A	Naton	NE102A	NE104	NE111	Pilot B	Pilot U
L_p [b]	100	80	70	55	62	45	58	60	50	60	67
Δt (ns)[c]	21.5	4.2	2.4	3.2	1.12[d]	2.6	3.7	2.0	1.55	2.8	1.20[d]
$M = L_p/\Delta t$	4.7	19.1	29.2	17.2	55.4	17.3	15.7	30.0	32.3	21.4	55.8

[a] Solutions in toluene with solute concentration in g l^{-1} shown in brackets.
[b] Assumed relative intensity of prompt component.
[c] Fwhm of prompt component time distribution, obtained from ref. 57 except for (d).
[d] Obtained from EMI Nuclear Enterprises Ltd., Edinburgh (December 1977).

TABLE 5
Time resolution measurements.

First author	Year	Scintillator	Timing res. (fwhm)	Ref.
1) Bengtson	1970	NE111	132 ps (^{60}Co $\gamma\gamma$) 216 ps (^{22}Na $\gamma\gamma$)	103
2) Bollini	1970	NE111	140 ps (540 MeV p in transit)	104
3) Moszynski	1971	NE111	130 ps (200 keV e)	108
4) Dietz	1971	NE111, Naton 136	~200 ps (sec. e from HI)	109
5) Bialkowski	1972	NE111	130 ps (^{60}Co $\gamma\gamma$, 20% window) 195 ps (^{60}Co $\gamma\gamma$, 90% window)	105
6) Calligaris	1973	Foils of NE111, NE104, KL236	~250 ps for 1 MeV deposited by transiting proton	106
7) Pouthas	1977	NE111 foil	~200 ps (transiting HI)	107

pends on the intensity of the prompt component as well as the width Δt. A convienient measure of scintillator time resolution is thus the figure of merit or ratio $M = L_p/\Delta t$, where L_p is proportional to the intensity of the prompt component. Table 4 shows some values of M calculated from the data given by Birks and Pringle[57]).

The overall time resolution of a scintillator–photomultiplier detector may be estimated from the combined time response function of its two components as described by Lynch and others[96]). From the practical viewpoint however, measures of achieved time resolution (fwhm) are also of interest. Several measurements of time resolution in the range 120–250 ps (fwhm) have been reported for detectors consisting of small plastic scintillators (dimensions of a few cm or less) used with fast photomultipliers such as the Amperex XP-1020. Information and references[103–109]) to some of these measurements are summarized in table 5. The investigations of Calligaris et al.[106]) and Pouthas et al.[107]), both using thin plastic scintillator foils, included studies of the time resolution as a function of light output from the foil. Pouthas et al.[107]) using a thin foil of NE111 plastic scintillator, report that the time resolution (fwhm) R is related to the number of photomultiplier cathode electrons n by $R = 1700\ \text{ps}/\sqrt{n}$, as shown in fig. 18.

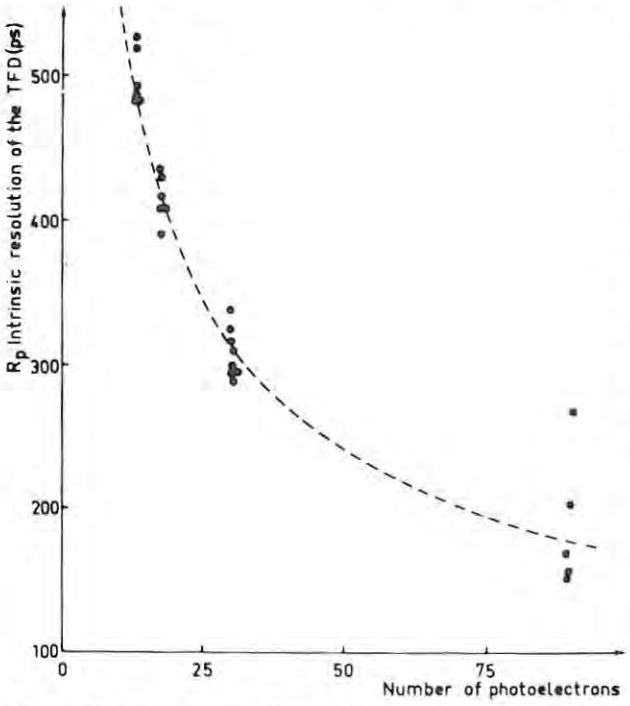

Fig. 18. Time resolution R (fwhm) of a thin foil detector (NE111 plastic scintillator) plotted as a function of the number of photocathode electrons per scintillation n [107]). The curve is calculated from $R = 1700/\sqrt{n}$ ps. (fig. from ref. 107).

Some further information about the time resolutions of both small and large organic scintillators can be found in refs. 110–119. Among these two papers dealing with the minimizing or compensating of optical time dispersion in large (>10 cm) scintillators may be specially noted. Poulet and Santoni[119]) describe time resolution measurements for a prototype plastic scintillator element (30×30 cm^2 sheet) of a four element hodoscope for high energy experiments. Using a single photomultiplier and no light guide they obtain an estimated time resolution of 520 ps (fwhm). Carlson et al.[120]) describe a cylindrical liquid scintillator (7.4 l of NE224, dimensions 18.2 cm diam., 29.2 cm length) for measuring the time-of-flight of neutrons entering parallel to the scintillator axis. Timing information from photomultipliers at each end of the cylinder is used to locate the point of neutron detection and to correct for optical time dispersion. The intrinsic compensated time resolu-

tion measured using ^{60}Co γ-rays is 0.66 ns and that measured using 17.1 MeV neutrons is 1.07 ns, including beam spread contributions. Several other experimenters, for example refs. 104, 121–124, have also used optical time differences to determine event position along a plastic or liquid scintillator and Bollini et al.[104]), for example, report a position resolution of ± 1.5 mm for high energy protons in NE111 plastic scintillator.

3.4. Pulse shape discrimination

The pulse shape discrimination (PSD) technique was originally developed[15]) as a method of neutron–gamma discrimination. It grew from the experimental observation of Wright[105]) which showed indirectly that the scintillation decay of anthracene was slower for α-particle scintillations than for electron scintillations. The true nature of the pulse shape differences was afterwards revealed by Owen[106]) who showed that they were caused by variations in the relative intensities of the prompt and delayed scintillation components (fig. 4). Fig. 19a shows, for example, some measurements by Kuchnir and Lynch[99]) which illustrate the different proportions of prompt and delayed components in the scintillation decay of the liquid scintillator NE218 when excited by incident neutrons and γ-rays respectively.

The early developments in pulse shape discrimination and PSD techniques were reviewed by Firk[127]) in 1961. Many new systems have been described and discussed since that time, for example as detailed in refs. 43, 78, 128–152. A typical PSD system will generate an output pulse the amplitude of which, S, depends on the shape of the scintillation, or. in other words, on the ratio of the intensities of the delayed and prompt components. Ideally S should characterize the shape uniquely and be independent of the response L. In practice S often depends on the response as well as the shape, but in any case different shapes (types of particle) define discrete loci in the LS-plane if a dual-parameter analysis is made of L and S. In one method of pulse shape discrimination[151,153–155]) the output S is obtained by integrating the prompt component and the total scintillation (or the delayed component) and comparing the two integrals. In another method[156]) the prompt component drives the final stage of the photomultiplier into space-charge saturation and thereby generates an output S which is shape dependent. In a third and widely used method[132,133]) the time difference is measured between the start of the scintillation and the time for the integral (fig. 19b) of the light output to reach some large fraction of its final value. This time difference is characteristic of the scintillation shape and hence of the type of particle, as can be seen from fig. 19b The method is often referred to as the zero crossing method of PSD because the second time measurement is made by a zero crossing discriminator operating on a double-differentiated signal. A number of PSD systems have been reported[137,142,151,152]) which are designed to operate with high stability at event rates up to 50 kHz.

While the main interest in PSD continues to be for its application in n–γ discrimination increasing interest is also being shown in other applications. Figs. 20 and 21 are examples of some of the detail that can be resolved by pulse shape analysis of scintillation events caused by fast neutrons. Fig.

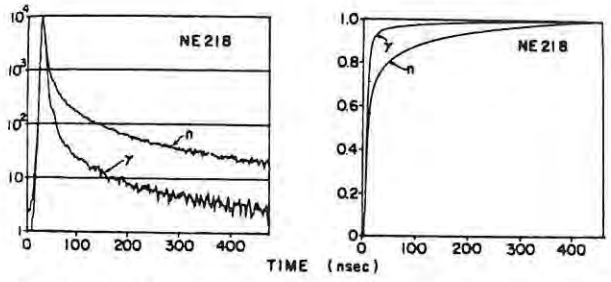

Fig. 19. (a) (Left): Measured light intensity vs time t [99]) for scintillations produced by γ-rays and neutrons in a NE218 liquid scintillator. (b) (Right): Integrals of measured curves on left, normalized at $t = 500$ ns (fig. from ref. 99).

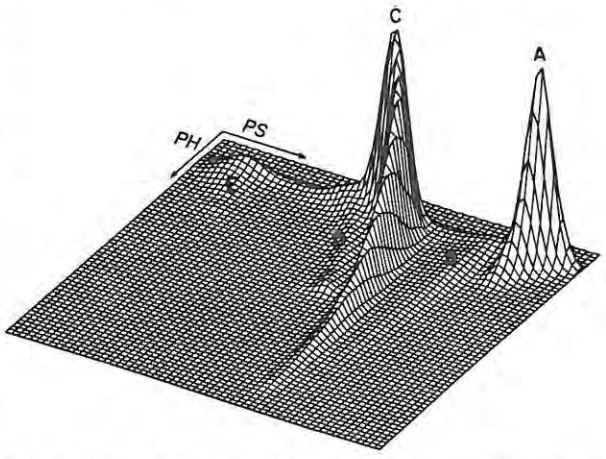

Fig. 20. Counts (vertical) as a function of response PH and pulse shape PS for events in a NE213 scintillator[78]) when exposed to radiation from a ^{7}Li target bombarded by 40 MeV protons. The features labelled A–E are discussed in the text (fig. from ref. 78).

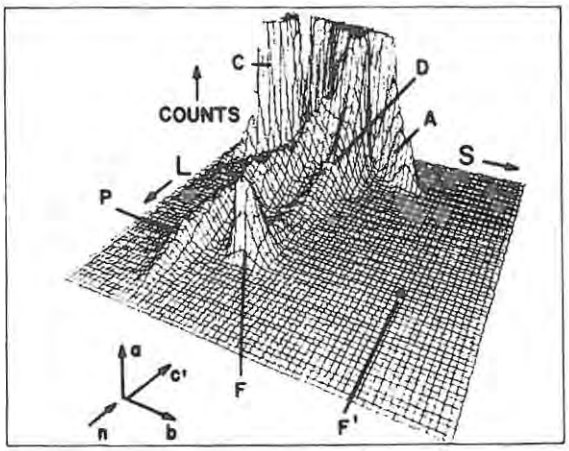

Fig. 21. Counts (vertical) as a function of response L and pulse shape S for events in a deuterated anthracene crystal[72]) when exposed to γ-rays and 21.6 MeV neutrons entering the crystal parallel to the artificial c'-axis. The features labelled C, P, D and A are discussed in the text. The characteristic deuteron forward recoil peak F moves to the point F′ in the LS plane if the incident neutron beam direction is aligned parallel to the crystal b-axis (fig. from ref. 72).

20 taken from St. Onge et al.[78]) shows the two-parameter pulse height × pulse shape distribution, or LS spectrum, for events in a NE213 liquid scintillator which was exposed to radiation from a ^{7}Li target bombarded by 40 MeV protons. The scintillator was the same as that referred to in fig. 17 and the maximum neutron energy was 37.5 MeV. The ridges labelled A–E in fig. 20 are associated with: A, Compton electrons, B, recoil protons which escape at the edge of the scintillator; C, recoil protons from n–p scattering; D, protons from the ^{12}C(n, p)^{12}B reaction in the scintillator; and E, α-particles from the ^{12}C(n, α)^{9}Be and ^{12}C(n, n′)3α reactions. The shift of D from C is attributed[78]) to the ^{12}B recoil which, consistent with its high ionizing power, appears to have a significant effect on the scintillation pulse shape even though it makes very little contribution to the response. The use of PSD to analyse the response of NE213 liquid scintillator to 3–75 MeV neutrons is further explored and discussed by Lockwood et al.[95]).

Fig. 21, taken from Steinbock et al.[72]), shows an LS spectrum obtained from a deuterated anthracene crystal (10 mm diam., 21 mm length) exposed to 21.6 MeV neutrons entering parallel to the crystal c'-axis. The ridges labelled C, P, D and A are associated with: C, Compton electrons; P, protons from the deuteron break-up reaction ^{2}H(n, 2n)^{1}H; D, deuterons from n–d elastic scattering; and A, α-particles from reactions on carbon, as described for fig. 20. The peak F corresponds to forward recoiling deuterons associated with the strong backward peak in the angular distribution for n–d elastic scattering. Similar spectra to fig. 21 were obtained[157]) using the deuterated liquid scintillator NE230 and the results were analysed to determine total cross sections for the breakup reaction relative to the elastic scattering cross section. Proton–alpha discrimination has also been used to study the (n, α) and (n, n′)3α reactions on ^{12}C using the liquid scintillator NE213[158]) or a stilbene crystal[43]).

Many organic scintillators exhibit pulse shape differences sufficient for PSD and comparisons have been made[132,142,149,151,153,154,159–165]) of n–γ discrimination characteristics of different scintillators and PSD systems. The common organic crystal scintillators, with the exception of diphenylacetylene, show good PSD and so do most liquid scintillators based on the common solvents, xylene, toluene and benzene, provided dissolved oxygen is removed. Most plastic scintillators show relatively poor PSD properties, consistent with the low proportion of delayed component in their scintillation decays. Since PSD performance varies with scintillator response L, or associated electron energy, quantitative comparisons of PSD characteristics are made at discrete electron energies or as a function of electron energy. The PSD resolution at a given response L can be expressed in terms of the projected S distribution in a cut across the LS spectrum (see e.g. figs. 20 and 21) at that value of L. For a projected distribution containing only electron (γ) and proton (n) groups the n–γ PSD resolution may be expressed as the ratio[151,153,159,161]) of the separation of the groups to their individual or summed widths (fwhm) or as the peak-to-valley ratio[159]) of the distribution. Alternatively a level of S may be determined corresponding to some specific rejection efficiency (e.g. 99%) for electrons and the PSD efficiency expressed[154]) as the percentage of protons for which S exceeds this level. The PSD efficiency then corresponds to the efficiency with which protons are accepted, as a function of proton energy, at a given rejection efficiency for electrons.

Different authors have used different methods to compare n–γ discrimination efficiencies. For further details reference should be made to the original papers, for example refs. 153, 154, 159, 161, each of which give comparisons between several

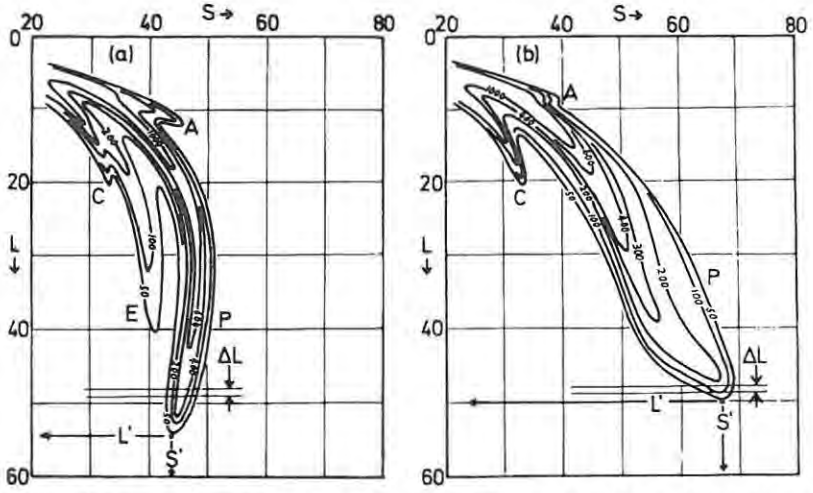

Fig. 22. Contours of equal count rate for *LS* spectra obtained when 21.6 MeV neutrons enter a 1.5 cm^3 anthracene crystal[71]) moving: (a) parallel to the artificial *c'*-axis; and (b) parallel to the *b*-axis of the crystal. The ridges in the spectra are attributed to: Compton electrons (C); recoil protons (P); escaping recoil protons (E); and α-particles from reactions on carbon (A). The point (*L'*, *S'*) corresponds to forward proton recoils (fig. from ref. 71).

different scintillators. The pulse shape discrimination properties of large liquid scintillators are size-dependent[160]), as might be expected from optical dispersion effects on the scintillation pulse shape. Nevertheless good n–γ discrimination has been reported for several large scintillators[120,144,165–167]), some involving light transmission over distances up to 1 m. Another factor requiring attention when using a PSD system is its sensitivity to temperature changes, as observed and studied by Weinert[168]) and by Chalupka et al.[169]). On the basis of Weinert's findings the complete detector head including scintillator (NE213), photomultiplier and preamplifier should be stabilized to ± 1 °C in order to achieve stable PSD operation.

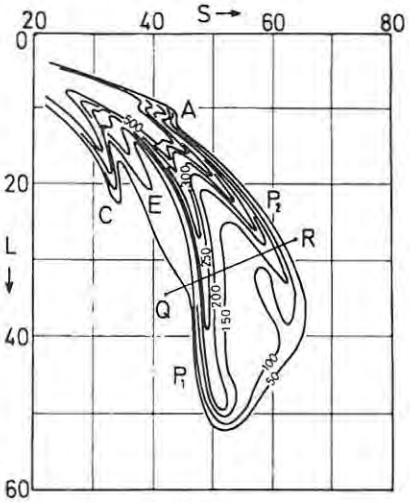

Fig. 23. Contour plot obtained[171]) as for fig. 22 but with neutrons entering the crystal in a direction lying in the *bc'*-plane and making an angle of 60° with the *c'*-axis. The ridges C, E and A identify as in fig. 22. The proton ridge P broadens into left and right recoil components, P_1 and P_2. The line QR represents the locus of a constant proton recoil angle in the *LS* plane (fig. from ref. 171).

3.5. Scintillation anisotropy of organic crystals

The better known organic crystal scintillators including anthracene, stilbene, terphenyl and quaterphenyl, all exhibit significant response anisotropies similar to those for α-particles and protons on anthracene, as illustrated in figs. 12 and 14. However, of these crystals only anthracene shows an appreciable degree of pulse shape anisotropy. Fig. 22 shows contour plots of response-pulse shape distributions (*LS* spectra) obtained[71]) from a 1.5 cm^3 anthracene crystal irradiated by 21.6 MeV neutrons entering in directions parallel to: (a) the artificial *c'*-axis; and (b) the *b*-axis of the crystal. The points (*L'S'*) at the limits of the proton ridges P correspond to 21.6 MeV forward recoiling protons and show the variations that occur in *L* and *S* for a 90° change of proton direction in the crystal *bc'*-plane. A similar effect occurs in deuterated anthracene and the point corresponding to forward deuteron recoils moves from F to F' in fig. 21, for example, when the incident neutrons enter this crystal moving parallel to the *b*-axis instead of the *c'*-axis.

The directional effects in anthracene and deuterated anthracene have been used[72,170,171]) to determine left–right asymmetries and hence polariza-

tions in n–p and n–d elastic scattering. Fig. 23 shows an *LS* spectrum obtained[170,171]) under the same conditions as fig. 22 but with the incident neutrons entering the *bc'*-plane in a direction making an angle of 60° with the *c'*-axis. The proton ridge broadens out and forms two distinct components P_1 and P_2 which correspond to recoils towards opposite sides of the neutron beam direction. These components can therefore be identified with left and right recoils, or vice versa, thereby enabling the asymmetry in elastic scattering of a polarized incident neutron beam to be determined[170]). The directional effects in anthracene are sufficiently large as to permit left-right asymmetry measurements to be made down to recoil proton energies of about 5 MeV [171]).

4. Some applications of organic scintillators

The suitability of an organic scintillator for a particular application may often be judged directly from the scintillator characteristics considered in section 3. Even when this is the case however, a reference to a similar application may be very helpful. Many of the applications of organic scintillators may conveniently be grouped under the headings: neutron detection; loaded scintillators; large area and large volume scintillators; thin film detectors; and applications in the medical, biological and associated fields. Before dealing with these topics however, we shall mention a few applications which do not fall neatly into one or other of these categories.

Organic scintillators are often used[11]) for the detection and spectrometry of β-rays because backscattering at organic surfaces is less than at surfaces of detectors composed of higher-Z elements. Plastic scintillators are particularly suitable[21]) because they can be shaped in a well geometry to further reduce the backscattering effect. A recent example of a detection system for β spectrometry is that described by Wohn et al.[172]) for the study of β spectra from short-lived gaseous fission products. Plastic scintillators are also used [173]) for the detection of secondary electrons ejected by heavy ions, nuclear recoils and fission fragments. The detection of recoil nuclei from β decay and α decay, using plastic scintillators, is reported for example by McFarlane et al.[174]) and Batty et al.[175]). The use of stilbene crystal scintillators, with pulse shape discrimination, for the routine monitoring of laboratories for α contamination is described by Shani and Cojocaru[176]).

4.1. NEUTRON DETECTION

The need for fast efficient neutron detectors has always been a strong motivating force in the development of organic scintillators. Boron-loaded liquids and plastics have been developed[177–181]) for detection of low energy neutrons (<0.05 MeV) and n–p scattering in organic scintillators is the standard method of neutron detection at higher energies. In addition, large cadmium-loaded or gadolinium-loaded organic scintillators are used[182–185]) to detect neutrons with high efficiency over a wide energy range. Neutrons are captured in the loaded element with the release of γ-rays, after being moderated to low energies by elastic scattering in the organic system.

The properties of neutron detectors based on n–p proton recoils have been studied in great detail. At energies less than about 12 MeV n–p scattering is the dominant neutron interaction in hydrocarbon media but at higher energies interactions with the carbon component become increasingly important. A number of studies and calculations have been reported[186–192]) which deal with the primary interaction processes and associated neutron detection efficiencies. Time resolution and n–γ discrimination are often critical factors in the assessment of detector performance and a variety of neutron detectors have been designed with the emphasis differently divided between these criteria and the criterion of neutron detection efficiency. Response (pulse height) resolution is also an important factor, especially in applications where the pulse height spectrum is unfolded[187,193–198]) in order to derive the incident neutron spectrum.

Neutron detection by proton recoil in organic scintillators is more fully discussed in other articles[199,200]) in this volume. Neutron detection by deuteron recoil in a deuterated organic liquid or crystal[72,157,201]) should perhaps be more fully exploited than it has been to date. Using pulse shape discrimination to separate recoil deuterons from both break-up protons and Compton electrons (fig. 21) a recoil deuteron spectrum may be obtained with a characteristic forward recoil peak (and low valley) for each energy in the incident neutron spectrum. The line shape obtained from the deuterated scintillator is therefore much sharper than that from a proton recoil detector. This should make the process of determining the neutron spectrum from the deuteron spectrum simpler and more accurate than the corresponding process for a normal hydrocarbon scintillator.

4.2. Loaded liquid and plastic scintillators

The chemistry of organic scintillators sometimes facilitates the inclusion of appreciable quantities of foreign elements or compounds whose presence may assist the detection process without seriously degrading the scintillation process. The better known examples are the neutron capturing elements, boron, cadmium and gadolinium, and the elements tin, lead and fluorine which have applications in X-ray and γ-ray detection.

Boron-loaded liquid scintillators contain typically 1–5% (wt.) boron (usually enriched in ^{10}B) in the form of methyl borate. Neutron capture results in charged particles and γ-rays from the reaction $^{10}B(n,\alpha)^7Li^* \rightarrow {}^7Li + \gamma(0.48\,MeV)$ and these products can be detected in 4π geometry in the scintillator. Boron-loading is used for neutron detection[177]) with pulse shape discrimination if required[178–180]), or as a means of suppressing the 2.3 MeV γ-ray from neutron capture in hydrogen in large scintillators[184]). A boron-loaded plastic scintillator is described by Anisimova et al.[181]). Cadmium- and gadolinium-loaded scintillators are described in refs. 182–185.

Fluorine-loaded scintillators such as NE226 are based on organic compounds in which fluorine is substituted for hydrogen. They can be effectively hydrogen–free and are therefore suitable for applications requiring a low sensitivity to neutrons. They can also be used to study the interactions of neutrons with carbon or fluorine[202,203]) and Van Moellendorff and Slobodrian[202]), for example have used pulse shape discrimination to identify carbon recoils from neutron elastic scattering in NE226. Macklin et al.[204,205]) describe the use of NE226 liquid scintillator for neutron capture cross section measurements in the 30–220 keV incident neutron energy range. Weston and Todd[206]) describe measurements of the scintillation pulse shapes of this scintillator.

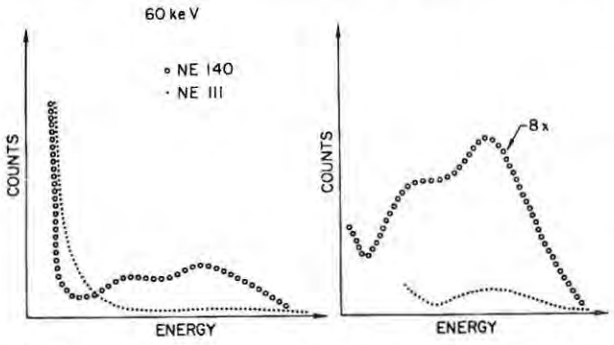

Fig. 24. Comparison of pulse height spectra obtained[212]) using NE140 (5% Sn) and NE111 plastic scintillators for 60 keV γ-rays (^{241}Am). The spectra were recorded under identical conditions (fig. from ref. 212).

Tin and lead loaded plastic scintillators containing up to ~7% (wt.) of the loaded element are attracting increasing interest[207–211]) in the detection of X-rays in the 5–100 keV energy region. Photoelectric absorption in the loaded element leads to a high X-ray detection efficiency at low energy (see fig. 24) while maintaining a low efficiency at high energies. The energy resolution is modest but high count rates can be handled. Erikson et al.[212]), Becker et al.[207]) and Cho et al.[208]) discuss the use of NE140 tin-loaded (5%) and Pilot lead-loaded plastic scintillators in low energy–high rate applications. The lead loaded scintillator has also been used in fast timing measurements[211]).

4.3. Large area and large volume scintillators

Liquid and plastic organic scintillators offer the simplest and most economical means of providing extended dense detecting media for nonrelativistic particles. Plastic scintillators are particularly suited to applications requiring detecting units of large area ($>1\,m^2$) and modest thickness (<10 cm). Plastics with high scintillation transmission efficiencies and fast time response characteristics[213,214]) have been developed (e.g. Pilot Y and NE110). They are used in nuclear physics to obtain large solid angles for the detection of neutrons[215,216]) and high energy charged particles, for example ^3He ions of energy up to 430 MeV[217]). They are also used as 4π anticoincidence shields[218,219]) for Ge(Li) and NaI(Tl) γ-ray spectrometers.

Many applications of large area scintillation counters may be found in the fields of high energy and cosmic ray physics. They are used in hodoscopes[220–222]) and in multiple detector telescopes[223,224]) designed to recognise a specific type of event promptly from a particular coincidence/anticoincidence pattern in the detector array and to trigger associated detectors when necessary. A recent example is the proton trigger for the CERN omega spectrometer, described by Ghidini et al.[225]) which uses a NE110 plastic scintillator sheet of dimensions $2\,m \times 1\,m \times 5$ cm.

Another type of multiple scintillator detector which has been used for several years in high energy physics is the laminated detector consisting of plastic scintillator sheets separated by sheets of

lead or steel. High energy particles or photons develop an electron shower as they traverse the metal plates and the electrons are detected in the plastic. Recent examples of such detectors are the steel and scintillator sandwich developed by Marshak and Schmüser[226]) for GeV protons and neutrons and the 0.03–1 GeV γ-ray detector (lead and plastic sandwich developed by Abrams et al.[227]) for the investigation of kaon decays.

A fast time response and a uniform pulse height response are sometimes essential requirements in high energy and cosmic ray applications. Some investigations aimed at optimizing these characteristics in large area scintillators are described in refs. 119, 214, 216, 220.

The use of large volume liquid scintillators has grown considerably since their potential was demonstrated by Cowan and Reines[182]). Similar large liquid scintillators have been used extensively and for some time to study γ-rays and neutrons from nuclear reactions and nuclear fission. A recent description of a 200 l liquid scintillator for neutron capture studies is given by Hellstrom and Beshai[184]). The use of gadolinium-loaded (0.5% wt.) and cadmium-loaded (1.0 % wt.) liquid scintillators (200–500 l) in studies of neutrons from (n, 2n), (γ, n) reactions and nuclear fission is discussed in refs. 185, 228.

The demand for large detectors has stimulated the development of new low-cost, high-flash-point liquid scintillator solvents[229–231]) such as 1, 2, 4 trimethylbenzene and mineral oil, which, when suitably purified have good light transmission properties[232]) and efficient scintillation characteristics. A recent example of an extremely large liquid scintillator system is the total absorption hadrom calorimeter described by Benevenuti et al.[233]) for the study of neutrino interactions. This detector uses 68 m^3 of the liquid scintillator NE235 in which the solvent is mineral oil. Other examples of uses of large volume scintillators in high enrgy and cosmic ray applications are given in refs. 229, 234–236.

4.4. Thin film detectors

A significant advance in the field or organic scintillators in recent years has been the development, led by Muga et al.[237–249]), of thin film plastic scintillators. The thin film detectors are easy to fabricate, even in foils as thin as 20 μg/cm^2. They are useful detectors for registering the passage of heavy ions and their scintillation characteristics are ideally suited for time-of-flight measurements[237,250]).

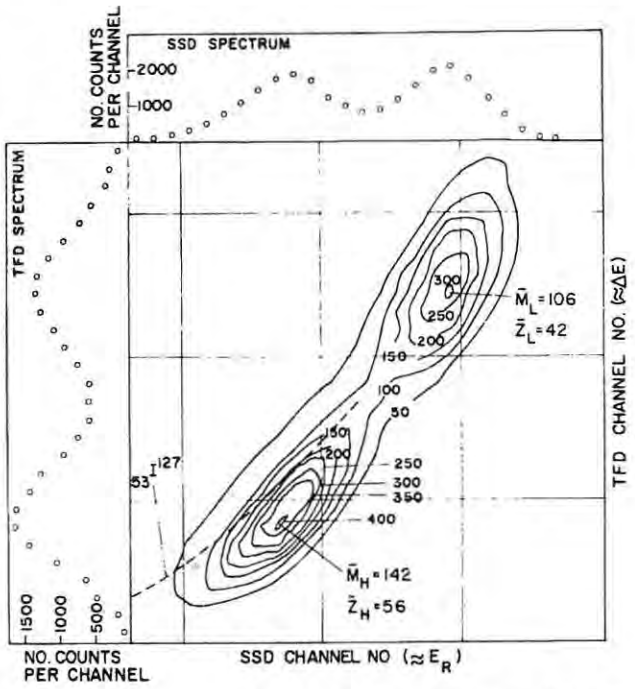

Fig. 25. Contour plot of a $\Delta E \cdot E$ spectrum obtained[238]) from ^{252}Cf fission fragments using a thin film plastic scintillator (TFD) as transmission (ΔE) detector and a semiconductor detector (SSD) as E detector. The projected spectra on the E and ΔE axes are shown and the dashed curve shows the locus of the $\Delta E \cdot E$ response to accelerated ^{127}I ions (fig. from ref. 238).

The preparation and mounting of thin film detectors is described by several authors, for example refs. 239, 242, 251, 252. The energy loss and straggling of α-particles in thin scintillator foils is discussed by Geissel et al.[253]) and the pulse height resolution of these detectors is discussed by Batsch et al.[254]). Their use as transmission (ΔE) detectors in counter telescopes is considered by Muga et al.[238]) and Gamp et al.[255]) and is illustrated by the contour plot (fig. 25) obtained by Muga et al.[238]) for fission fragments from a ^{252}Cf source.

The main interest to date in thin film scintillators has been their application in time-of-flight systems[109,255-257]) for heavy ions and fission fragments. The plastic scintillator foil is an effective transmission detector in a time of flight telescope because it can be made sufficiently thin to transmit even low energy heavy ions, because relatively large active areas are readily obtainable and because multiple scattering and energy straggling ef-

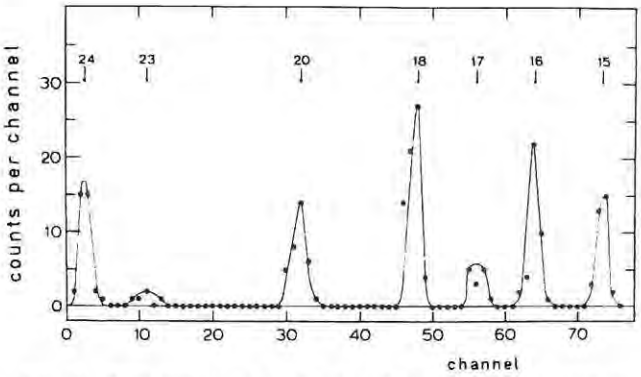

Fig. 26. Mass separation by time of flight of reaction products obtained by bombarding a target containing ^{7}Li and ^{12}C with 50 MeV ^{16}O ions[256]). The time spectrum is shown of products of one discrete energy and different masses in the range $A = 15-24$. The data were taken with a time resolution of 500 ps (fwhm) and a flight path of 1.5 m, using a thin film plastic scintillator as the transmission detector (fig. from ref. 256).

fects in the foil can be kept small[253,256]). Fig 26 shows an example of the mass separation obtained by Gelbke et al.[256]) in the analysis of reaction products obtained by bombarding a target containin g ^{7}Li and ^{12}C with 50 MeV ^{15}O ions.

4.5. Applications in the medical and biological fields

Organic scintillators have two important types of application in medicine and biology. One concerns the detection and measurement of γ radioactivity, natural or artificial, in the human body or in other biological systems. The detection may be accomplished by an organic scintillator scanning or surrounding the biological system. The second type of application is that of measuring the level of radioactivity in a sample obtained from a biological system. This is often accomplished by means of 4π internal counting of the sample in a liquid scintillator.

The estimation of body radioactivity may be more quickly made by using a 4π detector such as a large liquid scintillator[258]). Alternatively a system of several detectors may be disposed about the subject to form a "whole body monitor" covering a significant fraction of the 4π solid angle. Some whole body monitors consisting of arrays of plastic scintillators are described in ref. 259.

The measurement of radioactivity in biological samples dissolved, suspended or immersed in liquid scintillators is one of the busiest and most important fields of application of organic scintillators. Developments in this field are reviewed regularly at international conferences on liquid scintillation counting, the first of which was held in 1957[16]). The proceedings of these conferences[16,17,260–268]) together with other texts[21,24,25]) contain a comprehensive literature on the relevant methods and techniques of this field. The theoretical background of the 4π internal counting technique has recently been reviewed by Gibson[269]). The improvements in instrument performance over the period 1954–1972 are summarized by Horrocks[24]) as shown in table 6, in terms of the efficiencies and background levels for counting the β emitters ^{3}H and ^{14}C.

Until recently routine liquid scintillation measurements of biological and environmental samples were effectively confined to β and γ emitters. Although it was known since 1954 [270]) that α emitters could be measured by similar methods, internal liquid scintillation counting of α-particles was discouraged by the requirements of sample preparation and the high background count levels of liquid scintillators compared with other methods of α detection. These problems have recently been greatly alleviated by advances introduced by McDowell et al.[271–273]). They have developed liquid–liquid extraction procedures which allow selective extraction of α emitters directly into the liquid scintillator and they have introduced pulse shape discrimination techniques which reduce background count rates to <0.01 per minute. McDowell and Weiss[274]) describe the application of these α detection methods to the measurement of plutonium in bone and tissue samples.

Table 6

Improvements in liquid scintillation counting performance, 1954–1972[24]).

Year	^{3}H		^{14}C	
	Counting efficiency (%)	Background (cpm)	Counting efficiency (%)	Background[a] (cpm)
1954	10	80	75	60
1962	25	55	80	30
1964	40	30	85	25
1969	60	20	90	16
1972	65	18	97	11

[a] Above ^{3}H point.

This review was prepared during a sabbatical leave spent at the University of Birmingham. I

thank my hosts for their hospitality during this period and I thank the U.K. Science Research Council, the South African Council for Scientific and Industrial Research and the University of Cape Town for their financial support. I also thank Mr. D. Aliaga-Kelly of EMI Nuclear Enterprises Ltd., Edinburgh for his assistance in obtaining reference material and I am indebted to the authors of figs. 3–26 for permission to reproduce these figures.

References

1) H. Kallmann, Natur und Technik (July 1947); I. Broser and H. Kallmann, Z. Naturforsch. **2a** (1947) 439 and 642.
2) P. R. Bell, Phys. Rev. **73** (1948) 1405.
3) W. S. Koski and C. O. Thomas, Phys. Rev. **76** (1949) 308.
4) J. B. Birks, Proc. Phys. Soc. **A63** (1950) 1044.
5) G. T. Reynolds, F. B. Harrison and G. Salvani, Phys. Rev. **78** (1950) 488.
6) H. Kallmann, Phys. Rev. **78** (1950) 621.
7) M. Ageno, M. Chiozotto and R. Querzoli, Acad. naz. Lincei **6** (1949) 626 and Phys. Rev. **79** (1950) 720.
8) M. G. Schorr and F. L. Torney, Phys. Rev. **80** (1950) 474.
9) G. B. Collins, Phys. Rev. **74** (1948) 1542.
10) H. Kallmann and M. Furst, *Liquid scintillation counting* (eds. C. G. Bell and F. N. Hayes; Pergamon, London, 1958) p. 3.
11) J. B. Birks, *The theory and practice of scintillation counting* (Pergamon, London, 1964).
12) T. A. King and R. Voltz, Proc. Roy. Soc. A, **289** (1966) 424.
13) R. Voltz, J. Lopes da Silva, G. Laustriat and A. Coche, J. Chem. Phys. **45** (1966) 3306.
14) R. Voltz and G. Laustriat, J. Physique **29** (1968) 159.
15) F. D. Brooks, *Liquid scintillation counting* (eds. C. G. Bell and F. N. Hayes; Pergamon, London 1958) p. 268.
16) C. G. Bell and F. N. Hayes, eds., *Liquid scintillation counting* (Pergamon, London, 1958).
17) A. A. Noujaim, C. Ediss and L. I. Weibe, eds., *Liquid scintillation science and technology* (Academic Press, New York, 1976).
18) F. D. Brooks, Prog. Nucl. Phys. **5** (1956) 252.
19) J. B. Birks, Proc. Univ. New Mexico Conf. on *Organic scintillation detectors*, 1960 (USAEC, Washington, TID7612, 1961) p. 12.
20) J. B. Birks, *Physics and chemistry of the organic solid state* (eds. D. Fox, M. M. Labes and A. Weissberger; Interscience, New York, 1965) p. 434.
21) E. Schram and R. Lombaert, *Organic scintillation detectors* (Elsevier, Amsterdam, 1963).
22) J. B. Birks, *Photophysics of aromatic molecules* (Wiley, London, 1970).
23) I. B. Berlman, *Energy transfer parameters of aromatic compounds* (Academic Press, New York, 1973).
24) D. L. Horrocks, *Applications of liquid scintillation counting* (Academic Press, New York, 1974).
25) A. Dyer, *An introduction to liquid scintillation counting* (Heyden, London-New York-Rheine, 1974).
26) F. R. Lipsett, Progr. Dielectrics **7** (1967) 321; Mol. Crystals **5** (1968) 9; Mol. Crystals **6** (1969) 175.
27) A. S. Davydov, *Theory of molecular excitons* (McGraw-Hill, New York, 1962).
28) G. N. Fowler, Mol. Phys. **8** (1964) 375.
29) S. Singh, W. J. Jones, W. Siebrand, B. P. Stoicheff and W. G. Schneider, J. Chem. Phys. **42** (1965) 330.
30) M. Iannuzzi and E. Polacco, Phys. Rev. Lett. **13** (1964) 371.
31) S. Czarnecki, Bull. Acad. Polon. Sci. Ser. sci. math. astr. and phys. **9** (1961) 561.
32) J. Jortner, S. A. Rice, J. L. Katz and Sand Il-Choi, J. Chem. Phys. **42** (1965) 309.
33) J. B. Birks, Chem. Phys. Lett. **7** (1970) 293.
34) P. Avakian, E. Abramson, R. G. Kepler and J. C. Caris, J. Chem. Phys. **39** (1963) 1127.
35) R. G. Kepler, J. C. Caris, P. Avakian and E. Abramson, Phys. Rev. Lett. **10** (1963) 400.
36) J. L. Hall, D. A. Jennings and R. M. McClintock, Phys. Rev. Lett. **11** (1963) 364.
37) J. B. Birks, Acta Phys. Polon. **26** (1964) 367; J. B. Aladekomo and J. B. Birks, Proc. Roy. Soc. **A284** (1965) 551; T. Azumi and S. P. McGlynn, J. Chem. Phys. **41** (1964) 3131.
38) J. B. Birks and L. G. Christophorou, Nature **197** (1963) 1064.
39) B. Stevens, Nature **192** (1961) 725.
40) A. Meyer and R. B. Murray, Phys. Rev. **128** (1962) 98.
41) R. Voltz, H. du Pont and G. Laustriat, J. Physique **29** (1968) 297.
42) J. Lopes da Silva and R. Voltz, Rev. Phys. Appl. **7** (1972) 127.
43) G. Laustriat, Mol. Crystals **4** (1968) 127.
44) J. B. Birks, Proc. Phys. Soc. **79** (1962) 494; E. Brannen and G. L. Olde, Rad. Res. **16** (1962) 1.
45) L. M. Bollinger and G. E. Thomas, Rev. Sci. Instr. **32** (1961) 1044.
46) J. B. Birks, Proc. Phys. Soc. **A64** (1951) 874.
47) C. N. Chou, Phys. Rev. **87** (1952) 376 and 904.
48) G. T. Wright, Phys. Rev. **91** (1953) 1282.
49) D. Blanc, F. Cambou and Y. G. de Lafond, Compt. Rend. **254** (1962) 3187; and J. Phys. Rad. **25** (1964) 319.
50) F. D. Bechetti, C. E. Thorn and M. J. Levine, Nucl. Instr. and Meth. **138** (1976) 93.
51) M. L. Muga and J. D. Bridges, Nucl. Instr. and Meth. **134** (1976) 143.
52) S. P. Ahlen, B. G. Cartwright and G. Tarle, Nucl. Instr. and Meth. **147** (1977) 321.
53) F. N. Hayes, D. G. Ott and V. N. Kerr and B. S. Rogers, Nucleonics **13** no. 12 (1955) 38.
54) J. B. Birks, J. Phys. **B1** (1968) 946.
55) J. B. Birks and J. C. Conte, Proc. Roy. Soc. **A303** (1968) 85.
56) Th. Förster, Z. Naturforsch. **4a** (1949) 321.
57) J. B. Birks and R. W. Pringle, Proc. Roy. Soc. Edinburgh **A70** (1971/72) 233.
58) R. W. Pringle, L. D. Black, B. L. Funt and S. Sobering, Phys. Rev. **92** (1953) 1582.
59) M. Furst and H. Kallmann, Phys. Rev. **97** (1955) 583.
60) G. Germai, Int. J. Appl. Rad. Isotop. **21** (1970) 487.
61) P. H. Heckmann, Z. Physik **157** (1959) 139; P. H. Heckmann, H. Hanson and A. Flammersfeld, Z. Physik **162** (1961) 84; P. H. Heckmann, W. Sander and A. Flammersfeld, Z. Physik **165** (1961) 12; W. F. Kienzle and A. Flammersfeld, Z. Physik **165** (1961) 1.
62) J. Weiss, Z. Physik **203** (1967) 37.

63) F. I. Kratochwill, Z. Physik **234** (1970) 74.
64) G. Bonsch and A. Flammersfeld, Z. Physik **236** (1970) 305.
65) E. Berkhan, Z. Physik **178** (1964) 101; K. Wick and A. Flammersfeld, Z. Physik **204** (1968) 164; W. Brand, R. Dobrin, H. Jack, R. L. Aubert and S. Roth, Can. J. Phys. **46** (1968) 537.
66) W. F. Kienzle, Z. Naturforsch **19a** (1964) 756.
67) J. H. Coon (unpublished) quoted by C. D. Swartz and G. E. Owen, *Fast neutron physics*, part 1 (eds. J. B. Marion and J. L. Fowler; Interscience, New York, 1960) p. 211.
68) K. Tsukuda and S. Kikuchi, Nucl. Instr. and Meth. **17** (1962) 280.
69) K. Tsukada, S. Kikuchi and Y. Miyagawa, Nucl. Instr. and Meth. **37** (1965) 69.
70) D. B. Oliver and G. F. Knoll, IEEE Trans. Nucl. Sci. **NS-15**, no. 3 (1968) 122.
71) F. D. Brooks and D. T. L. Jones, Nucl. Instr. and Meth. **121** (1974) 69.
72) M. Steinbock, F. D. Brooks and I. J. van Heerden, Proc. 4th Int. Symp. on *Polarization phenomena in nuclear reactions* (eds. W. Grüebler and V. König; Birkhauser Verlag, Basel, 1976) p. 475.
73) K. Wille, Z. Physik **241** (1971) 55.
74) G. E. Owen and C. D. Swartz, *Fast neutron physics*, part 1 (eds. J. B. Marion and J. L. Fowler; Interscience, New York, 1960) p. 211.
75) M. E. Toms, IEEE Trans. Nucl. Sci. **NS-17** (1970) 107.
76) S. T. Thornton and J. R. Smith, Nucl. Instr. and Meth. **96** (1971) 551.
77) Nuclear Enterprises Ltd., Edinburgh, U.K., Bulletin 404 (1973).
78) R. St. Onge, A. Galonsky, R. K. Jolly and T. M. Amos, Nucl. Instr. and Meth. **126** (1975) 391.
79) E. Langenscheidt, Nucl. Instr. and Meth. **91** (1971) 237.
80) T. G. Miller, Rev. Sci. Instr. **36** (1965) 847.
81) W. Schoett and A. Flammersfeld, Z. Naturforsch **21a** (1966) 1075.
82) O. Dietzsch, Ann. Acad. Brasil Genc. **39** (1967) 221.
83) K. H. Maier and J. Nitschke, Nucl. Instr. and Meth. **59** (1968) 227.
84) D. L. Smith, R. G. Polk and T. G. Miller, Nucl. Instr. and Meth. **64** (1968) 157.
85) R. L. Craun and D. L. Smith, Nucl. Instr. and Meth. **80** (1970) 239.
86) T. G. Masterson, Nucl. Instr. and Meth. **88** (1970) 61.
87) F. Titus, Nucl. Instr. and Meth. **89** (1970) 93.
88) R. C. Webb, M. G. Hauser and R. E. Mischke, Nucl. Instr. and Meth. **88** (1970) 22.
89) A. Bertin, A. Vitale and A. Placci, Nucl. Instr. and Meth. **91** (1971) 649.
90) R. Katz, S. C. Sharma and M. Homayoonfar, Nucl. Instr. and Meth. **100** (1972) 13.
91) H. H. Knox and T. G. Miller, Nucl. Instr. and Meth. **101** (1972) 519.
92) W. Bertl, W. Breunlich, A. Chalupka and S. Tagesen, Nucl. Instr. and Meth. **104** (1972) 205.
93) R. Madey and F. M. Waterman, Nucl. Instr. and Meth. **104** (1972) 253.
94) M. Buenerd, D. L. Hendrie, U. Jahnke, J. Mahoney, A. Menchaca-Rocha, C. Olmer and D. K. Scott, Nucl. Instr. and Meth. **136** (1976) 173.
95) L. A. Lockwood, C. Chen, L. A. Frilling, D. Swartz, R. N. St. Onge, A. Galonsky and R. R. Doering, Nucl. Instr. and Meth. **138** (1976) 353.
96) F. J. Lynch, IEEE Trans. Nucl. Sci. NS-22 (1975) 58.
97) A. Houdayer, S. K. Mark and R. E. Bell, Nucl. Instr. and Meth. **59** (1968) 319.
98) J. Kirkbride, E. C. Yates and D. G. Crandall, Nucl. Instr. and Meth. **52** (1967) 293.
99) F. T. Kuchnir and F. J. Lynch, IEEE Trans. Nucl. Sci. NS-15, no. 3 (1968) 107.
100) R. Kunze and R. Langkau, Nucl. Instr. and Meth. **91** (1971) 667.
101) T. M. Kelly, J. A. Marrigan and R. M. Lambrecht, Nucl. Instr. and Meth. **109** (1973) 233.
102) Th. Binkert, H. P. Tschanz and P. E. Zinsli, J. Luminescence **5** (1972) 187.
103) B. Bengtson and M. Moszynski, Nucl. Instr. and Meth. **81** (1970) 109.
104) D. Bollini, P. Dalpiaz, P. L. Frabetti, T. Massam, F. Navach, F. L. Navarria, M. A. Schneegans and A. Zichichi, Nucl. Instr. and Meth. **81** (1970) 109.
105) J. Bialkowski and M. Moszynski, Nucl. Instr. and Meth. **105** (1972) 51.
106) F. Calligaris, C. Cernigoi, P. Ciuti and R. Giacomich, Nucl. Instr. and Meth. **107** (1973) 213.
107) J. Pouthas, S. Agarwal, M. Engrand and C. Pisani, Nucl. Instr. and Meth. **145** (1977) 445.
108) M. Moszynski and B. Bengtson, Nucl. Instr. and Meth. **91** (1971) 73.
109) E. Dietz, J. v. Czarnecki, W. Patscher, W. Schäfer and R. Bass, Nucl. Instr. and Meth. **108** (1973) 607.
110) C. Cerniogi, N. Grion, G. Pauli and B. Saitta, Nucl. Instr. and Meth. **144** (1977) 479.
111) B. Bengtson and M. Moszynski, Nucl. Instr. and Meth. **75** (1969) 152.
112) S. Cochavi, D. B. Fossan, S. H. Henson, D. E. Alburger and E. K. Warburton, Phys. Rev. **C2** (1970) 2241.
113) B. Bengtson, J. Jensen, M. Moszynski and H. L. Nielsen, Nucl. Phys. **A159** (1970) 249.
114) L. Karlsson, Nucl. Instr. and Meth. **100** (1972) 193.
115) P. B. Lyons and J. Stevens, Nucl. Instr. and Meth. **114** (1974) 313.
116) T. Batsch and M. Moszynski, Nucl. Instr. and Meth. **123** (1975) 341.
117) R. B. Knowlen and A. A. O'Dell, Nucl. Instr. and Meth. **78** (1970) 300.
118) C. A. Baker, C. J. Barry, B. E. Bonner, P. Ford, E. Freedman, C. Tschalar and L. E. Williams, Nucl. Instr. and Meth. **85** (1970) 259.
119) M. Poulet and A. Santroni, Nucl. Instr. and Meth. **148** (1978) 359.
120) J. D. Carlson, R. W. Finlay and D. E. Bainum, Nucl. Instr. and Meth. **147** (1977) 353.
121) J. V. Geaga, G. J. Igo, J. B. McClelland, M. A. Nasser, S. Sander, H. Spinka, J. B. Carroll, D. Frederickson, V. Perez-Mendez and E. T. B. Whipple, Nucl. Instr. and Meth. **141** (1977) 263.
122) V. Giordano, C. Manduchi, M. T. Russo-Manduchi and G. F. Segato, Nucl. Instr. and Meth. **135** (1976) 483.
123) G. C. Neilson, C, Glavina, W. K. Dawson, K. V. K. Iyengar and W. J. McDonald, Nucl. Instr. and Meth. **81** (1970) 301.
124) B. Ghidini et al., Nucl. Instr. and Meth. **125** (1975) 357.
125) G. T. Wright, Proc. Phys. Soc. **B69** (1956) 358.

126) R. B. Owen, IRE Trans. Nucl. Sci. NS-5, no. 3 (1958) 198.
127) F. W. K. Kirk, *Fast neutron physics*, part 2 (eds. J. B. Marion and J. L. Fowler; Interscience, New York, 1963) p. 2237.
128) A. Suhami and D. Ophir, Nucl. Instr. and Meth. **30** (1964) 141.
129) G. Walter, A. Huck, J. P. Trevetin and A. Coche, J. Phys. Rad. **24** (1963) 1017.
130) G. Walter and A. Coche, Nucl. Instr. and Meth. **23** (1963) 147.
131) Y. Takami and M. Hosoe, Nucl. Instr. and Meth. **31** (1964) 347.
132) M. L. Roush, M. A. Wilson and W. F. Hornyak, Nucl. Instr. and Meth. **31** (1964) 112.
133) T. K. Alexander and F. S. Goulding, Nucl. Instr. and Meth. **13** (1961) 244.
134) W. Sweirner, Nucl. Instr. and Meth. **39** (1966) 343.
135) B. Sabbah and A. Suhami, Nucl. Instr. and Meth. **58** (1968) 102.
136) C. E. Hollandsworth and W. P. Bucher, Rev. Sci. Instr. **39** (1968) 165.
137) R. St. Onge and J. A. Lockwood, Nucl. Instr. and Meth. **69** (1969) 25.
138) J. B. Czirr, Nucl. Instr. and Meth. **72** (1969) 23.
139) A. Adam, J. Cabe, M. Cance, M. Laurat and J. C. Ponce, Rev. Phys. App. **4** (1969) 262.
140) J. Kahane, R. Sené, P. Delpierre and M. Heyman, Rev. Phys. Appl. **4** (1969) 257.
141) G. White, Nucl. Instr. and Meth. **45** (1966) 270.
142) I. Taylor and J. Kalyna, Nucl. Instr. and Meth. **88** (1970) 267.
143) L. J. Heistek and L. van der Zwan, Nucl. Instr. and Meth. **80** (1970) 213.
144) R. R. Fullwood, Nucl. Instr. and Meth. **93** (1971) 235.
145) H. Nakamura, F. Reide and T. Yuasa, Nucl. Instr. and Meth. **108** (1973) 509.
146) M. Forte, A. Konsta and C. Maranzana, *Nuclear electronics*, vol. 1 (IAEA, Vienna, 1962) p. 277.
147) J. D. Dewendra and R. B. Galloway, Nucl. Instr. and Meth. **125** (1975) 503.
148) P. Sperr, H. Spieler, M. R. Maier and D. Evers, Nucl. Instr. and Meth. **116** (1974) 55.
149) G. White, Proc. 2nd Ispra *Nuclear electronics* Symp., 1975 (Euratom, 1975) p. 447.
150) C. L. Morris, J. E. Bolger, G. W. Hoffmann, C. F. Moore, L. E. Smith and H. A. Thiessen, Nucl. Instr. and Meth. **137** (1976) 397.
151) G. White, Nucl. Instr. and Meth. (in press).
152) P. Plischke, V. Schröder, W. Scobel, L. Wilde and M. Bormann, Nucl. Instr. and Meth. **136** (1976) 579.
153) F. D. Brooks, Nucl. Instr. and Meth. **4** (1959) 151.
154) F. D. Brooks, R. W. Pringle and B. L. Funt, IEEE Trans. Nucl. Sci. NS-7, nos. 2-3 (1960) 35.
155) M. Forte, Nuovo Cim. Ser. 10, Suppl., **9**, no. 2 (1958) 390; Proc. Geneva Conf. on *Peaceful uses of atomic energy*, 1958 (U.N., Geneva, 1959) Session A18, p. 167.
156) R. B. Owen, Nucleonics **17** (1959) 92.
157) G. Pauletta and F. D. Brooks, Nucl. Phys. **A255** (1975) 267.
158) D. Kopsch and S. Cierjacks, Nucl. Instr. and Meth. **54** (1967) 277.
159) J. B. Czirr, Nucl. Instr. and Meth. **88** (1970) 321.
160) J. Kalyna and I. Taylor, Nucl. Instr. and Meth. **88** (1970) 277.
161) R. A. Winyard, J. E. Lutkin and G. W. McBeth, Nucl. Instr. and Meth. **95** (1971) 141.
162) R. A. Winyard and G. W. McBeth, Nucl. Instr. and Meth. **98** (1972) 525.
163) D. B. Syme and G. I. Crawford, Nucl. Instr. and Meth. **104** (1972) 245.
164) T. G. Miller, Nucl. Instr. and Meth. **63** (1968) 121.
165) A. Bertin, A. Vitale and A. Placci, Nucl. Instr. and Meth. **68** (1969) 24.
166) W. P. Poenitz, Nucl. Instr. and Meth. **109** (1973) 413.
167) D. Evers, E. Spindler, P. Konrad, K. Rudolph and W. Assmann, Nucl. Instr. and Meth. **124** (1975) 23.
168) M. Weinert, Nucl. Instr. and Meth. **108** (1973) 401.
169) A. Chalupka, G. Stengl and H. Vonach, Nucl. Instr. and Meth. **144** (1977) 167.
170) D. T. L. Jones and F. D. Brooks, Nucl. Phys. **A222** (1974) 79.
171) F. D. Brooks and D. T. L. Jones, Nucl. Instr. and Meth. **121** (1974) 77.
172) F. K. Wohn, J. R. Clifford, G. H. Carlson and W. H. Talbot, Nucl. Instr. and Meth. **101** (1972) 343.
173) B. W. Ridley, Nucl. Instr. and Meth. **14** (1961) 231; N. R. Daly, Rev. Sci. Instr. **34** (1963) 1116; H. M. Gibbs and E. D. Cummins, Rev. Sci. Instr. **37** (1966) 1385; W. A. P. Young, R. G. Ridley and N. R. Daly, Nucl. Instr. and Meth. **51** (1967) 257; F. Brouillard and O. Godart, Nucl. Instr. and Meth. **74** (1969) 141.
174) R. D. McFarlane, D. F. Torgerson, Y. Fares and C. A. Hassell, Nucl. Instr. and Meth. **116** (1974) 381.
175) C. J. Batty, A. I. Kilvington and A. Marinov, Nucl. Instr. and Meth. **99** (1972) 179.
176) G. Shani and M. Cojocaru, Nucl. Instr. and Meth. **146** (1977) 531.
177) L. M. Bollinger and G. E. Thomas, Rev. Sci. Instr. **28** (1957) 489.
178) L. Sutterlin, Atomkernenergie **12** (1967) 287.
179) E. A. Rajo, G. J. Videla, M. A. Molinari, O. A. Lires and L. H. Casas, Int. J. App. Rad. Isotop. **15** (1964) 611.
180) H. E. Jackson and G. E. Thomas, Rev. Sci. Instr. **36** (1965) 419.
181) G. I. Anisimova, L. S. Danelyan, A. F. Zhigach, V. R. Lazarenko, V. N. Siryatskaya and P. Z. Sorokin, Instr. Exp. Tech. **1** (1969) 48.
182) C. L. Cowan, F. Reines, F. B. Harrison, E. C. Anderson and F. N. Hayes, Phys. Rev. **90** (1953) 493.
183) J. W. Boldeman, J. Nucl. Energy **22** (1968) 63.
184) J. Hellstrom and S. Beshai, Nucl. Instr. and Meth. **101** (1972) 267.
185) J. B. Parker, P. Fieldhouse, L. M. Harrison and D. S. Mather, Nucl. Instr. and Meth. **60** (1968) 7; S. Signarbieux, M. Ribrag, J. Poitou and J. Matuszek, Nucl. Instr. and Meth. **95** (1971) 585; H. Beil, R. Bergère and A. Veyssière, Nucl. Instr. and Meth. **67** (1969) 293; R. Bergère, H. Beil and A. Veyssière, Nucl. Phys. **A121** (1968) 463; H. Beil, R. Bergère and A. Veyssière, Rev. Phys. Appl. **4** (1969) 249; M. Soleilhuc, J. Frehaut and J. Gauriau, J. Nucl. Energy **23** (1969) 257.
186) A. B. Smith, P. Guenther and R. Sjoblom, Nucl. Instr. and Meth. **140** (1977) 397.
187) V. Verbinski, W. R. Burrus, T. A. Love, W. Zobel, N. W. Hill and R. Textor, Nucl. Instr. and Meth. **65** (1968) 8.
188) Y. Furuta, S. Kinbara and K. Kaieda, Nucl. Instr. and Meth. **84** (1970) 269; S. Mubarakmand and M. Anwar, Nucl. Instr. and Meth. **93** (1971) 515; H. J. Kellermann and R. Langkau,

Nucl. Instr. and Meth. **94** (1971) 137.
189) D. Hermsdorf, K. Pasieka and D. Seeliger, Nucl. Instr. and Meth. **107** (1973) 259.
190) M. Drosg, Nucl. Instr. and Meth. **105** (1972) 573.
191) M. Bormann, R. Kühl, K. Schäfer and U. Seebeck, Nucl. Instr. and Meth. **88** (1970) 245.
192) W. Lindstrom and B. D. Anderson, Nucl. Instr. and Meth. **98** (1972) 413.
193) W. R. Burrus and V. Verbinski, Nucl. Instr. and Meth. **67** (1969) 181.
194) M. M. Holland, R. C. Minehart and S. E. Sobottka, Nucl. Phys. **A147** (1970) 249; E. A. Stroker, C. E. Burgart, T. A. Love and R. M. Freestone, Nucl. Instr. and Meth. **97** (1971) 275; T. A. Khan, J. S. Hewitt and K. G. McNeill, Can. J. Phys. **47** (1969) 1037.
195) L. C. Northcliffe, C. W. Lewis and D. P. Saylor, Nucl. Instr. and Meth. **83** (1970) 93.
196) W. Meyer and S. Prigl, Trans, Am. Nucl. Sci. **16** (1973) 361.
197) C. W. Lewis and J. M. Blair, Nucl. Instr. and Meth. **35** (1965) 261.
198) R. H. Johnson, D. T. Ingersoll, B. W. Wehring and J. J. Dorning, Nucl. Instr. and Meth. **145** (1977) 337.
199) J. A. Harvey, these proceedings.
200) F. W. K. Firk, these proceedings.
201) B. A. Benetski, E. M. Burymov and I. M. Frank, Yad. Fiz. **8** (1968) 920 [Sov. J. Nucl. Phys. **8** (1969) 534].
202) U. von Moellendorff and R. J. Slobodrian, Nucl. Instr. and Meth. **120** (1974) 257.
203) C. M. Bartle, Nucl. Instr. and Meth. **117** (1974) 469.
204) R. L. Macklin and B. J. Allen, Nucl. Instr. and Meth. **91** (1971) 565.
205) B. J. Allen and R. L. Macklin, Phys. Rev. **C3** (1971) 1737.
206) L. W. Weston and J. H. Todd, Nucl. Instr. and Meth. **86** (1970) 205.
207) J. Becker, L. Eriksson, L. C. Momberg and Z. H. Cho, Nucl. Instr. and Meth. **123** (1975) 199.
208) Z. H. Cho, C. M. Tsai and L. A. Eriksson, IEEE Trans. Nucl. Sci. **NS-22** (1975) 72.
209) N. Benczer-Koller and T. Fink, Nucl. Phys. **A161** (1971) 123.
210) A. Schaarschmidt and H. Durner, Nucl. Instr. and Meth. **105** (1972) 497.
211) H. Abou-Leila, S. M. Darwish, A. A. El Kamhawy, H. A. Ismail and S. M. El Habis, Atomkernergie **28** (1976) 131.
212) L. A. Eriksson, C. M. Tsai, Z. H. Cho and C. R. Hurlbut, Nucl. Instr. and Meth. **122** (1974) 373.
213) B. Bärs and E. Markkanen, Nucl. Instr. and Meth. **99** (1972) 419.
214) A. V. Nemarov and I. G. Feldman, Instr. Exp. Tech. **15** (1972) 1351.
215) C. Cernigoi, N. Grion, G. Pauli and B. Saitta, Nucl. Instr. and Meth. **144** (1977) 479.
216) F. Ashton, H. J. Edwards and G. N. Kelly, Nucl. Instr. and Meth. **93** (1971) 349.
217) D. Frederickson, J. Carroll, M. Gotein, R. Kline, B. MacDonald, V. Perez-Mendez and A. Stetz, Nucl. Instr. and Meth. **107** (1973) 205.
218) S. R. Lewis and N. H. Shafrir, Nucl. Instr. and Meth. **93** (1971) 317; J. A. Cooper, L. A. Rancitelli and R. W. Perkins, J. Radioanal. Chem. **6** (1970) 147; J. A. Cooper and R. W. Perkins, Nucl. Instr. and Meth. **94** (1971) 29; J. A. Cooper, Anal. Chem. **43** (1971) 838.
219) D. C. Camp, C. Gatrousis and L. A. Maynard, Nucl. Instr. and Meth. **117** (1974) 189.
220) M. H. La Pointe, B. G. Rennex, F. Siohan and J. R. Wayland, Nucl. Instr. and Meth. **89** (1970) 291.
221) M. W. Collins, A. E. Groome and P. R. Norton, Nucl. Instr. and Meth. **117** (1974) 339.
222) S. F. Saterlie and D. R. Tompkins, Rev. Sci. Instr. **46** (1975) 857.
223) W. R. Webber and J. Kish, Nucl. Instr. and Meth. **99** (1972) 237.
224) E. Heidbreder, K. Pinkau, C. Reppin and V. Schönfelder, Nucl. Instr. and Meth. **88** (1970) 137.
225) B. Ghidini et al., Nucl. Instr. and Meth. **147** (1977) 313.
226) M. L. Marshak and P. Schmüser, Nucl. Instr. and Meth. **80** (1970) 77.
227) R. J. Abrams, A. S. Carroll, T. F. Kycia, K. K. Li, J. Menes, D. N. Michael, P. M. Mockett and R. Rubinstein, Nucl. Instr. and Meth. **107** (1973) 569.
228) H. Nifenecker, Nucl. Instr. and Meth. **81** (1970) 45.
229) R. B. Wilson, P. D. Cross and B. W. Sooler, J. Sci. Instr. **40** (1963) 127.
230) J. C. Barton, A. Crispin and M. Slade, J. Sci. Instr. **41** (1964) 736.
231) A. V. Voevodskii, V. L. Dadykin, O. G. Ryazhskaya, Instr. Exp. Tech. **1** (1970) 92.
232) E. Berkowitz, Nucl. Instr. and Meth. **73** (1969) 225.
233) A. Benvenuti, D. Cline, W. T. Ford, R. Imlay, T. Y. Ling et al., Nucl. Instr. and Meth. **125** (1975) 447.
234) T. L. Jenkins and F. Reines, IEEE Trans. Nucl. Sci. **NS-11**, no. 3 (1964) 1.
235) K. W. Chen, P. A. Crean, J. T. Dakin and M. G. Hauser, Nucl. Instr. and Meth. **88** (1970) 219.
236) A. M. Preszler, G. M. Simnett and R. S. White, Phys. Rev. Lett. **28** (1972) 982; R. T. Grannan, R. Koga, W. A. Millard, A. M. Prezzler, G. M. Simnett and R. S. White, Nucl. Instr. and Meth. **103** (1972) 99.
237) M. L. Muga, D. J. Burnsed, W. E. Steeger and H. E. Taylor, Nucl. Instr. and Meth. **83** (1970) 135.
238) M. L. Muga, Nucl. Instr. and Meth. **95** (1971) 349.
239) M. L. Muga, D. J. Burnsed and W. E. Steeger, Nucl. Instr. and Meth. **104** (1972) 605.
240) M. L. Muga, Nucl. Instr. and Meth. **105** (1972) 61.
241) M. L. Muga, G. L. Griffith, H. W. Schmitt and H. E. Taylor, Nucl. Instr. and Meth. **111** (1973) 581.
242) M. L. Muga, Univ. of Florida Nuclear Chemistry Progress Rep. ORO-2843-23 (1973) (NSA 29-15679).
243) P. Braun-Munzinger and C. K. Gelbke, Nucl. Instr. and Meth. **114** (1974) 141.
244) M. L. Muga, A. Chem, G. Griffith, H. S. Plendl, R. Eaker and R. Holub, Nucl. Instr. and Meth. **119** (1974) 255.
245) M. L. Muga, *Physics and chemistry of fission – 1973*, vol. 2 (IAEA, Vienna, 1974: STI/PUB/347) p. 451.
246) M. L. Muga, Nucl. Instr. and Meth. **124** (1975) 541.
247) M. L. Muga and G. Griffith, Nucl. Instr. and Meth. **109** (1973) 289.
248) M. L. Muga and D. Burnsed, Rev. Sci. Instr. **47** (1976) 924.
249) M. L. Muga and M. Diksic, Nucl. Instr..and Meth. **132** (1976) 553.
250) K. Ettling and W. von Witsch, Nucl. Instr. and Meth. **148** (1978) 299.
251) N. N. Ajitanand and K. K. Iyengar, Nucl. Instr. and Meth. **133** (1976) 71.

252) R. K. Batra and A. C. Shotter, Nucl. Instr. and Meth. **124** (1975) 101.

253) H. Geissel, K. Güttner, S. Hoffmann and G. Munzenberg, Nucl. Instr. and Meth. **144** (1977) 465.

254) T. Batsch and M. Moszynski, Nucl. Instr. and Meth. **125** (1975) 231.

255) A. Gamp, W. Bohne, P. Braun-Munzinger and C. K. Gelbke, Nucl. Instr. and Meth. **120** (1974) 281.

256) A. Gelbke, K. D. Hildenbrand and R. Bock, Nucl. Instr. and Meth. 95 (1971) 397.

257) T. M. Cormier, R. S. Galik, E. R. Cosman and A. J. Lazzarini, Nucl. Instr. and Meth. **119** (1974) 145.

258) E. C. Anderson, R. L. Schuch, J. D. Perrings and W. H. Langham, Nucleonics **14**, no. 1 (1956) 1; E. C. Anderson, *Liquid scintillation counting* (eds. C. G. Bell and F. N. Hayes; Pergamon, London, 1958) p. 211.

259) T. A. Iinuma and P. R. J. Burch, Nucl. Instr. and Meth. **16** (1962) 247; P. A. Delwaide, Int. J. App. Rad. Isotop. **20** (1969) 623; P. A. Delwaide, J. Nucl. Med. **11** (1970) 19.

260) *Organic scintillation detectors*, Proc. Univ. New Mexico Conf. 1960, TID-7612 (A.E.C., Washington, 1961).

261) D. L. Horrocks, ed., *Organic scintillators* (Gordon and Breach, New York, 1968).

262) E. D. Bransome, ed., *The current status of liquid scintillation counting* (Grune and Stratton, New York, 1970).

263) D. L. Horrocks and C. T. Peng, eds., *Organic scintillators and liquid scintillation counting* (Academic Press, London, 1971).

264) A. Dyer, ed., *Liquid scintillation counting*, vol. 1 (Heyden, London, 1971).

265) M. A. Crook, P. Johnson and B. Scales, eds., *Liquid scintillation counting*, vol. 2 (Heyden, London, 1972).

266) P. E. Stanley and B. A. Scoggins, eds., *Liquid scintillation counting* (Academic Press, New York, 1974).

267) M. A. Crook and P. Johnson, eds., *Liquid scintillation counting*, vol. 3 (Heyden, London, 1974).

268) M. A. Crook and P. Johnson, eds., *Liquid scintillation counting*, vol. 4 (Heyden, London, 1976).

269) J. A. B. Gibson, *Liquid scintillation science and technology*, (eds. A. A. Noujaim, C. Ediss and L. I. Weibe; Academic Press, New York, 1976) p. 153.

270) J. K. Basson and J. Steyn, Proc. Phys. Soc. A67 (1954) 297.

271) W. J. McDowell, *Organic scintillators and liquid scintillation counting* (eds. D. L. Horrocks and C. T. Peng; Academic Press, New York, 1971) p. 937.

272) J. H. Thorngate, W. J. McDowell and D. J. Christian, Health Phys. **27** (1974) 123.

273) J. N. McKilveen and W. R. Johnson, Health Phys. 28 (1975) 5.

274) W. J. McDowell and J. F. Weiss, *Liquid scintillation science and technology* (eds. A. A. Noujaim, C. Ediss and L. I. Weibe; Academic Press, New York, 1976) p. 17.

F.D. Brooks
Development of organic scintillators
Nucl. Instr. and Meth. 162 (1979) 477-505

D.T.L. Jones, F.D. Brooks, S. Wynchank and I.J. van Heerden
Differential dose measurements with T(d,n) and ^{252}Cf neutron sources
Proc. 5th Int. Conf. on Medical Physics, ed. E.H. Frei (Belinson Center, Jerusalem, 1979) p 57.1

DIFFERENTIAL DOSE MEASUREMENTS WITH T(d,n) and ^{252}Cf NEUTRON SOURCES

57.1

D.T.L. Jones, F.D. Brooks[†], S. Wynchank[†] and I.J. van Heerden[≠]

Karl Bremer Hospital and National Accelerator Centre, P.O. Karl Bremer 7531, Republic of South Africa

[†]Department of Physics, University of Cape Town [≠]Southern Universities Nuclear Institute

INTRODUCTION

In neutron therapy we are concerned with mixed beams of neutrons and gamma rays. The effects produced by neutrons with energies below 30 MeV are believed to be primarily due to recoil protons, with smaller contributions from heavier recoil charged particles and reaction products.

It is well known that the RBE of ionizing radiations is LET dependent. Compton electrons produced by incident gamma rays are low-LET radiations, while protons (or heavier particles) have low-LET at high energy and high-LET at low energy. Each proton which is brought to rest in a medium therefore produces some high-LET radiation (at the end of its range) and some low-LET radiation if the energy is high enough.

To correctly assess the biological effect of neutron irradiation we therefore need to, firstly, separate the electron and proton contributions and, secondly, to determine the energy of individual protons in order to divide this energy between high- and low-LET. It is strictly speaking incorrect simply to integrate all the energy deposited by the protons and regard this as high-LET.

In this work we have used the pulse shape discrimination properties of an organic scintillator to separate the protons and electrons produced in a tissue equivalent phantom in T(d,n) and ^{252}Cf fields and to measure the energy spectra, so that the high-LET component of the fields could be estimated correctly.

METHOD

The measurements were made at the Southern Universities Nuclear Institute, Faure, Cape. Neutrons of 22 MeV were produced in the forward direction by bombarding a tritium gas target with 5 MeV deuterons from the CN Van de Graaff accelerator. For these measurements a special collimator was constructed. This consisted of 350 mm of steel placed next to the source with 350 mm of wax and water behind the steel. The collimator system presented a 100 mm x 100 mm field at a distance of 0.8 m from the source.

The ^{252}Cf source was a short after-loading needle of active length 15 mm with nominal mass of 0.5 μg on loan from the IAEA. It was suspended in the phantom to simulate interstitial implant conditions. The phantom itself consisted of a perspex trough (600 x 275 x 300 mm) filled with a tissue equivalent liquid (1).

The detector consisted of an anthracene ($C_{14}H_{10}$) scintillation crystal (25 mm diameter x 25 mm long) attached by means of a 10 cm long perspex light guide to a photomultiplier tube. The detector was fitted with a pulse shape discriminator (2) which gave both energy and particle identification. It was therefore possible to simultaneously separate and record events which produced electrons and those which produced protons and to measure the energies deposited by the individual particles in the detector. The energy-loss spectra for the protons and electrons were therefore determined simultaneously.

With the sources fixed measurements were made with the detector at different positions in the phantom in order to obtain information about the depth dose characteristics of the high- and low-LET components of the sources. The operating threshold of the detector corresponded to an energy of 50 keV for electrons and 400 keV for protons.

RESULTS

It is known (3) that at LET $\geq$ 50 keV.μm^{-1} there is a sharp steplike increase in RBE. We therefore use this LET-value as the boundary between "low-LET" and "high-LET" radiation. For protons an LET (or specific energy loss in tissue) of $\geq$ 50 keV.μm^{-1} is realized only at energies $\leq$ 400 keV. This means that effectively a proton has high-LET only over the last 400 keV of its range. Thus for a proton depositing, for example, 2 MeV of energy in the detector, 0.4 MeV was considered as high-LET radiation and 1.6 MeV as low-LET radiation. Electrons detected in the crystal were classified as having low-LET over their full range. The energy deposited by each particle was determined from known scintillation response curves (4).

The results of some of the measurements are given in Fig. 1. These data have not been corrected for geometrical effects, for effects due to the non-tissue equivalence of the probe, or for events which went undetected due to the finite operating threshold of the detector. The upper figure shows the central axis depth dose distributions of the total dose (expressed as a percentage of the surface dose) and the high-LET fraction of the total dose for the T(d,n) source. The 50% depth dose occurs at 130 mm and the proportion of high-LET radiations decreases with increasing depth, as expected.

The dose measurements for the ^{252}Cf source (lower figure) are normalised to 100% at 10 mm (the closest distance which could be studied). The dose falls to half of this value 19 mm further away. The fraction of high-LET radiations also decreases at large distances, but is higher at small distances than for the T(d,n) source.

CONCLUSION

The results obtained illustrate the viability of this technique for differentiating between high- and low-LET radiations from neutron sources. The technique is absolute in that the energy deposited is directly determined. The method is independent of neutron and gamma spectral details and of knowledge of fluence, or fluence-to-dose conversion factors. On the other hand the method is limited by the detector threshold and the fact that the detector is not strictly tissue equivalent. However, corrections can be made for these effects and it is possible that this technique could find application in neutron therapy.

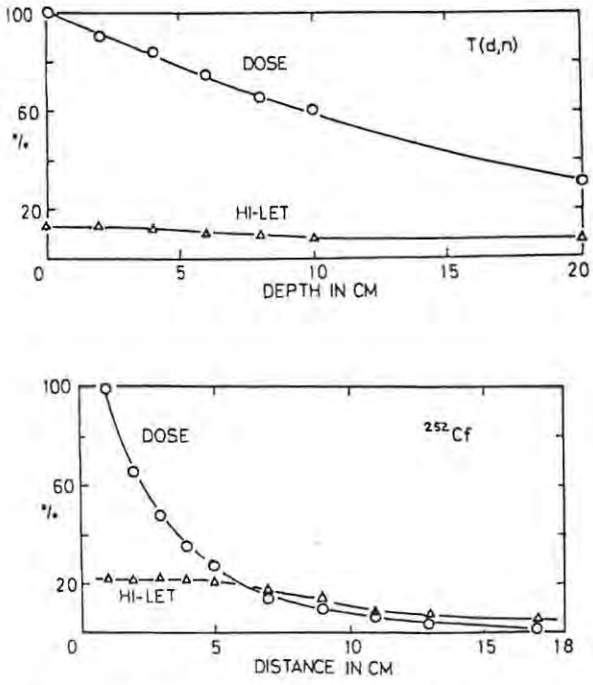

Fig. 1. Dose distributions from T(d,n) and ^{252}Cf sources

REFERENCES

1. L.J. Goodman, Health Physics 16 (1969) 763

2. F.D. Brooks, Nucl. Instr. and Meth. 4 (1959) 151

3. M.L. Boone and A.L. Wiley, IEEE Trans. on Nucl. Sc. NS-18 (1971) 36

4. J.B. Birks, The Theory and Practice of Scintillation Counting, Pergamon Press (1964)

SUMMARY

A new technique has been developed to study the distribution of high- and low-LET radiations from neutron sources within a tissue equivalent phantom. The method utilizes the pulse shape discrimination properties of an anthracene scintillation crystal in order to differentiate between protons and electrons detected in the crystal and to measure the energy deposited by these secondary particles. Protons with energies less than 400 keV are classified as high-LET radiations. For both 22 MeV neutrons from the T(d,n) reaction and for ^{252}Cf neutrons it was found that the high-LET fraction decreased with depth in the phantom. The method has several advantages and could find application in neutron therapy.

Nuclear Instruments and Methods 180 (1981) 165–171

A HIGH FLUX ASSOCIATED PARTICLE NEUTRON SOURCE

C.M. BARTLE *, F.D. BROOKS
Department of Physics, University of Cape Town, Rondebosch 7700, Cape Town, South Africa

D.T.L. JONES
Karl Bremer Hospital and National Accelerator Centre, Karl Bremer 7531, South Africa

W.R. McMURRAY and R. VERBRUGGEN
Southern Universities Nuclear Institute, Faure 7131, South Africa

Received 8 July 1980

An associated particle system for neutron production using the $^{2}H(d, n)^{3}He$ reaction is described. The system employs a thin-walled scattering chamber, an assembly to rotate a deuterated polyethylene target and a magnetic analyzer for recoil particle separation in high flux applications. Neutron beam intensities of up to 1000 s^{-1} are routinely obtainable.

1. Introduction

Measurements using neutrons produced with the $^{2}H(d, n)^{3}He$ reaction often are improved in precision by detecting the associated ^{3}He ions [1–4]. A monoenergetic neutron beam of absolutely determined flux is defined by detecting the neutrons in time coincidence with the ^{3}He ions. The ^{3}He ions are usually detected in a surface barrier detector which subtends a small solid angle at the target. The profile of the neutron beam is determined by the size of both the deuteron beam and the collimator in front of the surface barrier detector, although other factors such as multiple scattering and kinematic effects also play a role in determining the neutron beam profile.

As an example, if the collimator subtends an angle of 0.4 msr at the target and the deuteron beam spot size is 1.5 mm in diameter, a tagged neutron beam 3–4° wide (fwhm) can be achieved for deuterons in the 2–5 MeV range. In a typical application, the cross sections of neutron induced reactions on nuclei incorporated in organic or inorganic scintillators are measured [5–7]. In this type of experiment the scintillator physically encompasses the electronically defined neutron beam and serves as both target and detector. Reaction cross sections are then deduced from the ratio of the coincidence rate (between events in the scintillator and ^{3}He detector) and the ^{3}He detection rate.

In many experiments of this type a neutron rate of about 50 s^{-1} is sufficient to give the required statistical accuracy in the measurement after a few hours of data accumulation. In these experiments the background count rate in the scintillator is typically a few kHz and a higher tagged neutron flux is avoided to minimize pile-up effects. However, there are applications, e.g. in scattering and polarization studies and with detectors having low neutron detection efficiencies, where increased neutron intensity is desirable.

Increased neutron beam intensity is achieved by increasing the incident deuteron beam current or the target thickness. However, limitations are imposed by the amount of current which the target can withstand and by the count rate (mainly due to elastically scattered deuterons) which the surface barrier detector can tolerate without deterioration.

An experimental system is described here in which a relatively intense monoenergetic neutron beam has been produced by means of improved target fabrication and by optimization of the ^{3}He detection system.

* Present address: Institute of Nuclear Sciences, Private Bag, Lower Hutt, New Zealand.

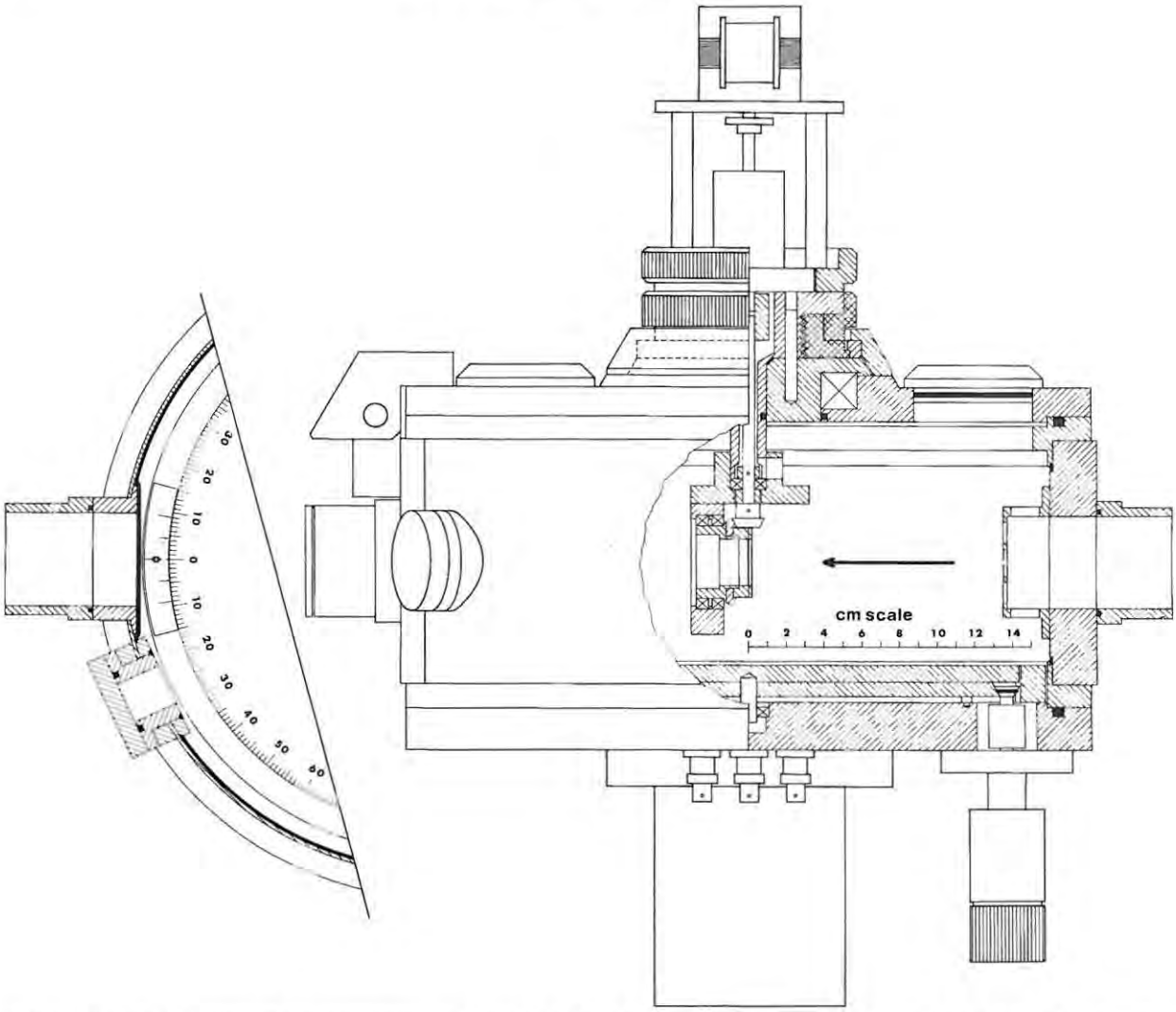

Fig. 1. Schematic diagram of the scattering chamber. The surface barrier detector usually positioned on the rotatable circular table is not shown.

2. Target chamber and components

A thin-walled, 34 cm diameter aluminium scattering chamber, constructed at the Southern Universities Nuclear Institute, while having similar features to some earlier chambers [2–4], incorporates a number of improvements. Cross sectional drawings of the chamber are shown in fig. 1, and an overall view is shown in fig. 2. The wall of the chamber is made of aluminium sheet 1.5 mm thick and is essentially transparent to MeV neutrons.

A deuterated polyethylene target is used and is mounted on an annular ring with an internal diameter of 25 mm. It is rotated by a motor mounted outside the chamber. The axis of rotation of the target does not coincide with the axis of the deuteron beam which thus sweeps out a circular path on the foil.

The rotary motion is transmitted to the target by means of a ferrofluidic rotary feedthrough * and a bevel gear and pinion drive mechanism. The target is rotated at 5 Hz and by periodically moving the target vertically (i.e. exposing a new path) its lifetime can be considerably extended.

The deuteron beam is collimated to 1.5 mm in diameter before entering the chamber. After passing

* Type SB-253-B-N-026. Manufactured by the Ferrofluidics Corp., Burlington, Massachusets 01803, U.S.A.

Fig. 2. A view of the target chamber and magnetic analyzer.

through the target it is stopped 2 m downstream in a shielded beam dump.

3. Target preparation and performance

Selfsupporting deuterated polyethylene foils, even when rotated at high speeds, typically have a lifetime of only a few minutes for incident beam currents of the order of 2 μA. The foils can however be strengthened considerably by evaporating thin layers of carbon onto both sides of the polyethylene as proposed by a number of workers [9–11]. It has been found that these target sandwiches with thicknesses in the 200–400 μg cm^{-2} range rotated at 5 Hz can withstand 2.5 μA of 5 MeV deuterons for long periods. The deuterated polyethylene foil is prepared from the powdered form * using a procedure described previously [8]. One carbon layer is evaporated onto the foil using a carbon arc (arc voltage 150 V) while it is still attached to the glass slide on which it was formed. After floating the foil off the slide in a water bath, the other carbon layer is evaporated onto the reverse side.

Fig. 3 is an electron microscope photograph of the cross section of a typical target. In this example, the deuterated polyethylene layer is approximately 1.2 μm thick (corresponding to an areal density of 120 μg cm^{-2}) and the carbon layers sandwiching the target are approximately 0.25 μm thick. The thickness of the deuterated polyethylene layer, which was nominally 400 μg cm^{-2} (based on the mass of polyethylene dissolved in the solvent) was found on examination to vary between 100 μg cm^{-2} and 300 μg cm^{-2} over the 2.5 cm diameter foil.

Typical yield characteristics of a target sandwich are shown in fig. 4. It can be seen from the figure that, after an initial rapid fall off, the yield remains fairly constant for a long period. This type of behaviour has been observed previously with such targets [9].

4. Magnetic analysis of the recoil ions

When incident deuteron beams of more than 2 μA are used with thick targets ($\geqslant$200 μg cm^{-2}), the high flux of elastically scattered deuterons causes damage to the solid state detector as well as producing severe pile up effects which limits the resolution of the ^{3}He events. A simple electromagnetic analyzer has been employed to partially screen the detector from these elastically scattered deuterons. The magnetic analyzer

* Available from Merck Sharp and Dohme, Pointe-Claire/Dorval, Quebec, Canada.

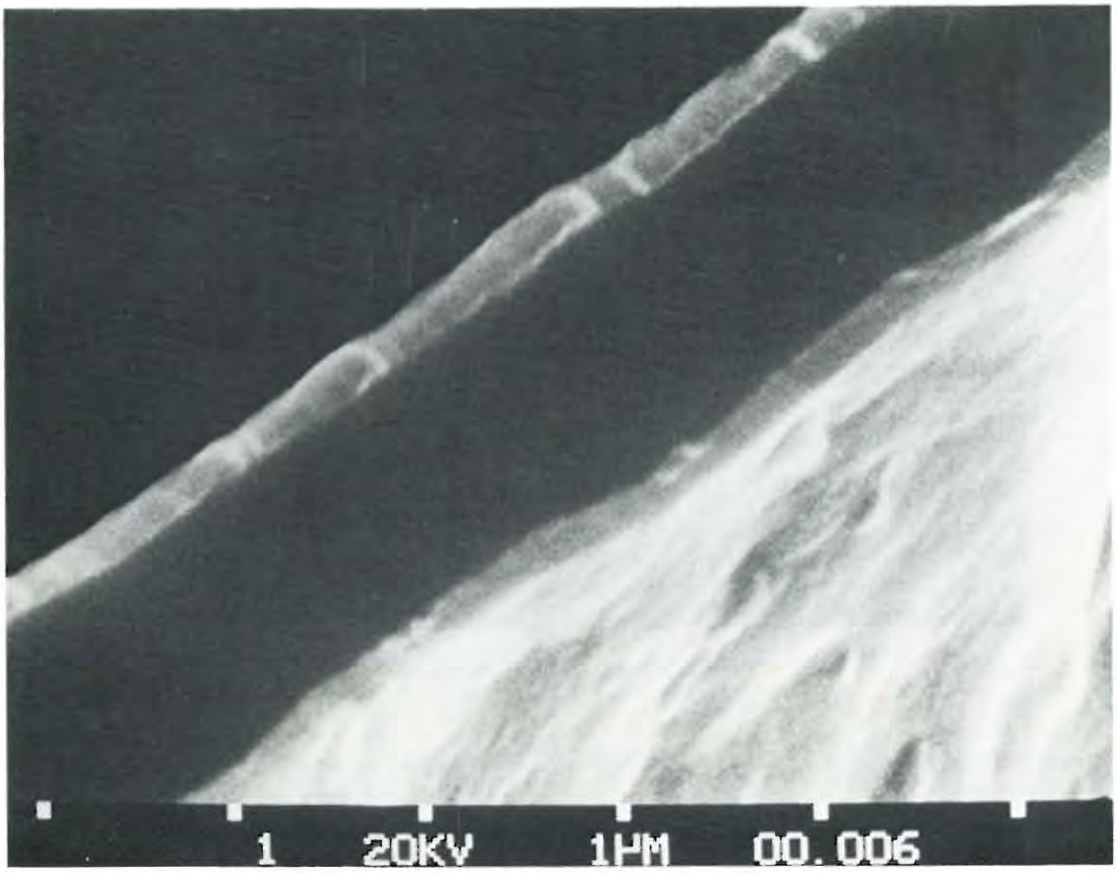

Fig. 3. An electron microscope photograph of a sectioned edge of a deuterated polyethylene target sandwiched between two carbon layers. The horizontal scale shown is in units of micrometers.

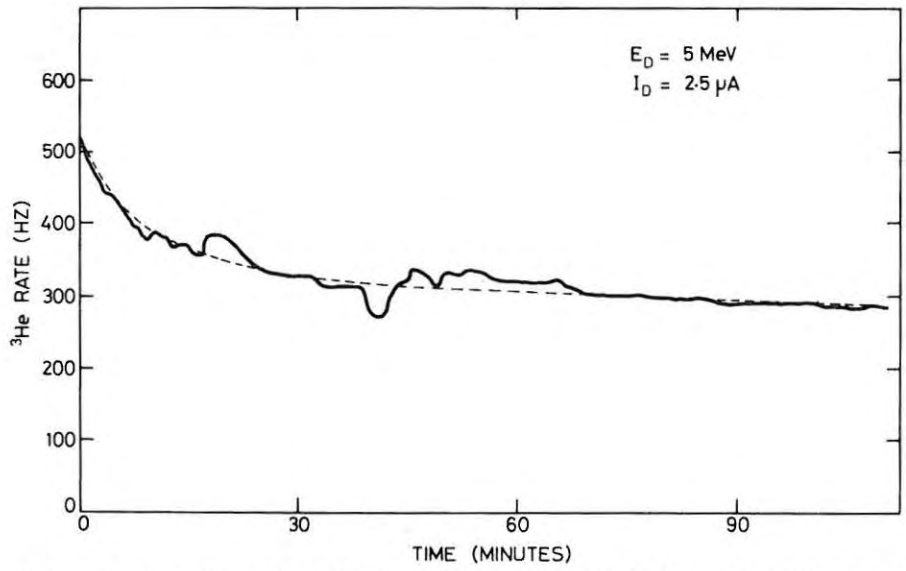

Fig. 4. The ^{3}He yield as a function of time for a 200 μg cm^{-2} thick "sandwiched" deuterated polyethylene target bombarded with 2.5 μA of 5 MeV deuterons. The ^{3}He particles are detected at 25° in a solid angle of 0.4 msr. Local variations in yield (continuous line) are due to variations in the beam current. The target was rotating at 5 Hz while the deuteron beam was displaced 6 mm from the axis of rotation.

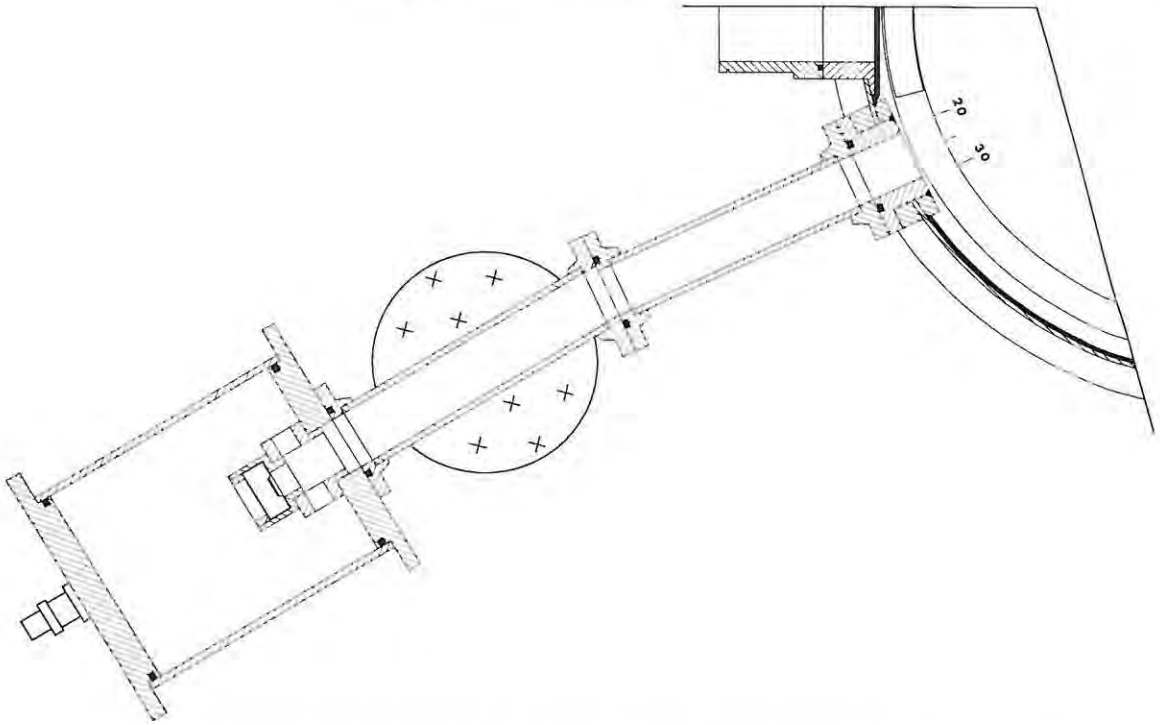

Fig. 5. Plan of the magnetic analyzer attached to the target chamber. Crosses indicate the magnetic field region.

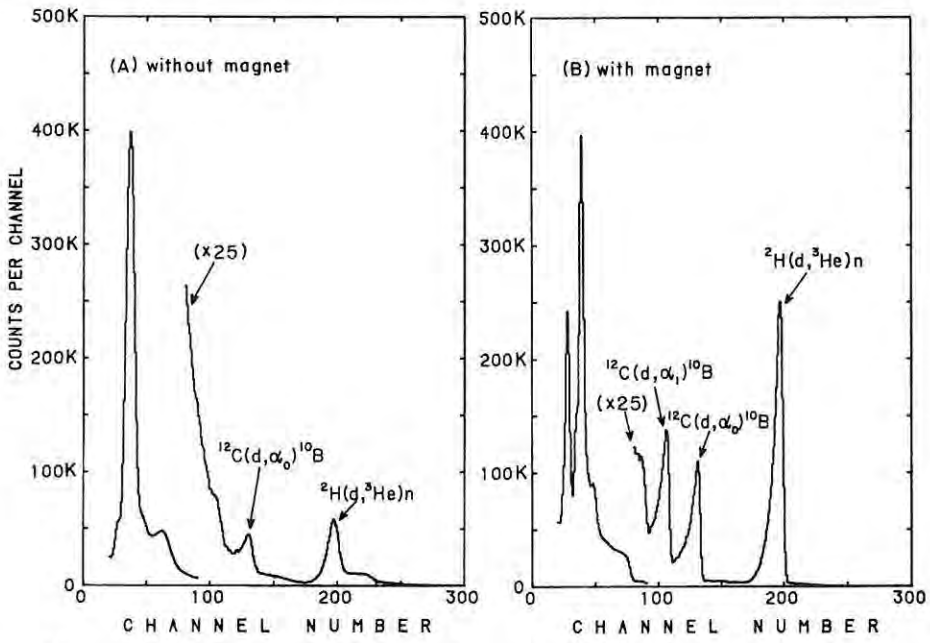

Fig. 6. Charged particle spectra obtained with a 30 μm thick silicon surface barrier transmission detector positioned at 25° to the 5 MeV incident deuteron beam. Spectrum (A) was obtained without magnetic analysis while for spectrum (B) magnetic analysis of the recoil charged particles was employed. The spectra are recorded for approximately the same number of elastically scattered deuterons (channels 25–45).

attached to a port positioned at 25° relative to the deuteron beam direction is shown in fig. 2. A schematic figure of the magnetic analyzer attachment is given in fig. 5.

The magnet has polepieces with circular cross section 10 cm in diameter and provides a field of 0.6 T. For 5 MeV incident deuterons this is sufficient to separate the elastically scattered deuterons and the 5.3 MeV ^{3}He recoil particles by approximately 3 mm at the exit of the field region.

The ^{3}He detector is a 30 μm thick silicon surface barrier transmission detector. This detector is of sufficient thickness to stop up to 5.5 MeV ^{3}He particles, while only absorbing a small part of the energy of the elastically scattered deuterons. Correct selection of the surface barrier detector thickness ensures that the elastically scattered particle events do not obscure the ^{3}He events [2–4].

Fig. 6 shows typical charged particle spectra without (fig. 6A) and with (fig. 6B) magnetic analysis. As can be seen from the figure, the magnetic analysis greatly improves the quality of the spectrum. In particular the resolution of the ^{3}He group is superior due to the reduction in the number of pile up events.

5. The neutron beam characteristics

The direction and angular spread of the neutron beam are known from the kinematic conditions, ^{3}He acceptance angle and deuteron beam spot size. However, it is important that the neutron beam profile be measured, firstly in order to assess effects such as multiple scattering of deuterons and ^{3}He ions in the target, and secondly to check the alignment of the apparatus.

In order to accomplish this a small cylindrical plastic scintillator (NE 102A) which subtends 1° at the neutron source is scanned across the beam in both the horizontal and vertical planes. Typically a coincidence timing resolution of 1 ns (fwhm) was obtained.

Measured horizontal and vertical neutron beam profiles are shown in fig. 7 for the calculated kinematic conditions: $E_d = 5$ MeV; $\theta_{He} = 25°$; $E_n = 3$ MeV; $\theta_n = 104.6°$. Magnetic analysis was used for these measurements. As can be seen from the figure the angular width is 3° in both the vertical and horizontal planes while the centre of the neutron beam coincides almost exactly with the direction given by the kinematic calculations.

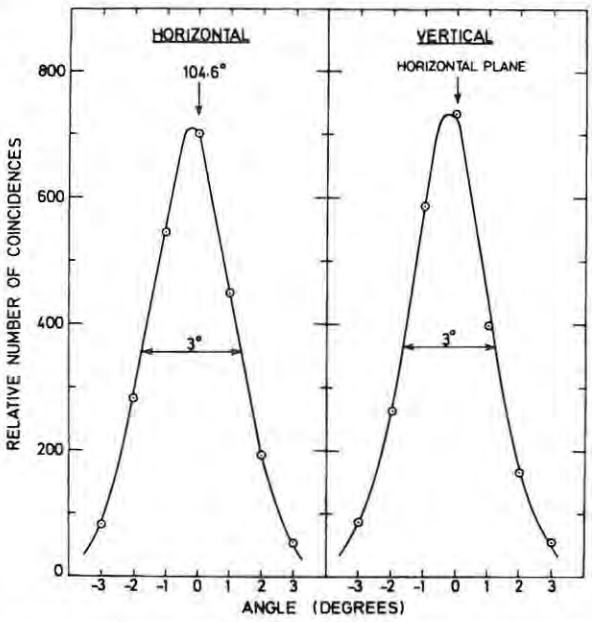

Fig. 7. Horizontal and vertical neutron beam profiles measured at $E_d = 5$ MeV, $\theta_{He} = 25°$ with a magnetically analysed charged particle beam. The charged particle detector subtended an angle of 0.4 msr at the target and the deuteron beam spot size was 1.5 mm in diameter.

6. Conclusion

An associated particle system for electronic collimation of a neutron beam from the ^{2}H(d, n)^{3}He reaction is described. Using deuterated polyethylene foils sandwiched between carbon layers and magnetic analysis of the emitted recoil particles a relatively intense neutron beam compared with that obtained from earlier systems can be achieved, while retaining good ^{3}He particle resolution. Using targets 400 μg cm^{-2} thick and with deuteron beam currents of 2.5 μA it was possible to achieve ^{3}He rates (and therefore neutron rates) of up to 1000 s^{-1}.

The authors are indebted to the South African Council for Scientific and Industrial Research and the Atomic Energy Board for financial assistance.

References

[1] H.H. Barschall, L. Rosen and R.F. Taschek, Rev. Mod. Phys. 24 (1952) 1.
[2] D.G. Schuster, Nucl. Instr. and Meth. 76 (1969) 35.
[3] C.M. Bartle and P.A. Quin, Nucl. Instr. and Meth. 121 (1974) 119.

[4] C.M. Bartle, D.W. Gebbie and C.L. Hollas, Nucl. Instr. and Meth. 144 (1977) 437.
[5] C.M. Bartle, Nucl. Instr. and Meth. 124 (1975) 547.
[6] C.M. Bartle, Nucl. Instr. and Meth. 117 (1974) 569.
[7] C.M. Bartle, Nucl. Phys. A330 (1979) 1.
[8] C.M. Bartle and H.O. Meyer, Nucl. Instr. and Meth. 112 (1973) 615.
[9] G.E. Tripard and B.L. White, Rev. Sci. Instr. 38 (1966) 435.
[10] L.M. Makosky and C. Hojvat, Nucl. Instr. and Meth. 74 (1969) 342.
[11] R.C. McFadden and P.W. Martin, Nucl. Instr. and Meth. 113 (1973) 601.

C.M. Bartle, F.D. Brooks, D.T.L. Jones, W.R. McMurray and R. Verbruggen
A high flux associated particle neutron source
Nucl. Instr. and Meth. 180 (1981) 165-171

Nuclear Physics **A362** (1981) 173–188;

NEUTRON-PROTON BREMSSTRAHLUNG AT 4.8 MeV

J. WHITTAKER and F. D. BROOKS
Physics Department, University of Cape Town, Rondebosch 7700, South Africa

and

I. J. VAN HEERDEN
Southern Universities Nuclear Institute, Faure, CP, 7131, South Africa

Received 25 August 1980
(Revised 17 December 1980)

Abstract: The differential cross section for neutron-proton bremsstrahlung has been measured at an incident energy of 4.8 MeV and outgoing nucleon angles of $\theta_n = 35°$, $\theta_p = 25°$. An upper limit of $d^2\sigma/d\Omega_n d\Omega_p = 210\ \mu b \cdot sr^{-2}$ was obtained. The experimental method was unusual in that the hydrogen target was a stilbene scintillation crystal, which also served as recoil proton detector, and the bremsstrahlung photon was detected in addition to the two nucleons. A theoretical estimate of the cross section corresponding to that measured in this experiment was made using an on-shell approximation and gave a result of $89\ \mu b \cdot sr^{-2}$. The measured upper limit exceeds this and other theoretical predictions but nevertheless represents a marked improvement over previous measurements of n-p bremsstrahlung at energies below 100 MeV.

E | NUCLEAR REACTIONS ^{1}H(n, np), $E = 4.8$ MeV; measured $\sigma(\theta_n, \theta_p)$ bremsstrahlung.

1. Introduction

In the past 15 years, nucleon-nucleon bremsstrahlung (NNB) has received attention as a possible means of investigating the 2-nucleon interaction off the energy shell. However, NNB cross sections are small ($\simeq 10^{-5}$ NNB events per NN elastic scatter in typical geometries), which makes measurements difficult. Most of the effort has been devoted to proton-proton bremsstrahlung (ppB) as both calculation and experiment are easier than for neutron-proton bremsstrahlung (npB). The range of 3.5 to 730 MeV has been covered by ppB experiments, and the recent trend has been to measure cross sections at a number of outgoing nucleon angles simultaneously [1]).

One of the main aims of NNB experiments has been to test 2-nucleon potentials which appear to satisfy the on-shell data. However, with increasing sophistication of experiment and calculation, as uncertainties of measurement have been reduced, so also have the predicted off-shell effects. The result is that even the latest comprehensive ppB experiments [1]) are unable to show convincingly whether or not

particular potentials are satisfactory off-shell [2]). In contrast to ppB there have been few reported npB measurements, and below 100 MeV the best result is an upper limit of 400 $\mu b \cdot sr^{-2}$ (Harvard geometry) at 14.4 MeV [ref. [3])]. Cross sections for npB are higher than for ppB [e.g. by a factor of 10 at 60 MeV, ref. [4])], but this advantage is outweighed by the experimental difficulties.

Nevertheless, npB data are necessary for a complete picture of the off-shell 2-nucleon interaction; moreover, it has been predicted that npB cross sections are more sensitive to off-shell effects than ppB [ref. [4])]. The present work was therefore initiated with the aim of measuring the low-energy npB cross section to higher accuracy than previously achieved and to enable, if possible, a critical comparison with theoretical predictions. Although the latter objective was not realized a significant improvement in precision was achieved through the application of a new technique in which a thick target was used and the bremsstrahlung photon was detected in coincidence with both outgoing nucleons.

2. Experimental

Many of the NNB measurements have used an arrangement known as Harvard geometry, in which the two outgoing nucleons are observed in directions coplanar with the incident beam, and the photon is not detected. Elastic NN scatters are excluded by specifying outgoing nucleon angles θ_1 and θ_2 such that $\theta_1+\theta_2$ is less than 90°, and the NNB events are selected by their position in the E_1-E_2 plane (see fig. 1). Harvard geometry has been popular because each event is kinematically overdetermined and high selectivity is then possible. An event is described by nine variables (3 energies, 6 angles) of which five are independent when energy and momentum are conserved; assuming point detectors, six variables are determined

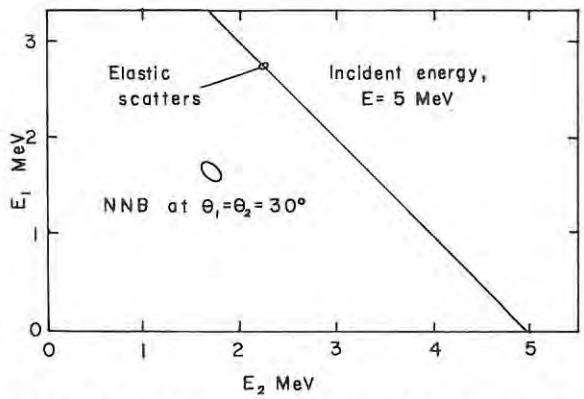

Fig. 1. Kinematic restrictions for NNB events. The periphery of the small region is the allowed locus for coplanar NNB events at $\theta_1 = \theta_2 = 30°$, $E = 5$ MeV, as the photon emission angle rotates through 360°. E_1 and E_2 are the outgoing nucleon energies. Non-coplanar events would populate the inside of the region.

in a Harvard measurement. For ppB, the proton directions, and thus the event itself, can be defined within narrow limits by the use of suitable detectors, for example multiwire proportional chambers or proton counter telescopes. With sufficient precision, at the expense of event rates, background can be reduced to a negligible level.

In comparison with ppB, npB measurements are more difficult because of the relatively poor quality and intensity of available neutron sources, and the problem of identifying npB neutrons in a high background of other neutrons. Furthermore, in low-energy ($\lesssim$ 20 MeV) experiments the target thickness must be less than about 10 mg · cm^{-2} if the outgoing proton is to emerge for detection and energy measurement. This can lead to prohibitively low event rates. In the present work the problem of the short proton range was overcome by using a stilbene scintillation crystal (volume 15 cm^3) as proton target and by detecting the npB proton internally in the crystal (see 1 or 2 in fig. 2). The outgoing neutron was detected in a liquid scintillator (NE 213, volume 250 cm^3, indicated by 3 in fig. 2) which employed pulse shape discrimination (PSD) to reject gamma rays. The energy of the npB proton was determined from the response of the target stilbene crystal (1 or 2 in fig. 2) but its direction remained unknown. To regain sufficient selectivity for npB events a triple coincidence was imposed, requiring detection of the npB photon in a second stilbene crystal (2 or 1 in fig. 2). The two crystals were complementary in that either one functioned as target and proton spectrometer while the other detected the photon, with PSD used to identify events showing a proton in one crystal and a photon in the other. All detectors were as large and as close together as practical in order to

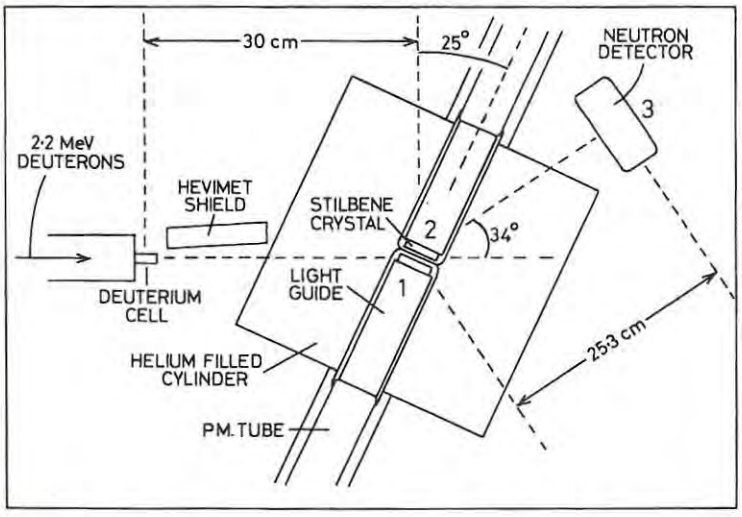

Fig. 2. Experimental geometry. The deuteron energy after traversing the entrance window to the deuterium cell was 1.6 MeV, giving neutrons of energy 4.8 MeV at angle 0°.

maximise the observed npB event rate. A wax (CH_2) disc was set between the stilbene crystals to prevent protons from escaping from one crystal into the other.

The choice of 4.8 MeV as the incident energy resulted from two requirements, effective particle separation by PSD, and the avoidance of certain types of multiple scattering event. The PSD resolution is poorer at lower energies whilst at higher energies, events such as an np elastic scatter, $^1H(n, n)^1H$ where the scattered neutron then rescatters inelastically from carbon, $^{12}C(n, n' \gamma)$, are possible. The particles produced by this combination are n, p and γ which in certain kinematic regions can mimic npB (fig. 3). Indeed, we have estimated that with the particular geometry used, if the incident energy were high enough (e.g. 14.6 MeV), then this mimic event would be some 50 times more probable than npB. Similar double scatters where ^{12}C is replaced by any nucleus with an excited state below $\simeq$ 3 MeV would have occurred even at 4.8 MeV incident energy if such nuclei had been present in appreciable concentration close to the stilbene crystals. To avoid this problem the stilbene detectors were designed so as to exclude elements other than C, H and O in the light collection system and air (^{14}N) was excluded by surrounding the targets with helium gas. Mimic events of the above type, originating from elements outside the helium chamber, were eliminated by means of the extra time delay between the signals from the two stilbene detectors.

The PSD system for the stilbene detectors was designed to be effective at low energies and was based on space-charge saturation in the region around the final dynode of the photomultiplier tube in a manner similar to that reported by Owen [5]). Effective separation down to $\simeq$ 1 MeV for protons and $\simeq$ 0.3 MeV for (Compton) electrons was achieved (fig. 4).

The only experimental restriction on the directions of the outgoing npB nucleons was that imposed by the geometry of the neutron detector. This implied that the energies E_n and E_p were restricted by kinematics to the area bounded by the lines $\theta_n = 25°$ and 45° in fig. 5. Now it was desired that the experimental results should

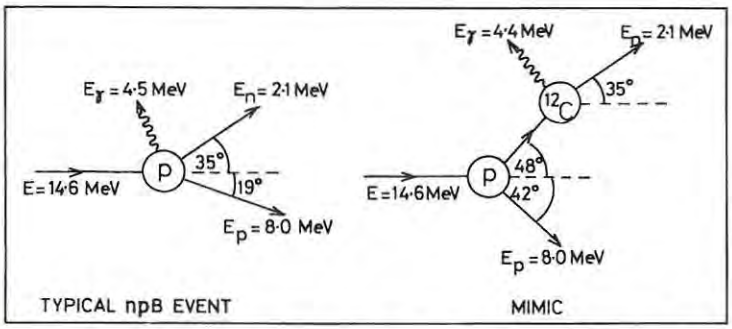

Fig. 3. Mimic event of the type $^1H(n, n)^1H \rightarrow {}^{12}C(n, n'\gamma)^{12}C$. The only observable difference between this and npB is the proton angle θ_p. The missing 0.1 MeV in the mimic event is the energy of the carbon recoil.

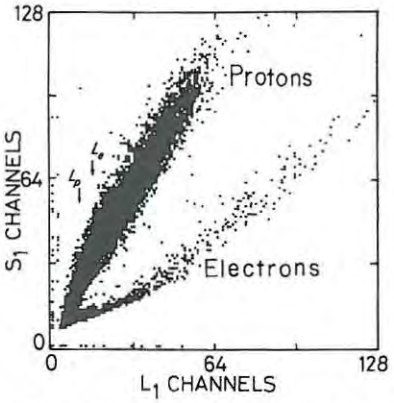

Fig. 4. Sample of raw data events from detector 1, plotted versus pulse height L_1 and pulse shape S_1. The lower limits on L_1, indicated by L_p and L_e, were imposed when separating protons from electrons in the data reduction and correspond to energy thresholds of 1 MeV and 0.34 MeV, respectively.

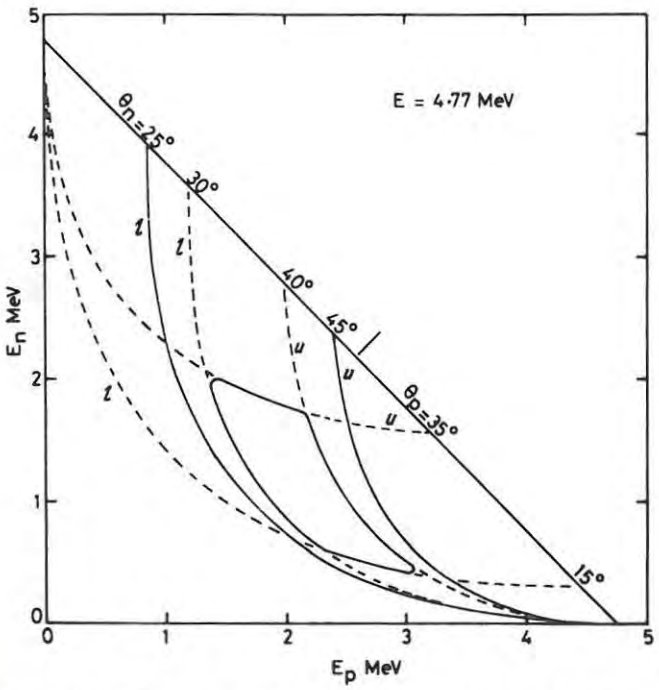

Fig. 5. Kinematic bounds (u = upper bound, ℓ = lower bound) in the $E_p - E_n$ plane. The lines $\theta_n = 25°$ and 45° show the bounds defined by the angular acceptance of the neutron detector. The kinematic region selected for analysis is bounded by $\theta_p = 15°$–$35°$, $\theta_n = 30°$–$40°$.

be expressed in terms of Harvard geometry, and this requires both outgoing nucleon angles to be defined. This was effectively achieved in the analysis by selecting events in the inner area of fig. 5 corresponding to $\theta_p = 15°$ to 35°, $\theta_n = 30°$ to 40°. The nucleon energies for this selection were obtained from the pulse height and time of flight, respectively. The average observed angle θ_p was thus 25° and this led to the orientation of the stilbene crystals as shown in fig. 2; the photon angular distribution from npB is close to dipole about the outgoing proton [6]) hence the stilbene crystal axes were set normal to the proton direction in order to maximise the photon detection probability.

The neutron source for the experiment was a deuterium gas cell in which the ^{2}H(d, n)^{3}He reaction was produced by 1.6 MeV deuterons from the SUNI 5.5 MV Van de Graaff accelerator. The resulting flux of neutrons ($\simeq 4 \times 10^7$ sr$^{-1} \cdot$ s^{-1}) caused high count rates of typically 50 kHz at the stilbene detectors. To prevent the recording of incorrect pulse-height and pulse-shape information at these rates, pile-up rejection was used on these detectors and particular attention was given to the electronics processing the detector signals in order to minimise dead time.

3. Data reduction

In all, 2.75×10^6 events from 125 h running were recorded on magnetic tape, an event being a coincidence in which all three detectors fired, with the further condition that the particle discriminator on the neutron detector (detector 3) had signalled a neutron. Information per event consisted of pulse-heights (L) from all three detectors, pulse-shape parameters (S) from the stilbene crystals (detectors 1 and 2) and times between the signals from detectors 1 and 2 (T_1) and 1 and 3 (T_2). The particle discrimination information for detectors 1 and 2 had not yet been applied and the large majority of recorded events contained protons in both detectors corresponding to an np elastic scatter in each crystal, with a random particle in detector 3. The first cut was thus to select events with a proton in detector 1 and a photon in detector 2 (p-γ events) and vice versa (γ-p events). This was done by defining boundaries on the $L-S$ plane for each detector corresponding to the proton and electron ridges (fig. 4). This initial cut removed 99.5 % of the raw data collected and set effective bias levels of 1.0 MeV for protons and 0.34 MeV for electrons in the stilbene detectors.

A sample of the p-γ data after this cut is shown in fig. 6 as a scatter plot with respect to T_1 and T_2. If npB events are present, they lie in the region labelled 1, which corresponds to a coincidence between detectors 1 and 2 within $T_1 = \pm 2.0$ ns, and the neutron time of flight T_2 covers the range of neutron energies specified in fig. 5. Evidently region 1 also contains a high proportion of accidental triple coincidences in which one or other, or both, particles recorded in detectors 2 and 3 are not correlated with the proton recorded in detector 1. These random coincidences lead to the prominent ridge structure seen in fig. 6. The vertical ridge is

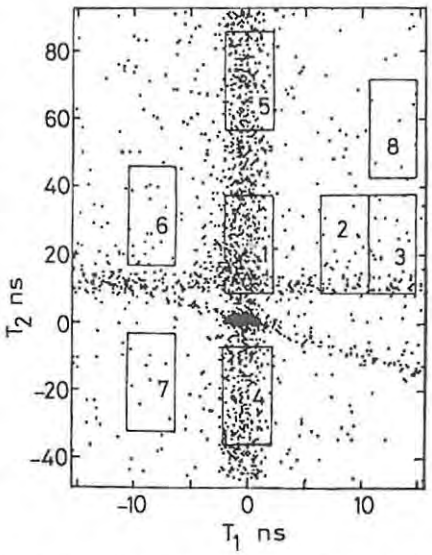

Fig. 6. A sample ($\sim$ 10 %) of the p-γ events, after applying the PSD cuts, plotted versus p-γ delay time T_1 and p-n neutron flight time T_2. If npB events are present they will lie in region 1. Regions 2–8 were used to estimate the contributions of different types of background event (see text).

associated with triple coincidences made by randoms in the neutron detector (3) in accidental coincidence with true p-γ coincidences between detectors 1 and 2. The horizontal ridge is associated with randoms in the photon detector (detector 2) in accidental coincidence with true n-p elastic scatter coincidences between detectors 1 and 3. The sloping ridge is attributed to true γ-γ coincidences between detectors 2 and 3 in random coincidence with protons in detector 1. This type of coincidence arises from the small fraction of gammas which bypass the pulse shape discriminator of detector 3. It is clear that most of the accidental coincidences in region 1 of fig. 6 arise from the randoms in the neutron detector which are responsible for the vertical ridge.

Regions 2–8 in fig. 6 were defined for the purpose of estimating the contributions of different types of accidental coincidences. Triple random coincidences, corresponding to uncorrelated particles in all three detectors, were monitored in regions 7 and 8. These were assumed to be present equally in all regions. Regions 2 and 3 contained events having a random in the photon detector (detector 2) and regions 4 and 5 contained events with a random in the neutron detector (detector 3). Region 6 was defined to identify events with a random proton (detector 1) in accidental coincidence with a true γ-n coincidence between detectors 2 and 3. However, it was consistently found that all the events of region 6 could be attributed to other origins already represented in the other regions, hence this region was disregarded in the further data reduction.

The remainder of the analysis was therefore confined to events in regions 1–5

and 7–8 and made use of all the remaining information recorded for each event to eliminate non npB data as far as possible. The pulse-height information L_1, L_2 and L_3, from the three detectors provided respectively: the proton energy E_p; a lower limit for the photon energy E_γ (derived from the detected Compton electron energy); and a lower limit for the neutron energy E_n (derived from the recoil proton energy in the neutron detector). For events in regions 1–3 E_n was independently determined from the measured neutron time of flight T_2 and events showing neutron energies inconsistent with the lower limit were discarded. The energy information was also used to check energy conservation within each event and to discard events which failed to meet this criterion. Events in regions 4–8 were processed in the same way as in regions 1–3 except for the calculation of the neutron energy E_n. The time of flight T_2 was random for these events since the events were all random neutron events. To facilitate analysis and enable valid background subtraction therefore, the T_2 values in each of these regions were first increased (or decreased) by the constant required to bring the T_2 limits of the region into line with those of region 1. In principle this approach is the same as the delayed coincidence method used by Edgington *et al.* [7]).

At this stage a more stringent coincidence window corresponding to -1.1 ns $< T_1 <$ 1.1 ns was introduced for regions 1, 4 and 5 only. The purpose of this measure was to discriminate against mimic events involving an np elastic scatter ^{1}H(n, n)^{1}H followed by an inelastic scatter X(n, n′γ)X (as discussed in sect. 2) where X is on or outside the wall of the helium chamber. The original time window of -2 ns $< T_1 <$ 2 ns was retained for the other regions (in which the event rate was independent of T_1) in order to obtain statistically more accurate estimates of the corresponding random coincidence rates.

The surviving events for the γ-p data from region 1 are projected on the $E_p - E_n$ plane in fig. 7a. The geometry of the neutron detector should confine npB events to the demarcated area in this diagram. However, the density of events in this area is not obviously enhanced over that for neighbouring areas.

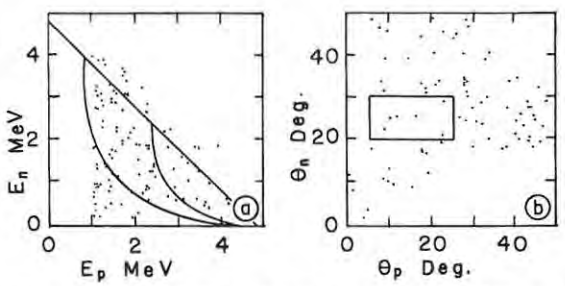

Fig. 7. Surviving γ-p events from region 1 plotted: (a) versus E_p and E_n; (b) versus θ_p and θ_n as derived from (a). In (a), any npB events should lie within the area indicated, which is bounded by $E_p + E_n = 4.8$ MeV and $25° < \theta_n < 45°$. The rectangle in (b) indicates the ranges of θ_p and θ_n within which the final count was made for the calculation of the npB cross section.

In preparation for the final cut of the analysis the data were first transformed to the $\theta_p - \theta_n$ plane, as shown in fig. 7b. This transformation was facilitated by the kinematics of npB at low incident energy ($E \ll mc^2$ where m is the nucleon mass), which show that the photon momentum is much smaller than the nucleon momenta and that, in the limit the angles θ_p and θ_n can be calculated as unique functions of E_p and E_n.

Events lying in the angular ranges $\theta_n = 30°$ to $40°$ and $\theta_p = 15°$ to $35°$ were now selected as shown by the box in fig. 7b for region 1 of the γ-p data. This reduced the field of npB candidates (before making background corrections) to 6 from the γ-p data (fig. 7b) and 3 from the p-γ data (not shown). Backgrounds were estimated from similar projections of the events of regions 2–5, 7, 8 on the $\theta_p - \theta_n$ plane. The corrected npB count N_{br} was then given by

$$N_{br} = N_1 - \tfrac{1}{2}(N_2 + N_3) - \tfrac{1}{2}(N_4 + N_5) + \tfrac{1}{2}(N_7 + N_8) = \sum_i f_i N_i, \qquad (1)$$

where f_i is the number of events in region i and the second, third and fourth terms represent averages of the random photon, random neutron and triple random coincidence backgrounds respectively, each of which is estimated in two different regions (fig. 6). The fourth term is added because triple random events are already included in both the second and third terms and are therefore doubly subtracted. Finally, compensation had to be made for the restricted T_1 window applied to regions 1, 4 and 5. This was done by proportionally reducing the weighting factors f_i of eq. (1) for the second and fourth terms corresponding to regions 2, 3, 7 and 8.

Using eq. (1) with this provision, the nett numbers of npB events after background subtraction were 0.3 p-γ events and 1.2 γ-p events. However these numbers were not used directly in evaluating the npB cross section, as the detection probability varied with respect to θ_p and θ_n. It was thus necessary to weight each event individually to make the result a true average over the observed angular range. This procedure is dealt with in the next section.

4. Calculation of cross section

An ideal Harvard geometry experiment has coplanar point detectors for the two outgoing nucleons, and no photon detector, and the number of observed npB events N_{br} may be expressed:

$$N_{br} = k e_n e_p \delta\Omega_n \delta\Omega_p \mathrm{d}^2\sigma/\mathrm{d}\Omega_n \mathrm{d}\Omega_p, \qquad (2)$$

with $k = Ftn_p$, where F is the incident neutron flux, t the target thickness, n_p the proton density in the target; $e_n(e_p)$ the neutron (proton) detection efficiency; $\delta\Omega_n(\delta\Omega_p)$ the solid angle subtended by (point) neutron (proton) detector and $\mathrm{d}^2\sigma/\mathrm{d}\Omega_n \mathrm{d}\Omega_p$ the Harvard cross section.

In this experiment, there was no restriction on coplanarity, and the photon detector imposed limits on the observed photon direction. In order to arrive at a

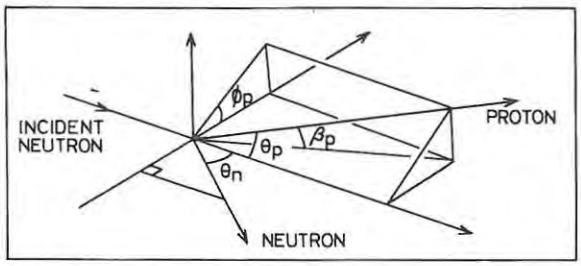

Fig. 8. Definition of noncoplanarity angle, β_p. The experimental plane is taken to include the incident and scattered neutrons.

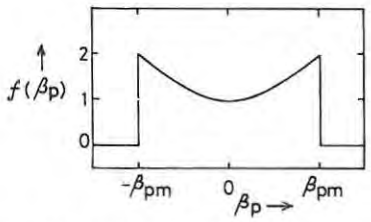

Fig. 9. Distribution of npB events with respect to the non-coplanarity angle β_p given by [8]) $f(\beta_p) = f(0)\{1+(\beta_p/\beta_{pm})^2\}$.

Harvard cross section, these different geometries had to be reconciled, and the necessary tools were derived from the known npB photon angular distribution which, at the low energy of this experiment, has a dipole pattern about the recoil proton direction [6]).

It can be shown [8]) that the dipole photon distribution leads to a parabolic distribution of events with respect to the non-coplanarity angle β_p (fig. 8) such that the cross section at the kinematic limit is double that for coplanar events (fig. 9). Averaging over this distribution, this means that if the proton detector is extended out of the plane so as to observe a finite range of angles β_p such that this range exceeds the kinematic limit β_{pm}, then the cross section is higher by a factor of $\frac{4}{3}$ than the corresponding coplanar cross section. The observed solid angle $\delta\Omega_p$ then becomes $\delta\Omega_p = 2\delta\theta_p\beta_{pm}$. This $\frac{4}{3}$ factor continues to apply if the neutron detector is similarly also enlarged to cover a range of angles $2\beta_n$ where $\delta\Omega_n = 2\delta\theta_n\beta_n$ (equivalent to rotation of the experiment about the incident neutron direction). Finally, taking the proton detection efficiency e_p as unity, and including the photon detection efficiency e_γ, eq. (2) is rewritten:

$$\frac{d^2\sigma}{d\Omega_n d\Omega_p} = \frac{N_{br}}{\frac{16}{3}ke_n e_\gamma \delta\theta_n \delta\theta_p \beta_n \beta_{pm} C}, \tag{3}$$

where the factor C is inserted to correct for npB events lost outside the time window on T_1 (see sect. 3).

Eq. (3) is not yet completely suitable for the experiment as it contains terms which are functions of θ_n and θ_p, and is thus only valid for small $\delta\theta_n$ and $\delta\theta_p$. These angle-dependent factors are e_n which is a function of E_n and thus of θ_n and θ_p, β_{pm} which is related to θ_n and θ_p by kinematics, and β_n which varies with θ_n as a result of the cylindrical shape of the neutron detector. In order to express the npB cross section as a true average over the full ranges $\Delta\theta_n$ and $\Delta\theta_p$ of nucleon angles selected for analysis, it was necessary to calculate the above factors for each remaining event in the foreground and background regions according to the position of the event on the $\theta_n-\theta_p$ plane. Replacing N_{br} of eq. (3) by a sum over all events, and including the background subtraction of eq. (1), the npB cross section was then calculated from

$$\frac{d^2\sigma}{d\Omega_n d\Omega_p} = \frac{3}{16ke_\gamma C\Delta\theta_n\Delta\theta_p}\sum_{i=1}^{R}\sum_{j=1}^{N_i}\frac{f_i}{e_{n_{ij}}\beta_{n_{ij}}\beta_{pm_{ij}}}, \tag{4}$$

where R is the number of regions and N_i and f_i are the number of events and the weighting factor [eq. (1)] respectively, for region i.

Expressing the cross section in the compact form

$$d^2\sigma/d\Omega_n d\Omega_p = y\sum_i\sum_j w_{ij}, \tag{5}$$

in which y and w_{ij} are defined as implied in eq. (4), the standard deviation of the result was calculated from

$$\varepsilon(d^2\sigma/d\Omega_n d\Omega_p) = y[\sum_i\sum_j (w_{ij})^2]^{\frac{1}{2}}. \tag{6}$$

We now describe how some of the quantities in eq. (4) were determined. Firstly, the parameter $k = Ftn_p$ was obtained by counting np elastic scatters which were coincidences between the proton and neutron detectors with the photon coincidence requirement removed. This method was adopted as all the factors in k contribute to the npB rate and to the elastic scattering rate, and the cross section for the latter is well known, whereas F and t would be difficult to determine by a more direct method. Furthermore, absolute values of the neutron-detection efficiency e_n are now unnecessary; relative values of e_n as a function of recoil neutron energy E_n were obtained from

$$e_n(E_n) = (1-E_B/E_n)\{1-\exp(-\sigma_{el}(E_n)n_H x)\} \tag{7}$$

where E_B is the proton bias level in detector 3, $\sigma_{el}(E_n)$ the total np elastic cross section at energy E_n, x the detector thickness and n_H the proton density in the detector.

The photon detection efficiency e_γ was established by calculation. For a photon of energy E_γ emitted from detector 1 and detected in detector 2, e_γ may be written

$$e_\gamma(E_\gamma) = \frac{n_e}{4\pi V_1}\int_{T_b}^{T_{max}}\frac{d\sigma_\gamma(E_\gamma)}{dT}\,dT\int_{det\,1}dV_1\int_{det\,2}dV_2\left(\frac{g\exp(-\sigma_\gamma n_e l)}{l^2}\right), \tag{8}$$

where n_e is the electron density in stilbene; dV_1, dV_2 volume elements in detectors 1, 2; σ_γ the cross section for Compton scattering; T the Compton electron energy; T_b the electron bias level (0.34 MeV); T_{max} the maximum Compton electron energy from a photon of energy E_γ; l the distance between volume elements dV_1 and dV_2; and g is a correction function folding in the dipole photon distribution. The factor g is given by $g = \frac{3}{2}\sin^2\theta'$, where θ' is the angle between the recoil proton and the photon, and the normalisation is such that the average value of g is unity ($\bar{g} = \int g d\Omega / \int d\Omega = 1$). The two volume integrals act to average over all positions for the npB process in detector 1 and to add the probabilities of photon detection for all volume elements of detector 2.

The efficiency e_γ was evaluated numerically [8]) from eq. (8) using the Klein-Nishina formula [9]) for the Compton cross section and it was found that e_γ was constant within 2 % over the range of E_γ observed. The values of e_γ were 0.0125 (p-γ events) and 0.0147 (γ-p events), where the differences are due to the slightly different volumes of the stilbene crystals. Estimates of errors in these figures due to multiple Compton scattering and electron escapes led to the conclusion that these effects could be disregarded. The calculations of e_γ were checked by measuring count rates from a ^{60}Co source of known activity.

Finally the correction factor C was estimated from a T_1 coincidence spectrum taken using a ^{22}Na source placed between the stilbene crystals. The coincidence peak observed was close to gaussian in shape with a FWHM of 1.8 ns. The factor C was calculated from the integral of this peak between the limits set by the T_1 window.

After adding the p-γ and γ-p data the cross section result given by eqs. (5) and (6) can be stated as

$$d^2\sigma/d\Omega_n d\Omega_p = 60 \pm 150\ \mu b \cdot sr^{-1}$$

or as an upper limit, including one standard deviation, of 210 $\mu b \cdot sr^{-2}$. The large uncertainty arises from the small number of true npB events and the large number of background events which had to be subtracted. Other sources of error such as uncertainties in calculated detection efficiencies are negligible in comparison and have been disregarded.

5. Discussion

Table 1 lists the present results together with the results, at or near to θ_n, $\theta_p = 30°$, 30° (Harvard geometry), of all known previous measurements of the npB cross section.

There have been several predictions of the npB cross section at the higher energies corresponding to the Davis and Harwell measurements and the results agree reasonably well with experiment. The work at these energies has established the basic techniques for npB calculations but there are still difficulties with the assess-

TABLE 1

Results of npB experiments at or near θ_n, θ_p = 30°, 30° (Harvard geometry)

Energy (MeV)	Source	θ_n, θ_p	$d^2\sigma/d\Omega_n d\Omega_p$ ($\mu b \cdot sr^{-2}$)	Ref.	Year
208	U.C. Davis	30°, 30°	35 ± 14	[10]	1968
130	Harwell	32°, 29°	77 ± 32	[7]	1974
14.4	Zagreb	30°, 30°	< 400	[3]	1970
14	UCLA	30°, all	< 170 [a]	[11]	1967
4.8	this work	35°, 25	60 ± 150 or < 210		1980

[a]) Single differential cross section $d\sigma/d\Omega_n$ in $\mu b \cdot sr^{-1}$. This result implies an upper limit to $d^2\sigma/d\Omega_n d\Omega_p$ of the order of 3 mb · sr^{-2}.

ment of the contributions to the npB amplitude from meson-exchange scattering. However, differences between the later calculations [12]) based on potential models, are small compared with the uncertainties of the experimental results.

Calculations of npB cross sections at low energy (< 20 MeV) are simpler in several ways, for instance internal scattering contributions should be negligible and only s-wave scattering need normally be considered in the NN interaction. However, there have been few reported predictions, probably because of the scarcity of data for comparison. Of the predictions shown in fig. 10, that of Baier *et al.* [13]) at 10.5 MeV can be disregarded because their one-boson-exchange model does not correctly reproduce the s-wave phase shifts [14]). McGuire [14]) reported two sets of calculations; his "O" curve was obtained by extrapolating known values of on-shell phase-shifts into the equivalent off-shell quantities, the quasi-phases [see e.g. Sobel [15]) for definition], using a prescription based on one-pion exchange. For curve "O_{el}" the quasi-phases were replaced by the on-shell phase-shifts. McGuire's object was mainly to find those kinematic regions where off-shell effects are most

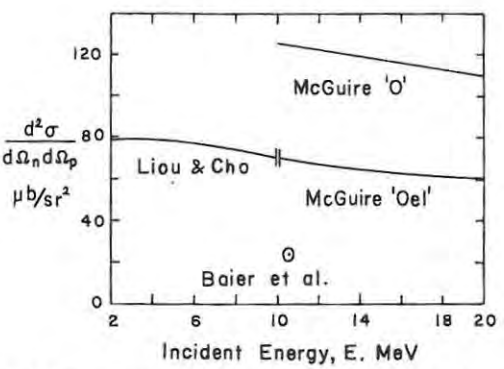

Fig. 10. Calculated values of the npB cross section (Harvard geometry, θ_n, θ_p = 30°, 30°) at low incident neutron energy. The results of McGuire [14]), Liou and Cho [16]) and Baier *et al.* [13]) are shown (see text).

marked, rather than to predict reliable values of cross sections by means of the "O" results.

The calculation of Liou and Cho [16]) is the only one known at the energy of this experiment. They used the Hamada-Johnston potential and evaluated the npB amplitude in the laboratory frame; it was then necessary to include a rescattering term to satisfy gauge invariance. If the amplitude is evaluated in the c.m. frame as is usual, then the rescattering contribution is negligible at these energies [6]) so their procedure seems cumbersome.

For comparison with Liou and Cho's result, we have made calculations using an on-shell approximation similar to that of Signell [6]). The method consists of a simple replacement of the off-shell NN transition amplitudes which occur in the npB amplitudes by their on-shell counterparts; these were then obtained from effective-range parameters. Internal scattering and magnetic-moment contributions were disregarded.

Table 2 summarises the results of the different predictions where extrapolation to the energy and angles of this experiment has been made where applicable. There is good agreement between McGuire's "O_{el}" result, Liou and Cho's result and the present calculation, with McGuire's "O" result standing alone. McGuire used a similar technique for calculating ppB cross sections [17]) and higher energy npB cross sections [4]) and has achieved general agreement with experiment except at very forward angles for ppB [18]). However, the differences between "O" and "O_{el}" are of the same magnitude or smaller than the experimental uncertainties. The difference between "O" and "O_{el}" is much larger in the energy region under consideration than in most others; it is thus suggested that the "O" calculation may exaggerate the off-shell effects, a conclusion also drawn by Edgington *et al.* [7]) for similar predictions at 130 MeV. Furthermore, if the npB cross section is indeed much higher than obtained in the present calculation, then the only possible explanation would seem to be that the off-shell NN amplitudes are very different from the on-shell values, in other words, that the approximation itself is bad. This is unlikely

TABLE 2

Predictions of npB cross sections (Harvard geometry)

Source	$d^2\sigma/d\Omega_n d\Omega_p$ ($\mu b \cdot sr^{-2}$)		Ref.
	E = 10 MeV θ_n, θ_p = 30°, 30°	E = 4.8 MeV θ_n, θ_p = 35°, 25°	
McGuire "O"	125	140 [a])	[14])
McGuire "O_{el}"	70	83 [a])	[14])
Liou & Cho	70	84 [b])	[16])
this work	76	89	

[a]) Extrapolated from 10 MeV, θ_n, θ_p = 30°, 30° result.
[b]) Extrapolated from 4.8 MeV, θ_n, θ_p = 30°, 30° result.

as on-shell calculations of ppB cross sections using a similar method have achieved close agreement with more precise calculations and experiment at 20 MeV [ref. [19])] and lower energies [20]).

The balance of the evidence therefore favours an npB cross section of 80–90 $\mu b \cdot sr^{-2}$ for the incident energy of 4.8 MeV and angles $\theta_n = 35°$, $\theta_p = 25°$, and suggests that off-shell effects are indeed small at these energies and angles. The measured upper limit from this experiment exceeds both this value and the higher cross section based on McGuire's "O" calculation.

The question arises as to what npB measurements, if any, might be attempted in the future. The present experimental method appears to be capable of only marginal improvement in accuracy, but it is feasible that this improvement could be sufficient to test McGuire's "O" result. The Low theorem [21]) which states that the first two terms of a series expansion of the NNB amplitude in powers of the photon energy can be exactly calculated from on-shell information, implies that off-shell effects play the greatest part when, at a given incident energy, the photon energy is maximised. In Harvard geometry, this means that one should work at small angles of the outgoing nucleons (θ_n, $\theta_p \lesssim 10°$). Some such experiments have been undertaken for ppB [ref. [22])] but they are difficult. However, low-energy npB measurements at small angles may be possible using the techniques of this work. Moreover, predictions using the on-shell approximation imply that the low-energy npB cross section increases towards small θ_n and θ_p. On the other hand, Fearing [23]) claims that a further parameter, Δm^2 which increases with incident energy, should be maximised to obtain the largest off-shell dependence. If this is so, then the low-energy region even with small θ_n and θ_p may not be a useful one.

To sum up, the present experiment has succeeded in providing a more accurate result than comparable earlier measurements and probably approaches the limit of precision attainable. However, in the tradition of earlier NNB experiments, it has failed to distinguish the relevant predictions and thus falls short of contributing any new knowledge of the off-shell dependence of the 2-nucleon interaction. The possibility exists that the experimental technique which has been developed could be refined to the extent that McGuire's "O" calculations could be tested, and modified so that small-angle measurements could be made. Some theoretical guidance as to the value of such work would be helpful.

We thank the South African Council for Scientific and Industrial Research for supporting this work and for a bursary to one of us (J.W.), the staff of SUNI for their cooperation and Mr. P. A. Back for constructing the equipment used.

References

1) L. G. Greeniaus, J. V. Jovanovich, R. Kercher, T. W. Millar, C. A. Smith and K. F. Suen, Phys. Rev. Lett. **35** (1975) 696;
B. M. K. Nefkens, O. R. Sander and D. I. Sober, Phys. Rev. Lett. **38** (1977) 876

2) J. V. Jovanovich, Proc. Int. Conf. on nucleon-nucleon interactions, ed. D. F. Measday *et al.*, Vancouver 1977 (AIP Conf. Proc. No. 41, AIP, New York, 1978) 451
3) M. Furic, V. Valkovic, D. Miljanic, P. Tomas and B. Antolkovic, Nucl. Phys. **A156** (1970) 105
4) J. H. McGuire and W. A. Pearce, Nucl. Phys. **A162** (1971) 573
5) R. B. Owen, Nucleonics **17**, No. 9 (1959) 92
6) P. Signell, Adv. Nucl. Phys. **2** (1969) 223
7) J. A. Edgington, V. J. Howard, I. M. Blair, B. E. Bonner, F. P. Brady and M. W. McNaughton, Nucl. Phys. **A218** (1974) 151
8) J. Whittaker, Ph.D. Thesis, University of Cape Town, 1979 (unpublished)
9) R. D. Evans, The atomic nucleus (McGraw-Hill, New York, 1955)
10) F. P. Brady, J. C. Young and C. Badrinathan, Phys. Rev. Lett. **20** (1968) 750;
F. P. Brady and J. C. Young, Phys. Rev. **C2** (1970) 1579; **C7** (1973) 1707
11) J. W. Verba, I. Slaus, J. R. Richardson, L. S. August, W. T. H. Van Oers and R. F. Carlson, Proc. Int. Nuclear Physics Conference, Gatlinburg 1966 (Academic Press, New York, 1967) 619
12) L. S. Celenza, B. F. Gibson, M. K. Liou and M. I. Sobel, Phys. Lett. **41B** (1972) 283;
V. R. Brown and J. Franklin, Phys. Rev. **C8** (1973) 1706;
G. E. Bohannon, Phys. Rev. **C17** (1978) 865
13) R. Baier, H. Kuhnelt and P. Urban, Nucl. Phys. **B11** (1969) 675
14) J. H. McGuire, Phys. Rev. **C1** (1970) 371
15) M. I. Sobel, Phys. Rev. **138** (1965) B1517; **156** (1967) 1553
16) M. K. Liou and K. S. Cho, Nucl. Phys. **A145** (1970) 369
17) J. H. McGuire and W. A. Pearce, Nucl. Phys. **A162** (1971) 561
18) J. H. McGuire, Phys. Lett. **40B** (1972) 41
19) P. Signell and D. Marker, Phys. Lett. **26B** (1968) 559
20) T. K. Dahlblom and A. M. Green, Phys. Lett. **41B** (1971) 23;
B. Frois, M. Irshad, C. R. Lamontagne, V. Von Moellendorf, R. Roy and R. J. Slobodrian, Phys. Lett. **53B** (1974) 341;
M. Suter, W. Wolfi, G. Bonani, Ch. Stoller and R. Miller, Phys. Lett. **58B** (1975) 36
21) F. E. Low, Phys. Rev. **110** (1958) 974
22) A. Willis, V. Comparat, R. Frascaria, N. Marty, M. Morlet and N. Willis, Phys. Rev. Lett. **28** (1972) 1063;
J. Sanado, K. Kondo and S. Seki, Nucl. Phys. **A203** (1973) 388
23) H. W. Fearing, Phys. Rev. Lett. **42** (1979) 21

J. Whittaker, F.D. Brooks and I.J. van Heerden
Neutron-proton bremsstrahlung at 4.8 MeV
Nucl. Phys. A362 (1981) 173-188

F.D. Brooks, P.M. Lister, J.M. Nelson and K.M. Dhuga
Vector analysing powers for the $^{12}C(\vec{d},n)^{13}N$, $^{9}Be(\vec{d},n)^{10}B$ and $^{28}Si(\vec{d},n)^{29}P$ reactions
A.I.P. Conf. Proc. 69 (1981) 656-658

VECTOR ANALYSING POWERS FOR THE $^{12}C(\vec{d},n)^{13}N$, $^{9}Be(\vec{d},n)^{10}B$ AND $^{28}Si(\vec{d},n)^{29}P$ REACTIONS

F.D. Brooks
Dept. of Physics, Univ. of Cape Town, Rondebosch 7700, South Africa

P.M. Lister, J.M. Nelson and K.S. Dhuga
Dept. of Physics, Univ. of Birmingham, Birmingham, B15 2TT, England

ABSTRACT

Vector analysing powers have been measured for the $^{12}C(\vec{d},n)^{13}N$, $^{9}Be(\vec{d},n)^{10}B$ and $^{28}Si(\vec{d},n)^{29}P$ reactions at E_d = 12.3 MeV. The results obtained for transitions to the ground state of ^{13}N and the 1.38 and 1.95 MeV states of ^{29}P agree well with DWBA predictions at forward angles and demonstrate the j-dependence of the analysing power.

INTRODUCTION

As a spectroscopic tool in the study of proton transfer reactions the $(\vec{d},n)$ reaction is a potentially strong competitor to the $(\vec{^3He},d)$ reaction because of the more intense polarized beams which are available for deuterons than for ^3He ions. However, this advantage may be offset by limitations imposed by the efficiency and energy resolution of available neutron spectrometers, especially when neutron energies exceeding 10 MeV are involved. We report here on some $(\vec{d},n)$ studies made using a new type of deuteron recoil spectrometer in conjunction with the 12.3 MeV vector polarized deuteron beam of the Birmingham University Radial Ridge Cyclotron.

EXPERIMENTAL

The neutron spectrometer consisted of a deuterated anthracene scintillation crystal (10 mm diam. × 21 mm length) placed 10-20 cm away from the target under study. Recoil deuterons from D(n,n)D elastic scattering in the crystal were internally detected and were separated from breakup protons (from D(n,2n)H reactions in the crystal) and gamma background by pulse shape discrimination. The spectrum of recoil deuterons produced by monoenergetic neutrons (E_n > 5 MeV) contains a prominent forward recoil peak with a sharp cutoff at its high energy limit, thus giving the deuterated scintillator a lineshape which is particularly suitable[1] for neutron spectrometry. By folding in the correct lineshape the neutron spectum may be extracted from the observed recoil deuteron spectrum. Fig. 1 shows an example of a neutron spectrum obtained from measurements of the $^{9}Be(d,n)^{10}B$ reaction. Vector analysing powers were determined from neutron spectra obtained simultaneously for the "up" and "down" spin states of the incident polarized deuteron beam.

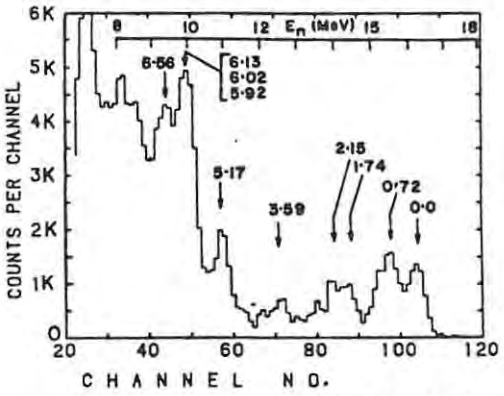

Fig.1. Neutron spectrum obtained from the $^{9}Be(d,n)^{10}B$ reaction at $\theta_{lab}=20^{0}$. Arrows show the expected positions of peaks corresponding to transitions to different levels in ^{10}B.

RESULTS AND DISCUSSION

Fig.2 shows analysing powers obtained for transitions to different final states in the $^{12}C(\vec{d},n)^{13}N$ reaction, together with data from refs.[2-4]. The data for the ground states are in good overall agreement at forward angles but diverge at $\theta_{cm}>45^{o}$. The DWBA predictions shown by the solid line were obtained using the computer code NELMAC[5] which includes corrections for non-locality and finite range. Optical-model parameters were obtained from refs.[6,7]. The agreement between theory and the present data is very good for the ground state transition in this reaction.

The central and lower sections of fig.2 show results for the reactions leading to the unbound 2.37 MeV state and the 3.51-3.56MeV doublet in ^{13}N. For the 2.37 MeV state the DWBA calculation was performed in the weakly-bound-nucleon approximation where the unbound proton is treated as being bound by a small (10 keV) amount. The fit to the data is reasonable at forward angles, both for our data and for those of Tenhaken and Quin[4].

Figs.3(a) and (b) show analysing powers for transitions to different final states in the reactions $^{9}Be(\vec{d},n)^{10}B$ and $^{28}Si(\vec{d},n)^{29}P$ respectively. Optical model para-

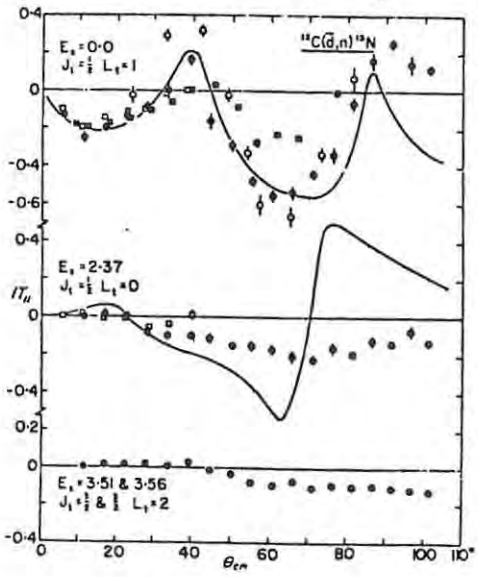

Fig.2. Analysing powers for the $^{12}C(\vec{d},n)^{13}N$ reaction leading to the ground, 2.37 MeV and (3.51 & 3.56) MeV states of ^{13}N.
Data shown are:
● present work (at 12.3 MeV);
○ Krämmer et al[2] (at 10.0 MeV);
■ Hilscher et al[3] (at 8.5 MeV);
□ Tenhaken and Quin[4] (at 9.7 MeV).
Curves show DWBA predictions.

eters for the DWBA calculations were taken from refs.[8,9] and from refs.[6,10]. Since no experimental spin-orbit parameters were available for ^{10}B+n, the spin-orbit parameters of Bechetti and Greenlees[6] were taken in conjunction with parameters from ref.[9]. The DWBA describes the overall features of the data quite well and achieves satisfactory fits to the data for the 1.38 MeV and 1.95 MeV states of ^{29}P (fig.3(b)) at forward angles. The analysing powers for these transitions show a j-dependence at forward angles similar to that found in many neutron transfer reactions. Vector analysing powers have also been determined for other final states in the ^{9}Be($\vec{d}$,n)^{10}B and ^{28}Si($\vec{d}$,n)^{29}P reactions and DWBA analyses of these data and the data shown in fig. 3 are in progress.

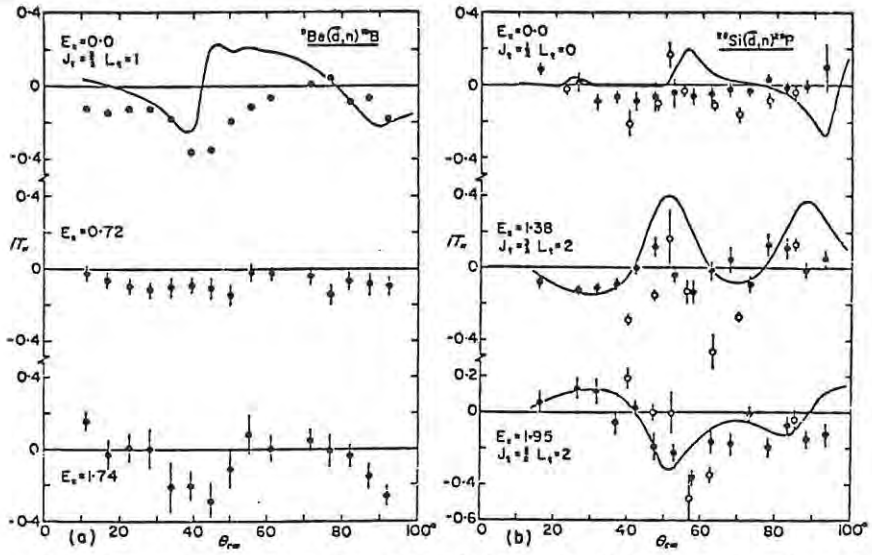

Fig. 3. Analysing powers for transitions to different final states in : (a) the ^{9}Be($\vec{d}$,n)^{10}B reaction; and (b) the ^{28}Si($\vec{d}$,n)^{29}P reaction Data shown are: ● present work; ○ Krämmer et al[2](taken at 10.0 MeV). Curves show DWBA predictions.

REFERENCES

1. F.D. Brooks, Nucl. Instr. and Meth., 162, 477 (1979).
2. P. Krämmer et al, Proc. 4th Int. Symp. on Polarization Phenomena (Birkhauser Verlag, Basel, 1976) p.651.
3. D. Hilscher, J.C. Davis and P.A. Quin, Nucl. Phys., A174, 417(197
4. R.K. Tenhaken and P.A. Quin, Nucl.Phys.,A271, 173 (1976).
5. J.M. Nelson and B.E.F. Macefield, Birmingham Univ. Rept.No.74-9 (unpublished).
6. F.D. Bechetti and G.W. Greenlees, Phys. Rev., 182, 1190 (1969).
7. C.E. Busch et al., Nucl. Phys.,A223, 183 (1974).
8. K.I. Zaika et al., Sov. J. Phys. , 13, 553 (1971).
9. J.A. Cookson and J.G. Lock, Nucl. Phys., A146,417 (1970).
10. A.K. Basak et al., Nucl. Phys., A295, 111 (1978).

F.D. Brooks, W.A. Cilliers and M.S. Allie
Response of thin NE102A scintillator films to fission fragments
Nucl. Instr. and Meth., A240 (1985) 338-342

Nuclear Instruments and Methods in Physics Research A240 (1985) 338–342
North-Holland, Amsterdam

RESPONSE OF THIN NE102A SCINTILLATOR FILMS TO FISSION FRAGMENTS

F.D. BROOKS, W.A. CILLIERS and M.S. ALLIE

Department of Physics, University of Cape Town, Rondebosch, Cape, 7700, South Africa

Received 27 December 1984 and in revised form 26 March 1985

The pulse height response of NE102A plastic scintillator films to fragment ions from ^{252}Cf spontaneous fission has been investigated as a function of fragment time-of-flight and film thickness t in the range 1–15 μm. For velocities close to the two peaks in the fragment velocity spectrum and for films of either $t \geq 9$ μm or $t \leq 3$ μm, an approximately linear relationship between response and fragment velocity is found. For films of thickness 3–6 μm or for fragments from symmetric or highly asymmetric fission, deviations from the linear dependence are observed. The response increases rapidly with film thickness in the range $t = 3$–6 μm and saturates at $t \geq 9$ μm for both light and heavy fragments. The possible role of surface effects in these phenomena is discussed.

1. Introduction

Thin film plastic scintillators (TFPS) display some useful and convenient features for the detection of heavy ions [1–3] and fission fragments [4–10]. They are simple to prepare [7,11] and the TFPS signal has good timing characteristics [5,12–14] and can also provide useful information, for example about the mass distribution in fission [5,8]. TFPS characteristics have been studied and the TFPS scintillation mechanism has been discussed [1–3,14–19] with reference to models of the scintillation process in other organic systems [20,21]. These studies have indicated [1–3,16–19] that the specific luminescence versus specific energy loss relationship traditionally used [20–22] to interpret the scintillation pulse height versus energy dependence is perhaps inappropriate for TFPS systems. They suggest instead that the elementary variables which determine the TFPS pulse height response to heavy ions are the ion velocity and the (velocity-dependent) effective ion charge.

The main aim of the present work was to study the TFPS pulse height response as a function of film thickness and ion velocity for fragment ions from ^{252}Cf spontaneous fissions. The range of thickness studied, 1–15 μm ($\sim$ 0.1–1.5 mg cm^{-2}), corresponded approximately to the range ($\sim$ 20 μm) of ^{252}Cf fragments in NE102A plastic. The upper limit of 15 μm also ensured that the alpha background from ^{252}Cf produced pulses much smaller than those produced by the fragments in the TFPS.

Although previous work on TFPS characteristics is extensive it does not, to our knowledge, include an investigation in which the velocity and thickness variables were studied simultaneously. Information on TFPS response as a function of thickness is contradictory, one set [7] showing saturation of the response to both light and heavy fragments for $t \geq 9$ μm while another [6] shows saturation only for the light fragment. Data are also available from measurements on multiple stacks of thin films [3,5]. However, it cannot be assumed that these laminated films will give results equivalent to those obtained from a single film of the same total thickness, since surface effects [20] can modify the scintillation mechanism at the interfoil boundaries and since nonradiative energy transfer processes, which are known to be important in the scintillation mechanism [20–22] are bound to be affected by these interfaces.

A further objective of the present work was to assess the suitability of the TFPS for use as a fragment detector in a subsequent experimental study of neutron emission in spontaneous fission. The dependence of TFPS pulse height response on fragment velocity was of particular interest for this application.

2. Experiments

Thin films of NE102A plastic scintillator were prepared by a method based on the technique described by Ajitanand and Iyengar [7]. A standard solution of 12 g l^{-1} of NE102A in scintillation-grade xylene was prepared. A measured quantity of this standard solution (or an appropriately diluted solution) was transferred by means of a glass syringe onto the carefully cleaned and levelled photocathode face of a photomultiplier tube (RCA 8575) mounted in a bell jar. The bell jar was slowly evacuated so as to ensure that a clear, unform and bubble-free NE102A TFPS remained attached to the photocathode face after the xylene had evaporated.

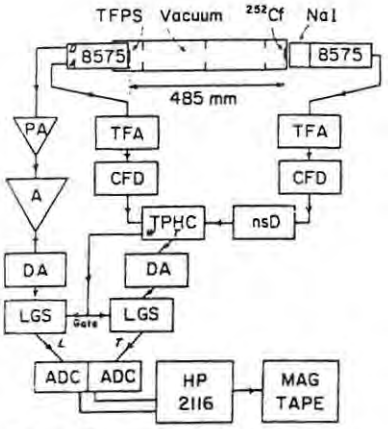

Fig. 1. Schematic and block diagram of the experimental arrangement. The NIM modules (Ortec or Canberra) were: TFA, timing filter amplifer; CFD, constant fraction discriminator; nsD, nanosecond delay; TPHC, time-to-pulse-height converter; DA, delay amplifier, LGS, linear gate and stretcher; A and PA, linear amplifier and preamplifier.

The thickness t of the film was calculated from the known amount of NE102A transferred in the solution, the film area and the density of NE102A (assumed to be 1.032 g cm^{-3}). An independent check made using an optical interferometric technique showed that this method was capable of making films of thickness within 10% of the calculated value and uniform to 5% or better over an area of 3 cm^2.

The photomultiplier with TFPS attached was mounted at the end of an evacuated tube containing an electrodeposited ^{252}Cf source of strength ~ 0.2 μCi (fig. 1). The flight path from the open surface of the source to the TFPS was 485 mm. A sodium iodide scintillation detector (50 mm diameter × 50 mm crystal), mounted immediately behind the source, to detect fission gamma rays, provided a fission time-zero signal. The time-of-flight T of the fragments to the TFPS was measured together with the pulse height response L of that detector, using the electronic arrangement shown in fig. 1. Data were written to magnetic tape, event-by-event, in two-parameter format (L and T) for subsequent off-line analysis. Time-of-flight singles spectra were accumulated and displayed during data acquisition, to monitor the stability of the T coordinate. These checks verified that the positions of the light and heavy fragment peaks in the T spectrum were, as expected, stable and independent of TFPS thickness. The zero of the time-of-flight scale was determined by recording an additional two-parameter spectrum for one of the TFPS, in which the TFPS detector was moved in so as to reduce the fragment flight path from 485 mm to 10 mm. The light and heavy fragments were then separated by means of the L coordinate and their positions (peak centres) in the T spectra obtained at 485 mm and 10 mm respectively were compared so as to determine the $T = 0$ channel by assuming that T is proportional to flight path length for each fragment. The time calibration is estimated to be accurate to < 0.5 ns.

3. Results

Raw data obtained using a 12.0 μm TFPS are shown in the density plot (fig. 2) of number of events as a function of L and T. The predominantly asymmetric mass division in ^{252}Cf fission is responsible for the structure of this plot, the two peaks corresponding to the maxima associated with the light and heavy fragments. A monotonic dependence of L on T (and hence of L on the fragment velocity, which is directly related to T) is clearly apparent in fig. 2. Similar distributions, differing only in their detailed L dependence, were obtained for all other film thicknesses studied.

The two-parameter spectra were analysed by projecting either: (a) cuts at different discrete T values onto the L axis; or (b) cuts at different discrete L values onto the T axis. Fig. 3 shows examples of these two types of projected spectra, obtained from the L–T spectrum (fig. 2) for a 12 μm TFPS. Projected spectra like these, from cuts through the centres of the light and heavy fragment peaks, were used to determine the (L, T) coordinates of these peaks for each film studied. Cuts taken at L values *off* the fragment peaks were also

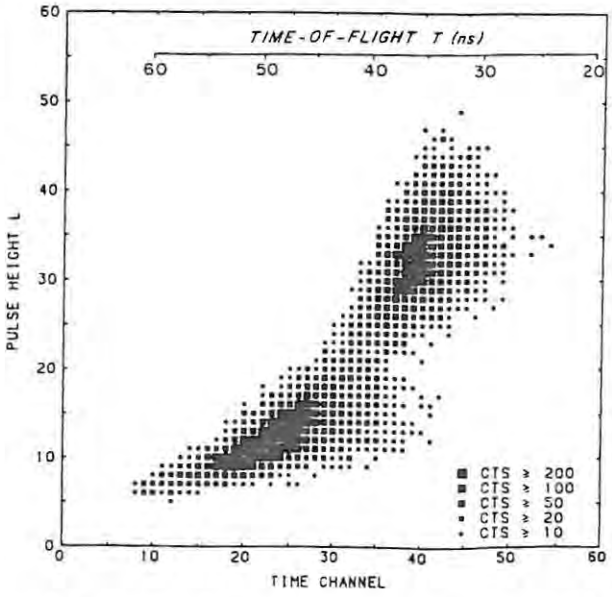

Fig. 2. Density plot of counts as a function of time channel and of pulse height L obtained using a 12.0 μm thick TFPS. The two prominent peaks are associated with the light and heavy fragments respectively from ^{252}Cf fission.

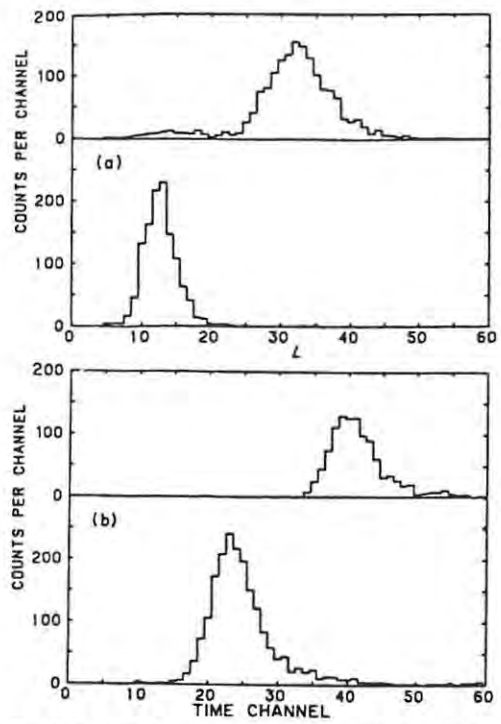

Fig. 3. Projected spectra from ordinate and abscissa cuts across the two-parameter spectrum (12 μm TFPS) shown in fig. 2: (a) projected L spectra from cuts at the time channels 24 (lower panel) and 39 (upper panel); and (b) projected T spectra from cuts at the abscissae $L=12$ (lower panel) and $L=32$ (upper panel). The lower panels in (a) and (b) correspond to cuts through the heavy fragment peak and the upper panels to cuts through the light fragment peak.

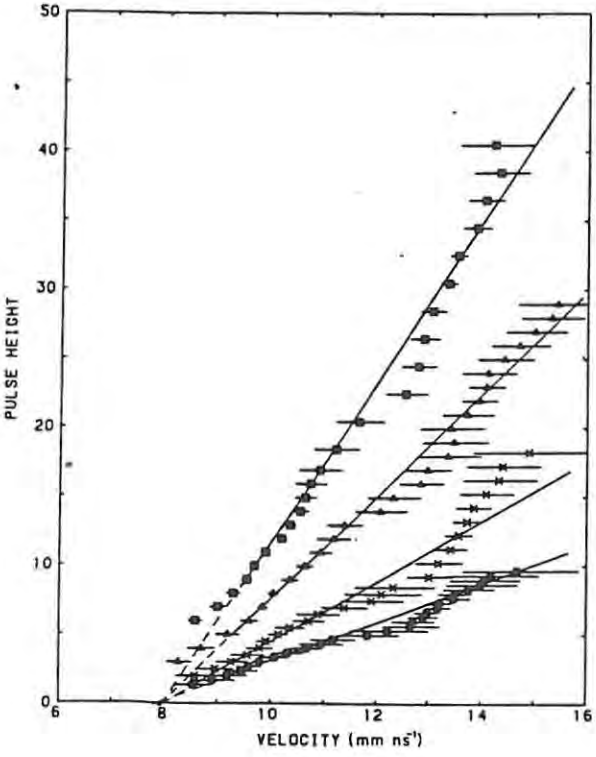

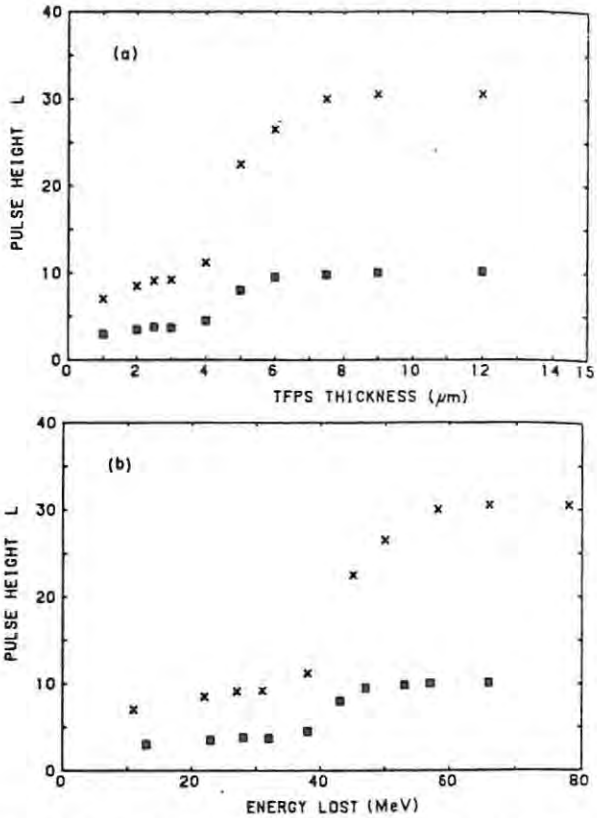

Fig. 5. TFPS pulse height response L to the light fragment (crosses) and heavy fragment (squares) as a function of: (a) TFPS thickness t; and (b) energy lost in the TFPS.

projected and analysed in this way, to determine most probable values of T over the full range of L covered in the measurements. The (L, T) coordinates obtained in this way are less precise than those obtained *on* the fragment peaks however, because the finite resolution of the pulse height and time-of-flight measurements can distort the observed L–T dependence and this distortion is greater for cuts off the fragment peaks than for cuts on the peaks. No attempts were made to correct for the distortion but uncertainties representing the limits of the associated systematic errors on the T-measurements were estimated. Fragment velocities v (and uncertainties) were then calculated from the T data.

Results showing L versus v for four of the ten TFPS thicknesses studied are presented in fig. 4. The straight lines shown in this figure are not fits to the data, but lines drawn through the two most accurately defined

Fig. 4. TFPS pulse height response L as a function of fragment velocity v for four different TFPS thicknesses: 1.0 μm (circles); 4.0 μm (crosses); 5.0 μm (triangles); and 12.0 μm (squares). The error bars represent systematic uncertainties in the v measurements (see text). The straight lines are defined by two points only for each thickness, namely the points derived from the centres of the light and heavy fragment peaks in the L–T spectra (e.g. fig. 2).

points, namely those corresponding to the centres of the light and heavy fragment peaks, as indicated above. The pulse heights L corresponding to these peaks are also plotted as a function of TFPS thickness and of energy lost in the TFPS, in figs. 5a and b respectively. The data in fig. 5b were derived from those in fig. 5a using the recent direct measurements by Batra and Shotter [23] of the energy loss (as a function of t) of ^{252}Cf fission fragments in NE102A TFPS.

4. Discussion

The two most striking features of the present results are perhaps the step-like variation of the response versus TFPS thickness characteristic (fig. 5a) and the linear trends shown in the response versus velocity dependence (fig. 4). Some previous work [9] has indicated a linear variation of L versus v for fission fragments incident on TFPS. The present data (fig. 4) show an approximately linear dependence of L on v for TFPS thicknesses corresponding to the plateau regions of fig. 5a, that is $t = 1$–3 μm and $t \gtrsim 9$ μm. For these thicknesses the lines (fig. 4) defined by the coordinates of the centres of the light and heavy peaks are consistent with the experimental data over a substantial fraction of the velocity range studied. Notable deviations from the lines occur at the velocities corresponding to symmetric fission (~ 12.5 mm ns^{-1}) and highly asymmetric fission ($\lesssim 9$ mm ns^{-1} and $\gtrsim 14.5$ mm ns^{-1}). However, these particular velocities correspond to minima in the velocity distribution for ^{252}Cf fission fragments. Thus a large proportion of the fragments have velocities in the region over which the straight line is a good approximation to the TFPS response, for TFPS of $t = 1$–3 or > 9 μm. It is also noted that the linear approximations for all TFPS thicknesses extrapolate (fig. 4) to a common $L = 0$ intercept at $v = (7.8 \pm 0.2)$ mm ns^{-1}.

The linear approximation is useful for estimating the accuracy with which fragment velocity can be determined from the TFPS response measurement alone. For the 12 μm TFPS for example, the pulse height resolution (fwhm) for the heavy fragment (fig. 3a) converts via the appropriate line in fig. 4 to a velocity uncertainty of ± 0.5 mm ns^{-1}, or a velocity resolution of $\pm 5\%$ (fwhm 9%). For the light fragment the corresponding figures are ± 0.8 mm ns^{-1} or $\pm 6\%$ (fwhm 12%) for the same TFPS. These estimates will apply for fragments close to the heavy and light fragment peaks respectively. For other regions, e.g. the symmetric fission region, the data shown in fig. 4 may be used to correct for systematic deviations from the linear response function. Thus the pulse height response for TFPS of thickness $\gtrsim 12$ μm provides a simple means for determining fragment velocities to ± 5–6% accuracy over the full range of the ^{252}Cf fission fragment spectrum.

The step-like variation of L with TFPS thickness (fig. 5a) is surprising and may have important implications concerning the scintillation mechanism in TFPS. For light ions on plastic scintillators it seems to be established [20–22] that only singlet excitations of the polymer molecules lead to significant light emission; or, in other words, that in plastics the delayed triplet–triplet component, important in other organic scintillators (liquid and crystal) is insignificant in comparison with the prompt component. It is likely, though not yet demonstrated, that this may also hold true for heavy ions in plastic scintillators. Two distinct primary excitation regions have been identified [21] in the excitation of the prompt component by *light* ions in organic scintillators. These are the molecular excitations produced directly by the incident particle in the "core" of dense excitation (diameter ~ 0.03 μm) which it forms around its path and the excitations to a radius of ~ 1 μm outside this core, produced by secondary electrons (δ-rays) ejected from the core. For heavy ions or fission fragments it is suggested [16,17] that the excitation density in the core will be extremely high, that scintillation emission from this region will consequently be strongly suppressed relative to that from the outer secondary electron region, and that the latter is therefore the dominant source of the scintillation emission.

If one assumes that the plastic scintillator is perfectly homogeneous, that its physical and chemical composition are independent of thickness and, for the moment, that the range of diffusion of excitation energy by nonradiative transfer processes is 1 μm or less, then the present data (fig. 5a) for L vs t yield, by simple differentiation, the specific luminescence $\mathrm{d}L/\mathrm{d}x$ as a function of x, the distance along the fission fragment track in the plastic. The results would indicate large variations in $\mathrm{d}L/\mathrm{d}x$ with x, showing maxima at $x \lesssim 1$ μm and $x \approx 4.5$ μm. It is conceivable that fluctuations in the charge of the fragment ion immediately after entering the TFPS could lead to fluctuations in the specific energy loss $-\mathrm{d}E/\mathrm{d}x$ and hence in $\mathrm{d}L/\mathrm{d}x$ for $x < 1$ μm. For $x > 1$ μm however, it is clear that $-\mathrm{d}E/\mathrm{d}x$ varies smoothly [23] with distance x along the fragment track. In particular there is no reason to expect any unusual fluctuation of $-\mathrm{d}E/\mathrm{d}x$ at $x = 4.5$ μm. It seems more likely that the *apparent* increase in $\mathrm{d}L/\mathrm{d}x$ at this depth is an artefact associated with some other phenomenon which appears or disappears at a film thickness of ~ 4.5 μm. Batsch and Moszynski [14,15] for example, have reported fluctuations in the timing characteristics and pulse height resolution characteristics of NE102A TFPS at thicknesses of ~ 3 μm. They suggest that the surface effects involving the loss or quenching of excitation energy could be responsible for these fluctuations. Using the surface effect model proposed by Birks [20] to analyse their data, they estimate a mean free path of ~ 7 μm for nonradiative

transfer of excitation energy in the plastic.

It is therefore suggested that the sudden change in TFPS response at $t = 4.5$ μm (fig. 5a) might be due to surface effects. When the film thickness is decreased a critical thickness, dependent on the range of the nonradiative energy transfer process in the plastic, is eventually reached. Below this thickness the TFPS characteristics are dominated by the properties of the surface regions, which show a poorer scintillation efficiency than the inner region of a thicker TFPS. Surface properties as well as the range of the nonradiative transfer process may also be sensitive to the method used to prepare the TFPS. Further experiments with ions of known charge and mass as well as with fission fragments will be required to explore and test these suggestions. One test which should be informative is an accurate comparison of the response of a stack of several thin TFPS with that of a single TFPS of the same total thickness and composition. In the meanwhile it would seem premature to interpret the TFPS scintillation process in terms of the specific luminescence dL/dx derived from response–thickness (L versus t) measurements.

We thank the South African Council for Scientific and Industrial Research for their financial support and Mr. D. Momsen for his assistance in the construction of the apparatus used. We also thank Dr. D.W. Mingay, of NUCOR, South Africa, for some stimulating discussions on these topics.

References

[1] L. Muga and G. Griffith, Nucl. Instr. and Meth. 109 (1973) 289.
[2] L. Muga, Nucl. Instr. and Meth. 124 (1975) 541.
[3] M.L. Muga, G.L. Griffith, H.W. Schmitt and H.E. Taylor, Nucl. Instr. and Meth. 111 (1973) 581.
[4] L. Muga, A. Clem, G. Griffith, H.S. Plendl, R. Eaker and R. Holub, Nucl. Instr. and Meth. 119 (1974) 255.
[5] L. Muga, A. Clem and G. Griffith, in: Physics and Chemistry of Fission, vol. 2 (IAEA, Vienna, 1974) p. 451.
[6] R.K. Batra and A.C. Shotter, Nucl. Instr. and Meth. 124 (1975) 101.
[7] N.N. Ajitanand and K.N. Iyengar, Nucl. Instr. and Meth. 133 (1976) 71.
[8] N.N. Ajitanand, K.N. Iyengar and S.R.S. Murthy, Phys. Rev. C18 (1978) 1745.
[9] W.J. McDonald, A.I. Kilvington, C.J. Batty and J.L. Weil, Nucl. Instr. and Meth. 115 (1974) 185.
[10] P. Plischke, W. Scobel and R. Wien, Nucl. Instr. and Meth. 203 (1982) 419.
[11] M.L. Muga, D.J. Burnsed and W.E. Steeger, Nucl. Instr. and Meth. 104 (1972) 605.
[12] A. Gelbke, K.D. Hildenbrand and R. Bock, Nucl. Instr. and Meth. 95 (1971) 397.
[13] G. Bendiscioli, V. Filippini, G. Fumagalli, E. Lodi Rizzini, C. Marciano, C. Milani, A. Rotondi and A. Venaglioni, Nucl. Instr. and Meth. 206 (1983) 471.
[14] T. Batsch and M. Moszyński, Nucl. Instr. and Meth. 123 (1975) 341.
[15] T. Batsch and M. Moszyński, Nucl. Instr. and Meth. 125 (1975) 231.
[16] L. Muga and G. Griffith, Phys. Rev. B9 (1974) 3639.
[17] L. Muga and M. Diksic, Nucl. Instr. and Meth. 122 (1974) 553.
[18] M.L. Muga and J.D. Bridges, Nucl. Instr. and Meth. 134 (1976) 143.
[19] L. Muga and G. Griffith, Phys. Rev. B8 (1973) 4069.
[20] J.B. Birks, The Theory and Practice of Scintillation Counting (Pergamon, London, 1964).
[21] R. Voltz, J. Lopes da Silva, G. Laustriat and A. Coche, J. Chem. Phys. 45 (1966) 3306; R. Voltz and G. Laustriat, J. Physique 29 (1968) 159;
R. Voltz, H. Du Pont and G. Laustriat, J. Physique 29 (1968) 297;
J. Lopes da Silva and R. Voltz, Rev. Physique Appl. 7 (1972) 127.
[22] F.D. Brooks, Nucl. Instr. and Meth. 162 (1979) 477.
[23] R.K. Batra and A.C. Shotter, Nucl. Instr. and Meth. B5 (1984) 14.

Nuclear Physics **A465** (1987) 429–444
North-Holland, Amsterdam

ANGULAR DISTRIBUTION OF NEUTRONS FROM $^2H(\gamma, n)^1H$ AT $E_\gamma = 2.75$ MeV

F.D. SMIT and F.D. BROOKS

Department of Physics, University of Cape Town, Rondebosch, Cape, 7700, South Africa

Received 10 September 1986

Abstract: The angular distribution of neutrons from deuteron photodisintegration by 2.75 MeV gamma rays was measured at six laboratory angles between 30° and 135°. The dipole cross section ratio derived from the measurements, $\sigma_m/\sigma_e = 0.290 \pm 0.021$, is consistent with theoretical calculations which include contributions from meson-exchange currents and isobar configurations.

E | NUCLEAR REACTION $^2H(\gamma, n)$, $E = 2.75$ MeV; measured photodisintegration $\sigma(\theta)$; deduced dipole σ(ratio), meson exchange; isobar configuration roles. Enriched target.

1. Introduction

In 1972 Riska and Brown [1]) resolved a long-standing discrepancy of about 10% between theory [2]) and the experimental value [3]) for the radiative capture cross section of protons for thermal neutrons. They showed that the capture cross section was enhanced by 9.7% when contributions from meson-exchange currents (MEC) and isobar configurations (IC) were included in the M1 transition amplitude which dominates thermal n-p capture. Their results stimulated new interest in both the n-p capture reaction and its inverse, deuteron photodisintegration. Work published since 1972 on the $^2H(\gamma, n)^1H$ reaction has been confined to energies well above the photodisintegration threshold (2.225 MeV) and has been motivated largely by interest in further evidence of sub-nucleonic degrees of freedom in this reaction. The MEC and IC contributions may be expected to manifest themselves more clearly in deuteron photodisintegration close to threshold ($E_\gamma < 3$ MeV) however, since the M1 transition contributes significantly to the cross section at these low energies. No new experimental data appear to have been reported on deuteron photodisintegration in this energy range since 1965; and the data published up to that time are in disagreement with one-another.

The differential cross sections for photoproton and photoneutron emission at centre-of-mass angle θ relative to the incident photon direction in the $^2H(\gamma, n)^1H$ reaction may be written [4,5])

$$\sigma(\theta) = a + b \sin^2\theta + c \cos\theta + d \sin^2\theta \cos\theta + e \sin^4\theta, \quad (1)$$

$$\sigma(\theta) = a + b \sin^2\theta - c \cos\theta - d \sin^2\theta \cos\theta + e \sin^4\theta, \quad (2)$$

respectively, where a-e are energy-dependent coefficients. At energies very close to threshold only dipole transitions need be considered and eqs. (1) and (2) reduce to

$$\sigma(\theta) = a + b \sin^2 \theta, \tag{3}$$

in which the first and second terms represent the M1 and E1 components respectively. By integrating over the 4π solid angle it may then be shown that the dipole cross section ratio τ, the ratio of the photomagnetic and photoelectric components of the total cross section, is given by

$$\tau = \sigma_m/\sigma_e = 3a/2b. \tag{4}$$

Thus, in the threshold energy limit, τ may be obtained directly from a simple measurement of the photoproton or photoneutron angular distribution. Absolute measurements of $\sigma(\theta)$ are not required to obtain τ. Furthermore, since the inclusion of MEC and IC in calculations at these energies affects the photoelectric cross section much less than the photomagnetic cross section [6]), the change in τ will be (eq. (4)) proportional to that in σ_m. In addition, since $\sigma_e > \sigma_m$ for photon energies >2.4 MeV, the fractional change in τ due to MEC and IC contributions will be larger at these energies than the associated fractional change in the total cross section $(\sigma_m + \sigma_e)$. These factors therefore combine in such a way that a relative measurement of $\sigma(\theta)$ for the $^2H(\gamma, n)^1H$ reaction at $E_\gamma = 2.75$ MeV provides a more sensitive probe of MEC and IC contributions than, for example, an absolute measurement of the total cross section at the same energy.

The values of τ previously reported [7-14]) at threshold energies were all measured prior to 1952 and were derived from angular distribution or cross section ratio measurements, assuming validity of the dipole approximation of eq. (3). In 1981 however Holt [15]) reported measurements of differential cross section ratios at slightly higher energies, from which he deduced that higher order ($L > 1$) multipole contributions were significant at photon energies as low as 3.5 MeV. The validity of the dipole approximation may be tested by checking the symmetry implied by eq. (3), of the angular distribution about $\theta = 90°$. This symmetry is broken by the third and fourth terms of eqs. (1) and (2), which increase in importance as the contributions of higher order multipoles become significant. The contributions from the $\sin^4 \theta$ terms of eqs. (1) and (2) are less important and may be neglected at threshold energies.

Most of the measurements reported in the threshold region [7-14]) were made at the photon energies conveniently provided by the radioactive sources ^{72}Ga (2.50 MeV), radiothorium (2.62 MeV) and ^{24}Na (2.75 MeV). The uncertainties quoted for these measurements vary considerably and there are irreconcilable discrepancies between the measurements which quote the highest accuracies. Calculations of photodisintegration which include MEC and IC contributions and extend to low energies have been reported by Hadjimichael [16]), by Arenhövel *et al.* [17]) and by Rustgi *et al.* [18]). None of these papers presents explicit values for τ at threshold

energies. However from the data or Arenhövel *et al.* [17]) it can be seen, as we shall describe presently, that the inclusion of MEC and IC contributions may be expected to lead to an increase of 10-20% in τ at the incident photon energy of 2.75 MeV.

The present experiment was initiated with the interest in MEC and IC contributions foremost in mind and also with a view to investigating the contributions [15]) of higher order multipoles ($L \geq 2$) at low incident energies. The experiment consisted of a measurement of the angular distribution from 30° to 135° of photoneutrons from the $^2H(\gamma, n)^1H$ reaction for $E_\gamma = 2.75$ MeV. We have employed a method in which the photoneutron and photoproton are detected in coincidence, thus obtaining a cleaner signature than the previous experiments in which only one nucleon or the other was detected.

2. Experimental

Six independent series of experimental runs were made, each of duration approximately two weeks and spaced at intervals of 1-3 months. The first three series were exploratory runs which were used to optimize the experimental arrangement. The results presented here are those obtained in the final runs referred to below as series A, B and C respectively. These runs were carried out at the Van de Graaff Laboratory of the South African National Accelerator Centre (NAC) at Faure, near Cape Town.

Each series incorporated both photodisintegration measurements and experiments to calibrate, *in situ*, the energy-dependence of the efficiency of the neutron detector used in the photodisintegration measurements. The NAC 5.5 MV Van de Graaff was used via the $^{23}Na(d, p)^{24}Na$ reaction to make ^{24}Na sources of activity about 5 mCi for the photodisintegration measurements and, via the $^7Li(p, n)^7Be$ reaction, to provide monoenergetic neutrons of energy in the range 180-350 keV for the neutron detector calibration.

2.1. PHOTODISINTEGRATION MEASUREMENTS

The ^{24}Na sources (half-life 15 hours) were prepared by bombarding a fused pellet (3 mm diam.) of sodium metaborate embedded in the base of a small graphite crucible (25 mm diam.) with 5 MeV deuterons. Two such pellets were used in alternating 12 hour shifts, one being recharged by the accelerator in a well shielded target cell while the other provided gammas for the photodisintegration experiment. The photodisintegration experiment was mounted away from the target cell, close to the end of one of the Van de Graaff beam lines, in a position convenient for the efficiency calibration runs (sect. 2.2).

The incident gamma spectrum was monitored throughout the photodisintegration measurements by a 100 cm^3 Ge(Li) detector placed at a distance of 4.2 m from the source (see fig. 1a). The flux of 2.75 MeV gammas was recorded by scaling the counts in a single channel analyser window centred on the corresponding total energy peak

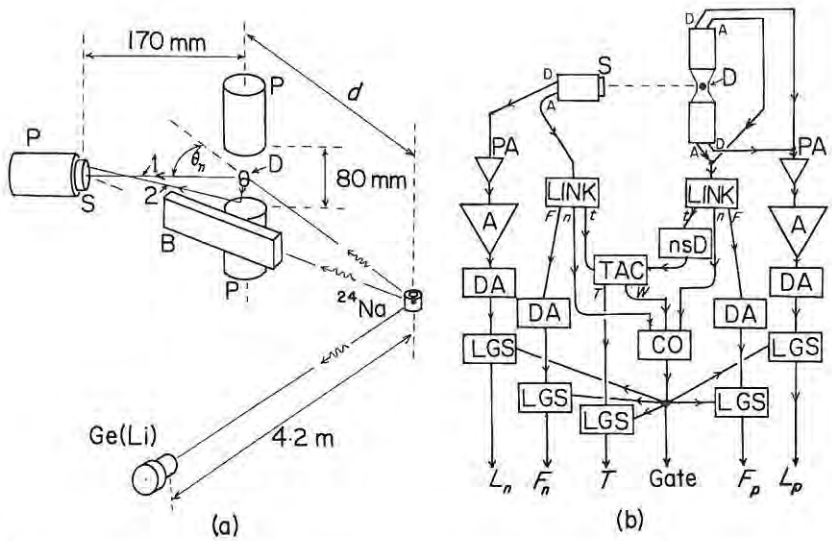

Fig. 1. Arrangements for the photodisintegration experiment, showing: (a) the experimental geometry; and, (b) an abridged block diagram of the electronic system. Labels in (a) show: deuterated anthracene crystal D; stilbene crystal S; hevimet shadow bar B; and neutron paths for a true coincidence (1) and an in-scattered background coincidence (2). Crystal D was supported by a light aluminium reflector (not shown in (a)) linking the upper and lower photomultipliers P. In (b) t, n and F indicate the timing, neutron and fast integral outputs respectively, of the LINK systems model 5010 pulse shape discriminators. Other standard NIM modules (Ortec or Canberra) shown in (b) are: linear amplifiers A and preamplifiers PA; delay amplifiers DA; time-to-pulse-height converter TAC; nanosecond delay nsD; coincidence CO; and linear-gate-and-stretchers LGS. The data-acquisition system consisted of five Canberra Model 8080 ADC's interfaced via a PDP 11/34 minicomputer to magnetic tape.

and was also determined after each run from the integral of this peak in the recorded spectrum. These measurements also verified that the incident gamma spectrum above 2.2 MeV contained no other gamma peaks of significant intensity.

Deuteron photodisintegrations produced by the 2.75 MeV gamma rays in a deuterated anthracene scintillation crystal (10 mm diam. × 20 mm long cylinder, D : H > 99) were studied. The photoprotons were detected in the crystal and the associated photoneutrons were detected in delayed coincidence in a stilbene crystal (40 mm diam. × 10 mm thick) at a distance of 170 mm. The photoproton energy was indicated by the pulse height L_p of the deuterated anthracene output signal and the photoneutron energy by the neutron time-of-flight T between the two crystals. The arrangement of the crystals and the photomultiplier tubes used to view them (RCA 8850 and 8575) is shown in fig. 1a. The phototubes viewing the deuterated anthracene were set back a distance of 40 mm from the crystal in order to facilitate the separation of true photoneutron coincidences (path 1 in fig. 1a) from in-scattered photoneutron coincidences (e.g. path 2) by time-of-flight. The difference in T for a 0.26 MeV neutron over the direct path 1 and any path such as 2, involving scattering on solid material outside the crystal was $\geqslant$4 ns.

A simplified block diagram of the detector electronics is shown in fig. 1b. The pulse height measurements L_p and L_n for protons and neutrons respectively were obtained from linear outputs taken from the ninth dynodes of the photomultipliers. The anode outputs of the photomultipliers were fed to LINK model 5010 pulse shape discriminator units [19]), which provided outputs for fast timing and pulse shape discrmination (PSD). The two photomultipliers viewing the deuterated anthracene were connected in parallel and their operating voltages were adjusted to match their individual pulse height responses to the 60 keV gamma rays from ^{241}Am.

The first level of selection for candidate photodisintegration events required neutron logic signals (n in fig. 1b) from the two LINK 5010 units together with a coincident logic signal (W in fig. 1b) from the TAC. For events which satisfied this condition the TAC output T, the pulse height outputs L_p and L_n and two additional "fast integral" outputs F_p and F_n, derived from simple internal modifications in the LINK units, were digitized and written to buffer tape for subsequent off-line analysis. The n-γ discrimination thresholds of the LINK units were set low enough to ensure that more than 98% of the detected photoprotons and photoneutrons passed the first (on-line) level of selection. The fast integral outputs F_p and F_n were used to impose stricter pulse shape discrimination against gammas during the subsequent off-line analysis, as described below.

The LINK pulse shape discriminators, which are based on a Harwell design [20]), incorporate pile-up rejection electronics and provide busy outputs for the monitoring of dead time. With singles count rates ranging as high as 2 kHz and 20 kHz in the stilbene and deuterated anthracene respectively these facilities were essential to the present experiment. The PSD technique employed in the LINK [20]) is based on comparison of two integrals of the scintillation decay. The first, which we refer to as the fast integral, is obtained by integrating from the start of the scintillation for a period of the order of the lifetime of the fast component of the scintillation decay (~3 ns for stilbene and ~20 ns for deuterated anthracene). The second integral is obtained by integrating for a period of about 500 ns. Minor internal modifications were made to the LINK units used, in order to extract the fast integral signals F_p and F_n in fig. 1b. The analogue processing within the LINK units was then emulated digitally in the off-line analysis of the buffered data, by computing pulse shape parameters S_p and S_n for each event from equations of the form

$$S = kL - F + C, \tag{5}$$

in which k and C are constants and L is the associated linear pulse height (fig. 1b) which may be assumed to be proportional to the long-period integral within the LINK. The values of k and C were chosen so as to simplify the application of the final pulse shape discrimination cuts in the analysis, as described below.

Figs. 2 and 3 show some two-parameter distributions from multiparameter off-line analysis of calibration runs and of a set of photodisintegration runs obtained at $\theta_n = 90°$ in series B. Fig. 2 shows plots of counts, versus S and L, obtained from

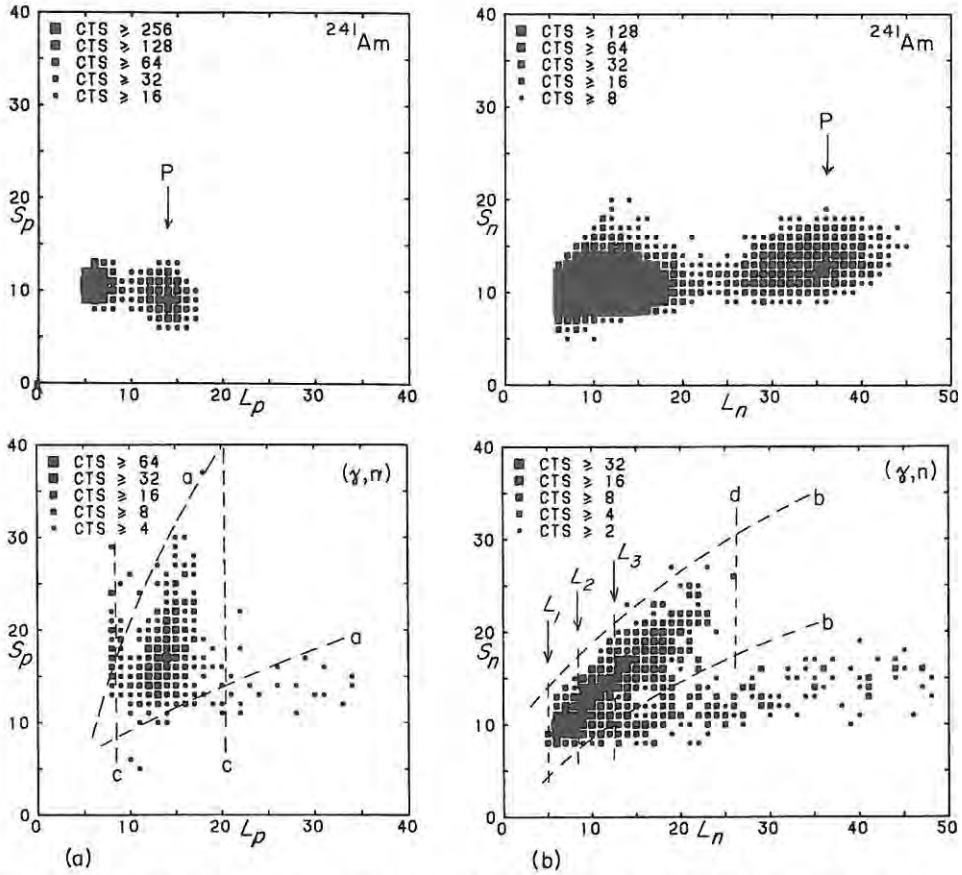

Fig. 2. Density plots of counts versus pulse height L and pulse shape S: (a) for the deuterated anthracene crystal; and (b) for the stilbene crystal. Upper panels display calibration spectra obtained using a sealed ^{241}Am source and show peaks P corresponding to the 60 keV gamma-ray. Lower panels show spectra obtained from the summed photodisintegration runs taken at $\theta_n = 90°$ in the series B experiments. The cuts applied when obtaining the spectra in these lower panels were b, d, e and L_1 for (a) and a, c and e for (b). The cuts are identified as follows: PSD cuts selecting photoprotons and photoneutrons, a and b respectively; photoproton pulse height window c; photoneutron pulse height window, d together with either L_1, L_2 or L_3; and photoneutron time-of-flight window e (see fig. 3).

^{241}Am calibration runs (upper panels) and from the photodisintegration runs (lower panels). A point of interest is the fact that the deuterated anthracene pulse height response L_p to 260 keV photoprotons is approximately the same as that to 60 keV electrons (fig. 2a), whereas the stilbene pulse height response to 260 keV protons, judged from the upper limit of the recoil proton distribution for 260 keV photoneutrons in fig. 2b, is only about two thirds of that to 60 keV electrons. The response in fig. 2a is enhanced by the fact that the artificial c'-axis of the deuterated anthracene crystal was aligned with the neutron-proton axis SD in fig. 1a and thus with the photoproton direction preferentially selected by the coincidence system. The c'-

direction is associated with enhanced pulse height response for anthracene crystals [21]). This pulse height anisotropy characteristic of anthracene therefore provided a measure of angular selection for the photoprotons in this experiment, by discriminating against accidental coincidences associated with photoprotons moving in off-axis directions.

The final PSD cuts applied to the deuterated anthracene and stilbene detectors are indicated by the lines a in fig. 2a, and b in fig. 2b. The photoproton pulse height window is indicated by lines c in fig. 2a. The upper limit of the photoneutron pulse height window is shown by d in fig. 2b. The levels L_1, L_2 and L_3 shown in this figure indicate three different neutron detection thresholds (lower limits for this window) used in the analysis.

Fig. 3 shows a two-parameter distribution of counts versus L_p and T. The most prominent features are the ridge and the peak at channels $T = 39.5$ and 27.5 respectively. The ridge is attributed to Compton coincidences, a small fraction of

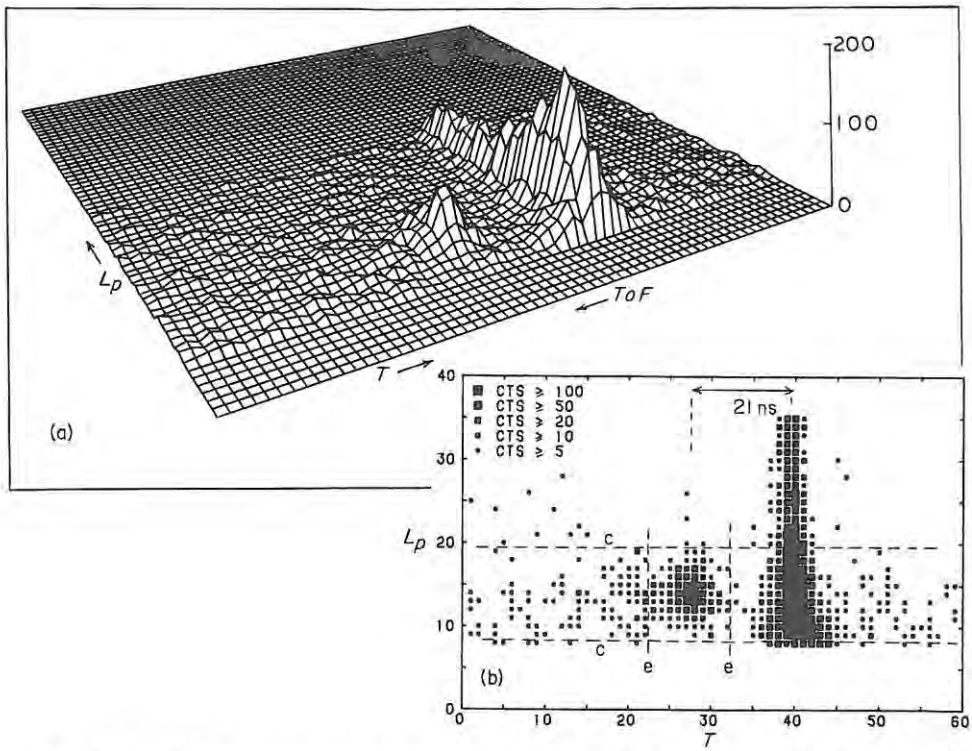

Fig. 3. Perspective view (a) and density plot (b) of counts versus photoproton pulse height L_p and photoneutron time-of-flight T, obtained from an analysis of the summed $\theta_n = 90°$ runs of series B, with cuts a, b, d and L_1 (see fig. 2) applied. The ridge centred at channel $T = 39.5$ is associated with Compton scattering coincidences. The peak centred at channel $T = 27.5$ is attributed to photodisintegration events. The cuts indicated in (b) are the photoproton pulse height window c and the photoneutron time-of-flight window e.

which are not filtered out by the PSD cuts, and the peak is attributed to photoneutron-photoproton coincidences. The photoproton window, as in fig. 2a, is indicated by lines *c* in fig. 3 and a time-of-flight window selecting the photodisintegration peak is indicated by the lines *e*. The distribution shown in fig. 3 was obtained with cuts a, b, d and L_1 (see fig. 2) applied, the distribution in fig. 2a with cuts b, d, e and L_1 applied and that in fig. 2b with cuts a, c and e applied.

Photodisintegration runs were made at the six laboratory angles $\theta_n = 30°$, 45°, 60°, 90°, 120° and 135°. For each angle the photoneutron yield was determined as outlined more fully below, by integrating the counts in the photoneutron peak, by correcting for background, geometry, dead time losses and relative detection efficiency of the neutron detector and by normalizing to a constant flux of incident 2.75 MeV gamma rays, as measured by the Ge(Li) monitor.

The dead time for the gamma spectrum measurement was monitored by feeding pulser signals at 130 Hz into the test input of the Ge(Li) preamplifier and comparing the integral under the resulting pulser peak in the spectrum with the real pulser integral, monitored by scaler. The pulser signals were also used to monitor the dead times in the photodisintegration experiments by recording pulser signals in anticoincidence with the busy outputs of the TAC and the two LINK units. The dead time fractions for the gamma spectrum measurements were typically $\leqslant 5\%$ while those for the photodisintegration detection system depended on the source strength and experimental geometry and varied significantly with the source decay during a 12 hour run. For the runs of series A and B the distance *d* in fig. 1a was 180 mm and the dead times measured over 12 hour runs varied between 8–25% depending on θ_n. The series C runs were made with $d = 240$ mm, and thus lower count rates, expressly in order to check the reliability of the dead time monitoring procedures. The dead times measured in this series ranged from 5–13%.

2.2. CALIBRATION OF THE NEUTRON DETECTOR EFFICIENCY

The efficiency of the stilbene detector used to detect the photoneutrons depends on the neutron angle θ_n, due to the kinematic variation of the photoneutron energy, from 0.24 MeV at $\theta_n = 135°$ to 0.29 MeV at $\theta_n = 30°$. The form of this dependence is sensitive to the PSD settings, through the action of the PSD cut (b in fig. 2b) and to the neutron detection threshold (L_1, L_2 or L_3 in fig. 2b). The variation of neutron detection efficiency with energy was therefore determined independently in each series of runs, under conditions identical to those used for the photodisintegration measurements. A ^{6}Li-loaded glass scintillator (Nuclear Enterprises NE905, 40 mm diam. × 12.5 mm thick) provided a convenient secondary reference standard for these calibrations. The energy-dependence of the neutron detection efficiency of the NE905 was determined from an independent comparison with a standard long counter (30 cm diam × 35 cm wax moderator). The long counter efficiency may be assumed to be constant to within 2% over the limited energy range (0.2–0.3 MeV) of interest.

The comparisons between the stilbene and NE905 detectors were made by delivering a pulsed proton beam onto a thin lithium metal target placed at the end of the Van de Graaff beam line adjacent to the photodisintegration experiment. The stilbene detector was moved to a position 40 cm from this target at an angle of 10° to the proton beam, without disturbing the electronics or cabling of the photodisintegration experiment in any way other than as described below. The NE905 detector was placed in a symmetrical position at the same distance and angle on the opposite side of the proton beam direction. Timing signals from the NE905 were fed in parallel with those from the stilbene detector to the start input of the TAC and the TAC stop (fig. 1b) was taken from the proton beam pulse instead of the deuterated anthracene. Apart from these changes the electronics for the stilbene detector remained identical to that used in the photodisintegration experiment. The stilbene outputs (L_n, F_n, and T), were recorded in multiparameter on buffer tape together with the multiplexed T output from the NE905. The off-line analysis was made using the same cuts (b, d and L_1, L_2 or L_3 in fig. 2b) as used in the photodisintegration experiment. Stilbene and NE905 time-of-flight spectra, determined by the common TAC and thus with identical dead times, were obtained from these analyses. The relative efficiency of the stilbene detector was then determined as a function of threshold setting L_n and incident neutron energy from the ratio of the neutrons recorded by two detectors for the ground state transition in the $^7Li(p, n)^7Be$ reaction. Relative efficiencies were measured in this way for 12 different neutron energies in the range 180–340 keV.

3. Results

The raw data from the three series of photodisintegration measurements consisted of 54 runs, each of 10–12 hours duration. Each series was analysed independently. After correcting for dead-time losses and normalizing to the same incident gamma flux, time-of-flight spectra were obtained by projecting the photoproton cut of the L_p–T spectrum (fig. 3) onto the T-axis. Runs at the same angle were first checked for internal consistency and then summed in subsequent analyses. Two or three analyses were made in which different neutron detection thresholds (L_1, L_2 or L_3 in fig. 2b) were used.

Fig. 4 shows two sets of projected T-spectra obtained from the summed runs of series B and illustrates how a higher neutron detection threshold improved the signal-to-background ratio for photoneutrons, but at the expense of a reduced photoneutron yield. The photoneutron peaks (fig. 4) were integrated after estimating background levels from the flat regions of the projected spectra themselves and setting T-limits to discriminate against externally scattered neutrons as mentioned earlier, with reference to fig. 1a. The integrals of the photoneutron peaks were then corrected for the energy-dependence of the neutron detection efficiency using the calibration data measured as described in sect. 2.2. The yields calculated for each series at the three different neutron detection thresholds (and therefore with different

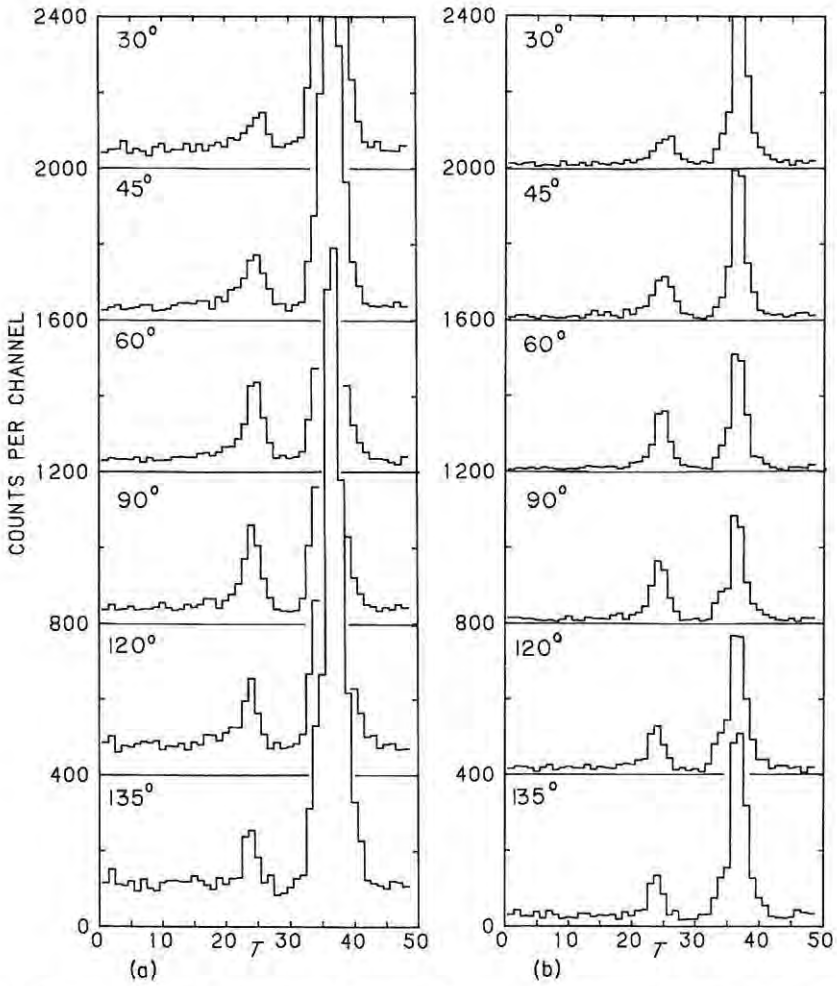

Fig. 4. Projected T-spectra for events satisfying cuts a, b, c and the photoneutron pulse height windows (a) L_1 and d; and (b) L_3 and d (see fig. 2). The spectra shown are the series B data for laboratory angles $\theta_n = 30°$, 45°, 60°, 90°, 120° and 135° respectively, normalized to the same flux of incident 2.75 MeV gamma rays and offset by multiples of 400 counts.

neutron detection efficiencies) were checked for consistency and then combined to give a single value for the measured yield at each angle for the series. These consistency checks were important in that they confirmed that the neutron detection efficiency calibrations were reliable.

The neutron yields were corrected for the effects of scattering of photoneutrons within the deuterated crystal. On the one hand this scattering removes some neutrons originally emitted in the direction of the stilbene detector, thus reducing the observed yield. On the other hand, some photoneutrons originally emitted in other directions may be scattered towards the stilbene, thus increasing the observed yield, unless

the energy loss in scattering is sufficient to permit time-of-flight discrimination (fig. 4) against these neutrons. Monte-Carlo calculations were made to estimate corrections for these effects and the correction factors obtained ranged between 1.01 and 1.12 at different angles.

The corrected results obtained from the A, B and C series are presented in table 1 as relative differential cross sections $\sigma(\theta)$. They have been reduced to a common arbitrary scale by normalizing the sum $\sum \sigma(\theta)$ to the same value for each series. A weighted average $\sigma(\theta)$ was calculated for each of the six angles, weighting in proportion to the inverse square of the uncertainty. The final uncertainties shown in table 1 were dominated by the counting statistics of the photodisintegration measurements.

TABLE 1

Angular distribution data

θ	$\sigma(\theta)$ (arbitrary units)			
	A	B	C	weighted average
30°	10.9 ± 1.0	10.4 ± 1.1	10.8 ± 2.8	10.7 ± 0.7
45°	16.9 ± 1.2	18.2 ± 1.1	19.9 ± 3.4	17.7 ± 0.8
60°	22.8 ± 1.4	23.6 ± 1.3	22.8 ± 2.7	23.2 ± 0.9
90°	29.6 ± 2.0	29.6 ± 1.5	30.0 ± 3.9	29.6 ± 1.1
120°	2.21 ± 2.2	21.2 ± 1.6	22.1 ± 4.5	21.6 ± 1.2
135°	17.3 ± 2.7	16.9 ± 1.8	13.9 ± 3.6	16.6 ± 1.4
a/b	0.199 ± 0.024	0.191 ± 0.022	0.184 ± 0.055	0.193 ± 0.015

4. Discussion and conclusions

The averaged angular distribution data are plotted against centre-of-mass angle θ in fig. 5. The data are symmetric about $\theta = 90°$ within the accuracy of the measurement and do not therefore provide evidence of contributions from multipoles $L \geq 2$. It should be noted that this is the first time that direct and unambiguous measurements have been reported at backward angles for the angular distribution in deuteron photodisintegration at 2.75 MeV. Previous angular distribution measurements either assumed symmetry about 90° [ref. [8])], or were confined to forward angles [9-12]) or were indirect insofar as they inferred the photoproton angle from a measurement of its energy [14]).

The angular distribution data (table 1 and fig. 5) have been fitted by weighted least squares (weighting in proportion to the inverse square of the estimated uncertainty) to the dipole approximation of eq. (3) to obtain values for the scale-independent ratio a/b. The values obtained from fits to the individual data sets A, B and

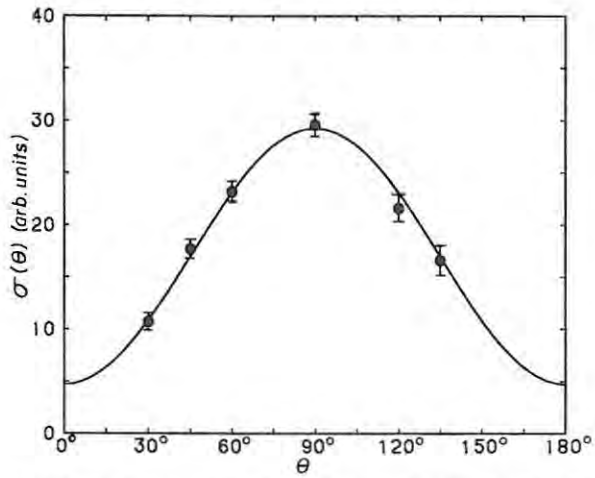

Fig. 5. Angular distribution of neutrons from deuteron photodisintegration by 2.75 MeV gamma rays (weighted mean values) and least squares fit to eq. (3), which led to the value $a/b = 0.193 \pm 0.014$.

C and to the weighted mean of the combined data are presented in the bottom row of table 1 and are consistent. A single least squares fit to the combined data (18 points) of series A, B and C has also been made and leads to the value $a/b = 0.193 \pm 0.014$. Taking this as our best estimate for a/b we obtain for the dipole cross section ratio (eq. (4)) $\tau = 3a/2b = 0.290 \pm 0.021$. This result is listed in table 2 and displayed in fig. 6, together with published values of τ at or near to $E_\gamma = 2.75$ MeV.

The presentation in fig. 6 distinguishes between measurements based on proton detection (crosses), on neutron detection (triangle and squares) and our measurement by neutron-proton coincidence (circle). The proton-detecting experiments all used active targets consisting of deuterium-filled proportional counters but varied considerably in method used to define or determine the photoproton angle. Lassen [8])

TABLE 2

Measurements of τ for $E_\gamma = 2.75$ MeV

N	Author and reference	No. of angles	τ
1	Lassen [8])	6	0.264 ± 0.063
2	Woodward & Halpern [9])	5	0.49 ± 0.07 [a])
3	Meiners [11])	2	0.304 ± 0.060
4	Meiners [11])	2	0.318 ± 0.012
5	Genevese [12])	4	0.295 ± 0.036
6	Hammermesh & Wattenberg [10])	2	0.31 ± 0.07
7	Bishop *et al* [14])	[b])	0.247 ± 0.007
8	this work	6	0.290 ± 0.021

[a]) measured at $E_\gamma = 2.71$ MeV.
[b]) angular distribution obtained from energy spectrum (see text).

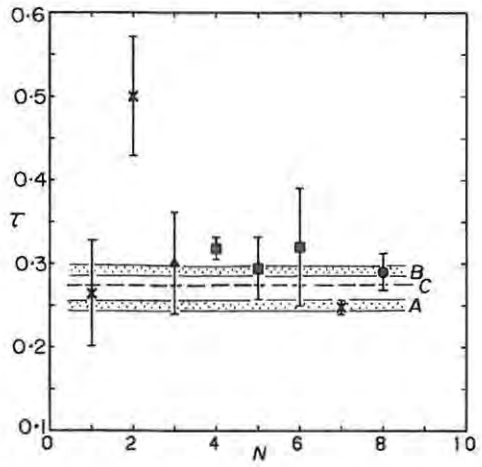

Fig. 6. Display of measurements and calculations of the dipole cross section ratio τ for deuteron photodisintegration at $E_\gamma = 2.75$ MeV. Data identified by the arbitrary ordinate value N (see table 2) are from proton-detecting measurements (crosses), neutron-detecting measurements (triangle and squares) and the present n-p coincidence measurement (circle). Band A shows the range of τ-values from calculations [22]) which do not include MEC or IC. Band B shows range calculated assuming MEC and IC contributions estimated from the results of Arenhövel *et al.* [17]). The dashed line C shows the value obtained from a recent calculation by Arenhövel and Miller [23]) based on the Paris potential and including MEC and IC contributions.

($N = 1$ in fig. 6) used single counter geometry and Woodward and Halpern [9]) ($N = 2$) used a triple counter telescope for this purpose. Bishop *et al.* [14]) ($N = 7$) derived the photoproton angular distribution from the energy spectrum measured by their counter.

The neutron-detecting experiments ($N = 3$–6 in fig. 6) all made use of heavy water targets (masses 1–35 g) and had to contend with problems arising from multiple neutron scattering in the target. One of these experiments ($N = 3$) used an activation method for neutron detection. The others ($N = 4$–6) used moderator-surrounded BF_3 proportional counters. Multiple scattering corrections were estimated by a method of extrapolation to zero target thickness, based on comparisons between measurements made on targets of different thickness or deuterium content. Extensive precautions were taken [10–12]) in these experiments to minimize the backgrounds caused by neutrons scatttering off the experimental surroundings into the neutron detectors.

It should be noted that the combination of time-of-flight, pulse shape discrimination and multiparameter analysis in our experiment was highly effective in discriminating against backgrounds and that the multiparameter method made it possible to estimate background levels simply and confidently. We also consider that the use of Monte Carlo calculations to estimate corrections for neutron scattering within the active target (deuterated crystal) represents a significant improvement over the methods used in the earlier neutron-detecting experiments.

The dipole cross section ratios obtained from the neutron-detecting experiments (fig. 6 and table 2) agree with one another. Those from the proton-detecting experiments show a wide spread and include both the lowest value [14]), which also has the smallest quoted uncertainty, and the highest value [9]). The latter value, by Woodward and Halpern [9]) is for a photon energy of 2.71 MeV, slightly lower than that of the other data (2.75 MeV) and was measured by the end-point technique, using a bremsstrahlung beam. The lower photon energy might be partially responsible for the higher result. Apart from the high value of Woodward *et al.* [9]) the most significant discrepancy within the data of fig. 6 is that between the two most accurate measurements, those by Bishop *et al.* [14]) ($N=7$) and Meiners [11]) ($N=4$); and this discrepancy seems to be irreconcilable within the uncertainties quoted. Our result ($N=8$) is closer to the measurement of Meiners than to that of Bishop *et al.* However, it is clear that more accurate measurements will be needed to resolve this disagreement in the experimental data.

Calculations of threshold photodisintegration cross sections [22]) which do not include exchange current contributions lead to dipole cross section ratios in the range $\tau = 0.249 \pm 0.006$ for $E_\gamma = 2.75$ MeV, as illustrated by the band A in fig. 6. Although there have been no calculations reported at this energy which include exchange currents and also quote values of τ, a value may be estimated from the results of Arenhövel *et al.* [17]). They concluded that the MEC + IC contribution would enhance the total cross section for deuteron photodisintegration by about 6% at threshold and by about 3.5% at the incident photon energy of 2.75 MeV. If we assume that this increase may be attributed entirely to enhancement of the photomagnetic component σ_m and let p represent the fractional increase in the total cross section, then the dipole cross section ratio must change by a factor ϕ given by

$$\phi = 1 + p(1 + \tau^{-1}), \tag{6}$$

where τ is the value calculated without including MEC or IC. Thus for $p = 0.035$ and $\tau = 0.25$ we obtain $\phi = 1.175$, implying a 17.5% increase in τ for $E_\gamma = 2.75$ MeV, to the value of 0.293 ± 0.007, as indicated by band B in fig. 6. Our result is consistent with this value.

The calculation of Arenhövel *et al.* [17]) was made using the Hamada-Johnston potential. They point out that their MEC contribution of 6% at threshold agrees with that used by Riska and Brown [1]) in the calculation of the thermal n-p radiative capture cross section. They also note however that their IC contribution at threshold is 0.9%, compared with the 3% used by the latter authors, and indicate that this discrepancy may be attributed to differences in the methods used to normalize the deuteron wave function in the presence of IC. It would be interesting to see how calculations based on other approaches or potential forms fare in predicting the low-energy deuteron photodisintegration observables, particularly the dipole cross section ratio.

The preliminary results of some new calculations by Arenhövel and Miller [23]), based on the Paris potential have recently been communicated to us and are as follows, for incident photon energy of 2.75 MeV. Their calculation not including MEC or IC gave an angular distribution which we have fitted to eq. (2), obtaining the following values for the coefficient ratios: $a/b = 0.165$; $c/b = 0.001$; $d/b = 0.046$; and $e/b = 0.0007$. Their calculation including MEC and IC led to the same values for all but the first of these ratios and this ratio increased to the value of $a/b = 0.183$. Thus the inclusion of MEC and IC raises the dipole cross section ratio τ from 0.248 to 0.275. The former value lies at the centre of band A and the latter value is indicated by the dashed line C in fig. 6. Our result is thus also consistent with this calculation, in which the MEC + IC contributions lead to an increase of about 11% in τ.

It is also interesting to note evidence of higher multiple contributions implied by the asymmetry about 90° of the calculated [23]) photoneutron differential cross sections $\sigma(\theta)$. Introducing the ratio $R(\theta)$ defined by

$$R(\theta) = \sigma(\pi - \theta)/\sigma(\theta), \tag{7}$$

we find $R(45°) = 1.05$ and $R(60°) = 1.04$ from the Paris potential calculations [23]), while our measurements (table 1) give $R(45°) = 0.93 \pm 0.09$ and $R(60°) = 0.93 \pm 0.06$. The experimental values are thus systematically lower than the calculated ratios but the discrepancy is small and of doubtful significance. The proximity of all these R values to unity, on the other hand, validates the use of the dipole approximation (eq. (3) in the analysis to obtain τ-values.

The angular distribution of the polarization of photoneutrons from deuteron photodisintegration by unpolarized incident 2.75 MeV photons has been measured by Jewell *et al.* [24]). Their results have a scale uncertainty of about 10%, associated with the calibration of their polarization analyser. They disagree by a larger margin of 15–30% with several calculated polarization values [18,23–25]), the magnitude of the measured polarization being systematically smaller than that of the theoretical calculations in every case. This discrepancy has attracted comment and discussion [25,26]) and it seems unlikely that an explanation will be found in terms of MEC and IC effects in the calculations. Arenhövel *et al.* [17]) find that the photoneutron polarization is relatively insensitive to MEC and IC contributions at this energy. Rustgi *et al.* [18]) suggest that the investigations of another polarization observable, the asymmetry function measured using a polarized photon beam, should also be useful in the study of exchange current effects at low energies.

Thus, in addition to being difficult to perform, photoneutron polarization measurements at threshold energy do not promise to reveal much about MEC and IC contributions. Angular distribution experiments on the other hand are relatively straightforward and lead directly to the dipole cross section ratio τ which is sensitive to MEC and IC contributions. The data now available at 2.75 MeV exhibit inconsistencies but tend to indicate values higher than the $\tau = 0.245 \pm 0.006$ predicted by

calculations which do not include MEC+IC contributions. Further calculations of τ at threshold energies would be of interest as well as further experimental measurements, preferably measurements made using coincidence methods of the type we have outlined here.

We thank the Foundation for Research Development of the South African CSIR for their financial support and for a bursary awarded to one of us (FDS). We also thank Drs. H. Arenhövel and H.G. Miller for providing advance information of their calculations based on the Paris potential, Drs. H.G. Miller and D.W. Mingay for stimulating discussions, Mr. P.A. Back for his assistance in the construction of experimental equipment and the staff of the NAC Van de Graaff group for their cooperation and assistance during the experimental runs.

References

1) D.O. Riska and G.E. Brown, Phys. Lett. **38B** (1972) 193
2) N. Austern and E. Rost, Phys. Rev. **117** (1959) 1506;
H.P. Noyes, Nucl. Phys. **74** (1965) 508
3) A.E. Cox, S.A.R. Wynchank and C.H. Collie, Nucl. Phys. **74** (1965) 497;
D. Cokinos and E. Melkonian, Phys. Rev. **C15** (1977) 1636
4) M.L. Rustgi, W. Zernik, G. Breit and D. Andrews, Phys. Rev. **120** (1960) 1881
5) F. Partovi, Ann. of Phys. **27** (1964) 79
6) J.L. Friar and S. Fallieros, Phys. Lett. **114B** (1982) 403; Phys. Rev. **C29** (1984) 1645
7) G.A.R. Graham and H. Halban, Rev. Mod. Phys. **17** (1945) 297
8) N.O. Lassen, Phys. Rev. **75** (1949) 1099
9) W.M. Woodward and I. Halpern, Phys. Rev. **76** (1949) 107
10) B. Hamermesh and A. Wattenberg, Phys. Rev. **76** (1949) 1405
11) E.P. Meiners, Phys. Rev. **76** (1949) 259
12) F. Genevese, Phys. Rev. **76** (1949) 1288
13) G.R. Bishop, H. Halban, P.F.D. Shaw and R. Wilson, Phys. Rev. **81** (1951) 219
14) G.R. Bishop, L.E. Beghian and H. Halban, Phys. Rev. **83** (1951) 1052;
G.R. Bishop and R. Wilson, in Handbuch der Physik, ed. S. Flügge, vol. 42 (Springer, Berlin, 1957) p. 309
15) R.J. Holt, IEEE Trans. Nucl. **NS-28** (1981) 1279
16) E. Hadjimichael, Phys. Lett. **46B** (1973) 147
17) H. Arenhövel, W. Fabian and H.G. Miller, Phys. Lett. **52B** (1974) 303
18) M.L. Rustgi, R. Vyas and M. Chopra, Phys. Lett. **50** (1983) 236
19) LINK Model 5010 Pulse Shape Discriminator, from LINK SYSTEMS Halifax Rd., High Wycombe, Bucks, England HP12 3SE
20) J.M. Adams and G. White, Nucl. Instr. Meth. **156** (1978) 459
21) F.D. Brooks and D.T.L. Jones, Nucl. Instr. Meth. **121** (1974) 69
22) H.C. Bethe and C. Longmire, Phys. Rev. **77**(1950) 647;
E.E. Salpeter, Phys. Rev. **82** (1951) 60;
L. Hulthén and B.C.H. Nagel, Phys. Rev. **90** (1953) 62;
L. Hulthén and M. Sugawara in Handbuch der Physik, ed. S. Flügge, vol. 39 (Springer, Berlin, 1957) p. 1
23) H. Arenhövel and H.G. Miller, private communication
24) R.W. Jewell, W. John, J.E. Sherwood and D.H. White, Phys. Rev. **B71** (1965) 119
25) M.L. Rustgi, R. Vyas and O.P. Rustgi, Phys. Rev. **C29** (1984) 1580
26) J.M. Cameron, Can. J. Phys. **62** (1984) 1019;
M.L. Rustgi, R.D. Nunemaker and R. Vyas, Can. J. Phys. **62** (1984) 1064

F.D. Smit and F.D. Brooks
Angular distribution of neutrons from $^{2}H(\gamma,n)^{1}H$ at E_{γ} = 2.75 MeV
Nucl. Phys. A465 (1987) 429-444

Muon Catalyzed Fusion 2 (1988) 85–92

PULSED MUONS FOR μCF EXPERIMENTS AT RAL

F.D. BROOKS, J.D. DAVIES, G.J. PYLE, G.T.A. SQUIER

Department of Physics, University of Birmingham, Birmingham B15 2TT, U.K.

and

G.H. EATON

Rutherford Appleton Laboratory, Chilton, Didcot, OX0N OX11 0QX, U.K.

An intense, pulsed muon beam has been constructed at ISIS, the spallation neutron source of the Rutherford Appleton Laboratory. Both facilities are driven by 800 MeV protons having a 10^{-5} duty cycle. The facility is described and the performance of the muon beam given. Two μCF experiments in active preparation and benefiting from the very low duty cycle are described, viz a direct measure of the μα sticking coefficient, W_s, and a determination of the μ ^{4}He X-ray spectrum following sticking.

1. Introduction

The advantages of pulsed, low energy muons for many experiments in many disciplines are well recognised and several expensive schemes have been proposed for providing the initial, pulsed protons. It was suggested that the unusual time structure of the proton synchrotron that drives the spallation neutron source (SNS) at the Rutherford Appleton Laboratory could provide (a) pulsed neutrinos from the SNS for the cost of the floor space for the detector (b) pulsed muons for the price of the beam line and a small reduction in the spallation neutron yield. The beam line elements have been 'acquired' at very low cost and muons are now being used for experiments.

2. The ISIS facility

A rapid cycling, 50 Hz synchrotron with negative ion injection has recently been built to provide 180 μA of protons at 800 MeV. The extracted beam strikes a depleted uranium target to provide neutrons by spallation and fast fission; the beam and neutrons are pulsed so that Time-of-flight (TOF) can be used to determine neutron energies. Figure 1 shows the accelerator, target station and the various neutron beam lines. So far 45 μA at 750 MeV is routinely available with 90 μA and 800 MeV intended for later this year.

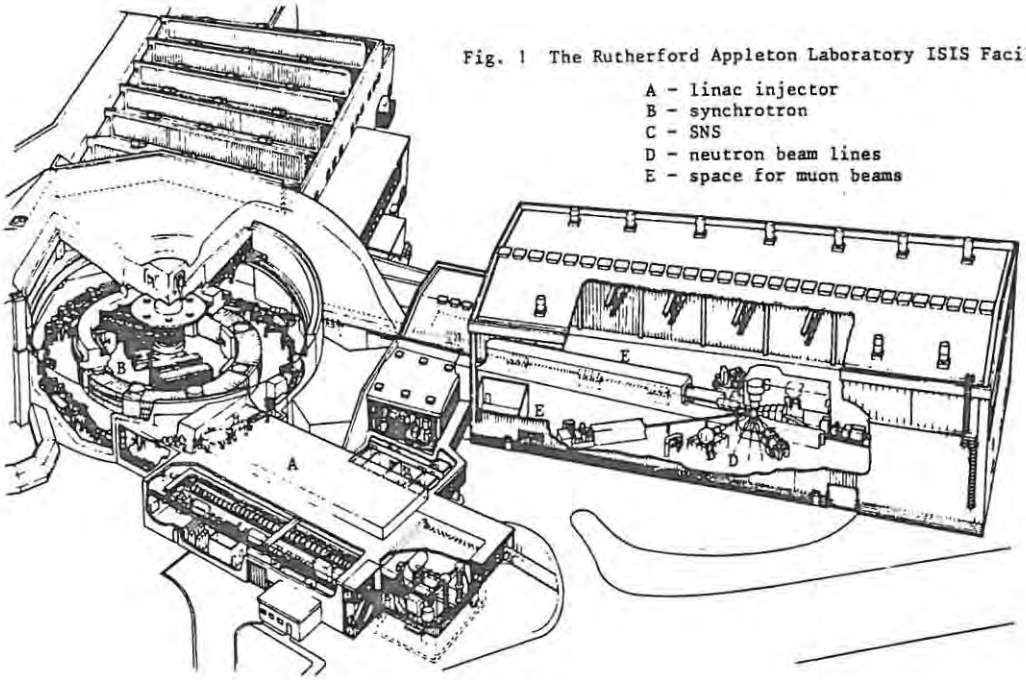

Fig. 1 The Rutherford Appleton Laboratory ISIS Facility.

A - linac injector
B - synchrotron
C - SNS
D - neutron beam lines
E - space for muon beams

Fig. 1.

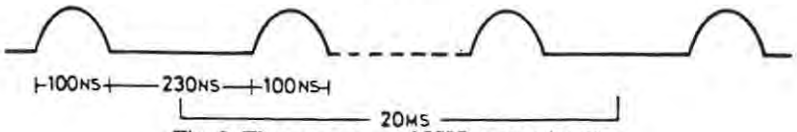

Fig. 2. Time structure of ISIS proton bursts.

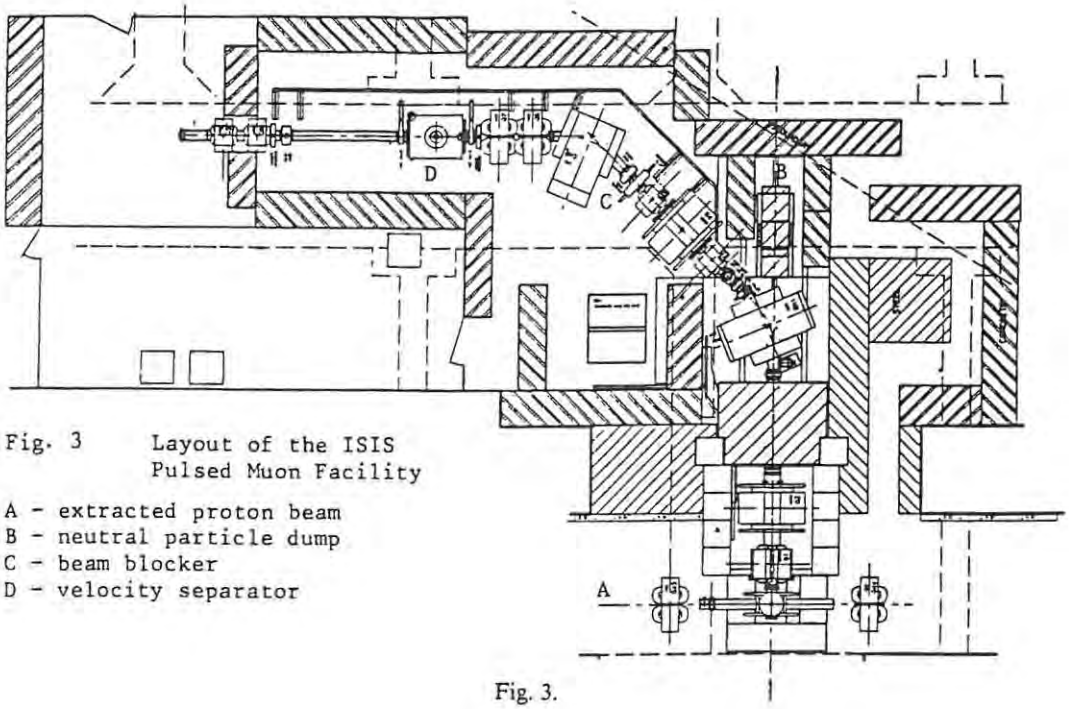

Fig. 3 Layout of the ISIS Pulsed Muon Facility

A - extracted proton beam
B - neutral particle dump
C - beam blocker
D - velocity separator

Fig. 3.

There are two bunches of protons on opposite sides of the accelerator and the fields of a kicker magnet triplet are ramped up between the bunches to provide single turn extraction of high efficiency. Figure 2 shows the proton time structure, two bunches, 330 ns apart, repeated every 20 ms. The SNS is also an intense source of neutrinos. Being pulsed enables ν types to be distinguished and the effects of cosmic ray background minimized. KARMEN is a large, liquid scintillator, neutrino facility presently being assembled.

Muons coming from pion decay in and around an intermediate target in the proton beam will have the time structure of fig. 2, broadened by the 26 ns pion life-time. A 2 cm thick graphite target will reduce the neutron yield from the spallation target by 5% and with the beam line of fig. 3 180 μA of protons should produce

$3 \cdot 10^6$ μ^+/s at 29 MeV/c – 'surface' muons for μSR

$6 \cdot 10^5$ μ^-/s at 60 MeV/c – 'cloud' muons for μCF

3. The muon beam

The 20 m long beam line [1] has a conventional double bend with large acceptance quadrupoles at the beginning and an almost parallel beam through a 1 m long crossed-field, velocity separator; the latter is used for particle separation and for rotating the plane of the muon polarization. The magnets operate from 150 MeV/c to below the 29 MeV/c of surface muons. All the beam elements and shielding have come from former British accelerators or on loan from CERN and DESY while France/Germany/Italy/Sweden/EEC have provided £0.5M towards a European μSR facility. The production targets are made from graphite and are edge-cooled with water.

The present beam can be further enhanced by the provision of a kicker magnet to separate the two pulses into different areas and/or time slice the pulses down to 5 ns. There is considerable space in the vicinity of the intermediate target, sufficient for a complex of muon beam lines; this would use the same intermediate production target and thus not affect the neutron yield.

4. Performance of the muon beam for μCF experiments

So far only thin production targets have been used but the muon intensities for 29 MeV/c μ^+ and 60 MeV/c μ^- accord with being pro-rata on the above numbers. A beam spot of $2\frac{1}{2} \times 2\frac{1}{2}$cm^2 at the focus at the position of the μCF target was measured; $\Delta p/p$ is $\pm 5\%$ with small beam divergence.

Neutron backgrounds and choice of target walls for μCF experiments have been determined with a 2 in. $\varnothing \times 2$ in. long NE 213 liquid scintillator using a LINK 5010 PSD to distinguish the neutrons. A threshold equivalent to 1 MeV neutron energy was set. TOF spectra were started with the pulses that also initiate proton extraction from the synchrotron, the jitter being ± 3 ns.

The general background was expected to come from the SNS, being degraded

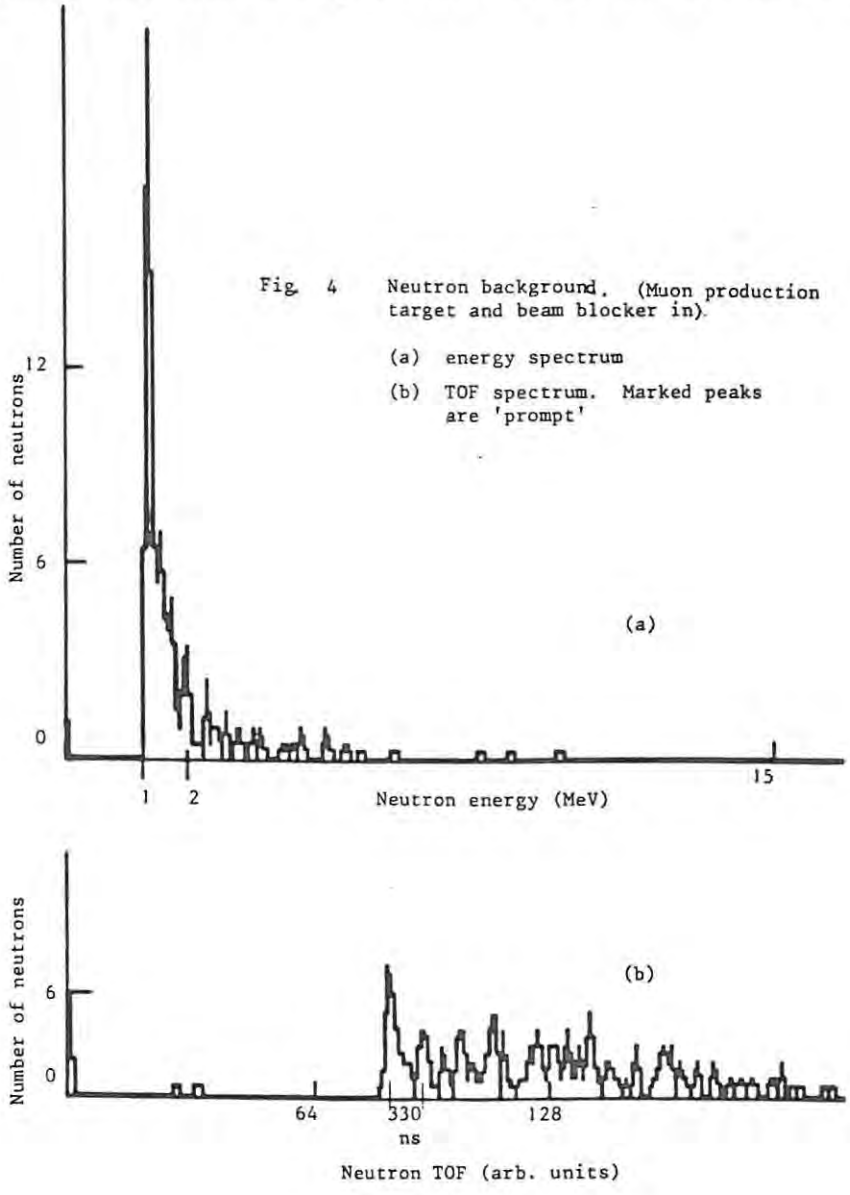

Fig. 4 Neutron background. (Muon production target and beam blocker in).
(a) energy spectrum
(b) TOF spectrum. Marked peaks are 'prompt'

Fig. 4.

in energy and delayed in time as it passed through the shielding with ~ 1 MeV particles delayed by ~ 1 μs expected in the muon experimental area. This background was found to be very low. However there was a large background from the neutral particle dump in the muon line; this protects against neutral background coming directly from the muon production target. So the beam line was roofed over with 90 cm thick concrete slabs, the neutral particle dump was enhanced and polythene shielding placed around the beam pipe. The background of figs. 4a – energy spectrum, 4b – time spectrum, was obtained for 10^{-1} coulombs of 750 MeV protons. This background is already satisfactorily low but will be further reduced by more than 50% when some obvious shielding holes are filled in.

Figure 5 (insert) shows the time spectrum of neutrons coming from a 60 MeV/c μ^- beam incident on a C target with an Al holder. The two (prompt) peaks come directly from the 'muon' pulses and their 330 ns separation provides a time calibration. Figure 5 (insert) shows the peaks on a X4 expanded time scale; the two contributions come from electrons and pions in the beam pulses and have the appropriate time separation. If the LINK 5010 selects 'γs' then there is a dramatic increase in the peaks associated with the beam pulse electrons

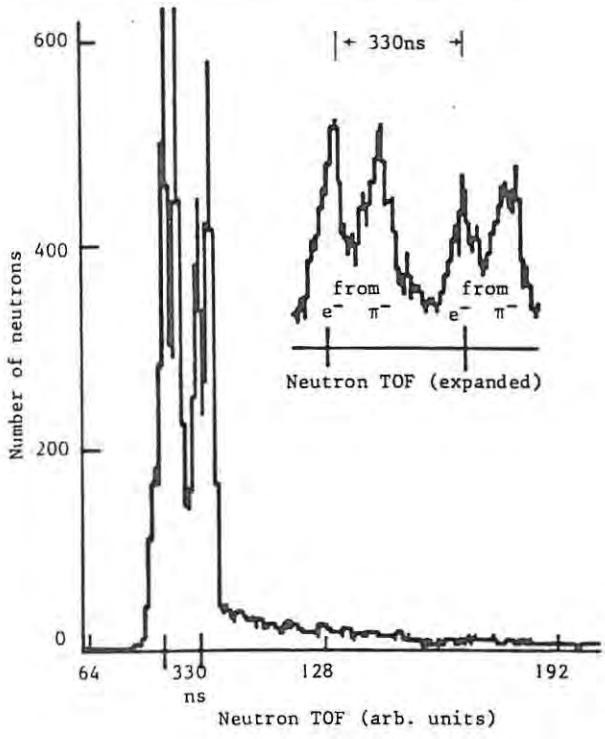

Fig. 5. Neutron time of flight spectra off an Al/C target. Insert – 'prompt' peaks on time-scale X4.

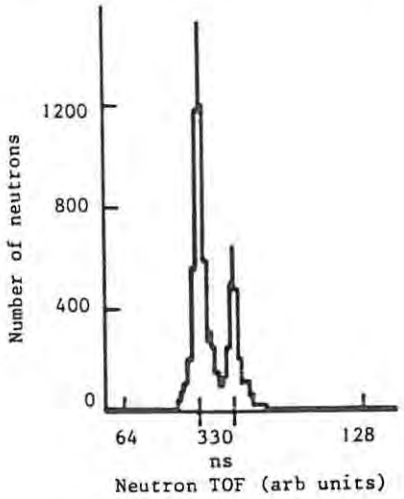

Fig. 6. Neutron time of flight spectrum off an Ag target.

(bpe). There are two exponentials in the tail, $\tau \sim 2$ μs from μC atoms and $\tau \sim 1$ μs from μAl atoms.

Stopping μ^- have an effective life-time $\tau_{\text{eff}} < \tau_{\text{free}}$ owing to muon capture. As the Z of the stopping target increases, τ_{eff} is ~ 2 μs up to $Z \sim 6$ and then falls steeply to ~ 100 ns at $Z \sim 48$ whence it levels off [2]. As the data is old and came from observing decay electrons, we verified this behaviour for neutrons from a range of target materials. Figure 6 shows the neutron time spectrum for a Ag target; an exponential with $\tau_{\text{eff}} \sim 100$ ns can be seen on the edge of the second peak. This second (prompt) peak is reduced in magnitude because of the LINK dead time in handling the showering of the bpe. $\tau_{\text{eff}} < 100$ ns was obtained for a Pb target but the showering was much greater.

The X-rays from μ^- stopping in a C target were examined with a SiLi detector having pulsed optical feedback: the efficiency was very low because of the optical resets necessitated by the 'γ flashes' coming from the bpe. Although we built a fast veto for the LINK 5010 and 'γ' flash protection is available for the SiLi pulse processing, the probability of systematic errors coming from the bpe is large, e.g., via pile-up of the long decay components of the NE 213. Therefore the BPE MUST BE REMOVED.

These electrons come from $\pi^0 \rightarrow \gamma\gamma$ in the production target with the γ showering there and in surrounding materials; hence their beam spot is larger than that of the μ^-. They were thus imperfectly removed when the velocity separator was used with ± 25 kV on the plates. 200 kV power supplies are being purchased. For a DC beam the dead time caused by these electrons is very small, i.e., ~ 50 Hz $\times 2$ μs $\sim 10^{-2}$%.

In accord with TRIUMF [3] data from a similar beam line we decreased the beam momentum $60 \rightarrow 50 \rightarrow 40$ MeV/c and obtained relative muon fluxes $0 \rightarrow 0.8 \rightarrow 0.4$. With $\Delta p/p = \pm 5\%$ then changing $60 \rightarrow 40$ MeV/c reduces the spread in range of stopping μ^- by $\times 5$, thus increasing the proportion of μ^- stopping in low density gas targets by more than $\times 2$ as the reduced degrader gives smaller coulomb scattering.

5. Some possible μCF experiments

S. Jones has reported [4a] on an experiment to measure directly W_s, the $\mu\alpha$ sticking coefficient, from the ratio

$$\frac{N[(\alpha\mu)^+ - \mathrm{n}]}{N[\alpha^{++} - \mathrm{n}]}$$

coincidences with a small, low density gas target. On an $E - \mathrm{TOF}$ plot $(\alpha - \mathrm{n})$ events were clearly seen and well separated from the region of $(\mu\alpha - \mathrm{n})$ coincidences; however any signal from the latter was buried under the background coming from the $> 99.9\%$ of the μ^- that stop in the target walls. The LAMPF group then suggested the experiment for the pulsed beam at ISIS using a target having high Z walls so that interactions therein would be complete within 300 ns of the pulse arrival; data taking could then start after this delay. The collaboration, including Bologna and Delft, are actively preparing apparatus. Compared with the original experiment there will be two $((\mu)\alpha - \mathrm{n})$ telescopes, Si surface barrier detectors only 20 μm thick to further reduce background and NE 213 neutron counters segmented to improve TOF. The target has been made from Ag since this construction material has the lowest Z (to reduce showering of any remaining electrons) with $\tau_{\mathrm{eff}} \lesssim 100$ ns.

G. Hartmann [4b] and K Nagamine [4c] have reported on experiments looking for the K_α X-rays following $\mu\alpha$ sticking. To reduce the background from bremsstrahlung of the tritium decay β^-, the SIN experiment used low C_T and neutron coincidences while results were sought at KEK with a pulsed beam. Using the improved beam at ISIS, a SiLi detector with Comptom suppression, GSPCs and a low mass system should enable K_α and K_β X-rays to be measured.

Acknowledgements

We would like to thank V.R. Bom, S.S. Jogpal, C.A. Scott, A. Zoccoli, Birmingham University, the Rutherford Appleton Laboratory and the Foundation of Research Development.

References

[1] G.H. Eaton et al., NIM 214 (1983) 151.
[2] G. Feinberg and L.M. Lederman, Ann. Rev. Nuc. Sci. 13 (1963) 431.
J. Yamazaki et al., Physica Scripta 11 (1975) 133.
[3] C.J. Oram et al., NIM 179 (1981) 95.
[4] (a) R. Gajewski and S.E. Jones, This volume, Ch. 2;
(b) F.J. Hartmann et al., This volume, Ch. 2;
(c) K. Nagamine et al., This volume, Ch. 2.

F.D. Brooks, W.A. Cilliers, B.R.S. Simpson, F.D. Smit, M.S. Allie, D.T.L. Jones, W.R.McMurray and J.V. Pilcher
Deuterated anthracene spectrometer for 5-30 MeV neutrons
Nucl. Instr. and Meth. A270 (1988) 149-156

Nuclear Instruments and Methods in Physics Research A270 (1988) 149–156
North-Holland, Amsterdam

DEUTERATED ANTHRACENE SPECTROMETER FOR 5–30 MeV NEUTRONS

F.D. BROOKS, W.A. CILLIERS, B.R.S. SIMPSON *, F.D. SMIT * and M.S. ALLIE
Physics Department, University of Cape Town, Rondebosch, Cape, 7700, South Africa

D.T.L. JONES, W.R. McMURRAY and J.V. PILCHER
National Accelerator Centre, Faure, Cape, 7131, South Africa

Received 7 December 1987

A neutron spectrometer consisting of a deuterated anthracene scintillation crystal and a pulse shape discriminator is described. Forward recoiling deuterons are selected by means of their pulse shape signatures, making use of the direction dependence of the pulse height response and scintillation decay characteristics of the crystal. The line shape of the spectrometer for monoenergetic neutrons is a single peak and the neutron energy resolution (FWHM) varies from 7% at 9 MeV to 3.5% at 22 MeV neutron energy.

1. Introduction

The demand for accurate neutron measurements in research associated with controlled nuclear fusion and with neutron therapy has stimulated interest in neutron spectrometers for the energy range 5–30 MeV. Important features sought in neutron spectrometers for these applications are typically a detection efficiency of at least a few percent and varying smoothly with neutron energy in this range and a knowledge of the relative efficiency of neutron detection as a function of energy, to an accuracy of a few percent. Energy resolution is less important in these applications, a FWHM of about 8% being acceptable for most purposes.

Time-of-flight methods [1] where applicable, or recoil proton techniques [2] based on organic scintillators such as the liquid NE213, are traditionally chosen to meet these requirements. We present here a new variant of the recoil spectrometer, based on the observation of recoil deuterons associated with neutron elastic scattering in a deuterated anthracene crystal. The deuterated anthracene spectrometer (DAS) has unique features which arise principally from two factors: firstly, from the prominent forward deuteron recoil peak associated with enhanced backscattering of neutrons in ^{2}H(n, n)^{2}H elastic scattering; and secondly, from the direction-dependent scintillation characteristics of deuterated anthracene, which are similar to those of natural anthracene [3]. These characteristics provide means for enhancing the forward recoil peak relative to other components in the pulse height spectrum and this leads to a spectrometer with a simple and convenient line shape – a single peak in the pulse height distribution for each energy group in the incident neutron spectrum.

The deuterated anthracene crystal may not be well-known as a scintillator. However it has been used previously, firstly to measure left–right asymmetries in n–d elastic scattering [4], secondly as a recoil spectrometer of the conventional type [5] and thirdly to investigate deuteron photodisintegration close to threshold [6].

2. The deuterated anthracene spectrometer (DAS)

The DAS (fig. 1) consists of a deuterated anthracene crystal (10 mm diameter × 21 mm, $D:H > 99$), mounted via a small perspex light pipe on an RCA 8575 photomultiplier tube which is connected to a Link Systems Model 5010 pulse shape discrimination (PSD) unit [7]. A simple internal modification was made to the LINK to extract an extra output pulse F proportional to the "short integral" in this unit. The short integral is the integral of the scintillation pulse over a period which is normally set to match the lifetime of the prompt component of the scintillation decay (~ 20 ns for anthracene). The "long integral" (L in fig. 1), is the standard integrated output provided by the LINK and is proportional to the integral of the scintillation pulse for about 500 ns. It therefore includes contributions from both prompt and delayed scintillation components. The outputs t, n and γ in fig. 1 are the logic

* Now at the National Accelerator Centre, Faure, Cape, 7131, South Africa.

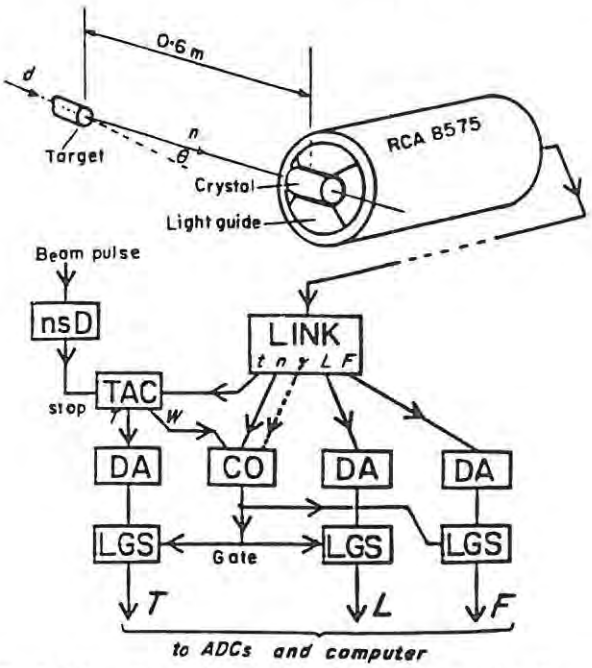

Fig. 1. Schematic and block diagram of the deuterated anthracene crystal spectrometer (DAS) as used in conjunction with a pulsed neutron source. The NIM modules are: a LINK Systems model 5010 pulse shape discriminator; nanosecond delay unit (nsD); time-to-pulse-height converter (TAC); delay amplifiers (DA); linear gate and stretchers (LGS); and universal coincidence (CO). The event gate is a twofold coincidence in CO. The gamma input to CO is enabled only for calibration runs.

signals provided from the LINK for fast timing and n–γ discrimination. The n or γ identification is based on a comparison of the internal signals corresponding to L and F. The external L and F signals are used here (fig. 1) for a finer pulse shape discrimination analysis, designed to separate the protons, deuterons and alphas resulting from neutron interactions within the crystal, and to sense recoil deuteron directions. This analysis was carried out off-line in the present work. It could be performed on-line by using a modified data-acquisition program.

The DAS as shown in fig. 1 used a pulsed neutron source and included a low-resolution (2 ns m^{-1}) measurement of the neutron time of fight. The three parameters, L, F and T, were digitised (12 bits) and written to an event tape by a data-acquisition system based on a PDP 11/34 computer. In the off-line analysis a shape parameter S was computed for each event, from

$$S = L - kF + S_0 \qquad (1)$$

where k and S_0 are constants. The constant k was set at the value $\langle L_d \rangle / \langle F_d \rangle$ where $\langle L_d \rangle$ and $\langle F_d \rangle$ are the average values of L and F respectively for deuterons, thus making $S \approx S_0$ for these particles. The constant S_0 was chosen so as to ensure that S was positive and lay in the range 0–4095 for all events accepted. With these values for k and S_0 the event distribution in the L–S plane resembles that of the display provided for setting up the LINK.

Fig. 2a shows an L–S distribution obtained using 21.9 MeV neutrons (from a ^{3}H(d, n)^{4}He source) incident on the DAS in a direction parallel to the artificial c'-axis of the deuterated anthracene crystal. Components or ridges which may be recognised in this spectrum are those associated with: Compton electrons (from background gammas); protons (from ^{2}H(n, 2n)^{1}H and ^{12}C(n, p)^{12}B reactions in the crystal); deuterons (from ^{2}H(n, n)^{2}H and ^{12}C(n, d)^{11}B); and alphas (from ^{12}C(n, α)^{7}Be and ^{12}C(n, n′)3α).

A projection (fig. 2b) of the deuteron ridge of fig. 2a on the L-axis shows evidence of the two deuteron components indicated above. Deuterons from the ^{12}C(n, d)^{11}B reaction ($Q = -13.7$ MeV) are significant at pulse heights L (channel no.) $\lesssim 35$ in fig. 2b. Recoil deuterons from ^{2}H(n, n)^{2}H are peaked at $L \approx 0$ and at the upper limit or edge of the spectrum, $L \approx 95$ in fig. 2b. These features correspond to the strong forward and backward peaking respectively, of neutrons in the differential cross section for ^{2}H(n, n)^{2}H. The minimum M at $L \approx 75$ in fig. 2b corresponds to the minimum in this cross section at $\theta_{cm} \approx 120°$.

The forward deuteron recoil (backward neutron scattering) peak at $L \approx 90$ in fig. 2b is important to the operation of the DAS. The anisotropic scintillation properties of the crystal may be used, as we outline below, to select only these forward recoiling deuterons and thereby to obtain a pulse height spectrum in which the line shape for monoenergetic neutrons is a single peak.

Fig. 3 shows a pair of L–S distributions obtained using 21.9 MeV neutrons: one (fig. 3a) for neutrons incident in the direction parallel to the c'-axis of the crystal; and the other (fig. 3b) for neutrons incident parallel to the crystal b-axis. Note that, as for natural anthracene crystals [3], the position in the L–S plane of the deuteron forward recoil peak is particularly sensitive to the incident neutron direction. For the neutrons incident parallel to the b-axis (fig. 3b) the forward recoil peak extends to higher S values than other deuteron or proton components of the distribution. A similar pattern is found in the L–S distributions obtained for other incident neutron energies. From measurements of the position of the forward recoil peak as a function of incident neutron energy a line or cut AB (fig. 3b) may be defined which separates the forward recoil peaks from other components in the spectra. Events with S-values above this line then correspond to forward recoiling deuterons only and projection of these

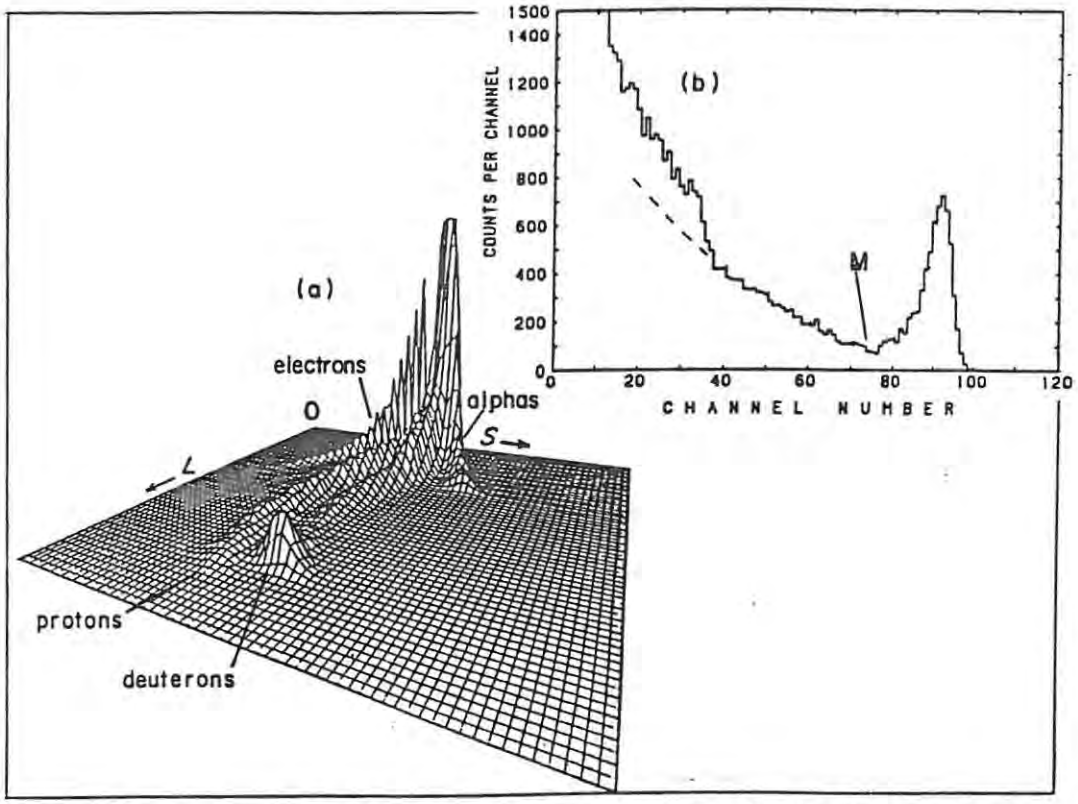

. 2. Perspective view (a) of counts vs pulse height L and pulse shape S obtained when 21.9 MeV neutrons are incident along the ificial c'-axis of the deuterated anthracene crystal. The electron component in (a) is due to Compton scattering of background nmas in the crystal. The proton, deuteron and alpha components in (a) are due to neutron interactions with the ^{2}H and ^{12}C nuclei the crystal (see text). The pulse height spectrum (b) was obtained by projecting the deuteron component (ridge) of (a) onto the L-axis.

ents onto the L-axis leads to a pulse height spectrum ntaining a peak for each energy group in the incident utron spectrum.

Fig. 4 shows projected spectra obtained in this way r monoenergetic neutrons of energies 21.9 and 16.9 eV respectively. The forward recoil peaks, have been librated in terms of incident neutron energy, for use a spectrometer, although they actually correspond to uterons of energies 19.5 and 15.0 MeV respectively. ıe spectrum for 21.9 MeV neutrons shows an ad- tional component at low pulse heights, due to detec- ɔn of the (n, d), (n, α) and (n, n′)3α reactions on ^{12}C the scintillator. This component can be removed by ıposing a further two-parameter cut derived from the w resolution time-of-flight measurement T, as de- ribed in section 4 below.

The energy resolution of the DAS may be specified terms of the widths (FWHM) of the projected pulse ight groups obtained for monoenergetic neutrons. leasurements of the energy resolution obtained from e projected spectra in fig. 4 are shown in fig. 5, from which it may be seen that $\Delta E/E \approx 4\%$ for neutrons of energy 20 MeV.

3. Determination of the relative efficiency $\epsilon(E)$

The relative neutron detection efficiency $\epsilon(E)$ of the DAS may be determined by comparing the peak area (fig. 4) measured for monoenergetic neutrons with the integral of the deuteron forward recoil peak, measured under the same conditions and for the same number of incident neutrons N_0, but with the neutrons incident parallel to the c'-axis instead of the b-axis. Let $N_b(E)$ represent the peak area measured for N_0 incident neutrons of energy E in fig. 4 and $N_c(E)$ the integral (for the same number N_0 of incident neutrons) of the counts from the minimum M to the upper limit of the deuteron peak in the corresponding projected c'-axis spectrum such as fig. 2b. Forward recoiling deuterons are very cleanly separated from other components in the L–S spectrum measured in the c'-orientation (fig. 2a). Thus

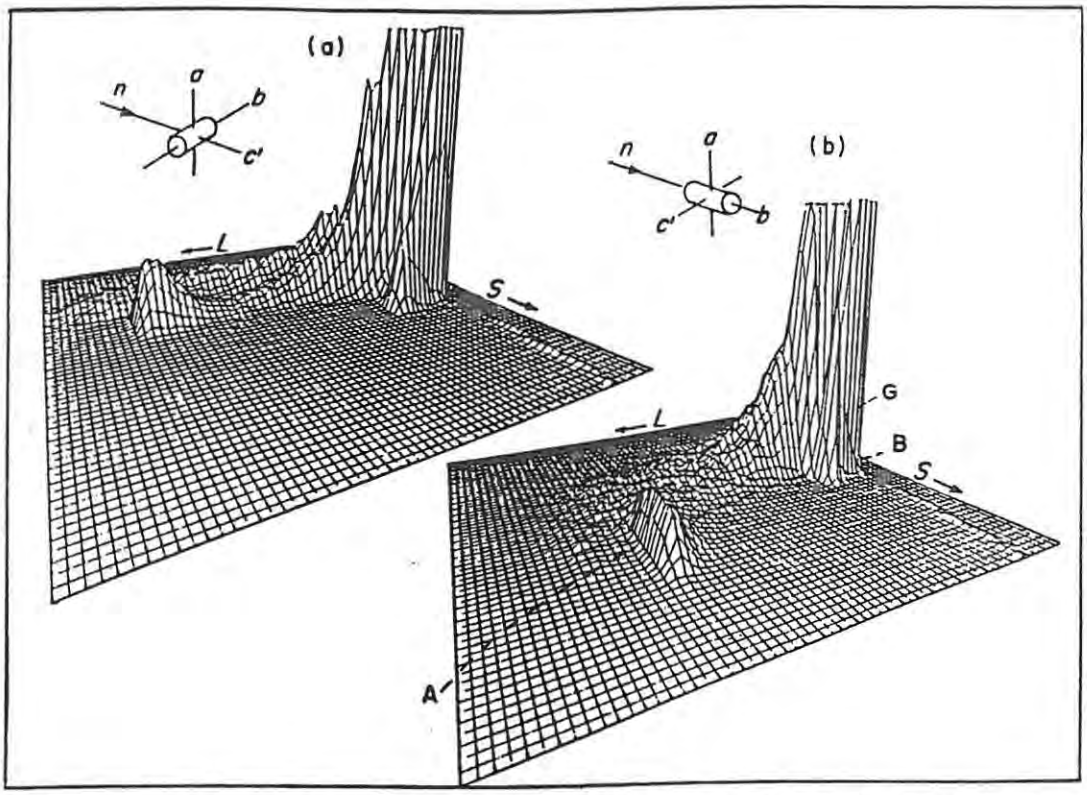

Fig. 3. Perspective views of counts vs L and S obtained for 21.9 MeV neutrons incident on the deuterated anthracene crystal in directions parallel to different crystal axes: (a) the artificial c'-axis; and (b) the b-axis. The cut AB in (b) is used to select forward recoiling deuterons (see text). The component G in (b) is due to neutron interactions with carbon. The insets in (a) and (b) show the orientation of the mutually perpendicular a-, b- and artificial c'-axes of the crystal to the incident neutron beam.

after making a small correction for escaping deuterons (see later) $N_c(E)$ represents the number of deuteron forward recoils resulting from N_0 incident neutrons and the ratio $R(E)$, defined by

$$R(E) = N_b(E)/N_c(E), \qquad (2)$$

represents the fraction of these forward recoils which pass the cut AB of fig. 3b, for measurements in the b-orientation.

Since the dimensions of the crystal are small in comparison with the mean free paths of 5–30 MeV neutrons in it, we may assume that $N_c(E)$ is proportional to $\sigma_P(E)$, where $\sigma_P(E)$ is a total cross section obtained by integrating the n–d differential elastic scattering cross section over the angular range $\theta_{cm} = \theta_M$ to π, and θ_M corresponds to the minimum M in fig. 2b. Since the cross section is a minimum at θ_M the integral $N_c(E)$ will not be sensitive to slight inaccuracies in locating the lower limit M for the integration.

The relative efficiency $\epsilon(E)$ is proportional, in first approximation, to $R(E)$ and $\sigma_P(E)$. Thus

$$\epsilon(E) = KR(E)\sigma_P(E), \qquad (3)$$

where K is a constant. Values of $\epsilon(E)$ were determined from measurements of $R(E)$ for monoenergetic neutrons of energies 8.6, 16.7 and 21.9 MeV in combination with values of $\sigma_P(E)$ taken from a previous evaluation [8] made in the course of a study of the ^{2}H(n, 2n)^{1}H reaction. A correction (~ 4%) for edge effects, arising from the escape of recoil deuterons from the crystal, was included in the calculation. The values of $\epsilon(E)$ obtained from these measurements decreased by 54% over the energy range from 8 to 22 MeV. The variation of $\epsilon(E)$ at intermediate energies was determined by interpolation from these values.

4. Neutron spectrum from the ^{19}F(d, n)^{20}Ne reaction

The performance of the DAS was demonstrated by measuring the spectrum of neutrons emitted at laboratory angle 10° from the ^{19}F(d, n)^{20}Ne reaction produced by 4.8 MeV incident deuterons. A 20 μg cm^{-2} CaF_2 target was bombarded by a pulsed deuteron beam and the DAS was mounted 0.6 m from this target. The neutron time of flight to the DAS was recorded together with the pulse heights L and F (fig. 1). A simultaneous

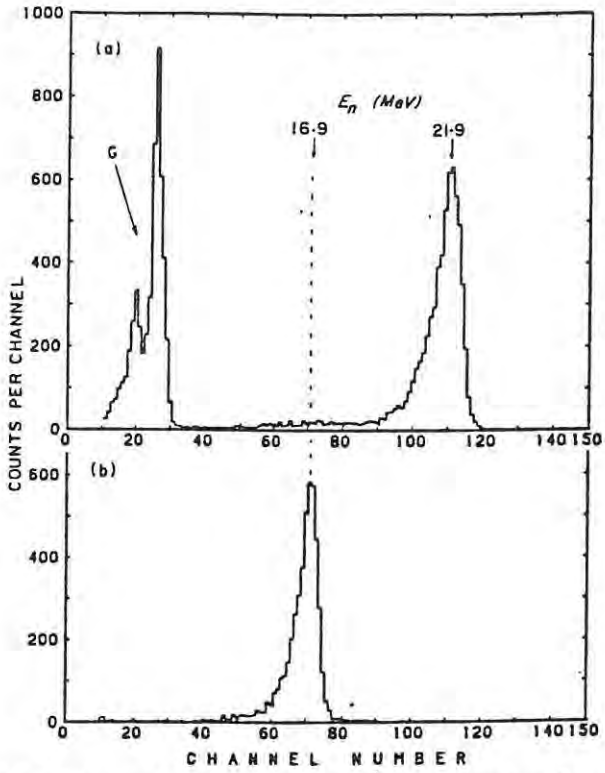

Fig. 4. Projected pulse height spectra for events satisfying the cut AB of fig. 3b, obtained using: (a) 21.9 MeV; and (b) 16.9 MeV neutrons incident along the *b*-axis of the crystal. The component G in (a), which corresponds to component G of fig. 3b, may be excluded by imposing a further cut in the $T-L$ plane (see fig. 6). The forward recoil peaks in (a) and (b) are calibrated in terms of the associated incident neutron energies.

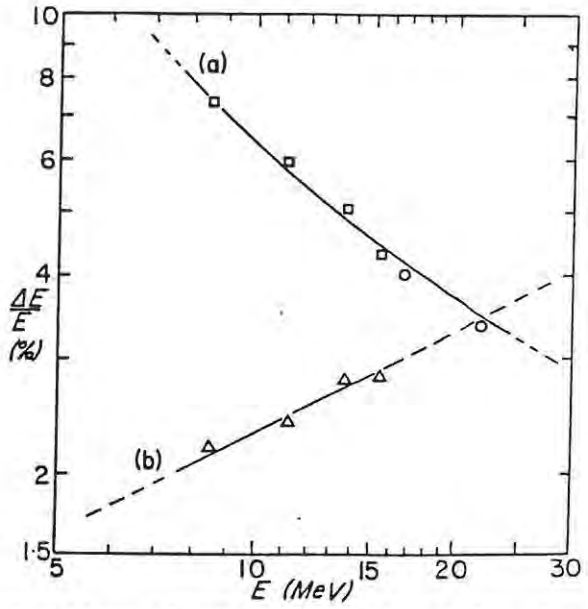

Fig. 5. Measured FWHM energy resolution $\Delta E/E$ as a function of neutron energy E for: (a) the DAS (circles and squares); and (b) the NE213 time-of-flight spectrometer (triangles). Circles in (a) show measurements made from fig. 4. Squares (a) and triangles (b) show measurements from peaks 0, 1, 2 and 5 of spectra in fig. 7.

and independent time of flight measurement of the neutron spectrum was made using an NE213 liquid scintillation detector placed 6.06 m away from the target in a direction at 10° to, and on the opposite side of, the deuteron beam.

Raw data obtained from the DAS are displayed in fig. 6, which shows plots of counts versus pulse height L and TAC output T for events which satisfy the cut AB of fig. 3b. The peaks numbered 0–5 in this figure are identified as forward deuteron recoils associated with the neutron groups from transitions to the ground state (0) and excited states (1–5) of ^{20}Ne in the ^{19}F(d, n)^{20}Ne reaction. Peaks 1–5 are attributed to the excited states at 1.74, 4.20, 4.96, 5.62 and 6.80 MeV respectively. The component labelled 6 in fig. 6 is associated with a group of several states in ^{20}Ne with excitation energies ranging from 7.16–9.15 MeV.

The structure labelled G in fig 6 is a low pulse height component from interactions of high energy neutrons with ^{12}C. It is similar to the component G in figs. 3b and 4 and may be excluded from the final projected L spectrum by imposing the $T-L$ cut indicated by the line CD, shown in fig. 6 and rejecting events with T-coordinates exceeding this cut.

The events selected for the final pulse height spectrum are thus those which satisfy two conditions: (1) the $L-S$ cut AB in fig. 3; and (2) the $L-T$ cut CD in fig. 6. These cuts ensure that only forward deuteron recoils contribute to the final pulse height spectrum and consequently that each discrete energy group in the incident neutron spectrum produces one peak only in the final spectrum.

The pulse height spectrum obtained from the data shown in fig. 6 has been regrouped in bins of equal energy, correcting for the nonlinear response of anthracene to deuterons [9] and for the measured energy dependence of the relative efficiency $\epsilon(E)$ of the DAS. The resulting energy spectrum is shown in fig. 7a. The associated energy spectrum measured simultaneously by time of flight, using the NE213 detector at 6.06 m, and corrected for the energy dependence of the efficiency of this detector, is shown for comparison in fig. 7b. Further measurements of $\Delta E/E$ for both the DAS, and the time-of-flight spectrometer were made from peaks 0, 1, 2 and 5 of fig. 7 and have been included in fig. 5.

5. Discussion

The spectra (fig. 7) obtained using the DAS and the time-of-flight detector agree well on the energies mea-

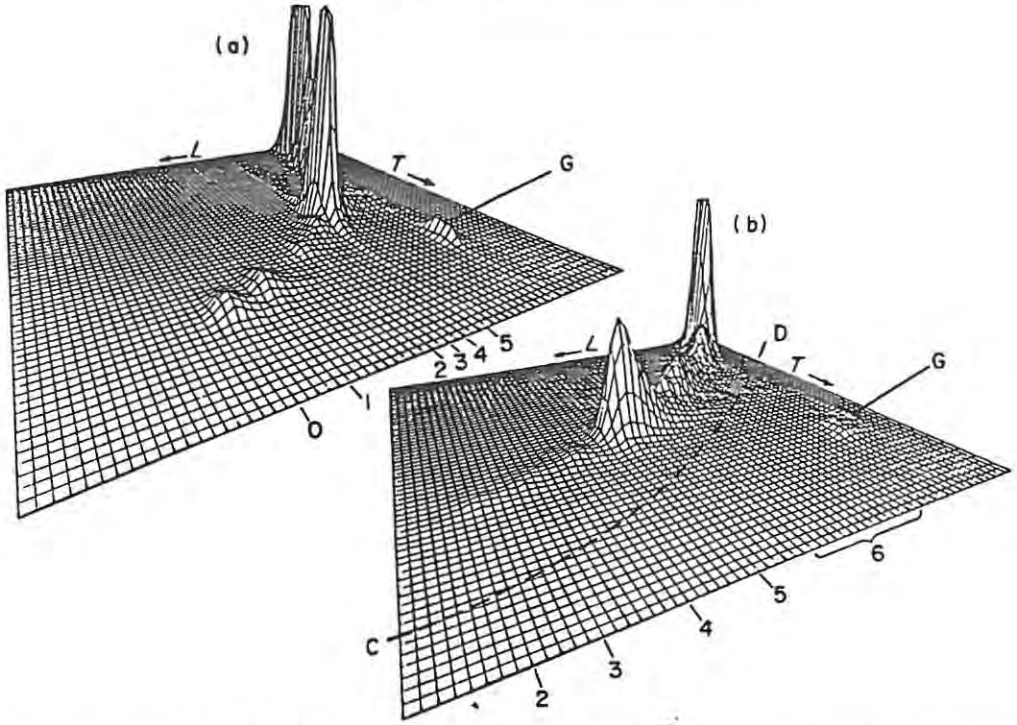

Fig. 6. Perspective views of counts vs pulse height L and TAC output T measured by the DAS for neutrons from the $^{19}F(d, n)^{20}Ne$ reaction at deuteron energy 4.8 MeV and lab angle 10°. Note that T is complementary to the neutron time of flight (see fig. 1). View (b) is an expanded display of the low-L region of view (a), with the L-dispersion increased by a factor of 3. Peaks labelled 0–5 are identified with transitions to different final states in ^{20}Ne (see text). The cut CD is used (see text) to exclude the low-L component G (see also figs. 3 and 4) associated with high-energy neutrons. The upper limits of the counts scales in (a) and (b) are 2000 counts per channel.

sured for peaks 0–5. The peak P in fig. 7b, which is not present in fig. 7a, is attributed to gamma rays originating from an upstream collimator slit in the deuteron beamline. Pulse shape discrimination was not applied on the NE213 detector during these measurements. Peak P was identified as a gamma peak by making an additional run using a shorter flight path. A comparison of relative peak intensities from the two spectra in fig. 7 also shows reasonable agreement if allowance is made for the different backgrounds of the two detectors and for the uncertainties introduced when correcting for the calculated energy dependence of the detection efficiency of the NE213 detector.

The main feature distinguishing the DAS from other single-detector, recoil scintillation spectrometers [2,3] is its inherent facility for selecting forward deuteron recoils. The other types of spectrometer depend on a computation to unfold the neutron spectrum from a measured pulse height spectrum and data of high statistical accuracy are required to unfold accurately, because the line shapes of the spectrometers include a wide range of recoil proton or recoil deuteron energies. The relatively sharp (forward-recoil) line shape of the DAS (fig. 4) has the advantage that the pulse height spectrum obtained after applying the cuts AB of fig. 3b and CD of fig. 6, is directly related to the neutron spectrum. If these cuts were implemented on-line, through use of a suitable data acquisition program, then the neutron spectrum could be displayed as it accumulated.

The time-of-flight parameter T (fig. 1) is not essential to the operation of the DAS. For measurements on a nonpulsed neutron beam, for example, the four electronic units on the left of fig. 1 would be omitted and only the parameters L and F would be recorded. Such measurements would then lack the facility of eliminating the low pulse height component associated with high energy neutrons (G in figs. 4 and 6) by means of a cut in the T–L plane, such as CD in fig. 6. Some other way of removing or correcting for the component G would be required if this component was significant.

The energy dependence of the energy resolution of the DAS (fig. 5a) shows $\Delta E/E$ proportional to $E^{-1/2}$ at high energies, as would be expected on the assumption that ΔE is governed predominantly by photoelectron statistics at the photomultiplier cathode. The nonlinear energy response of the crystal to deuterons accounts for the deviation from the $E^{-1/2}$ dependence at lower energies.

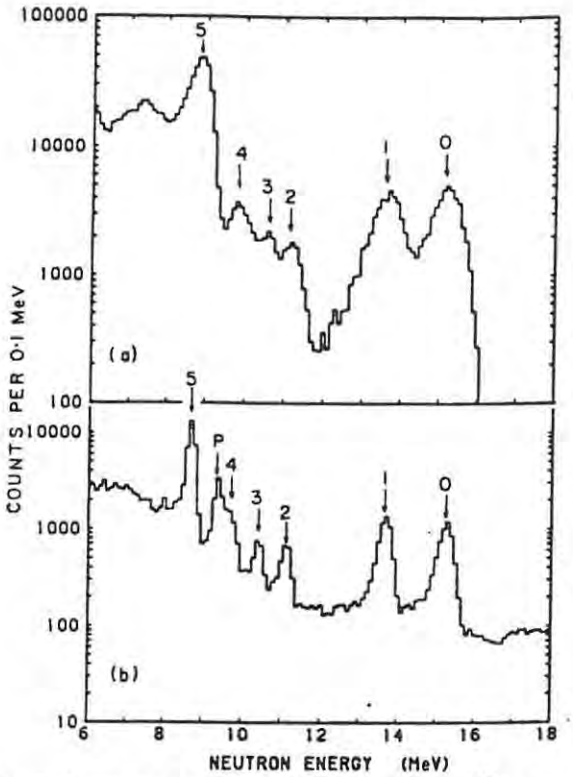

Fig. 7. Neutron spectra measured for the $^{19}F(d, n)^{20}Ne$ reaction at 4.8 MeV incident deuteron energy and laboratory angle 10°, using: (a) the DAS; and (b) the NE213 TOF spectrometer. The peaks 0–5 are identified as in fig. 6. Peak P in (b) is a spurious gamma peak (see text).

For the time-of-flight spectrometer timing uncertainties rather than distance uncertainties are expected to govern the energy resolution, so that $\Delta E/E$ should be proportional to $E^{1/2}$. Values of $\Delta E/E$ (fig. 5b) obtained from the data of fig. 7b are consistent with the expected variation of $\Delta E/E$ with E, and indicate a time-of-flight resolution of 215 ps m^{-1}, corresponding to a timing uncertainty of 1.3 ns (FWHM) for the pulsed beam and NE213 detector system at a flight path of 6 m.

The energy resolution characteristics displayed by the DAS are therefore seen to meet the requirements specified for neutron measurements in fusion research and neutron therapy. The resolution attained may also be suitable for certain nuclear physics experiments such as studies of pre-equilibrium emission of neutrons in neutron reactions at intermediate energies, or studies of few-nucleon systems in the same energy range. The energy resolution could be improved, for example, by using a selected photomultiplier of a type with superior characteristics, e.g. RCA8850 instead of RCA8575. Even with such improvements however, the potential of the DAS for nuclear structure studies is likely to be severely restricted by its limited energy resolution.

For the particular deuterated anthracene crystal used in this work, which was a cylinder of diameter 10 mm and length 21 mm, the crystal b-axis happened to lie parallel to the cylindrical axis. The DAS operating with b-axis parallel to the neutron beam therefore presented the maximum possible thickness (21 mm) to the beam. The detection efficiency for neutrons entering the crystal in this orientation is estimated to be a few percent in the energy range 5–30 MeV. The fact that the energy dependence of the relative detection efficiency can be measured effectively in situ and with minimum reliance on calculation should prove especially convenient. The efficiency measurement can be made as described here, using a set of monoenergetic neutron sources. Alternatively, a high-resolution time-of-flight measurement could be made with the DAS several metres away from an intense pulsed neutron source providing a wide range of neutron energies.

Finally, looking toward further possibilities at higher neutron energies, we note (fig. 5) that $\Delta E/E$ improves with increasing energy for the DAS in contrast to the time-of-flight spectrometer, for which the opposite is true. However, for work at neutron energies exceeding 60 MeV the dimensions of the present crystal begin to be outstripped by the recoil deuteron range and edge (i.e. deuteron escape) effects will become increasingly severe. An alternative to obtaining a larger crystal might be to add a deuterated liquid or plastic scintillator so as to form an extended telescope with the deuterated crystal as the final detecting element, still performing the key task of selecting the forward recoil peak.

Acknowledgements

We thank the Foundation for Research Development for financial support and for bursaries awarded to three of us (B.R.S.S., F.D.S. and M.S.A.). We also thank Mr. P.A. Back for his assistance in the construction of experimental equipment and the staff of the NAC Van de Graaff group for their cooperation and assistance during the experimental measurements.

References

[1] F.W.K. Firk, Nucl. Instr. and Meth. 162 (1979) 539.
[2] W.R. Burrus and V.V. Verbinski, Nucl. Instr. and Meth. 67 (1969) 181.
[3] F.D. Brooks and D.T.L. Jones, Nucl. Instr. and Meth. 121 (1974) 69.
[4] M. Steinbock, F.D. Brooks and I.J. van Heerden, Proc. 4th Int. Symp. on Polarization phenomena in nuclear reactions, eds. W. Gruebler and V Konig (Birkhäuser, Basel, 1976) p. 475.
[5] F.D. Brooks, P.M. Lister, J.M. Nelson and K.M. Dhuga, AIP Conf. Proc. (no. 69) on Polarization phenomena in

Nuclear Physics, eds. G.G. Ohlsen, R.E. Brown, J. Jarmie, W.N. McNaughton and G.M. Hale (American Institute of Physics, New York, 1981) p. 656.
[6] F.D. Smit and F.D. Brooks, Nucl. Phys. A465 (1987) 429.
[7] LINK Model 5010 Pulse Shape Discriminator, from LINK Systems, Halifax Rd., High Wycombe, Bucks, England HP12 3SE.
[8] G. Pauletta and F.D. Brooks, Nucl. Phys. A255 (1975) 267.
[9] F.D. Brooks, Nucl. Instr. and Meth. 162 (1979) 477.

Nuclear Physics **A505** (1989) 361–368
North-Holland, Amsterdam

ANALYZING POWER IN NEUTRON–PROTON SCATTERING AT 21.6 MeV

B.R.S. SIMPSON[1] and F.D. BROOKS

Physics Department, University of Cape Town, Rondebosch, 7700, South Africa

Received 16 June 1989

Abstract: The analyzing power in neutron–proton elastic scattering at 21.6 MeV was measured using polarized neutrons from the ^{3}H(d, $\vec{n}$)^{4}He reaction. The results agree with recent measurements and with revised earlier data in the vicinity of 22 MeV. The combined data give $\Delta^{P}_{LS} = (0.847 \pm 0.019)°$ and $\Delta^{D}_{LS} = (0.100 \pm 0.008)°$ and are consistent with predictions made from the Paris potential.

E

NUCLEAR REACTION ^{1}H(polarized n, n), $E = 21.6$ MeV; measured $A_y(\theta)$; deduced spin–orbit splitting parameters. Anthracene crystal target.

1. Introduction

Significant systematic errors have been noted recently [1–3]) in low-energy neutron–proton analyzing power $A_y(\theta)$ measurements made using polarized neutron beams from ($\vec{d}$, $\vec{n}$) polarization transfer reactions. This situation highlights the need for independent np experiments using different techniques and alternative sources of neutrons. Furthermore, for phase-shift analyses such as that now in progress in Nijmegen [2]), it is especially important that the accuracy of available $A_y(\theta)$ data be critically assessed, in order to identify discrepancies and, where possible, to resolve these discrepancies.

In this paper we consider the np analyzing power data at neutron energies 21–22 MeV. The $A_y(\theta)$ data of Morris *et al.* [4]) and Jones and Brooks [5]), hereafter referred to as MT and JB respectively, were important in an earlier evaluation and phase analysis of the np and pp data from 20–30 MeV, by Bohannon *et al.* [6]) in 1976. Morris *et al.* [4]) and Haeberli [7]) have noted discrepancies between the MT and JB data and Brock *et al.* [8]) have suggested that the JB data require adjustment from their published values to take into account revised values for the incident neutron polarization assumed in these measurements. We re-examine the MT and JB data in the light of these comments and together with more recent $A_y(\theta)$ measurements at 22 MeV, reported from Karlsruhe [9]). We also report new measurements of $A_y(\theta)$ at 21.6 MeV incident neutron energy.

[1] Present address: National Accelerator Centre, P.O. Box 72, Faure, 7131. South Africa.

2. New measurements of $A_y(\theta)$ at 21.6 MeV

The new measurements were made using an improved anthracene polarimeter based on that originally used by JB [5,10]). The improvements were designed: (i) to reduce systematic errors associated with instrumental asymmetries; and (ii) to calibrate, directly, the method the anthracene polarimeter uses to determine the neutron scattering angle. The anthracene polarimeter measures the left–right asymmetry of the associated recoil proton in np scattering without detecting the scattered neutron. The scatterer is an anthracene scintillation crystal which also detects the recoil proton. The method utilizes the directional sensitivity of the scintillation characteristics of the crystal [5,10]) to measure left–right asymmetries of recoil protons. The pulse height and pulse shape outputs from the crystal are the basic observables from which this asymmetry and also the associated neutron c.m. scattering angle θ are determined. The pulse height and pulse shape outputs are sensitive to the direction of the recoil proton relative to the axes of the crystal [10]). The crystal was mounted on a rotating holder with the axis of rotation accurately aligned to the incident neutron beam direction (fig. 1). It could thus be easily and accurately "flipped" through 180° about the neutron beam direction, so as to alternate between the two symmetrical orientations in which its own axes were aligned so as to give maximum sensitivity for left–right asymmetry measurements [5,10]). The alignment and symmetric design of this system, including for example the use of two stationary photomultipliers to view the crystal (fig. 1), ensured that instrumentally-based asymmetries were kept to a minimum in the measurements. In addition, the offline analysis of the data included checks designed to identify and correct residual instrumental asymmetries without interfering with the true asymmetries originating

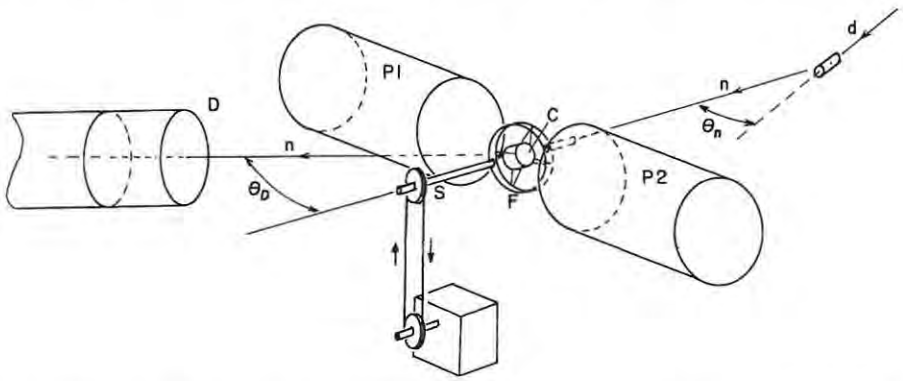

Fig. 1. Anthracene polarimeter (schematic) showing the crystal C mounted on a light aluminium frame F attached to a light, hollow rotating shaft S. The crystal is removed when aligning the axis of rotation parallel to the incident neutron beam. A light aluminium housing (not shown) supports S and encloses the photomultipliers P1 and P2 which remain stationary in the laboratory. The neutron detector D (NE213 liquid scintillator, 50 mm diam × 50 mm), at angle θ_D to the neutron beam, is used to calibrate the measurement of the neutron scattering angle by C (see text).

in np scattering. These checks and correction procedures were themselves exhaustively tested and checked, using artificial data sets generated by computer.

The measurement of the scattering angle θ from the pulse height and pulse shape data was calibrated by using an additional scintillator detector (NE213, 50 mm diam × 50 mm – see fig. 1) to record coincidentally-detected scattered neutrons. Coincidences identified using the neutron time-of-flight between the two scintillators were recorded with the second detector placed at different laboratory angles in the range 20°–80°. Coincidence events constituted a small sample of the scatters recorded by the anthracene. They were tagged throughout the experiment and the tagged events, taken over the range of associated c.m. scattering angles used, formed the basis for the calibration of the scattering angle measurement.

The scintillation polarimeter has a number of advantages. For example: (i) It has a detection efficiency approaching 100% because essentially all primary scatters, including non-planar events, are detected; (ii) data are collected simultaneously over a wide range of scattering angles; and (iii) multiple neutron scattering is estimated to have a negligible effect on the observed asymmetry because of the small (<3 cm^3) size of the scintillation crystal target. It is also noted that, since only primary scatters in a single detector are observed, the instrumental effect due to the strong p-wave resonance in neutron scattering from ^{12}C, as described in ref. [3]), is avoided. The analyzing power at 21.6 MeV was measured using neutrons from the ^{3}H(d, $\vec{n}$)^{4}He reaction as this was the only convenient source of polarized neutrons locally available. While inferior, in terms of neutron polarization obtained, to a ($\vec{d}$, $\vec{n}$) source, the (d, $\vec{n}$) reaction is however free of the systematic effects recently discovered in ($\vec{d}$, $\vec{n}$) sources and associated with the variation of neutron flux across the scattering sample [1,2]). Tritium in a gas cell at 0.75 atm was bombarded with 5.0 MeV pulsed deuterons produced by the 5.5 MV Van de Graaff accelerator at the National Accelerator Centre, Faure. The deuterons were delivered in 1 ns pulses at 500 ns intervals with a mean current of about 1 μA. Neutrons emitted at angles $\theta_n = 0°$ or 20° to the deuteron beam were used in the experiments. The unpolarized 22 MeV neutron beam emitted at 0° was used to collect null polarization data in order to monitor instrumental asymmetries, of whatever origin, in the experiment. For the analyzing power measurements, the neutron reaction angle selected was 20°, providing an incident neutron beam of polarization 0.25 ± 0.01 according to ref. [11]). In each case the primary component in the neutron spectrum was selected by time-of-flight measured over a 0.30 m flight path from the tritium target to the crystal. Approximately one third of the beam time was devoted to null runs, which were alternated with polarization runs at intervals of 1 or 2 days.

Facilities for rapid reversal of the incident neutron beam polarization, now so common in polarization experiments, were not available. Using the modified anthracene polarimeter however, this disadvantage is offset by the ease with which the crystal may be flipped through 180° about the beam axis, as described earlier. This inverts the measuring laboratory, in effect, instead of the beam polarization.

The crystal was flipped in cycles of 1–2 min, depending on the event rate, and events recorded in the two different crystal orientations were tagged for identification in the subsequent offline analysis. The primary data recorded in the experiment were thus the pulse height and pulse shape coordinates (two parameters) for each event, tagged according to crystal orientation and recorded on event (magnetic) tape.

In the offline data reduction the two-parameter spectra were divided into bins, each bin corresponding to a certain range of recoil angles as outlined in ref. [10]). However, the following important modifications were made to the procedures described in ref. [10]): (a) the angle bins were defined using the direct calibration data obtained coincidentally in the runs; (b) improved methods [12]) were used to detect and remove residual instrumental asymmetries and to correct for the effects of recoil proton escape from the crystal on the measurement; and (c) an error in eq. (15) of ref. [10]) which leads to an underestimate of the uncertainty on the experimentally measured left-right asymmetry, was corrected.

With reference to point (c), let N_{AL}, N_{BL}, N_{AH} and N_{BH} represent the basic information (number of counts) recorded for a particular angle bin, $\theta \pm \Delta\theta$. Subscripts A and B denote the two orientations of the crystal and subscripts L and H denote lower and higher values of the pulse shape coordinate as defined in ref. [10]). Then, assuming an equal number of events N in the A and B orientations, the asymmetry $\varepsilon(\theta)$ is obtained as in ref. [10]) eq. (12), from

$$\varepsilon(\theta) = (\pi/4N)(N_{AL} + N_{BH} - N_{AH} - N_{BL}) , \tag{1}$$

where $N = N_{AL} + N_{AH} = N_{BL} + N_{BH}$. The statistical uncertainty $\Delta\varepsilon(\theta)$ is incorrectly estimated in ref. [10]). Deriving from Bernoulli statistics, it can be shown [12]) that $\Delta\varepsilon(\theta)$ should be estimated from

$$\Delta\varepsilon(\theta) = (\pi/2N)\{[N_{AL}(N - N_{AL})/N] + [N_{BH}(N - N_{BH})/N]\}^{1/2} . \tag{2}$$

The analyzing power is obtained from

$$A_y(\theta) = \varepsilon(\theta)/P_0 , \tag{3}$$

where P_0 is the incident neutron beam polarization.

The data were analyzed using four angle bins of full width corresponding to 20° c.m. scattering angle (10° lab angle) and a fifth bin covering the range $\theta = (77.5 \pm 2.5)°$. This smaller bin was imposed by the electronic threshold of the measurement. The results are shown in table 1. The angles listed are the centres of the angle bins used and correspond within 0.5° to the associated mean c.m. scattering angles. The final $A_y(\theta)$ values are weighted averages of results from four internally consistent independent experimental runs, made using two different anthracene crystals, one crystal being a cylinder (15 mm diam × 15 mm) and the other irregularly shaped, of volume 1.5 cm^3. The final values of $A_y(\theta)$ for each scattering angle were obtained by weighting the four individual measurements each by the inverse squares of their statistical errors when determining the average. The results listed in table 1 include

TABLE 1

The present np analyzing power values at 21.6 MeV

θ (deg)	$A_y(\theta)$	$\Delta A_y(\theta)$	
		(partial)	(total)
77.5 ± 2.5	0.0575	0.0065	0.0073
90 ± 10	0.0469	0.0031	0.0046
110 ± 10	0.0372	0.0036	0.0050
130 ± 10	0.0278	0.0042	0.0054
150 ± 10	0.0089	0.0066	0.0074

corrections for instrumental asymmetries which were determined from the associated null runs made at source reaction angle $\theta_n = 0°$. The uncertainties $\Delta A_y(\theta)$ shown in table 1 are the partial statistical uncertainties (column 3) calculated from eq. (2) for the uncorrected measurements alone and the total statistical uncertainties (column 4) which include an additional component ΔA_{null}, associated with the introduction of the correction for instrumental asymmetries. A value of $\Delta A_{\text{null}} = 0.0034$ was estimated from the uncertainties determined (using eq. (2)) from the null measurements, averaged over angle. The total uncertainties (column 4) were obtained by adding ΔA_{null} in quadrature to the partial uncertainties (column 3). The 4% uncertainty in the incident beam polarization adds a proportional systematic uncertainty to the data in table 1. This is small in comparison with the statistical uncertainties shown in the table.

3. Discussion

The present measurements (table 1) are plotted in fig. 2 together with the Karlsruhe data [9]) and two other sets of measurements, set A and set B, which have been derived from the earlier JB [5]) and MT [4]) data, as follows. The JB data have been revised to take into account the more recent polarization values of Smith and Thornton [11]) for the ^{3}H(d, $\vec{n}$)^{4}He reaction used in the experiment. The corrected data have been obtained from the original left-right asymmetry data given in the Ph.D thesis of Jones [13]), by recalculating the weighted average analyzing power for each angle using the revised incident neutron beam polarization data. The corrected data are shown as set A in table 2. They differ only marginally from the values calculated by Brock *et al.* [8]), who first indicated the need for this correction.

The data labelled set B in fig. 2 were calculated as follows from the MT data [4]). We note that the incident neutron polarization of $P_0 = 0.35$ quoted by MT is consistent with the data of ref. [11]) for the energy and angle of their measurement. However, if one refers to the measured asymmetries quoted in table 1 of MT it appears that their analyzing powers have been calculated using $P_0 = 0.50$ instead of $P_0 = 0.35$. Using $P_0 = 0.35$ we obtain the values listed and plotted as set B in table 2 and fig. 2.

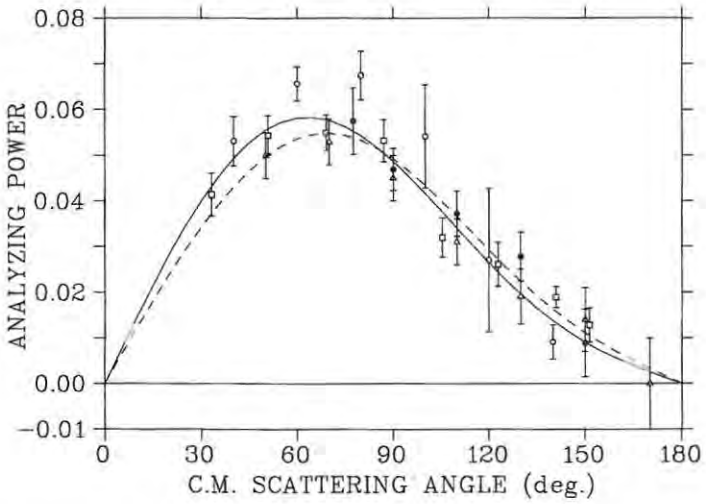

Fig. 2. Analyzing power in np elastic scattering at 21.1–22 MeV, showing experimental data (table 2) from set A (triangles), set B (open circles), Karlsruhe [9]) (squares) and the present measurements (solid circles). The broken curve shows the fit (based on eq. (4)) to the combined experimental data, excluding set B. The continuous curve shows the prediction calculated from the Paris potential.

The agreement between the experimental data in fig. 2 is satisfactory, except for the systematically higher values of set B. The situation is very different from that noted in earlier comparisons [4,6–8]).

To facilitate further comparisons it is convenient to parameterize the experimental data and theoretical predictions in a form suggested by Mutchler and Simmons [14]). They show that for orbital angular momenta up to $L_{max} = 2$, the product of analyzing power and differential cross section can be fitted by the function

$$A_y(\theta)\sigma(\theta) = \sin\theta(A + B\cos\theta)\,, \tag{4}$$

TABLE 2

Revised analyzing powers calculated from the JB data [5]) (set A) and the MT data [4]) (set B)

SET A (21.6 MeV)		SET B (21.1 MeV)	
θ (deg)	$A_y(\theta)$	θ (deg)	$A_y(\theta)$
50	0.050 ± 0.004	40	0.0531 ± 0.0054
70	0.053 ± 0.004	60	0.0657 ± 0.0037
90	0.045 ± 0.004	80	0.0675 ± 0.0053
110	0.031 ± 0.004	100	0.0541 ± 0.0113
130	0.019 ± 0.005	120	0.0270 ± 0.0157
150	0.014 ± 0.006	140	0.0091 ± 0.0038
170	0.000 ± 0.008		

where θ is the c.m. scattering angle. The parameters A and B are related to the phase parameters Δ^{l}_{LS} representing combinations of triplet l-wave phase shifts arising from the spin-orbit part of the nucleon-nucleon interaction. Approximations for the Δ^{l}_{LS} are derived from expressions given by Chisholm *et al.* [15]), where it is assumed that the phase shifts for $L \geqslant 1$ are small, and the mixing parameter is zero:

$$\Delta^{\mathrm{P}}_{LS} = 4k^2A/(12\sin^2({}^3\mathrm{S}_1)),$$
$$\Delta^{\mathrm{D}}_{LS} = 4k^2B/(60\sin^2({}^3\mathrm{S}_1)), \qquad (5)$$

where k is the centre-of-mass wave number of the incident neutron. The magnitude of the analyzing power depends on the spin-orbit splitting Δ^{P}_{LS} of the $T=1$ triplet P-waves, whereas the shape relates to the spin-orbit splitting Δ^{D}_{LS} of the $T=0$ triplet D-waves.

A least squares fit to eq. (4) was made for each of the following data sets: the present data; the Karlsruhe [9]) data; and the set A data (revised JB) of table 2. The set B data have been omitted because the validity of the procedure used to derive them from the MT values is questionable. A fit was also made to the combined data (3 sets) and this is shown together with the experimental data in fig. 2. The A and B values obtained from these fits are shown in table 3.

The data are also compared in fig. 2 with the analyzing power at 21.6 MeV as predicted by the Paris potential. No cogniscance was taken of the Mott-Schwinger interaction which leads to large negative values of $A_y(\theta)$ at very forward angles as shown in ref. [2]). The Paris potential phase shifts at 21.6 MeV were available and A and B have been calculated directly from eq. (5) and the p- and d-wave spin-orbit combinations of these phase shifts:

$$\Delta^{\mathrm{P}}_{LS} = \tfrac{1}{12}(-2{}^3\mathrm{P}_0 - 3{}^3\mathrm{P}_1 + 5{}^3\mathrm{P}_2),$$
$$\Delta^{\mathrm{D}}_{LS} = \tfrac{1}{60}(-9{}^3\mathrm{D}_1 - 5{}^3\mathrm{D}_2 + 14{}^3\mathrm{D}_3). \qquad (6)$$

The A and B values that were determined thus are shown together with those from the least squares fits in table 3. The values of A and B derived from the fit to the combined data show good agreement with those obtained from the Paris potential.

TABLE 3

Comparison of A and B [see eq. (4)] from fits to the analyzing power data and as derived from the Paris potential phase shifts

	Energy (MeV)	A (fm^2)	B (fm^2)
present	21.6	0.1687 ± 0.0077	0.0844 ± 0.0218
set A	21.6	0.1578 ± 0.0037	0.1096 ± 0.0089
Karlsruhe [9])	22 ± 1.5	0.1699 ± 0.0070	0.0990 ± 0.0128
combined	21.6	0.1688 ± 0.0038	0.0994 ± 0.0079
Paris potential	21.6	0.1555	0.1064

None of the analyzing power measurements at 21–22 MeV show any indication of zero crossing at large scattering angles, which implies that any F-wave contribution is very small. This is in agreement with the 25 MeV np analyzing power measurements made at Wisconsin [1]).

To summarise, the previous discrepancies in np analyzing power values in the vicinity of 21.6 MeV appear to be resolved, with the three data sets, set A (revised JB), Karlsruhe and the present results showing good agreement. A fit to the combined np data of these sets gives (for $^3S_1 = 84.0°$) $\Delta^P_{LS} = (0.847 \pm 0.019)°$ and $\Delta^D_{LS} = (0.100 \pm 0.008)°$. A proper assessment of whether or not there is evidence for isotopic spin splitting of the triplet P-wave phase shifts (i.e. $\Delta^P_{LS}(\mathrm{np}) - \Delta^P_{LS}(\mathrm{pp})$) in the vicinity of 25 MeV may now be possible by including the data under discussion in an updated phase shift analysis.

We are grateful to Prof. H.G. Miller for supplying the Paris potential phase shift parameters, to Dr. D.T.L. Jones for valuable discussions, to Mr. P.A. Back for construction of equipment and to the staff of the NAC Van de Graaff for their assistance. We also thank the Foundation for Research Development for financial support and a bursary to one of us (BRSS).

References

1) J. Sromicki, D. Holslin, M.D. Barker, P.A. Quin and W. Haeberli, Phys. Rev. Lett. **57** (1986) 2359
2) W. Tornow, C.R. Howell, M.L. Roberts, P.D. Felsher, Z.M. Chen, R.L. Walter, G. Mertens and I. Šlaus, Phys. Rev. **C37** (1988) 2326
3) D. Holslin, J. McAninch, P.A. Quin and W. Haeberli, Phys. Rev. Lett. **61** (1988) 1561
4) C.L. Morris, T.K. O'Malley, J.W. May, Jr. and S.T. Thornton, Phys. Rev. **C9** (1974) 924
5) D.T.L. Jones and F.D. Brooks, Nucl. Phys. **A222** (1974) 79
6) G.E. Bohannon, T. Burt and P. Signell, Phys. Rev. **C13** (1976) 1816
7) W. Haeberli, AIP Conf. Proc. on nucleon-nucleon interactions, Vancouver, 1977, ed. H.W. Fearing, D.F. Measday and A. Strathdee (American Inst. of Phys., New York, 1978) p. 1
8) J.E. Brock, A. Chisholm, J.C. Duder, R. Garrett and J.L. Poletti, Nucl. Phys. **A361** (1981) 368
9) J. Wilczynski, J. Hansmeyer, F.P. Brady, P. Doll, W. Heeringa, J.C. Hiebert, H.O. Klages and P. Plischke, Nucl. Phys. **A425** (1984) 458
10) F.D. Brooks and D.T.L. Jones, Nucl. Instr. Meth. **121** (1974) 77; **121** (1974) 69
11) J.R. Smith and S.T. Thornton, Nucl. Phys. **A187** (1972) 433
12) B.R.S. Simpson, Ph.D thesis, (1986) University of Cape Town
13) D.T.L. Jones, Ph.D thesis, (1972) University of Cape Town
14) G.S. Mutchler and J.E. Simmons, Phys. Rev. **C4** (1971) 67
15) A. Chisholm, J.C. Duder, R. Garrett and J.L. Poletti, Phys. Rev. **C21** (1980) 1653

B.R.S. Simpson and F.D. Brooks
Analyzing power in neutron-proton scattering at 21.6 MeV
Nucl. Phys. A505 (1988) 361-368

FIRST DIRECT MEASUREMENT of $\alpha - \mu$ STICKING in $dt - \mu$CF

M.A. Paciotti, O.K. Baker, J.N. Bradbury, J.S. Cohen, M. Leon,
H.R. Maltrud, L.L. Sturgess,
Los Alamos National Laboratory, Los Alamos, N.M.,

S.E. Jones, P. Li, L.M. Rees, E.V. Sheely, J.K. Shurtleff, S. F. Taylor,
Brigham Young University, Provo, Utah,

A.N. Anderson,
Idaho Research, Boise, Idaho,

A.J. Caffrey, J.M. Zabriskie
Idaho National Engineering Laboratory, Idaho Falls, Idaho

F.D. Brooks, W.A. Cilliers, J.D. Davies, J.B.A. England, G.J. Pyle, G.T.A. Squier,
University of Birmingham, Chilton, England

A. Bertin, M. Bruschi, M. Piccinini, A. Vitale, A. Zoccoli,
University of Bologna, Bologna, Italy

V.R. Bom, C.W.E. van Eijk, H. de Haan,
Delft University of Technology, Holland, and

G.H. Eaton,
Rutherford-Appleton Laboratory,
Didcot, Oxfordshire.

ABSTRACT

Both $(\alpha\mu)^+$ and α particles have been observed in coincidence with fusion neutrons in a gaseous $D-T$ target at 2.8×10^{-3} liquid-hydrogen density. The initial muon sticking probability in muon-catalyzed $d-t$ fusion, measured directly for the first time, is $(0.80 \pm 0.15 \pm 0.12$ systematic)% in agreement with 'standard' theoretical calculations. However, this measured value does not support those theories that invoke special mechanisms to alter the initial sticking value.

INTRODUCTION

There has been a need for some time for a direct measurement of the $\alpha - \mu$ sticking probability in muon-catalyzed $d-t$ fusion.[1] The muon loss due to this sticking phenomenon is the most severe limitation to the ultimate fusion yield χ. The sticking probability, ω_s, has been inferred from the total muon loss rate after detailed corrections[2,3,4,5], and from x-ray measurements[6,7] plus cascade calculations[8,9]. Vorobyov expects that the LNPI direct ionization chamber method, so successful in $dd - \mu CF$, will work for measuring sticking in $dt - \mu CF$;[10] so far an upper limit of 1% comes from this work.[11]

The present paper describes the first direct measurement of the $\alpha - \mu$ sticking probability, using a low density ($\approx 10^{-3}$ *lhd*) $D-T$ mixture.[12] As such, it comes very close to measuring the initial sticking probability in $dt - \mu CF$. Extension of the this work is presently underway at Rutherford-Appleton Laboratory (RAL).[13]

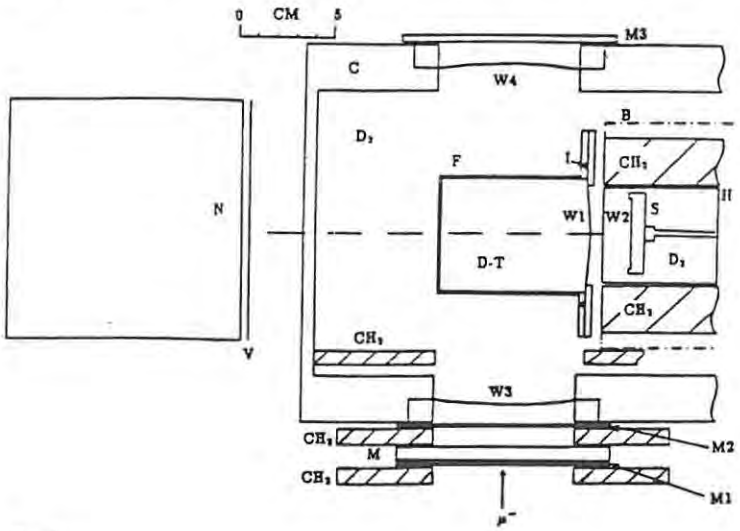

Fig. 1.

F: Beryllium target flask, 6.4 cm diameter, 7.6 cm long; cylindrical walls are 1.5 mm thick; contains $D-T, C_t = 0.4$.
W1,W2: 1.5 micron mylar windows aluminized 1600 $\mathring{A}$ on T_2 side.
I: Pure indium 'O'-ring sealing the target window.
S: Silicon surface barrier detector, 1000 mm^2, 100 microns thick.
M1,M2,M3: Muon telescope counters, each 1.6 mm thick
N: Neutron counter, Bicron liquid scintillator (BC-501), 12.7 *cm* in diameter and 12.7 cm in depth; 1.6 mm veto counter in front.
B: Dotted line indicates poletip of 1 kG permanent magnetic field.
C: Secondary container for D_2, 12 *l* volume, Al walls, Lucite lid, all seals Viton 'O'-rings.
W3,W4: Heat treated Al beam entrance and exit windows, 0.13 mm thick.
H: Detector housing, sealed, cooled, and moveable; contains D_2.
M: Moderator for slowing down 60-MeV/c μ^- beam.
V: Charged particle veto counter.

M.A. Paciotti, O.K. Baker, J.N. Bradbury, J.S. Cohen, M. Leon, H.R. Maltrud, L.L. Sturgess, A.N. Anderson, A.J. Caffrey, J.M. Zabriskie, F.D. Brooks, W.A. Cilliers, J.D. Davies, J.B.A. England, G.J. Pyle, G.T.A. Squier, A. Bertin, M. Bruschi, M. Piccinini, A. Vitale, A. Zoccoli, V.R. Bom, C.W.E. van Eijk, H. de Haan and G.H. Eaton
First direct measurement of alpha-muon sticking in d-t muon-catalyzed fusion
A.I.P. Conf. Proc. 181 (1989) 38-51

The CONCEPT of the LAMPF EXPERIMENT

The $(\alpha\mu)^+$ ions produced by "sticking" events and the α-particles formed in the remaining 99^+ % majority of events are detected in coincidence with the 14.1 MeV neutron and are easily separable by range in the low pressure $D-T$ gas; the density is dictated by the very limited ranges of these ions. The fact that the ions are produced at 180° from the neutrons is useful for background rejection. Triggers due to (μ^-, pn) and $(\mu^-, p2n)$ captures in the target flask are substantially suppressed since the charged particle is not similarly correlated in angle with the neutron[14]. Beryllium, chosen for its good properties in containing tritium and its very low muon-capture probability, is the best target material for use in the LAMPF beam structure. The full μ^- beam is directed on the target to achieve an adequate event rate; many muons are therefore present in the target at one time, and there is then almost no possibility to measure the fusion time with respect to the muon arrival time. (This will be possible using the RAL pulsed muon beam.) Even though high-Z materials do not exhibit many charged particles in coincidence with neutrons, the high capture probability produces overwhelming singles rates in both neutron and silicon detectors.

LAYOUT

Features of the setup are shown in Fig. 1. Most important, the silicon detector must be protected from tritium beta radiation. T_2 diffuses out through the target window W1, limited primarily by the aluminum coating, at a measured rate of 2.5% per day and is diluted by the large volume of the secondary container. The second window W2 then keeps this dilute mixture at a distance from the detector where the intervening D_2 region is guarded by a magnetic field. The detector housing is sealed except for a long pressure-equilibrating capillary, necessary when the detector housing is cooled; cooling to -7° C improved the timing resolution from 3.5 to 3.0 ns. Target filling is challenging since the windows cannot support much differential pressure; as a molecular sieve cold trap cleans the incoming premixed $D-T$ gas, D_2 is admitted to the secondary container at a rate that maintains low differential pressure. Backgrounds are measured in an identical apparatus filled entirely with D_2 and normalized to incoming muons. A ^{233}U source, insertable between W1 and W2, gave identical energy and timing calibrations for each apparatus.

The character of the LAMPF experiment is revealed by typical rates; both peak rates during the LAMPF pulse and average rates are given in Table I. (During this particular run period, a thin production target caused the rates to be reduced by a factor of 3 below normal.) The neutron rate n is taken after pulse-shape discrimination[15]; the α rate includes noise; $\alpha\cdot(\gamma+n)$ is the trigger rate formed with a 150 ns coincidence width. Clearly the fusion process in not observable in either the neutron or the α-singles rate.

TABLE I. Typical rates.

RATE	*M1M2M3*	$\gamma+n$	n	α	$\alpha\cdot(\gamma+n)$
Peak/s	2.6×10^6	1.5×10^4	560	1440	2.8
Average/s	1.4×10^4	810	30	80	0.15

SYSTEMATIC EFFECTS

The factor 4 ratio between $(\alpha\mu)^+$ and α ranges was utilized by two different schemes; in an earlier experiment both ions were detected concurrently, while for the latest data, optimum detection of each ion required different fill pressures. Table II compares merits and systematic effects for each method. At 650 Torr the experiment is severely rate-limited and (at LAMPF) background-limited. We could not have been certain that $(\alpha\mu)^+$ had been seen without a higher density run. Using the dual pressure scheme, a strong $(\alpha\mu)^+$ signal is seen. However, the usefulness of the data may be limited by the systematic uncertainty of yield χ scaling with density ϕ. This scheme presents a good opportunity to measure stripping effects.

TABLE II. Systematic effects.

$(\alpha\mu)^+$ and α detected concurrently :

1) Single fill, $\phi = 1.0\times10^{-3}$ *lhd*, 650 Torr.
2) α's are collected from only 1/2 of target volume nearest the window.
3) μ^- stopping distribution must be well known.
4) α ranges must be known very well.
5) Gas impurity only affects the fusion yield χ , not the sticking result.
6) Slightly lower stripping since $(\alpha\mu)^+$ energies are higher.
7) No $t\mu$, $d\mu$ diffusion effect.
8) C_t only alters the yield χ.

Separate $D-T$ fills for $(\alpha\mu)^+$ and α observation :

1) Two fills, $\phi = 7.6\times10^{-4}$ $(490\ Torr)\alpha$ and $\phi = 2.8\times10^{-3}(1800\ Torr)(\alpha\mu)^+$.
2) Both ions are collected from the full target volume.
3) Assume muon stopping rate and distribution scales with density ϕ. The μ^- stopping distribution only comes into stripping and diffusion corrections.
4) Most uncertainty in range cancels out.
5) Gas impurity necessitates an important systematic correction.
6) Stripping is higher but still well known.
7) $t\mu$ and $d\mu$ may diffuse to the walls at the low density.
8) C_t change due to tritium diffusing out the window will alter the fusion yield at each pressure and thereby confuse the normalization.

A Monte Carlo code is useful for evaluating these systematic effects, but the experiment is not so complicated that the code is essential to the analysis. Figure 2 displays the distributions of fusion events in the dual-pressure scheme, reflecting principally the muon stopping distribution, detector solid angles, and particle range. α-particles originating near the back of the flask fall below the 0.7 MeV threshold and are not detected. The code finds a 93% active volume, whereas the $(\alpha\mu)^+$ active volume is 100%. According to the prescription, we could have used about 460 Torr to avoid this correction, but we favored instead a slightly higher density to obtain a higher χ. The overall efficiency is small (0.08% per stopped μ^-), independent of density, and, aside from the volume correction, cancels out of the sticking result.

Variation in the muon stopping intensity within the target volume was measured by counting the ^{56}Mn activation[16] of thin iron foils placed inside the non-tritiated target. Compared with the central maximum, the intensity falls to 1/2 along the axis near the window and the back wall. The predicted stop rate in hydrogen, based on these foils, was 4.7×10^{-4} μ^- stopped per incident μ^- at 490 Torr.

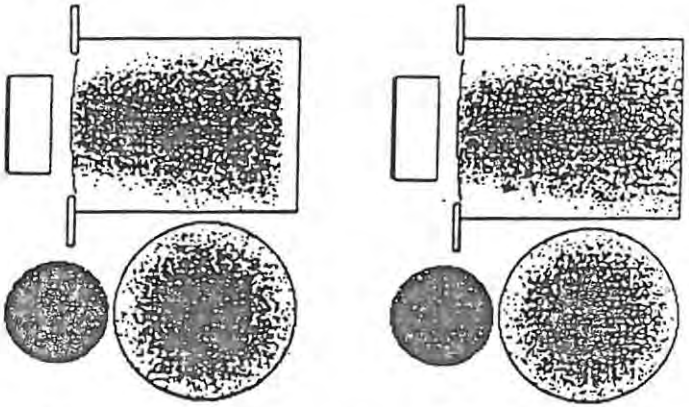

Fig. 2. Left side: 490 Torr; α. Active volume is 93% of target volume. Right side: 1800 Torr; $(\alpha\mu)^+$ ions are detectable from the full target volume. Here, the α's , having about 1/4 the range of the $(\alpha\mu)^+$ ions, are below threshold. The α locus at the detector and the projection along the target axis of the fusion distribution are shown below.

The Monte Carlo uses the Bichsel range code,[17] which was verified by degrading five α energies from the ^{233}U source through various gas thickness obtained by moving the detector. These checks were done between data runs utilizing the same windows and fill gas as fusion particles. Good consistency was obtained, and we conclude that the calculated range of a 3.5-MeV α degraded to the 0.7 MeV threshold was verified to about 2 mm.

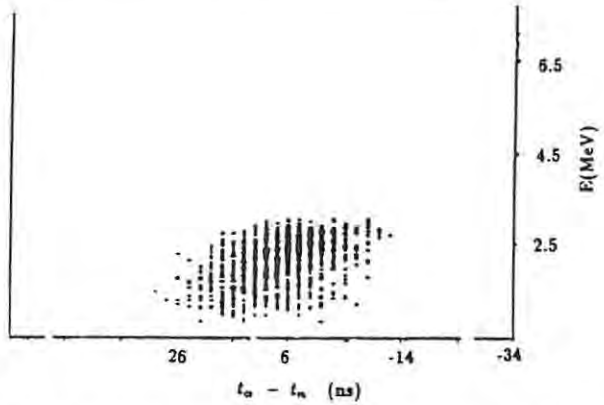

Fig. 3. Monte Carlo prediction for $(\alpha\mu)^+$ at 1800 Torr. Time vs energy correlation is evident. The higher energy $(\alpha\mu)^+$'s arrive early.

Corrections for stripping are easily and accurately given by the Monte Carlo using the energy-dependent stripping cross sections for $D-T$ gas, aluminum, mylar, and D_2 gas.[18] Table III lists stripping for the several materials assuming an average energy at each position. It can be used to assess the relative effect of the gas and of the windows, which are approximately equal.

TABLE III. Stripping probabilities.

STRIPPING MATERIAL	*STRIPPING PROBABILITY*
3.9 *cm avg.* $D-T$ *pathlength at* 1800 *Torr*	6.5%
1600 Å Al coating on target window	1.3%
1.5 *micron mylar target window*	4.0%
1.0 *cm* D_2 *at* 1800 *Torr*	1.0%
1600 Å Al coating on detector window	1.1%
1.5 *micron mylar detector window*	3.9%
1.5 *cm* D_2 *at* 1800 *Torr*	2.1%

However note that many of the stripped $(\alpha\mu)^+$ still have enough energy to be detected above threshold as α particles, particularly if the stripping occurs in

the detector window or the last 1.5-cm D_2 region. The net result after the code has considered all of the above (stopping distribution, solid angle, energy loss, stripping at proper energies, and detection threshold) is that only 16% of the initially produced $(\alpha\mu)^+$ are unobserved. This effective stripping, $R_{eff} = 0.16$, is quite small considering that more efficient strippers such as aluminum and mylar have been introduced. Stripping is significantly less than that seen when the ion is allowed to stop fully in a medium[8], and convinces us that initial sticking is close at hand in this direct method. Verification of stripping calculations could be accomplished in these experiments, for example, by testing the effect of additional mylar. Reduced backgrounds at RAL will also be helpful. Fusion α particles generated between W1 and W2 could simulate $(\alpha\mu)^+$ events; however, C_t is so low there that the correction to ω_s^o is estimated to be much less than 1% of ω_s^o and is therefore neglected.

DATA

The pulse-shape discrimination[15] picture is given in Fig. 4 showing the location of the cut that selects the approximately 4% neutron signal from the remaining γ's that arise mainly from muon-decay electrons.

The α-data are presented first since the signal is so prominent (Fig. 5). Only the neutrons have been selected, and prompt muons have been rejected. The time difference between the α-ion and the fusion neutron is plotted along the abscissa while the ion energy is plotted along the ordinate. The box drawn shows the region where the α's are expected from Monte Carlo predictions. The position of the box along the time axis cannot be known from measurement, so the α-data themselves are used as a guide to positioning the box. $(\alpha\mu)^+$ ions are also expected in this plot, but with such low rate that background masks them.

The $(\alpha\mu)^+$ spectrum for all data taken at 1800 Torr is shown in Fig. 6, where the axes are the same as in Fig. 5. A quick comparison with its companion background plot shows a strong signal, but of course not as clean as the α data. The coincident background, which extends from threshold to well above the maximum $(\alpha\mu)^+$ energy, comes from from μ^- capture in the beryllium target flask; protons, deuterons, tritons, and alphas, are emitted in coincidence with neutrons. Non-coincident background, in the wings of the time distribution, originates from a variety of sources producing singles, including scattered muons which cannot be completely rejected and products from μ^- capture in beryllium, polyethylene, and aluminum.

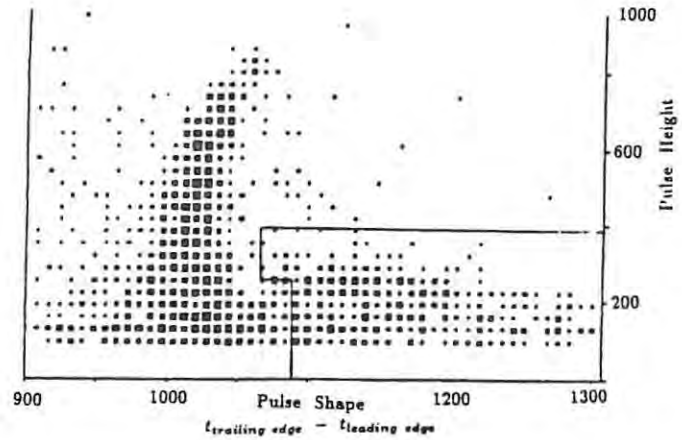

Fig. 4. Neutron separation by pulse shape.

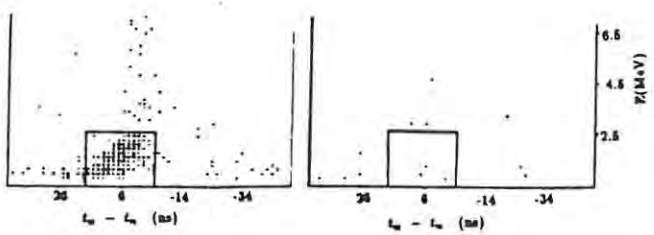

Fig. 5. α data on the left. Background on the right for 1/7 number of incident muons.

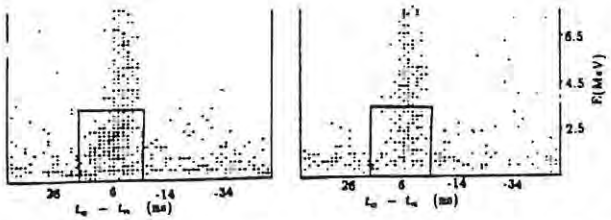

Fig. 6. The $(\alpha\mu)^+$ spectrum for all data taken at 1800 Torr. Background is shown on the right for 3/4 number of incident muons.

Table IV lists the raw numbers obtained from the data.

TABLE IV. Raw Data.

PRESSURE	*REGION*	*COUNTS*	*M1.M2.M3*
1800 *Torr*	$(\alpha\mu)^+$	115	16.7×10^9
1800 *Torr*	*Background*	90	29.1×10^9
490 *Torr*	α	295	7.2×10^9
490 *Torr*	*Background*	3	1.05×10^9

PURITY OF $D-T$ GAS

An anticipated source of trouble was impurities in the $D-T$ mixture. (See table II.) The mylar window precludes a high-temperature bakeout of the target, and there just is not enough gas to overpower small fixed amounts of contaminants as there is for the high-pressure targets.[12] The procedure used was to fill first to 1800 Torr and to collect $(\alpha\mu)^+$ data, then to bleed the gas pressure down to 490 Torr and collect α data. In this way, the same gas was used for the measurement and for the normalization. Time-dependent evolution of contaminants from the walls by tritium is not prevented by this procedure, but none was evident. A second 1800-Torr data run produced 30% more $(\alpha\mu)^+$ than did the first 1800-Torr fill when normalized to entering muons while no changes were evident in the background. It was not possible to accomplish the bleed procedure for this fill, and so confident normalization is lacking for more than 1/2 of the $(\alpha\mu)^+$ counts in Fig. 6. The direction of the observed effect is consistent with a cleaner mixture being obtained for the second fill following tritium scouring of the surfaces occuring during the first fill. Contamination

of the D_2 in the secondary container could also contaminate the target gas by diffusion through the window; we expect less such impurity for a second fill. Although the increase is not statistically conclusive, its direction reinforces our belief that it is due to a change in gas properties. Consequently, only the first set of runs at 1800 Torr were used in deriving the sticking probability, the data appearing in Table IV. If impurity did cause the change in χ, we estimate about 600 ppm (with the Z of nitrogen) was present.

RESULTS

The initial sticking probability is given by

$$\omega_s^o = \frac{N_{\alpha\mu}}{N_\alpha + N_{\alpha\mu}}. \qquad (1)$$

Here

$$N_{\alpha\mu} = \frac{n_{\alpha\mu}}{N\varphi^2(1 - R_{eff})}, \qquad (2a)$$

$$N_\alpha = \frac{n_\alpha}{N\phi^2\ 0.93} \qquad (2b)$$

where n_α ($n_{\alpha\mu}$) is the number of doubly (singly) charged ions detected, R_{eff} is the effective stripping, and 0.93 the active volume for α. N is the number of incident muons in each case (normalization to the high-energy coincident background was shown to be equivalent). We assume for now that both the number of μ^- stopped and the yield χ are proportional to ϕ. (See the next section.) The result is $\omega_s^o = (0.80 \pm 0.14)\%$ (statistical error).

ω_s^o measured in the 650-Torr experiment is $(0.91 \pm 0.3)\%$ (statistical error).[19] The error is larger since fewer $(\alpha\mu)^+$ were observed in the presence of substantial background.

SYSTEMATIC UNCERTAINTY

We now examine systematic uncertainties for items in Table II listed under "*Separate $D-T$ fills for $(\alpha\mu)^+$ and α*". The $t\mu$ and $d\mu$ diffusion distances are limited by the muon lifetime at such low pressures and could become somewhat longer due to diffusion while the atoms are still epithermal. We estimate this distance to be about 1 cm at 490 Torr, somewhat smaller than the dimensions of the target. No correction is made at this time; generalization of Cohen's solution to the time-dependent Boltzmann equation[20] to get the spatial extent would be appropriate for a good estimate.

The most important uncertainty is a consequence of the use of two different densities in making the measurements. At our densities thermalization times equal or exceed the muon lifetime. Therefore most of the molecular formation will occur in the epithermal (transient) region where $\lambda_{dt\mu}$ is rapidly changing, and the yield χ may then not scale with density as assumed above. Table V attempts to outline the scope of this problem. Thermalization times, as well as average temperature and remaining triplet fraction at a relevant time of 2 μs (all from ref. 20) tell us that at the lowest density the $t\mu$ atoms remain hot, and the triplet quenching is not complete. The muon lifetime then selects rather different slices of the epithermal transient for each density. (See survey of experimental low-density transients in refs. 21 and 22 and calculated transient effects in ref. 23)

TABLE V. Density Effect.

QUANTITY	490 *Torr*	1800 *Torr*
Density ϕ	7.6×10^{-4}	2.8×10^{-3}
Thermalization time	6 μs	1.6 μs
Average temperature at 2 μs	$540K$	$340K$
$t\mu$ *triplet fraction at 2* μs	0.33	0.04
Average $\lambda_{dt\mu}$	1.5×10^8	1.3×10^8
Extrapolated q_{1s} *from ref.*26	0.77	0.66

Next, let's see how large the effect is likely to be. Turning to Leon[24] to estimate singlet and triplet formation rates for our mixture at the two average temperatures, we find a higher rate for the less-thermalized, low-density case. The rates given in the Table V do not include screening effects,[25] but these will not alter the relative magnitudes. Nor should extension to the theory of direct molecular formation[23] seriously alter the relative magnitudes since the molecular-formation rates as a function of temperature still have similar shapes.

Other quantities remaining for discussion are q_{1s} and λ_{10}. An extrapolation of the Menshikov and Ponomarev q_{1s} is presented in Table V for each density[26];

here the strongest density dependence is predicted at low density. The direction of the q_{1s} density dependence is to offset the increased formation rate expected at the low density. In this simplified treatment, the 0.33 triplet fraction remaining in the 490 Torr sample has little effect on the conclusion; in the event that λ_{10} is actually larger than calculated[27], the triplet fraction could approach zero without largely affecting the $\lambda_{dt\mu}$ listed in the table.

Some comments are in order: 1) Expected epithermal enhancement of $\lambda_{dt\mu}$ makes the q_{1s} density dependence more important in determining yield at $C_t = 0.4$. Hence the RAL experiment may find a larger optimum C_t where the higher yield would be welcome. 2) λ_{10} effects would likely enter in a important way if a proper evaluation over the complete epithermal peak were done. 3) Thermalization could be more rapid than reported. 4) We should pay attention to the plunging cycle rates at low density,[4,5] keeping in mind that the lowest-density points (ϕ=1%) are already heavily into the epithermal region. But simply taking $\chi = \phi\lambda_c/\lambda_o = 0.08/\mu^-$ (450 Torr) with λ_c at $45/\mu s$ gives a predicted rate for *our* experiment that agrees with the absolute number of muon stops in the mixture found by foil activation. Unfortunately the foil test disagrees badly (by a factor of 2) with the number of stops estimated from beam properties. We might otherwise have hoped to bracket the extent of the epithermal enhancement at low densities (subject to assumptions about gas purity). 5) We anticipate that the RAL pulsed-beam data will add to the understanding of this low density region and answer some of the questions raised by the LAMPF experiment.

The initial C_t of 0.4 falls with time, and ionization chamber measurements indicate C_t dropped to 0.38 at the end of the data collection on the first 1800 Torr fill and to 0.37 at the end of the 490-Torr data collection. This small change is significant only if the optimum C_t is much higher so that 0.4 is on the rising edge of the λ_c vs C_t curve instead of at the plateau where we intended it to be.

Variations in ω_s^o depending on cuts used have been evaluated in the thesis of Li[19]; the rms scatter amounts to about 0.06% which we add to the statistical error. Based on the reliability of the above assumptions, we believe it unlikely that the density effect will alter ω_s^o by more than 15%. Accordingly a systematic uncertainty is quoted with the result: $\omega_s^o = (0.80 \pm 0.15 \pm 0.12$ systematic)% Subsequent experiments or calculations on the density effect can be used to correct this result.

The 650-Torr sticking measurement, as outlined in Table II, does not contain uncertainly due to the density effect, and its consistent value of (0.91 ± 0.3)% (statistical error), adds confidence to our conclusion.

CONCLUSION

In conclusion, we report a measurement of the initial $\alpha - \mu$ sticking probability in muon catalyzed $d-t$ fusion at low density. ω_s^o, measured directly for the first time, is $(0.80 \pm 0.15 \pm 0.12$ systematic)% in agreement with 'standard'

theoretical calculations[28,29,30] and not supporting those theories that invoke special mechanisms to alter the initial sticking.[31,32,33] The reported value contains only a 16% correction to the observed sticking due to stripping. Additional experiments are underway at the Rutherford-Appleton Laboratory where a high-Z target in the pulsed muon beam produces lower backgrounds. Direct normalization to neutron singles, transient observation, and reactivation tests should be possible.

ACKNOWLEDGEMENTS

We wish to thank R. H. Sherman of the Los Alamos National Laboratory for making a test of the cleanliness in tritium of the thin mylar coated with aluminum. Little impurity was seen in his Raman spectrometer, giving us confidence to proceed.

This work is supported by the U. S. Department of Energy Division of Advanced Energy Projects.

REFERENCES

1. Panel discussion on the Future of μCF, C. Petitjean Chairman, Muon Cat. Fusion 1, 391 (1987)
2. S.E. Jones *et al.*, Phys. Rev. Lett. 56, 588, (1986).
3. C. Petitjean *et al.*, Muon Cat. Fusion 1, 89 (1987).
4. C. Petitjean *et al.*, Muon Cat. Fusion 2 37 (1988).
5. See both W. H. Breunlich and C. Petitjean, μCF Workshop, Sanibel Island (1988).
6. H. Bossy *et al.*, Phys. Rev. Lett. 59, 2864, (1987).
7. K. Nagamine *et al.*, Muon Cat. Fusion 1, 137 (1987).
8. J.S. Cohen, Phys. Rev. Lett. 58, 1407 (1987).
9. V. E. Markushin, Muon Cat. Fusion 3, 395 (1988).
10. A. A. Vorobyov, Muon Cat. Fusion 2 17 (1988).
11. G. Semenchuk, private communication (1986).
12. S. E. Jones *et al.*, Muon Cat. Fusion 1, 121 (1987).
13. J. Davies, μCF Workshop, Sanibel Island (1988).
14. N. C. Mukhopadhyay, Phys. Reports 30, 98, (1977).
15. A. J. Caffrey *et al.*, Muon Cat. Fusion 1, 53 (1987).
16. G. Heusser and T. Kirsten, Nucl Phys. *A*195, 369 (1972).
17. H. Bichsel, Private communication.
18. J.S. Cohen, Phys. Rev. *A*37, 2343 (1988).
19. P. Li, Thesis, Brigham Young University, unpublished (1988).
20. J.S. Cohen, Phys. Rev. *A*34, 2719 (1986).
21. W. H. Breunlich *et al.*, Muon Cat. Fusion 1, 67 (1987).
22. C. Petitjean *et al.*, Muon Cat. Fusion 2 37 (1988).
23. J. S. Cohen and M. Leon, Phys. Rev. Lett. 55, 52 (1985).

24. M. Leon, Phys. Rev. Lett. 52, 605(1984) and corrected figures in 52, 1655 (1984) (Caution is advised due to the emergence of the sub-threshold resonances as strong contributors to the molecular formation).
25. J. S. Cohen and R. L. Martin, Phys. Rev. Lett. 53, 738 (1984).
26. L. I. Menshikov and L. I. Ponomarev, Pisma Zh. Eksp. Teor. Fiz. 39, 542 (1984) [Sov. Phys. JETP Lett. 39, 663 (1984)].
27. M. Leon, μCF Workshop, Sanibel Island (1988).
28. L. N. Bogdanova *et al.*, Nucl Phys. *A*454, 653 (1986).
29. D. Ceperley and B. J. Alder, Phys. Rev. *A*31, 1999 (1985).
30. Chi-Yu Hu, Phys. Rev. *A*34, 2536 (1986).
31. J. Rafelski and B. Müller, Phys. Lett. 164*B*, 223 (1985).
32. M. Danos, B. Müller, and J. Rafelski, Muon Cat. Fusion 3 (1988).
33. M. Danos, L.C. Biedenharn, A. Stahlhofen, , μCF Workshop, Sanibel Island (1988).

μCF THOUGHTS FROM BIRMINGHAM AND THE RUTHERFORD APPLETON LABORATORY

J.D. Davies, F.D. Brooks, W.A. Cilliers,
J.B.A. England, G.J. Pyle, G.T.A. Squier,
University of Birmingham, U.K.

A. Bertin, M. Bruschi, M. Piccinini, A. Vitale, A. Zoccoli,
University of Bologna, Bologna, Italy

S.E. Jones, P. Li, L.M. Rees, E.V. Sheeley,
J.K. Shurtleff, S.F. Taylor
Brigham Young University, Provo, Utah, USA

G.H. Eaton
Rutherford Appleton Laboratory, U.K.

B. Alper
UKAEA Culham Laboratory, U.K.

V.R. Bom, C.W.E. van Eijk, H. de Haan
Delft University of Technology, Holland

A.N. Anderson
Idaho Research, Boise, Idaho, USA

A.J. Caffrey, J. Zabriskie
Idaho National Engineering Laboratory, Idaho Falls, Idaho, USA

M.A. Paciotti, O.K. Baker, J.N. Bradbury, J.S. Cohen, M. Leon,
H.R. Maltrud, L.N. Sturgess
Los Alamos National Laboratory, Los Alamos, N.M. 87545, USA

ABSTRACT

This paper gives some ideas to be learnt from magnetic confinement fusion and briefly describes the pulsed muon beam at ISIS, progress with the measurement of W_s(the μα sticking coefficient), future beam plans and possible experiments.

INTRODUCTION

μCF has had considerable progress; its continuation requires new ideas to be widely discussed at workshops like this. Thought must be given to collective and critical planning, exploiting resources, expanding funding and to acquainting those in authority or having influence, non readers of the specialised science publications, of μCF. Inter alia, there have been general articles in Nature, the New Scientist and Scientific American. Amusingly it was the latter that led to articles in the Economist, the (British) Times and BBC radio.

IDEAS FROM MAGNETIC CONFINEMENT FUSION

This subject was investigated last November at JET (Joint European Torus and 20km from ISIS) in a STOA Workshop of the European Parliament and EEC. Significant points included there no longer being an urgent need for fusion. Although magnetic confinement research has made considerable expensive progress, it has technical problems and a goal in the distant, costly future. Nevertheless it should not be abandoned but slowed and savings made. However research is not viable at less than the current European spend. The USA STARFIRE had reached similar conclusions. Mention was made of ITER - the start of a joint European, Japanese, USA, USSR project. The lesson for μCF is obvious - we must plan a world programme. Invited as an alternative method of fusion, μCF was presented as interesting physics with basic parameters made with relatively small scale, low cost equipment divorced from the large, expensive apparatus, the accelerator, which was provided anyway for other purposes. Progress was rapid with 'a low cost, long shot' possibility of energy production. Support for ISIS experiments by Culham, the British fusion centre, was mentioned.

In the future 550 fusions/μ could provide energy break-even, heat + heat. If > 20% of the power output is required to drive the complex then the financial cost of such becomes too high. Therefore, in some sense, economic break-even requires 2500 fusions/μ .

THE ISIS PULSED MUON BEAM

The synchrotron sends protons in 50Hz pulses to make neutrons by spallation and fast fission at a distant uranium target: each pulse contains 2 bunches, 330ns apart.. Recently the complex has run for appreciable periods at 750 Mev and 90 μa. The surface/cloud muon beam[1,2] is taken off a thin, intermediate transmission target. The raison-d'être of ISIS, so far, is to appear as a pulsed reactor; so the aims are long, steady runs and very low backgrounds. There is a very good cave around the muon target from which leak-paths are enthusiastically sought and blocked. Improved exit collimation from the cave to protect downstream magnets has also decreased external backgrounds.

The performance of the muon beam is given in table 1; ± 55kv on the velocity separator and a simple collimator reduced the electron contamination by x50. With little advertising for its first full year, the beam has been oversubscribed by x2½, mainly μSR experiments. A problem with having no switchyard is interchanging experiments.

A DIRECT MEASURE OF W_s, THE μα STICKING COEFFICIENT

This continues the LAMPF[3] determination of the ratio of $\frac{\mu\alpha - n}{\alpha - n}$

J.D. Davies, F.D. Brooks, W.A. Cilliers, J.B.A. England, G.J. Pyle, G.T.A. Squier, A. Bertin, M. Bruschi, M. Piccinini, A. Vitale, A. Zoccoli, S.E. Jones, P. Li, L.M. Rees, E.V. Sheeley, J.K Shurtleff, S.F. Taylor, G.H. Eaton, B. Alper, V.R. Bom, C.W.E. van Eijk, H. de Haan, A.N. Anderson, A.J. Caffrey, J. Zabriskie, M.A. Paciotti, O.K. Baker, J.N. Bradbury, J.S. Cohen, M. Leon, H.R. Maltrud and L.N. Sturgess
μCF thoughts from Birmingham and the Rutherford Appleton Laboratory
A.I.P. Conf. Proc. 181 (1989) 52-58

coincidences with a small, low density gas target described at the workshop. That experiment had a large 'α'-n background from the > 99.9% of the μ^- that stopped in the target walls with general accelerator background contributing to the high neutron count rate. Data were taken at 490mm Hg target pressure to see α-n coincidences and at 1800mm for μα-n since the event rate increased approximately as the square of the D-T density.

These backgrounds could be avoided by using a pulsed beam, target walls having high Z and delaying counting by ½ μs. As the atomic number of an elemental stopping medium is increased the effective muon life-time falls from τ=2 μs for Z ~ 6 to 100ns for Z ~ 48 where it then flattens.

Figure 1 shows the apparatus modified for use at RAL. The target flask is made from silver since this is the structural material having τ_μ (effective) < 100ns and of the lowest Z to reduce showering. There are 2 NE213 neutron counters to improve timing and the Si surface barrier α-detector was thinned to 50μ to reduce background.

The neutron backgrounds were examined as functions of energy and time after the muon pulse. That which was non muon-induced became softer with increasing time and came principally from the muon production target. The muon-induced background had an energy spectrum of time-independent shape but magnitude decaying with the τ_μ ~ 1μs characteristic of μ^--Al interactions. So the beam-pipe end-flange and target outer vessel were covered with 3mm of Pb. For E_n > 3 Mev this was still the dominant background and tests indicated an origin in the downstream beam-pipe - this will be lined with copper in future.

There is a tremendous flux of particles and energy during the beam burst - principally from the e/π contamination. Inhibiting each of the signal paths inside the LINK n/γ discriminator protected the neutron channel. Little background can get above the 0.6 Mev α counter threshold and pile-up was measured at 1½%. However the very many sub-threshold pulses during the burst cause a 50ns time walk and jitter in the pre-amp. If this cannot be inhibited then a thin scintillator will be used to take advantage of a photo-multiplier's stability.

μα-n events at 1520mm Hg target pressure and α-n coincidences at 765 and 490mm were clearly seen in the raw, on-line data as were fusion neutron singles at the same densities. The neutron data should provide the cross normalisation between high and low pressure required for this and the LAMPF experiments and also explore this region of epithermal production.

THE FUTURE

A grant application is being prepared for a kicker magnet to spatially separate the muon bunches; this will double the number of completed μSR experiments, as they use only a fraction of the available beam, and considerably improve their frequency range. The undeflected beam position would then be available for more permanent experiments such as μCF.

There are space and plans for a purpose-built muon beam on the other side of the proton beam and sharing the production target; a switch-yard would reduce background and permit the beam to alternate between 'permanent' experiments. Table 1 also gives the parameters of a 'conventional' decay channel at ISIS with a superconducting solenoid. The total fluxes of decay and cloud beams are comparable. As μCF experiments use only a small fraction of the μ^- stopping volume then the cloud beam would give much higher event rates and better signal to noise because of its smaller $\frac{\Delta p}{p}$ and spot size. The major advantage of the decay channel is the negligible π^- and e^- contamination (the latter only with an ultra-thin, solenoid window) n.b. a π^- gives 140 Mev of background but a large fraction of the muon mass goes into the neutrino. For the present beam a recently installed double collimator should enable higher separator volts to reduce the e^- contamination by much more than x50. Next year we aim to considerably reduce the π^- contamination with a thin degrader at an upstream focus at the expense of ~ 25% increase in $\frac{\Delta p}{p}$. The choice of beam is open.

SOME POSSIBLE EXPERIMENTS

These are mentioned to illustrate the power of the facility.
μ^3He and μ^4He cascade x-rays

(A) Scavenging by He from excited (μ-hydrogen isotope) atoms can be distinguished from that via the ground or meso-molecular state; the former will dominate during the burst and the latter afterwards. Suppression of e/π contamination from the target and charged particles from the detector - GSPC or Compton suppressed SiLi - by a solenoid magnet will be required.

(B) The state of the 'stuck' μα, following D-T fusion, as it slows may be followed from the changes in yield of several spectral lines as functions of density.

Exploration of epithermal production and low temperature plasma.

The 'μt' intermediate state is created with 19ev and its thermalisation is sufficiently slowed at low densities that it spends significant time with energies equivalent to the required high temperatures. Neutron singles will explore $10 \rightarrow \frac{1}{2}\rho_{STP}$ and α-n coincidences densities below $1\rho_{STP}$.

Low temperature plasma.

This can be achieved with the pulsed, θ-pinch of a solid D-T filament.

Hyperfine studies

A pulsed CO laser could induce $(\mu t)_s \rightarrow (\mu t)_t$ with polarized $(\mu t)_t$ being detected by transverse μSR.

REFERENCES

1. G. Eaton et al., NIM A269, 483 (1988).
2. F.D. Brooks et al., Muon Catalyzed Fusion 2, 85 (1988).
3. See M.A. Paciotti, these proceedings.

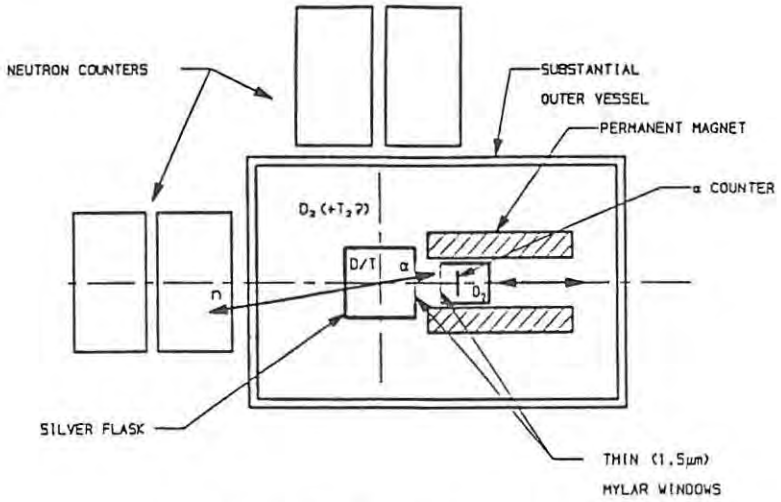

Fig. 1. Apparatus for measuring W_s.

Table 1

Column 1 - Performance of the ISIS surface/cloud pulsed muon beam
Column 2 - Calculate performance of a decay beam using an existing superconductor solenoid.
Both from a 1cm production target and 90 μa protons.

		Surface/Cloud		Decay
Beam spot		2x3cm²	FWHM	6x6cm²
Δp/p		5%(cloud)		12%
Intensity	29	~1.5 $10^6 \mu^+$/s		negligible
at MeV/c	40	6 $10^4 \mu^-$/s		30% less
	60	1.5 $10^5 \mu^-$/s		equal
	100	"cloud" 30% less than "decay"		
π contam.		between 3:1 and		very low
e contam.		1:1 π or e : μ		low (?)
Polarized μ		at 29 Mev/c only		yes

J.D. Davies, J.B.A. England, G.J. Pyle, G.T.A. Squier, F.D.Brooks, W.A. Cilliers, A. Bertin, M. Bruschi, M. Piccinini, A. Vitale, A. Zoccoli, S.E. Jones, V.R. Bom, C.W. van Eijk, H. de Haan, A.N. Anderson, M.A. Paciotti, G.H. Eaton and B. Alper
A direct measurement of the alpha-muon sticking coefficient in muon-catalysed d-t fusion
J. Phys. G: Nucl. Part. Phys. 16 (1990) 1529-1537

J. Phys. G: Nucl. Part. Phys. **16** (1990) 1529–1537. Printed in the UK

A direct measurement of the alpha–muon sticking coefficient in muon-catalysed d–t fusion

J D Davies†, J B A England†, G J Pyle†, G T A Squier†, F D Brooks†, W A Cilliers†, A Bertin‡, M Bruschi‡, M Piccinini‡, A Vitale‡, A Zoccoli‡, S E Jones§, V R Bom||, C W E van Eijk||, H de Haan||, A N Anderson¶, M A Paciotti+, G H Eaton$ and B Alper*

† School of Physics and Space Research, University of Birmingham B15 2TT, UK
‡ Dipartimento di Fisica dell'Universitá, and Istituto Nazionale di Fisica Nucleare, Sezione di Bologna, Italy
§ Brigham Young University, Utah, USA
|| Delft University of Technology, The Netherlands
¶ Idaho Research, Boise, Idaho, USA
+ Los Alamos National Laboratory, Los Alamos, New Mexico, USA
$ Rutherford Appleton Laboratory, UK
* UKAEA, Culham, UK

Received 21 May 1990

Abstract. A direct method of determining the alpha–muon sticking coefficient ω_0 following muon-catalysed d–t fusion, by measuring the ratio of $(\alpha\mu)$–neutron coincidences to neutron singles, is described. Initial measurements have used a low-pressure D–T gas target and the pulsed muon beam at the ISIS facility of the Rutherford Appleton Laboratory and give a preliminary result of $\omega_0 = 0.0069 \pm 0.0040 \pm 0.0014$(sys).

1. Introduction

Negatively charged muons catalyse d–t fusion via the resonant formation of a muonic molecule in which the dtμ positive ion replaces a deuterium nucleus in the D_2 molecule. The fusion reaction $d + t \rightarrow \alpha(3.5\,\text{MeV}) + n(14.1\,\text{MeV})$ occurs rapidly by barrier penetration and the muon is generally released and so can catalyse further fusions during its 2.2 μs lifetime. However, there is a small probability ω_0 that the muon will be captured by the alpha particle produced in the fusion and, unless it is detached during the slowing down of the $(\alpha\mu)^+$ ion (i.e. reactivated), it will be removed from the catalysis cycle. The effective sticking coefficient ω is thus less than ω_0 and can be written

$$\omega = \omega_0(1 - R) \tag{1}$$

where R is the muon reactivation coefficient, which is obtained by integrating the muon stripping probability over the whole $\alpha\mu$ range. The sticking coefficient ω_0 is a basic observable in the theoretical description [1–4] of muon-catalysed fusion. Ultimately the number of fusions per muon is limited to ω^{-1}, thus accurate measures of ω_0 and R are important in assessing future possibilities of economical energy generation by this process.

0954-3899/90/101529 + 09 $03.50

Theory gives $\omega_0 = 0.0089$–0.0093 [5, 6] and $R = 0.37$ [7] at liquid D–T densities, ρ_l, with only a small density dependence for ω via R, e.g. $R = 0.30$ at $0.1\rho_l$. Experimental measurements agree around $\omega = 0.0041$ for ρ_l [8–13], which is about six standard deviations less than theory, but vary between 0.005 ± 0.001 [9, 11] and 0.010 [8] at low densities; this allows the possibility of a large density dependence and even lower values of ω. These measurements are indirect and observe either the time evolution of the fusion neutrons or the K_α line from muonic helium using liquid targets [10, 13]. For the former ω is one of several parameters determined simultaneously from the analysis and represents a small loss term at long times; there is considerable controversy about the large corrections which increase in significance as the density is reduced. Obtaining ω from muonic x-ray measurements depends on untested cascade calculations. The present experiment [14], and an associated experiment [15] at the LAMPF facility of the Los Alamos National Laboratory (LANL), aim to determine ω_0 directly, in low-density conditions, from measurements of $\alpha\mu$–n coincidences. In the LANL experiment the coincidence rate is measured using D–T gas targets at two different pressures. At the higher pressure (1800 Torr) only $\alpha\mu$, being singly charged, can make coincidences, whereas α, being doubly charged, are ranged out in the D–T gas and the target windows, before they can reach the α detector. At the lower pressure (490 Torr) α as well as $\alpha\mu$ can make coincidences. The sticking coefficient may be calculated from the ratio of the coincidence rates provided the ratio of fusion rates at the two pressures is known.

The present work follows a different approach, exploiting the characteristics of the pulsed muon beam [14, 16, 17] of the ISIS facility at the Rutherford Appleton Laboratory (RAL) to obtain low backgrounds, thus allowing measurements of single neutron events from low-density D–T targets. A single set of measurements is made using a D–T target at a pressure of 1509 Torr and selecting only $\alpha\mu$–n events in the coincidence measurement. The ratio of these coincidences to the neutron singles, which originate from all fusions, is measured. This ratio is proportional to the sticking coefficient ω_0 and the constant of proportionality is simply the probability that a collinear $\alpha\mu$ associated with a detected fusion neutron reaches the α detector and is registered. For gas densities such that the $\alpha\mu$ have sufficient range to reach the detector, the probability factor is determined by geometrical considerations and in-flight stripping and may be estimated to better than 10% from Monte Carlo calculations. The sticking coefficient ω_0 is thus determined directly from the experimental measurement of the coincidence-to-singles ratio.

We report here on the characteristics and performance of this new direct method for determining the alpha–muon sticking coefficient and present a preliminary result obtained by this technique.

2. Experimental details

The experiment used a pulsed beam of negative muons having a small spot size, momentum 40 MeV/c and $\Delta p/p \simeq 5\%$, provided by the cloud muon facility [16, 17] associated with the ISIS proton synchrotron at RAL. Figure 1 shows the gas target together with the three NE213 liquid scintillators employed for neutron detection and the surface barrier detector (SBD) used to detect $\alpha\mu$. The silver target cell (a cube of side 70 mm) contained a D–T mixture at a pressure of 1509 Torr. The cell was housed in a substantial aluminium vessel containing D_2 gas at the same pressure

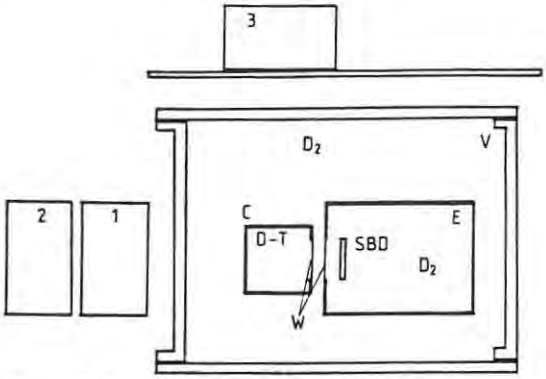

Figure 1. Experimental arrangement (schematic) viewed looking downstream along the muon beam, showing: silver target cell C containing D–T mixture; aluminised Mylar windows W; surface barrier detector SBD; and NE213 scintillation detectors 1–3. The enclosure E and the outer vessel V were filled with D_2 gas at the same pressure as the target.

as the cell and separated from the D–T mixture by an aluminised Mylar window (thickness 1.5 μm Mylar + 0.08 μm Al) to permit $\alpha\mu$ to exit to the SBD. The SBD, area 1000 mm^2 and only 50 μm thick (to reduce background), was enclosed in its own D_2 environment, at the same pressure and with an identical entrance window for the $\alpha\mu$. As in the LAMPF experiment [15], this dual window arrangement was designed to protect the SBD against the formidable tritium beta activity (750 Ci) present in the target cell. The arrangement ensured that tritium diffusing through the first window was diluted in the large outer D_2 volume adjoining the inter-window region, thereby reducing the rate of tritium diffusion through the second window, to the SBD. Diffusion through the first window reduced the tritium fraction in the target cell from its initial value of 45% to 38% over the period of the measurements (2 d).

The three NE213 detectors (figure 1), each 13 × 13 cm in area and 7 cm thick, used pulse shape to discriminate against gammas. Detectors 1 and 2 were placed so that either, in conjunction with the SBD, could register collinear $\alpha\mu$–n coincidences. Detector 3, by registering orthogonal coincidences, provided a measure of the coincidence background. The muon beam incident on the target was monitored by integrating a time-gated signal from a plastic scintillator 0.05 mm thick in transmission geometry, close to the entrance window of the target cell.

The incident muon beam entered the target cell normal to the plane of figure 1. At the target pressure used, about 1% of the muons stopped in the target gas, the rest stopping in the walls of the silver target cell. The muon lifetime in silver is reduced from 2200 ns to 90 ns by weak interaction processes. Thus, by delaying the start of data taking until 500 ns after the beam pulse, the effects of prompt background from muon interactions in the silver were greatly reduced. This delay also reduced the effects of high-energy background from the ISIS beam dump and the muon production target in the proton beam. The inside of the aluminium containment vessel was lined with lead to capture (rapidly) stray scattered muons and the entire detector system was shielded with lead and polythene (not shown in figure 1).

Signals from the scintillation detectors were processed in Link Systems pulse

shape discriminators (Models 5010 or 5020); these had been modified to allow the processing circuitry to be inhibited until a preset time (0.5 μs) after the second muon pulse in the ISIS beam time structure [17] and to provide an output signal F proportional to the fast scintillation component from NE213, as well as the standard signal L, which is proportional to the total light output. Signals from the SBD were processed using a conventional charge-sensitive preamplifier and slow amplifier system and the relative timing T_c between coincident NE213 and SBD signals was obtained via a TAC. The SBD timing signals were derived using crossover timing because preliminary attempts to use a fast voltage-sensitive preamplifier in the timing circuit revealed a poor signal-to-noise ratio of 3:1, due to the large capacitance (2200 pF) of the detector. A signal from any NE213 detector within the time window 0.5–7.5 μs after arrival of the second muon pulse and satisfying the condition $L > L'$, where L' is the pulse height corresponding to a 2 MeV proton, was defined as an event. The pulse heights L and F from the three NE213 detectors were recorded on tape or disc for all events, together with the event time T_μ relative to the second muon pulse, which was measured using a second TAC. The pulse height from the SBD and the output T_c from the associated TAC were also recorded, together with the L, F and T_μ outputs, for SBD–NE213 coincidences. The following constraints were applied in the off-line analysis of all events, including both coincidences and singles: (i) events in which more than one of the NE213 detectors responded were rejected; (ii) pulse shape discrimination based on comparison of the L and F outputs of the NE213 detectors was implemented so as to select neutron events and reject gamma events; and (iii) an event time cut of $T_\mu = 1$–7.5 μs was imposed, to discriminate against a background component showing a decay constant of 0.9 μs and attributed to muon capture in the aluminium beam pipe. Additional constraints, described below, were applied in the analysis of the coincidence events.

In addition to the runs made using the D–T target, a second, nominally identical SBD and target system filled with H_2 gas was used to determine backgrounds. Some additional runs were also made with the D–T target at lower pressures (710 and 490 Torr) to check the performance of the coincidence system under conditions in which α–n as well as $\alpha\mu$–n coincidences could be detected. After checking consistency between runs made under the same conditions, the raw data were summed to form single D–T (1509 Torr) and single H_2 runs for each of the three NE213 detectors. Figure 2 shows the pulse height spectra obtained from the three NE213 detectors for these summed runs. The background spectra measured using the H_2 target and shown by circles were measured for a smaller number of incident muons than the spectra measured using the D–T target (histograms) and have been multiplied by a factor of 1.96. This factor was determined by referring to the number of neutrons recorded at short event times, $T_\mu \leqslant 0.7$ μs, at which background dominates strongly, so that the number of neutrons in the normalised background run should approach closely to that in the D–T run. Recoil protons (0–14 MeV) from the d–t fusion neutrons can be identified clearly above background in the spectra from all three detectors in figure 2.

The off-line analysis of the neutron–SBD coincidence data included a further cut, applied to the L outputs of the NE213 detectors to select pulse heights in the range corresponding to recoil proton energies of 2.4–15 MeV. Figure 3 shows plots of $\alpha\mu$ energy against coincidence time delay for these data, presenting the H_2 background runs and the D–T runs in the left and right panels respectively. The coincidence data obtained using the D–T target (figure 3), if projected onto the T_c axis, show a

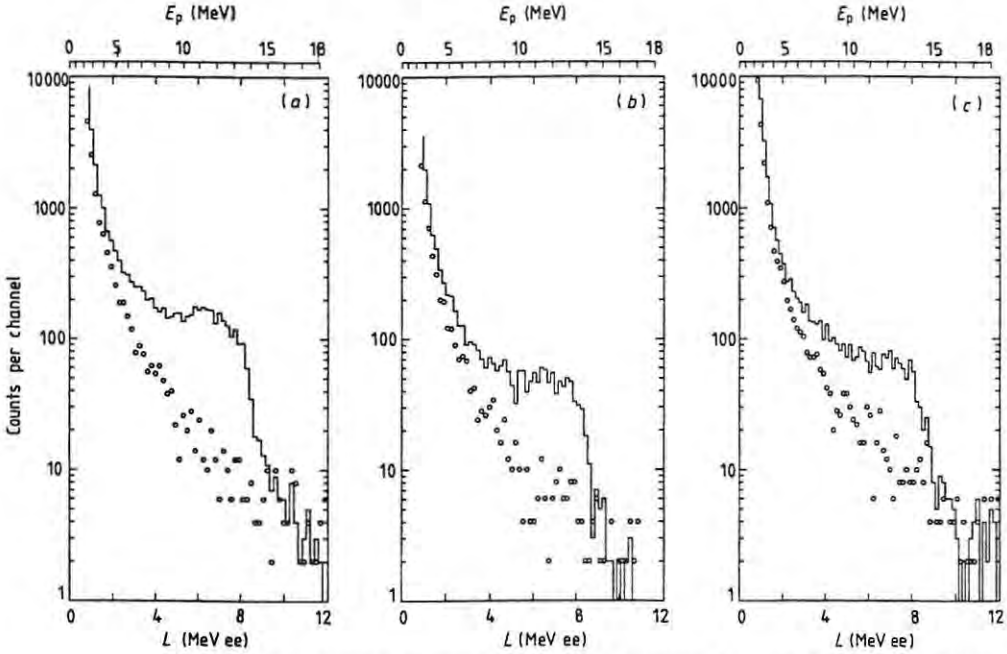

Figure 2. Pulse height spectra obtained from detectors 1–3 ((*a*)–(*c*) respectively) for muons incident on the D–T target (histograms) and the H_2 target (circles). The H_2 spectra have been normalised as described in the text. The pulse height scales, L, are calibrated in units of MeV ee (MeV electron equivalent), that is units which represent the electron energy required to give the pulse height indicated. The corresponding proton energies are shown above.

peak of FWHM about 28 ns at $T_c = 138$ ns, with a low intensity tail stretching out to about $T_c = 350$ ns. Better timing resolution (FWHM = 12 ns) was observed in tests made using a ^{252}Cf spontaneous fission source. The timing degradation under beam conditions was investigated and it appeared to be a result of slight baseline fluctuations in the output from the SBD to the crossover timing, coming from the very many small (and occasional large) SBD signals at beam arrival time ($T_\mu \leqslant 0$). A generous time window of $T_c = 50$–350 ns (figure 3) was used to select $\alpha\mu$–n coincidences from the D–T runs, in order to ensure that events in the wings of the coincidence peak were not lost. The corresponding time window for runs taken with the H_2 target was $T_c = 100$–400 ns, the shift of 50 ns being introduced to compensate for variations in the crossover timing characteristics of the different SBDs used with the H_2 and D–T targets respectively.

The energy window used on the SBDs to select $\alpha\mu$–n coincidences was set at 1.5–3.6 MeV (figure 3), the threshold of 1.5 MeV being chosen so as to exclude the small number of detected α–n coincidences produced by fusions in the region close to the exit window of the D–T target. Monte Carlo simulations show that the α from these fusions are not ranged out by the windows and the intermediate D_2 gas, and may reach the SBD with energies up to about 1 MeV, thus contributing to the events which are observed in this region of figure 3. The $\alpha\mu$ reaching the SBD have energies between 1 and 3 MeV, depending on their point of origin within the D–T target cell and whether the muon is stripped from the alpha in the gas or Mylar windows, en route to the detector. The fraction φ of the $\alpha\mu$ directed towards the SBD which reaches the SBD with energy exceeding 1.5 MeV was estimated from

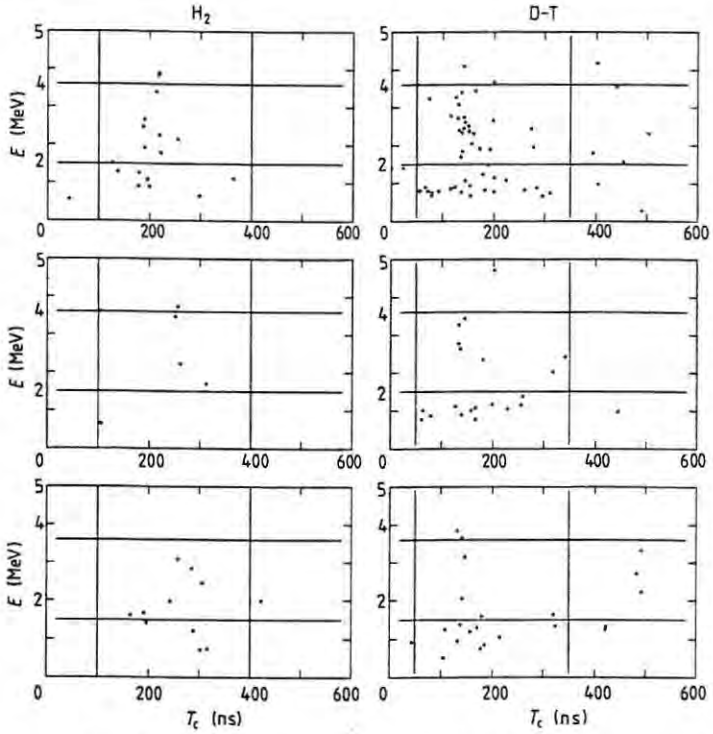

Figure 3. Coincidence events as function of $\alpha\mu$ energy E and coincidence time difference T_c. Panels top-to-bottom show data from detectors 1–3, left panels obtained using the H_2 target and right panels the D–T target. The lines within the panels show the cuts imposed on T_c and E in the analysis leading to the coincidence data in table 1. The number of incident muons for the H_2 data was estimated to be about half that for the D–T data.

Monte Carlo simulations based on the stripping calculations of Cohen [18] and was found to be $\varphi = 0.84$ for the conditions of this experiment.

The data obtained from detector 1 using the H_2 target show a concentration of events (figure 3) at times $T_c = 200 \pm 30$ ns, indicating that a significant fraction of these events are real coincidences rather than accidental coincidences. The data from detectors 2 and 3, H_2 target, show lower coincidence rates and no evidence of concentration at $T_c \approx 200$ ns. These features, together with the fact that detector 1 was closer to, and less shielded from, the muon beam (figure 1) than detectors 2 and 3, suggest that the real coincidence component from detector 1 is beam-associated. The real coincidences may be due, indirectly, to muons which find their way into light elements (H, C or Al) in, or close to, the beam and thus survive, as muonic atoms or muo-molecules, to event times $T_\mu > 1\,\mu$s, before being captured by nuclei. Energetic charged particles and neutrons emitted in coincidence from the ensuing nuclear interactions could be responsible for the real coincidence component, which would thus also be present as a real coincidence background (RCB) in the data taken using the D–T target.

The levels of RCB present in the D–T coincidence data from detectors 1 and 2 were estimated in two ways: (i) from the measurements made using the H_2 target; and (ii) from the coincidences recorded by detector 3 for the D–T target. The

Table 1. Numbers of coincidences and neutron singles.

		Coincidences			
Detector	Singles, N_n	Raw	RCB	Accidental	N_c
1	8417 ± 157	24	11	4	9 ± 6
2	4291 ± 121	7	4	0	3 ± 3

orthogonal geometry of detector 3 with respect to the SBD implies that all such coincidences should be attributed to background and the time distribution of the D–T data from this detector (figure 3) shows further evidence of the RCB component. Method (i), after normalising the H_2 data by a factor of two, as used for the singles spectra (figure 2), indicated RCB levels of 16 and 6 events for detectors 1 and 2 respectively. Method (ii), assuming an isotropic distribution of the RCB and normalising by the ratios (1.23 and 0.62) of the singles neutron rates of detectors 1 and 2 to that of detector 3, indicated levels of 5 and 2 events for the two detectors. Since fusion competes with the suggested RCB mechanism, for muons surviving beyond 1 μs, we expect a lower RCB rate per muon in the D–T target than in the H_2 target, and hence that method (i) will overestimate the RCB. Method (ii), in contrast, may be expected to underestimate the RCB, since this background, by its nature, is likely to contain fewer orthogonal coincidences than collinear coincidences. The averages of the values obtained from methods (i) and (ii) have therefore been used, giving RCB levels of 11 and 4 events for detectors 1 and 2 respectively, as shown in table 1.

The numbers of accidental coincidences shown in table 1 were estimated from the numbers of events within the E window but outside the T_c windows in figure 3. The increased accidental coincidence rate seen with the D–T target as compared with the H_2 target (figure 3) can be attributed to the significantly higher (fusion) neutron rate associated with the D–T target (figure 2). The numbers of single events shown in the table were estimated by integrating the spectra of figure 2 (corrected for background) between the same pulse height limits (corresponding to $E_p = 2.4$–15 MeV) as applied in the coincidence analysis.

3. Results and discussion

The number N_n of singles neutrons registered by an NE213 detector, for N_0 d–t fusions in the target, may be written

$$N_n = \varepsilon N_0 \tag{2}$$

where ε is the relevant detection efficiency of the neutron detector.

Assuming that all α–n coincidences are excluded by the SBD energy window (figure 3), the number N_c of real fusion coincidences registered between this neutron detector and the SBD is given by

$$N_c = \varepsilon \omega_0 \varphi B N_0 \tag{3}$$

where the factor B represents the probability that the extrapolated geometric path of a collinear $\alpha\mu$ associated with a detected fusion neutron intersects the SBD and φ represents the fraction of these particles which reach the detector with energy

greater than the threshold (1.5 MeV). The product φB may be estimated to better than 10% from Monte Carlo calculations. The sticking coefficient ω_0 is thus, from equations (2) and (3), given by

$$\omega_0 = N_c/\varphi B N_n \tag{4}$$

and is thus obtained directly from the measurements N_c and N_n.

Monte Carlo calculations give B values of 0.155 and 0.176 for the coincidences from detectors 1 and 2 respectively. With the value $\varphi = 0.84$ and the data of table 1, we obtain $\omega_0 = 0.0082 \pm 0.0055$ from detector 1 and $\omega_0 = 0.0047 \pm 0.0047$ from detector 2. A slight improvement in accuracy is obtained by combining the data for both detectors and using a B factor estimated for the combined detector system. This gives the result

$$\omega_0 = 0.0069 \pm 0.0040 \pm 0.0014(\text{sys})$$

for the initial sticking coefficient, the systematic uncertainty reflecting an allowance for a 10% uncertainty in the Monte Carlo estimations of φB and for some systematic error in the data reduction procedures.

The preliminary value reported from the direct measurement of ω_0 at LANL is [15] $\omega_0 = 0.0080 \pm 0.0015 \pm 0.0012(\text{sys})$. This was obtained from the ratio of coincidence rates measured using a target geometry similar to that of the present experiment, at D–T pressures of 1800 and 490 Torr. It was not possible to measure neutron singles rates in the LANL experiment, hence the sticking coefficient was determined by assuming that the fusion rate per incident muon scales as the square of the D–T target gas pressure p. Scaling as p^2 is based on the expectation that: (i) the number of muon captures forming $d\mu$ or $t\mu$; and (ii) the formation rate of $dt\mu$ are each proportional to the target density, and hence to the pressure. However, the decrease with pressure may not be linear for the former because of the increasing fraction of muons that, having stopped in the gas, are transferred to the target walls, or for the latter, because of the increasing importance of epithermal $dt\mu$ production [19], that is direct $dt\mu$ formation during the increasingly longer thermalisation time of the muonic atom. The data obtained at 710 and 490 Torr demonstrate that the dependence of the fusion rate on pressure could be determined by extending the present experiment. This would be equivalent to measuring the $dt\mu$ formation rate at high temperatures [20].

The present preliminary result is consistent with the LANL value [15] and is independent of theoretical assumptions concerning the mechanism of muon-catalysed fusion. The LANL value, in contrast, depends on the assumed p^2 dependence of the fusion rate in D–T targets, which still needs to be tested experimentally. The indirect experiments that determine ω, and hence ω_0, from the time evolution of fusion neutron emission [8, 9, 11, 12] are inherently vulnerable to systematic errors, for example through their dependence on knowledge of neutron detection efficiencies. The density dependence assigned to q_{1s}, the fraction of muons that reach the $d\mu$ ground state, is also important in evaluating these measurements [21] and the difference between $\omega = 0.005$ [9, 11] and $\omega = 0.010$ [8] reported for low densities could arise from this source. The need for a more accurate measurement of ω_0 obviously remains. The present method, used in conjunction with the RAL pulsed muon source, should be capable of meeting this need.

These investigations have been supported in part by the Science and Engineering

Research Council, the Foundation for Fundamental Research on Matter (FOM), the Netherlands Organisation for Scientific Research (NWO) and the Foundation for Research Development (FRD). We gratefully acknowledge helpful discussions with J S Cohen concerning the evaluation of muon-stripping effects. Two of us (FDB and WAC) record our thanks for hospitality extended by the University of Birmingham.

References

[1] Breunlich W H, Kammel P, Cohen J S and Leon M 1989 *Ann. Rev. Nucl. Part. Sci.* **39** 311
[2] Leon M 1989 *AIP Conf. Proc.* **181** 94
[3] Ponomarev L I and Fiorentini G 1987 *Muon Catalyzed Fusion* **1** 3
[4] Ponomarev L I 1988 *Muon Catalyzed Fusion* **3** 629
[5] Hayward S F, Monkhorst H M and Szalewicz K 1988 *Phys. Rev.* A **37** 3393
[6] Kamimura M 1989 *AIP Conf. Proc.* **181** 330
[7] Cohen J S 1987 *Phys. Rev. Lett.* **58** 1407
[8] Jones S E *et al* 1983 *Phys. Rev. Lett.* **51** 1757; 1986 *Phys. Rev. Lett.* **56** 588
[9] Breunlich W H *et al* 1987 *Phys. Rev. Lett.* **58** 329
[10] Bossy H *et al* 1987 *Phys. Rev. Lett.* **59** 2864
[11] Petitjean C 1989 *Fusion Engng Design* **11** 255
[12] Nagamine K *et al* 1988 *Muon Catalyzed Fusion* **2** 73
[13] Nagamine K 1990 *μCF89, Oxford, RAL Report Number 90-022*
[14] Alper B *et al* 1990 *μCF89, Oxford, RAL Report Number 90-022*
[15] Paciotti M A *et al* 1989 *AIP Conf. Proc.* **181** 38
[16] Eaton G H *et al* 1988 *Nucl. Instrum. Methods* A **269** 483
[17] Brooks F D, Davies J D, Pyle G J, Squier G T A and Eaton G H 1988 *Muon Catalyzed Fusion* **2** 85
[18] Cohen J S 1988 *Phys. Rev.* A **37** 2343
[19] Cohen J S and Leon M 1985 *Phys. Rev. Lett.* **55** 52
[20] Kammel P 1985 *Lett. Nuovo Cimento* **43** 349
[21] Jones S E 1989 *AIP Conf. Proc.* **181** 2
Anderson A N 1989 *AIP Conf. Proc.* **181** 57

Muon Catalyzed Fusion 5/6(1990/91)405–411

SIMULATION AND EMULATION OF DIRECT MEASUREMENTS OF ω_0 IN dt μCF

C.G.L. HENDERSON, F.D. BROOKS and W.A. CILLIERS
Department of Physics, University of Cape Town, Rondebosch 7700, South Africa

G.J. PYLE and G.T.A. SQUIER
School of Physics and Space Research, University of Birmingham, Birmingham B15 2TT, UK

Monte Carlo simulations have been used to model and study characteristics of alpha–neutron coincidence detection systems used in direct experimental measurements of the initial sticking coefficient ω_0 in dt μCF. Some characteristics of these systems have also been measured experimentally, using the ^{3}H(d, n)^{4}He reaction to emulate dt μCF.

1. Introduction

Several of the direct methods proposed or used to measure sticking coefficients in muon catalyzed fusion [1] depend on differences in stopping powers to distinguish singly- and doubly-charged fusion products. In the experiment of the RAL collaboration [2], for example, range differentiation occurs in the gas (D–T and D_2) and the thin mylar windows (fig. 1(a)) traversed by the α or $\alpha\mu$ en route to the surface barrier detector (SBD). At a target pressure of 1500 Torr, most of the $\alpha\mu$ which are emitted towards the SBD reach this detector with energy exceeding 1.5 MeV, whereas α are either ranged out in the gas and target windows or arrive at the SBD with $E < 1.5$ MeV. A threshold of 1.5 MeV therefore selects only $\alpha\mu$ for measurement of coincidences with fusion neutrons detected by the NE213 scintillators (fig. 1(a)). The number of coincidences N_c and neutron singles N_n are recorded simultaneously. All fusions contribute to the neutron singles; thus, after subtracting backgrounds, the initial sticking coefficient ω_0 is obtained directly from the ratio of coincidences to singles,

$$\omega_0 = N_c/\phi B N_n, \tag{1}$$

where B is the probability that the extrapolated geometric path of a collinear $\alpha\mu$ associated with a detected fusion neutron intersects the SBD, and ϕ is the fraction of coincident $\alpha\mu$ on such paths which reach the SBD with energy exceeding the threshold of 1.5 MeV. The factors B and ϕ are estimated from Monte Carlo simulations (MCS) based on stopping power data, neutron cross sections [3] and muon stripping data [4].

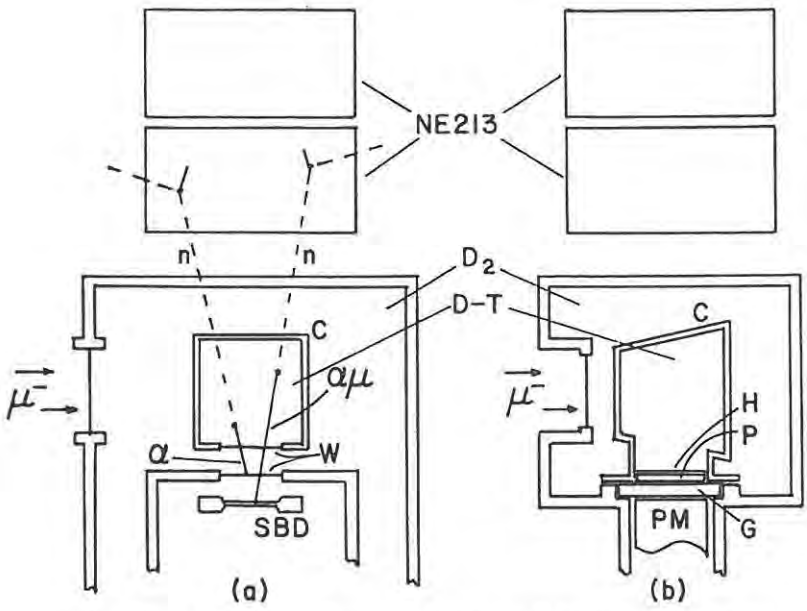

Fig. 1. Schematic diagrams of: (a) the RAL detection system; and (b) a proposed alternative system in which a 0.1 mm thick plastic scintillator P, protected by a 1.6 μm havar barrier H, detects the αμ. W are thin, aluminium-coated mylar windows, G is a glass window and the D–T target cells C are made of silver.

The low background levels attainable [2] using the RAL pulsed muon beam should allow the ratio N_c/N_n to be measured to a few percent. A comparable precision is therefore demanded in the calculation of B and ϕ, in order to determine ω_0 accurately. We report here on simulations of the RAL experiment and of an alternative geometry (fig. 1(b)). In order to check the MCS, we have also used the ^{3}H(d, n)^{4}He reaction to emulate dt μCF experimentally, and compared α–n coincidence measurements made in this way with those predicted by the simulations.

2. Monte Carlo simulations (MCS)

Simulations of the μCF experiments (fig. 1) were initiated by estimating the spatial distribution of fusions in the D–T targets using the code DEGRAD. An arbitrary sticking fraction of 0.5 was assumed in order to determine the characteristics of the two types of fusion with similar statistical accuracy, and the histories of individual collinear fusion pairs, n and α or n and αμ, were simulated. The α and αμ were tracked with energy decreasing in steps of 1–10 keV, using the data calculated by Cohen [4] to estimate the probability of muon stripping at each point along the αμ path. Neutron interactions with both the carbon and the hydrogen components of the scintillators were considered and neutron histories, including multiple scatterings,

were followed until the neutron either escaped from the system or dropped to an energy less than 0.1 MeV. The output from the MCS included detector efficiencies and singles and two-parameter spectra in addition to the B and ϕ factors.

3. Emulation of dt μCF

Alpha–neutron coincidences imitating those from dt μCF were obtained by using a DC deuteron beam to induce the reaction ^{3}H(d, n)^{4}He in a tritium gas target (fig. 2(a)) at a pressure of 400 Torr. An aperture A (diam. 2 mm) on the side of the cell, sealed by a 1.6 μm havar window, allowed α emitted at 90° to the deuteron beam to escape to the detector D, which was either an SBD or a thin NE102 plastic scintillator. The incident energy was adjusted so that deuterons entering the T_2 gas were degraded to 108 keV (the energy of the well-known resonance for this reaction) at the intersection of the beam with the α exit direction. Coincident 14.1 MeV neutrons emitted at the associated angle of 84° were detected in the NE213 scintillator, using a LINK 5010 pulse shape discriminator to reject gamma background events. The correct deuteron energy was easily found by tuning the beam energy for maximum coincidence rate using a smaller neutron detector (50 mm diam.) placed at the associated neutron angle.

Measured and simulated response functions (pulse height spectra) for an NE213 detector (130 × 130 × 70 mm) that was used in the RAL experiment are shown in fig. 2(b). The histogram shows the spectrum measured using the emulation system (fig. 2(a)). Curve M shows the simulated spectrum from the MCS and curves A–E show the components of M. Spectra M and A–E have been convoluted with a Gaussian distribution to simulate the pulse height resolution of the system. The width of this Gaussian was adjusted for best fit at the 14.1 MeV recoil proton edge and constrained to vary as $\sqrt{L}$ for other pulse heights L.

Several features of the response function M are clarified by reference to the components A–E. The main component A, due to n–p elastic scattering, shows a rise at high pulse heights which is due to neutrons undergoing multiple n–p scattering in the detector. The steep rise at low pulse heights is attributed to neutron reactions on the carbon component of the scintillator, particularly ^{12}C(n, α)^{9}Be (component B) and ^{12}C(n, n′)3α (component C). Components D and E are associated with the n–p scattering (proton recoils) of neutrons which have first been degraded by scattering on carbon, elastic scattering in the case of D and inelastic scattering to the ^{12}C 4.43 MeV level in the case of E. It is evident that neutron interactions with carbon have a significant effect on the response function at 14.1 MeV and should be considered when using low thresholds for neutron detection in dt μCF.

The arrangement of fig. 2(a) may also be used to determine the absolute efficiency of the NE213 detetctor for detecting 14.1 MeV neutrons, provided every α detected is associated with a neutron entering the NE213. Preliminary measurements by this method give efficiencies consistent with those estimated from the MCS.

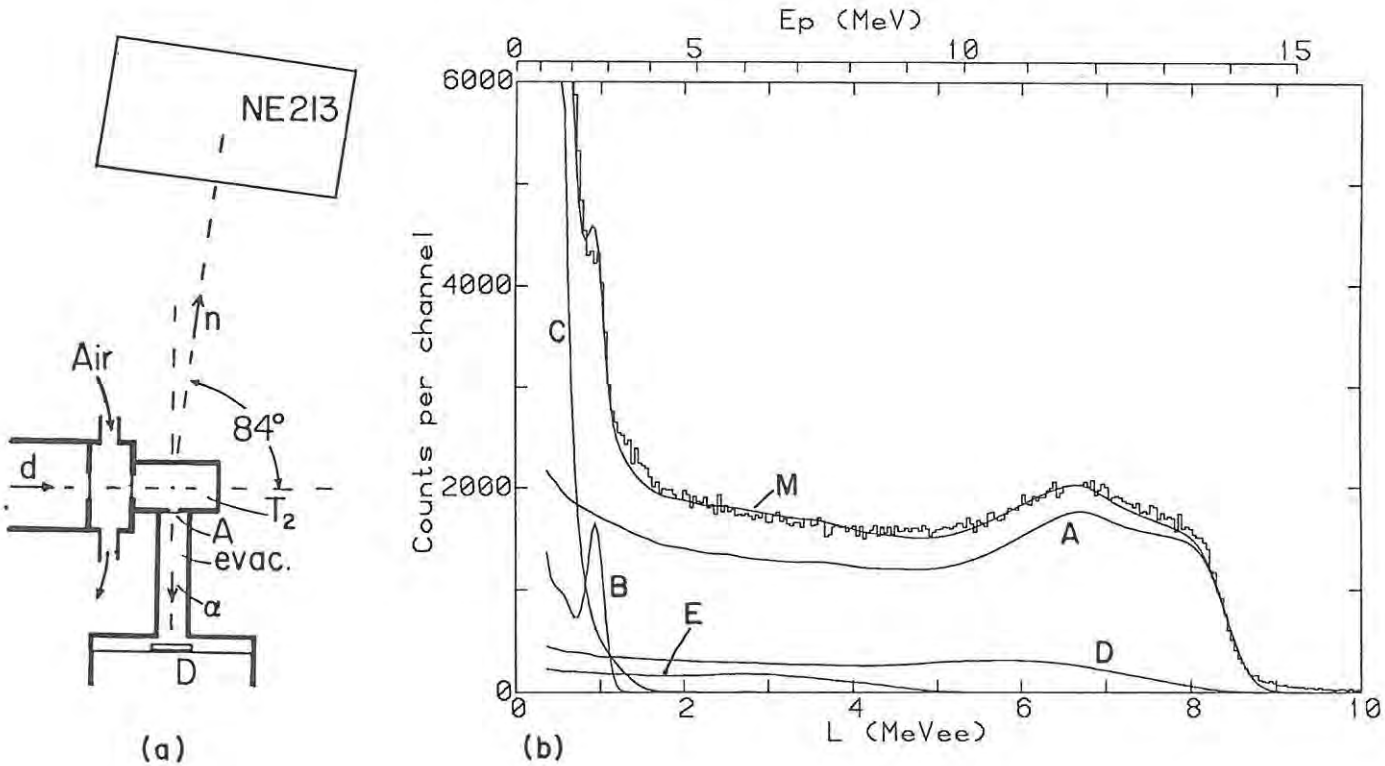

Fig. 2. (a) Schematic diagram of the system for emulating μCF experiments via the ^{3}H(d, n)^{4}He reaction. (b) Response function of NE213 detector (130 × 130 × 70 mm) for 14.1 MeV neutrons, showing experimental measurement (histogram), Monte Carlo simulation M and components A–E of M. The NE213 pulse height L is calibrated in MeV electron equivalent. The calibration against proton energy is shown above.

Absolute neutron detection efficiencies, although essential for some other μCF experiments, are not required for the sticking experiments considered here.

4. Coincidence distributions and backgrounds

The agreement between the simulated and emulated response functions (fig. 2(b)) lends confidence to the MCS and encourages its use in calculations of B and ϕ and in studies of other features of μCF experiments. Figure 3 shows, for example, simulations of the numbers of coincidences as a function of the time difference $T = T_\alpha - T_n$ between neutron and alpha detection and either: (a) the energy E measured by the SBD, or (b) the pulse height L measured by the plastic scintillator. In the simulations for the RAL system, we assume a time resolution of 3.0 ns (FWHM) and an energy resolution of 0.15 MeV (FWHM) at 3.5 MeV (varying as $\sqrt{E}$ at other energies) for the SBD. The alternative system (fig. 1(b)), which detects alphas in a thin plastic scintillator protected from the beta activity of the tritium by a thin (1.6 μm) havar barrier [5], achieves better timing, but at the expense of considerably degraded energy resolution. In the simulations for this system, we use the data obtained from the emulation experiments (section 3); a time resolution of 1.0 ns (FWHM) and pulse height resolution of 50% (FWHM) for 1.5 MeV alphas, varying as $\sqrt{L}$ for other energies.

The discrete loci of $\alpha\mu$–n coincidences in the E–T or L–T planes in fig. 3 provide the means for identifying and measuring sticking in these experiments. The events below these loci include the small fraction of α which reach the SBD or the plastic scintillator and some of the small fraction $(1 - \phi)$ of $\alpha\mu$ which are stripped of their μ before reaching the SBD (fig. 3(a)) or the havar barrier (fig. 3(b)). The MCS did not simulate any background coincidences, whereas actual experiments would generate background due to both accidental coincidences (from non-associated particles) and real coincidences (from associated, non-fusion particles). Experience at RAL [2] showed fewer accidental coincidences (which spread evenly in the T coordinate) than real coincidence background (RCB) events. Muon–nucleus interactions in the material surrounding the D–T gas (cell walls and alpha detector) are a possible source of the RCB. The target cells (fig. 1) are made from high-Z material (silver) so as to remove muons not captured in the D–T gas (the vast majority) very rapidly and the RAL data analysis excludes events earlier than 1 μs after the beam pulse to allow time for this muon scavenging to be completed. Muon–nucleus interactions in the surroundings may nevertheless persist beyond 1 μs, at a low level, if, for example: (a) a small fraction of dμ or tμ atoms formed in the D–T target gas diffuse slowly to the cell walls, or (b) multiple scattering leads to a few muons capturing in light elements ($Z < 15$) in or near to the alpha detector. In either case, since 40 MeV or more energy may be released in a muon–nucleus interaction, the products responsible for the RCB signals are likely to include some high-energy particles and the spread in T for RCB events should therefore be less than for fusion events. If

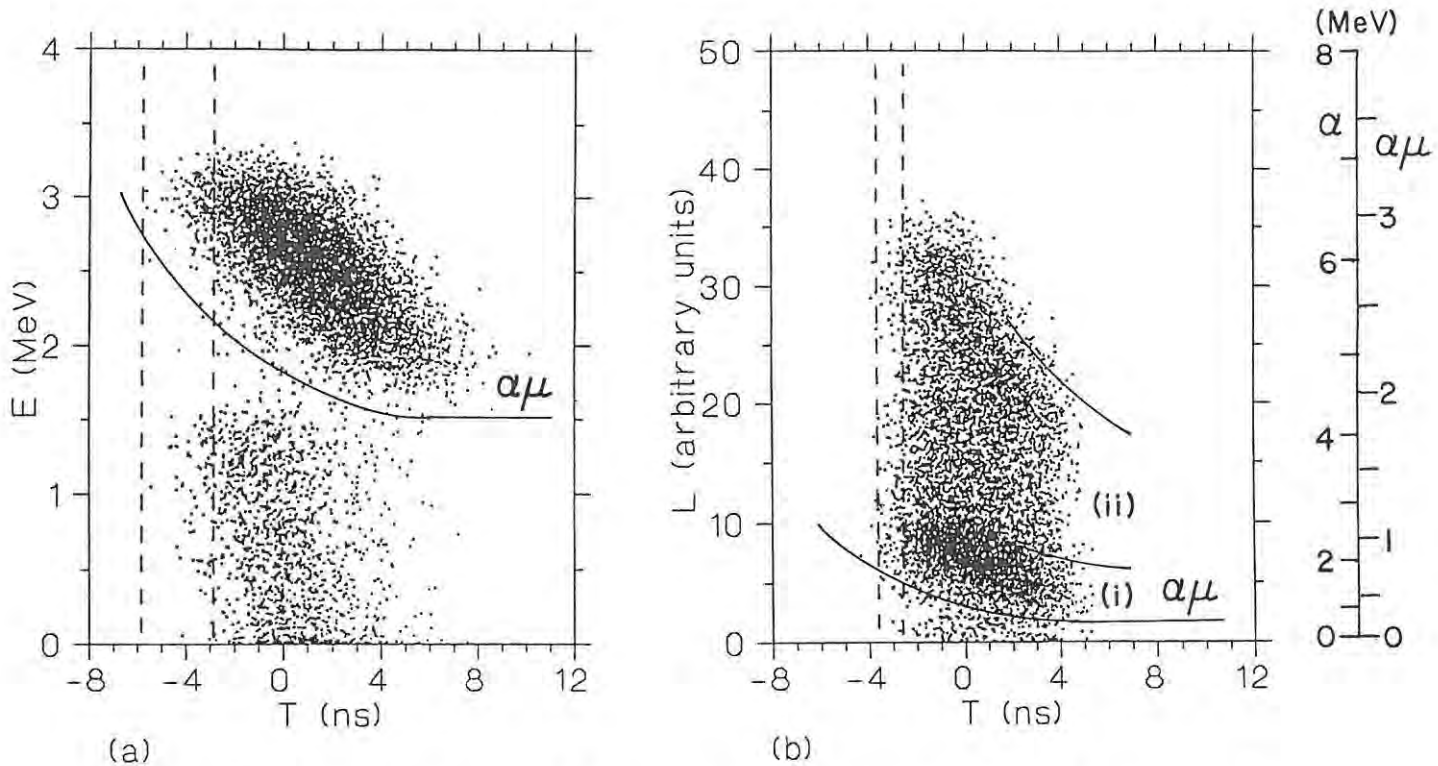

Fig. 3. Monte Carlo simulations of coincidences as a function of the alpha–neutron time difference T and detected α or $\alpha\mu$ energy E (or pulse height L) for: (a) the RAL system (fig. 1(a)) at a target pressure of 1500 Torr, and (b) the alternative system (fig. 1(b)) at a target pressure of 1800 Torr. The solid lines indicate cuts to select $\alpha\mu$ and the dashed lines show FWHM for the time distributions of RCB originating in or near to the alpha detectors. In (b) $\alpha\mu$ which are: (i) stripped in the havar, and (ii) remain unstripped for part or all of their path in the plastic are indicated. The calibrations of the plastic scintillator pulse height scale against energy, for α and $\alpha\mu$, respectively, are shown on the right-hand side.

all RCB were due to mechanism (b) alone, for example, then time distributions of these events should form groups of FWHM corresponding to the system time resolution and located as shown by the dashed lines in fig. 3. Time resolution may therefore be important for discriminating against RCB.

The simulation (fig. 3(b)) for the alternative system (fig. 1(b)) shows the $\alpha\mu$ locus broadening into two regions corresponding to $\alpha\mu$ which: (i) are stripped in the havar, or (ii) remain unstripped for part or all of their passage to rest in the plastic. The well-known saturation quenching effects in organic scintillators are responsible for this broadening. Quenching is smaller (and thus pulse height is larger) for (ii) than for (i) because the charge of the particle over part of its path in the plastic is half that of a bare alpha.

The results of the simulations (fig. 3) show that both of the systems considered (fig. 1) should discriminate effectively against α–n coincidences. The RAL system (fig. 1(a)) gives better separation than the alternative system (fig. 1(b)) using the plastic scintillator, but may be inferior to the plastic in discriminating against RCB due to poorer time resolution. If the RCB is indeed due to high-energy particles mimicking the $\alpha\mu$ in the fusion signature, then discrimination against this background could be enhanced by inserting a second scintillator of longer scintillation decay time between the plastic and the glass window in fig. 1(b), to form a phoswich. Fusion signals would then be characterised by a fast component alone (plastic only), whereas RCB signals would contain both slow and fast components. Pulse shape discrimination could then be used to discriminate against RCB. Tests made using the emulator system (fig. 2(a)) have verified that a detector of this type will operate successfully.

Acknowledgements

We thank the Science Research Council (UK) and the Foundation for Research Development (SA) for financial support, the RAL collaboration for stimulating discussions, A.P. Back, S.S. Jagpal and D. Momsen for technical support, and M.S. Allie, A. Buffler, M.J. Oliver and H.W. Schmitt for their assistance during the experiments.

References

[1] W.H. Breunlich, P. Kammel, J.S. Cohen and M. Leon, Ann. Rev. Nucl. Part. Sci. 39(1989)311.
[2] J.D. Davies et al., J. Phys. G16(1990)1529.
[3] *CINDA 76/77* (IAEA, Vienna, 1977).
[4] J.S. Cohen, Phys. Rev. A37(1988)2343.
[5] W.A. Cilliers and F.D. Brooks, this volume.

C.G.L. Henderson, F.D. Brooks, W.A. Cilliers, G.J. Pyle and G.T.A. Squier
Simulation and emulation of direct measurements of ω_0 in dt μCF
Muon Catalyzed Fusion 5/6 (1990/91) 405-411

TESTS OF PLASTIC SCINTILLATORS AS ALPHA DETECTORS IN dt μCF

W.A. CILLIERS and F.D. BROOKS
Department of Physics, University of Cape Town, Rondebosch 7700, South Africa

Thin plastic scintillators are considered for the detection of alphas from muon-catalyzed fusion in D–T gas targets. Tests show that barriers of havar foil (1.6 μm) or aluminium oxide (0.3 μm) provide adequate protection of the scintillator against tritium decay betas and restrict diffusion of tritium into the scintillator to within acceptable limits over periods of eight days or longer.

1. Introduction

The detection of α and $\alpha\mu$ emitted from D–T gas targets in experiments to measure, directly, the sticking coefficient in dt μCF [1–3] can present difficulties. A barrier is needed to protect the detector from the activity (typically >500 Ci) of betas and bremsstrahlung from the decay of tritium in the target. The α and $\alpha\mu$ reaching the barrier may be degraded to energies as low as 2 MeV in their passage through the target gas. The barrier must be thin enough to transmit these particles without additional energy loss of more than about 0.8 MeV. It must also limit diffusion of tritium into the detector itself to a tolerable level over a period long enough to complete an experimental run, typically 1–2 weeks.

The systems used by the LAMPF [2] and RAL [3] collaborations have incorporated surface barrier detectors (SBD), protected from the tritium by double windows of thin aluminised mylar and layers of D_2 gas between the windows and the SBD. Leakage or diffusion of tritium through the windows can be a worry in such systems, and it has also been suggested [4] that the better time resolution that should result from replacing the SBD by a plastic scintillator might improve discrimination against coincidence backgrounds. We report here on tests that have been carried out to assess the feasibility of alternative detection systems of this type, a thin plastic scintillator protected by a barrier consisting of either a thin foil of the alloy havar (plain or with surfaces oxidised) or a thin coating of aluminium oxide applied to the plastic.

2. Experiments and results

The tests on different barriers were made using the arrangement shown in fig. 1, incorporating a metal housing H with a cylindrical cavity C (10 mm diam. × 30 mm) to contain the tritium. A ^{210}Po α-source S1 was mounted at one end of C and the other end was sealed to the barrier B under test by a viton O-ring V. The

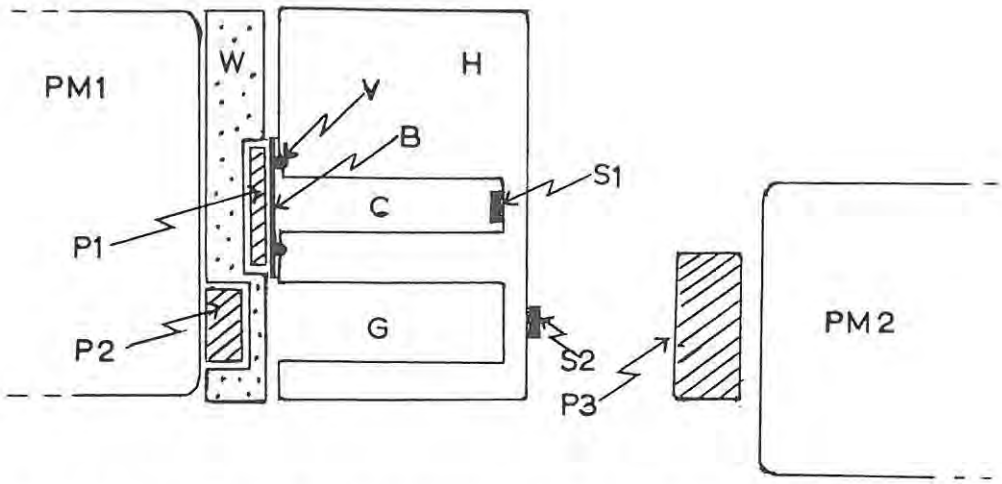

Fig. 1. Schematic diagram of the arrangement used for the tests, showing tritium cell C, ^{210}Po source S1, ^{22}Na source S2, barrier B, perspex window W, and plastic scintillators P1–P3.

0.1 mm thick NE118 plastic scintillator P1, beneath B, and the photomultiplier tube PM1 on the opposite side of the perspex window W were coupled to W by means of silicone jelly. A second plastic scintillator P2 (15 mm diam. × 5 mm) was coupled to PM1 beneath the hollowed-out section G, which allowed 0.5 MeV gammas from the ^{22}Na source S2 easy access to this scintillator. Annihilation quanta from S2 could thus make coincidences between P2 and the third plastic scintillator P3 (10 mm diam. × 20 mm), on photomultiplier PM2 in fig. 1.

The barriers tested included: (i) a 1.6 μm thick foil of the alloy havar, (ii) a similar foil, but with surfaces chemically oxidised beforehand, and (iii) a coating, applied to the plastic by electron beam vacuum evaporation, consisting of a 0.3 μm thick layer of aluminium oxide (Al_2O_3) deposited on top of a light-reflecting layer of aluminium, 0.3 μm thick. All these barriers are thin enough to be suitable for use in a sticking coefficient experiment. They were chosen for study because havar is readily available as thin foil, well-known for its use in vacuum windows, and because certain oxides, particularly aluminium oxide [5], are well-known for their good properties as barriers against gaseous diffusion. Assembly of the plastic scintillator P1 on the window W and of havar foils on the plastic (in (i) and (ii)) was carried out under vacuum so as to avoid trapping and subsequent release of air bubbles beneath B or in the optical coupling jelly between P1 and W.

Two different types of tests were made in the experiments. In the first type, the singles pulse height spectrum from PM1 was monitored, once or twice daily, for up to 8 days after loading the cell C with tritium to a pressure of 450 Torr. Source S2 was removed for these tests, hence the spectrum (fig. 2(a)) consisted of a peak from the alphas and a group at low pulse heights which included contributions

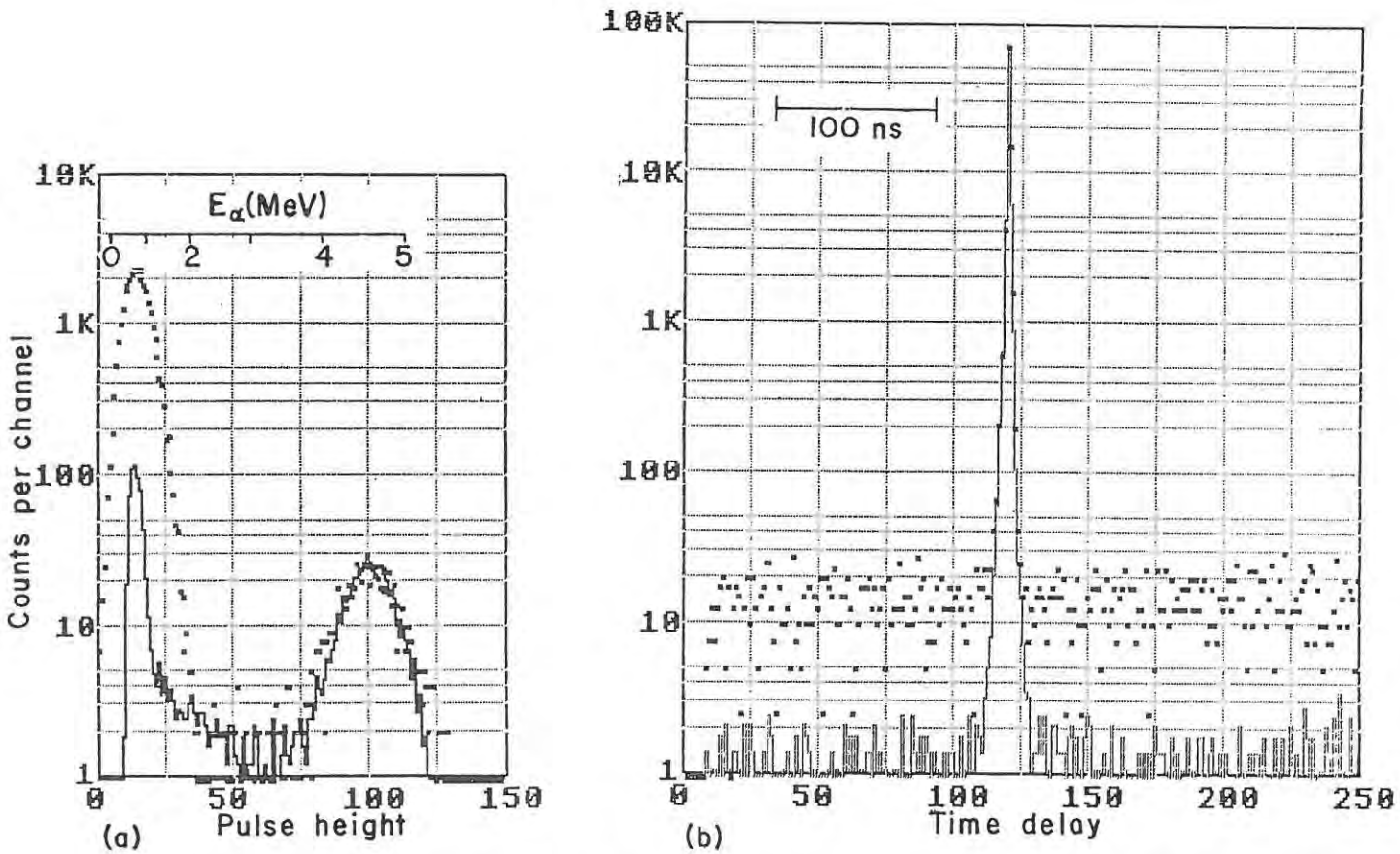

Fig. 2. Data obtained using the aluminium oxide barrier, showing: (a) pulse height spectra obtained (with source S2 removed) before (histogram) and 25 hours after (points) introducing tritium into the cell C, and (b) coincidence time delay spectra observed using a threshold corresponding to 0.7 MeV alpha energy on PM1, before (histogram) and 100 hours after (points) introducing tritium. The two spectra in (a) are normalised to the same live time, and likewise for (b).

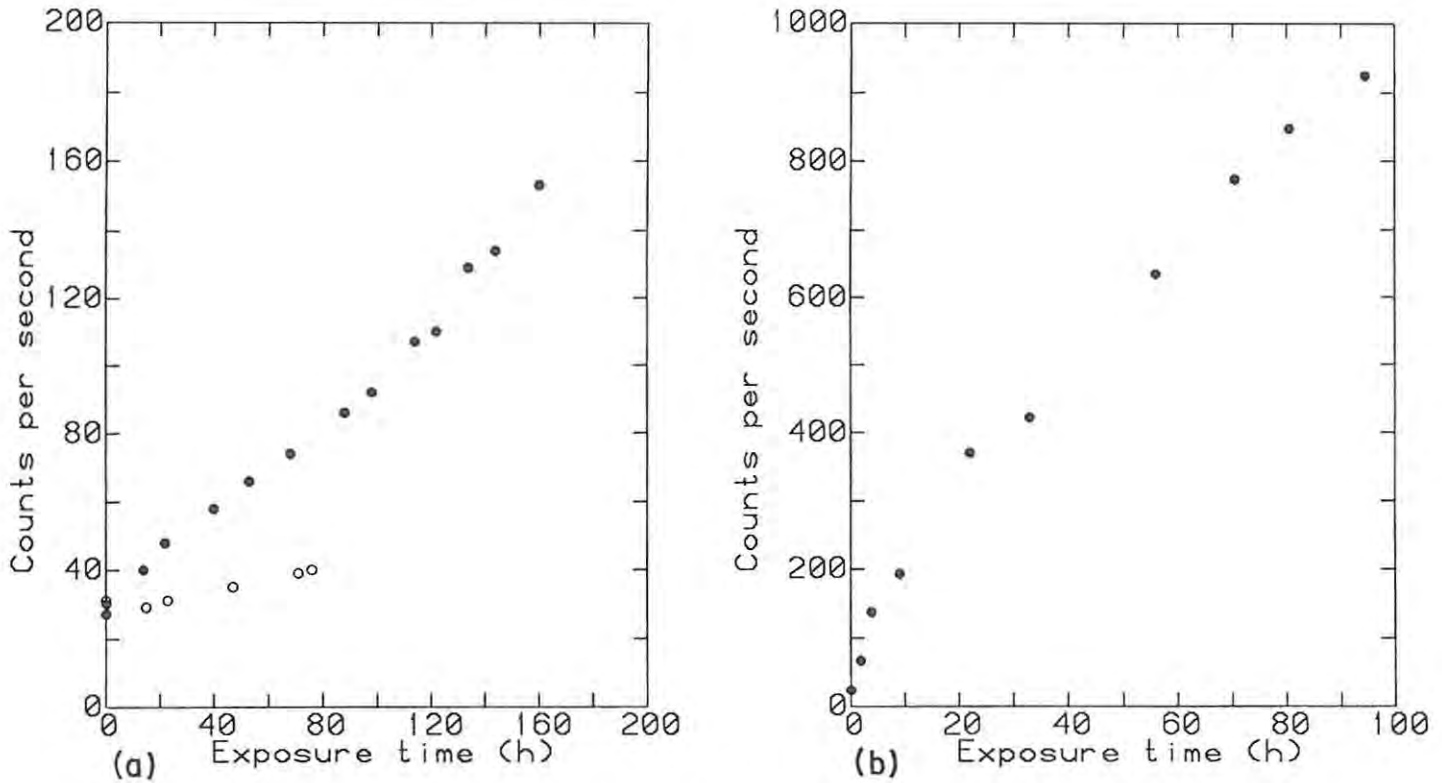

Fig. 3. Count rates from PM1 operating at a threshold corresponding to an alpha energy of 0.7 MeV, as a function of hours exposed to tritium for: (a) the havar (open circles) and oxidised havar (solid circles) barriers, and (b) the aluminium oxide barrier.

from any tritium activity reaching P1. The second type of test consisted of coincidence measurements between PM1 and PM2 made with source S2 in position. Real coincidences from annihilation quanta detected in P2 and P3 were thus viewed against the background of accidental coincidences contributed mainly by tritium activity detected in P1, thus imitating the situation in the sticking experiment in which true α–n coincidences have to be recognized against accidental background from a similar source.

A conventional fast timing system (timing filter amplifier plus constant fraction discriminator) was used to process the signals from PM2. The signals from PM1 were processed by a Link Systems type 5010 pulse shape discriminator [6], which was used as a fast gated integrator. This unit supplied both the integrated output (integration time 30 ns) for the pulse height measurements and the fast timing output for the coincidence measurements. The results from the latter are presented as coincidence time delay spectra (fig. 2(b)).

Pulse height spectra (fig. 2(a)) taken immediately before introducing tritium into the cell C, and 25 hours later, show the sharp increase that occurs in the low pulse height component after exposure to tritium. The growth of this component with length of exposure was monitored by recording the count rate above a threshold of 0.7 MeV alpha energy at regular intervals over periods lasting up to 8 days. Figure 3 shows results obtained for the three difference types of barriers tested. Time delay spectra obtained using the same threshold on PM1 were also recorded regularly. The spectra (fig. 2(b)) taken immediately before introducing the tritium and again 105 hours later show that the fraction of accidental coincidences observed at this threshold increased by a factor of 15 over this period.

3. Discussion

The results in fig. 3 show some systematic trends and some surprising and unexpected features. The rates observed using the havar foils increase approximately linearly with length of exposure. Their rates of increase can be expressed in terms of diffusion or leakage constants of: (i) $D = 0.25$ counts $s^{-1}\,h^{-1}$ for havar, and (ii) $D = 0.60$ counts $s^{-1}\,h^{-1}$ for oxidised havar. The increase for aluminium oxide is nonlinear at first but approaches linear after about 20 hours exposure, as it drops to a rate corresponding to $D = 7.5$ counts $s^{-1}\,h^{-1}$. The higher value for the aluminium oxide barrier may be partially due to its much smaller thickness. The absence, for all the barriers tested, of any noticeable step increase in the count rate immediately after introducing tritium into the cell is significant. This implies that betas or bremsstrahlung originating from within the tritium gas volume and penetrating through the barrier must contribute relatively little to the count rate. The effects seen are, on the contrary, consistent with penetration or leakage of tritium into the plastic and its decay there afterwards.

The higher value of D for oxidised havar than for plain havar was unexpected. However, subsequent checks have shown that it is extremely difficult to select very

thin foils which are completely free of tiny pinholes or other small flaws which might permit slow leakage of tritium. The different results obtained for oxidised and plain havar foils may therefore have more to do with the condition of the foils than the presence or absence of oxidised surface layers. There was also evidence, noted after the tests, that the aluminium oxide barrier may have been slightly damaged by contact with the O-ring V in fig. 1. Thus, leakage may also have contributed to the relatively high D value measured for this barrier.

The time delay spectrum observed after 100 hours exposure to tritium (fig. 2(b)) represents the accidental coincidence rate measured in the "worst" conditions encountered in these tests, "worst" since this spectrum was recorded at the time when the singles rate from P1 was highest (about 1 kHz), as can be seen from fig. 3(b)). Given that the ratio of true P2–P3 coincidences to P3 singles was 0.0012, we can use data from this spectrum to estimate the accidental coincidence count rate expected in a sticking coefficient experiment made using an aluminium oxide coated detector operating at a threshold of 0.7 MeV for alphas, as follows. The true fusion coincidences from a sticking coefficient experiment will be spread over a coincidence delay time range of about 10 ns, as can be seen from fig. 3(b) of ref. [4]. For a time window of this width bracketing the coincidence peak in fig. 2(b), the ratio of accidental to real coincidences is about 0.0009; hence, the ratio of such accidentals to the singles in P3 is about 1.1×10^{-6}. For the neutrons detected in the sticking coefficient experiment, we can assume this same value for the ratio of accidental coincidences to single neutrons if the area of the α-detector and the exposure to tritium activity are the same as in the tests. Scaling up by a factor of 50 to adjust for the higher target pressure and larger detector used in the sticking experiment, we estimate a value of 5.5×10^{-5} for the "worst" ratio of accidental coincidences to single neutrons that might be expected using the plastic scintillator systems that we have considered here. This is significantly lower than the corresponding ratio of 5×10^{-4} reported [3] for the RAL experiment.

We therefore conclude that thin plastic scintillators protected by barriers of havar or aluminium oxide will be viable as detectors of the α and $\alpha\mu$ from muon catalyzed fusion in D–T gas targets. The reliability of havar barriers might perhaps be improved by applying thin coats of aluminium oxide, to plug pinholes or other small flaws which are difficult to detect. However, plain aluminium oxide should be the best, as well as the most economical, of the barriers tested here, if applied in coatings about 0.5 μm thick. The possibility of using aluminium oxide as a tritium barrier on semiconductor detectors also looks promising and will be investigated shortly.

Acknowledgements

We acknowledge the support of the SA Foundation for Research Development, and thank Drs. A.N. Anderson and R. Pretorius and Messrs.

G. Ackermann, A.P. Back, D. Boulton, J.E. McLeod, D. Momsen and H.W. Schmitt for their advice and assistance.

References

[1] W.H. Breunlich, P. Kammel, J.S. Cohen and M. Leon, Ann. Rev. Nucl. Part. Sci. 39(1989)311.
[2] M.A. Paciotti et al., AIP Conf. Proc. 181(1989)38.
[3] J.D. Davies et al., J. Phys. G16(1990)1529.
[4] C.G.L. Henderson et al., this volume.
[5] K.R. Lawless, Rep. Progr. Phys. 37(1974)231.
[6] J.M. Adams and G. White, Nucl. Instr. Meth. 156(1978)459.

W.A. Cilliers and F.D. Brooks
Tests of plastic scintillators as alpha detectors in dt μCF
Muon Catalyzed Fusion 5/6 (1990/91) 413-419

Neutron fluence and kerma spectra of a p(66)/Be(40) clinical source

D. T. L. Jones, J. E. Symons, and T. J. Fulcher
Division of Medical Radiation, National Accelerator Centre, P.O. Box 72, Faure, 7131 South Africa

F. D. Brooks, M. R. Nchodu, M. S. Allie, A. Buffler and M. J. Oliver
Department of Physics, University of Cape Town, Rondebosch, 7700 South Africa

(Received 11 November 1991; accepted for publication 24 January 1992)

High-resolution neutron fluence spectra have been measured in the National Accelerator Centre's p(66)/Be(40) neutron therapy beam by the pulsed-beam time-of-flight method. ICRU muscle kerma spectra have been derived from the fluence spectra. Spectral changes resulting from different irradiation conditions have been quantified in terms of the average neutron energy and the fractional low-energy (<16 MeV) contribution. The changes observed with different thicknesses of polyethylene filtration are consistent with changes in quality parameters determined in biological and microdosimetric experiments. The dosimetry parameters $(K^{\text{tissue}}_{A150})_N$ and $(W_{\text{gas}})_N$ calculated for the measured spectra agree with the values recommended in the neutron dosimetry protocol. The shapes of the present fluence spectra differ from previous measurements of $p(>40)$/Be spectra. In particular, they differ significantly from the spectrum measured by recoil techniques in an identical neutron therapy unit at the Clatterbridge Hospital, UK. The reasons for the difference are not known.

Key words: neutrons, therapy, spectra

I. INTRODUCTION

Most of the newer neutron therapy facilities utilize the reaction of protons up to energies of 66 MeV on thick beryllium targets ($p+{}^9\text{Be}\rightarrow n+{}^9\text{B}-1.85$ MeV, plus several breakup reactions). Beam quality depends on the incident proton energy, precise details of the target construction (particularly the Be thickness and the type and thicknesses of backstop materials), filtration, shielding, and collimation. Different facilities are therefore likely to have beams with somewhat different quality even if the incident proton energies are similar. An appropriate unambiguous way of specifying beam quality is by means of a neutron energy spectrum.[1]

Knowledge of neutron therapy beam spectra is important since neutron interaction cross sections and kerma factors[2] as well as biological effects[3] are energy dependent. The sources of the largest uncertainties when neutron doses are derived from tissue-equivalent ionization chamber measurements are the energy-dependent factors $(W_{\text{gas}})_N$ (the energy required to produce an ion pair in TE gas) and $(K^{\text{tissue}}_{A150})_N$ (the tissue/A150 kerma ratio).[4] Spectral information is of interest when clinical data are exchanged between different centers and when radiobiological or dosimetric intercomparisons are undertaken. Neutron beam spectra are also used as inputs to certain treatment planning programs,[5] to calculate the energy deposited in various tissues and dosimetry materials, to provide information for shielding calculations and to aid in the interpretation of biological phenomena.

Measurements of thick-target p/Be spectra in air for proton energies greater than 35 MeV have been made most often by the pulsed-beam time-of-flight (TOF) technique,[6–15] but recoil spectrometry[16,17] has also been used. Recently, a novel method that involves the iterative fitting of water-attenuation data has been employed to derive a spectrum.[18] Only the most recent measurements[17,18] have actually been made in a clinical beam whereas all the other measurements have been made in a nonclinical environment. The earlier TOF measurements made at the University of California, Davis[6,7,10] have been questioned.[9,16,19] It was averred[9,19] that there were errors present in the version of the neutron detection efficiency code[20] which was used to derive energy spectra from the TOF spectra. The spectra were also considered unreliable[16] because of the poor resolution at high energies as a result of the short flight paths used. Subsequent measurements at proton energies up to 46 MeV[11–13,15,16] indicated that the main features of p/Be fluence spectra were a relatively intense low-energy component attributed to evaporation neutrons (the relative magnitude of this component depending on target thickness and beam filtration), followed by a region of approximately constant fluence from about 10 MeV to near the kinematic limit and then a steep decrease to the maximum energy. This "standard" shape was adopted by Awschalom *et al.*[21] for their extensive calculations of kerma for p(41)/Be and p(66)/Be neutrons in various materials. For the higher energy beam, the spectrum was simply scaled from lower energy measurements.[11,13]

The shapes of the two clinical beam spectra measured recently at $E_p=45$ MeV[18] and $E_p=62$ MeV[17] are very different from each other and neither show the characteristics of the standard shape. Furthermore, the only previous measurements of p/Be spectra at proton energies greater than 60 MeV, viz at 65.4 MeV[6] and at 90–101 MeV[8,14] reveal bell-shaped distributions in the higher energy regions. The shape of these spectra have little in common with the standard spectral shape or with the most recent clinical beam measurements.[17,18] The need therefore exists

 0094-2405/92/51285-08$01.20

for definitive high-resolution measurements of high energy *p*/Be spectra.

At the National Accelerator Centre (NAC) we have the unique capability of measuring high-resolution TOF spectra *in situ* in the *p*(66)/Be(40) neutron therapy beam.[22] Here, TOF spectra have been measured under different irradiation conditions and both fluence and muscle kerma spectra have been obtained from the measured data. From these spectra various quality-related factors have been derived. The values of some parameters of importance in neutron dosimetry have also been determined.

II. EXPERIMENTAL METHODS

Briefly, the NAC's neutron therapy system[22] consists of an isocentric gantry capable of $\pm 185°$ rotation and includes a collimator with a continuously variable aperture providing rectangular field sizes from 5×5 cm^2 to 30×30 cm^2 at a source-to-axis distance (SAD) of 150 cm. Neutrons are produced by the reaction of 66-MeV protons on a copper-backed 19.6-mm-thick Be target in which the proton beam dissipates 40 MeV. The neutron beam is modified by 0.8-cm-thick iron flattening filters and a 2.5-cm-thick polyethylene $[(CH_2)_n]$ hardening filter (H). One flattening filter (F1) is always in the beam and is used for fields with sides $\leqslant$16 cm in length while for fields with longer sides an additional filter (F2) is placed in the beam. This large-field filter combination is designated F12. Three tungsten wedge filters (W1, W2, W3) can be inserted in the beam to tilt the beam profiles at a depth of 10 cm in water by 25°, 35°, and 45°, respectively. The "book-end" collimator consists of five layers of four interlocking blocks of iron and borated polyethylene, geared to provide a tapered aperture and is rotatable through 360°.

The neutron detector was a cylindrical 5 cm long by 5-cm-diam NE213 liquid scintillator coupled to a RCA8850 photomultiplier tube. The scintillator was oriented with its symmetry axis parallel to the direction of the neutron beam and was mounted in the treatment room in open geometry at a flight path of 6.06 m from the Be target. The center of the scintillator was 94 cm from the concrete wall of the room. For all the measurements, the gantry rotation angle was set at 270° to provide a horizontal beam. The use of pulse shape discrimination (PSD) allowed neutron- and gamma-induced events in the scintillator to be distinguished. Standard pulsed-beam TOF techniques were used: The time reference signal was derived from the rf cycle of the injector cyclotron which under normal conditions is operated at a frequency of 16.373 MHz (pulse separation=61 ns) for 66-MeV protons. Pulse selection (1 in 5) was used to give a frequency of 3.275 MHz and pulse separation of 305 ns. In order to prevent overlapping of events from successive beam pulses the lower limit of detection was thus 2.1 MeV (neutron energy). In practice, however, a slightly higher minimum threshold was required to eliminate electronic noise and to provide adequate gamma discrimination without loss of any neutron events.

Three-parameter event-by-event data acquisition was used: Each event was characterized by a pulse height (L), a PSD signal (S) (Link Systems Model 5010 pulse shape discriminator) and the TOF relative to the cyclotron rf (T). To reduce the count rates to acceptable levels proton beam currents of 1 nA or less were used. In order to achieve these beam currents the widths of two pairs of slits in the low-energy (E_p=3.15 MeV) beam line (between the injector cyclotron and the main cyclotron) are reduced, thus ensuring that the 66-MeV beam remains focussed on the Be target. The low currents used precluded the accurate measurement of target charge since the target leakage current was of the same order as the beam current. Such leakage currents are negligible relative to the proton beam currents of 25–30 μA used for patient treatment. The emphasis in the present work is in any case on spectral shapes rather than on absolute yields. Dead times in the detection system were negligible.

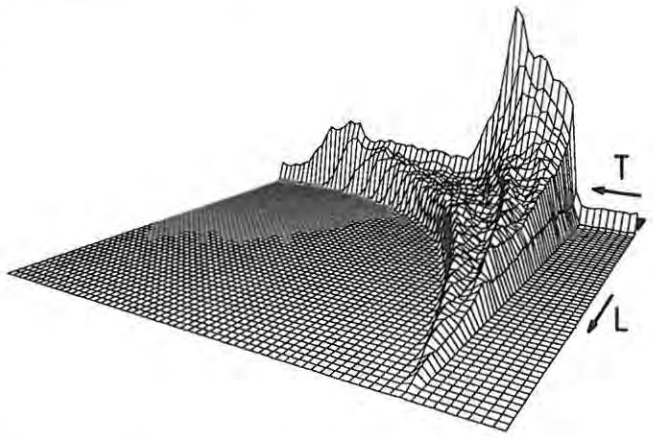

FIG. 1. A typical T-L spectrum (counts versus time-of-flight versus pulse height) measured in the 10×10 cm^2 clinical beam. The ridge due to prompt gamma rays is not shown.

The FWHM of the prompt γ-ray peak in the TOF spectra was typically 1.4 ns indicating an overall time resolution of the detection system of $\pm$0.7 ns. This translates to an energy resolution of $\pm$1.5 MeV at 60 MeV and $\pm$0.1 MeV at 10 MeV for the flight path of 6.06 m. (The flight path uncertainty makes a negligible contribution to the energy resolution.) Except where otherwise stated all the spectra presented in this paper were determined with the neutron detection threshold (E_{th})set at 3.5 MeV, which corresponds to an equivalent electron energy of 1.3 MeV.[23] No time walk was observed in the T-L spectra above this threshold. TOF spectra were measured in air on the beam central axis for different field sizes and different filter combinations, while some off-axis measurements were also made.

III. RESULTS

A typical T-L spectrum is shown in Fig. 1 while illustrative TOF spectra are shown in Fig. 2. These latter spectra were derived from event-by-event data with two different neutron detection thresholds of 4.8 MeV and 10.7 MeV respectively imposed. For the 4.8-MeV threshold two spectra are shown: one without PSD operative and the other

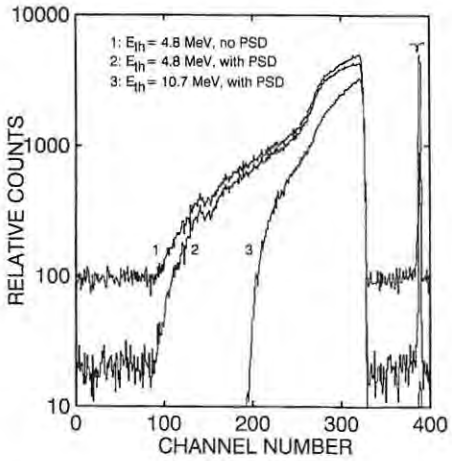

FIG. 2. Time-of-flight spectra in the 10×10 cm^2 clinical beam showing the prompt gamma peak. These spectra were derived from the same three-parameter spectrum with the conditions imposed in each case indicated in the legend. The time scale calibration is 0.594 ns per channel and the flight path was 6.06 m.

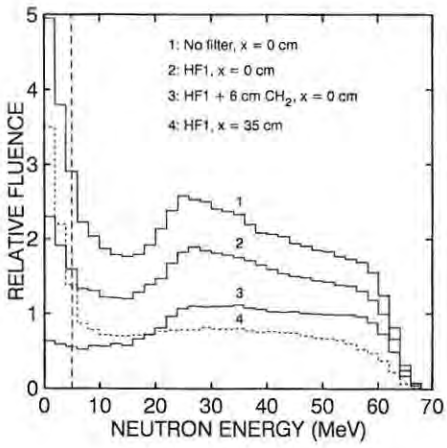

FIG. 3. Neutron fluence spectra in a 10×10 cm^2 field for various irradiation conditions as indicated in the legend. The spectra are arbitrarily scaled for clarity. HF1 is the clinical filter (H=2.5 cm CH_2, F1=iron flattering filter for small fields) and x is the off-axis distance. The neutron detection threshold was 3.5 MeV. The portions of the curves to the left of the dashed vertical line indicate exponential extrapolation to zero energy.

with a PSD cut set to eliminate most of the gamma rays, but allowing all neutron events to be counted. The spectrum obtained with the 10.7-MeV threshold has the same PSD cut imposed. The very sharp low-energy cutoffs provide very accurate measures of the detection thresholds. In the cases illustrated, one channel corresponds to energy bins of about 0.03 MeV and 0.1 MeV at 4.8 MeV and 10.7 MeV, respectively. The thresholds determined in this way were found to be in good agreement with thresholds determined from pulse height spectra measured with radioactive sources providing high-energy gamma ray reference points. Appropriate NE213 response functions,[23] which were confirmed by the present measurements, were then used to determine the corresponding neutron energy.

The fact that there are essentially no events below the low-energy cutoff or between the prompt gamma ray peak and the neutron kinematic limit in the PSD-gated spectra indicates that there is negligible room-scattered background. Further evidence of the detection of negligible numbers of scattered neutrons is the very sharp maximum pulse-height (L) edge in the T-L spectrum (Fig. 1). Scattered high-energy neutrons would take a longer time to reach the detector than primary neutrons of the same energy. They would therefore appear as events in the T-L spectrum of large pulse height, but at a time corresponding to a lower energy primary neutron, i.e., beyond the primary maximum pulse-height edge. There is no evidence of this. Measurements with a 1-m-long iron shadow bar and at shorter flight paths confirmed the essentially scatter-free experimental conditions.

All the TOF spectra were converted to fluence energy spectra using the SCINFUL detection efficiency code.[24] To test the consistency of the code several TOF spectra were derived from the same run with the off-line imposition of different detection thresholds and these were converted to fluence spectra. In the region above the highest threshold, it was found that these spectra were consistent, thus lending credence to the efficiency calculations. The efficiencies of the detector calculated[25] with the older Stanton code[20] were similar at low energies to those obtained with SCINFUL for the same detection thresholds, but diverged at high energies. At 60 MeV, the efficiency calculated with the Stanton code exceeds that calculated with SCINFUL by 19%. The gross features of the spectra were largely independent of the efficiency code used, but spectra derived with SCINFUL were harder. The spectra were corrected for attenuation in the 4.56 m of air between the gantry axis and the detector position. This attenuation was 3.4% at 5 MeV and 2.3% at 60 MeV, respectively.

Selected, arbitrarily-scaled neutron fluence spectra are shown in Fig. 3. These spectra were all obtained with a neutron detection threshold of 3.5 MeV. In order to derive quantitative information, all the spectra were exponentially extrapolated from threshold to the E=0-MeV axis. This appears to be a reasonable approach as such an extrapolation for the unfiltered beam approximates that of an evaporation distribution[21] (see Fig. 6). An important application of the measurement of neutron therapy beam spectra is the calculation of kerma in various tissues and materials. The lowest energy neutrons contribute relatively little to energy absorption and the shape of the fluence spectrum in the low energy region therefore has only a small influence on total kerma.[21]

All the fluence spectra have been converted to ICRU muscle tissue[26] kerma spectra. The muscle tissue kerma spectra corresponding to the fluence spectra in Fig. 3 are shown in Fig. 4. These spectra were calculated using the ICRU muscle tissue kerma factors given by Caswell *et al.*[2] for energies below 15 MeV, and for energies above 15 MeV those given by Brenner.[27] These kerma factors were chosen because they are the most recent which have been published in the respective energy ranges.

The kerma spectra shown in Fig. 4 are represented as kerma fraction distributions in Fig. 5. Here, the data are

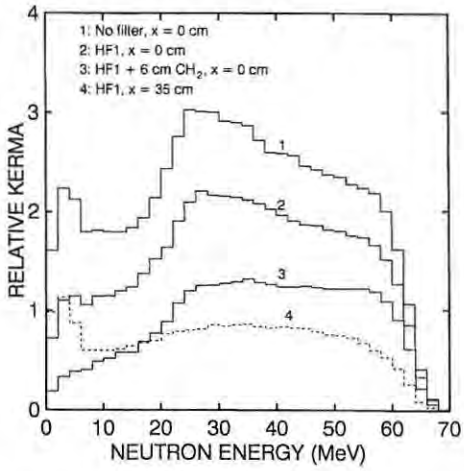

FIG. 4. ICRU muscle kerma spectra corresponding to the fluence spectra shown in Fig. 3. The spectra are arbitrarily normalized.

expressed as the total kerma contributed by neutrons with energies less than the abscissa energy. From these curves, it can be seen that the fraction of total kerma in the extrapolation region (below 4 MeV) is in all cases less than 10% of the total kerma.

In order to quantify the observed quality changes both fluence-weighted ($\bar{E}_F$) and kerma-weighted ($\bar{E}_K$) average neutron energies have been calculated. In addition, quality parameters which are termed "normalized fluence softness factors" (NFSF) and "normalized kerma softness factors" (NKSF) have been derived for all the fluence and muscle kerma spectra, respectively. These parameters are defined as follows for each filter (f), field size ($s\times s$) and off-axis distance (x):

$$\mathrm{NFSF}(f,s,x)=\frac{\mathrm{FSF}(f,s,x)}{\mathrm{FSF}(\mathrm{HF1},10,0)}=\left(\frac{\text{Fluence below 16 MeV}}{\text{Total fluence}}\right)\times\frac{1}{\mathrm{FSF}(\mathrm{HF1},10,0)},$$

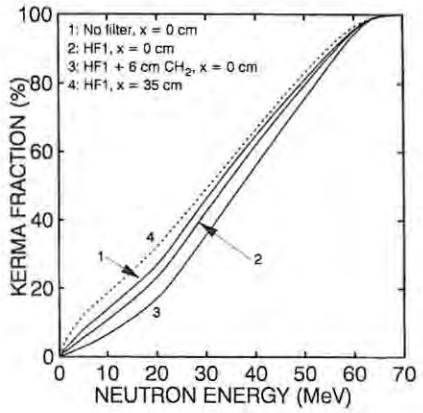

FIG. 5. Kerma fractions calculated from the spectra shown in Fig. 4.

TABLE I. Fluence- and kerma-weighted average energies ($\bar{E}_F$, $\bar{E}_K$) and normalized fluence and kerma softness factors (NFSF, NKSF) as a function of field size, filtration and off-axis distance (x). [H: Clinical hardening filter (2.5 cm CH_2), F1,F12: Iron flattening filters, and W2: Tungsten wedge filter].

Field size at isocenter (cm×cm)	Filtration	x (cm)	$\bar{E}_F$ (MeV)	$\bar{E}_K$ (MeV)	NFSF	NKSF
10×10		0	28.5	32.6	1.23	1.22
10×10	HF1	0	30.8	34.1	1.00	1.00
10×10	HF1+3 cm CH_2	0	33.3	35.9	0.78	0.80
10×10	HF1+6 cm CH_2	0	34.6	36.9	0.67	0.68
10×10	HF1	0	30.8	34.1	1.00	1.00
10×10	HF1	20[a]	30.8	34.0	0.99	0.99
10×10	HF1	25	28.1	32.0	1.25	1.25
10×10	HF1	35	25.3	30.7	1.57	1.52
10×10	HF1	0	30.8	34.1	1.00	1.00
10×10	HF12	0	31.4	34.4	0.93	0.94
10×10	HF1W2	0	32.7	35.5	0.84	0.85
5.5×5.5	HF1	0	31.3	34.4	0.94	0.95
10×10	HF1	0	30.8	34.1	1.00	1.00
20×20	HF1	0	30.2	33.7	1.06	1.05
29×29	HF1	0	29.8	33.5	1.11	1.09

[a] In penumbra

$$\mathrm{NKSF}(f,s,x)=\frac{\mathrm{KSF}(f,s,x)}{\mathrm{KSF}(\mathrm{HF1},10,0)}=\left(\frac{\text{Kerma below 16 MeV}}{\text{Total kerma}}\right)\times\frac{1}{\mathrm{KSF}(\mathrm{HF1},10,0)}.$$

The combination HF1,10,0 represents the reference clinical beam spectrum: HF1 filters (see above), 10×10 cm^2 field size, on the beam axis ($x=0$).

Details of the irradiation conditions for the measured spectra and the quality parameters which have been derived are given in Table I. The spectra for 20×20 cm^2 and 29×29 cm^2 field sizes were measured with the clinical F12 flattening filter combination. The quality parameters given in the Table I for these two field sizes have been corrected for the effect of filter F2. The uncertainties in the calculated parameters associated with the zero-energy extrapolation for the 10×10 cm^2 clinical beam spectrum are estimated to be 2.2%, 0.9%, 6.9%, and 4.4% for $\bar{E}_F$, $\bar{E}_K$, FSF and KSF, respectively.

IV. DISCUSSION

Generally the spectra and the quality parameters derived therefrom show the expected trends. The spectra harden significantly with increasing thicknesses of polyethylene filtration which preferentially filters out low-energy neutrons. The spectra soften with increasing distance from the geometrical beam edge. (The off-axis distance of $x=20$ cm is in the geometric penumbra of a 10×10 cm^2 field defined at the isocenter.) Some hardening is also observed with increasing thicknesses of metallic flattening and

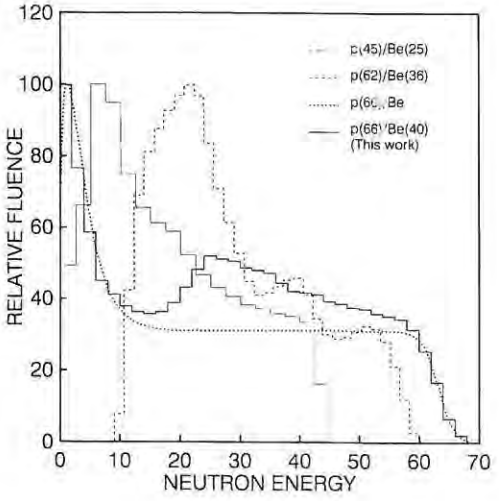

FIG. 6. Comparison of different fluence spectra normalized to 100 at maximum fluence. (1) $p(45)/Be(25)$: University of California—Los Angeles;[18] (2) $p(62)/Be(36)$: Clatterbridge Hospital, UK;[17] (3) standard $p(66)/Be$ spectrum scaled from lower energy spectra;[21] (4) $p(66)/Be(40)$: present work, 10×10 cm^2 unfiltered beam.

wedge filters while the spectra soften with increasing field size. The fluence-weighted average neutron energy (E_F) of 30.8 MeV for the 10×10 cm^2 clinical beam compares with a value of 27.6 MeV measured in air at the isocenter by microdosimetry.[28] The average neutron energies and normalized softness factors obtained for different polyethylene filter thicknesses are consistent with variations in both RBE and y^* (dose mean lineal energy corrected for saturation) values previously determined with different polyethylene filter thicknesses by radiobiological and microdosimetric methods respectively in the NAC clinical beam.[29]

Figure 6 shows the fluence spectrum for the 10×10 cm^2 unfiltered beam measured here together with other $p(>60)/Be$ spectra. The spectra are normalized to 100 at maximum fluence. The spectrum measured recently in the $p(45)/Be(25)$ neutron therapy beam at the University of California, Los Angeles[18] is also shown. Although the energy of this beam is much lower the spectrum is of interest because it was measured in a clinical environment. The experimental technique used was spectrum reconstruction by interative fitting of narrow beam water-attenuation data. Although this method has been used to determine megavoltage x-ray beam spectra,[30] it has not been used before for neutron beams. Ionization chambers were used to measure the separate neutron and gamma attenuation curves and these were placed at a distance of 2.20 m from the target. The field size defined at the isocenter was 4×4 cm^2. The $p(62)/Be(36)$ spectrum shown is the one measured recently in the neutron therapy beam at Clatterbridge Hospital, UK.[17] This spectrum was measured by NE213 scintillator recoil spectrometry in a 10×10 cm^2 field in air at the isocenter (SAD=150 cm). There was an iron flattening filter in the beam, but no other beam modifier was used. As mentioned above the $p(65.4)/Be$ spectra measured by Amols *et al.*[6] using the time-of-flight technique have been questioned due to resolution and detection efficiency problems[9,16] and are therefore not shown. The standard $p(66)/Be$ spectrum[21] is also shown. This spectrum was simply obtained by scaling $p(41)/Be$[11] and $p(46)/Be$[13] spectra.

The shapes of the spectra shown in Fig. 6 have quite different characteristics. It can be argued that the standard $p(66)/Be$ spectrum can be discounted because it is not necessarily valid to scale a spectrum from one energy to another. Furthermore, the original spectra[11,13] were measured with infinitely thick (stopping) targets whereas the other measurements shown here were made with targets in which only a fraction of the incident energy is dissipated. However, the NAC spectrum does agree most closely with this standard spectrum. The $p(45)/Be(25)$ spectrum differs markedly from the standard shape. There is no obvious explanation for this although it is possible that there are systematic errors in the experimental and fitting procedures used, as mentioned in the original paper.[18]

Of most significance are the differences observed between the NAC [$p(66)/Be(40)$] and Clatterbridge [$p(62)/Be(36)$][17] spectra. These two neutron therapy units are identical in every respect including target construction. The very slight differences in beam energy and target thickness should result in negligible differences in the spectral features. The construction of both targets is such that the energy of the proton beam exiting the beryllium is 26 MeV, which is dumped in water and copper. The Clatterbridge scintillator was covered by a 6.5-mm-thick lead cap, although this was actually only necessary for their measurements in phantom. No filtration was used for the NAC measurement shown here, while an iron flattening filter was used for the Clatterbridge measurement. None of these experimental differences can account for the gross difference in shape observed between the two spectra. Another difference is the fact that the NAC measurements were made at a distance of 6.06 m from the target whereas the Clatterbridge measurement was made at a SAD of 150 cm. However, in the present work spectra have also been measured on the gantry axis (SAD=150 cm) and these agree very well with those measured at longer flight paths, except in the high-energy region where the resolution at the short flight path is poor (±6 MeV at 60 MeV).

Although most of the data presented in this work are from a single experimental run, several sets of measurements have been made at different times over a period of a year, and the spectra obtained have always been reproducible within experimental error. As mentioned above, there is confidence in the detection efficiency calculations that are a potential source of error in this type of measurement. The entire experimental arrangement used here, including the detector, has been used in independent time-of-flight experiments on other beam lines. No unexpected results have been obtained. There is therefore confidence in the reliability of the present data. There appears to be no reasonable explanation for the differences between the NAC and Clatterbridge spectra, unless there is a systematic error in the recoil techniques used to derive the latter spectrum.

Energy-dependent differential linear attenuation coefficients were calculated for polyethylene from hydrogen and

carbon total cross sections.[31] Using these coefficients, fluence spectra were calculated from the reference spectrum for additional polyethylene thicknesses of 3 and 6 cm. The shapes of the calculated and measured spectra agreed almost exactly, thus lending further credence to the present data. The integral linear attenuation coefficient in polyethylene was calculated to be 0.087 cm^{-1}. Structure due to neutron resonant scattering in ^{12}C below 10 MeV was not observed because of the smearing effect of the relatively large energy bins (2 MeV).

It is interesting to note that a flat peak occurs in the NAC spectrum at an energy of about 0.4 of the maximum energy. This agrees approximately with the position of peaks observed in *p*/Be spectra measured at 90-101 MeV.[8,14] The NAC beam energy is about half way between these latter energies and the beam energies of 41 MeV[11] and 46 MeV[13] from which the standard spectrum was scaled. If the higher energy distributions were scaled to a beam energy of 66 MeV, appropriately normalized and added to the standard spectrum, a spectral shape very similar to that obtained in this work would be obtained.

Using the reference 10×10 cm^2 clinical fluence spectrum, the ratio of ICRU muscle tissue kerma to *A*150 kerma $[(K^{tissue}_{A150})_N]$ has been calculated for three different combinations of kerma factors, corresponding to the combinations[2,27,32–34] designated I, II, and IV by Awschalom *et al.*.[21] The results obtained for the *p*(66)/Be standard spectrum are 0.92, 0.96, and 0.98, respectively, whereas Awschalom *et al.* obtained values of 0.92, 0.95, and 0.98, respectively for the same kerma factor combinations. The value recommended in the neutron dosimetry protocol[35] for high-energy *p*/Be beams is 0.95. The kerma ratios obtained here vary by less than 1.0% between all the spectra. These ratios are also quite insensitive to the nature of the extrapolation to zero energy of the measured spectra—there is a difference of less than 0.2% between two extreme assumed extrapolations for the reference spectrum. Of course the kerma for individual materials are quite sensitive to such quality changes (variation of about 6% for both muscle and *A*150 for the reference spectrum). The effect of spectral variations on muscle kerma and kerma ratios has been examined in detail by Awshalom *et al.* .[21]

A fluence-averaged $(W_{gas})_N$ value (average energy required to produce on ion pair in TE gas) of 31.1 eV has been obtained for the reference spectrum using $(W_{gas})_N$ values given by Goodman and Coyne[36] up to neutron energies of 19 MeV. Above 19 MeV, a constant value of 31.0 eV was assumed. The recommended value of $(W_{gas})_C$ (average energy required to produce an ion pair in TE gas in the calibration photon beam) is 29.3 eV.[35] The value of W_N/W_C obtained here is 1.06 which agrees exactly with the protocol-recommended value of 1.06 ± 0.02.[35] The value of $(W_{gas})_N$ is also insensitive to the zero-energy extrapolation and a difference of 0.4% between two extreme extrapolations was found. $(W_{gas})_N$ varies by less than 0.5% between all the measured spectra for the standard zero-energy extrapolation.

V. CONCLUSIONS

Extensive high-resolution spectra have been measured in the NAC's *p*(66)/Be(40) neutron beam. The measurements comprise one of the very few spectral determinations in a *p*/Be therapy beam and probably the first made using the pulsed-beam time-of-flight method. The spectra are very sensitive to beam quality changes and parameters have been derived from the spectra to quantify these changes. The spectral changes observed with different thicknesses of polyethylene filtration exhibit the same trends as observed in biological and microdosimetry measurements. There is some uncertainty in the extrapolation of the spectra from the detection threshold to zero energy, but this is of little consequence for dosimetry since the kerma factors in this energy region are small.

The shapes of the spectra obtained do not agree with other measurements, although it can be argued that the shapes are intermediate between those measured at lower energies and those measured at higher energies. The differences observed between the NAC beam spectra and the one measured at an identical neutron therapy facility at Clatterbridge Hospital, UK by recoil spectrometry[17] cannot be explained except on the basis of systematic errors probably associated with the response function measurements.

The dosimetry parameters, $(K^{tissue}_{A150})_N$ and $(W_{gas})_N$, calculated for the 10×10 cm^2 clinical beam agree closely with those recommended in the international neutron dosimetry protocol.[35] Both parameters are very insensitive to quality changes, specially in the low-energy region. In view of the significant differences in shape between the spectra measured here and those assumed for previous *p*(66)/Be kerma ratio calculations,[21] a comprehensive re-evaluation of kerma ratios for other tissues and materials is required. Indications are, however, that the results obtained will not be very different, unless more definitive kerma factors become available. Further spectral measurements will incorporate accurate monitoring systems so that absolute yields and kerma can be calculated. It is also planned to extend this work to include spectral and angular distribution measurements of the *p*/Be reaction at various proton energies and for different target thicknesses.

[1]International Commission on Radiation Units and Measurements, "Clinical neutron dosimetry Part 1: Determination of absorbed dose in a patient treated by external beams of fast neutrons" (ICRU Rep. No. 45, Bethesda, Maryland, 1989).
[2]R. S. Caswell, J. J. Coyne, and M. L. Randolph, "Kerma factors of elements and compounds for neutron energies below 30 MeV," Int. J. Appl. Radiat. Isot. **33**, 1227–1262 (1982).
[3]M. Beauduin, J. Gueulette, V. Gregoire, B. de Coster, S. Vynckier, and A. Wambersie, "Practical problems caused by the comparison of clinical results of neutron therapy. Clinical RBE and clinical neutron potency factor, as a function of neutron energy. Survey of the literature," in *Proc. EULIMA Workshop on the Potential Value of Light Ion Beam Therapy*, EUR 12165 EN (CEC, Luxembourg, 1989) pp. 101–135.
[4]J. J. Broerse, B. J. Mijnheer, and J. R. Williams, "European protocol for neutron dosimetry for external beam therapy," Brit. J. Radiol. **54**, 882–898 (1981).
[5]M. F. Moyers, J. L. Horton, and A. L. Boyer, "A scatter model for fast neutron beams using convolution of diffusion kernels," Radiat. Prot. Dosim. **23**, 475–478 (1988).
[6]H. I. Amols, J. F. Dicello, M. Awschalom, L. Coulson, S. W. Johnsen, and R. B. Theus, "Physical characterization of neutron beams pro-

duced by protons and deuterons of various energies bombarding beryllium and lithium targets of several thicknesses," Med. Phys. **4**, 486–493 (1977).

[7]S. W. Johnsen, "Proton-beryllium production at 25–55 MeV," Med. Phys. **4**, 255–258 (1977).

[8]R. Madey, F. M. Waterman, and A. R. Baldwin, "Neutron spectra at 0° from 83.7 MeV deuterons and 100.2 MeV protons on beryllium," Med. Phys. **4**, 322–323 (1977).

[9]R. G. Graves, J. B. Smathers, V. A. Otte, P. R. Almond, and W. H. Grant, Communication in Med. Phys. **5**, 451–452 (1978).

[10]S. W. Johnsen, "Polyethylene filtration of 30 and 40 MeV *p*-Be neutron beams," Phys. Med. Biol. **23**, 499–502 (1978).

[11]R. G. Graves, J. B. Smathers, P. R. Almond, W. H. Grant, and V. A. Otte, "Neutron energy spectra of *d*(49)-Be and *p*(41)-Be neutron radiotherapy sources," Med. Phys. **6**, 123–128 (1979).

[12]F. M. Waterman, F. T. Kuchnir, L. S. Skaggs, R. T. Kouzes, and W. H. Moore, "Neutron spectra," Med. Phys. **6**, 160–161 (1979).

[13]F. M. Waterman, F. T. Kuchnir, L. S. Skaggs, R. T. Kouzes, and W. H. Moore. "Neutron spectra from 35 and 46 MeV protons, 16 and 28 MeV deuterons, and 44 MeV ^{3}He ions on thick beryllium," Med. Phys. **6**, 432–435 (1979).

[14]G. H. Harrison, E. K. Balcer-Kubiczek, and C. R. Cox, "Dosimetric properties of *p*(90)+(Be+Ta) and *p*(101)+(Be+Al) neutrons," Med. Phys. **7**, 348–351 (1980).

[15]R. F. Turco, R. Gahbauer, A. Rodriquez-Antimez, J. L. Horton, W. K. Roberts, and J. W. Blue, "Status report of the Cleveland Clinical Foundation National Aeronautics and Space Administration neutron therapy center," in *Treatment Planning for External Beam Therapy With Neutrons*, edited by G. Burger, A. Breit, and J. J. Broerse (Urban and Schwarzenberg, München, 1981) pp. 150–155.

[16]J. L. Ullman, N. Peak, S. W. Johnsen, S. Raventos, and P. Heintz, "Improved measurement of neutron spectrum from 35 MeV protons on thick beryllium," Med. Phys. **8**, 396–297 (1981).

[17]N. M. J. Crout, J. G. Fletcher, S. Green, M. C. Scott, and G. C. Taylor, "*In situ* neutron spectrometry to 60 MeV in a water phantom exposed to a cancer therapy beam," Phys. Med. Biol. **36**, 507–519 (1991).

[18]M. F. Moyers and J. L. Horton, "Determination of the neutron and photon spectra of a clinical fast neutron beam," Med. Phys. **17**, 607–614 (1990).

[19]S. W. Johnsen, Communication in Med. Phys. **5**, 452 (1978).

[20]N. R. Stanton, "A Monte Carlo program for calculating neutron detection efficiencies in a plastic scintillator," Ohio State University Report No. COO-1545-92 (1971).

[21]M. Awschalom, I. Rosenberg, and A. Mravca, "Kermas for various substances averaged over the energy spectra of fast neutron beams: A study in uncertainties," Med. Phys. **10**, 395–409 (1983).

[22]D. T. L. Jones, M. Yudelev, and W. L. J. Hendrikse, "Physical characteristics of the South African high energy neutron therapy facility," Radiat. Prot. Dosim. **23**, 365–368 (1988).

[23]V. V. Verbinski, W. R. Burrus, T. A. Love, W. Zobel, N. W. Hill, and R. Textor, "Calibration of an organic scintillator for neutron spectrometry," Nucl. Instr. Meth. **65**, 8–25 (1968).

[24]J. K. Dickens, "SCINFUL: A Monte Carlo based computer program to determine a scintillator full energy response to neutron detection for E_n between 0.1 and 80 MeV: Users' manual and fortran program listing," Oak Ridge National Laboratory, Rep. No. ORNL-6462 (1988).

[25]G. H. Harrison, Private Communication (1982).

[26]International Commission on Radiation Units and Measurements, "Tissue substitutes for radiation dosimetry and measurement" (ICRU Rep. No. 44, Bethesda, Maryland, 1989).

[27]D. J. Brenner, "Neutron kerma values above 15 MeV calculated with a nuclear model applicable to light nuclei," Phys. Med. Biol. **29**, 437–441 (1983).

[28]P. J. Binns and J. H. Hough, "Evaluation of average neutron energy from ionization-yield spectra," NAC Annual Report NAC/AR/90-1 (National Accelerator Centre, South Africa, 1990) p. 204.

[29]J. P. Slabbert, P. J. Binns, H. L. Jones, and J. H. Hough, "A quality assessment of the effects of a hydrogenous filter on a *p*(66)/Be(40) neutron beam," Brit. J. Radiol. **62**, 989–994 (1989).

[30]P. Huang, K. R. Kase, and B. E. Bjarngard, "Spectral characterization of 4 MV bremsstrahling by attenuation analysis," Med. Phys. **8**, 368–374 (1981).

[31]D. I. Garber and R. R. Kinsey, *Neutron cross sections: Volume II, Curves*, BNL 325 (Brookhaven National Laboratory, New York, 1976), 3rd ed.

[32]A. H. Wells, "A consistent set of kerma values for H, C, N, and O for neutrons of energies from 10 to 80 MeV," Radiat. Res. **80**, 1–9 (1979).

[33]M. A. Behrooz and D. E. Watt, "Kerma factors for neutrons of 14 MeV to 60 MeV in elemental H, C, N, and O," Radiat. Prot. Dosim. **1**, 291–297 (1981).

[34]P. J. Dimbylow, "Neutron cross-section and kerma value calculations for C, N, O, Mg, Al, P, S, Ar, and Ca from 20 to 50 MeV," Phys. Med. Biol. **27**, 1–9 (1982).

[35]B. J. Minjheer, P. Wootton, J. R. Williams, J. Eenmaa, and C. J. Parnell, "Uniformity in dosimetry protocols for therapeutic applications of fast neutron beams," Med. Phys. **14**, 1020–1026 (1987).

[36]L. J. Goodman and J. J. Coyne, "W_n and neutron kerma for methane-based tissue-equivalent gas," Radiat. Res. **82**, 13–26 (1980).

D.T.L. Jones, J.E. Symons, T.J. Fulcher, F.D. Brooks, M.R. Nchodu, M.S. Allie, A. Buffler and M.J. Oliver
Neutron fluence and kerma spectra of a p(66)/Be(40) clinical source
Medical Physics 19 (1992) 1285-1291

International Conference Proceedings

NUCLEAR TECHNIQUES FOR ANALYTICAL AND INDUSTRIAL APPLICATIONS

Mykonos, Greece, June 1992

Editors

George Vourvopoulos
Western Kentucky University, USA

Themis Paradellis
NCSR Demokritos, Greece

NUCLEAR TECHNIQUES FOR ANALYTICAL
AND INDUSTRIAL APPLICATIONS

Printed by Gerald Printing Service, Kentucky, USA

F.D.Brooks
Developments in neutron detection
Nuclear Techniques for Analytical and Industrial
Applications, ed. G. Vourvopoulos and T. Paradellis
(Western Kentucky University Press, 1993) 151-170

DEVELOPMENTS IN NEUTRON DETECTION

F.D. Brooks

Physics Dept., University of Cape Town, Rondebosch,
Cape, 7700 South Africa.

ABSTRACT: Neutron detection is reviewed with a view to its role in applications of nuclear techniques. Neutron detection methods used in various applications are discussed, for example: neutron radiography; nuclear fusion; exploration; industrial monitoring; surveillance; safeguards; waste management; neutron dosimetry; and neutron therapy.

1. INTRODUCTION

Measurements involving neutrons are not uncommon among the applications of nuclear techniques to areas beyond "pure" nuclear physics, as can be seen in the programme for this conference. Applications can require anything from the simple detection of neutrons, with or without knowledge of detection efficiency, to accurate measurements of neutron spectra or times of detection, with good discrimination against other types of radiation. In this paper we shall aim first to review recent developments in neutron detection, emphasising those aspects which seem to be particularly relevant to applications. Thereafter we shall consider some specific applications fields, aiming particularly to identify where new developments have advanced, or could advance, the field.

2. DETECTION AND MEASUREMENT OF NEUTRONS

Neutron detection has been reviewed many times during the sixty years that it has been practiced. A comprehensive review by Harvey and Hill[1] covers developments up to about 1979 for example, and much valuable information is also available in texts on radiation detection[2]. We concentrate here on

developments subsequent to 1979. For convenient presentation we divide the field into two regions, "low energy", arbitrarily defined as < 100 keV, and "higher energies" (> 100 keV). We consider the detection techniques available, the methods used to discriminate against gamma rays when detecting neutrons, neutron spectroscopy, the calibration of neutron detection efficiency and the timing resolution of neutron detectors.

2.1 Low Energy Neutron Detectors (< 100 keV)

Low energy neutrons are detected via charged particles, fast neutrons or gamma rays emitted promptly from an exothermic, neutron-induced nuclear reaction, or by detecting the radioactive decay of the product nucleus of such a reaction. Traditional examples of the activation method for low energy neutrons are[2] the neutron radiative capture reactions which produce ^{56}Mn, ^{108,110}Ag, ^{114,116}In, ^{165}Dy or ^{198}Au, from which beta or gamma decay is observed with half lives ranging between 72 s and 253 days.

Some details of the exothermic nuclear reactions commonly used for prompt detection of low energy neutrons are shown in Table 1. The reaction on ^{10}B, leading to emission of either α or $\alpha+\gamma$, has been familiar in neutron detection for many years and is used in conjunction with all the detector types listed in Table 1. Recent developments based on this reaction include BF_3 filled multiwire proportional chambers[3,4], a multistep avalanche gas detector[5], a track-etch detector[6] and thermoluminescent dosimeters[7,8].

The ^{6}Li(n,α)^{3}H reaction has become very popular for neutron detection during the last decade, especially in the form of the Li-glass scintillator[1,2]. New developments include renewed interest in pulse shape discrimination in these detectors[9] (see section 2.3) and the introduction of ^{6}Li-loaded liquid scintillators[10,11]. A flat response (i.e. energy-independent) detector has been developed[12], which is similar to the well known "long counter" for neutrons, but uses Li-glass scintillator fibres for neutron detection, instead of a BF_3 proportional counter.

TABLE 1: Reactions for detecting thermal neutrons

Reaction	Q (MeV)	σ (barn)[a]	Types[b]
^{3}He(n,p)^{3}H	0.76	5330	1 2 4
^{6}Li(n,α)^{3}H	4.78	940	3 4 5
^{10}B(n,α)^{7}Li	2.79	3840	1 2 3 4 5
^{235}U(n,f)	~ 180	582	1 3 4 5

[a] Cross section for thermal neutrons

[b] Types of detectors used with the reaction: 1, ion chamber/proportional counter; 2, MWPC; 3, semiconductor detector; 4, scintillator; 5, track-etch

The ^{3}He(n,p)^{3}H reaction is also a popular vehicle for thermal neutron detection, particularly in the field of applications, where its high thermal cross section (Table 1) and the convenience and simplicity of the ^{3}He proportional counter are attractive features. Recent developments include the proposal[13] for an improved gas filling (65% ^{3}He + 35% CF_4 instead of the traditional ^{3}He-Xe-CO_2 mixtures), to reduce wall effect and gamma sensitivity, and Monte Carlo calculations[14] of detector response functions for incident neutron energies up to 2 MeV. Also of interest is a proposal[15] for an in-core (reactor) neutron monitor based on a ^{3}He-Ne laser which is pumped or triggered by energy released in the nuclear reaction. New position sensitive detectors for thermal neutrons have also been described, based on the ^{3}He(n,p) reaction[16] and on neutron-induced fission of ^{235}U[17]. Two novel techniques also reported recently for thermal neutron detection involve the use of microchannel plates[18] and pyroelectric ceramics[19] respectively.

2.2 Higher Energy Neutron Detectors (> 100 keV)

Higher energy neutrons may be detected via the products of nuclear reactions, promptly or after a delay (activation), as for low energy neutrons. They may also be detected via recoils associated with neutron scattering or by moderation of the

neutron to thermal energy, followed by detection as for low energy neutrons[1,2]. Activation methods may be chosen to be sensitive to neutron energy by selecting an endothermic nuclear reaction with a suitable threshold energy. Interesting recent additions to the more traditional threshold activation methods[2] are: (i) the detection of betas from the short-lived (seconds) products of ^{238}U fission, induced by fast neutrons in a thick uranium radiator[20]; and (ii) the use of the $^{28}Si(n,p)^{28}Al$ reaction[21] to measure d-t fusion neutrons (14 MeV) in the presence of much stronger fluxes of d-d fusion neutrons (2.5 MeV) from the JET tokamak. Silicon semiconductor detectors have also been used for prompt measurement of 14 MeV neutrons from JET[22], via both the (n,p) and (n,α) reactions on ^{28}Si. Germanium detectors have been used for prompt neutron detection[23], by observing the discrete gamma energies associated with inelastic neutron scattering in Ge or in some other nearby target. The excellent energy resolution of this detector permits good discrimination against backgrounds and several gamma peaks may also be monitored simultaneously, to provide information at different neutron threshold energies.

In nuclear physics the standard method[1] for detecting neutrons of energy exceeding about 0.5 MeV is via recoil protons from n-p elastic scattering in an organic scintillator. In applications fields, however, the moderation plus capture (MPC) method, employing a thermal neutron detector (Table 1) embedded in polythene or wax, has traditionally been preferred for detecting MeV neutrons. MPC detectors are inferior to organic scintillators in timing resolution and neutron detection efficiency. Where timing is unimportant, as is often the case in applied work, the ease with which MPC detectors may be set up, with good discrimination against gammas, is appealing. Nevertheless the improved detection efficiency offered by recoil detectors may eventually see this type becoming more popular in applied work. A similar conclusion might be drawn from a comparison of different types of MeV neutron detector, presented recently by Sekimoto et al.[24].

A recent innovation in recoil detection is the composite scintillator consisting of a mixture of plastic and powdered BaF_2, of Kubota et al.[25]. An older idea[26] with some unique advantages, now being carried further[27,28], is to detect deuteron

recoils, instead of proton recoils, using a deuterated organic scintillator. We return to this in sections 2.4 and 3.7.

2.3 Discrimination Against Gamma Radiation

Gamma radiation is usually present when neutrons are being measured, hence neutron detectors must be insensitive to gammas or must incorporate some means for discriminating against this form of radiation. Proportional counter and ion chamber detectors for thermal neutrons are usually designed to be insensitive to gammas by limiting the dimensions and stopping power of the detecting medium so that Compton (or other) electrons from gamma interactions deposit much less detectable energy than the (short range) reaction products listed in Table 1. Pulse height discrimination can then be used to select neutrons and reject gammas, although pile-up (pulse superposition) problems can still arise in an extremely high gamma background.

The ^{6}Li-glass scintillation detector for thermal neutrons can be made thin (< 1 mm) so as to discriminate against gammas as outlined above for proportional counters. The comparatively short response time (< 3 ns) of the scintillator makes it less susceptible to pile-up problems than the proportional counters. Recoil detectors based on organic scintillators often use the pulse shape discrimination (PSD) technique to distinguish between gammas and neutrons. The PSD method[29] is based on the fact that for many scintillators, particularly the organic liquids and crystals, the "shape", or time distribution of the scintillation light emission, depends on the type of the particle responsible for the scintillation. Fig. 1, for example, compares the shapes of neutron and gamma scintillations from the liquid scintillator NE213. The signature which distinguishes proton scintillations (produced by neutrons) from electron scintillations (produced by gammas) is the larger proportion of slow decay component (fig. 1) for protons. The quality of discrimination obtained may be displayed by making a scatter plot of the number of events as a function of the scintillation pulse height L and pulse shape (or signature) S, where S is a signal whose amplitude depends on the fraction of slow component (tail) in the

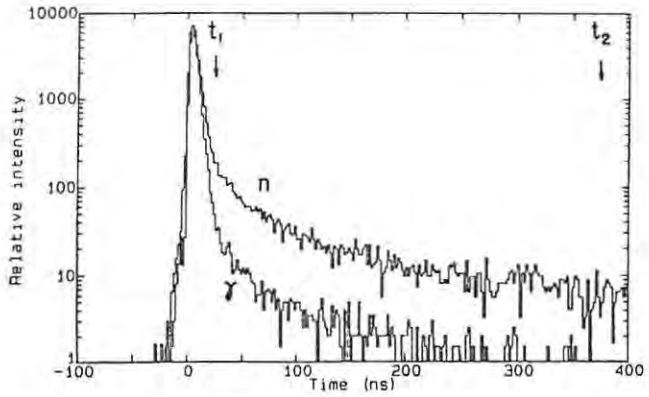

Fig. 1 Time-dependence of scintillations excited in NE213 liquid scintillator by neutrons and gammas from an AmBe source. The two histograms have been normalised to the same peak intensity.

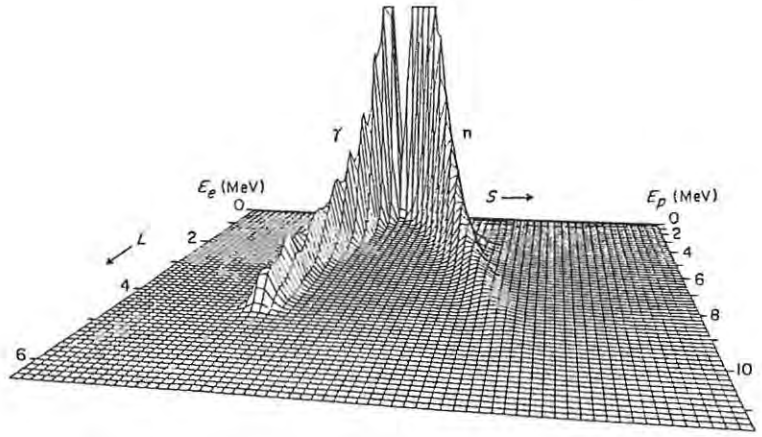

Fig. 2 Counts (vertical) as a function of pulse height L and pulse shape parameter S, observed from an NE213 liquid scintillator (50 mm diam. x 50 mm) irradiated by gammas and neutrons from an AmBe source. The pulse height scale is calibrated in electron energy on the left and in proton energy on the right. The Compton edge (4.2 MeV) and double escape peak (3.4 MeV) from the 4.4 MeV gamma are visible on the gamma ridge.

scintillation. The plot shown in fig. 2, for example, was obtained using a NE213 liquid scintillator in conjunction with an AmBe source, which provides a broad spectrum of neutron energies, extending to about 12 MeV, and gamma rays up to about 4.4 MeV. In this example the L and S signals were generated by a Link Systems Model 5010 Pulse Shape Discriminator[30,31] and were derived[27] from the integrals of the scintillation decay between time zero and times t_1 and t_2 respectively (see fig. 1). When liquid scintillators such as NE213 (Nuclear Enterprises) or BC501A (Bicron) are used optimum values for t_1 and t_2 are about 20 and 500 ns respectively.

Several new PSD systems have been described recently[10,11,32-41], all of which appear to provide excellent discrimination between neutrons and gammas when using liquid scintillators such as NE213 or BC501A. Zucker and Tsoupas[32] describe a system which can be assembled entirely from standard NIM and CAMAC modules and has been used for neutron energies ranging from < 0.1 MeV to 200 MeV. The system of Miller and McCollough[33] has been designed to perform PSD on either a scintillator or a hydrogen filled proportional counter. It is constructed as a single portable unit and requires only a PC to process the output information. The system of Bialkowski et al.[41] is designed to perform high precision PSD at high event rates. The systems of Heltsley et al.[35], Aleksan et al.[10,36] and Ait-Boubker et al.[11] use charge integrating ADCs and Aleksan et al.[36] also describe a system which uses a 100 MHz flash ADC.

New possibilities have become available recently[10,11,36] for using PSD in the detection of thermal and low energy neutrons. Aleksan et al.[10,36] and Ait-Boubker et al.[11] have shown that good PSD can be obtained using the new Li-doped liquid scintillator NE320 (see fig. 3). There is also new interest in PSD from Li-glass scintillators. This was reported by Coceva[42] many years ago but has not been widely exploited in the meanwhile, possibly because the discrimination obtainable was perceived to be of marginal value. Sakamoto[9] describes a Li-glass detector which he uses together with an Ortec 458 pulse-shape analyser to achieve PSD. Measurements of pulse shapes from a Li-glass scintillator (NE905) are shown in fig. 4. The difference between the decay shapes for thermal neutrons and gammas is clear and suggests that PSD should be

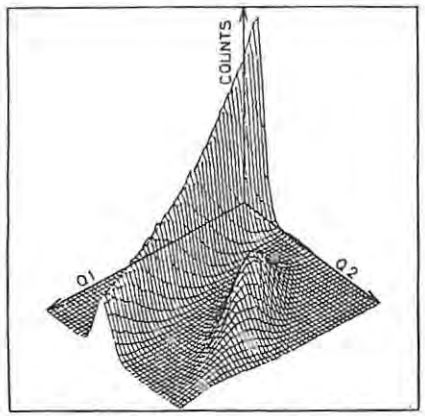

Fig. 3 Counts as a function of integrals Q1 and Q2 (corresponding to pulse height and pulse shape) obtained from a 6-litre ^{6}Li-doped liquid scintillator (NE320) irradiated by gammas and neutrons from an AmLi source. The ^{6}Li(n,α)^{3}H reaction produces the peak in the foreground. Gamma events fall on the ridge behind. Figure from Ait-Boubker *et al.*[11]

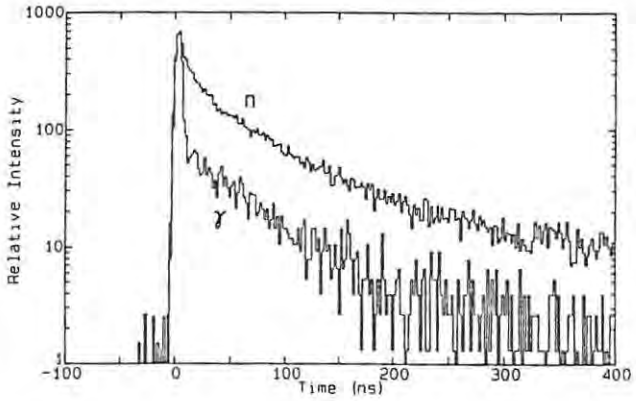

Fig. 4 Time dependence of scintillations excited by thermal neutrons and gammas in a NE905 ^{6}Li-glass scintillator (40 mm diam. x 12 mm). The two histograms have been normalised to the same peak intensity.

capable of achieving good discrimination against gammas in this detector. This has not yet been realised in practice however, and the reason could perhaps be that the PSD systems that have been used have been designed to suit the decay shapes of scintillators such as NE213 (fig.1) and BC501A rather than those of the glass scintillators themselves (fig. 4).

2.4 Neutron Spectroscopy

High-resolution neutron spectroscopy is widely used in nuclear physics, usually facilitated by high resolution time-of-flight systems[43] some of which cater for neutron energies up to several hundred MeV. Time-of-flight is also extensively used for high-resolution studies in condensed matter physics[44], at low neutron energies. Applications fields involving MeV neutron energies would probably benefit significantly if time-of-flight, or some other spectroscopy technique affording comparable energy resolution, were available at reasonable cost. Since this is not yet the case, applications which require neutron spectroscopy or neutron energy selection in the MeV range generally have to rely on simpler forms of spectrometer providing poorer energy resolution than time-of-flight. Methods which depend on measurements of pulse height spectra from detectors such as ^{3}He-filled[14], or hydrogen-filled[45] proportional counters or organic scintillators[1] are typical. Several developments have been reported recently[46-54] on the technique of proton recoil spectrometry using organic scintillators. Among these are three methods which strive to obtain a simpler (single peak) neutron lineshape by selecting events in which the neutron energy is totally absorbed. In one method[52] this is done by using a large scintillator. Another method[46,54] employs a boron-loaded liquid or plastic scintillator and uses the double-pulse technique in which a second pulse (from the capture reaction (Table 1)) signals that the neutron has been thermalised and absorbed. The third method[55], also double pulse, employs several thin Li-glass plates immersed in NE213 liquid scintillator to capture the thermalised neutron.

The deuterated organic scintillator offers another approach[26] towards obtaining a simple neutron lineshape in recoil spectrometry. The differential cross section

for n-d elastic scattering is significantly forward-backward peaked for E_n > 1 MeV, hence the associated recoil deuteron spectrum displays a prominent forward recoil peak at its upper limit, in contrast to the equienergy distribution of recoil protons from n-p elastic scattering. Deuterated scintillators therefore provide a more useful lineshape (a peak) than do natural organic scintillators (a plateau and edge), for monoenergetic neutrons. If a deuterated anthracene crystal scintillator is used, for example, and the anisotropic response and pulse shape characteristics of this detector are used to select the forward recoil peak, a resolution of 4-6% (FWHM) may be obtained for 10-17 MeV neutrons[27].

Other recent innovations in neutron spectrometers include the two detector time-of-flight system designed for measuring fusion neutrons from the JET Tokamak[56] and the system described by Balcazar et al.[57] which uses lithium fluoride and uranium oxide radiators sandwiched between track-etch detector foils to measure the spectra of neutrons emanating from a nuclear reactor.

2.5 Neutron Detection Efficiency

A knowledge of neutron detection efficiency may be of greater or lesser importance, according to the application under consideration. The review and text literature[1,2] provide useful efficiency data for many detector types and geometries. To accurately calibrate a specific detector a measurement using "tagged" neutrons from an associated particle source[58-60] might be more appropriate. Recent papers on recoil detectors also report response function data[61,62], detection efficiency data for high energy (25-360 MeV) neutrons[63,64] and useful techniques[65,66] for calibrating detection efficiency for low energy neutrons using ^{252}Cf spontaneous fission sources.

2.6 Timing Resolution

Timing resolution is clearly an important consideration in applications involving time-of-flight or coincidence measurements. For many applications outside

nuclear physics this is not the case. The timing resolution (FWHM) of neutron detectors ranges[1,2] from about 130 ps, for some plastic scintillators[67] to about 1 μs, for the proportional counters used to detect thermal neutrons, or even several μs for the MPC detectors, owing to the variable delay associated with neutron moderation. At the top of the range, the good timing resolution offered by plastic scintillators[67] is bought at the price of little or no capability to discriminate against gammas by pulse shape. Liquid scintillators can offer timing resolution of about 500 ps (FWHM) together with excellent PSD[29].

3. APPLICATIONS INVOLVING NEUTRON DETECTION

Applications of nuclear techniques which involve neutron detection encompass a diverse range of activities. In referring to some of these activities here we focus on the neutron detector in the system and, where appropriate, we speculate on how the application might possibly be enhanced by modifying the neutron detection technique.

3.1 Neutron Radiography

Neutron radiography is a specialist area with its own regular series of international conferences at which progress and developments in the field are regularly reviewed. Much of the activity involves radiography using thermal neutrons, for which a traditional detection system has been a radiator plate (eg of Gd), to generate gammas and x-rays from neutron capture, combined with photosensitive film to record the image[68,69]. Scintillator screens which incorporate neutron converter material (eg LiF-ZnS) and are viewed by TV cameras or other CCD equipment are also used. A recent example of these developments is the real-time thermal neutron radiography system described by Reuscher et al.[70]. Track-etch detectors have been used for more penetrating radiography with higher energy neutrons; for example, together with a ^{10}B radiator, for 25 keV neutrons[6], as well as directly, by observing proton recoils from n-p scattering of higher energy neutrons in track recording material[71].

3.2 Condensed Matter Physics

Condensed matter physics is now a major user of low energy neutrons and its needs, together with those of neutron radiography, have stimulated the development of position sensitive low energy neutron detectors. Developments to 1988 in this field were reviewed by Bateman[44] and have continued energetically since then as reported in refs.[3,4,18,72-75].

3.3 Nuclear Fusion

Neutrons are important in studies of nuclear fusion and the measurements required for these investigations often require a detailed knowledge of the detector properties. Neutron detection specific to this field is discussed in recent papers relating to 2.5 MeV neutrons from d-d fusion[24,28,76,77] and 14.1 MeV neutrons from d-t fusion[21,52,56,78]. Fig. 5 shows, for example, the measured and simulated response functions[78] of a NE213 scintillation detector (13 x 13 x 7 cm) used to observe 14 MeV neutrons from muon catalysed d-t fusion.

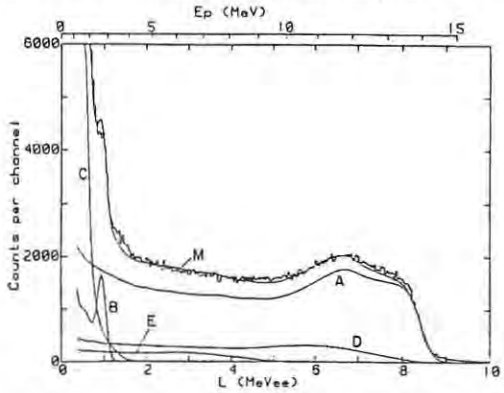

Fig. 5 Response function of a NE213 liquid scintillator (13x13x7 cm) for 14 MeV neutrons, showing experimental measurement (histogram) and Monte Carlo simulation (curve M). The pulse height L is calibrated in MeV electron equivalent (MeVee). The processes responsible for the components A-E of M are: A, n-p scattering, single and multiple; B, $^{12}C(n,\alpha)^{9}Be$; C, $^{12}C(n,n')3\alpha$; and D,E, n-p scattering following elastic (D) or inelastic (E) scattering on carbon. Figure from Henderson *et al*[78]

3.4 Exploration and Industrial Monitoring

Neutron probes are familiar in the exploration science of oil well logging[79] and also in on-line analysis and monitoring in the industrial environment. A well logging tool for porosity measurements, for example, may use an AmBe neutron source in conjunction with thermal neutron detectors such as ^{3}He-filled proportional counters, placed at different distances from the source, within the logging tool. Monte Carlo simulations have been employed[80] to explore the feasibility of making simultaneous measurements with combinations of different types of detector, such as thermal neutron, prompt gamma and epithermal neutron. It would be interesting to see this approach extended to incorporate trials with an even wider range of neutron detector types.

Neutron techniques in the on-line monitoring of industrial processes include measurements which sense or monitor the transmission, scattering or moderation of neutrons, for example in material being transported on conveyor belts or flowing through pipes. In fast neutron measurements to measure the moisture content of coke, for example[81], a MPC detector (Li-glass embedded in polythene) is used. In another application[82] the thermalisation of fast neutrons is monitored to determine the void fraction in the flow of boiling water through a small diameter (22 mm) pipe. The detector is a ^{3}He proportional counter housed in a cadmium chamber enclosing the pipe. A MPC(^{3}He) detector is used in another application in which wear of the refractory lining of an industrial furnace is monitored by means of the $^{9}Be(\gamma,n)$ reaction[83]. BeO test plates are mounted on the inner surface of the furnace and the neutron detector and 1.7 MeV gamma source are positioned outside, during measurements.

3.5 Nuclear Safeguards and Waste Management

Neutron techniques for assaying special nuclear materials such as fertile or fissile nuclides were reviewed by Zucker in 1982[84]. Subsequent developments include detection equipment for monitoring spontaneous fission neutrons emitted from nuclear warheads[85], in verification of the INF Treaty, and for monitoring

spontaneous fission in spent nuclear fuel[86,87]. Systems for detecting trace quantities of spontaneously fissioning nuclides[88] or of fissile nuclides[89], in the latter case with the aid of a neutron generator, are also described. In one of these applications[86] the neutron detector is a ^{235}U fission counter. All the other systems use MPC(^{3}He) detectors.

3.6 Detection of Hidden Explosives

Progress in the development of methods for the detecting hidden explosives, for example in airline baggage, is reviewed in other contributions to this conference. One approach is to use thermal neutron activation analysis[90], with particular interest in the 10.8 MeV gamma from neutron capture in ^{14}N. Another neutron method under study[91] is based on simultaneous measurements of scattering and transmission of fast neutrons from a ^{252}Cf source. An MPC neutron detector is used, enclosed in a cadmium sleeve to exclude background from neutrons moderated in the surroundings. The neutron is a potentially excellent probe for this application but the technology needed to realise this potential is still awaited. If a monoenergetic neutron source of sufficient intensity were available, together with a neutron detector spectrometer of adequate energy resolution, at reasonable cost, the prospects for using neutrons in baggage screening might look much better. The kinematics of neutron elastic scattering, for example, should provide a good basis for identifying and monitoring the light elements such as carbon, nitrogen and oxygen.

3.7 Medical Applications

Medical applications involving neutron detection include dosimetry measurements associated with neutron radiotherapy and measurements of the properties, such as energy spectra, of neutron therapy beams. These topics were reviewed[92] by the International Commission on Radiation Units and Measurements (ICRU) in 1989. Further work of interest in this field includes microdosimetric measurements for neutrons of energy above 20 MeV, using low

pressure proportional counters[93], the calibration of detector efficiencies up to 60 MeV for therapy measurements[94] and measurements of the neutron response of a thermoluminescent detector for applications in biomedical dosimetry[8].

The ICRU has stressed the need for accurate information about the spectra used in neutron therapy[92]. Some measurements made at neutron energies extending up to 63 MeV are shown below, to illustrate what may be done to meet this need. Fig. 6 shows the detail and quality of information obtainable from PSD when analysing the response of a NE213 scintillator (50 mm diam. x 50 mm) to quasi-monoenergetic neutrons of energy 63 MeV. Protons, deuterons, alphas and other

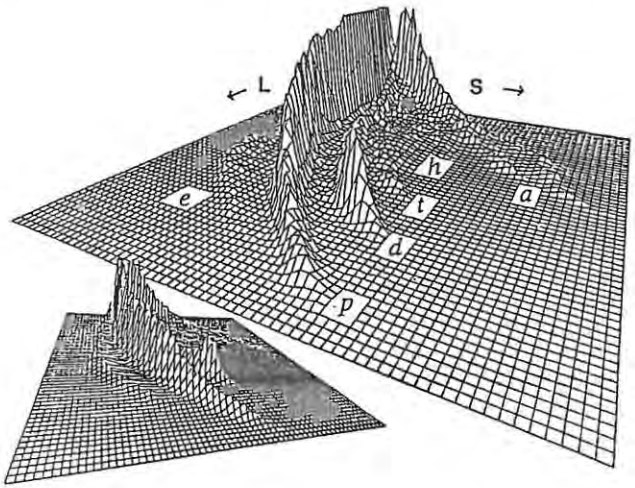

Fig. 6 Counts (vertical) as a function of pulse height L and pulse shape S for events produced by 6 MeV neutrons interacting with the hydrogen or carbon in a NE213 liquid scintillator (50 mm diam x 5 mm). The ridges are attributed to protons (p), deuterons (d), tritons (t) ^{3}He (h) and alphas (a released by the neutron interactions. Ridge e is attributed to protons which escape from th scintillator.

charged particles released by neutron interactions with hydrogen or carbon in the scintillator are clearly resolved from one-another and from the Compton electrons produced by gamma background. Proton events, for example, may be selected by imposing a suitable cut across the L-S plane (fig. 6). In fig. 7 the number of proton events is shown (vertical) as a function of pulse height L and time-of-flight T, for the broad spectrum of neutron energies (up to 63 MeV) from a p(66)/Be(40) neutron therapy beam[95], i.e. a beam produced by 66 MeV protons incident on a 40 MeV thick Be target. The edge which curves across the L-T plane (fig. 7) corresponds to forward recoil protons, i.e. protons of energy equal to that of the incident neutron, given by the neutron time-of-flight T. Fig. 8 shows another distribution against L and T obtained using the same incident beam, but with the NE213 scintillator replaced by a deuterated liquid scintillator (NE230) of similar size, and using PSD to select deuterons instead of protons. In this case the forward recoil deuterons form a distinctive ridge, corresponding to the peak referred to in section 2.4, instead of an edge. This useful feature allows the yield corresponding to forward recoils (backward neutron scattering) to be clearly identified and measured. The cross section corresponding to backward scattering is similarly well defined, therefore the incident neutron spectrum can be determined accurately by determining the integral over the forward recoil peak. Another useful feature of the deuterated detector is the shorter range of the deuteron in the scintillator, than for a proton of the same energy. This means that distortions due to the escape of recoiling particles from the scintillator (wall effect) are smaller.

4. CONCLUSIONS

Two general conclusions seem to emerge from this brief look at the state of neutron detection in nuclear applications fields. One conclusion is that neutron applications are handicapped, in comparison with those involving charged particles or gamma rays, by the present lack of a simple detector spectrometer offering good energy resolution and detection efficiency, for example, an energy resolution of about 3%, or better and a detection efficiency of at least 10% for 14 MeV neutrons. Some useful new applications might become possible if this

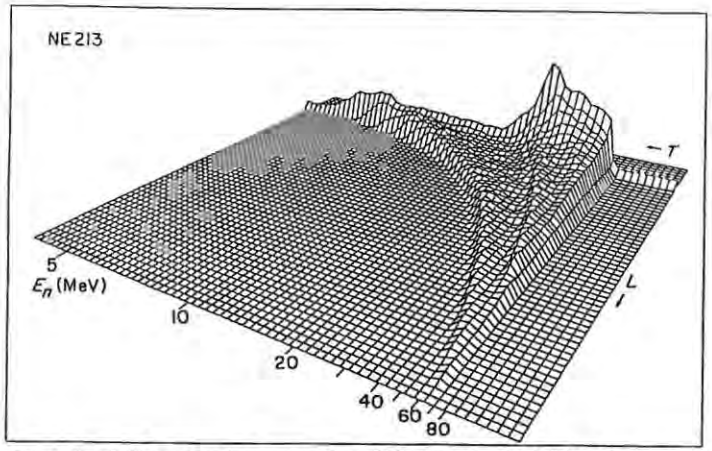

Fig. 7 Counts (vertical) as a function neutron time-of-flight T and pulse height L for proton events produced in a NE213 scintillator (50 mm diam. x 50 mm) by neutrons from a pulsed p(66)/Be(40) neutron therapy beam. The beam pulse width and neutron flight path were 1 ns and 6.06 m respectively. The edge corresponding to forward recoiling protons forms a "cliff" which extends from the far corner of the plot towards the foreground.

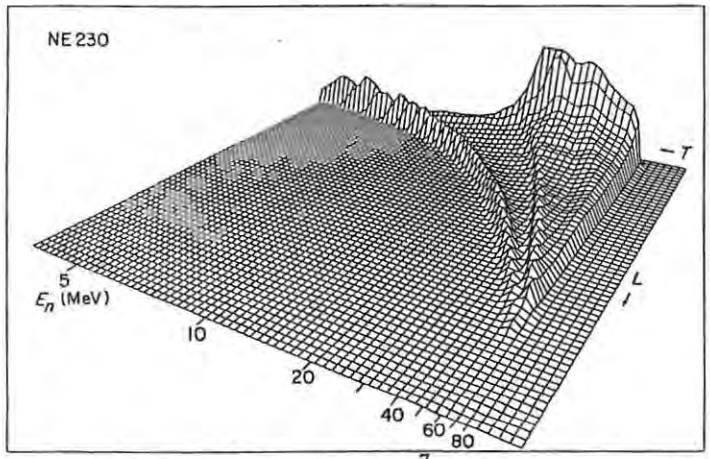

Fig 8. Counts (vertical) as a function of T and L, as for fig. 7, but for deuteron events produced in a NE230 deuterated liquid scintillator (40 mm diam. x 50 mm). The peak corresponding to forward recoiling deuterons forms a ridge which extends from the far corner of the plot towards the foreground.

deficiency were to be remedied in the foreseeable future. The other conclusion is that there could be advantages in introducing more of the standard and recently developed neutron detection techniques of nuclear physics into the applications fields. Liquid scintillator methods for fast neutrons and the ^{6}Li-doped liquid scintillator for thermal or epithermal neutrons, both of which discriminate efficiently against gammas by PSD (section 2.3), should be good candidates for replacing MPC detectors in many applications presently in use.

ACKNOWLEDGEMENTS

I am indebted to several colleagues and research students from the University of Cape Town and the National Accelerator Centre, Faure, South Africa, for assistance in the preparation of this paper: Dan Jones, Willem Cilliers, Roy McMurray, Saalih Allie, Andy Buffler, Colin Henderson, Rudolph Nchodu, Marian Oliver, Julian Symons and James Wanliss. I also thank the University of Cape Town and the Foundation for Research Development for their support.

REFERENCES

1 Harvey, J.A. and Hill, N.W., Nucl. Instr. and Meth. 162, 507 (1979).
2 Knoll, G.F., 'Radiation Detection and Measurement' (2nd ed.) John Wiley and sons, Inc. (1989).
3 Schefer, J. *et al.*, Nucl. Instr. and Meth. A310, 416 (1991).
4 Janson, M. *et al.*, Physica B 156/157, 584 (1989).
5 Anisimov, Yu.S. *et al.*, Nucl. Instr. and Meth. A273, 731 (1988).
6 Beynon, T.D. and Constantine, G., Nucl. Instr. and Meth. A264, 526 (1988).
7 Gauld, I.C. *et al.*, Nucl. Instr. and Meth. A251, 380 (1986).
8 Matsumoto, T., Nucl. Instr. and Meth. A301, 552 (1991).
9 Sakamoto, S., Nucl. Instr. and Meth. A299, 182 (1990).
10 Aleksan, R. *et al.*, Nucl. Instr. and Meth. A274, 203 (1989).
11 Ait-Boubker, S. *et al.*, Nucl. Instr. and Meth. A277, 461 (1989).
12 Spector, G.B. *et al.*, Nucl. Instr. and Meth. A309, 303 (1991).
13 Kopp, M.K. *et al.*, Nucl. Instr. and Meth. A201, 395 (1982).
14 Sailor, W.C. *et al.*, Nucl. Instr. and Meth. A270, 527 (1988).
15 Soramoto, S. *et al.*, Nucl. Instr. and Meth. A306, 524 (1991); Okamura A., *et al.*, Nucl. Instr. and Meth. A306, 530 (1991).

16 Zanevsky, Yu.V. *et al.*, Nucl. Instr. and Meth. A310, 362 (1991).
17 Mori, C. *et al.*, Nucl. Instr. and Meth. A310, 437 (1991).
18 Fraser, G.W. and Pearson, J.F., Nucl. Instr. and Meth. A293, 569 (1990).
19 Crestana, S.B. *et al.*, Nucl. Instr. and Meth. A311, 558 (1992).
20 August, R.A. *et al.*, Nucl. Instr. and Meth. A299, 33 (1990).
21 Sadler, G. *et al.* Rev. Sci. Instr. 61, 3175 (1990).
22 JET Team, Nuclear Fusion 32, 187 (1992)
23 Ejiri, H. *et al.*, Nucl. Instr. and Meth. A302, 482 (1991); Chung, C. and Chen, Y.R., Nucl. Instr. and Meth. A301, 328 (1991).
24 Sekimoto, H. *et al.*, Nucl. Instr. and Meth. A302, 150 (1991).
25 Kubota, S. *et al.*, Nucl. Instr. and Meth. A270, 598 (1988).
26 Benetskii, B.A. *et al.*, Yad. Fiz. 8, 920 (1968); tr. Sov. J. Nucl. Phys., 8, 534 (1969).
27 Brooks, F.D. *et al.*, Nucl. Instr. and Meth. A270, 149 (1988).
28 Roberts, D.A. *et al.*, Phys. Rev. C42, R1809 (1990).
29 Brooks, F.D., Nucl. Instr. and Meth. A162, 477 (1979).
30 LINK Model 5010 Pulse Shape Discriminator from LINK Systems, Halifax Road, High Wycombe, Bucks, England, HP13 3SE.
31 Adams, J.M. and White, G., Nucl. Instr. and Meth. 156, 459 (1978)
32 Zucker, M.S. and Tsoupas, N., Nucl. Instr. and Meth. A299, 281 (1990).
33 Miller, W.H. and McCollough, K., Nucl. Instr. and Meth. A299, 286 (1990).
34 Bose, S. *et al.*, Nucl. Instr. and Meth. A270, 487 (1988).
35 Heltsley, J.H. *et al.*, Nucl. Instr. and Meth. A263, 441 (1988).
36 Aleksan, R. *et al.*, Nucl. Instr. and Meth. A273, 303 (1988).
37 Harihar, P. *et al.*, Nucl. Instr. and Meth. A302, 469 (1991).
38 Moszynski, M. *et al.*, Nucl. Instr. and Meth. A307, 97 (1991).
39 Pai, S. *et al.*, Nucl. Instr. and Meth. A278, 749 (1989).
40 Harihar, P. *et al.*, Nucl. Instr. and Meth. A272, 763 (1988).
41 Bialkowski, J. *et al.*, Nucl. Instr. and Meth. A275, 322 (1989).
42 Coceva, C., Nucl. Instr. and Meth. 21, 93 (1963)
43 Firk, F.W.K., Nucl. Instr. and Meth. 162, 539 (1979)
44 Bateman, J.E., Nucl. Instr. and Meth. A273, 721 (1988).
45 Knauf, K. and Vorbrugg, W., Nucl. Instr. and Meth. A305, 419 (1991).
46 Feldman, W.C. *et al.*, Nucl. Instr. and Meth. A306, 350 (1991).
47 Olsson, N. and Trostell, B., Nucl. Instr. and Meth. A224, 142 (1984).
48 Grosshog, G. *et al.*, Nucl. Instr. and Meth. A249, 468 (1986).
49 Albergo, S. *et al.*, Nucl. Instr. and Meth. A311, 280 (1992).
50 Coelho, P.R.P. *et al.*, Nucl. Instr. and Meth. A280, 270 (1989).
51 Da Silva, A.G. *et al.*, Nucl. Instr. and Meth. A264, 381 (1988).
52 Dzhelepov, V.P. *et al.*, Nucl. Instr. and Meth. A269, 634 (1988).
53 Oyama, Y. and Mackwa, H., Nucl. Instr. and Meth. A245, 173 (1986).
54 Aoyama, T., *et al.*, 'Development of an electronically black neutron spectrometer using B-loaded liquid scintillators.', Proc. Sixth Workshop on Radiation Detectors and their Uses, KEK, Japan; Miyajima, M. and Sasaki, S. eds. p101 (1991).
55 Bertin, A. *et al.*, Nuovo Cim. 105, 751 (1992).
56 Elevant, T. *et al.*, Nucl. Instr. and Meth. A306, 331 (1991).
57 Balcazar, M. *et al.*, Nucl. Instr. and Meth. A299, 147 (1990).

58 Bartle, C.M. *et al.*, Nucl. Instr. and Meth. 180, 165 (1981).
59 Cherubini, R. *et al.*, Nucl. Instr. and Meth. A269, 623 (1988).
60 Guillaume, G. *et al.*, Nucl. Instr. and Meth. A277, 458 (1989).
61 Saraf, S.K. *et al.*, Nucl. Instr. and Meth. A268, 200 (1988).
62 Shin, K. *et al.*, Nucl. Instr. and Meth. A308, 609 (1991).
63 Byrd, R.C. and Sailor, W.C., Nucl. Instr. and Meth. A274, 494 (1989).
64 Paticchio, V. *et al.*, Nucl. Instr. and Meth. A305, 150 (1991).
65 Cub, J. *et al.*, Nucl. Instr. and Meth. A274, 217 (1989).
66 Gul, K. *et al.*, Nucl. Instr. and Meth. A278, 470 (1989).
67 Moszynski, M. and Bengston, B. Nucl. Instr. and Meth. 142, 417 (1977).
68 Barton, J.P., 'Neutron Radiography -- accomplishments and potential.', The Neutron and its Applications, Schofield, P., ed, p447, *The Institute of Physics* (1982).
69 Walker, J., 'Uses of Neutrons in Engineering and Technology', in ref. 68, p435 (1982).
70 Reuscher, J.A. *et al.*, Nucl. Instr. and Meth. A299, 434 (1990).
71 Ikeda, Y. *et al.*, Nucl. Instr. and Meth. A276, 183 (1989).
72 Johnson, R.G., Nucl. Instr. and Meth. A263, 427 (1988).
73 Wilkinson, C. and Lehmann, M.S., Nucl. Instr. and Meth. A310, 411 (1991).
74 Heiderich, M. *et al.*, Nucl. Instr. and Meth. A305, 423 (1991).
75 Crawford, R.K. *et al.*, Nucl. Instr. and Meth. A299, 17 (1990).
76 Menlove, H.O. and Miller, M.C., Nucl. Instr. and Meth. A299, 10 (1990).
77 Bonazzola, G.C. *et al.*, Nucl. Instr. and Meth. A299, 25 (1990).
78 Henderson, C.G.L. *et al.*, Muon Catalyzed Fusion 5/6, 405 (1990/91).
79 Ellis, D.V., Well Logging for Earth Science, Elsevier, New York, 1987.
80 Oraby, M. *et al.*, Nucl. Instr. and Meth. A299, 674 (1990).
81 Sowerby, B.D. and Watt, J.S., Nucl. Instr. and Meth. A299, 642 (1990).
82 Waller, E.J. and Hussein, E.M.A., Nucl. Instr. and Meth. A299, 670 (1990).
83 Staicu L. and Apostol, I, Nucl. Instr. and Meth. A196, 511 (1982).
84 Zucker, M.S., 'Neutron Techniques in Safeguards', in ref. 68, p463 (1982).
85 Ewing, R.I. and Marlow, K.W., Nucl. Instr. and Meth. A299, 559 (1990).
86 Williams, J.A. *et al.*, Nucl. Instr. and Meth. A299, 187 (1990).
87 Fehlau, P.E. *et al.*, Nucl. Instr. and Meth. A299, 29 (1990).
88 Gotoh, H. *et al.*, 'Detection of trace amounts of spontaneously fissioning nuclides', in ref 54, p116 (1991).
89 Haruyama, M. *et al.*, 'Non destructive detection of trace amounts of fissile material using a neutron generator', in ref. 54, p125 (1991).
90 Shea, P. *et al.*, Nucl. Instr. and Meth. A299, 444 (1990).
91 Hussein, E.M.A. *et al.*, Nucl. Instr. and Meth. A299, 453 (1990).
92 'Clinical Neutron Dosimetry Part 1: Detection of absorbed dose in a patient treated by external beams of fast neutrons', ICRU report 45 (1989).
93 Schrewe, U.J. *et al.*, Nucl. Instr. and Meth. A299, 226 (1990).
94 Crout, N.M.J. *et al.*, Nucl. Instr. and Meth. A277, 664 (1989).
95 Jones, D.T.L. *et al.*, Medical Physics, to be published October 1992.

Physics Letters B 314 (1993) 173–178
North-Holland

PHYSICS LETTERS B

Differential cross section for n–p radiative capture at $E_n = 63.4$ MeV

M.S. Allie [a], F.D. Brooks [a], D.G. Aschman [a], A. Buffler [a], W.A. Cilliers [a], R.W. Fearick [a], C.G.L. Henderson [a], M.J. Oliver [a], M.R. Nchodu [a], S.M. Perez [a], D. Steyn [a], W.R. McMurray [b], B.R.S. Simpson [b], F.D. Smit [b], H.G. Miller [c], K. Bharuth-Ram [d] and I.J. van Heerden [e]

[a] *Department of Physics, University of Cape Town, Rondebosch 7700, South Africa*
[b] *National Accelerator Centre, Faure 7131, South Africa*
[c] *Department of Physics, University of Pretoria, Pretoria 0002, South Africa*
[d] *Department of Physics, University of Durban-Westville, Durban 4000, South Africa*
[e] *Department of Physics, University of the Western Cape, Bellville 7535, South Africa*

Received 3 May 1993; revised manuscript received 5 July 1993
Editor: R.H. Siemssen

The angular distribution of photons from n–p radiative capture of 63.4 MeV neutrons has been measured. Data taken at eight n–γ laboratory angles (45°–150°) were transformed to deuteron photodisintegration cross sections at the equivalent laboratory energy, $E_\gamma = 33.9$ MeV, and analysed in combination with independent measurements of the 0° and 180° cross sections. Legendre polynomial coefficients obtained from the analysis are consistent with values reported from global fits and deviate marginally from predictions based on the Bonn and Paris potentials.

Searches now being made for evidence of sub-nucleonic degrees of freedom in nuclei have led to renewed interest [1,2] in deuteron photodisintegration and its inverse, neutron–proton radiative capture. These reactions have been a rich source of information about the N–N interaction for many years. Conventional theories which include relativistic corrections and assume only nucleon, meson and isobar degrees of freedom, have achieved considerable success [1–4] in explaining data from deuteron photodisintegration and n–p capture at photon energies up to about 40 MeV. Experimental data [5,6] for the total photodisintegration cross section are consistent with values predicted by the theory in this energy range [1,2]. The theory also appears to be in reasonable agreement with most differential cross section measurements [1–4], a notable exception being the data of Stephenson et al. [7] for photon energies in the range 2–18 MeV. Global fits, in which Legendre polynomials are used to describe the cross section data over an extended range of energy and angle [5,8–10], may be used to compare a larger set of experimental data with theory. Such comparisons [1,2] have shown discrepancies between the Legendre polynomial coefficients derived from experiment and theory, thus raising doubts as to whether the conventional theory [11,12] is entirely adequate, even at low energies.

Differential cross sections for deuteron photodisintegration at $E_\gamma < 40$ MeV have been obtained mainly from measurements of the angular distributions of photoprotons or photoneutrons. A number of measurements, e.g. refs. [13–16], of differential cross sections corresponding to photoproton angles 0° and 180° have been obtained from the inverse reaction, n–p capture, at equivalent incident neutron energies ($E_n < 80$ MeV). However, angular distribution data for intermediate angles, obtained from n–p capture, are scarce. For incident neutron energies 19–50 MeV, Fink et al. [10] have reported measurements at photon laboratory angles 55°, 90° and 125°. Data from n–p capture measurements are especially useful for comparison with those obtained from photodisintegration because the experimental techniques, and hence sources of error, are quite different. We have therefore determined the differential cross section for deuteron photodisintegration at the incident photon energy of 33.9 MeV by measuring the angular distri-

bution of photons from n–p radiative capture at $E_n = 63.4$ MeV. Measurements at eight n–γ laboratory angles were transformed by means of detailed balance so as to obtain differential cross sections for the ^{2}H(γ, p)n reaction at eight γ–p centre-of-mass angles between 27° and 126°. These data were then analysed in combination with independent measurements [16–18] of the 0° and 180° cross sections.

The experimental arrangement for the angular distribution measurements is shown in fig. 1. A 66 MeV pulsed proton beam from the $k = 200$ cyclotron of the South African National Accelerator Centre (NAC), Faure, was directed through a natural lithium metal target (2 mm thick) and deflected into a shielded beam dump. Pulsed neutrons from the (p, n) reaction on lithium emerged from an aperture (50×50 mm^2) in the shielding ahead of the target (fig. 1). An NE213 liquid scintillator (50 mm diam.×50 mm) was placed 5.9 m from the neutron source, and protons in the NE213 constituted the target for the n–p radiative capture reaction. Time-of-flight was used to select the strong forward peak ($E_n = 63.4$ MeV) in the neutron spectrum, corresponding to the transitions ^{7}Li(p, n)^{7}Be(gs + 0.43 MeV).

The angular distribution of gammas from n–p radiative capture in the NE213 scintillator was determined by observing coincidences between this scintillator and (any one of) the eight identical NaI(Tl) crystals surrounding it (fig. 1). The crystals (75 mm diam.×125 mm) were mounted in identical lead shields and a 5 mm thick lead plate was mounted over the entrance window to each crystal to remove

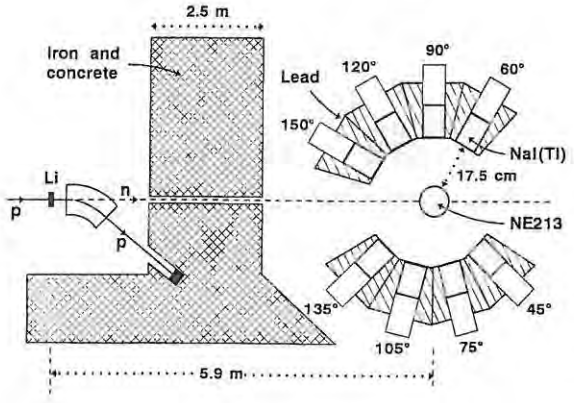

Fig. 1. Experimental arrangement (schematic).

charged particles. The gamma flight time over the 175 mm gap between the NE213 cell and the crystals (fig. 1) was used to reject backgrounds due to non-relativistic particles detected in the latter. Signals from the NE213 detector were fed to a modified Link Systems Model 5010 Pulse Shape Discriminator, which provided two outputs from which the NE213 pulse height L and pulse shape S were derived [19] in the offline analysis. The two outputs from the Link were recorded event by event on magnetic tape, together with the pulse height from the NaI(Tl), the incident neutron time-of-flight and the coincidence time delay between NE213 and sodium iodide. A pattern register was used to record the gamma detector active in the event and to veto events in which more than one such detector registered. The design of the electronic system ensured that the same dead time was effective for all the NaI(Tl) detectors. Three sets of measurements, each 60–80 hours in duration, were made. After checking that the angular distribution was consistent, within statistical accuracy, over the three sets, the data were combined for final analysis.

Fig. 2a shows a perspective view of number of events against NE213 pulse height L and pulse shape S, for coincidences in which the NaI(Tl) crystal located at $\theta_{n\gamma} = 90°$ (lab), detected a gamma of energy greater than 12 MeV. Events corresponding to protons, deuterons and alphas detected in the NE213 produce the ridges labelled p, d and α respectively in the L–S plane (fig. 2a) and n–p radiative captures from a sharp peak which can be clearly identified on the deuteron ridge. Similar peaks were observed in the L–S distributions recorded for coincidences at the other values of $\theta_{n\gamma}$. Events on the deuteron ridge (d–γ coincidences) were selected by a cut in the L–S plane and projected onto the L-axis to give the deuteron pulse height spectra shown in fig. 2b, for different $\theta_{n\gamma}$. The peaks corresponding to n–p capture stand out clearly and display the expected kinematic shift with detection angle.

The n–p capture peaks (fig. 2b) were integrated after correcting for background, mainly due to the ^{12}C(n, dγ)^{11}B reaction. A fraction of the events in these peaks will be due to n–p radiative captures induced by neutrons which have scattered on C or H nuclei in the scintillator, prior to undergoing capture. Monte Carlo calculations showed that this fraction amounted to (2–3)% of the peak area at each angle,

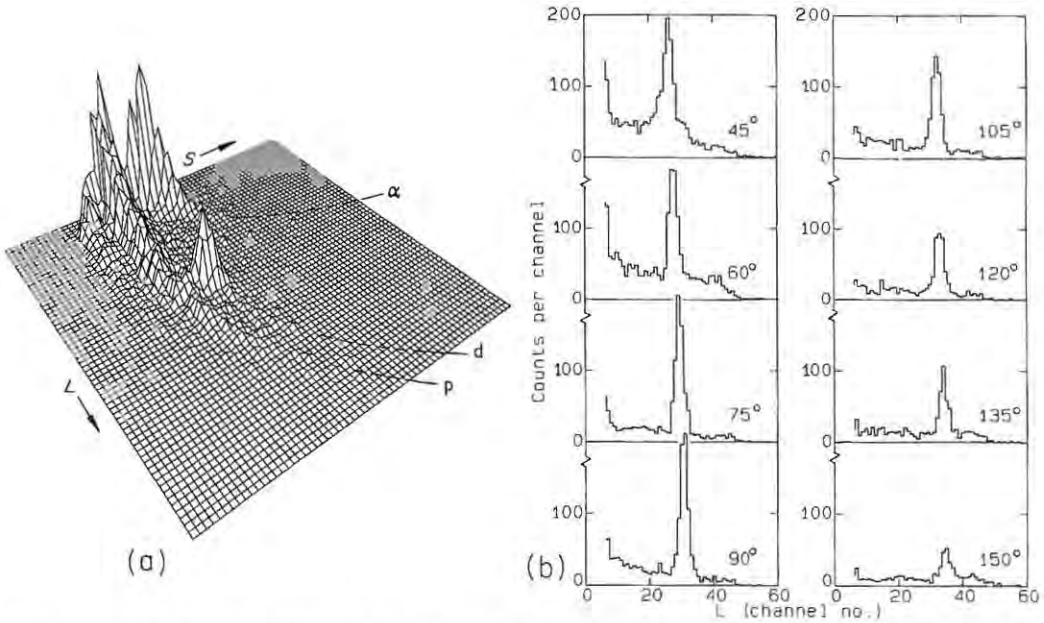

Fig. 2. (a) Counts (vertical) versus NE213 pulse height L and pulse shape S, for coincidences between the NE213 and the NaI(Tl) crystal positioned at $\theta_{n\gamma}=90°$ (lab), showing ridges due to protons (p), deuterons (d) and alphas (α) detected in the NE213. The sharp peak on the deuteron ridge is the signature for n–p radiative capture. (b) Projected NE213 pulse height spectra for coincidences identified as deuterons in NE213 and gammas in NaI(Tl), for different $\theta_{n\gamma}$(lab).

and hence that the angular distribution was not significantly distorted by this effect. The peak intensities were converted to relative differential cross sections for n–p radiative capture by using the code ESTE [20] to correct for the variation of gamma detection efficiency with $\theta_{n\gamma}$. Detailed balance was used to convert to differential cross sections for proton emission in the inverse reaction, deuteron photodisintegration at the corresponding laboratory photon energy of 33.9 MeV. The results, normalised as outlined below to an absolute scale, are listed in table 1 and plotted in fig. 3a. The angles $\theta_{\gamma p}^{cm}$ and $\Delta\theta_{\gamma p}^{cm}$ in this table show, respectively, the centroid angle and the spread (FWHM) in angle of detection for each gamma detector, calculated by Monte Carlo simulation, allowing for the variation of the differential cross section over the solid angle subtended by the detector. The uncertainties shown for $d\sigma/d\Omega$ are statistical only. Systematic errors introduced in the calculations of cross sections are estimated to be less than 5%.

In order to make a meaningful Legendre polynomial fit to the differential cross section for photodisintegration it is important to have data covering the range 0°–180°. The present measurements cover the range $\theta_{\gamma p}^{cm}=27°$–126°. However, groups at Mainz [17,18] and at Louvain [16] have recently reported new absolute measurements at 0° and 180° for photon energies close to 34 MeV. These data are summarised in table 2 and the Mainz data are included in fig. 3a. A weighted least-squares Legendre polynomial fit, in which the present data were normalised as follows, was made to the combined data set shown

Table 1
Differential cross sections for ^{2}H(γ, p)n, $E_\gamma=33.9$ MeV.

$\theta_{\gamma p}^{cm}$ (deg)	$\Delta\theta_{\gamma p}^{cm}$ (deg)	$\frac{d\sigma}{d\Omega}\left(\frac{\mu b}{sr}\right)$
27.3	20	13.2(22)
39.8	19	21.4(18)
52.6	19	25.7(16)
66.1	18	33.3(18)
80.1	17	37.5(18)
94.7	17	29.9(14)
110.0	16	21.6(13)
126.0	15	19.1(15)

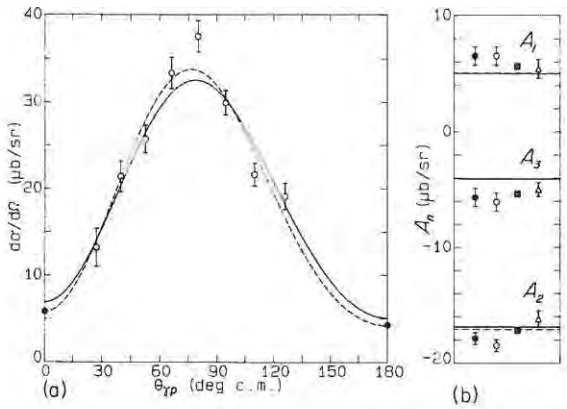

Fig. 3. (a) Differential cross section for ^{2}H(γ, p)n at E_γ(lab) = 33.9 MeV, showing present data (open circles), Mainz data [17,18] (solid circles), least-squares fit (dashed curve) and Bonn prediction [11] (solid curve). (b) Legendre polynomial coefficients, (a)–(f) from table 3: (a) Bonn prediction (solid lines); (b) Paris prediction (dashed lines); (c) fit to present and Mainz data (solid circles); (d) fit to present and Louvain data (open circles); and global fits (e) Rossi et al. [5] (squares) and (f) De Pascale et al. [8] (triangles). The uncertainties for set (e) (squares) are smaller than the point size.

Table 2
$d\sigma/d\Omega$ data for $\theta_{\gamma p}^{cm} = 0°$ and 180°, $E_\gamma \simeq 34$ MeV.

Group	Ref.	E_γ (MeV)	$d\sigma/d\Omega$ (μb/sr) [a]	
			$\theta_{\gamma p}=0°$	$\theta_{\gamma p}=180°$
Mainz	[17]	31.7(26)	5.83(6)	–
Mainz	[18]	33.9(29)	–	4.28(9)
Louvain	[16]	32.8	4.72(26)	3.93(40)

[a] Uncertainties are statistical only.

in fig. 3a. A scaling factor was introduced for the present data only, and was adjusted in the fitting procedure so as to equate the Legendre polynomial coefficient A_0 to the value 22.9 μb/sr [11,21], which corresponds to a total photodisintegration cross section $\sigma_T = 4\pi A_0 = 287$ μb. The present data are normalised, in other words, to a total photodisintegration cross section of 287 μb. This value, based on the Bonn r-space potential [11,21], is consistent, within 2%, with the cross section calculated from the Paris potential [12,21] and with the value obtained from the global fit of Rossi et al. [5], which is based on an extensive set of experimental data. It should also be noted that the absolute values assumed for the 0° and 180° differential cross sections have negligible influence on the normalisation procedure used. This is due to the effect of the sin θ factor introduced in the integration of the differential cross section to obtain the total cross section. Fitting was carried out using the matrix inversion technique [22], weighting each datum in proportion to the inverse square of its statistical uncertainty. Legendre expansions to orders 3, 4 or 5 were investigated using the χ^2/dof and the F-test [22] to monitor the quality of the fits. For fits to the present data combined with the Mainz (Louvain) data the χ^2/dof obtained for expansions to order 3, 4 or 5 were 2.2 (2.3), 2.7 (2.7) and 1.9 (2.1) respectively. The fits based on order 3 were preferred because the F-test indicated that the fits to higher orders gave A_4 and A_5 coefficients with rejection probabilities of 87% (96%) and 15% (19%) respectively.

The Legendre coefficients obtained from the third order fit to the combined present and Mainz data are listed as (c) in table 3. The differential cross section calculated from these coefficients is shown by the dashed curve in fig. 3a. The solid curve was calculated using coefficients (a) in table 3, predicted [11,21] by the Bonn potential. Other coefficients listed in table 3 are: (b), predicted [12,21] by the Paris potential with meson exchange currents (MEC), isobar configurations (IC) and relativistic corrections (RC) included; (d), obtained by fitting the present data in combination with the Louvain data instead of the Mainz data; and (e) and (f), calculated from global fits made by Rossi et al. [5] and De Pascale et al. [8] respectively, to extensive sets of experimental data. The Legendre coefficients A_1–A_3 from table 3 are also displayed in fig. 3b, to facilitate comparisons between them. The coefficient sets (c) and (d) were calculated without including systematic uncertainties. The effects of including systematic uncertainties (by addition in quadrature with statistical uncertainties) have been checked and found to produce no significant change to the values in table 3.

The present relative measurements of $d\sigma/d\Omega$ may be compared with other experimental data taken at the same or nearby photon energy by comparing ratios of the $n \geq 1$ Legendre coefficients to A_0. Such a comparison shows that the present data agree with those of Weissman and Schultz [23,24] at $E_\gamma = 35$ MeV, and also with other measurements [25,26] at

Table 3
Legendre polynomial coefficients (μb/sr) for $d\sigma/d\Omega$ at $E_\gamma = 33.9$ MeV. (a) Bonn r-space potential [11,21]; (b) Paris potential [12,21]; (c) present data and Mainz data [17,18]; (d) present data and Louvain data [16]; (e) global fit (Rossi et al. [5]); (f) global fit (De Pascale et al. [8]).

Set	A_0	A_1	A_2	A_3	A_4
(a)	22.9	5.00	−16.9	−4.09	−0.7
(b)	23.3	5.02	−17.1	−4.07	−0.6
(c)	22.9(5)	6.5(8)	−17.9(5)	−5.7(8)	-
(d)	22.9(5)	6.5(8)	−18.5(5)	−6.1(8)	-
(e)	22.8(1)	5.6(1)	−17.2(1)	−5.4(1)	−0.83(3)
(f)	21.9(8)	5.4(8)	−16.2(7)	−5.0(6)	−0.7

nearby energies. These measurements [23–26] are included in the data upon which the global fits [5,8] are based and from which coefficient sets (e) and (f) in table 3 are derived. The present values (sets (c) and (d)) for A_2 deviate from both the theoretical values (sets (a) and (b)) and the global fits (sets (e) and (f)), the deviation being larger in the case of set (d), obtained by analysis in combination with the Louvain data [16], than in set (c), obtained in combination with the Mainz data [17,18]. The two sets (c) and (d) are, however, consistent with one-another, for A_2 as well as for the other Legendre coefficients, thus showing that the analysis is insensitive to the values used for the 0° and 180° cross sections, within the ranges defined by the Mainz and Louvain data (table 2). The present values for A_1 and A_3 are consistent with those obtained from the global fits and larger in magnitude than predicted by theory, as is the case for the global fits for incident energies $E_\gamma = 20$–40 MeV [1,2].

It is perhaps significant that the values of A_1 and A_3 obtained from the present work confirm the deviation from theory indicated by the global fits at $E_\gamma = 34$ MeV [5,8], bearing in mind that the present data were obtained using a completely different technique based on n–p capture measurements. The discrepancy between theory and the global fit of Rossi et al. [5] for the A_3 coefficient amounts to several experimental standard deviations. The present value of A_3 ((c) or (d)) is not accurate enough to check this result convincingly. However, further measurements based on the n–p capture method or on photon tagging [27,28] should be able to attain the precision necessary to to this. In regard to the theoretical predictions, we note that calculations based on the Paris potential [12,21] demonstrate that, at this energy, inclusion of MEC/IC/RC increases the magnitude of the coefficient A_2 by $<6\%$ and has an even smaller effect ($<1\%$) on A_1 and A_3. The theoretical predictions are thus very insensitive to the MEC/IC/RC corrections, especially for the coefficients A_1 and A_3, hence it seems unlikely that these effects will account for the discrepancies suggested in fig. 3b.

In conclusion, the differential cross section for deuteron photodisintegration at $E_\gamma = 33.9$ MeV (lab) has been determined via the inverse reaction, n–p radiative capture, and found to deviate marginally from theoretical predictions. The deviations of the Legendre A_1 and A_3 coefficients are consistent with trends observed in previous direct photodisintegration measurements.

We wish to thank: the Foundation for Research Development for financial support; Dr. D. Reitmann and staff of the NAC for their cooperation in carrying out the experiments; Mr. P.A. Back and Mr. D. Momsen for constructing equipment used; and Dr. H. Arenhövel, Dr. P. Leleux and Dr. A. Zuchiatti for valuable discussions and for providing data and computer codes.

References

[1] H. Arenhövel and M. Sanzone, Photodisintegration of the deuteron: a review of theory and experiment, Few Body Systems, Suppl. 3 (Springer, New York, 1991).
[2] K.M. Schmitt, P. Wilhelm and H. Arenhövel, Few Body Systems 10 (1991) 105.
[3] W. Jaus and W.S. Woolcock, Nucl. Phys. A 431 (1984) 669.

[4] S. Ying, E.M. Henley and G.A. Miller, Phys. Rev. C 38 (1988) 1584.
[5] P. Rossi et al., Phys. Rev. C 40 (1989) 2412.
[6] P. Wauters et al., Few Body Systems 8 (1990) 1.
[7] K.E. Stephenson et al., Phys. Rev. C 35 (1987) 2023.
[8] M.P. De Pascale et al., Phys. Lett. B 119 (1982) 30.
[9] A.E. Thorlacius and H.W. Fearing, Phys. Rev. C 33 (1986) 1830.
[10] G. Fink et al., Nucl. Phys. A 530 (1991) 331.
[11] K.M. Schmitt and H. Arenhövel, Few Body Systems 7 (1989) 95.
[12] P. Wilhelm, W. Leidemann and H. Arenhövel, Few Body Systems 3 (1988) 111.
[13] J.F. Gilot et al., Phys. Rev. Lett. 47 (1981) 304.
[14] P. Michel et al., J. Phys. G 15 (1989) 1025.
[15] C. Dupont et al., Nucl. Phys. A 445 (1985) 13.
[16] A. Ninane et al., Phys. Rev. C 35 (1987) 402.
[17] A. Zieger et al., Phys. Lett. B 285 (1992) 1.
[18] A. Zieger et al., Phys. Lett. B 287 (1992) 51.
[19] F.D. Smit and F.D. Brooks, Nucl. Phys. A 465 (1987) 429.
[20] M.M. Taiuti et al., Nucl. Instrum. Methods 211 (1983) 135.
[21] H. Arenhövel, private communication.
[22] P.R. Bevington, Data reduction and error analysis for the physical sciences (McGraw-Hill, New York, 1969).
[23] B. Weissman and H.L. Schultz, Nucl. Phys. A 174 (1971) 129.
[24] F.W.K. Firk, Neutron capture gamma-ray spectroscopy, eds. Robert E. Chrien and Walter R. Kane (Plenum, New York, 1979) pp. 245–263.
[25] L. Allen, Phys. Rev. 98 (1955) 705.
[26] Y.M. Shin et al., Nucl. Phys. A 154 (1970) 482.
[27] P.T. Debevec et al., Phys. Rev. C 45 (1992) 904.
[28] K.-H. Krause et al., Nucl. Phys. A 549 (1992) 387.

M.S. Allie, F.D. Brooks, D.G. Aschman, A. Buffler, W.A. Cilliers, R.W. Fearick, C.G.L. Henderson, M.J. Oliver, M.R. Nchodu, S.M. Perez, D. Steyn, W.R. McMurray, B.R.S. Simpson, F.D. Smit, H.G. Miller, K. Bharuth-Ram and I.J. van Heerden

Differential cross section for n-p radiative capture at E_n = 63.4 MeV

Physics Letters B314 (1993) 173-178

Hyperfine Interactions 82 (1993) 327–335

Techniques for measuring initial sticking in d–t fusion

C.G.L. Henderson, F.D. Brooks and W.A. Cilliers

Department of Physics, University of Cape Town, Rondebosch 7700, South Africa

Monte Carlo simulations are used to compare experimental techniques for the direct measurement of the initial sticking coefficient ω_s^0 in muon-catalyzed d–t fusion. Three methods based on observing alpha–neutron coincidences from fusions in a low-density D_2–T_2 gas target are investigated. The experimental systems use either a surface barrier detector or a thin plastic scintillator to detect the α and αμ, and mylar windows or a thin coating of aluminium oxide to protect this detector from the tritium activity in the target.

1. Introduction

One of the promising methods for obtaining an accurate measure of the initial sticking coefficient ω_s^0 in muon-catalyzed d–t fusion is the method [1] based on observing α–n coincidences from fusions occurring in a low-density ($\rho < 3 \times 10^{-3} \rho_0$) D_2–T_2 gas target. The selection of a collinear coincidence between the α (or αμ) and neutron allows good discrimination against backgrounds. The difference in the rates of energy loss for α (doubly charged) and αμ (singly charged) in the gas provides the means for determining the proportion of αμ. Corrections for the effects of muon stripping in the target gas are small.

Collaborations using the muon beam facilities of LAMPF, at Los Alamos [1], and ISIS, at the Rutherford–Appleton Laboratory (RAL) [2], have reported measurements by this method. In both experiments the α and αμ were detected by a surface barrier detector (SBD) mounted in a pure D_2 environment and protected from the high tritium activity (> 500 Ci) of the target gas by means of a pair of thin mylar windows (fig. 1a). The hazards associated with experiments in which large quantities of tritium are contained by thin windows naturally encourage consideration of alternative solutions to the problems of measuring α–n and αμ–n coincidences in experiments of this kind. Two such alternatives, referred to as geometries B and C respectively, are proposed here and compared by means of Monte Carlo calculations [3] with a third system (geometry A), similar to that used in the LAMPF and RAL experiments. Geometries B and C use a SBD and a thin plastic scintillator, respectively, for α-detection. Both employ a thin (2.5 μm) layer of aluminium oxide (ALOX), deposited on the detector surface by means of electron beam vacuum evaporation, as a barrier against tritium.

2. System characteristics and simulations

The main features of geometries A, B and C are illustrated in panels (a) of figs. 1–3. Each geometry uses a target cell of volume 300–400 cm^3. In geometry A the gas is contained in a silver-walled cubical cell of side 70 mm (fig. 1a), as in the RAL experiment [2]. A change to a truncated conical shape is proposed in geometries B and C (figs. 2a and 3a), to follow the broadening of the multiply scattered incident muon beam as it progresses through the target entrance wall and gas. From a larger set of simulations made at various gas pressures we present only results from those made at pressure 1510 Torr, the pressure for which the minimum energy of an $\alpha\mu$ reaching the detector is about 2 MeV.

The procedure for Monte Carlo simulations followed that outlined in a previous paper [3]. The distribution of fusion sites within the target cell was assumed to be axially symmetric and Gaussian in profile, with FWHM increasing with the depth of penetration [3]. A value of $\omega_s^0 = 0.01$ was used in simulations of the actual experiments and further simulations were also made using the artificially high value of $\omega_s^0 = 0.5$, in order to determine characteristics of events involving sticking to a similar statistical accuracy as for those not involving sticking.

The neutron detector was a cell of the liquid scintillator NE213, size

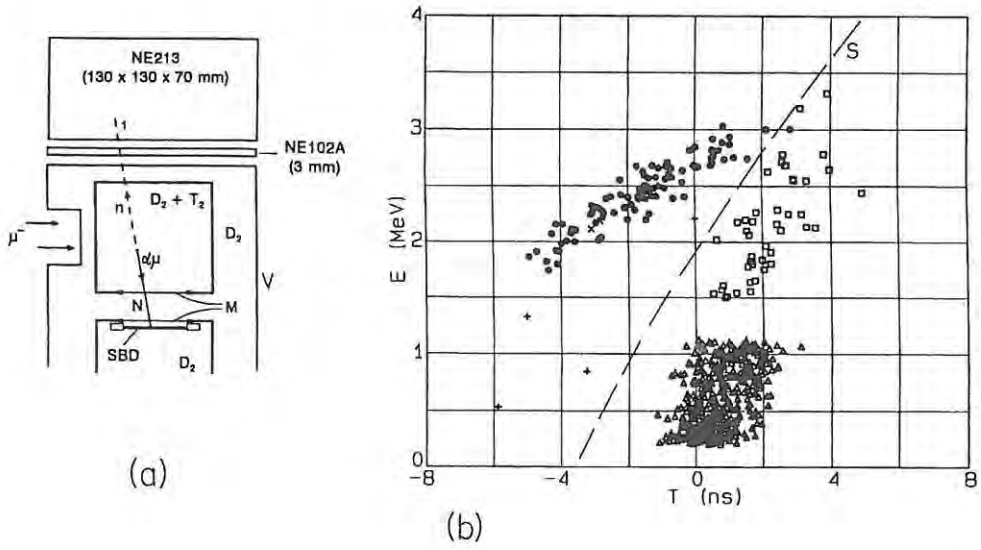

Fig. 1. Geometry A: (a) experimental arrangement (schematic); and (b) scatter plot showing simulated coincidences as a function of observed energy E and time difference T between neutron and alpha detection. Events in which an $\alpha\mu$ enters the SBD intact are indicated by solid circles. Events in which the μ is stripped from an $\alpha\mu$ before detection are shown as plus signs and crosses, for stripping in the target gas and the mylar windows, respectively. α–n events are shown as triangles (fusions in the target) and squares (fusions in the neck region N). The cut S is designed to select $\alpha\mu$–n events.

13 × 13 × 7 cm, the centre of which was located at a distance of 18 cm from the muon beam axis (all geometries). The system time resolution (for coincidence measurements) was assumed to be 1.2 ns (FWHM) for all geometries. An energy resolution of 2% (FWHM) at 3 MeV was assumed for the SBD in geometries A and B and a pulse height resolution of 30% (FWHM) at pulse height $L = 150$ keVee (see section 6) was assumed for the scintillator in geometry C. The E and L resolutions were scaled by $\sqrt{N}$ statistics for other energies.

3. Results for geometry A

In geometry A (fig. 1a) the α or αμ which are associated with fusion neutrons detected by the NE213 cell may escape through the mylar windows M and the "neck region" N of the outer D_2-filled containment vessel V, heading towards the SBD. For N_0 fusions occurring in the target cell, let the number of neutrons detected be N. Then

$$N = \epsilon N_0 , \tag{1}$$

where ϵ is the detection efficiency of the NE213 cell for 14.1 MeV fusion neutrons emitted from a spatial distribution of points corresponding to that of the fusion sites within the target. To determine the number N_c of α and αμ that are registered by the SBD in coincidence with these N neutrons, we need consider only the associated, collinear α and αμ whose paths are directed towards the SBD. If we apply a cut, as described below, to select only coincidences in which an αμ is detected then

$$N_c = \epsilon N_0 \omega_s^0 B \phi , \tag{2}$$

where B is a geometrical factor which represents the probability that the direction of the collinear αμ intersects the SBD and ϕ is the probability that an αμ on such a path reaches the SBD and satisfies the cut which is imposed to select αμ events. The probabilities B and ϕ are determined in the Monte Carlo calculation [3]. From eqs. (1) and (2)

$$\omega_s^0 = (1/B\phi) N_c/N , \tag{3}$$

showing how ω_s^0 follows directly from the measured ratio N_c/N of coincidence to single neutron rates and the calculated product $B\phi$.

The cut for discriminating between α–n and αμ–n coincidences is based on measurements of E, the energy deposited in the SBD, and the relative time delay T between α or αμ detection (T_α) and neutron detection (T_n). Thus

$$T = T_n - T_\alpha . \tag{4}$$

Consider a fusion which releases a neutron and an αμ along the axis labelled (1) in fig. 1a and leads to a coincidence being detected. If this event were to be repeated exactly, except that an α was released instead of an αμ, then the α would lose energy

faster than the αμ on its way to the SBD. A lower E would therefore be measured for the α than for the αμ and the time T_α would be slightly longer, making T smaller. The parameters E and T also depend on the position at which the fusion occurs, thus events corresponding to αμ–n coincidences and α–n coincidences respectively are distributed across different regions of the E–T plane (fig. 1b) as indicated by the solid circles and triangles. The solid circles in this plot indicate αμ which reach the SBD without the μ being stripped from the α. The energy E measured by the SBD is not significantly affected if stripping occurs in the detector itself. The triangles in fig. 1b represent only a small fraction (8%) of the potential α–n coincidence candidates that were tracked in the Monte Carlo simulation. For most of these candidates, that is fusions in which the neutron was detected and the direction of the associated α intersected the SBD, the α was ranged out in the target gas or the mylar windows and was therefore not detected. The few (8%) α–n coincidences that *are* observed are those which originate from fusions occurring within a limited region of the target gas near to the SBD. This also accounts for these events (triangles in fig. 1b) being located at larger values of T.

The Monte Carlo simulation [3] used values from the theoretical calculations of Cohen [4] to estimate the probability of muon stripping during the passage of the αμ through the target gas and mylar windows. Events in which stripping occurs in the gas and windows are indicated by diagonal crosses and plus signs, respectively, in fig. 1b. The fraction of αμ affected by stripping is very small in this geometry.

In an ideal situation, in which the windows M are completely impermeable to D_2 and T_2, the only events in fig. 1b would be those described above and a cut such as that indicated by the line S should separate αμ from α almost perfectly. Experience has shown, however, that D_2 and T_2 may diffuse through thin mylar windows such as used in the RAL experiment [2]. A low concentration of T_2 then builds up in the outer vessel V and fusions catalyzed by muons scattered into the "neck region" N between the mylar windows lead to the additional α–n events indicated by squares in fig. 1b. The small energy gap between the triangles and squares corresponds to the energy lost by a fusion α in traversing the upper mylar window in fig. 1a, which thus applies only to the target fusions (triangles). The proportion of "neck fusions" (fusions from region N) among the detected coincidences will depend on the permeability of the mylar windows to tritium and the profile of the incident muon beam and is difficult to predict. The number shown in fig. 1b is a very rough estimate based on the experience [2] over a single run which lasted for 5 days. The presence of a large number of neck fusions would complicate the positioning of cut S if the system coincidence timing resolution was inferior to the value of 1.2 ns (FWHM) assumed in the simulations.

4. Results for geometry B

The most important difference between the proposed geometry B (fig. 2a) and

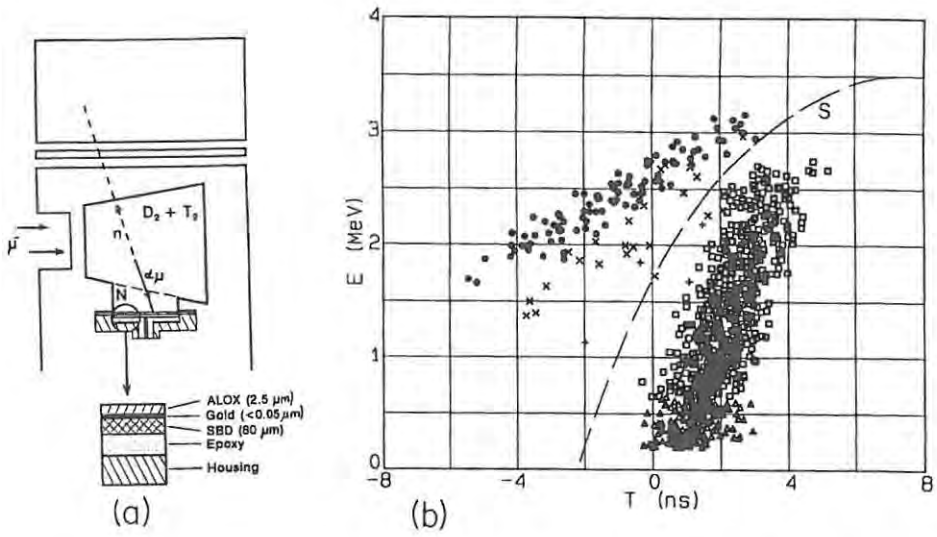

Fig. 2. Geometry B: (a) experimental arrangement (schematic); and (b) scatter plot, as for fig. 1, except that crosses indicate αμ–n events in which muon stripping occurs in the ALOX barrier.

geometry A is the replacement of the two mylar windows, M in fig. 1a, by the 2.5 μm thick ALOX barrier deposited directly on the entrance window of the SBD. An associated contribution [5] to this conference describes experimental tests which showed that an even thinner barrier (0.5 μm ALOX plus 0.2 μm gold) is effective in preventing tritium from diffusing into a SBD.

Fig. 2b shows the scatter plot of events as a function of E and T from the Monte Carlo simulation for geometry B. The coincidences are coded as in fig. 1b, except that crosses now indicate αμ that have been stripped in the ALOX barrier which replaced the mylar windows. Stripping is more likely in this barrier owing to the higher Z-values of its constituents. However, since the stripping occurs immediately in front of the SBD, the displacement of these events from the unstripped αμ is small and αμ may still be separated clearly from α by means of the cut S shown in fig. 2b.

The distinction between "neck fusions" (squares) and other α–n coincidences (triangles) is academic in geometry B, since the neck region N (fig. 2a) is contiguous with the remainder of the target cell. The results show, however, that good timing resolution is essential to discriminate between αμ–n events and α–n events in this geometry.

5. Results for geometry C

The evolution from geometry B to geometry C (fig. 3a) simply involves replacing the SBD by a thin plastic scintillator detector, an NE102A film, 80 μm thick,

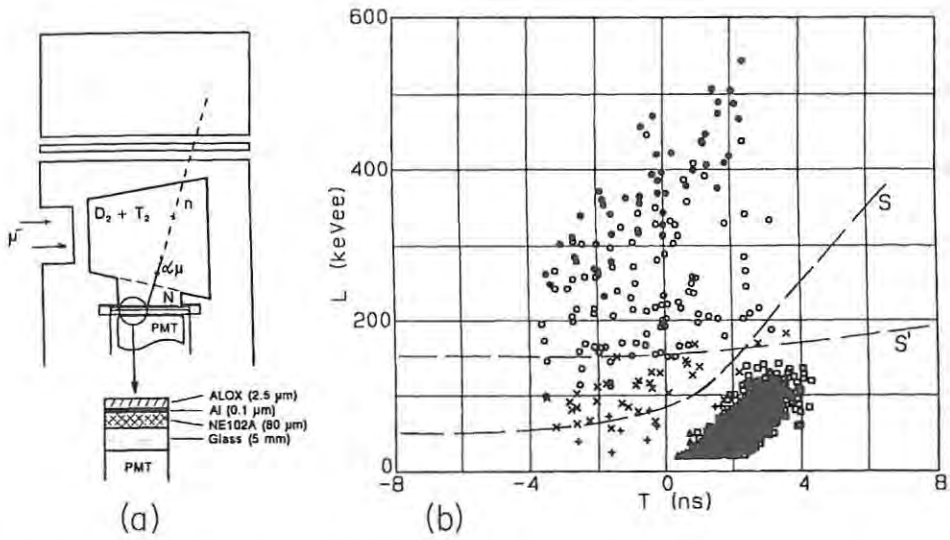

Fig. 3. Geometry C: (a) experimental arrangement (schematic); and (b) scatter plot showing simulated coincidences as a function of scintillator pulse height L and relative time difference T. αμ–n events are shown by solid circles (αμ brought to rest in scintillator without stripping), open circles (αμ stripped in scintillator before coming to rest), plus signs (αμ stripped in target gas) and crosses (αμ stripped in ALOX). α–n events are shown by triangles (fusions in conical section of target cell) and squares (fusions in neck region N). αμ–n events may be selected by one or other of the cuts, S and S'.

viewed through a glass window by a photomultiplier tube. The barrier protecting the detector against tritium is, as in geometry B, a 2.5 μm layer of ALOX. A 0.1 μm thick aluminium reflector is sandwiched between the ALOX and the NE102A to enhance light collection by the photomultiplier.

The pulse height response of the scintillator, unlike that of a SBD, depends on the rate of energy loss $-\mathrm{d}E/\mathrm{d}x$ of the incident particle, as well as on its energy E, and is a non-linear function of E [6]. The simulated results for geometry C are therefore presented as a scatter plot (fig. 3b) of events as a function of pulse height L and time difference T, with L calibrated in the units keVee. In these units, "keV electron equivalent", a pulse height of X keVee, for any particle, is the same as the pulse height produced by an electron of energy X keV. The Monte Carlo simulation [3] used the formula of Birks [6] to calculate the pulse height responses L, for α and αμ, shown in fig. 3b.

In fig. 3b, αμ which remain unstripped until the end of their range (defined as $E<0.1$ MeV for the purposes of the simulation) are shown as solid circles. It is interesting to note again [3] how the Birks formula predicts a considerably higher response L for these αμ than for α of the same energy (squares and triangles). This useful feature of geometry C should enhance the separation of αμ–n events from α–n events in the sticking experiment. The αμ which pass unstripped through the ALOX barrier and then strip in the plastic scintillator, before coming to rest, are

shown as open circles in fig. 3b. Those which strip in the barrier are shown as crosses. Two possible cuts, S and S′, for discriminating against α–n events are considered in fig. 3b. Cut S includes a substantial fraction of the αμ which are stripped in the ALOX barrier and would therefore require a smaller correction for events lost due to this process. For experimental reasons such as low pulse height backgrounds, however, it might be preferable to operate at a higher pulse height threshold, as indicated for cut S', and thus with a larger correction for lost αμ–n coincidences. The correction for these lost events, estimated from the Monte Carlo simulations [3], should be about 13% and 35% for cuts S and S′, respectively.

The ability of the plastic scintillator to discriminate between αμ and α could also lead to useful new applications in the experimental study of muon stripping. An additional layer of any element or compound could be deposited on top of the ALOX barrier in fig. 3a, for example. The numbers of events measured above the cut S or S′ (fig. 3b), with and without the additional layer, could then be compared to determine stripping cross sections as a function of αμ energy. This approach could also be used to estimate or check the stripping corrections required for the determination of ω_s^0 by method C.

6. Discussion

The data presented in figs. 1–3 simulate results that would be expected from experiments in which 100–200 αμ–n coincidence events are measured using geometries A, B or C, assuming a sticking coefficient $\omega_s^0 = 0.01$. In an experiment carried out using the RAL muon beam, for example, it should be possible to gather this number of events in about 24 hours. Table 1 shows data for the three geometries, obtained as for figs. 1–3 but with better statistical accuracy for the αμ–n events, by assuming the artificially high value of $\omega_s^0 = 0.5$ in the Monte Carlo simulations. The numbers shown are percentages of those fusion events in which: (a) sticking occurs; (b) the fusion neutron is detected; and (c) the direction of the associated αμ intersects the SBD (geometries A or B) or the scintillator (geometry C). Column 2

Table 1
Statistics for fusions in which sticking occurs, the neutron is detected and the αμ path intersects the αμ-detector.

Geometry	Percentage of αμ which:			
	enter detr. unstripped	are stripped		pass cut S (S′)
		in gas	in barrier	
A	83	9	8	93
B	70	8	22	92
C	70	8	22	87 (65)

of the table shows the fraction of αμ which reach the detector without being stripped. Stripping subsequent to this stage is insignificant in the detection process in a SBD (geometries A and B) but is important in the case of a scintillator (geometry C) as noted above. In geometry C the unstripped component of 70% in column 2 of the table comprises 23% which remain unstripped effectively until brought to rest in the scintillator and 47% which are stripped at some stage during the detection process. These two categories contribute the events shown as solid and open circles, respectively, in fig. 3b.

The third column in table 1 shows events in which αμ are stripped in D_2–T_2 gas within the target cell. These numbers include events in which the α resulting from this stripping is ranged out in the target gas or the tritium barrier, and is therefore not observed in the experiment. The 9%, 8% and 8% shown in column 3 for geometries A, B and C, respectively, include 5%, 4% and 4% corresponding to events which are ranged out in this way.

Column 4 of the table shows events in which the αμ is stripped in the mylar windows (geometry A) or the ALOX barrier (geometries B and C). The latter percentages could be reduced by a factor of 2 to 3, without difficulty, by reducing the thickness of ALOX from 2.5 μm to 0.8–1.2 μm, since thinner barriers have been shown to be suitable [5], as noted above. This should be useful in geometry C, in reducing the correction for αμ–n events lost below the cut S or S' (fig. 3b). It would not be expected to lead to any significant advantage in geometry B. The percentages in columns 2–4 of the table are the same for geometries B and C, as expected from the fact that the geometries (figs. 2a and 3a) are identical, except for the detectors used.

The last column of table 1 shows the percentages of the specified αμ–n events which satisfy the cuts S or S' (figs. 1b–3b) which are designed to reject α–n events. The rejection efficiency for α–n events is 99.99% or better in all cases, while over 90% of the αμ–n events are accepted in geometries A or B and 65–87% in geometry C, depending on which cut, S or S' (fig. 3b), is applied. The numbers in this column give the factor ϕ of eq. (2) (expressed as a percentage) for the different geometries.

A system timing resolution of 1.2 ns (FWHM) or better is essential in order to achieve an effective separation of αμ–n events from α–n events in geometries A and B, and also in geometry C, if cut S is used. This requirement is relaxed for cut S' of geometry C however (fig. 3b), due to the different pulse height response of the scintillator to αμ and α. Good timing resolution is nevertheless likely to be required in all geometries in order to discriminate against real coincidence backgrounds [5], which are expected to contribute events in the regions $T > 2$ ns in figs. 1b–3b.

Comparing the three geometries, geometry A offers the clearest separation of αμ–n events from α–n events, but only if diffusion of tritium through the mylar windows proves to be negligible. Even with the risk of such diffusion, the performance of geometry A may still be adequate but it will be no better than that of geometry B which is more robust and effectively eliminates the possibility of tritium leakage. Geometry C will be as robust as geometry B and should attain good timing resolu-

tion without difficulty or a special design of the α-detector. It is less efficient in selecting αμ–n events against α–n events however (table 1), and therefore more reliant on calculations, or other estimates, of the correction for event losses. The most promising system therefore appears to be geometry B, but geometry C also has some unique and promising features which could justify an experimental trial of this technique.

Acknowledgement

We thank the South African Foundation for Research Development for their support of this work, and the members of the RAL collaboration for stimulating discussions.

References

[1] M.A. Paciotti et al., AIP Conf. Proc. 181 (1989) 38.
[2] J.D. Davies et al., J. Phys. G16 (1990) 1529.
[3] C.G.L. Henderson et al., Muon Catal. Fusion 6 (1991) 405.
[4] J.S. Cohen, Phys. Rev. A37 (1988) 2343.
[5] W.A. Cilliers, F.D. Brooks and J.B.A. England, Proceedings of this Conference, Hyp. Int. 82 (1993) 337.
[6] J.B. Birks, Proc. Phys. Soc. A64 (1951) 874.

C.G.L. Henderson, F.D. Brooks and W.A. Cilliers
Techniques for measuring initial sticking in d-t fusion
Hyperfine Interactions 82 (1993) 327-335.

Hyperfine Interactions 82 (1993) 337–342

Detection of fusion alphas from D_2–T_2 gas targets

W.A. Cilliers, F.D. Brooks

Dept. of Physics, University of Cape Town, Rondebosch 7700, South Africa

and

J.B.A. England

Qpar Angus Ltd., Leominster, HR6 8RS, UK

Detectors for recording alphas from fusions in D_2–T_2 gas targets require protection against diffusion of tritium into the detector medium. Tests have been carried out on surface barrier detectors to determine the feasibility of using thin coatings of oxide and metal for this purpose. The results show that a layer of 0.5 μm aluminium oxide plus 0.2 μm gold provides effective protection for at least 280 h, without impairing the transmission of 2 MeV alphas into the detector. Tests of an alternative detector, a phoswich of thin film plastic and lithium-glass scintillators, are also described.

1. Introduction

The initial sticking coefficient ω_s^0 in d–t μCF may be measured directly [1,2] by observing alpha–neutron coincidences from fusions in a low-density (<2000 Torr) gaseous D_2–T_2 target. To achieve adequate event rates in an experiment of this type tritium fractions of 30-50% are required in the target gas, hence the target activity will typically exceed 500 Ci. A barrier is thus required to shield the α-detector from this activity (19 keV beta and associated bremsstrahlung) and to impede the diffusion of tritium into the detector. The barrier must be thin so that the 3.5 MeV α or αμ from fusion, which may be degraded to energies as low as 2 MeV in its passage through the gas, can reach the detector with sufficient energy to be recorded.

The coincidence measurements of ω_s^0 that have been reported to date [1,2] have used surface barrier detectors (SBD) to register the alpha and a pair of aluminium-coated mylar windows (1.5 μm) to isolate the SBD from the target gas. A possible alternative, a thin film plastic scintillator (TFPS) protected by a thin surface coating (0.3 μm) of aluminium oxide (ALOX), has been tested under conditions simulating the sticking experiment and found to operate satisfactorily [3]. In this paper

we report tests of a related alternative system, consisting of a SBD coated with a thin ALOX layer. We also describe tests of a modified TFPS detector [3] in the form of a phoswich, which may be capable of discriminating between alpha–neutron coincidences and particle–neutron coincidence backgrounds in the sticking experiment.

2. ALOX-coated surface barrier detector

Systems incorporating thin mylar windows have functioned successfully [1,2] but not without problems and anxiety. Operating with such fragile windows requires extreme care to avoid pressure differences across the mylar, particularly when filling the target or when adjusting the gas pressure. Experience has also shown [2] that the diffusion of tritium through thin mylar windows may be significant over the time required to gather data in a sticking experiment. An ALOX-coated SBD, like the ALOX-coated TFPS previously investigated [3], should avoid these problems since aluminium oxide layers are known [4] to be good barriers against tritium diffusion and because coating the detector surface ensures a stable physical support and avoids the possibility of a pressure gradient across the barrier.

The arrangement used to test the effectiveness of ALOX coatings as tritium barriers is shown in fig. 1. The SBD, area 20 mm^2, thickness 89 μm, fully depleted, was mounted in a recessed aluminium baseplate by means of epoxy cement (fig. 1a).

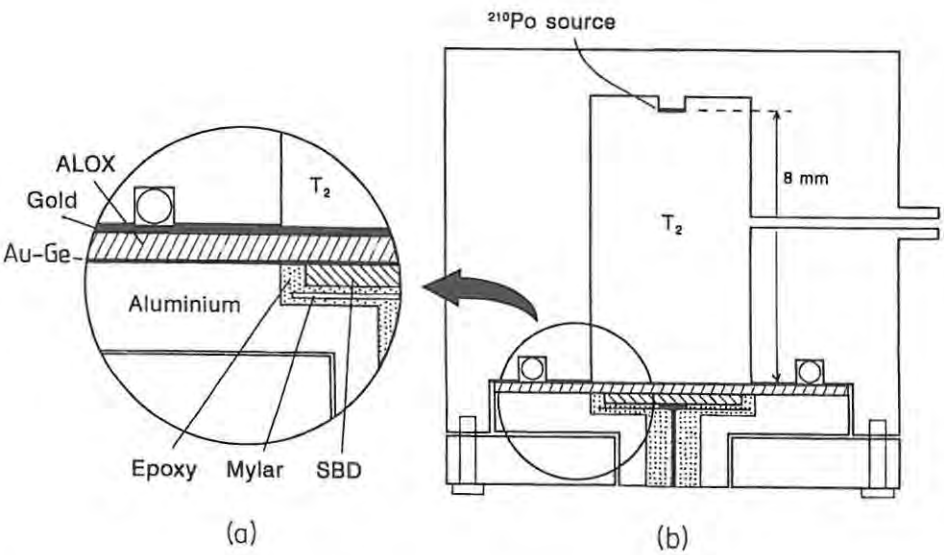

Fig. 1. Schematic diagrams of the experimental arrangement showing: (a) detail of the gold/ALOX barrier; and (b) the cell used for the tritium tests.

The Au–Ge eutectic layer (<0.05 μm) forming the entrance window to the diode extended over the epoxy onto the plate. An ALOX layer (0.5 μm) was deposited over this window by electron beam vacuum evaporation. The same technique was then used to add an outer layer (0.2 μm) of gold, extending to the edge of the baseplate so as to ensure a good mechanical seal over the ALOX. In a sticking experiment performed using a pulsed muon beam [2] the outer gold layer could also assist in scavenging muons which might otherwise find their way into the detector and cause coincidence backgrounds.

Not all types of surface barrier detector are likely to be suitable for the application of coatings of the type considered here. Normal silicon surface barrier detectors are not sufficiently ruggedized to allow glassy layers to be applied to their surfaces. Detectors made using the Au–Ge eutectic layer, developed by England and Hammer [5], which are touchproof in normal use, do, however, allow deposition of such layers. In addition, the window thickness for these detectors is much less than for the usual "touchproof" detectors, so that even after deposition of the additional layers described above, the α-particle resolution is still good. A detector of this type, provided by Qpar Angus, Leominster, UK, was used in these tests.

In the tests of the ALOX-coated SBD the test chamber (fig. 1b) was evacuated and then filled with tritium to a pressure of 600 Torr. The spectrum of alphas from the uncollimated ^{210}Po α-source (5.304 MeV) mounted in the chamber was measured before filling and monitored over periods varying from 15–70 h, commencing at different times after filling. Measurements continued for 280 h from the time of filling, after which the tritium was removed and the spectrum was remeasured with the cell evacuated. Fig. 2 shows two spectra, recorded over periods of 1–17 and 210–280 h, respectively, normalised to the same live time. At α-energies above about 1.2 MeV differences between the two spectra are insignificant. The spectrum taken at the later time shows a rise in count rate at $E_\alpha < 1.2$ MeV, which might perhaps be due to pulse pileup caused by diffusion of tritium through the ALOX into the SBD.

For 2 MeV α-particles entering a SBD via a barrier of the type tested (0.5 μm ALOX plus 0.2 μm gold) the energy deposited in the SBD will be 1.7 MeV. The tests therefore show that such a barrier should be effective in protecting the SBD from the effects of tritium radioactivity and tritium diffusion for at least 280 h. This should allow sufficient time to make useful measurements in a sticking experiment requiring detection of fusion alphas of energy 2 MeV or higher.

3. Tests of a TFPS phoswich detector

The tests reported [3] for ALOX barriers on thin film plastic scintillators involved ALOX coatings only (no gold) and the ALOX layer was thinner (0.3 μm) than in the SBD tests described above. The results obtained with the SBD suggest that the small effects which were attributed to tritium diffusion in the TFPS tests [3]

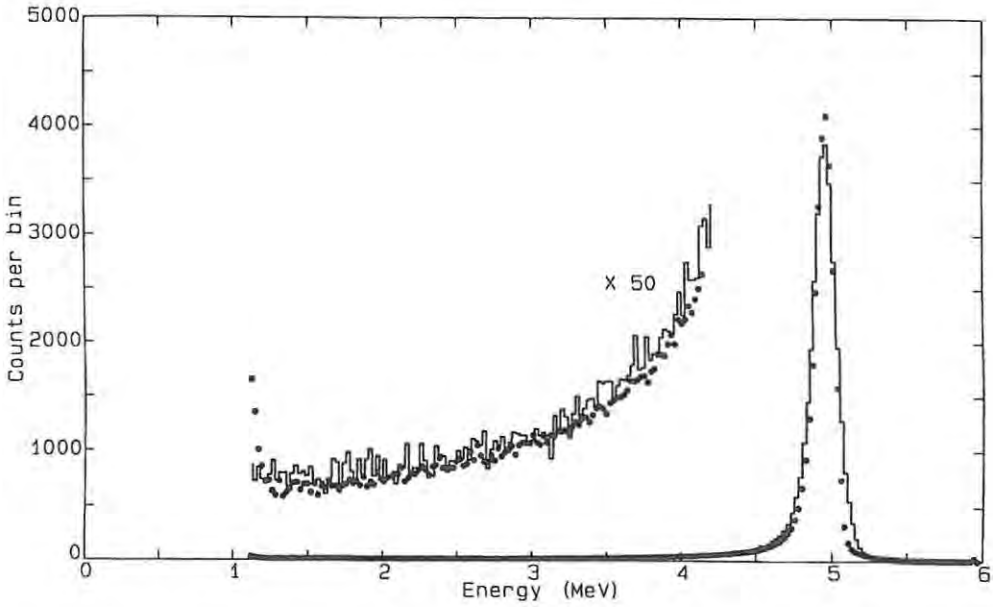

Fig. 2. Alpha spectra measured over the periods of 1–17 h (histogram) and 210–280 h (points) after loading the test cell with tritium. The spectra are normalised to the same live time.

should be reduced significantly if a barrier similar to that shown in fig. 1a were used. The TFPS therefore remains a promising option for α-detection in a sticking experiment.

Experience in the direct determination of ω_s^0 by measuring α–n coincidences has indicated the presence of a "real coincidence background" [2,6] which appears most likely to be due to charged particle–neutron coincidences arising from muon capture on low-Z nuclei located within, or near to, the α-detector. If the charged particle in this mechanism is lighter than the α then it may be possible to discriminate against this type of background by employing a phoswich detector consisting of a TFPS coupled to a second scintillator, of longer decay time, viewed by a single photomultiplier. The principle of operation is that the α or αμ from fusion should be stopped in the TFPS, thus giving a pulse of short decay time (<3 ns), whereas a lighter particle of sufficient energy should penetrate to the second scintillator, thus giving a pulse which includes both slow and fast decay components. Pulse shape discrimination (PSD) techniques can then be used to distinguish between true fusions and backgrounds of this type.

A phoswich consisting of a 20 μm thick NE102A TFPS coupled to a NE905 ^{6}Li-loaded glass scintillator (25 mm diam. × 3 mm thick disc) was used to test this scheme. The TFPS was prepared by an evaporation technique [7] directly on the surface of the NE905 disc. Measurements were made using a wax-moderated AmBe source (neutrons and gammas), to calibrate the NE905 response, and an ^{241}Am α-source placed at different distances (in air) above the NE102A layer, to

provide different incident alpha energies. Results taken with the α-source at 14 and 3 mm, respectively, from the phoswich are shown in fig. 3. The photomultiplier output signals were processed by a Link Systems model 5010 pulse shape discriminator unit and a two-parameter data acquisition system to obtain plots (fig. 3) showing event density as a function of the parameters L and S. The pulse height L, which is proportional to the total light in the scintillation, increases monotonically with particle energy for any given type of particle and is smaller for more heavily ionising particles. The pulse shape parameter S depends on the proportion of slow component in the scintillation and is therefore sensitive to the fraction of energy deposited by the particle in the NE905 sector of the phoswich. Events lying along the upper locus, labelled (1) in fig. 3, are attributed to neutron and gamma interactions in the NE905. Peak C is a convenient calibration reference provided by the ^{6}Li(n,α)^{3}H reaction ($Q = 4.8$ MeV) in the glass scintillator. Events in which energy is deposited predominantly in the NE102A lie along region (2) in fig. 3. With the α-source at distance 14 mm (fig. 3a) the α enter the NE102A in directions close to normal, with energy 4.0 MeV, and do not penetrate into the NE905. Most of these events therefore fall within the boundaries of the cut enclosing region (2) in fig. 3. With the source at distance 3 mm however (fig. 3b), alphas enter the phoswich with

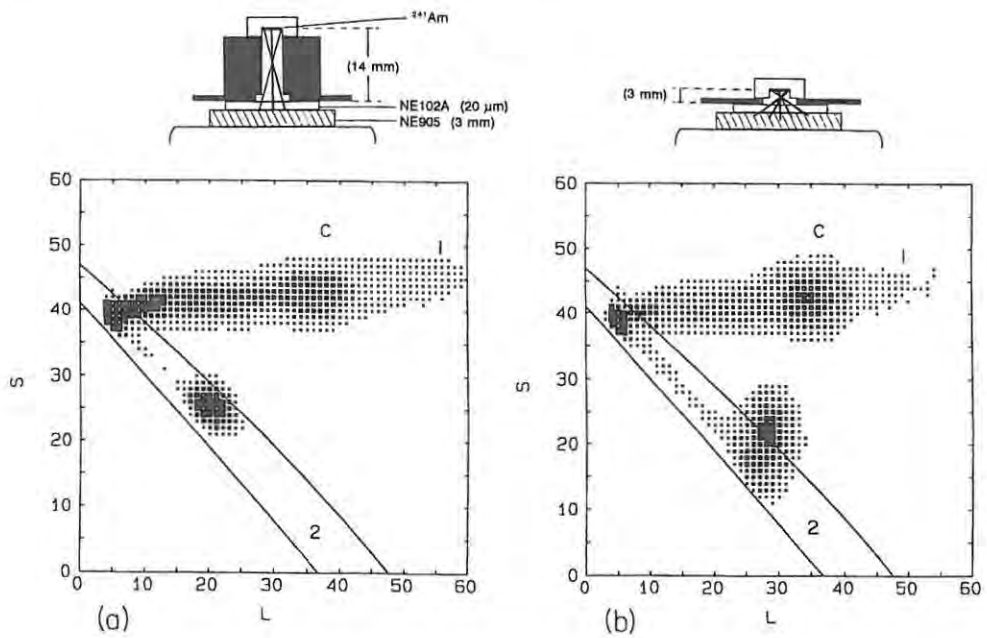

Fig. 3. Density plots of events as a function of pulse height L and pulse shape S, obtained with air gaps of: (a) 14 mm; and (b) 3 mm between the ^{241}Am source and the NE102A/NE905 phoswich. Locus (1) corresponds to events depositing energy in the NE905 only. Cut (2) selects events detected in the NE102A only. The points, in order of increasing size, indicate count thresholds of 20, 100, 500, 1000 and 2000.

energy 5.1 MeV and a wider range of incident angles. Those which enter at angles close to normal penetrate more deeply into the NE905 component. These events are seen to be displaced outside the cut enclosing region (2), towards higher S-values, thus confirming that the phoswich should be able to distinguish α or αμ events from backgrounds due to lighter particles which penetrate into the NE905. A thicker NE102A layer (80 μm) would be required in a sticking experiment, in order to stop both αμ and α of energy 3.5 MeV. The second scintillator need not be as thick as that used in the tests and could be of any type exhibiting a decay time significantly longer than that of NE102A.

4. Conclusions

The results of these tests suggest that the two types of α-detector considered, namely the ALOX-coated SBD and a TFPS phoswich equipped with a similar barrier, should both be suitable for detecting fusion alphas in a sticking experiment. Factors such as energy resolution, timing resolution or the nature and level of real coincidence background [6] in the experiment might indicate a clear preference for one detector or the other. It might be advantageous to compare the two types of detector in a preliminary sticking experiment by mounting one of each type on the same gaseous target system. Two similar detectors could be installed later, if the first run indicated a clear preference for one type over the other.

Acknowledgement

We thank the South African Foundation for Research Development for their support of this work, Mr. C.G.L. Henderson for his assistance in the experiments and analysis, and Dr. R. Pretorius, Mr. J.E. McLeod and Mr. H.W. Schmitt, of the National Accelerator Centre, Faure, S.A., for their assistance with the electron beam vacuum evaporation and the tritium experiments.

References

[1] M.A. Paciotti et al., AIP Conf. Proc. 181 (1989) 38.
[2] J.D. Davies et al., J. Phys. G16 (1990) 1529.
[3] W.A. Cilliers and F.D. Brooks, Muon Catal. Fusion 6 (1991) 413.
[4] K.R. Lawless, Rep. Progr. Phys. 37 (1974) 231.
[5] J.B.A. England and V.W. Hammer, Nucl. Instr. Meth. 96 (1971) 81.
[6] C.G.L. Henderson et al., Muon Catal. Fusion 6 (1991) 405.
[7] M.S. Allie et al., Nucl. Instr. Meth. A240 (1985) 338.

W.A. Cilliers, F.D. Brooks and J.B.A. England
Detection of fusion alphas from D_2-T_2 gas targets
Hyperfine Interactions 82 (1993) 337-342

F.D. Brooks, C.G.L. Henderson, M.S. Allie, A. Buffler, M.J. Oliver and M.R. Nchodu
Element analysis by scattered neutron spectrometry
Proceedings of the 5th International Conference on Applications of Nuclear Techniques - Neutrons and their Applications, Crete, June 1994 - to be published.

Element analysis by scattered neutron spectrometry

FD Brooks, CGL Henderson, MS Allie, A Buffler, MJ Oliver and MR Nchodu
Dept of Physics, University of Cape Town, Rondebosch, 7700 South Africa

DTL Jones, BRS Simpson, FD Smit and JE Symons
National Accelerator Centre, P.O. Box 72, Faure, 7131 South Africa

ABSTRACT

The lineshape of a neutron spectrometer[1] consisting of a single deuterated anthracene scintillation crystal has been investigated as a function of neutron energy from 7-30 MeV. The spectrometer has been used to study backscattering of 14 MeV neutrons by samples containing carbon, nitrogen and oxygen. The results indicate that it should be possible to analyse bulk samples for these elements by means of this technique.

1. INTRODUCTION

When a sample containing light elements such as C, N or O is bombarded with monoenergetic neutrons the energy spectrum of backscattered neutrons contains signatures characteristic of these elements and could therefore provide a means for identifying the elements and determining their concentrations. Like the well-known technique of Rutherford backscattering (RBS) "neutron backscattering" (NBS) would use the dependence of the backscattered energy on target nuclide mass to identify the scatterer. Whereas RBS, using charged particles, is confined to surface analysis, NBS would be suited to bulk analysis, and might consequently find application in the detection of hidden explosives. The practical realisation of both RBS and NBS depends on the availability of a detector-spectrometer for the backscattered particle which has good energy resolution and high detection efficiency together with low sensitivity to backgrounds. For example, an energy resolution of < 4% (FWHM) is required in order to resolve between neutrons elastically scattered by C, N and O. Semiconductor detectors are obviously ideal for RBS but no neutron spectrometer suitable for NBS seems to have emerged yet. In this work we consider using the deuterated anthracene neutron spectrometer (DANS)[1] for this purpose and describe tests to determine whether this detector will be capable of identifying the elements C, N and O in an NBS system. The tests (fig 1) included measurements of the lineshape and energy resolution of the DANS for monoenergetic neutrons in the energy range 7-30 MeV and exploratory measurements of the scattering of monoenergetic 14 MeV neutrons by samples containing C, N and O.

2. THE DEUTERATED ANTHRACENE NEUTRON SPECTROMETER

The deuterated anthracene spectrometer[1] consists of a single deuterated anthracene scintillation crystal (10 mm diam x 21 mm long) which detects neutrons by n-d elastic scattering. It utilises the anisotropy of the scintillation characteristics of anthracene crystal scintillators[2] to select the forward peak in the angular distribution of recoil deuterons associated with n-d elastic scattering. Fig 2 shows perspective views of events recorded as a function of pulse height L and pulse shape parameter[1] S when 14 MeV neutrons enter the crystal in directions parallel to either: (a) the crystal c'-axis; or (b) the crystal b-axis (perpendicular to c'). The direction-dependence is illustrated by the shift (fig 2) of the forward recoil peak P in the LS-plane as the incident neutron direction changes from c'-axis to b-axis. For neutrons incident in the direction parallel to the crystal

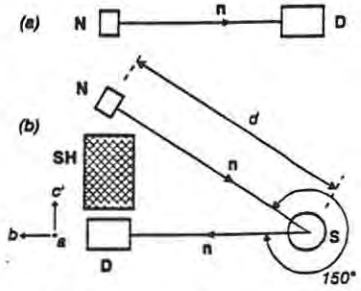

Fig 1. Experimental arrangements (schematic) for: (a) lineshape measurements; and (b) scattering measurements. N = pulsed neutron source. S = scattering sample. D = deuterated anthracene crystal. SH = shadow shield.

b-axis (fig 2b) forward recoils are selected by requiring events to fall on the high-S side of the cut FR shown in fig 2. The projected pulse height (L) spectrum for these events gives the DANS its simple (single peak) lineshape at low neutron energy, E_n < 16 MeV.

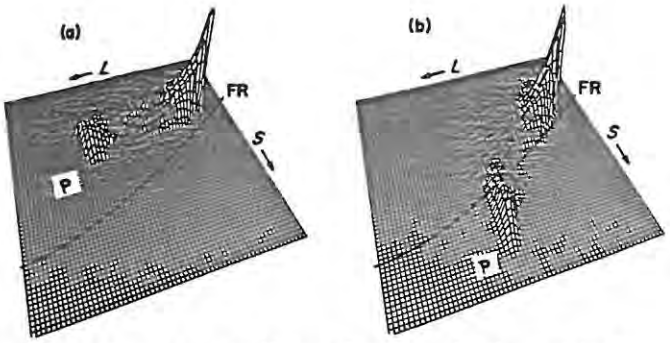

Fig 2. Counts (vertical) as a function of pulse height L and pulse shape parameter S produced by 14 MeV neutrons incident on the deuterated anthracene crystal in the mutually perpendicular directions parallel to: (a) the crystal c'-axis; and (b) the crystal b-axis. The peak P corresponds to forward deuteron recoils from n-d elastic scattering. The line FR shows the cut used to select deuterons recoiling parallel to the b-axis.

3. LINESHAPE MEASUREMENTS

The lineshape of the DANS was studied: (a) using pulsed 14.1 MeV neutrons, obtained from the $^3H(d,n)^4He$ reaction; and (b), as a function of neutron energy (7-30 MeV), by time-of-flight, using the continuous-spectrum (5-63 MeV) neutron beam provided by the neutron therapy facility[3] of the South African National Accelerator Centre (NAC). Fig 3a shows the lineshape measured for 14.1 MeV neutrons. The width (FWHM) of the forward recoil peak corresponds to a neutron energy spread of 0.73 MeV, or 5.2% of the incident neutron energy. The energy resolution of the DANS is determined by the accuracy with which the upper edge of this peak is measured, since the edge corresponds to the sharply defined upper limit in the continuum of recoil deuteron energies resulting from n-d elastic scattering. The observed edge is broadened by photomultiplier statistics and by imperfections in the crystal and the light collection efficiency. A measure of the energy resolution corresponding to the observed forward recoil edge is obtained by differentiating the spectrum $N(L)$ of fig 3a and plotting $-dN/dL$ versus L as shown in fig 3b. The width of the peak in fig 3b indicates an energy resolution of 2.4% (FWHM) for 14 MeV neutrons.

In the measurements made using the neutron therapy beam the flight path was 6.07 m and the observed time resolution was 1 ns (FWHM), giving an energy resolution (for time-resolved neutrons) varying from 1.3-2.5% (FWHM) for E_n = 7-30 MeV. Pulse height L, pulse shape S and time-of-flight T were recorded

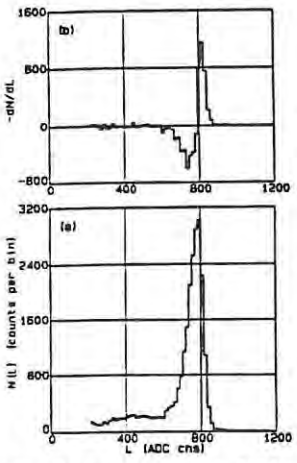

Fig 3. (a) Lineshape $N(L)$; and (b) $-dN/dL$ versus L, for 14.1 MeV neutrons.

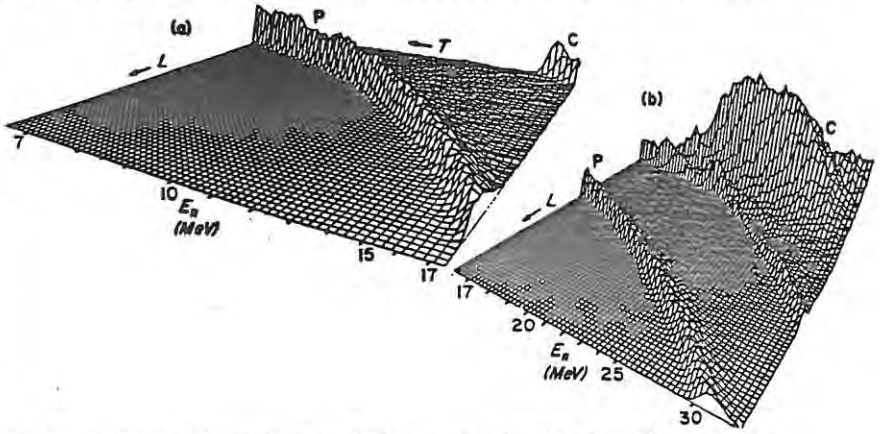

Fig 4. Number of events as a function of scintillation pulse height L and neutron time-of-flight T for events selected by the forward recoil cut FR (see fig 2). The T-scale is calibrated to neutron energy, P indicates the forward recoil peak and C indicates components from neutron reactions on carbon (see text).

for each event. After selecting forward recoil deuterons by the cut FR in the *LS* plane (fig 2), the pulse height spectrum at any discrete *T* gives the lineshape for the corresponding E_n. The plots in fig 4, showing number of events as a function of *L* and *T*, with *T* calibrated in terms of E_n, therefore present the lineshape as a function of E_n from 7-30 MeV. At E_n < 17 MeV (fig 4a) the lineshape is dominated by the forward recoil peak. At E_n > 17 MeV (fig 4b) products of the (n,d) and (n,α) reactions on the carbon within the scintillator contribute significantly to the low-*L* region. The edge resolution, as defined above (fig 3b), was determined as a function of E_n from the data of fig 4 and found to vary from 3.5% to 2.8% for E_n increasing from 7-12 MeV, levelling out at 2.5% for E_n > 17 MeV. These results suggest that the time-of-flight resolution of the system may have limited the resolution observed at the higher energies. The resolution observed over the full energy range investigated is nevertheless inside the limit (<4%) within which it should be possible to resolve backward elastic scattering from the elements C, N and O.

4. SCATTERING MEASUREMENTS

Scattering measurements were carried out using pulsed monoenergetic 14.1 MeV neutrons in an arrangement (fig 1b) similar to that envisaged for CNO monitoring. Neutrons from the source N are scattered by the sample S, through an angle of 150°, into the deuterated anthracene crystal D. The scattered neutrons enter the crystal moving parallel to the *b*-axis, as required for the DANS[1]. The shadow shield SH (10 cm W) deflects about 96% of the 14 MeV neutrons heading from N towards D. Even with this shield, however, the number of these direct background neutrons detected by D exceeds the number detected after scattering from a typical sample by a factor of about 10^5. The time-of-flight difference of about 11 ns between scattered and direct neutrons provides a means for discriminating against the latter. This was not very effective in the test experiments, however, because the time resolution of the (Van de Graaff) pulsed deuteron beam driving the neutron source was only 5 ns (FWHM). A very effective method for discriminating against direct neutrons is nevertheless provided by the direction sensitivity of the DANS, since these neutrons enter the crystal parallel to the *c'*-axis (fig 1b) and the vast majority of the events which they make consequently fail to pass the FR cut (see fig 2a). The fraction of detected, direct (background) neutrons which pass the FR cut is estimated at less than 10^{-5}, from the test measurements. The DANS, in other words, functions as a detector telescope which selects neutrons entering along the *b*-axis, thus discriminating in favour of neutrons scattered from S.

For 14.1 MeV incident neutrons in fig 1b the scattered neutron energy observed at detector angle 150° is 10.2, 10.7 or 11.1 MeV for elastic scattering on ^{12}C, ^{14}N or ^{16}O respectively. Lower energy neutron groups from inelastic neutron scattering are also present, at energies depending on the energy level structure of the scattering nuclides. Fig 5 shows event density as a function of *L* and *S* for a 14.1 MeV calibration run (fig 5a) and for a scattering run (fig 5b) taken using a 0.3 kg graphite scattering sample. The forward recoil peak P corresponding to 10.2 MeV neutrons from elastic scattering on ^{12}C projects clearly above the cut FR

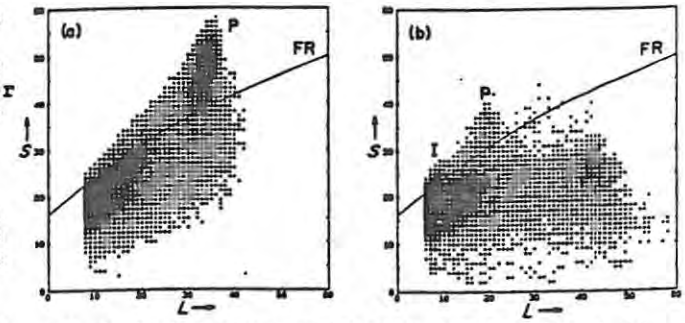

Fig 5. Event density as a function of pulse height *L* and pulse shape *S* observed in: (a) a 14.1 MeV calibration run; and (b) in a scattering run using a 0.3 kg graphite sample. The lines FR show the forward recoil cut. In (b), P and I show the forward recoil peaks associated with elastic and inelastic (4.43 MeV state) scattering on ^{12}C respectively. The points, in order of increasing size, represent count thresholds of 10, 20, 50, 100 and 200 in (a), and 2, 5, 10, 20 and 50 in (b).

in fig 5b, like that for 14.1 MeV neutrons in figs 5a and 2b. The low energy peak I, above cut FR (fig 5b) is attributed to 6.4 MeV neutrons from the inelastic scatterings on carbon which populate the 4.43 MeV state of ^{12}C. Fig 6 shows projected pulse height (L) spectra (histograms) for events satisfying the FR cut. Spectra are shown for scattering samples (mass 0.3-0.9 kg) of graphite (C), liquid nitrogen (N), water (H_2O) and alcohol (C+O) respectively and for a no-sample background run (Blank) as well as for the 14.1 MeV calibration run of fig 5a. The background spectrum shows an approximately linear dependence on pulse height L. The spectra obtained using scatterers show the expected increase in the upper limit of L as the scatterer is changed from C to N to O, due to the increase in backscattered neutron energy with increasing target nucleus mass. The strong peak at L = 320 channels in the spectra obtained from scatterers which contain carbon corresponds to the inelastic neutron group I (4.43 MeV level) referred to in fig 5b. The weaker peak observed at L = 380 channels, for nitrogen, is similarly attributed to inelastic neutron scattering in which the 3.95 MeV state of ^{14}N is populated. The relative intensities of the elastic and inelastic peaks for carbon and for nitrogen agree with estimates based on scattering cross section data and the calculated variation of detection efficiency with neutron energy for the DANS.

Using the lineshapes measured (section 3) for monoenergetic neutrons as a basis, the response functions of the DANS to the neutron spectra resulting from the scattering (elastic and inelastic) of 14.1 MeV neutrons on C, N and O respectively, at 150°, were calculated. Least squares fits were then made to the experimental data, representing each experimental spectrum as a combination of C, N and O components plus a background which drops linearly with increasing L. The smooth curves in fig 6 show the fitted spectra and the numbers to the right of the figure show the relative proportions of background, C, N and O components determined from the fitting. The C:N:O ratios obtained for the different samples are consistent with their known compositions. This demonstrates that the technique should be reliable for identifying these elements in a scatterer.

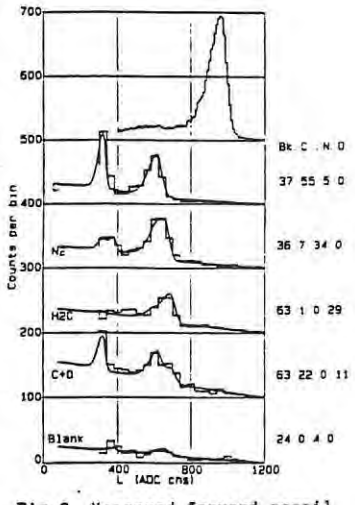

Fig 6. Measured forward recoil spectra (histograms) showing calibration peak for 14.1 MeV neutrons (top) and scattering spectra for no sample (blank) and for four different scatterers: graphite (C); liquid nitrogen (N); water (H_2O); and alcohol (C+O). Successive spectra are offset in multiples of 100 on the abcissa scale. The curves show least squares fits to the data. The numbers on the right indicate the relative proportions of background and of C, N and O respectively, determined from the fitting (see text).

5. CONCLUSIONS

The lineshape measurements show that the DANS has the energy resolution required to resolve the backward elastic scattering signatures of C, N and O for incident monoenergetic neutrons in the range 10-30 MeV. For the convenient incident neutron energy of 14.1 MeV, test experiments demonstrate that NBS signatures, including both elastic and inelastic, can be used to identify these elements reliably. Further work is needed to confirm that reliable quantitative measurements can be made of element concentrations. With improvements to the pulsed neutron source used in the scattering tests, a time resolution of < 1 ns (FWHM), similar to that obtained in the lineshape measurements (section 2), should be attained. This should make it possible to locate the depths of scattering sites in an extended sample volume to an accuracy of 5 cm (FWHM) from neutron time-of-flight measurements. As an alternative to using a pulsed neutron beam, 14 MeV neutrons obtained from the $^{3}H(d,n)^{4}He$ reaction, driven by a continuous deuteron beam might be considered. The time of neutron emission would then be indicated by detecting the associated alpha in a plastic scintillator or a fast surface barrier

detector (SBD). Since this technique also tags the direction of neutron emission a position-sensitive SBD or a matrix of SBDs might be employed in order to obtain information about the lateral distribution, as well as the depth distribution, of scattering sites within the sample volume. In such an arrangement, the position signals from the SBD would indicate the direction taken by the neutron, the time difference between the SBD and DANS would indicate the depth at which backscattering occured and the DANS would identify the scatterer as outlined in this paper.

The scattering experiments also confirm that the direction sensing capability of the DANS is effective in discriminating against the main source of background expected in an NBS system, that is neutrons heading directly from the source to the detector. The efficiency of the proposed NBS system can also be estimated from the fact that the data shown in figs 5b and 6, for the 0.3 kg graphite scattering sample, were obtained in 183 minutes of running time, using a deuteron beam current of 300 nA, with the deuteron energy degraded so that it matched the well-known resonance for the d-t reaction, E_d = 108 keV, at a point near the centre of a 3 cm long tritium gas target filled to a pressure of 0.8 Torr. The volume of the deuterated anthracene crystal was 1.65 cm^3. To reduce the measuring time to 90 seconds, for example, requires an improvement by a factor of about 120 in the overall efficiency. Such an improvement could be achieved by increasing the detector volume to 200 cm^3, for example by using four crystals, each 4 cm diam x 4 cm. To maintain the same event rate at a source to sample distance d larger than that used in the tests (30 cm) would require a further increase in the efficiency by a factor proportional to d^2. At today's retail prices the deuterated anthracene required to make a 50 cm^3 crystal would cost about US$4000, allowing for reasonable losses in purification and production.

We conclude that the DANS offers good prospects for monitoring light elements such as C, N and O by means of neutron backscattering and could therefore be useful in the detection of hidden explosives.

ACKNOWLEDGEMENTS

We thank the South African Foundation for Research Development for their support, the staff of the National Accelerator Centre, Faure, for their support and cooperation in carrying out the experiments, and Mr D Momsen, Mr D Boulton and Mr G Fowle for constructing the equipment used.

REFERENCES

1. F D Brooks, W A Cilliers, B R S Simpson, F D Smit, M S Allie, D T L Jones, W R McMurray and J V Pilcher, Nucl. Instr. & Meth. **A270** (1988) 149.

2. F D Brooks and D T L Jones, Nucl. Instr. & Meth. **121** (1974) 69.

3. D T L Jones, J E Symons, T J Fulcher, F D Brooks, M R Nchodu, M S Allie, A Buffler and M J Oliver, Med. Phys. **19** (1992) 1285.